Metropolitan Washington District of Columbia Coastal Storm Risk Management Feasibility Study

Appendix B: Hydraulics and Hydrology Analysis

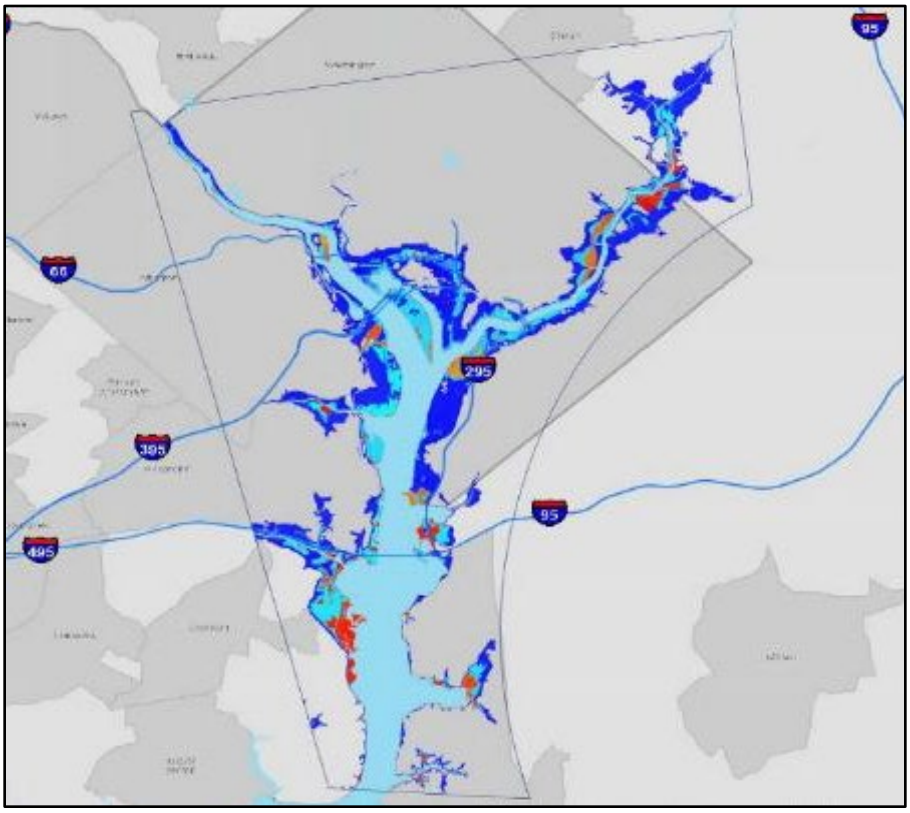

Northern Virginia

May 2022

US Army Corps of Engineers
Baltimore District

Metropolitan Washington Council of Governments

This page left intentionally blank.

TABLE OF CONTENTS

This page left intentionally blank.

1. Study Overview

1.1 Study Area

The DC Coastal study area is located within the northern Virginia side of the Potomac River as shown in Figure 1 below. The study area is along the Potomac River within the Middle Potomac River watershed,

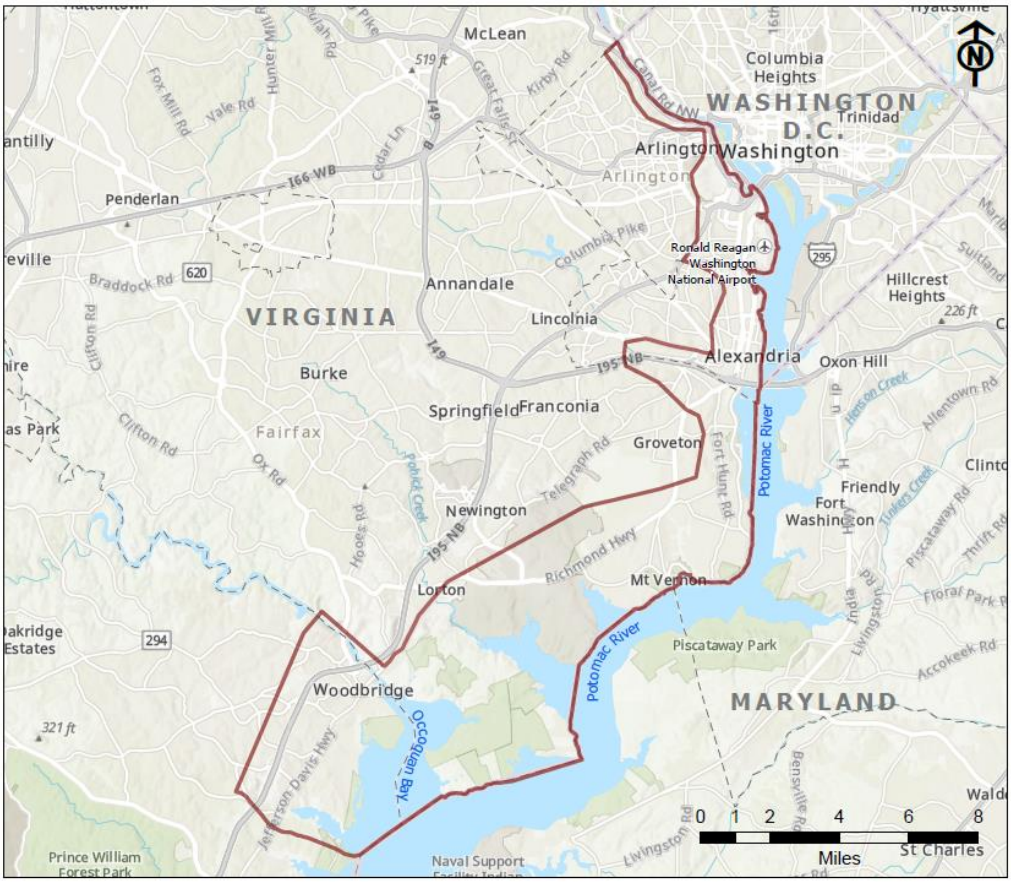

Figure 1 Location of District of Columbia Coastal Study Area

which encompasses Arlington County southward to the northern portion of Prince William County. It is situated within the western bank of the Potomac River where natural land subsidence, low-lying topography, and sea level changes has contributes to localized flooding. Northern Virginia has been impacted by numerous major tropical and extratropical events, most notably the Chesapeake and Potomac Hurricane of 1933, Hurricane Agnes (1972), Hurricane Floyd (1999), Hurricane Fran (1996), Nor'easter (1998), Hurricane Isabel (2003), Hurricane Irene (2011), and Hurricane Sandy (2012). Hurricane Isabel in 2003 resulted in extreme water levels and caused millions of dollars of damage to residences, businesses, and critical infrastructure. The goal of this study is to reduce coastal flood risk to populations, properties, infrastructure, and environmental and cultural resources, considering future climate and sea level change scenarios.

The Study evaluates project alternatives to assess flooding risks induced by coastal storms for the metropolitan area surrounding Washington, D.C. The Engineer Research Development Center (ERDC) utilized the NACCS study data and the latest bathymetric data available to model the coastal flood hazards along the Potomac River. This study applied USACE's Probabilistic Coastal Hazard Analysis (PCHA)

framework to quantify storm surge, leveraging existing synthetic tropical cyclones (TCs) from the North Atlantic Coast Comprehensive Study (NACCS). Using a reduced storm suite of synthetic TCs and the historical extratropical cyclones from NACCS, hydrodynamic model simulations were performed on an updated grid to produce storm responses at 23 save point locations (save points are locations within the model that save the storm information, such as tide and wave data) surrounding the D.C. Metropolitan area. Through application of the PCHA framework, the joint probability analysis of TC atmospheric-forcing parameters and their associate storm responses were assessed for the estimation of still water level (SWL) and annual exceedance frequencies (AEFs) ranging from 1-year to 10,000-year flooding events. The ERDC DC Metro model computed Water Surface Elevations (WSEL) at 13 different flood frequencies (1-, 2-, 5-, 10-, 20-, 50-, 100-, 200-, 500-, 1000-, 2000-, 5000-, and 10000-year flood) for 23 save points.

1.2 North Atlantic Coast Comprehensive Study

The North Atlantic Coast Comprehensive Study (NACCS) (2015) report detailed the results of a two-year long study by the U.S. Army Corps of Engineers which addressed coastal storm and flood risk to vulnerable populations, property, ecosystems, and infrastructure affected by Hurricane Sandy in the North Atlantic Region. The purpose of the study was to identify flood risk and then plan and implement strategies to reduce the risk now and in the future. The study also determined the magnitude and uncertainty of existing and future forcing conditions. The study's conclusions included a recommendation to use its findings to assess coastal engineering projects for coastal storm risk management and resiliency for the areas in the region from Virginia to Maine.

The NACCS included high-fidelity coastal numerical modeling of coastal hazards for the North Atlantic coast region including the study area. Storm surge and wave modeling results from these efforts in the DC Coastal study area were considered for this study.

The Coastal Hazards System (CHS) bias is the systematic deviation from the expected value and is calculated as the mean of the non-linear residual. The CHS includes tidal bias and Sea Level Change bias. The combined non-linear residual represents the summation of the individual biases. The NACCS study has bias as high as 0.8m for the northern part of the study area near Reagan National Airport. Because the study area is further inland from the coastline and has significantly high bias, after consultation with vertical team it was determined a refined ERDC modeling was required for this study to reduce uncertainty and bias.

1.3 Scope of Work for Refined Coastal Modeling

The Coastal Modeling scope includes additional statistical analysis of the NACCS Joint Probability Method (JPM) and Design of Experiments (DoE) approach for the selection of an optimal subset of the NACCS storms that specifically impact the District of Columbia (northern Virginia) study area and adequately represent the annual exceedance probability curves for this region. Modifications to the NACCS mesh were done to incorporate updated bathymetric and topographic data and increase spatial resolution for the study area. ADCIRC simulations were executed on the model mesh for each of the conditions identified in the storm selection procedure. Statistical (frequency) surge analyses were performed based upon the results of the subset of the synthetic storm simulations for the study area. Water level hazard curves (i.e., frequency distributions) were computed using the revised JPM. In addition to the expected

values, non-exceedance confidence limits (CL) were provided, including for best estimate/mean, in addition to 2%, 16%, 84%, 90%, and 98% confidence limits. Output products did include surfaces of storm peak surge elevations and inundation depths in the project area. Frequency distributions of inundation depth, and confidence intervals were provided at selected point locations.

2. Storm Climatology

Coastal flooding is primarily caused by rainfall, storm-induced water levels, and waves. For the northeastern U.S. Atlantic coastline, tides can have a significant influence on the degree of flooding given their large amplitudes. For the D.C. coastal area, tropical cyclones (TCs) and extratropical cyclones (XCs) have historically caused significant coastal flooding. The analysis conducted as part of this study for the quantification of coastal storm hazards focuses on the probabilistic characterization of storm forcing and responses for the study area. The primary goal of this study was the estimation of coastal storm hazards Annual Exceedance Probability (AEP) at the 23 save point locations relative to the D.C. Metropolitan (D.C. Metro) study area. Estimating these AEPs required the development of a joint probability model of TC atmospheric-forcing parameters and statistical analysis based on the StormSim-Stochastic Simulation Technique (StormSim-SST) for simulated responses of historical XCs.

Since the D.C. Metro study area was included within the NACCS, this study leveraged the storm suite and hydrodynamic modeling grids from the 2015 NACCS study. As a result of the NACCS, a storm suite was developed to cover the probability and parameter spaces of TCs from Virginia to Maine, which resulted in a suite of 1050 synthetic TCs. Coastal hazards within this region are also influenced by XCs, therefore 100 historical XCs were included as part of the NACCS storm suite. The TCs and XCs from the NACCS were leveraged for this study in order to quantify coastal storm wave and water level extremal statistics for the D.C. Metro study area. Although the hydrodynamic modeling grids were also leveraged, they were significantly updated to include changes in bathymetry and mesh resolution as well as mesh alterations to include the project alternatives.

3. Hydrodynamic Modeling & Results

3.1 Selection of the Reduced Storm Suite (RSS)

The goal of the storm selection is to find the optimal combination of storms, given a predetermined number of events to be sampled out of the 1,050-storm initial TC suite (ITCS), to obtain a reasonable estimation of the SWL hazard.

For this study, an RSS of 60 TCs was selected for simulating in the hydrodynamic models. However, the probabilistic analysis applied surge responses from only 58 storms in the RSS, since two of the hydrodynamic simulations were unstable. The storm parameters of these 58 TCs and detailed methodology for RSS are provided in ERDC's model report entitled "Probabilistic Coastal Hazard Analysis: DC Metropolitan Study" dated January 2022.

The storm responses for the XCs were leveraged from the NACCS simulations as it was not feasible under this study to produce updated simulations of these storms. Due to instabilities in the NACCS simulations, the probabilistic analysis of XC-induced surge relied on 94 of the 100 storms in the XC suite. Although these simulations do not include the effects of the updated mesh, the influence of the XCs on the final SWL AEPs within the study area is small, and the differences in surge between this modeling efforts and NACCS simulations are considered to be negligible.

3.2 ADCIRC Mesh Development

The ADCIRC mesh developed for the NACCS (Cialone et al. 2015) was modified to a provide detailed representation of the D.C. Metro study area. There were two major changes implemented in the NACCS grid specific to this project, that is, refinement of the study area and de-refining of a remote area (Long Island, NY) while the original boundary of the domain was not altered.

Refinement of the grid in the study area was necessary to fully capture and analyze the hydrodynamic processes in the area of interest. Moreover, this procedure facilitated the implementation of the complex levee system at the specific location as shown in figure 3. The purpose of grid de-refining is to reduce the mesh resolution in areas remote from the area of interest in order to

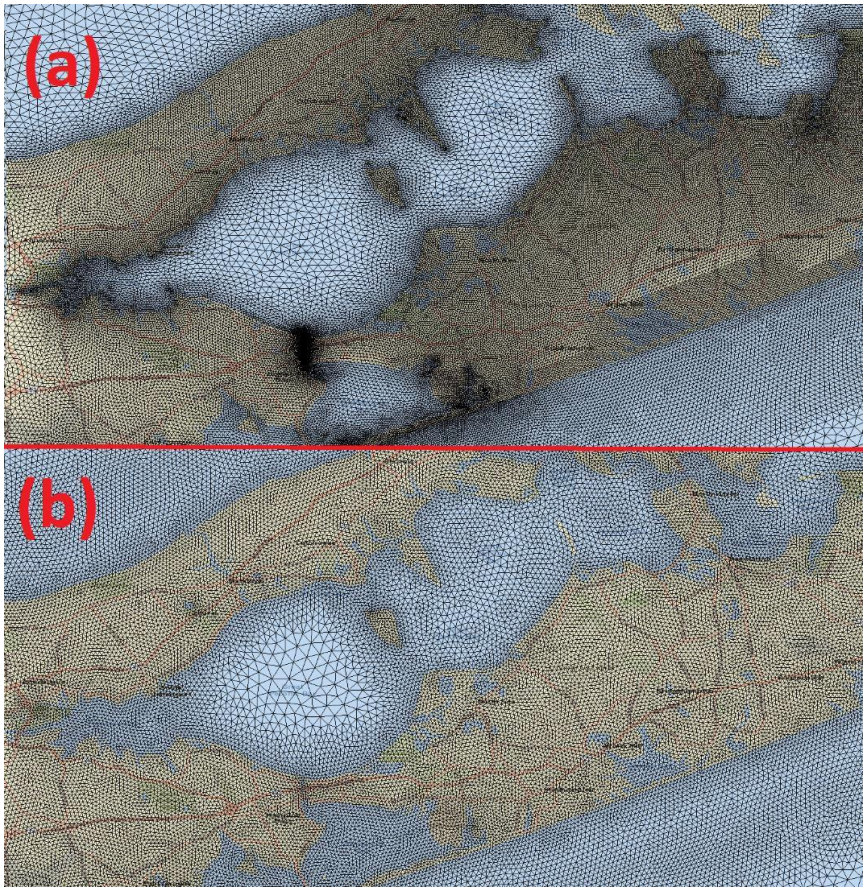

Figure 2. Long Island, NY area (a) before and (b) after de-refining.

decrease model simulation times without significantly affecting the flow volume exchange between the de-resolved region and the study area. The total number of 3.12 million nodes in the NACCS grid was reduced to 2.95 million (approximately a 6% reduction) in the D.C. Metro grid due to the Long Island, NY

region de- refining. Figure 2 shows the grid resolution before (a) and after (b) de- refining in the Long Island, NY area.

Figure 3 show the ADCIRC mesh elements and boundary in the D.C. Metro study area for the D.C. Metro mesh. The resolution of the NACCS grid was locally increased in order to facilitate implementation of the existing levee structures (indicated as green lines in Figure 3). Representing levees as ADCIRC weir-pair sub-grid features helps to maintain model stability. This is because the sub-grid scale formulation for weir-pairs prevents the model from transitioning from sub to supercritical flows during the course of the simulation in the event that the water elevation is high enough to overtop the structure. The D.C. Metro grid has a spatial resolution (element size) ranging from approximately 10 to 1000 m and MSL as the vertical datum.

Another noticeable difference between the NACCS grid and the D.C. Metro grid is the extent and boundary location in the Anacostia River. The NACCS grid was terminated southward from Route 50 in the D.C. Metro grid (Figure 4 shows a detailed view of the grid termination) in order to properly accommodate the in-flow boundary condition for the Anacostia River.

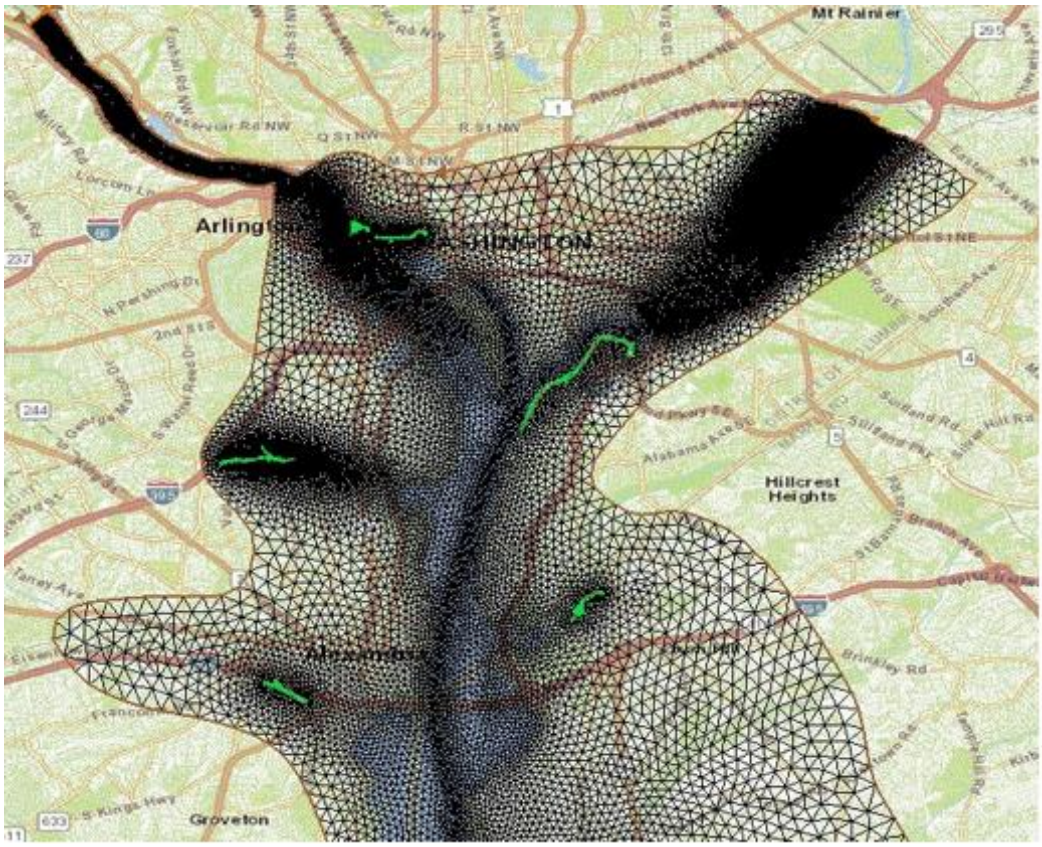

Figure 3. NACCS ADCIRC mesh in the D.C. Metro study area.

The final step in the grid modification was to update the bathymetry/topography in the study area with data from available latest LIDAR.

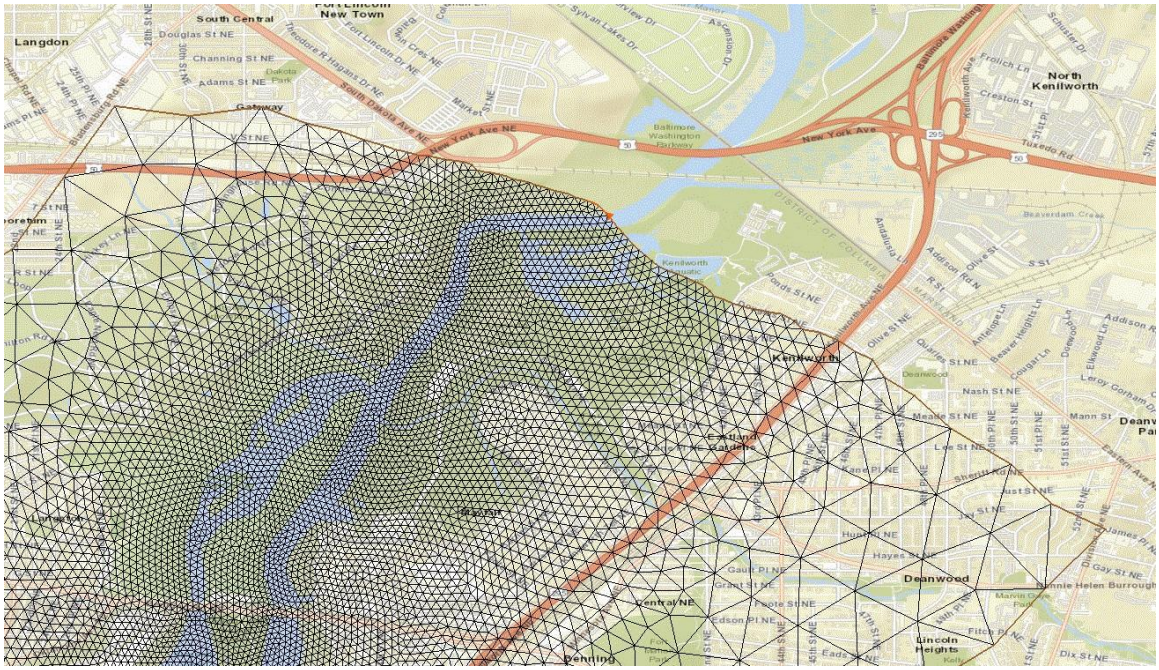

Figure 4. Zoom of ADCIRC grid at Anacostia River terminated boundary.

3.3 ADCIRC Simulation Results

For this study, the SWL AEFs were computed at the 23 save point locations surrounding the D.C. Metro study area as shown in Figure 5. The AEFs were computed ranging from 10 to 1x10-4 yr-1, and the hazard curves show the Best Estimate curve and the 90% CL. The ERDC modeling results are shown in Attachment #1. Also, included is the ERDC report entitled “Probabilistic Coastal Hazard Analysis: D.C. Metropolitan Coastal Study” dated January 2022 as Attachment # 2. Details on the modeling efforts and results for this study are described in Attachment #2.

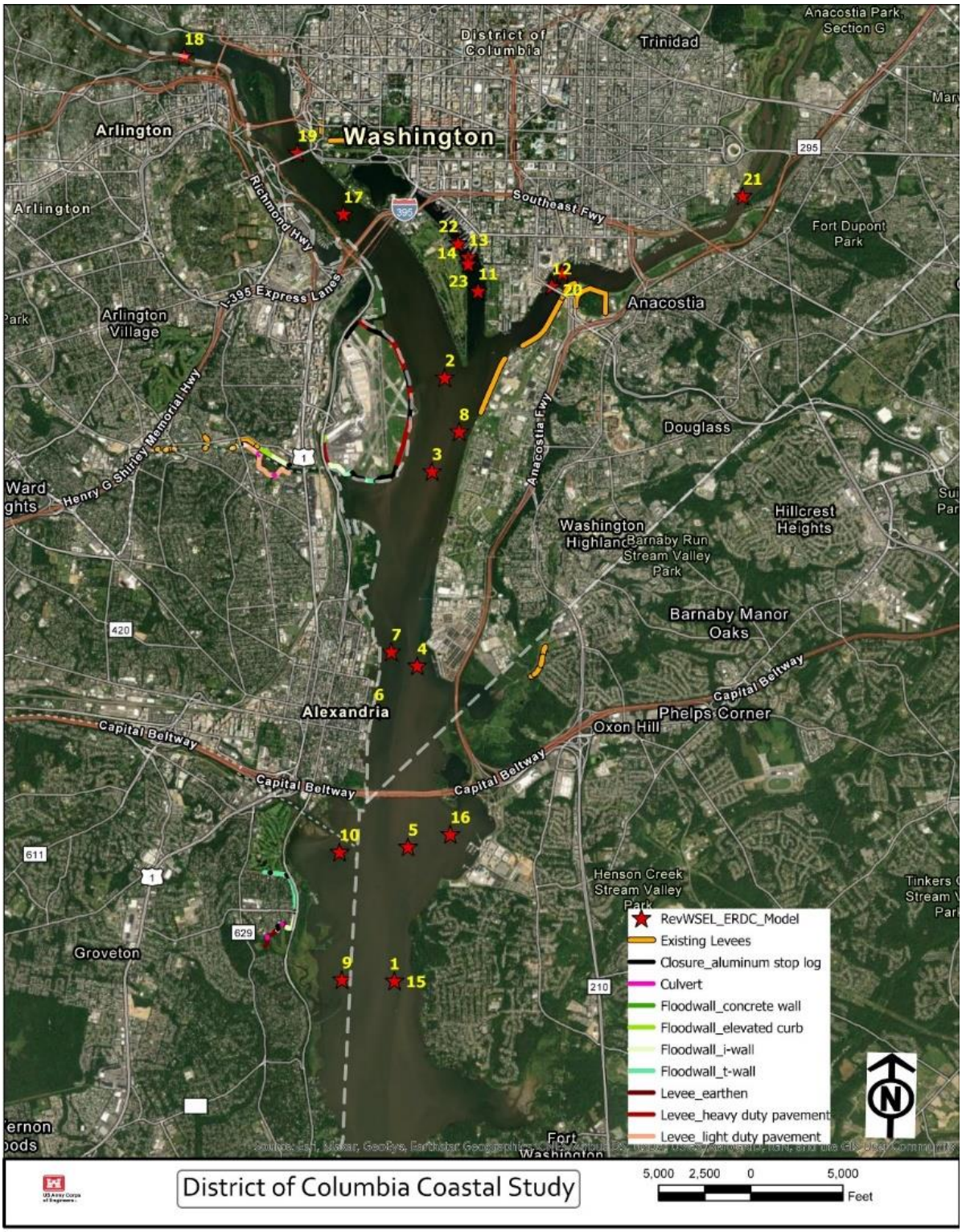

Figure 5. Save Point Locations Surrounding the D.C. Metro Study.

NACCS Save Points 5984, 14608 and 14731 are located near the proposed alternatives in 5 focus areas – Regan National Airport, Arlington Water Pollution Control Plant (WPCP), Old Town Alexandria, Four Mile Run and Belle Haven Areas. Maximum computed WSEL in feet NAVD88 is shown in the table below for these save points:

NACCS ID/ Virtual ID	1-year	2-year	5-year	10-year	20-year	50-year	100-year	200-year	500-year	1000-year	2000-year	5000-year	10000-year
5984/3	4.03	5.17	6.99	8.11	9.01	10.0	10.74	11.70	13.19	13.81	14.35	14.96	15.36
14608/7	3.92	4.89	6.45	7.46	8.31	9.28	10.03	11.11	12.50	13.14	13.72	14.28	14.67
14731/9	3.80	4.59	5.86	6.74	7.52	8.56	9.64	10.78	12.05	12.65	13.20	13.79	14.19

Based on the above WSEL for these NACCS IDs, level of performance is sought for the following level for structural measures in the following areas:

Project Area	NACCS ID/ Virtual ID	Level of Performance for Levees/Floodwalls ft NAVD88
Reagan National Airport	5984/3	14.3
Arlington WPCP	5984/3	14.3
Old Town Alexandria	14608/7	13.2
Four Mile Run	5984/3	13.9
Belle Haven	14731/9	13.0

For Old Town Alexandria, Four Mile Run, Reagan National Airport, Arlington WPCP and Belle Haven the level of performance is based on 100-year WSEL with approximately 95% confidence level and intermediate SLC curve through year 2080.

4 Climate Change

4.1 Introduction

Engineering and Construction Bulletin (ECB) 2018-14 requires USACE studies to provide a qualitative description of climate change impacts to inland hydrology and/or sea level change assessments as necessary. The objective of this ECB is to enhance USACE climate preparedness and resilience by incorporating relevant information about observed and expected climate change impacts in hydrologic analyses for new, and existing USACE projects

ECB 2018-14 requires at a minimum, a qualitative assessment of potential climate change threats and impacts that may be relevant to the recommended plan for the DC Coastal Study (hereinafter referred to as DC Coastal). DC Coastal Study included a large portion of study within District of Columbia and Northern Virginia. The primary focus for the study is within Regan National Airport, Cities of Arlington, Alexandria, and Belle Haven (New Alexandria).

4.2 Scope of Qualitative Analysis

ECB 2018-14 stipulates that for project areas at elevations less than or equal to 50 feet NAVD88, a determination should be made as to whether Sea Level Change (SLC) will affect flooding by increasing (or decreasing) water surface elevation of the project area. The entire project area is affected by coastal flooding from the Chesapeake Bay and area elevation is well below 50 feet NAVD88. Therefore, a SLC assessment is necessary for the DC Coastal Study.

The climate assessment for SLC follows the USACE guidance of Engineer Regulation (ER) 1100-2-8162, "Incorporating Sea Level Change in Civil Works Programs," and Engineer Technical Letter (ETL) 1100-2-1, "Procedures to Evaluate Sea Level Change: Impacts, Responses, and Adaptation." ER 1100-2-8162 and ETL 1100-2-1 provide guidance for incorporating the direct and indirect physical effects of projected future SLC across the project life cycle in managing, planning, engineering, designing, constructing, operating, and maintaining the federal projects. Planning studies and engineering designs over the project life cycle, for both existing and proposed projects, will consider alternatives that are formulated and evaluated for the entire range of possible future rates of SLC.

A qualitative analysis will provide the necessary information to support the assessment of climate change risk and uncertainties for the DC Coastal Study. The study is primarily focused on coastal flood risk reduction. Therefore, riverine hydrology is briefly reviewed as part of this qualitative assessments in section 3.6. The relevant climate variables identified for this study are temperature, precipitation, and relative sea level rise.

According to the Fourth National Climate Assessment (4th NCA) report on Region 2, The Chesapeake Bay watershed which includes the DC coastal study area, is experiencing stronger and more frequent storms, an increase in heavy precipitation events, increasing bay water temperatures, and a rise in sea level (though some of the increase in the bay area is contributed to subsidence). These trends vary throughout the watershed and over time but are expected to continue over the next century.

The District of Columbia and Commonwealth of Virginia climate is changing. The region has warmed by more than two degrees (F) in the last century, hot days and heavy rainstorms are more frequent, and the tidal Potomac is rising about one inch every eight years. In the coming decades, changing climate is likely to increase tidal flooding, cause more heavy rainstorms and sewer overflows, and increased risks to human health.

The earth climate is changing. It is estimated the people have increased the amount of carbon dioxide in the air by 40 percent since the late 1700s. Other heat-trapping greenhouse gases are also increasing. These gases have warmed the surface and lower atmosphere of our planet about one degree during the last 50 years. Evaporation increases as the atmosphere warms, which increases humidity, average rainfall, and the frequency of heavy rainstorms in many places—but contributes to drought in others.

Greenhouse gases are also changing the world's oceans and ice cover. Carbon dioxide reacts with water to form carbonic acid, so the oceans are becoming more acidic. The surface of the ocean has warmed about one degree during the last 80 years. Warming is causing snow to melt earlier in spring, and mountain glaciers are retreating. Even the great ice sheets on Greenland and Antarctica are shrinking. Thus, the sea level is rising at an increasing rate in some regions of the world.

4.3 Temperature

According to 4th NCA, warming rates on the Northeast Shelf have been higher than experienced in other ocean regions and climate projections indicate that warming in this region will continue to exceed rates expected in other ocean regions. Since 1950 there has been no trend in extremely hot days (maximum temperature above 100°F) in Washington, District of Columbia (D.C.) (Figure 6). However, from 2010 to

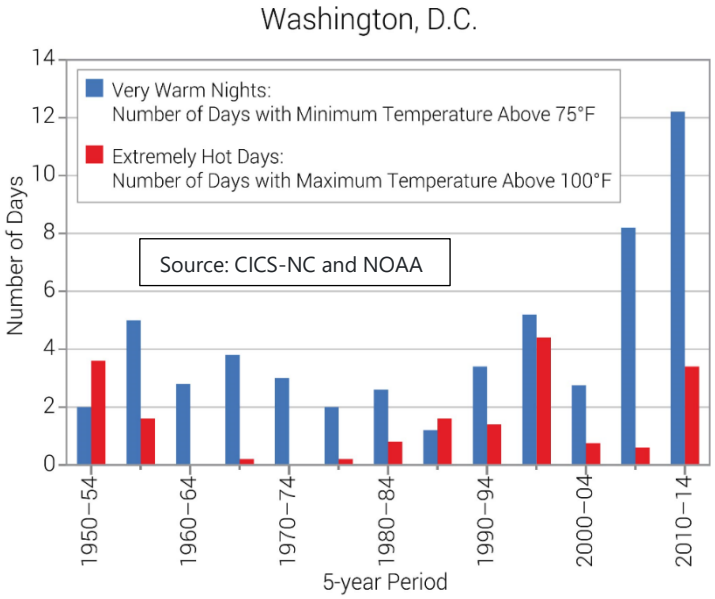

Figure 6 Observed and Projected Temperature

2014, D.C. averaged 12 very warm nights (nighttime minimum temperature greater than 75°F) per year compared to the 1950–2009 average of 3 very warm nights per year.

NOAA State summaries reported that temperatures have risen approximately 1.5°F in the

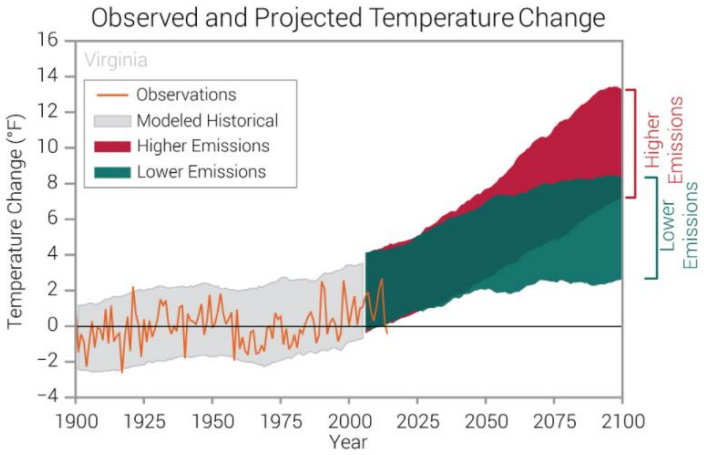

Figure 2 Observed and Projected Temperature for Virginia

Commonwealth of Virginia since the beginning of the 20th century. The 1930s and 1950s were very warm, followed by a period of generally below average temperatures during the 1960s through early 1980s (Figure 3).

Although the 5-year average highest number of very hot days (maximum temperature above 95°F) and corresponding number of very warm nights (minimum temperature above 75°F) occurred in the early 1930s (Figures 7a and 7b), gradual warming has occurred since the early 1990s.

Average annual temperatures during the 21st century (2000–2014) have exceeded the previous highs of the 1930s. A winter warming trend is reflected in the below average number of very cold nights

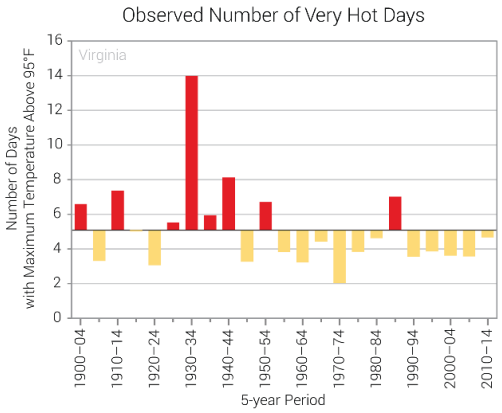

Figure 7a 5-year average number of very hot days

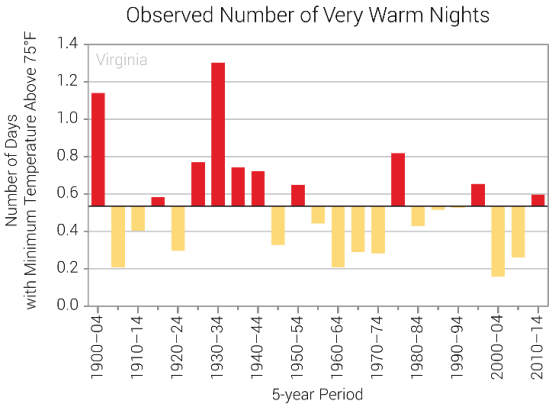

Figure 7b 5-year number of very warm nights

(minimum temperature below 0°F) since 1990 (Figure 8).

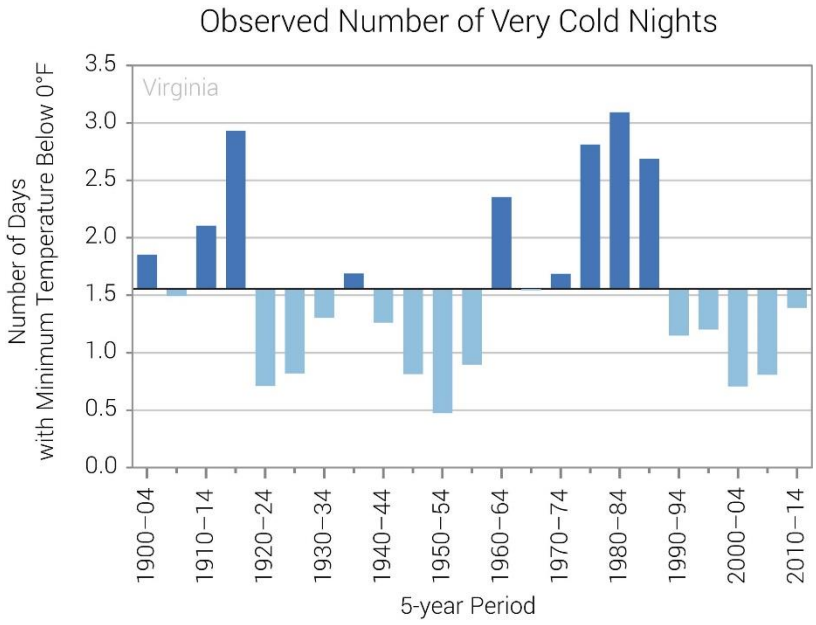

Figure 8 Average Number of Very Cold Nights

4.4 Precipitation

According to 4th NCA, historical precipitation differences across regions are apparent as increases have occurred in several regions and predominantly in the Northeast. A national average increase of 4% in annual precipitation since 1901 mostly a result of large increases in the fall season. Annual precipitation has increased by 5% to more than 15% in parts of the Northeast from the first half of the last century (1901–1960) compared to present day (1986–2015).

Regional changes in flood dynamics are likely to occur as a result of perturbations to precipitation and temperature conditions. Flood severity is a result of many interrelated factors including topography, soil moisture, precipitation amount, precipitation intensity, land cover, and others.

According to NOAA state climate change summary for the commonwealth of Virginia, there is no overall trend in average annual precipitation in Virginia (Figure 9), although over the past two decades (1995–2014), annual precipitation has been generally above the long-term average.

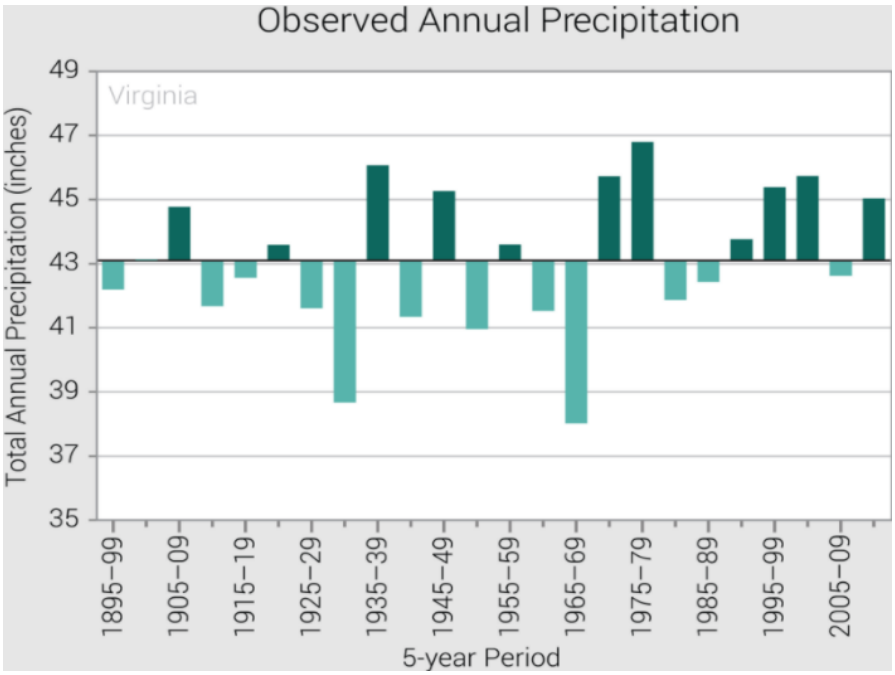

Figure 9 Observed Annual Precipitation

Average annual summer precipitation (Figure 10) has been below or near the long-term average during the most recent decade (2005–2014). There is an upward trend in the annual number of extreme precipitation events (precipitation greater than 2 inches) over the past two decades (1995–2014), with

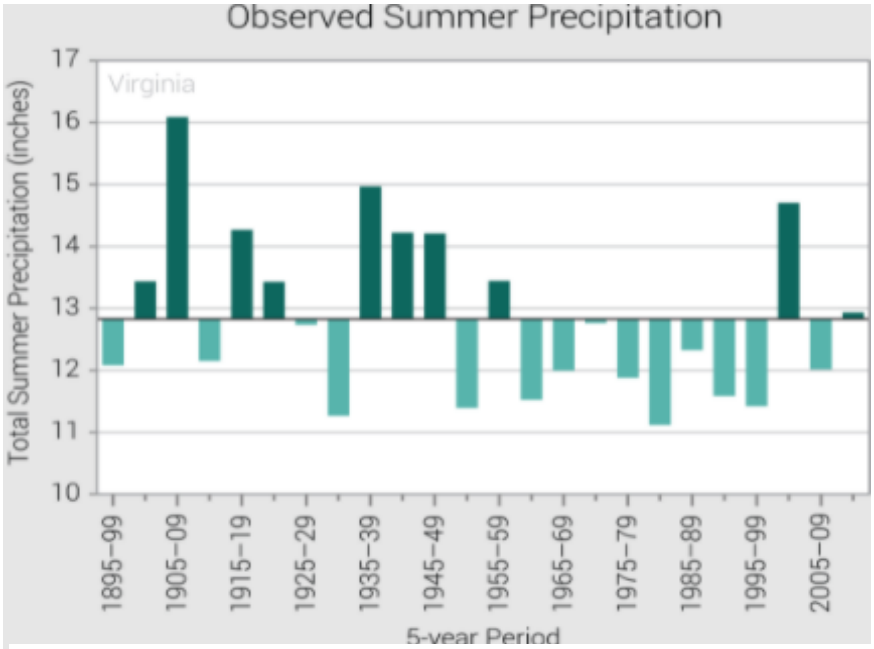

Figure 10 Events Observed Summer Precipitation

the number of such events in 1995–1999 surpassing record levels of the early 1940s (Figure 11).

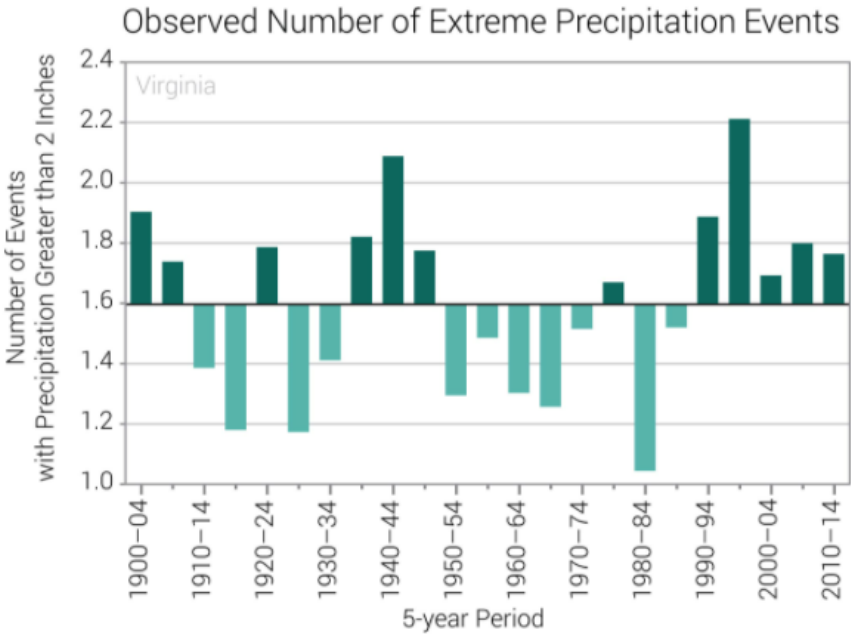

Figure 11 Observed Number of Extreme Precipitation

4.5 Sea Level Rise

Sea Level Rise (SLR) has been a persistent trend for decades in the United States and elsewhere in the world. SLR will likely continue beyond the end of this century. The USACE has developed two web-based SLC tools: Sea Level Change Curve Calculator and the Sea Level Tracker. Both tools provide a consistent and reproducible methods to visualize the dynamic nature and variability of coastal water levels at tide gauges, allowing comparison to the USACE projected SLC scenarios, and support simple exploration of how SLC has or will intersect with local elevation thresholds related to infrastructure (e.g., roads, power generating facilities, dunes), and buildings. Taken together, decision-makers can align various SLR scenarios with existing and planned engineering efforts, estimating when and how the sea level may impact critical infrastructure and planned development activities (USACE, 2018b).

Both the Sea Level Change Curve Calculator and the Sea Level Tracker are designed to help with the application of the guidance found in ER 1100-2-8162 and ETL 1100-2-1. The tools use equations in the regulation to produce tables and graphs for the following three SLC scenarios:

- Low estimate, which is based on historic trend and represents the minimum expected SLC.
- Intermediate estimate.
- High estimate, representing the maximum expected SLC.

The calculator accepts user input—including project start date, selection of an appropriate NOAA long-term tide gauge, and project life span—to calculate projected SLCs for the respective project. The Sea Level Tracker has more functionality for quantifying and visualizing observed water levels and SLC trends and projections against existing threshold elevations for critical infrastructure and other local elevations of interest (USACE, 2018b).

4.5.1 Historic and Existing Condition Sea-Level Change

Historically, the relative sea level trend for Washington DC is 3.33 millimeters/year with a 95% confidence interval of +/- 0.28mm/yr based on monthly mean sea level data from 1924 to 2018 which is equivalent to a change of 1.09 feet in 100 years. Details of historic trend is shown in NOAA chart below.

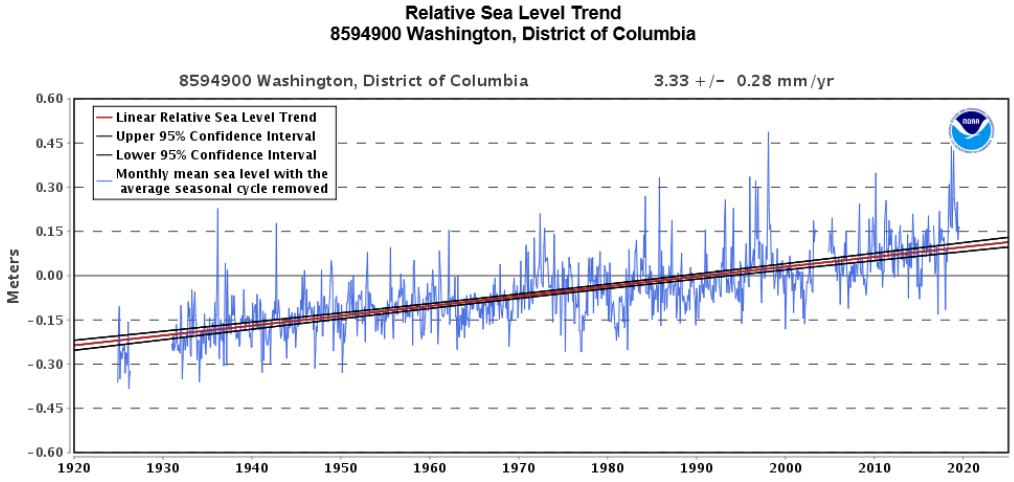

Figure 12 Historic Sea Level Changes for Washington DC

4.5.2 Potential Impacts to the Project from Sea-Level Change

The following analysis evaluates potential effects on recommended plan for the DC coastal study. For this analysis, the following years are evaluated:

- 2030 (beginning of the DC Coastal planning horizon at the start of construction)
- 2080 (50 years into the future, representing the DC Coastal future without project (FWOP) condition)
- 2130 (100 years into the future, representing the end of the DC coastal project planning life cycle)

Climate for which the project is designed can change over the planning life cycle of that project and may affect its performance, or impact operation and maintenance activities. Given these factors, the USACE guidance from ECB 2018-14, suggests that the project life cycle should be up to 100 years. For most projects, the project life cycle starts when construction is complete which typically corresponds to the time when the project starts accruing benefits. For some cases, however, the project life cycle starts before construction completion, typically because these projects start getting benefits during construction.

For the DC Coastal study, the project life cycle begins in 2030, when construction is planned to be completed. The 2080 and 2130 conditions could ultimately affect flooding due to SLC and local storm water runoff from Potomac River drainage basins. Hence, SLC considerations may result in an increase in hydraulic loading impacts on floodwalls/levees under future conditions. The magnitude of those impacts will depend on how soon the sea rises to a level that impacts project performance.

Sea levels relative to the Potomac River water surface elevation level are expected to rise, depending on the projected rates of rise for low (current historic trend), intermediate, and high scenarios. Figure 6 shows the estimated relative SLC from 2030 to 2130, calculated with the USACE Sea Level Change Curve Calculator, at the Washington DC Shores NOAA gauges which closest to the project sites.

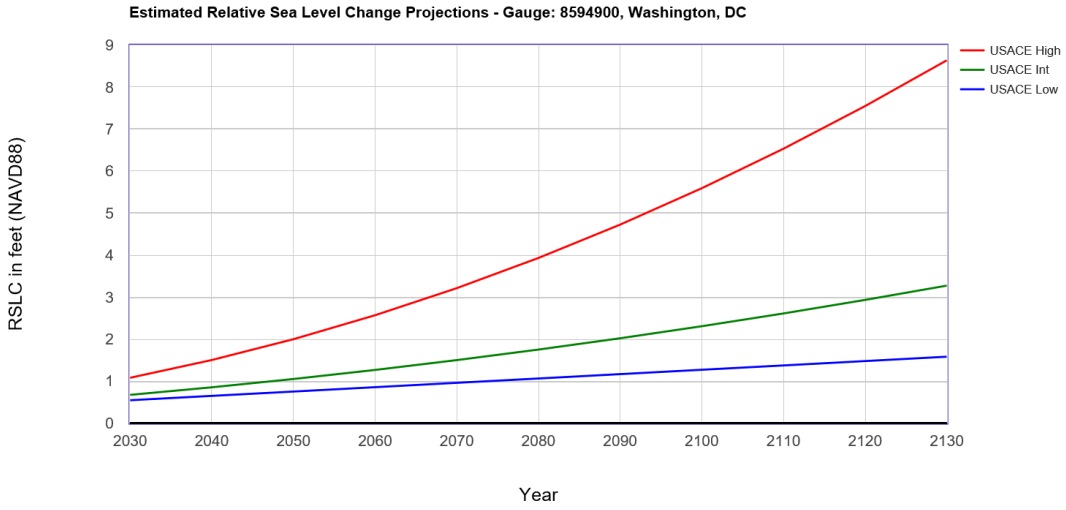

Figure 13 Sea Level Change Projections for Washington DC

Table 3 below shows estimated USACE Low, Intermediate, and High SLC projections at Washington DC Shores, in feet relative to NAVD88, from years 2030 to 2130. The USACE Seal level rise calculator is available at https://cwbi-app.sec.usace.army.mil/rccslc/slcc_calc.html

Table 3 DC Coastal Study Sea Level Rise Projection

Climate Change 8594900, Washington, DC NOAA's 2006 Published Rate: 0.01037 feet/yr All values are expressed in feet relative to NAVD88			
Year	**USACE Low**	**USACE Int**	**USACE High**
2030	0.54	0.67	1.08
2035	0.6	0.76	1.28
2040	0.65	0.85	1.5
2045	0.7	0.95	1.74
2050	0.75	1.05	2
2055	0.8	1.16	2.28
2060	0.86	1.27	2.57
2065	0.91	1.38	2.88
2070	0.96	1.5	3.21
2075	1.01	1.62	3.56
2080	1.06	1.75	3.93
2085	1.11	1.88	4.32
2090	1.17	2.02	4.73

2095	1.22	2.16	5.15
2100	1.27	2.31	5.59
2105	1.32	2.46	6.06
2110	1.37	2.61	6.54
2115	1.43	2.77	7.03
2120	1.48	2.93	7.55
2125	1.53	3.1	8.09
2130	1.58	3.27	8.64

ERDC environmental laboratory in Vicksburg, Mississippi assessed vulnerability of infrastructure systems in Northern Virginia. This vulnerability assessment focuses on seven sea level change scenarios. For each sea level rise scenario, the impacts to infrastructure systems are assessed for coastal storms with a 100-year return period and a 1000-year return period. These two levels of storm severity were selected to represent the weakest storm that might have any significant impact on infrastructure, and the most severe storm that might reasonably be expected to occur, respectively. Details on the vulnerability assessments are available in attachment 3 entitled "Northern Virginia Infrastructure System Vulnerability Assessment" dated May 19, 2022.

4.6 Climate Hydrology

It is expected that increased air temperatures and frequencies of drought, particularly in the summer months, will result in increased stream water temperatures, potentially affecting dissolved oxygen levels. Higher average and extreme temperatures combined with an increased annual rainfall in the region may lead to higher peak flows as well as more frequent low flows (USACE, 2015c).

4.6.1 Climate Hydrology Assessment tool (CHAT)

The Climate Hydrology Assessment tool (CHAT) [USACE, 2016a] allows users to access data concerning past (observed) changes as well as potential future (projected) changes to relevant hydrologic inputs. The qualitative analysis required by this ECB includes consideration of both past (observed) changes as well as potential future (projected) changes to relevant hydrologic inputs. A first-order statistical analysis of the potential impacts to particular hydrologic elements of the study can be very useful in considering future without project conditions (FWOP) and the potential direction of climate change.

The following figures were developed using the Online CHAT. These graphs show an increasing trend in the Annual Peak Instantaneous Stream Flow for the overall Potomac River Basin (HUC 0207). The P value for the trend line is 0.456754 which is greater than 0.05. A larger P value indicates very little statistical significance for the linear regression trend line.

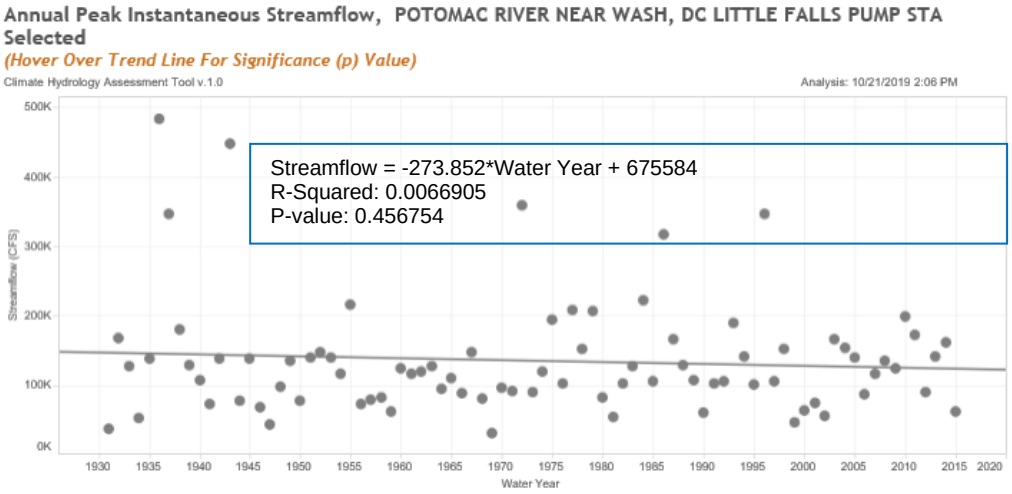

Figure 14 Annual Peak Linear Regression Trend

The following figure shows projected annual Maximum monthly stream flows. It follows the same trend line with a P value of 0.456754. However, the uncertainty with climate changed hydrology is high and not currently, readily quantifiable. The above trend line cannot be used for quantifying the potential changes due to climate change.

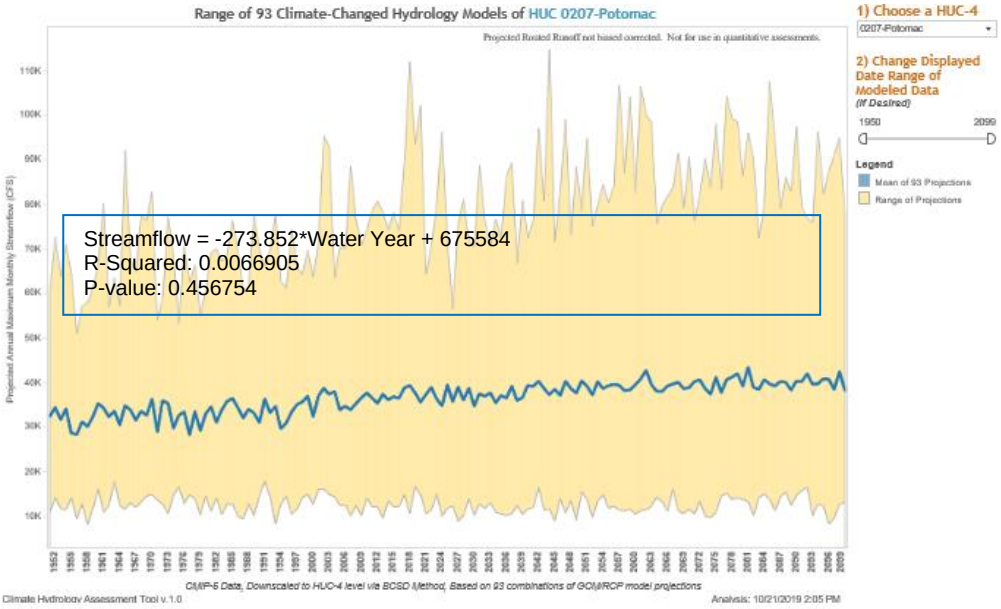

Figure 35 Trends in projected mean annual maximum monthly streamflow in HUC04 Potomac River Basin (HUC04 0207).

A statistical analysis of the projected hydrology for 2000-2100 indicates a statistically significant linear trend of increasing average annual maximum monthly flows (Figure 16). This increase is statistically significant (p-value < 0.05) and suggests the potential for future increases in streamflow relative to current

conditions. This trend is not consistent with an assessment of trends in observed annual peak streamflow. The results of these tools are only for qualitative assessments and cannot be used for quantitative assessments.

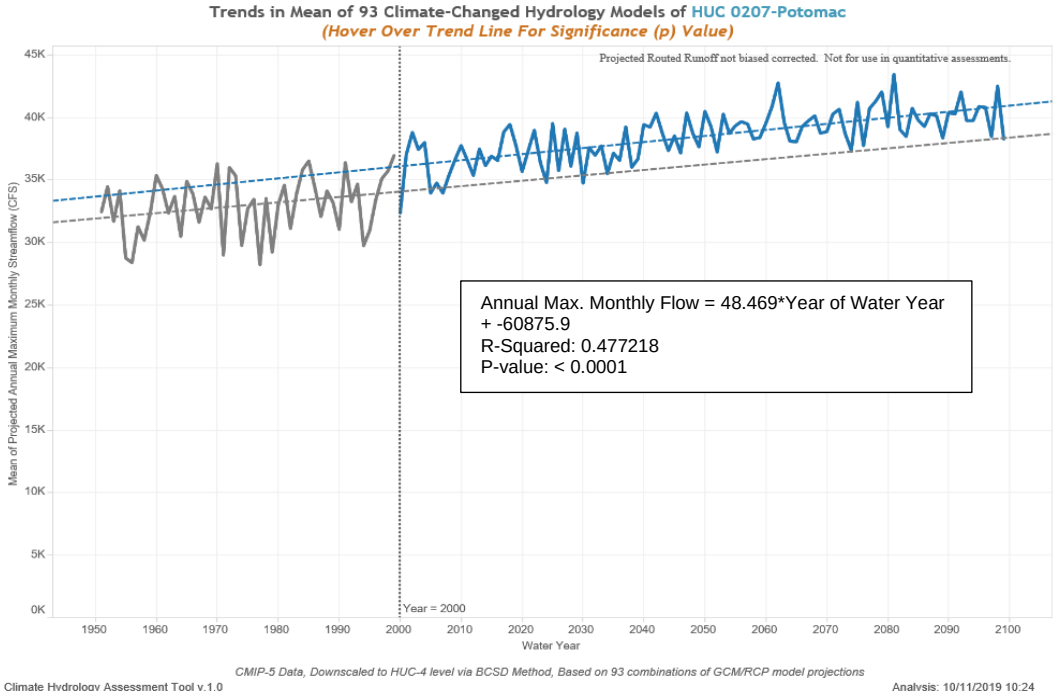

Figure 46 Projected mean annual maximum monthly streamflow in HUC04 Potomac River Basin (HUC04 0207).

4.6.2 Non-stationarity Detection Tool

The current guidance for detecting nonstationarities is the USACE ETL 1100-2-3, "Guidance for Detection of Nonstationarities in Annual Maximum Discharges." provides technical guidance on detecting nonstationarities in the flow record which may continue to impact flow into the future and should be considered in the FWOP project conditions.

The Nonstationarity Detection Tool (NSD) was developed to support ETL 1100-2-3. The USACE Responses to Climate Change (RCC) Program developed the tool to enable users to detect abrupt and slowly varying changes (nonstationarities) in observed, annual instantaneous peak discharges at USGS streamflow gauges with over 30 years of record. The tool allows users to conduct monotonic trend analysis on the data and any resulting subsets of stationary flow records identified.

Nonstationarities are identified when the statistical characteristics of a hydrologic data series are not constant through time. The NSD, however, is not a substitute for engineering judgment. Engineers are advised to use their judgment to consider the resilience of the system when incorporating the range of results in the hydrologic study or design results (USACE, 2016d)

It is up to the tool's user to determine which, if any, of the statistically significant nonstationarities identified by the NSD may be used to segment the data for hydrologic analysis. The user assesses the

relative “strength” of any nonstationarities detected to identify “strong” nonstationarities for use in further analyses. The tool applies several methods that assess nonstationarities in time series datasets driven by changes in the mean, variance/standard deviation, and in the distributional properties of the dataset.

The NSD was utilized for the Potomac River USGS gage 1646500 at Washington DC in accordance with ECB 2018-14. The tool analyzes whether the assumption of stationarity, which is the assumption that statistical characteristics of time-series data are constant over the period of record, is valid for a given hydrologic time-series data set. Similar to the CHAT analysis, the Potomac River gage was selected because it is closest to the project site and effect of the dam near gage (and project site) is insignificant.

Error! Reference source not found. shows the results from the tool applied to the period of record available at the Potomac River gage: 1930-2015. The tool’s default sensitivity parameters were applied to evaluate the stationarity of the streamflow record. The statistical methods collectively identified nonstationarities in 1938. The nonstationarity was identified using the Smooth Lombard Method.

A “strong” nonstationarity is one for which there is a consensus among a minimum of three nonstationarity detection methods (more than one test flagging a nonstationarity targeted at the same statistical property), robustness in detection of changes in statistical properties (tests flagging nonstationarities targeted at different statistical properties), and relatively large change in the magnitude of a dataset’s statistical properties (mean or standard deviation).

Based on these criteria, there is not enough strong evidence of statistical non-homogeneity in the 1938 event to warrant consideration within the decision making process. Because the detected nonstationarity is only indicated by a single test they do not meet the criteria of consensus, robustness, and magnitude, and are not considered strong, operationally significant nonstationarities.

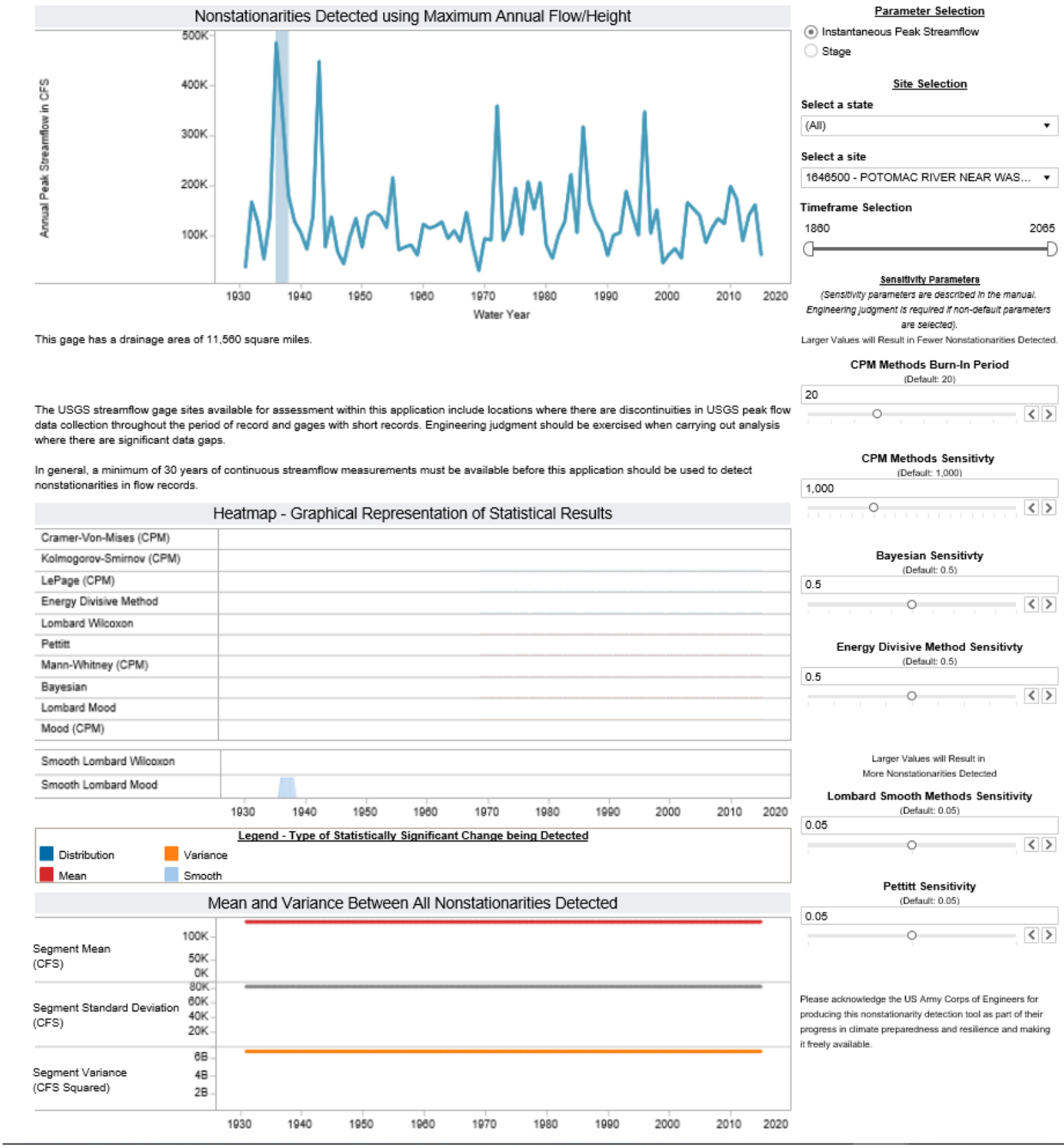

Figure 17 Output from Nonstationarity Detection tool – Potomac River near Project Site in Washington DC.

A monotonic trend analysis is conducted to identify statistically significant trends in peak streamflow. Detected nonstationarities are used to subdivide the period of record into stationary subsets, each of which are tested for the presence of monotonic trends. If no strong nonstationarities are identified within an annual instantaneous peak streamflow dataset, then the entire period of record could be assessed for monotonic trends. Because the nonstationarities identified are not considered operationally significant, the entire period of record of 1930-2015 was assessed.

Error! Reference source not found. shows a monotonic trend analysis using the Mann-Kendall Test and Spearman Rank Order test for time period 1930-2015. No statistically significant trend in annual peak streamflow was detected for the period of record.

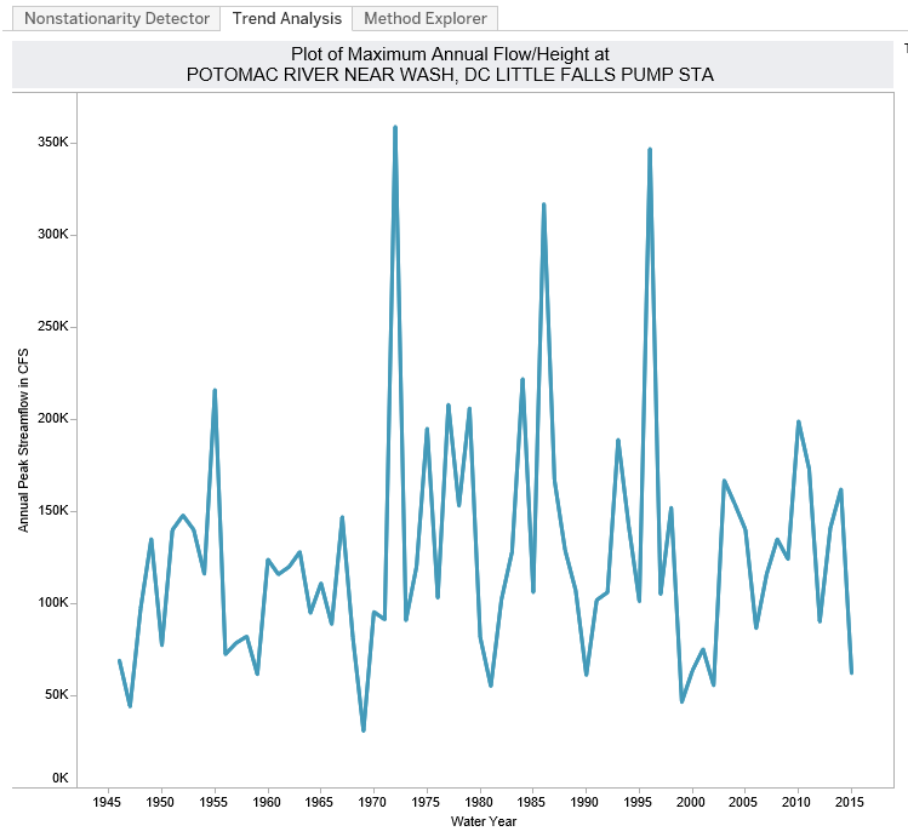

Figure 18 Monotonic trend analysis results.

4.7 Climate Risk

As discussed in Sections 4.5 and 4.6, the study area is most vulnerable to sea level rise, increases in precipitation frequency and intensity, and increases in air temperature. Per guidance in ECB 2018-14, Table 12-1 identifies risks resulting from changing climate conditions in the future. The table shows the major project feature, the trigger event (climate variable that causes the risk), the hazard (resulting dangerous environmental condition), the harms (potential damage to the project or changed project output), and a qualitative assessment of the likelihood and uncertainty of this harm. Note that not all impacts of climate change will result in increased risk.

Project benefits may change as a result of climate change due to sea level change. In addition, project benefits may be impacted by climate change due to inland hydrology. Changes to benefits due to climate change may occur due to increases in flooding produced by sea level rise, or flooding produced by a combination of precipitation and sea level rise. There may be positive impacts to the project from increased air temperatures.

Feature or Measure	Trigger	Hazard	Harm	Qualitative Likelihood
Floodwall	Increased sea level	Increased water levels and wave heights seaward of the floodwall	Increased SLR may increase frequency and magnitude of water level and wave loading on floodwall. Risk reduction level decreases while residual risk increases.	Likely
Closure Structures	Increased sea level	Increased water levels and wave heights seaward of closure structures	Increased SLR may increase frequency of structure closure, increasing operational costs. Frequency and magnitude of water level and wave loading may increase. Risk reduction level decreases while residual risk increases.	Likely
Pump Station	Increased sea level	Increased water levels to pump	Increased O&M costs associated with running pumps for a longer duration and with higher head differentials.	Likely
Pump Station, Elevated Gravity Inlet Piping	Increased extreme precipitation	Future flood volumes may be larger than present	Larger flood volumes may not be adequately captured by elevated gravity inlet piping and pumps. Water that cannot be pumped from interior may reduce project benefits or cause nuisance flooding. Current pump size may be able to handle increased water levels at a higher energy cost (longer pumping duration)	Somewhat Likely
Pump Station, Elevated Gravity Inlet Piping	Increased air temperatures	Increased evapotranspiration or drought	Decrease in flow volumes entering the elevated gravity inlet piping and through the pump station	Likely

5 Coastal Storm Damage Reduction Measures Considered

Proposed structural alternatives are considered in four areas i) Reagan National Airport, ii) Arlington WPCP, iii) Four Mile Run and iv) Belle Haven areas. These alternatives involve floodwall, levees and road raisings. The following figure shows structural alternatives considered and their locations. Details on these structural alternatives are shown in Civil Engineering appendix, section 2.4.

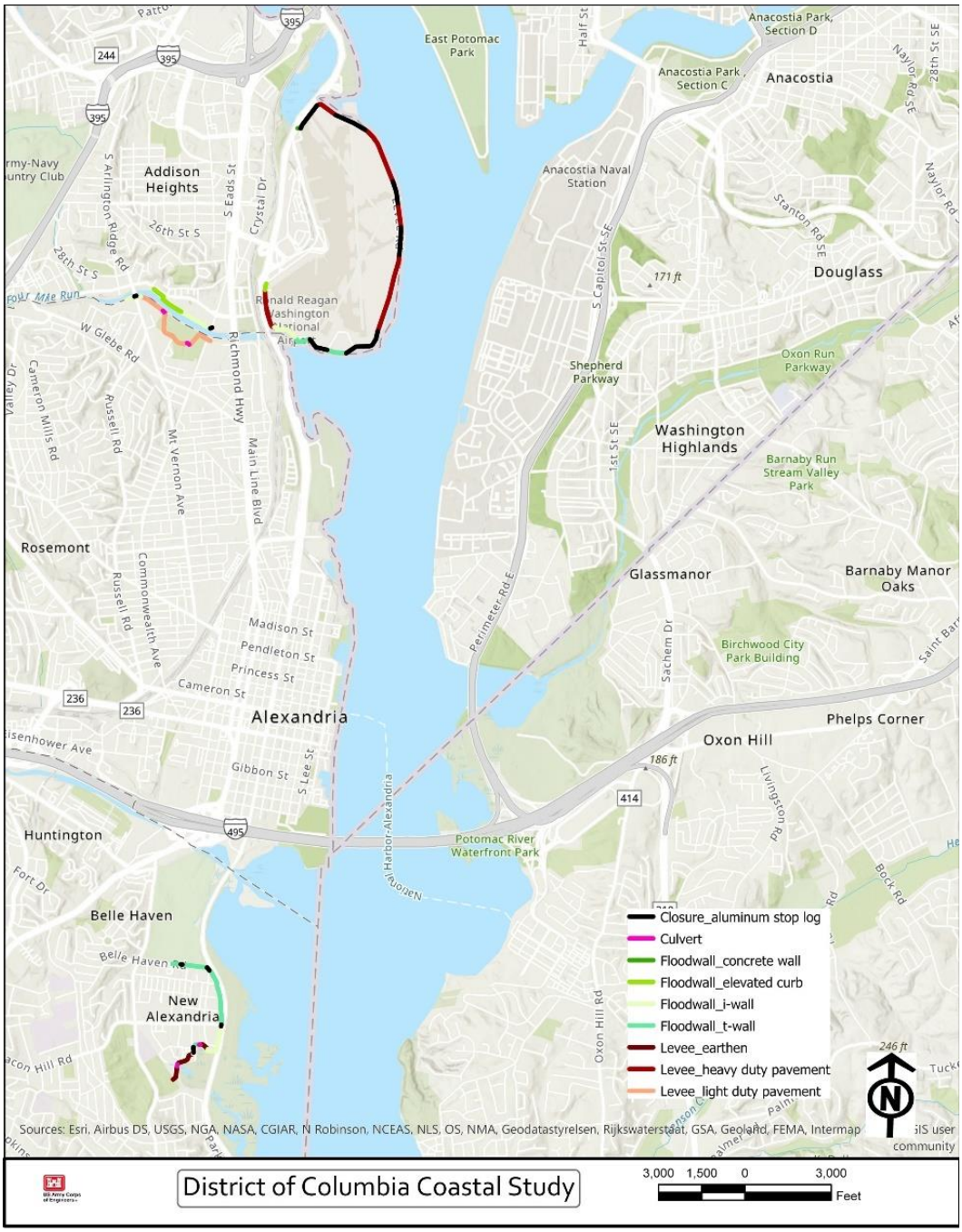

Figure 19 Monotonic trend analysis results

6 Summary and Conclusion

The water levels provided were extracted from the refined coastal modeling study performed by ERDC CHL in Vicksburg, Mississippi. The Model water surface elevations were performed for SLR through 2075. Therefore, the modeled WSEL were adjusted for anticipated changes due to sea level rise for another 5 years through year 2080. For designing structural alternatives of the project, we used 13.0 feet through 14.3 feet NAVD88 as the level of performance as outlined in Section 3.3. The level of performance is based on the 100-year WSEL with approximately 95% confidence level and intermediate SLC curve through year 2080.

Additional analysis will be performed by ERDC in near future to determine the effect of structural alternatives planned for this project. The goal of this additional modeling efforts is to determine if the structural alternatives would adversely affect flood hazards in any areas around these planned project elements.

7 References

HUC4 Level - The USACE online tool USACE Screening-Level Climate Change Vulnerability Assessment at https://maps.crrel.usace.army.mil/apex/f?p=201:2:5656654680613::NO:::

2016a – The USACE's online Climate Hydrology Assessment Tool available at https://maps.crrel.usace.army.mil/projects/rcc/portal.html

2016b – The USACE Nonstationarities Detection Tool available at http://corpsmapu.usace.army.mil/cm_apex/f?p=257:2:0::NO

2015C - Climate Change and Hydrology Literature Synthesis For The Us Army Corps Of Engineers Missions in The United States, MID-ATLANTIC REGION 2, MAY 2015, CDM Smith, et.al.

ER 1100-2-8162, Incorporating Sea Level Change In Civil Works Programs

ECB No. ECB 2018-14, Guidance for Incorporating Climate Change Impacts to Inland Hydrology in Civil Works Studies, Designs, and Projects

NOAA National Centers for Environmental Information | State Summaries 149-VA

NCA4 - The Fourth National Climate Assessment https://nca2018.globalchange.gov/

This page left intentionally blank.

Attachment # 1 ERDC Model Results

This page left intentionally blank.

Best Estimate WSEL in feet, NAVD88 datum

Latitude	Longitude	Virtual_ ID	NACCS _ID	1-year	2-year	5-year	10-year	20-year	50-year	100-year	200-year	500-year	1000-year	2000-year	5000-year	10000-year
38.765	-77.033	1	14607	3.772	4.56	5.82	6.69	7.46	8.47	9.51	10.60	11.88	12.48	13.06	13.62	14.02
38.855	-77.026	2	5982	4.067	5.32	7.27	8.45	9.38	10.40	11.10	11.89	13.33	13.98	14.51	15.14	15.54
38.841	-77.028	3	5984	4.030	5.17	6.99	8.11	9.01	10.01	10.74	11.70	13.19	13.81	14.35	14.96	15.36
38.812	-77.030	4	5987	3.927	4.90	6.45	7.47	8.35	9.36	10.20	11.40	12.77	13.38	13.94	14.52	14.90
38.785	-77.031	5	5991	3.854	4.69	6.05	6.98	7.83	8.91	9.97	11.17	12.50	13.10	13.64	14.21	14.61
38.805	-77.038	6	7757	4.017	4.99	6.47	7.47	8.35	9.44	10.58	11.92	13.19	13.74	14.26	14.86	15.25
38.814	-77.035	7	14608	3.923	4.89	6.45	7.46	8.31	9.28	10.03	11.11	12.50	13.14	13.72	14.28	14.67
38.847	-77.023	8	14609	4.042	5.22	7.10	8.26	9.17	10.16	10.83	11.59	13.01	13.67	14.23	14.85	15.25
38.765	-77.043	9	14731	3.797	4.59	5.86	6.74	7.52	8.56	9.64	10.78	12.05	12.65	13.20	13.79	14.19
38.784	-77.044	10	14735	3.853	4.69	6.04	6.97	7.82	8.90	9.91	11.11	12.43	13.04	13.60	14.16	14.57
38.868	-77.020	11	5878	4.101	5.35	7.30	8.51	9.47	10.55	11.30	12.18	13.64	14.29	14.83	15.47	15.91
38.869	-77.006	12	5980	4.076	5.29	7.24	8.44	9.41	10.46	11.17	11.95	13.31	14.01	14.56	15.22	15.63
38.873	-77.022	13	6137	4.202	5.41	7.35	8.54	9.50	10.58	11.33	12.24	13.76	14.41	14.94	15.59	16.03
38.873	-77.022	14	7841	4.227	5.48	7.41	8.63	9.65	10.85	11.89	13.32	14.73	15.42	16.02	16.82	17.32
38.765	-77.033	15	14607	3.970	4.75	6.06	6.95	7.82	9.34	10.86	12.18	13.37	13.93	14.48	15.16	15.62
38.787	-77.023	16	14732	4.019	4.85	6.24	7.20	8.11	9.49	11.00	12.38	13.64	14.24	14.78	15.49	15.93
38.879	-77.046	17	5978	4.366	5.82	7.88	9.20	10.33	11.70	12.71	13.79	15.05	15.75	16.38	17.18	17.74
38.902	-77.077	18	5919	4.559	6.44	8.90	10.43	11.74	13.20	14.10	14.88	15.69	16.21	16.78	17.37	17.96
38.888	-77.055	19	14611	4.402	6.00	8.17	9.54	10.70	12.02	12.95	13.79	14.80	15.42	16.04	16.78	17.35
38.871	-77.004	20	14612	4.087	5.30	7.25	8.45	9.42	10.48	11.20	11.99	13.40	14.08	14.64	15.32	15.73
38.883	-76.970	21	14733	4.112	5.27	7.23	8.45	9.43	10.48	11.21	11.99	13.41	14.16	14.71	15.45	15.86
38.875	-77.024	22	5979	4.050	5.27	7.25	8.46	9.44	10.51	11.22	11.97	13.21	13.89	14.46	15.10	15.50
38.872	-77.022	23	14610	4.054	5.29	7.25	8.44	9.39	10.41	11.10	11.83	13.18	13.85	14.42	15.05	15.45

90% Confidence Limit WSEL in feet, NAVD88 datum

Virtual_ID	NACCS ID	Latitude (deg)	Longitude (deg)	1-year	2-year	5-year	10-year	20-year	50-year	100-year	200-year	500-year	1000-year	2000-year	5000-year	10000-year
1	14607	38.765	-77.033	5.36	6.22	7.58	8.49	9.29	10.33	11.38	12.49	13.79	14.39	14.97	15.54	15.94
2	5982	38.855	-77.026	5.65	7.00	9.03	10.25	11.20	12.23	12.93	13.74	15.19	15.84	16.38	17.01	17.41
3	5984	38.841	-77.028	5.62	6.85	8.75	9.91	10.83	11.85	12.59	13.55	15.06	15.68	16.23	16.84	17.24
4	5987	38.812	-77.030	5.52	6.57	8.22	9.28	10.17	11.20	12.06	13.28	14.66	15.28	15.84	16.42	16.81
5	5991	38.785	-77.031	5.45	6.36	7.81	8.78	9.65	10.76	11.85	13.06	14.41	15.00	15.56	16.13	16.53
6	7757	38.805	-77.038	5.62	6.69	8.25	9.28	10.19	11.30	12.46	13.81	15.10	15.65	16.17	16.77	17.16
7	14608	38.814	-77.035	5.51	6.56	8.21	9.27	10.14	11.13	11.89	12.99	14.39	15.04	15.62	16.19	16.58
8	14609	38.847	-77.023	5.62	6.90	8.87	10.05	10.98	11.99	12.67	13.44	14.87	15.53	16.10	16.72	17.12
9	14731	38.765	-77.043	5.40	6.27	7.63	8.54	9.36	10.42	11.53	12.68	13.97	14.57	15.13	15.72	16.12
10	14735	38.784	-77.044	5.46	6.37	7.81	8.78	9.65	10.76	11.80	13.02	14.35	14.96	15.52	16.09	16.50
11	5878	38.868	-77.020	5.67	7.01	9.05	10.29	11.27	12.37	13.12	14.01	15.48	16.14	16.68	17.32	17.76
12	5980	38.869	-77.006	5.63	6.94	8.97	10.21	11.19	12.25	12.98	13.76	15.13	15.83	16.39	17.05	17.47
13	6137	38.873	-77.022	5.78	7.08	9.10	10.32	11.30	12.39	13.15	14.07	15.60	16.26	16.79	17.44	17.88
14	7841	38.873	-77.022	5.81	7.15	9.16	10.41	11.45	12.67	13.71	15.16	16.58	17.27	17.87	18.68	19.18
15	14607	38.765	-77.033	5.58	6.44	7.82	8.76	9.66	11.21	12.75	14.09	15.29	15.85	16.41	17.09	17.55
16	14732	38.787	-77.023	5.62	6.53	8.00	9.00	9.94	11.35	12.87	14.27	15.55	16.14	16.69	17.41	17.85
17	5978	38.879	-77.046	5.98	7.53	9.66	11.01	12.16	13.54	14.57	15.65	16.92	17.62	18.25	19.06	19.62
18	5919	38.902	-77.077	6.20	8.19	10.72	12.28	13.60	15.07	15.97	16.76	17.58	18.10	18.67	19.26	19.86
19	14611	38.888	-77.055	6.02	7.71	9.97	11.36	12.53	13.87	14.81	15.65	16.67	17.30	17.92	18.66	19.24
20	14612	38.871	-77.004	5.64	6.94	8.98	10.21	11.20	12.27	13.00	13.80	15.22	15.90	16.47	17.15	17.56
21	14733	38.883	-76.970	5.63	6.87	8.91	10.16	11.15	12.22	12.96	13.74	15.18	15.93	16.49	17.22	17.63
22	5979	38.875	-77.024	5.61	6.93	8.99	10.24	11.24	12.32	13.04	13.80	15.05	15.74	16.30	16.95	17.36
23	14610	38.872	-77.022	5.62	6.95	9.00	10.22	11.19	12.23	12.92	13.66	15.02	15.69	16.27	16.90	17.30

DCMetro, Surge+Tides: Storm 16

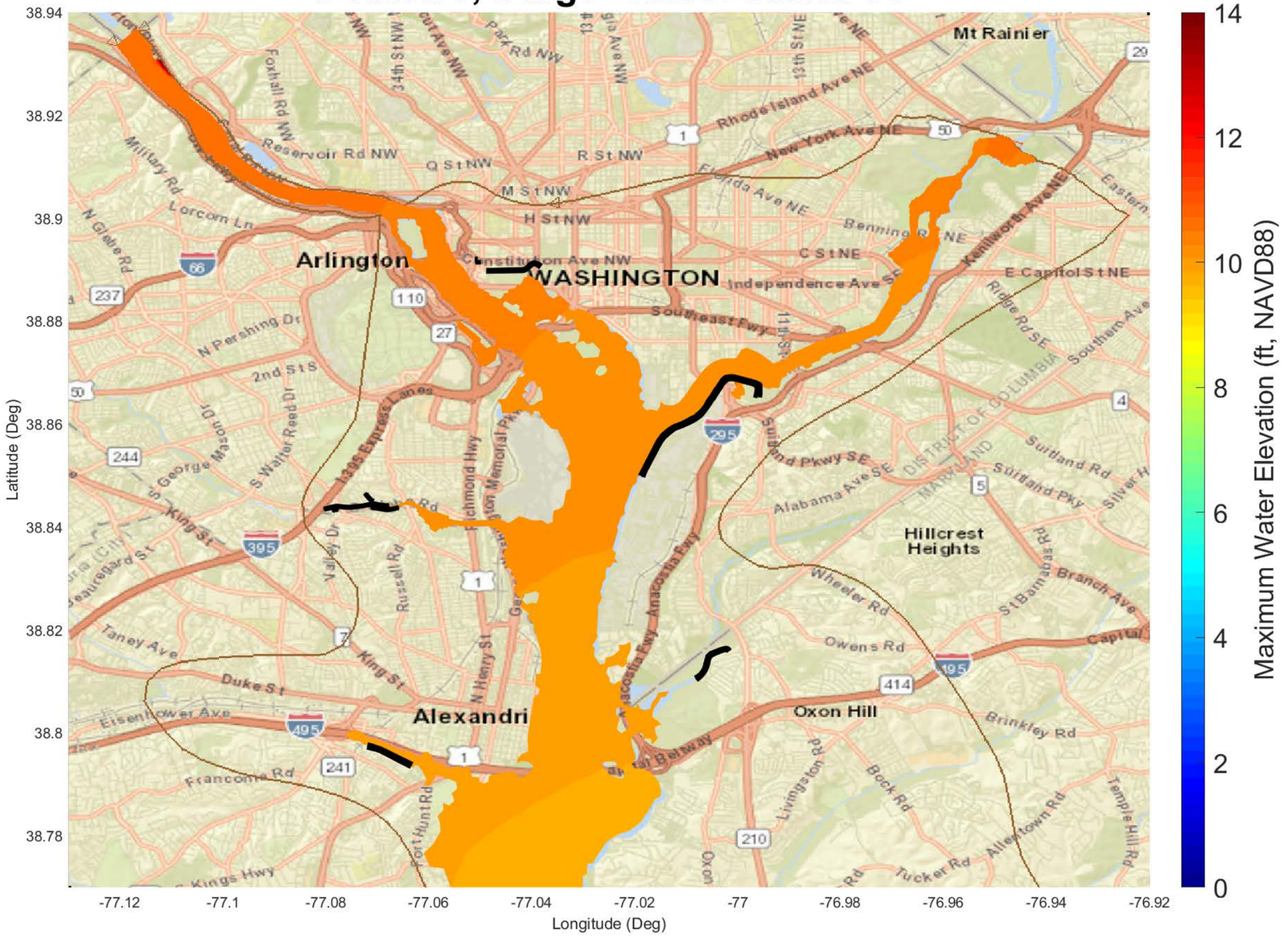

DCMetro, Surge+Tides: Storm 17

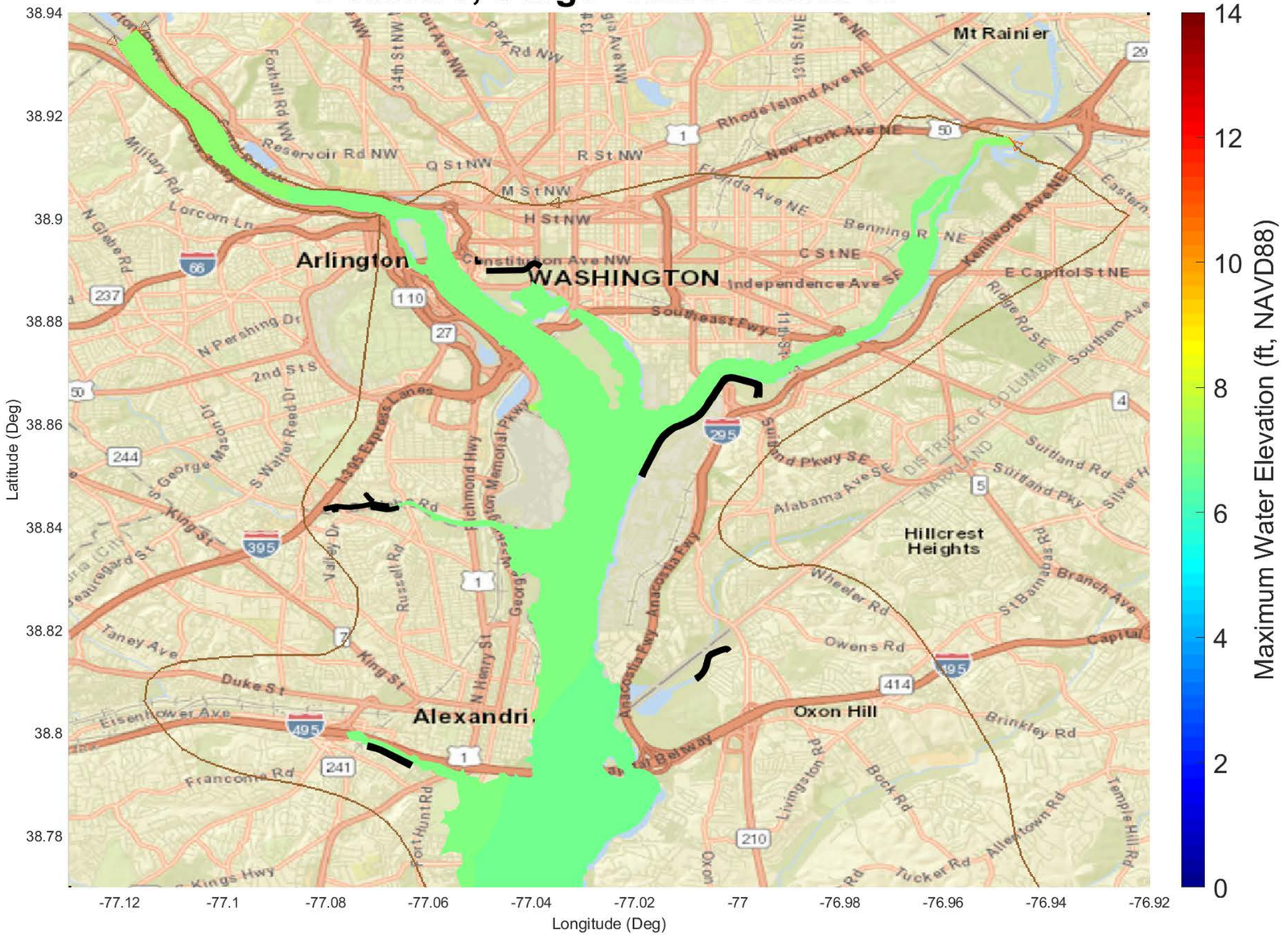

DCMetro, Surge+Tides: Storm 22

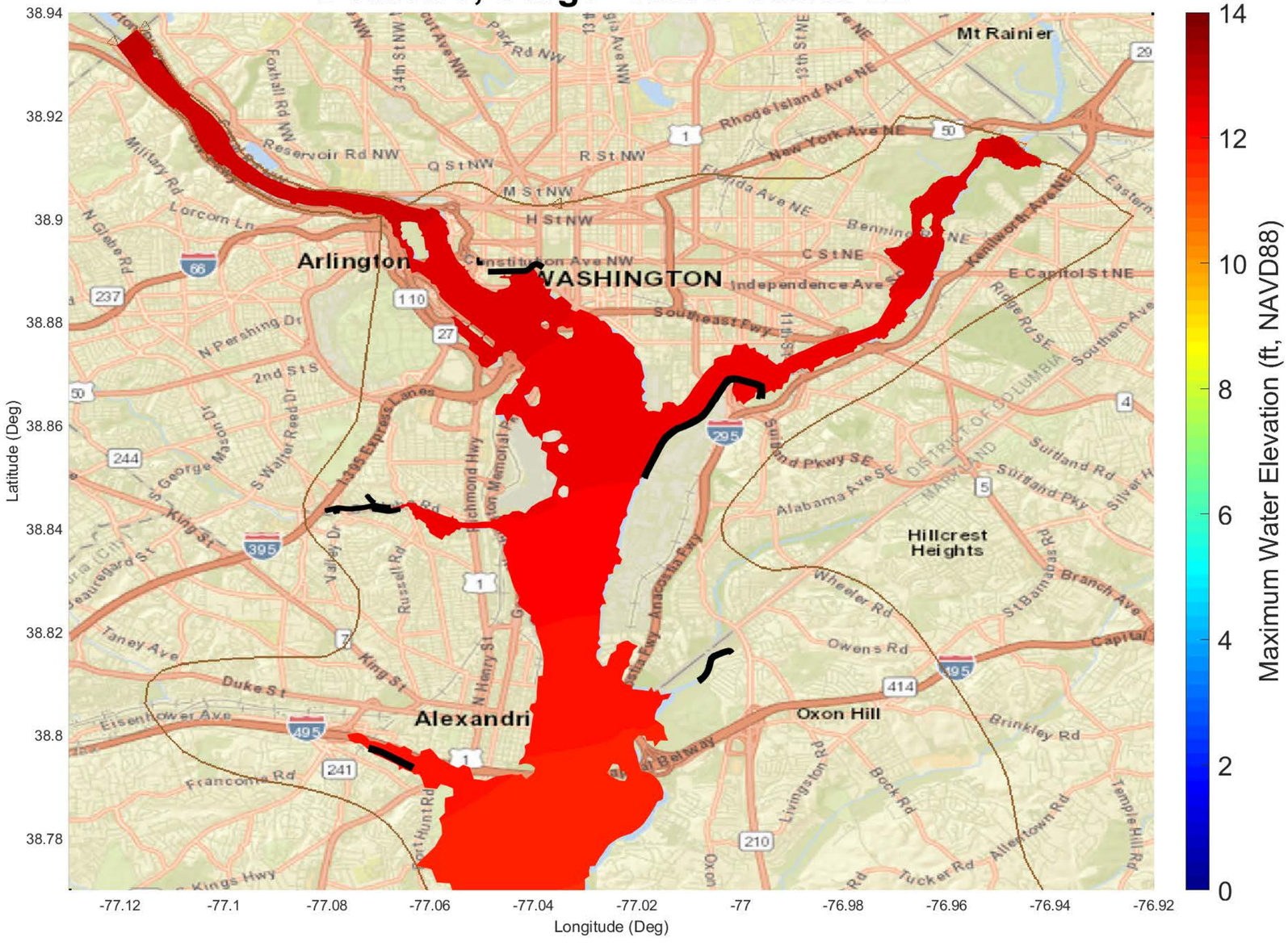

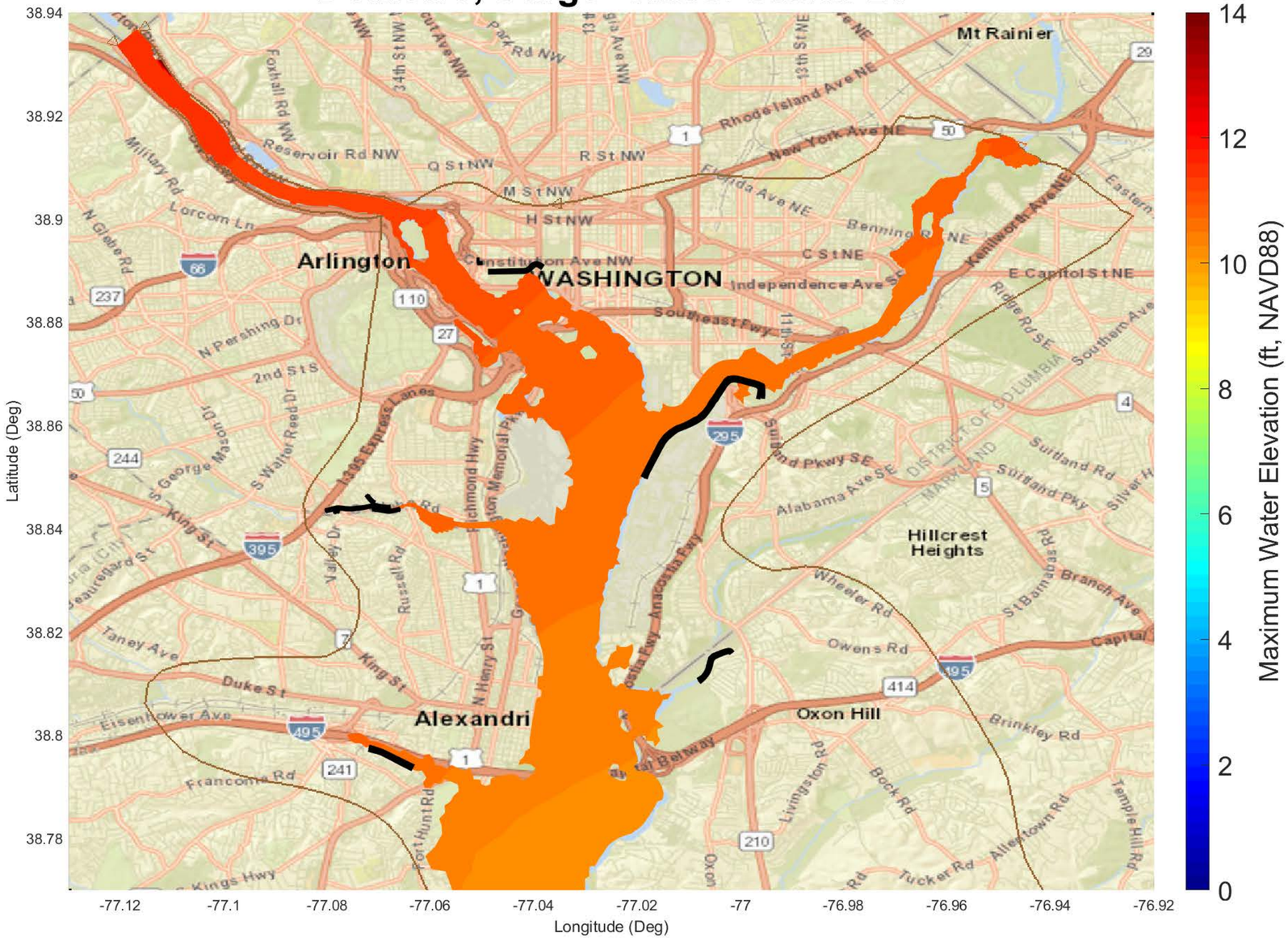
DCMetro, Surge+Tides: Storm 24
Latitude (Deg)
38.94
38.92
38.9
38.88
38.86
38.84
38.82
38.8
38.78
Longitude (Deg)
-77.12
-77.1
-77.08
-77.06
-77.04
-77.02
-77
-76.98
-76.96
-76.94
-76.92
Maximum Water Elevation (ft, NAVD88)
14
12
10
8
6
4
2
0
Arlington
WASHINGTON
Alexandri
Hillcrest Heights
Oxon Hill
Mt Rainier
Rhode Island Ave NE
New York Ave NE
Florida Ave NE
Benning Rd NE
Kenilworth Ave NE
E Capitol St NE
Ridge Rd SE
Southern Ave
Suitland Pkwy
Alabama Ave SE
Wheeler Rd
Owens Rd
Brinkley Rd
Capital Beltway
Reservoir Rd NW
Q St NW
R St NW
M St NW
H St NW
Constitution Ave NW
Independence Ave SW
Southeast Fwy
Foxhall Rd NW
Military Rd
Lorcom Ln
N Glebe Rd
N Pershing Dr
2nd St S
S Walter Reed Dr
George Mason Dr
S King St
Beauregard St
Taney Ave
Duke St
Eisenhower Ave
Francone Rd
Fort Hunt Rd
Kings Hwy
Valley Dr
Russell Rd
Richmond Hwy
N Henry St
Jefferson Memorial Pkwy
14th St Bridge Express Lanes
Anacostia Fwy
Livingston Rd
Bock Rd
Tucker Rd
Allentown Rd
Temple Hill Rd
St Barnabas Rd
Branch Ave
Park Rd NW
34th St NW
Mass Ave NW
13th St NW
Sixth Ave NW
Eastern
66
237
110
27
50
244
395
1
7
295
4
5
414
495
241
210
29

DCMetro, Surge+Tides: Storm 25

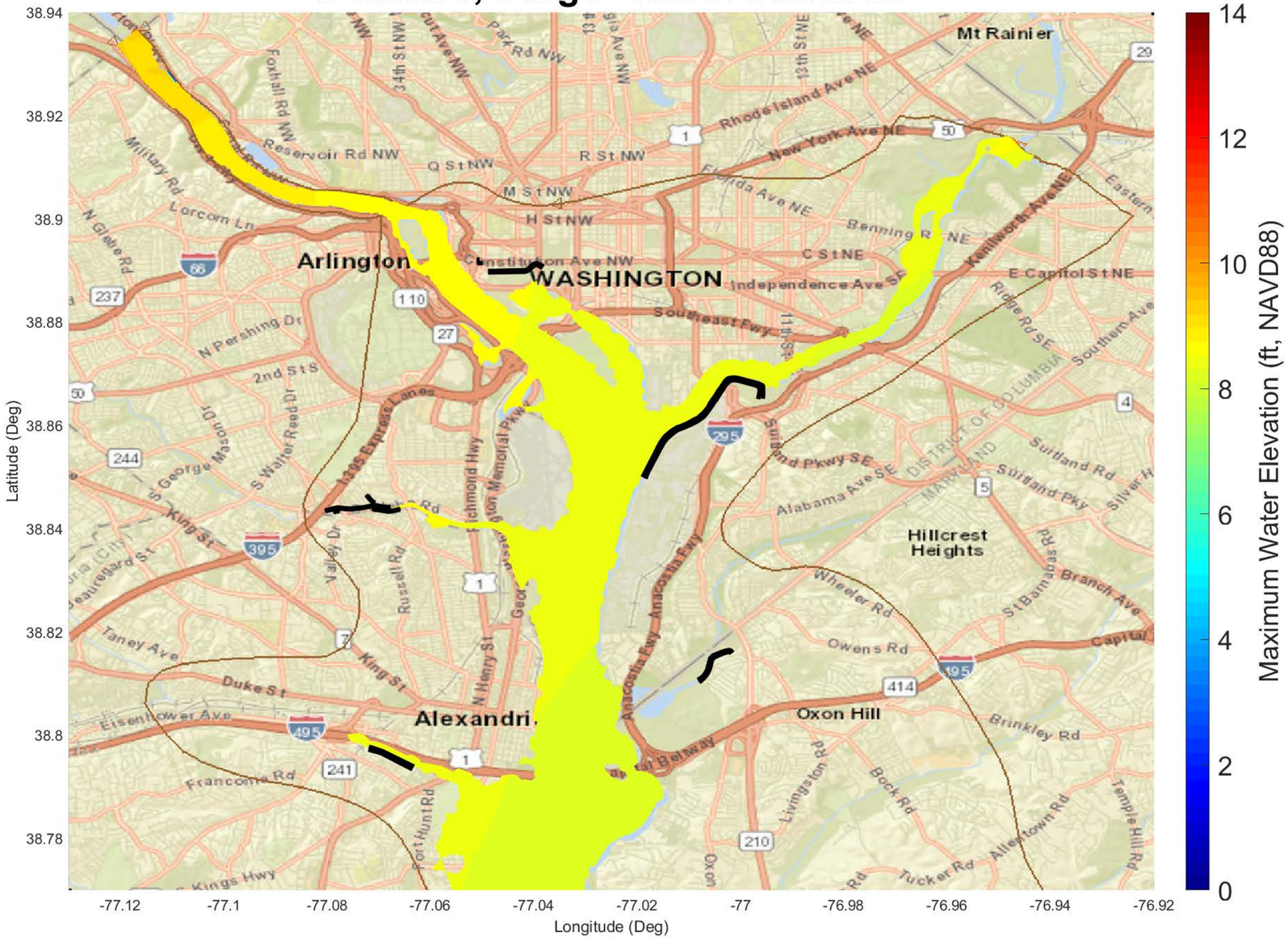

DCMetro, Surge+Tides: Storm 31

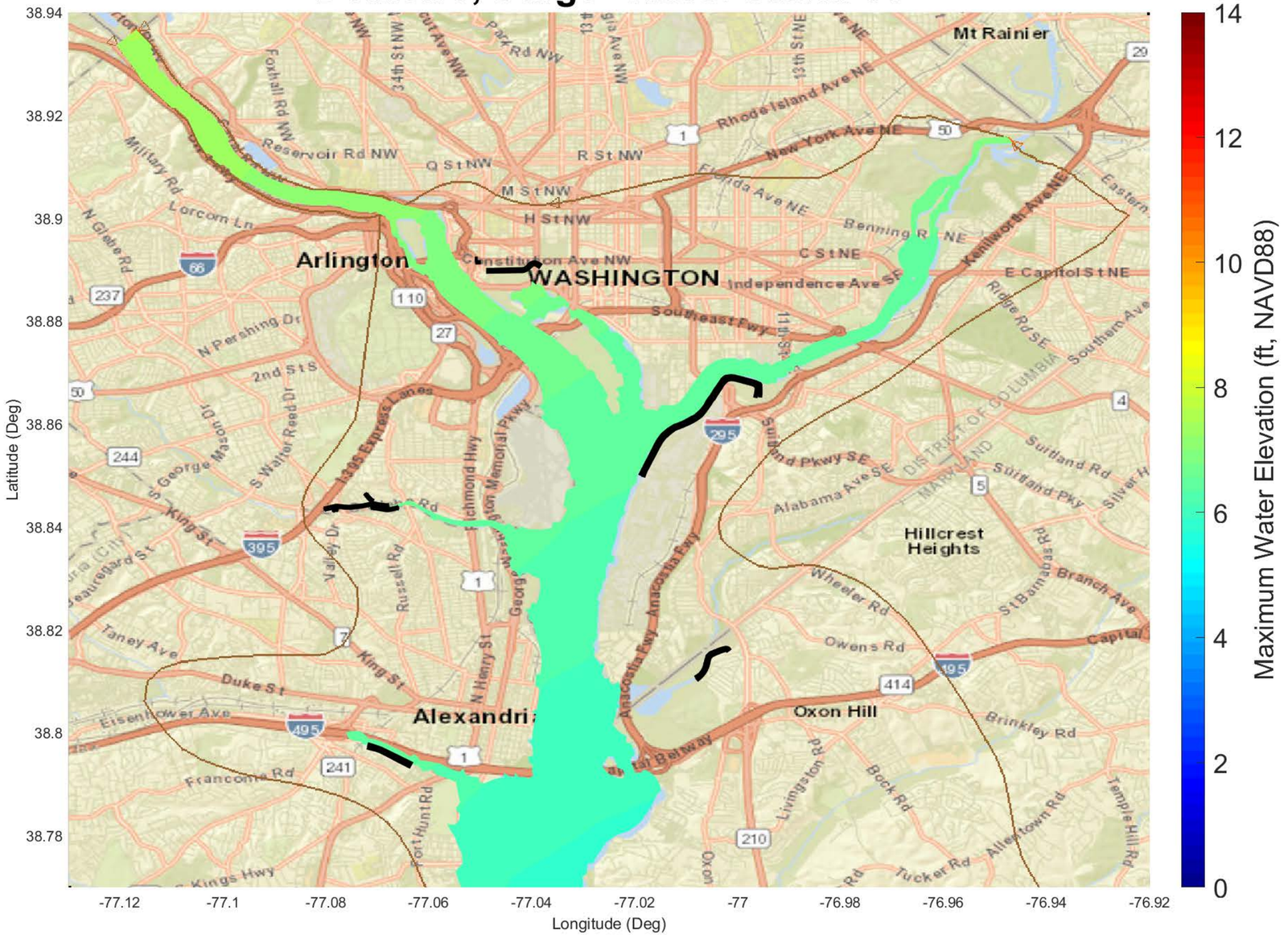

DCMetro, Surge+Tides: Storm 33

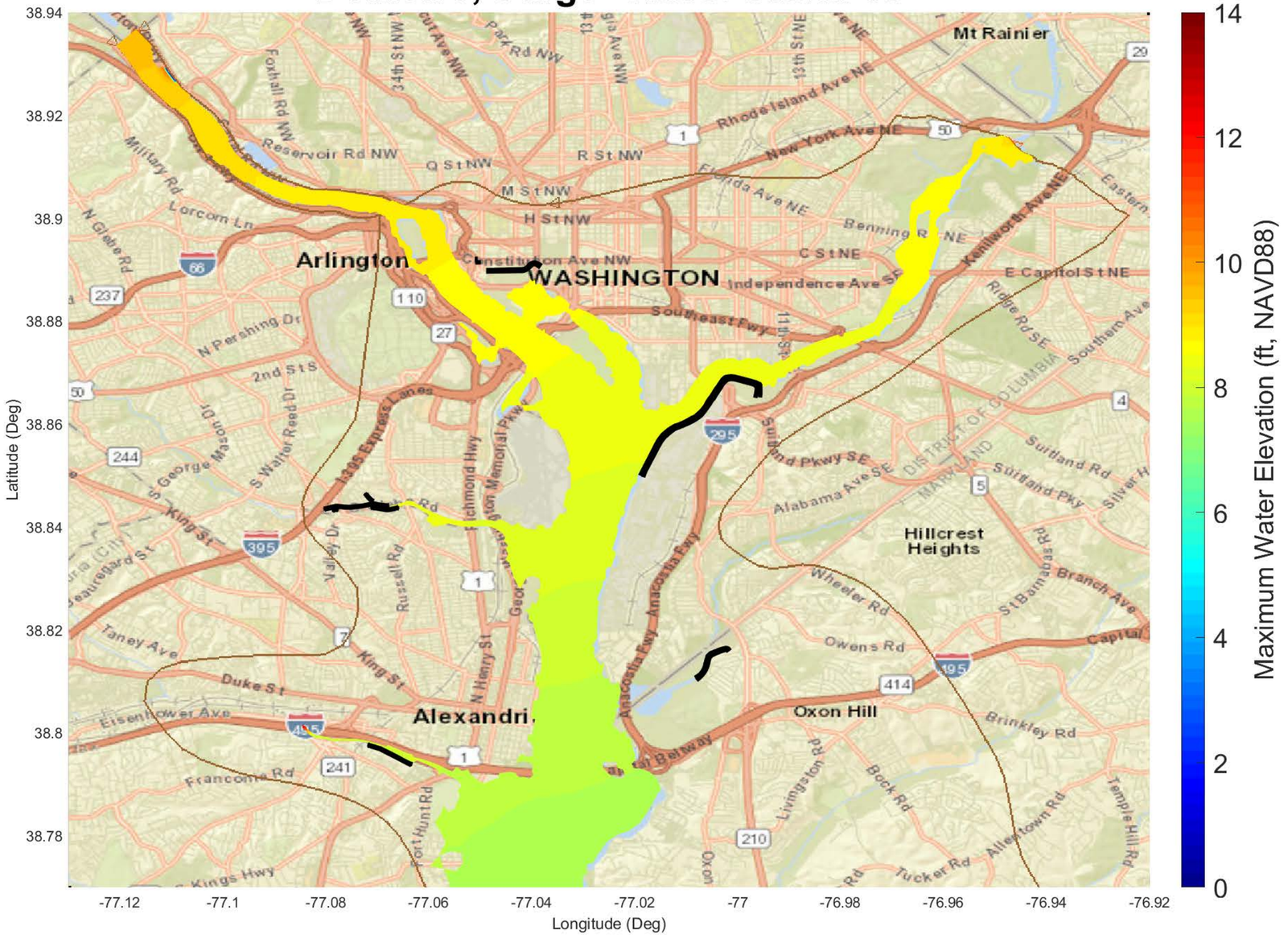

DCMetro, Surge+Tides: Storm 57

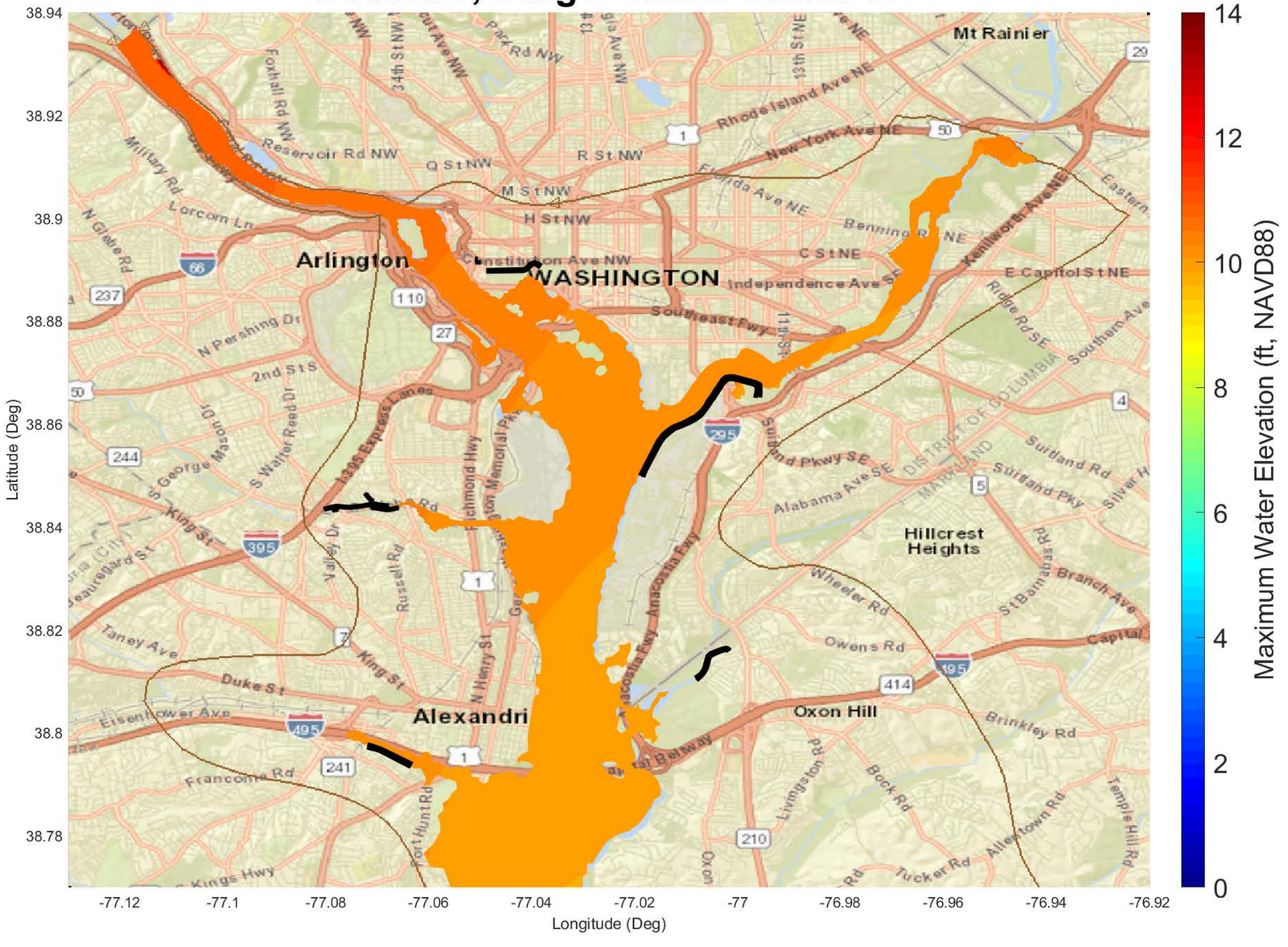

DCMetro, Surge+Tides: Storm 69

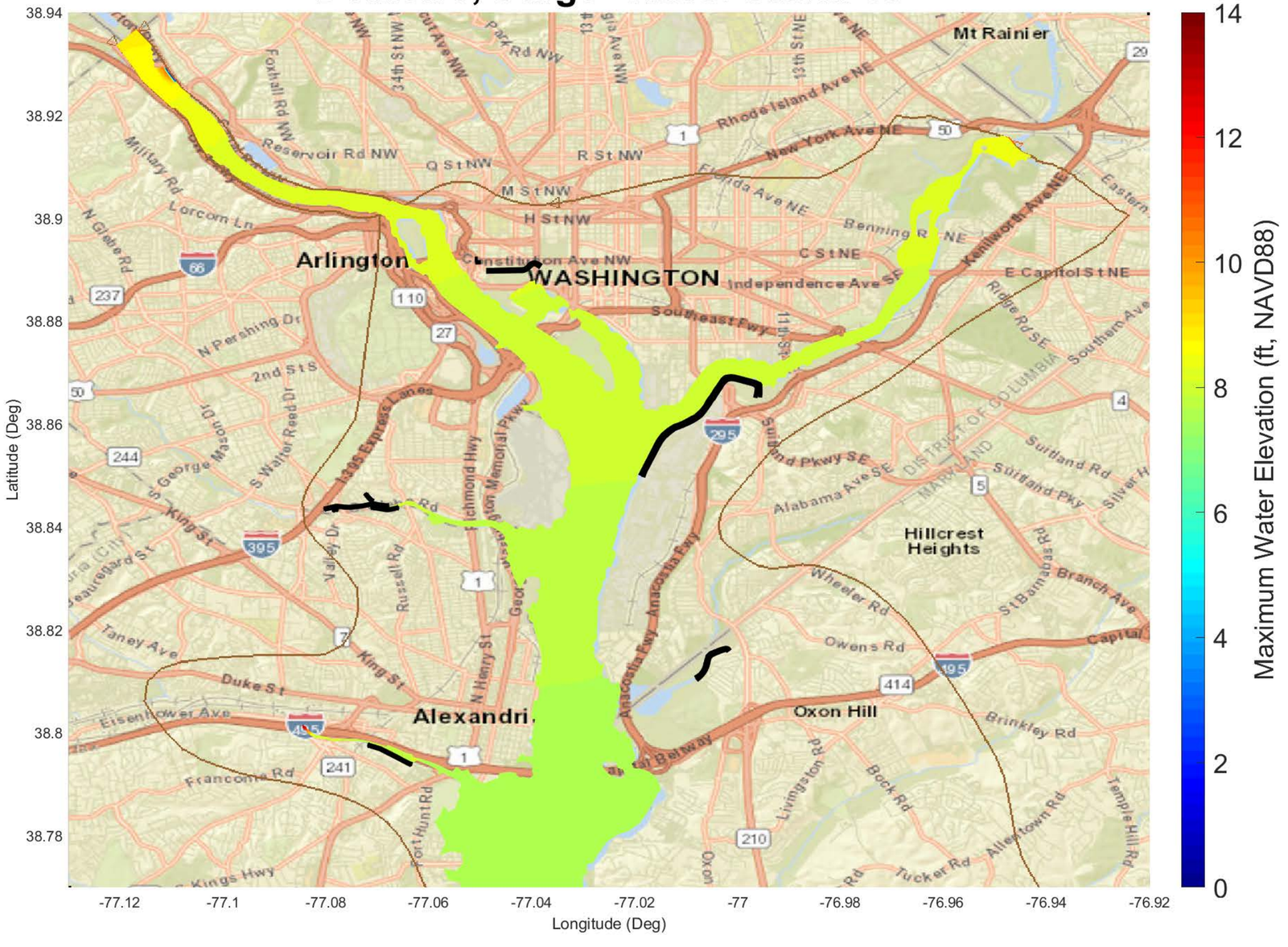

DCMetro, Surge+Tides: Storm 72

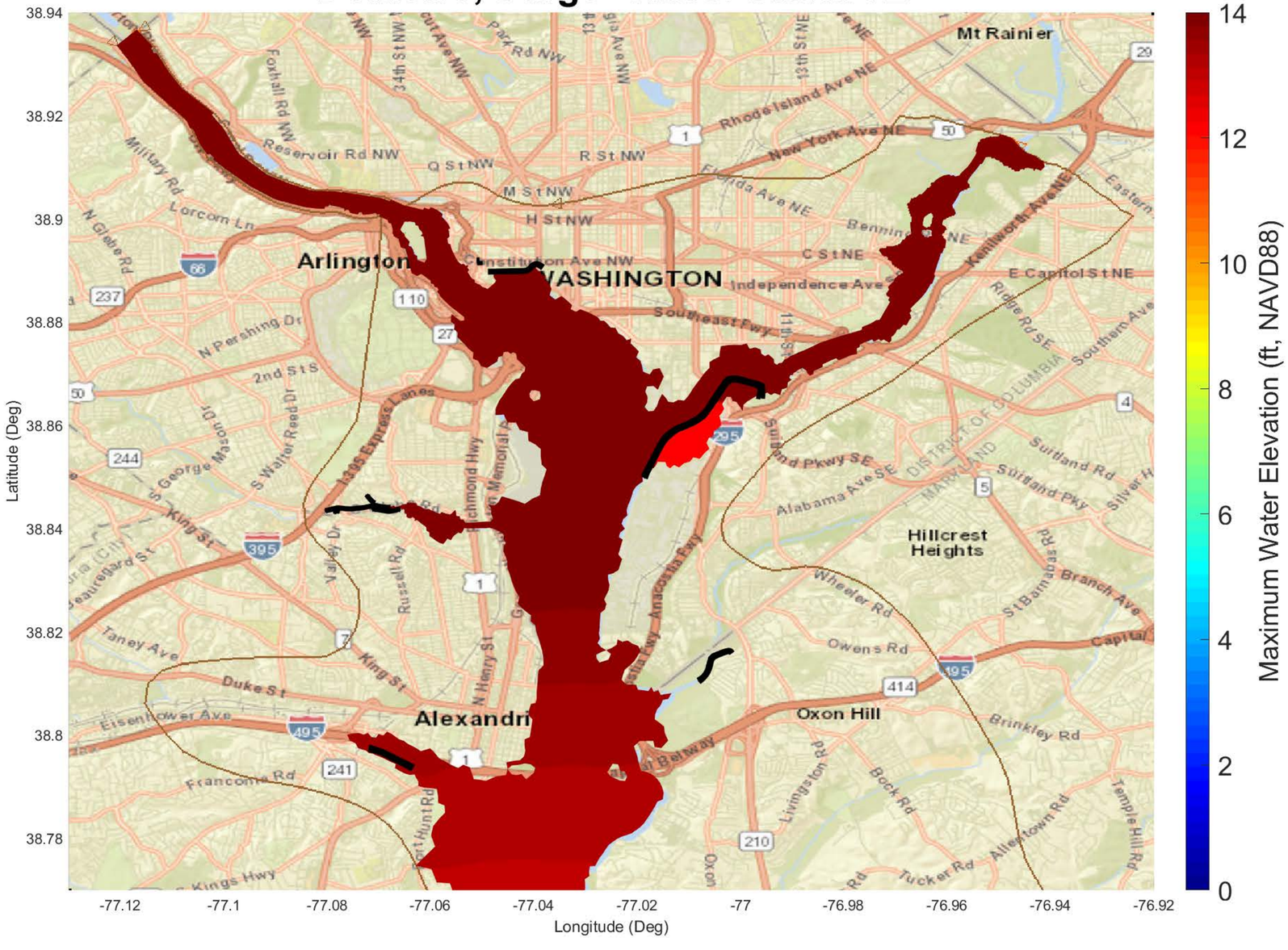

DCMetro, Surge+Tides: Storm 75

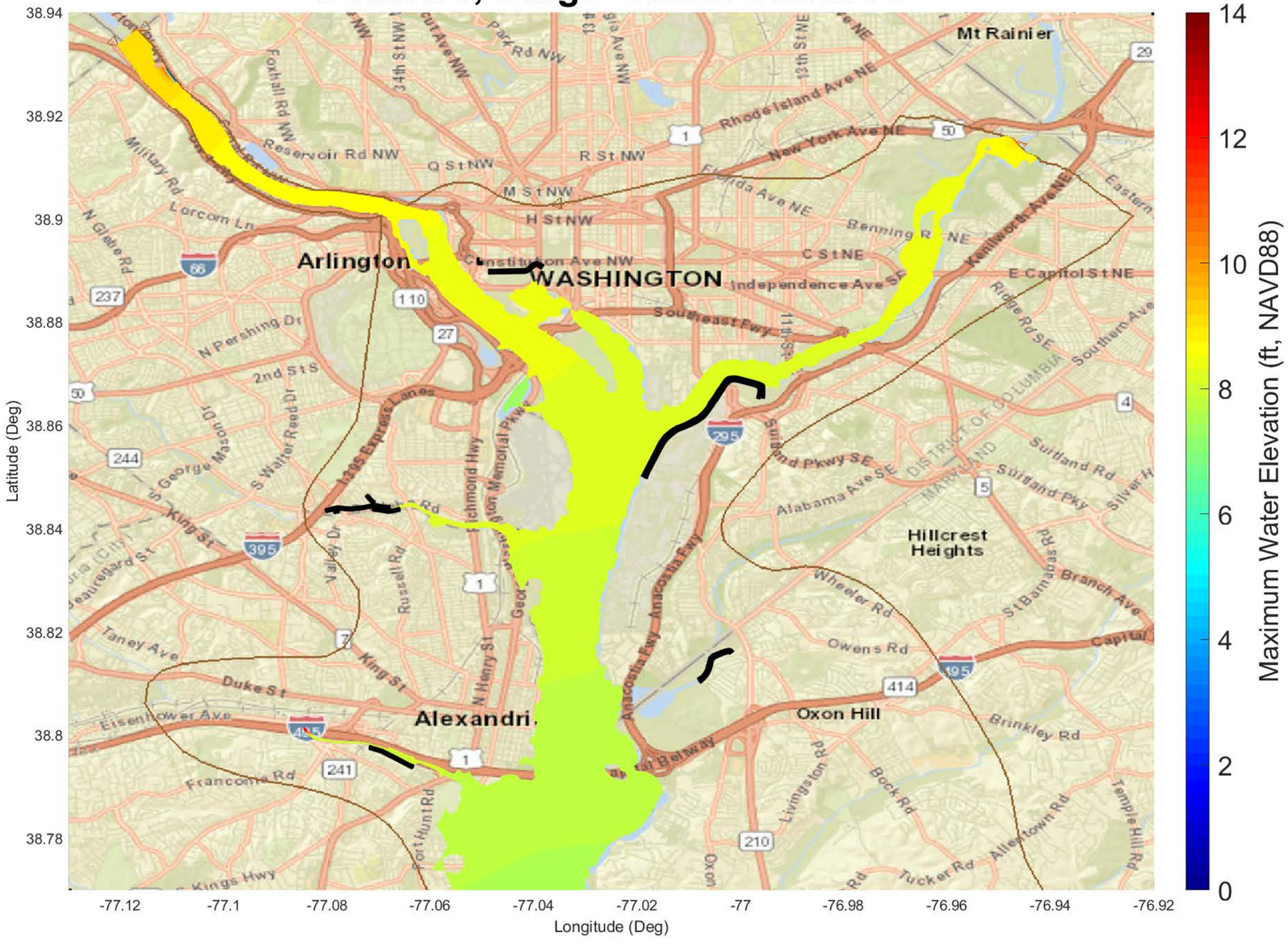

DCMetro, Surge+Tides: Storm 76

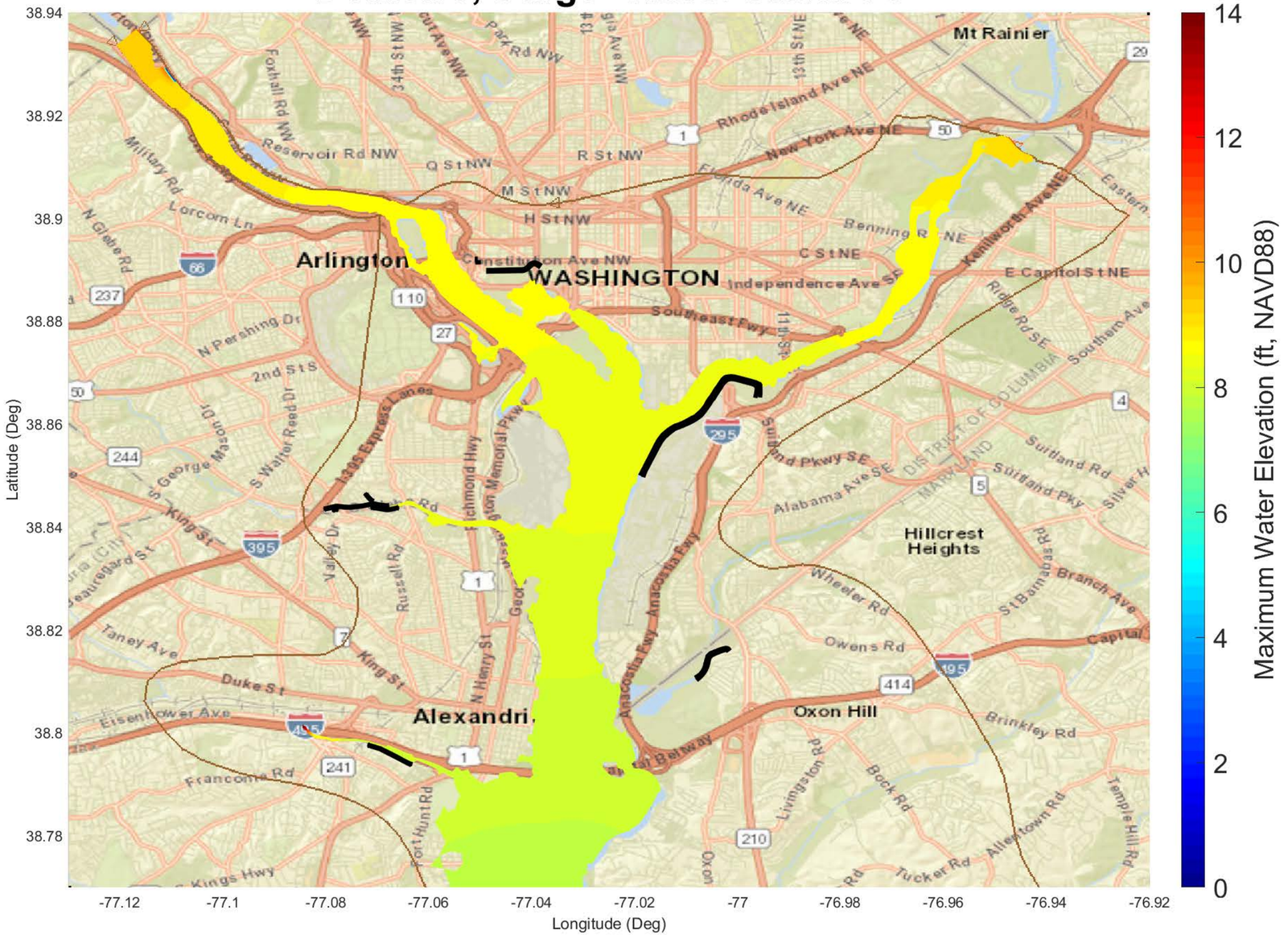

DCMetro, Surge+Tides: Storm 77

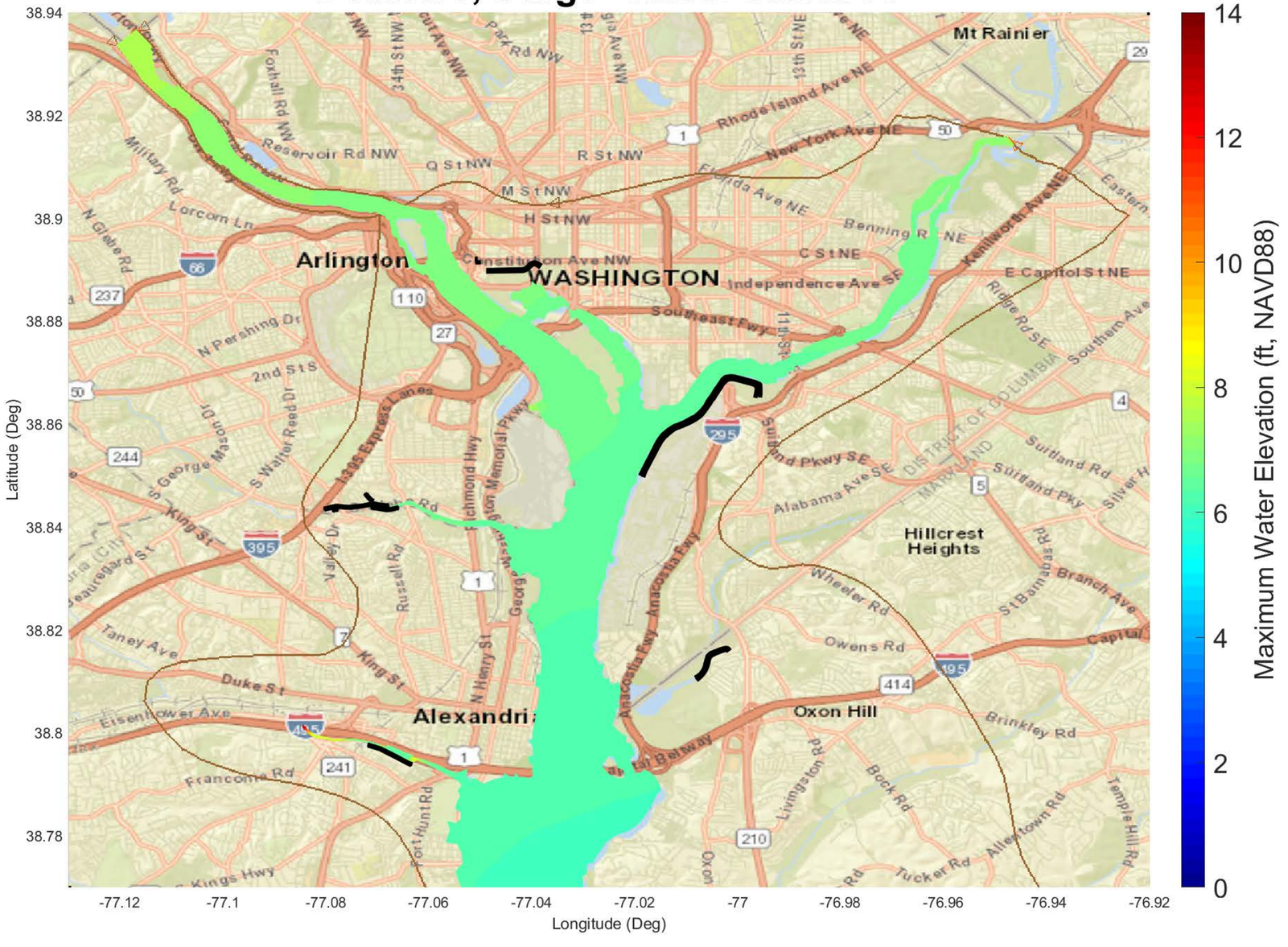

DCMetro, Surge+Tides: Storm 83

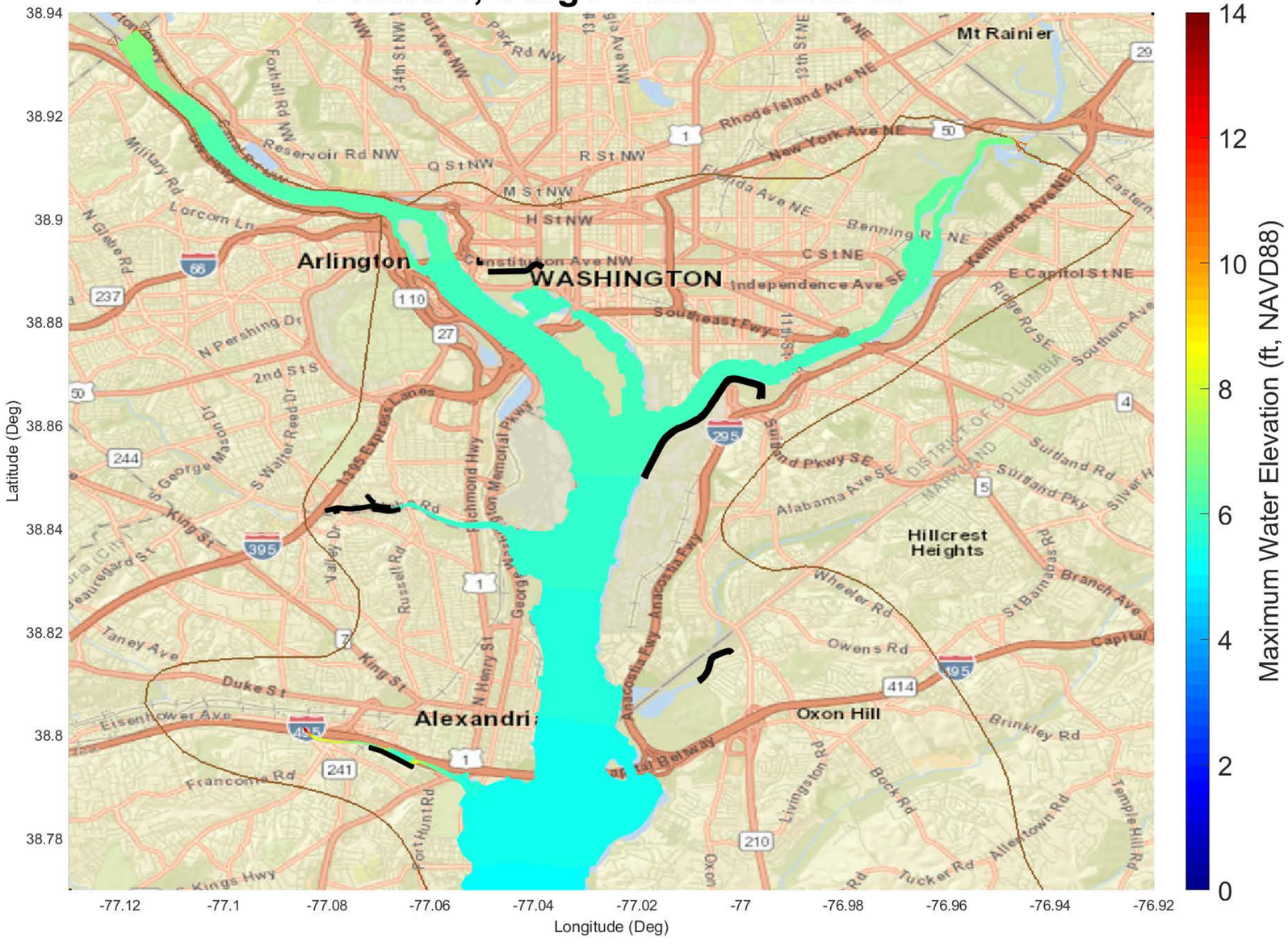

DCMetro, Surge+Tides: Storm 109

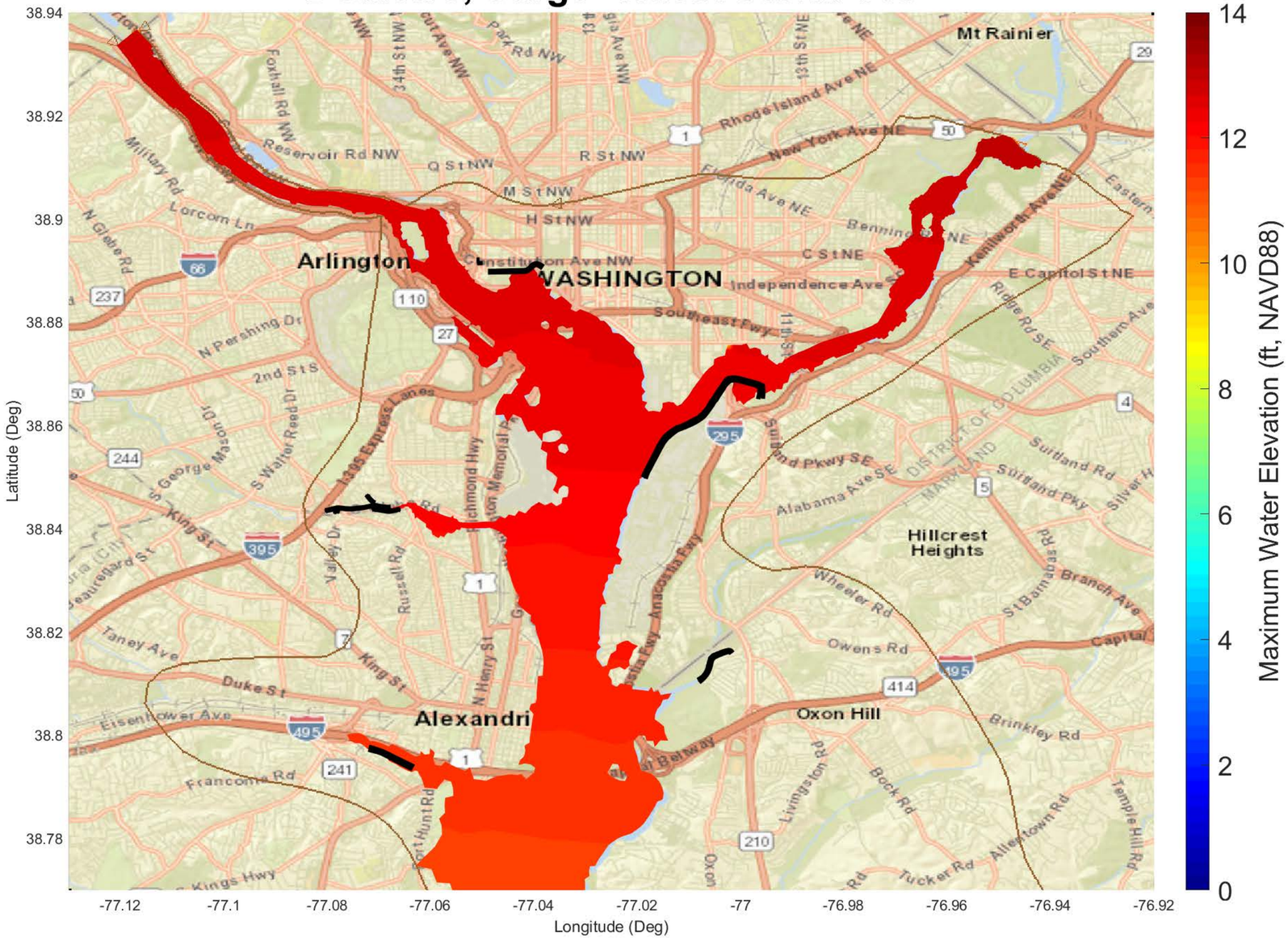

DCMetro, Surge+Tides: Storm 110

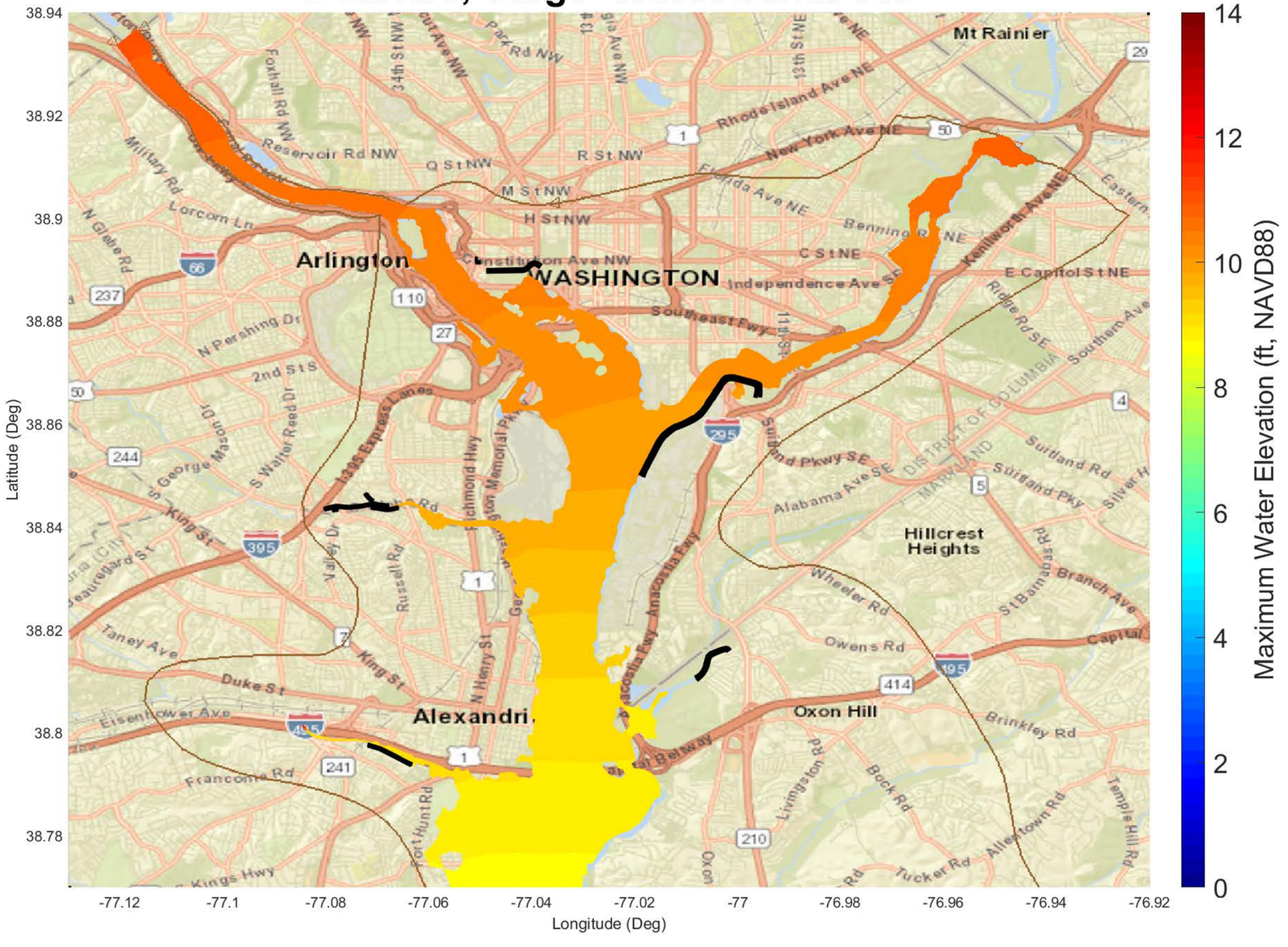

DCMetro, Surge+Tides: Storm 115

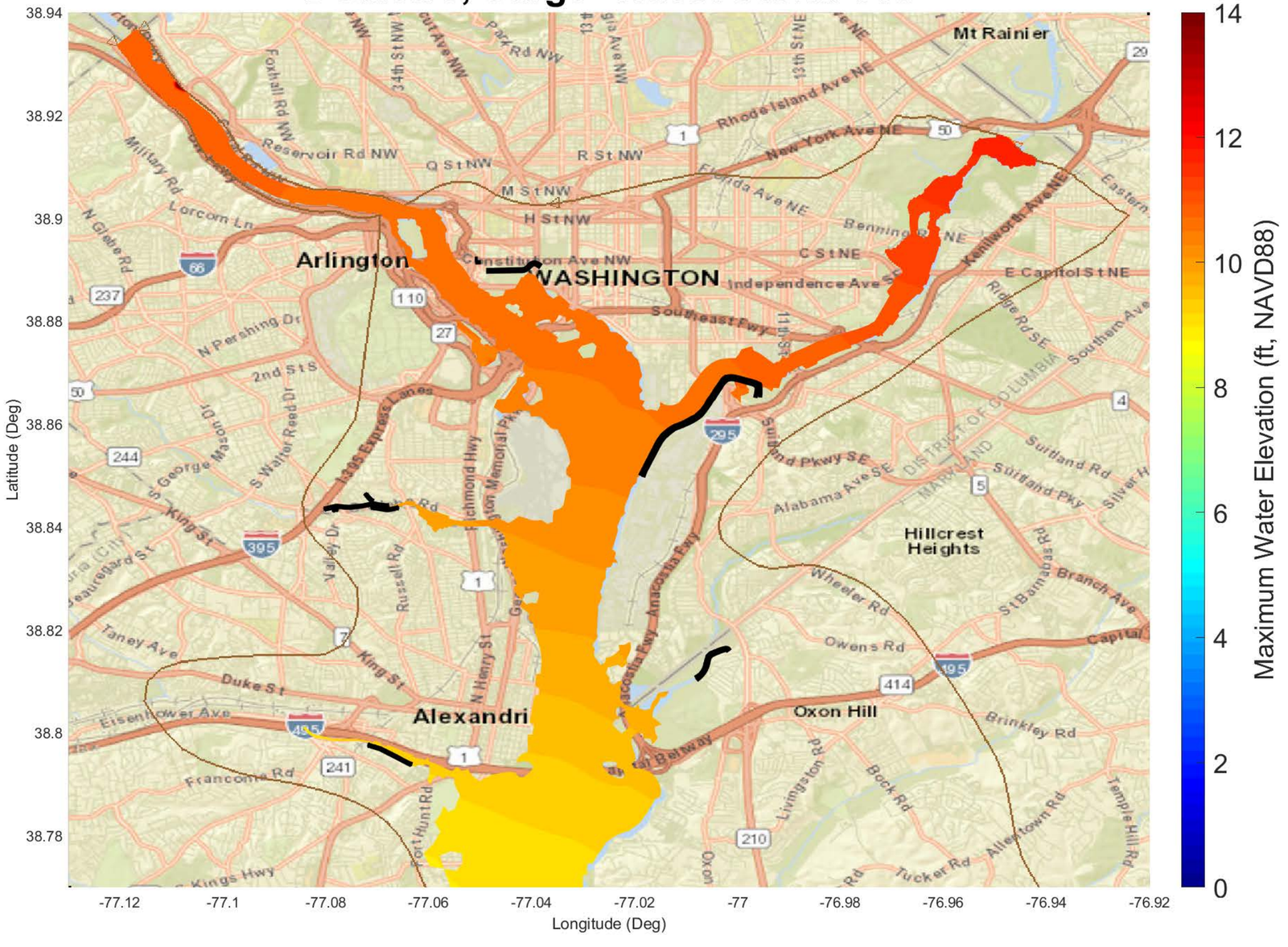

DCMetro, Surge+Tides: Storm 117

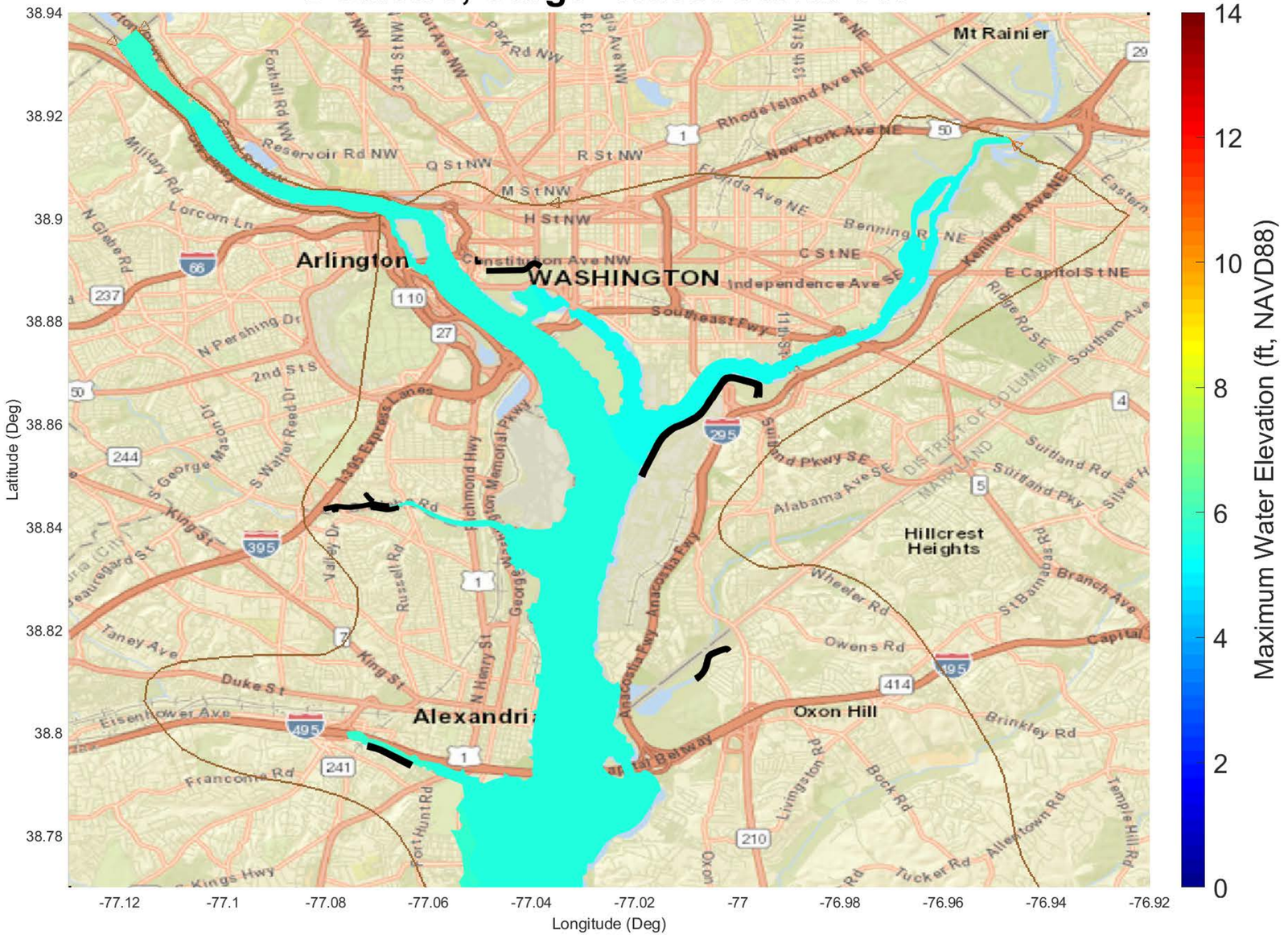

DCMetro, Surge+Tides: Storm 119

DCMetro, Surge+Tides: Storm 122

DCMetro, Surge+Tides: Storm 123

DCMetro, Surge+Tides: Storm 136

DCMetro, Surge+Tides: Storm 142

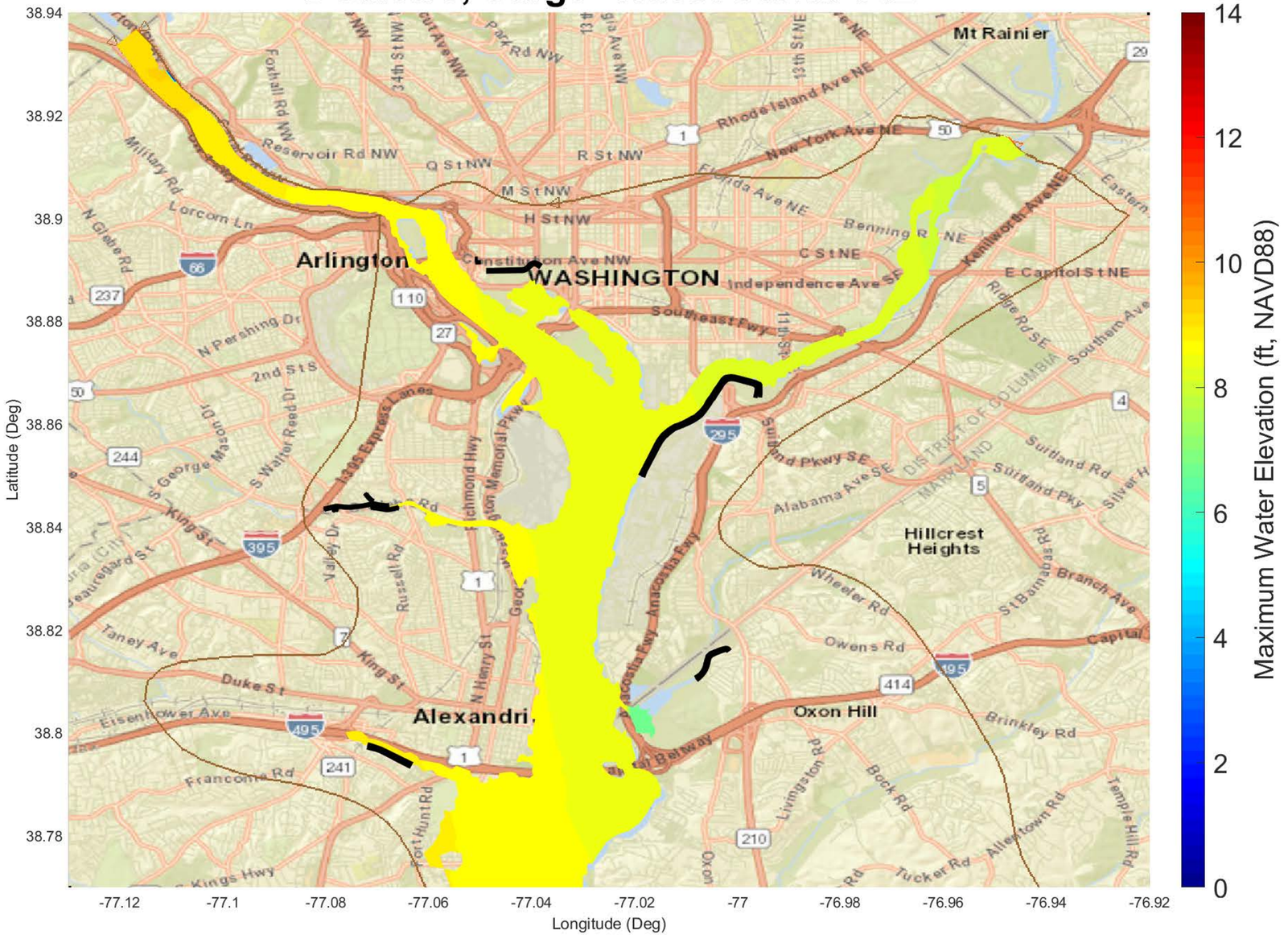

DCMetro, Surge+Tides: Storm 143

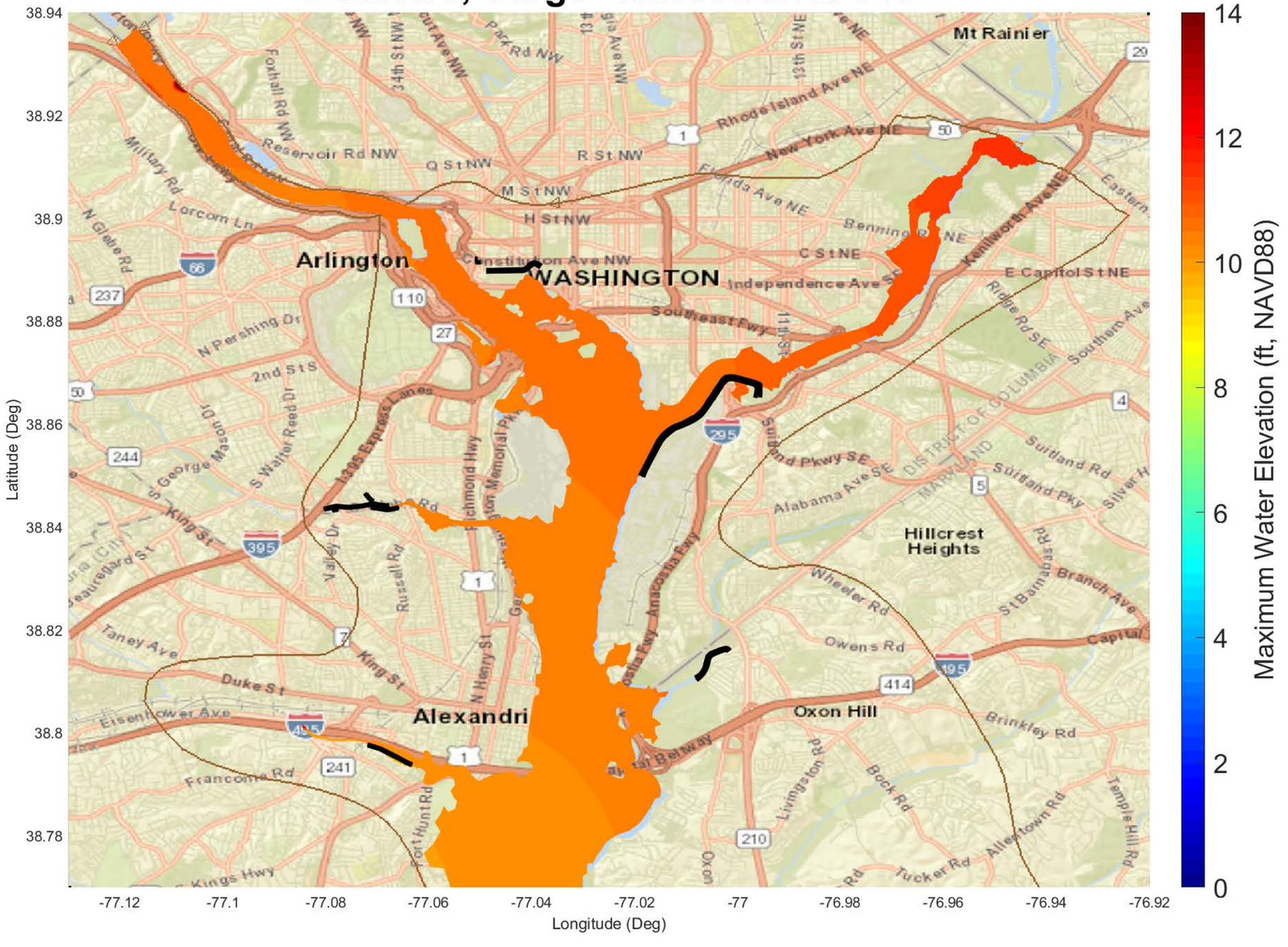

DCMetro, Surge+Tides: Storm 146

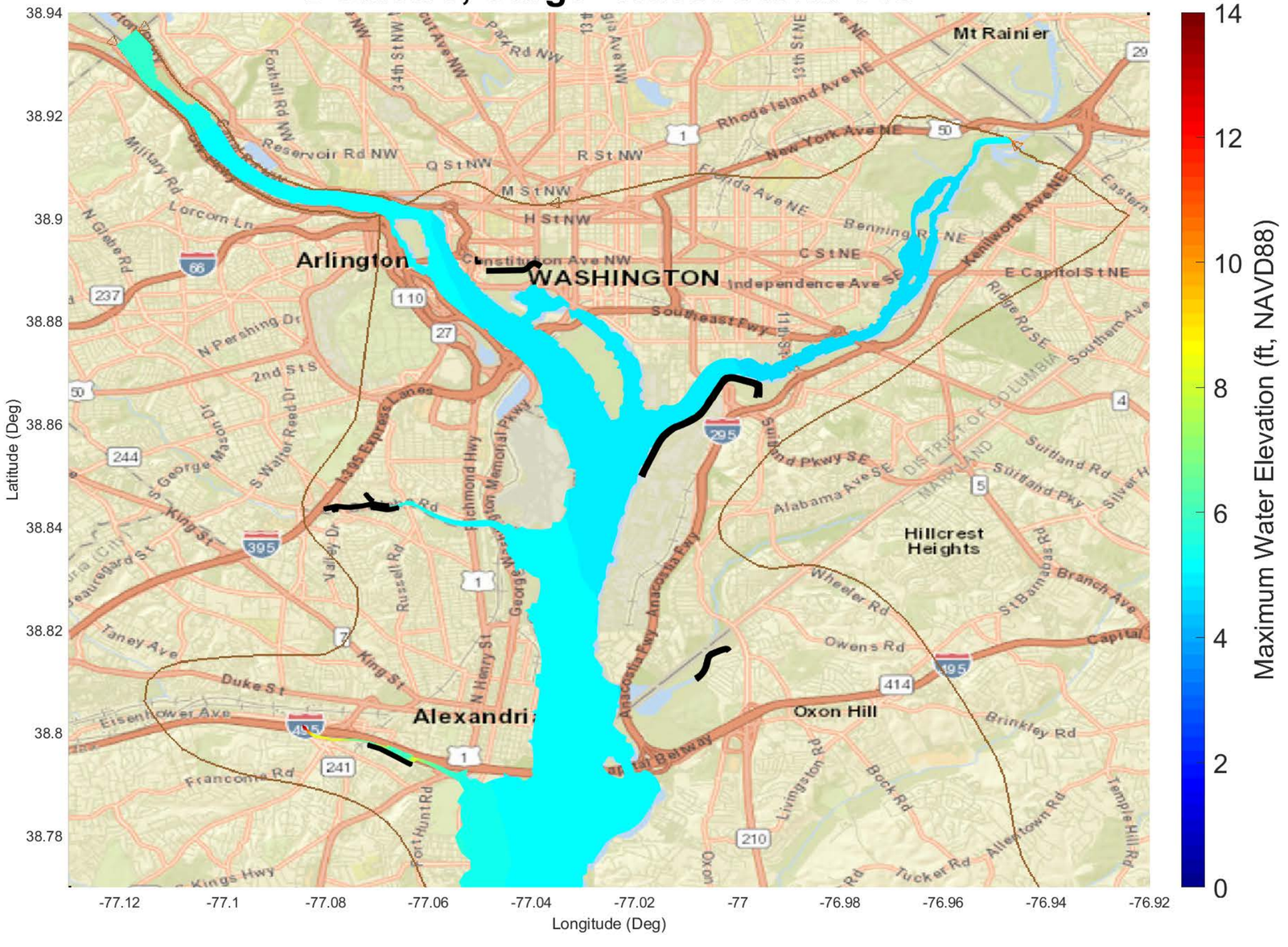

DCMetro, Surge+Tides: Storm 147

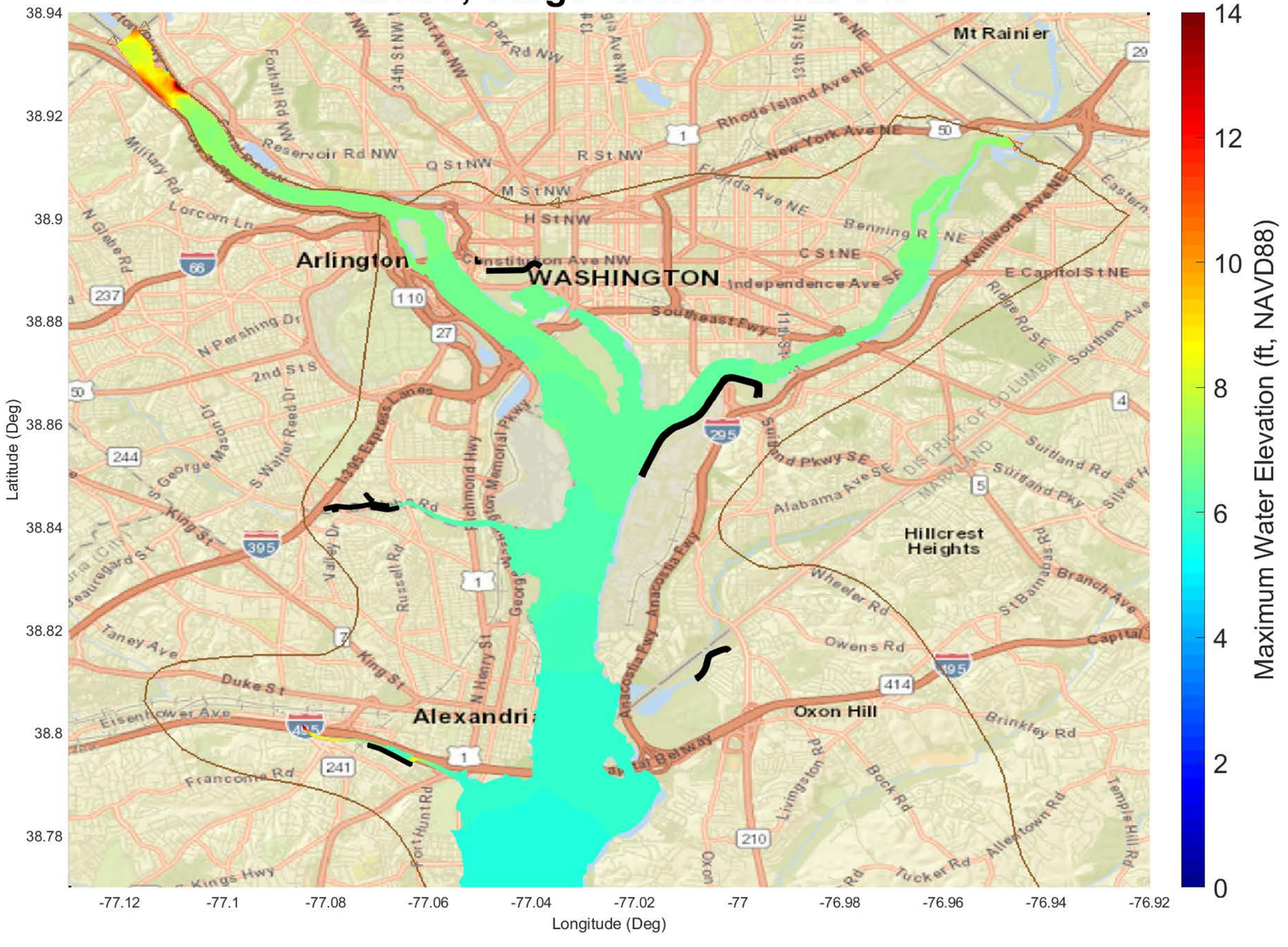

DCMetro, Surge+Tides: Storm 148

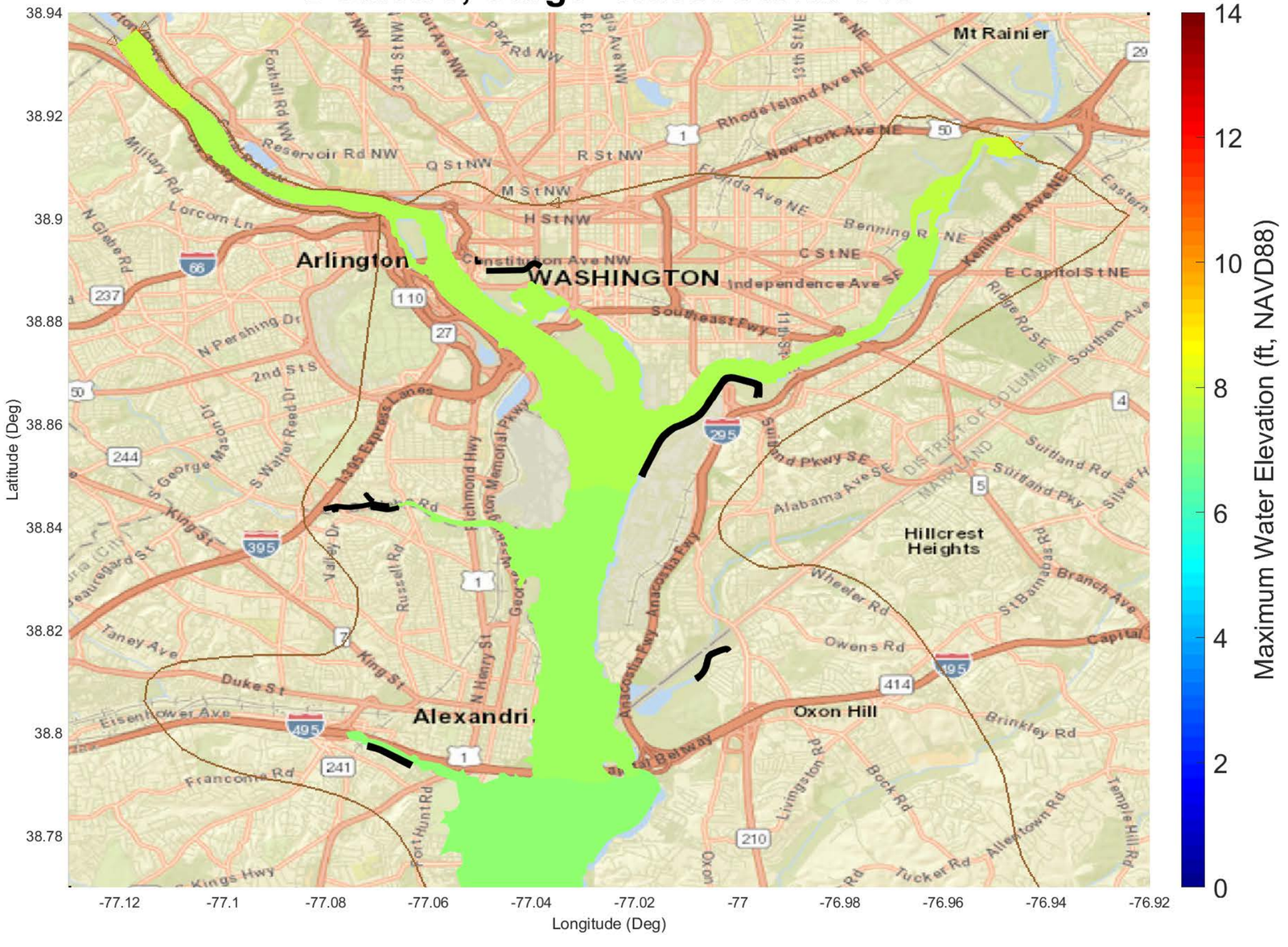

DCMetro, Surge+Tides: Storm 149

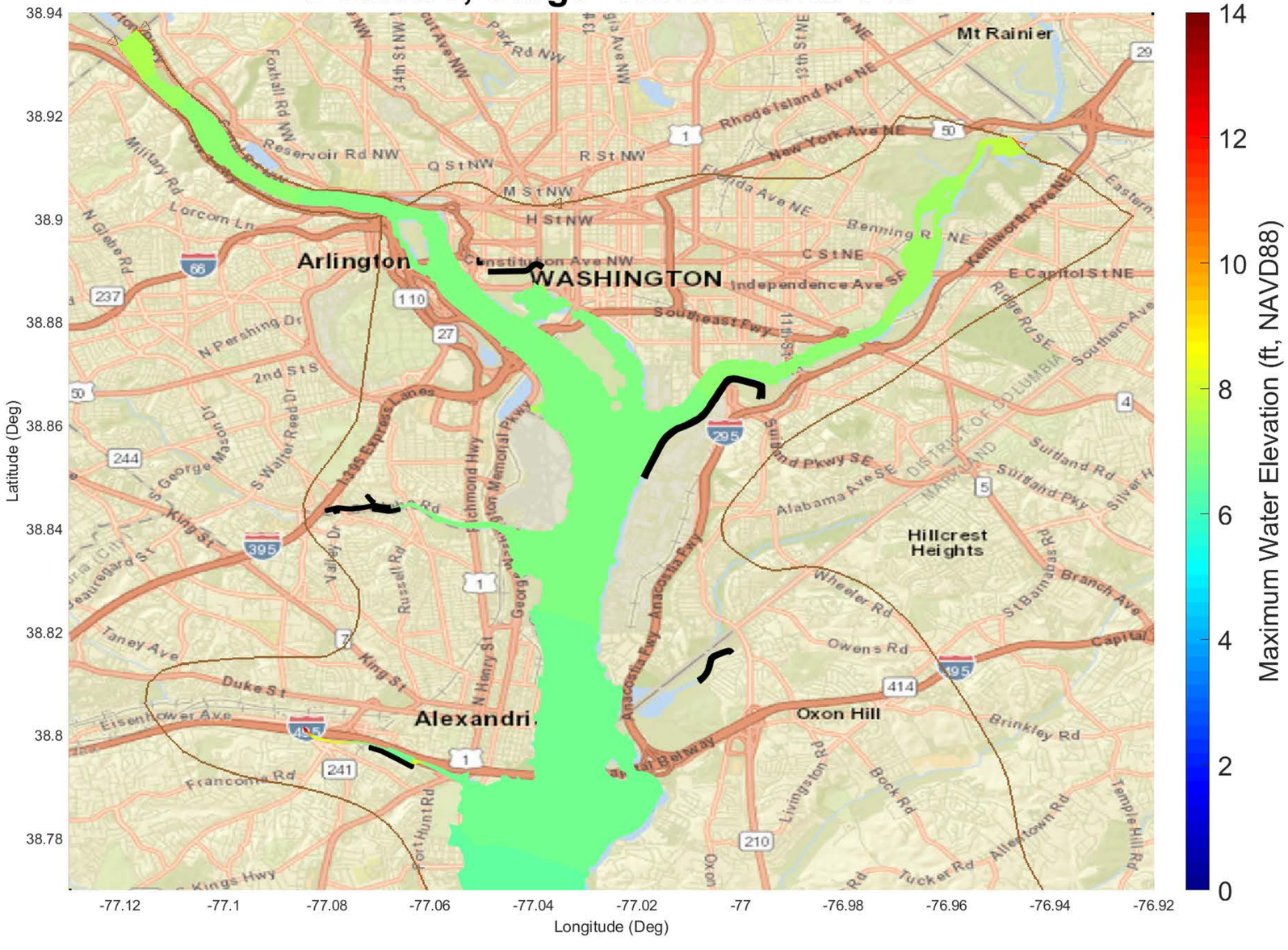

DCMetro, Surge+Tides: Storm 151

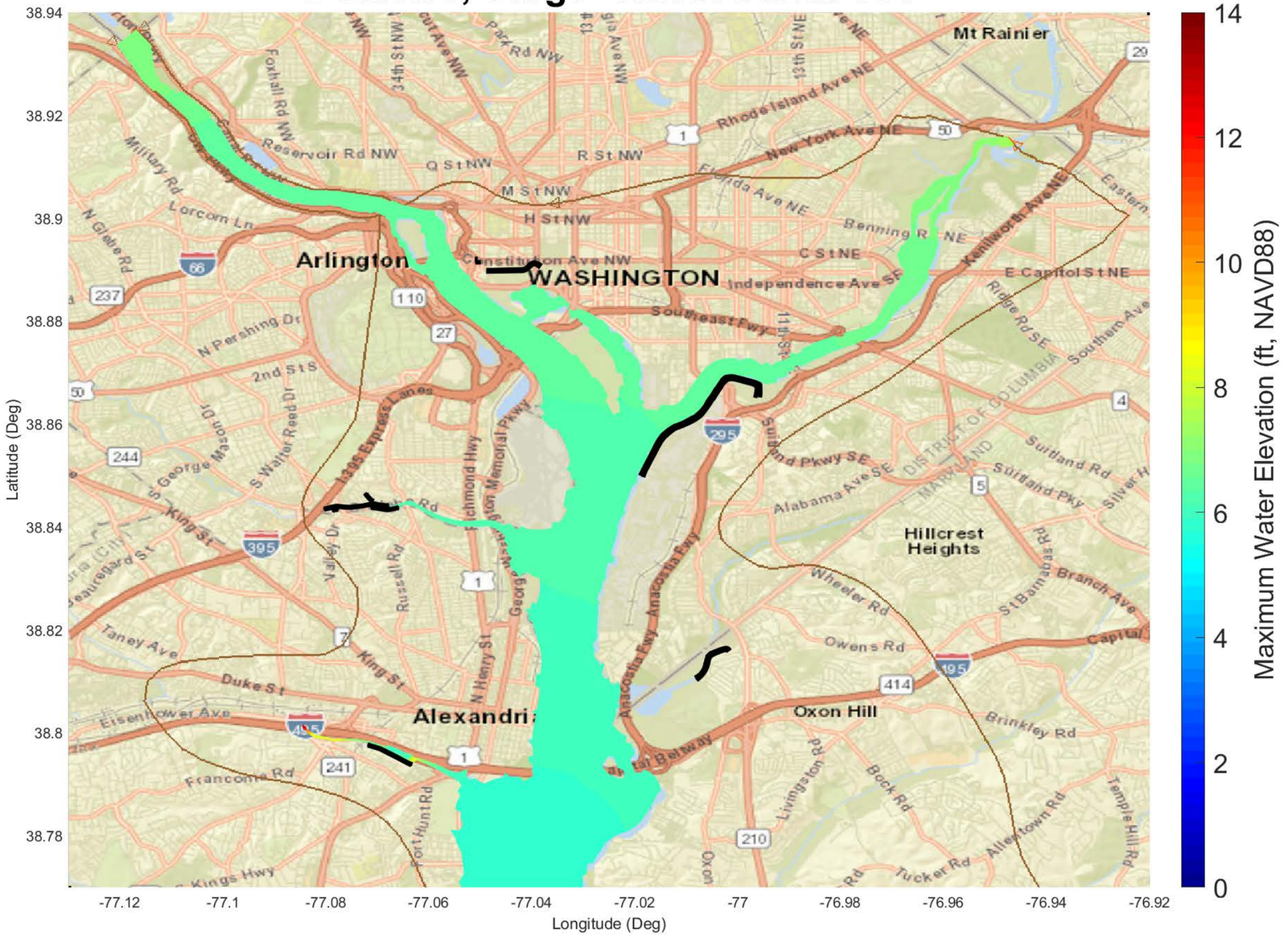

DCMetro, Surge+Tides: Storm 155

DCMetro, Surge+Tides: Storm 165

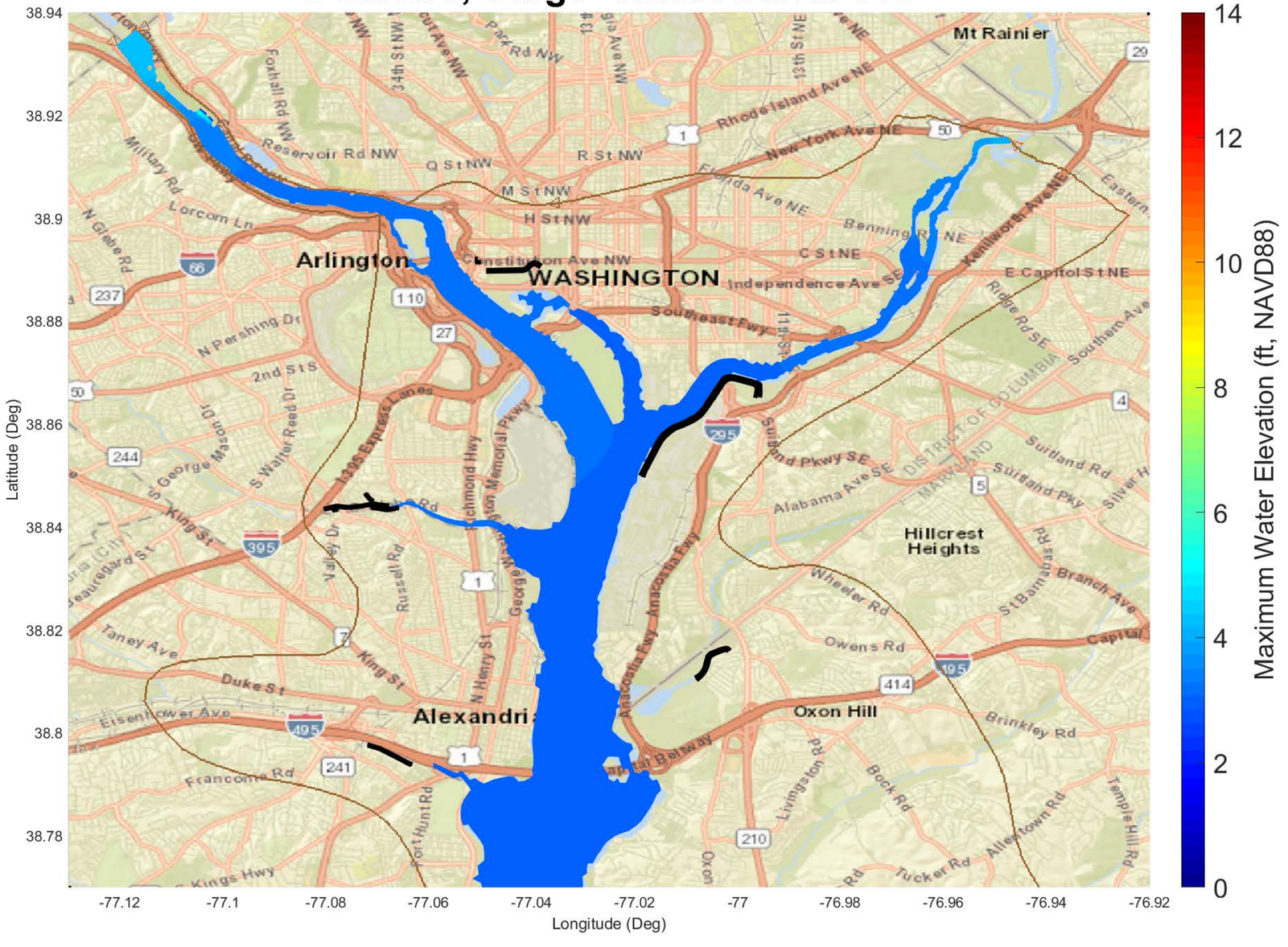

DCMetro, Surge+Tides: Storm 174

DCMetro, Surge+Tides: Storm 204

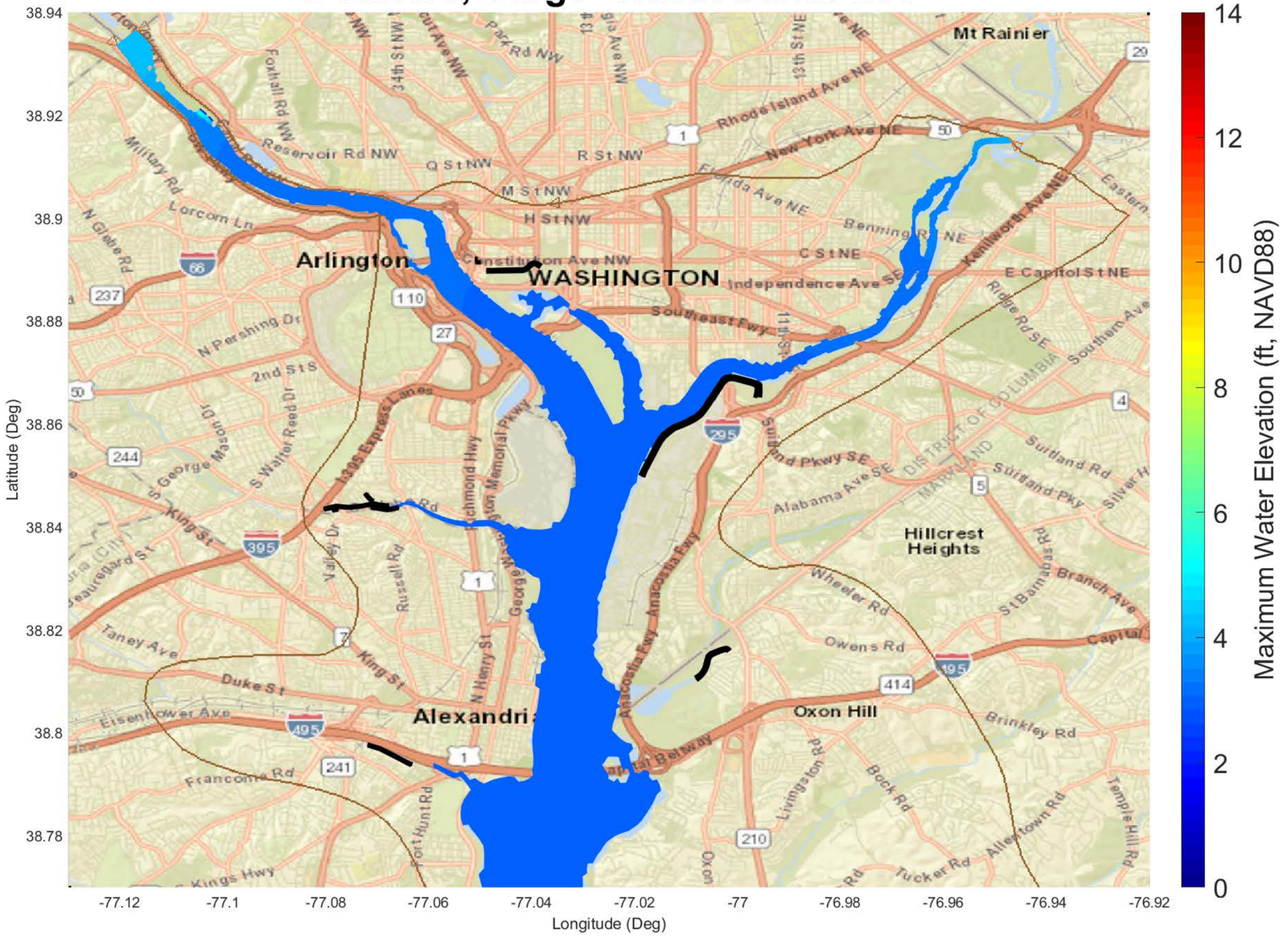

DCMetro, Surge+Tides: Storm 205

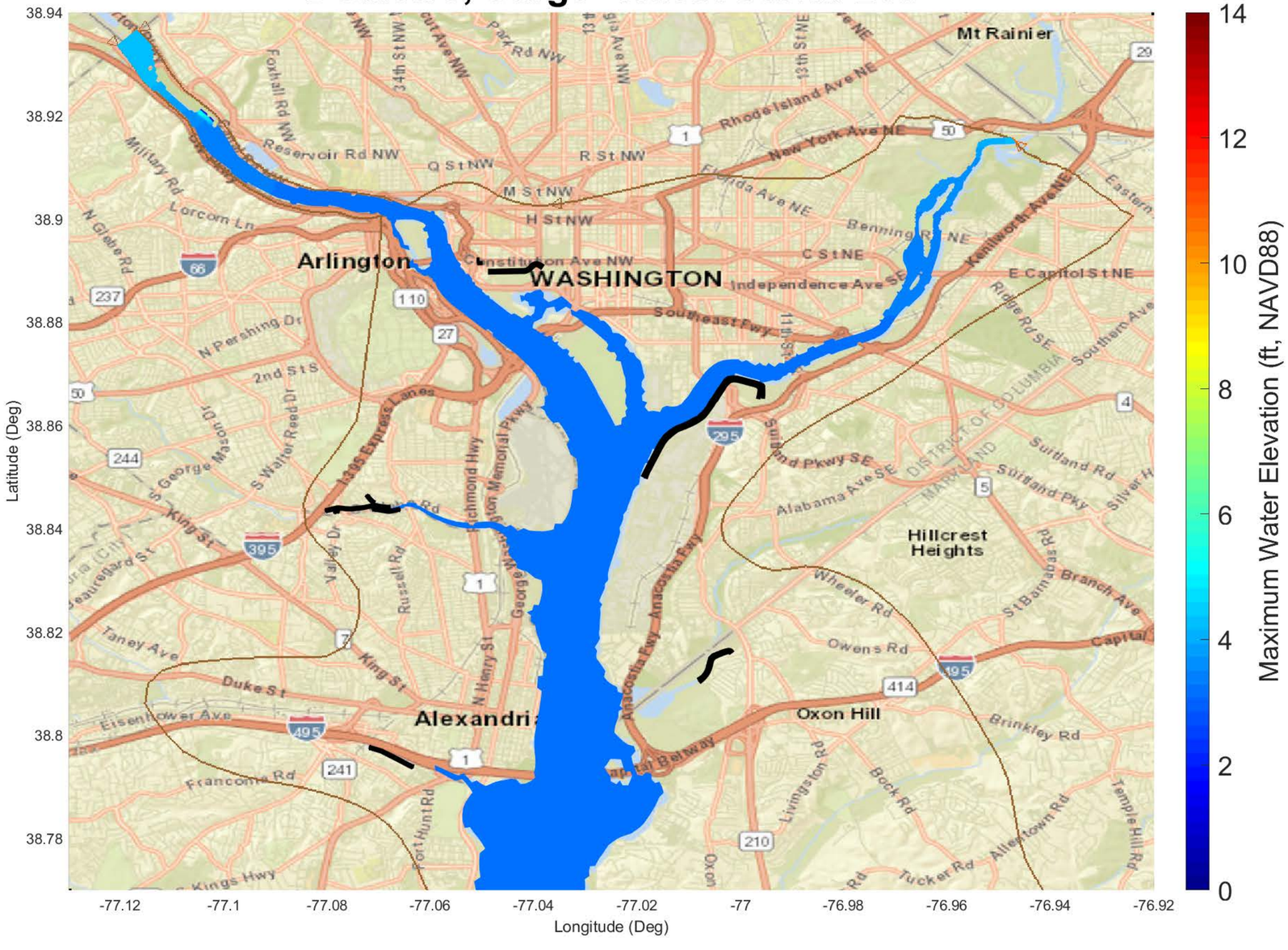

DCMetro, Surge+Tides: Storm 206

DCMetro, Surge+Tides: Storm 210

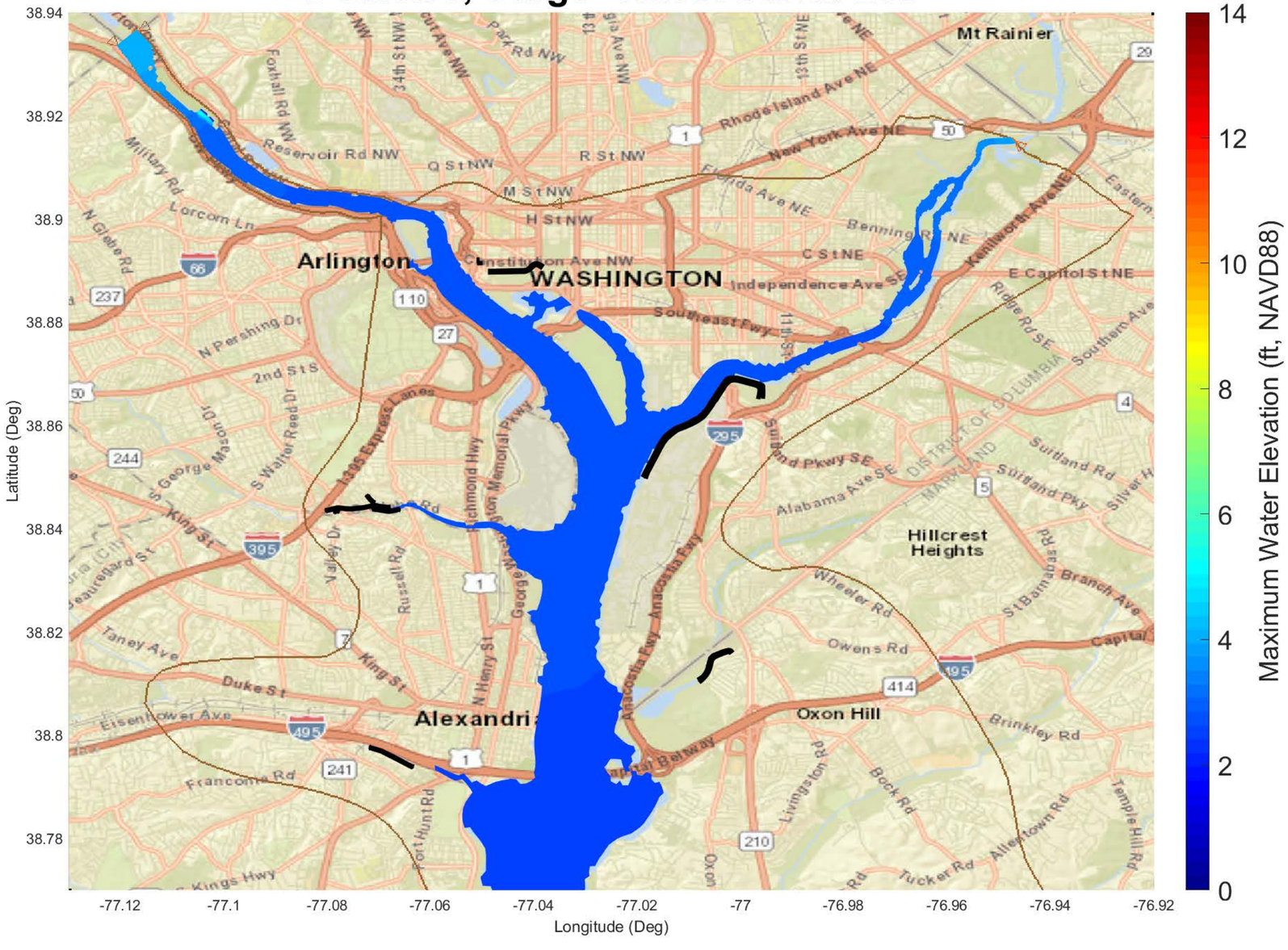

DCMetro, Surge+Tides: Storm 275

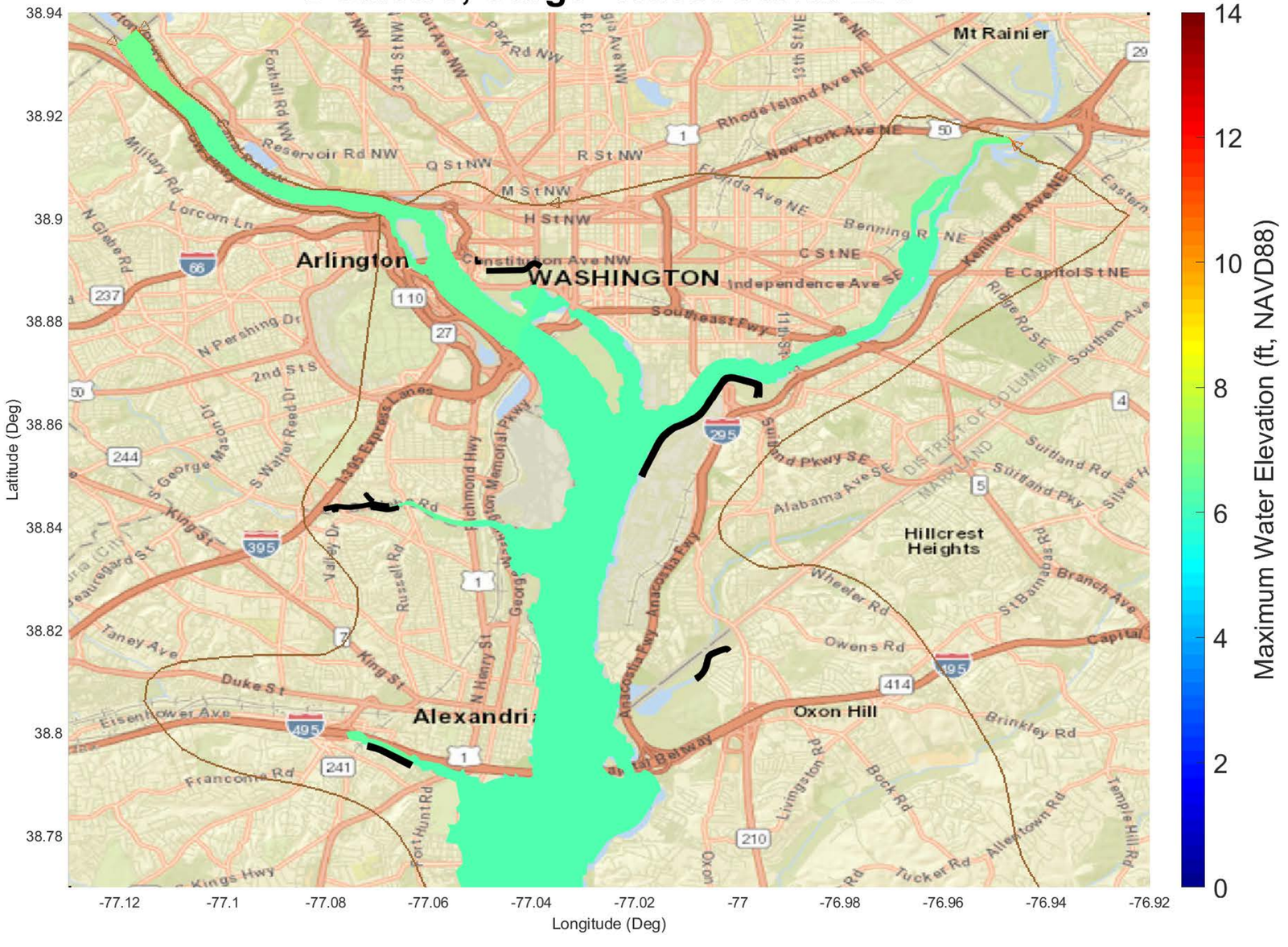

DCMetro, Surge+Tides: Storm 282

DCMetro, Surge+Tides: Storm 283

DCMetro, Surge+Tides: Storm 289

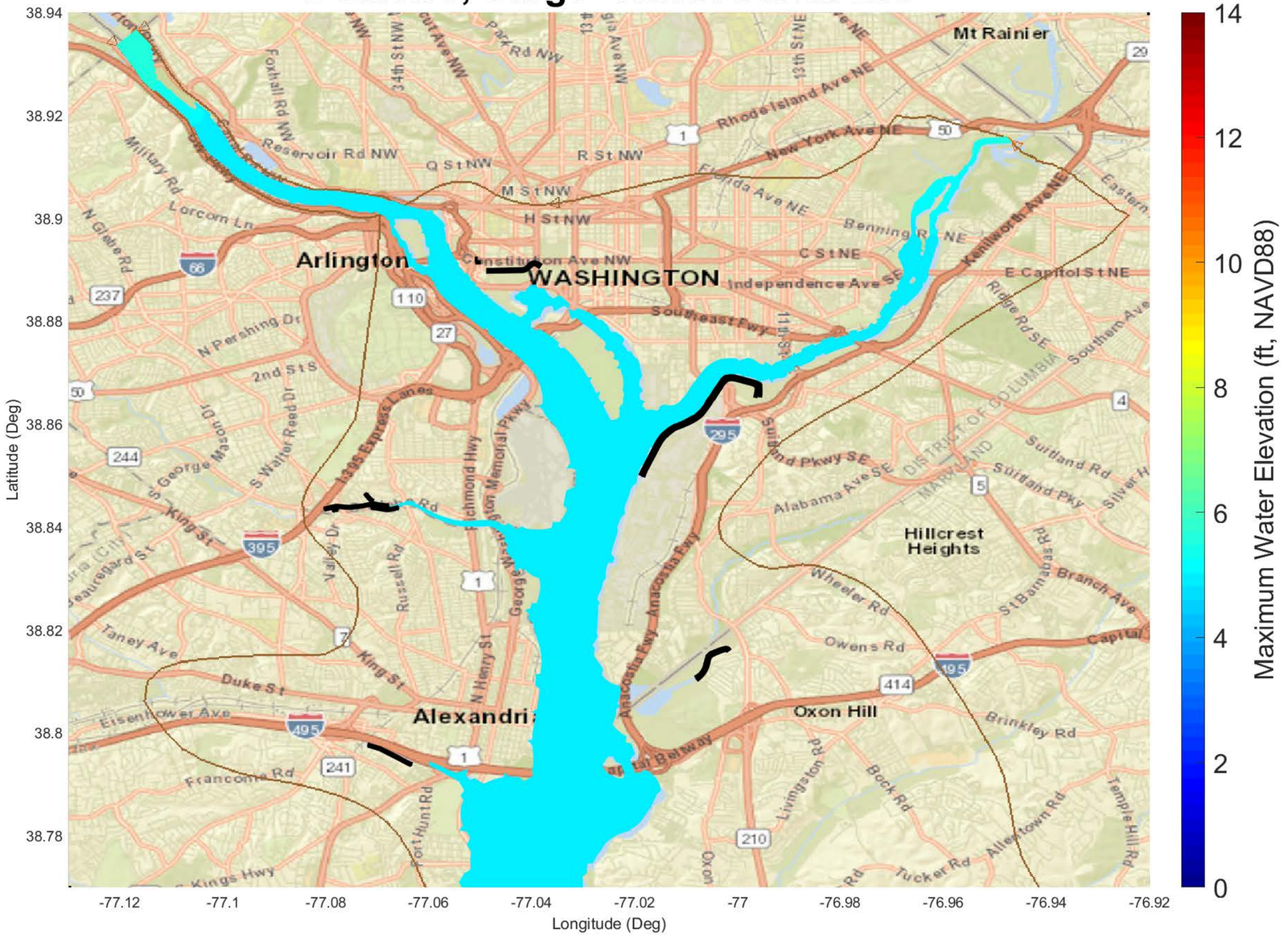

DCMetro, Surge+Tides: Storm 296

DCMetro, Surge+Tides: Storm 391

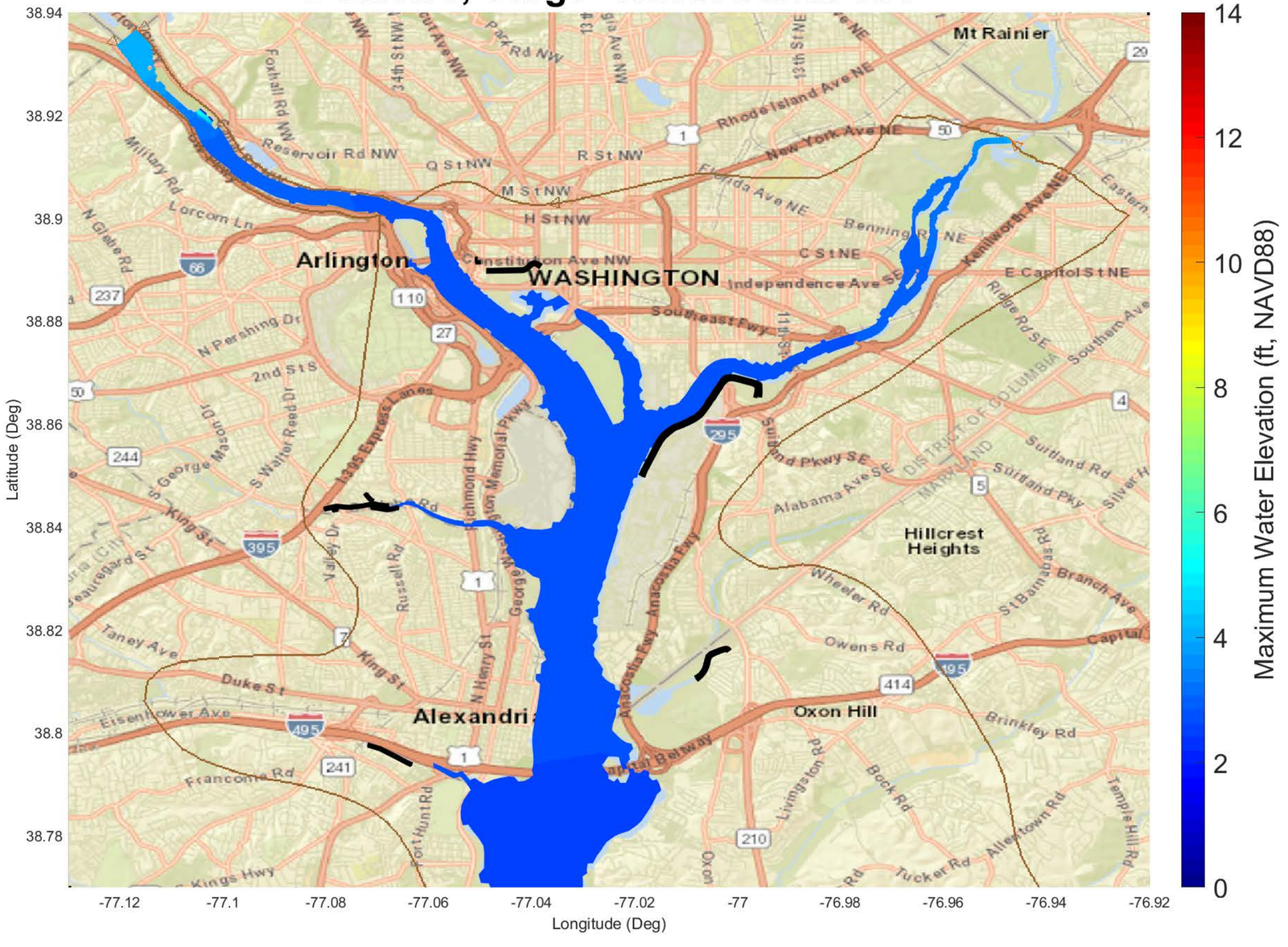

DCMetro, Surge+Tides: Storm 524

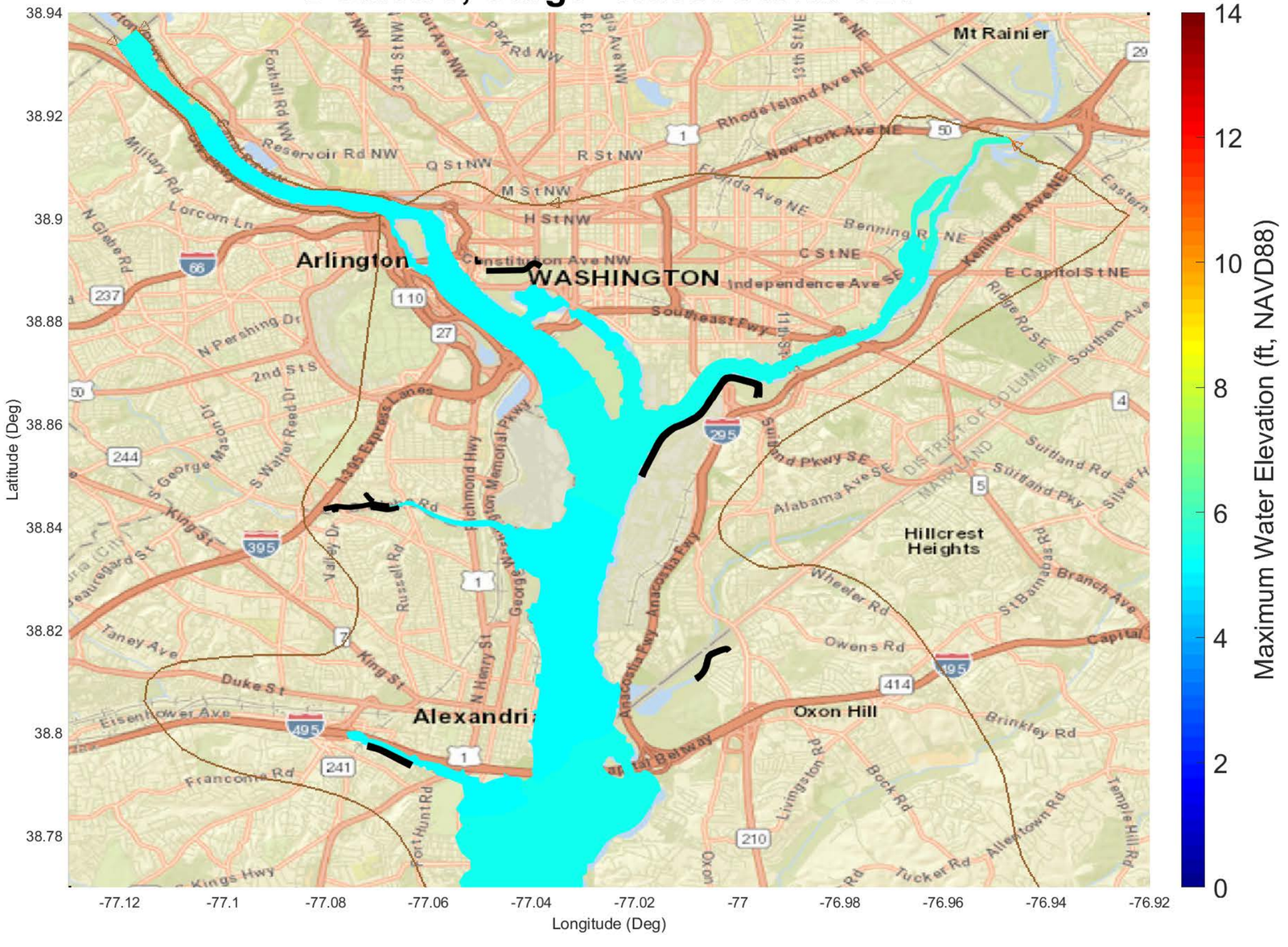

DCMetro, Surge+Tides: Storm 530

DCMetro, Surge+Tides: Storm 532

DCMetro, Surge+Tides: Storm 534

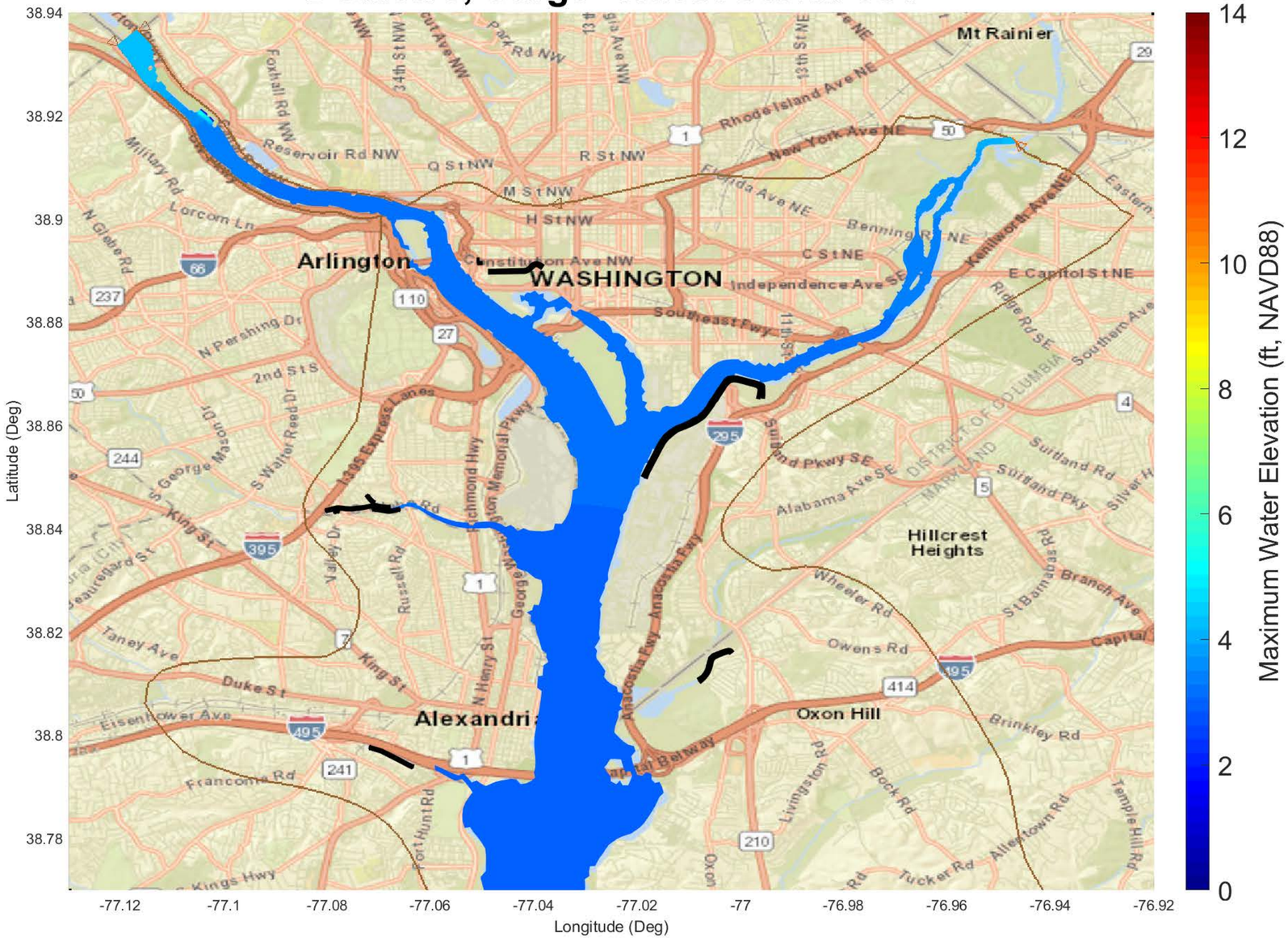

DCMetro, Surge+Tides: Storm 629

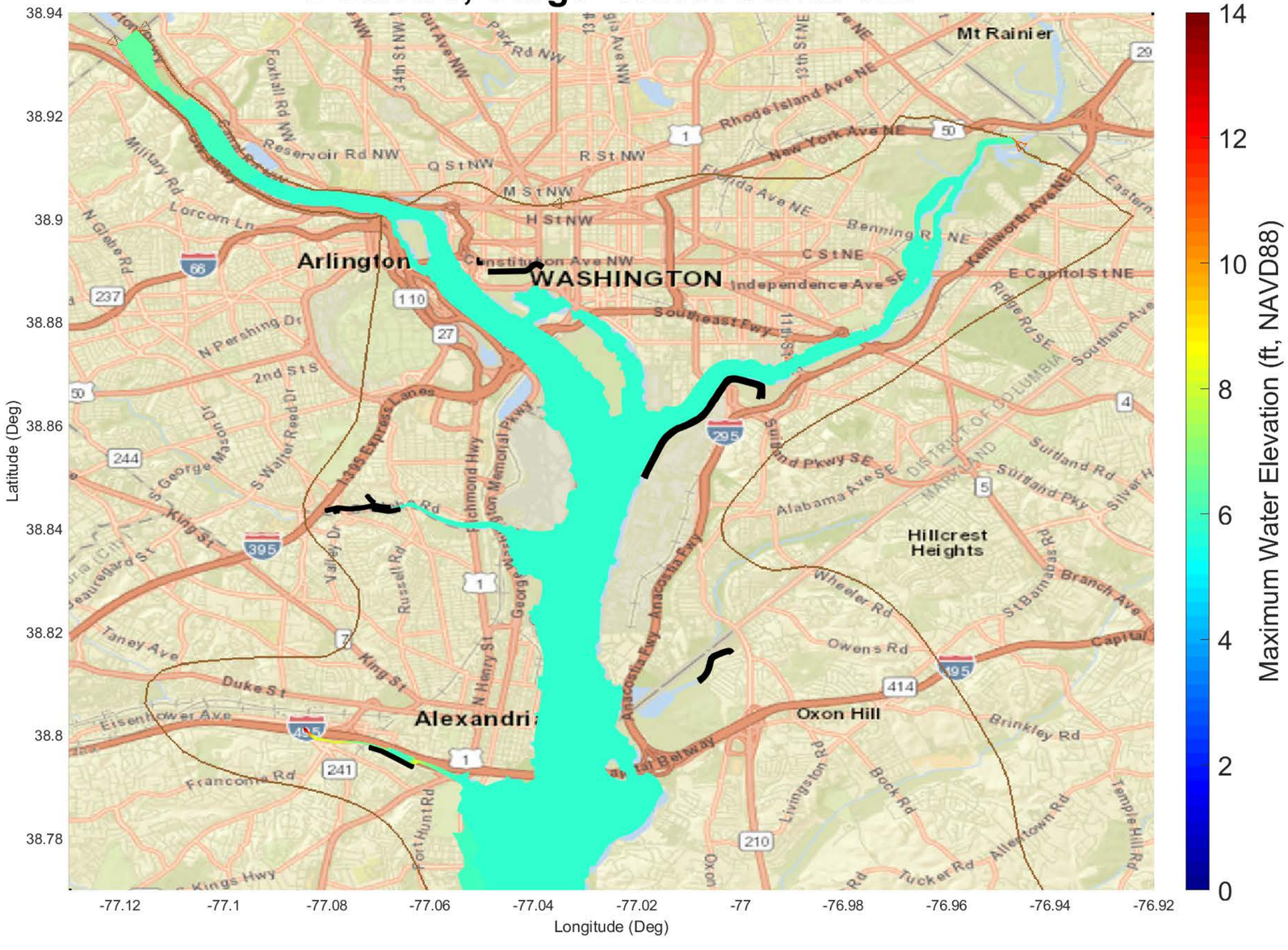

DCMetro, Surge+Tides: Storm 630

DCMetro, Surge+Tides: Storm 631

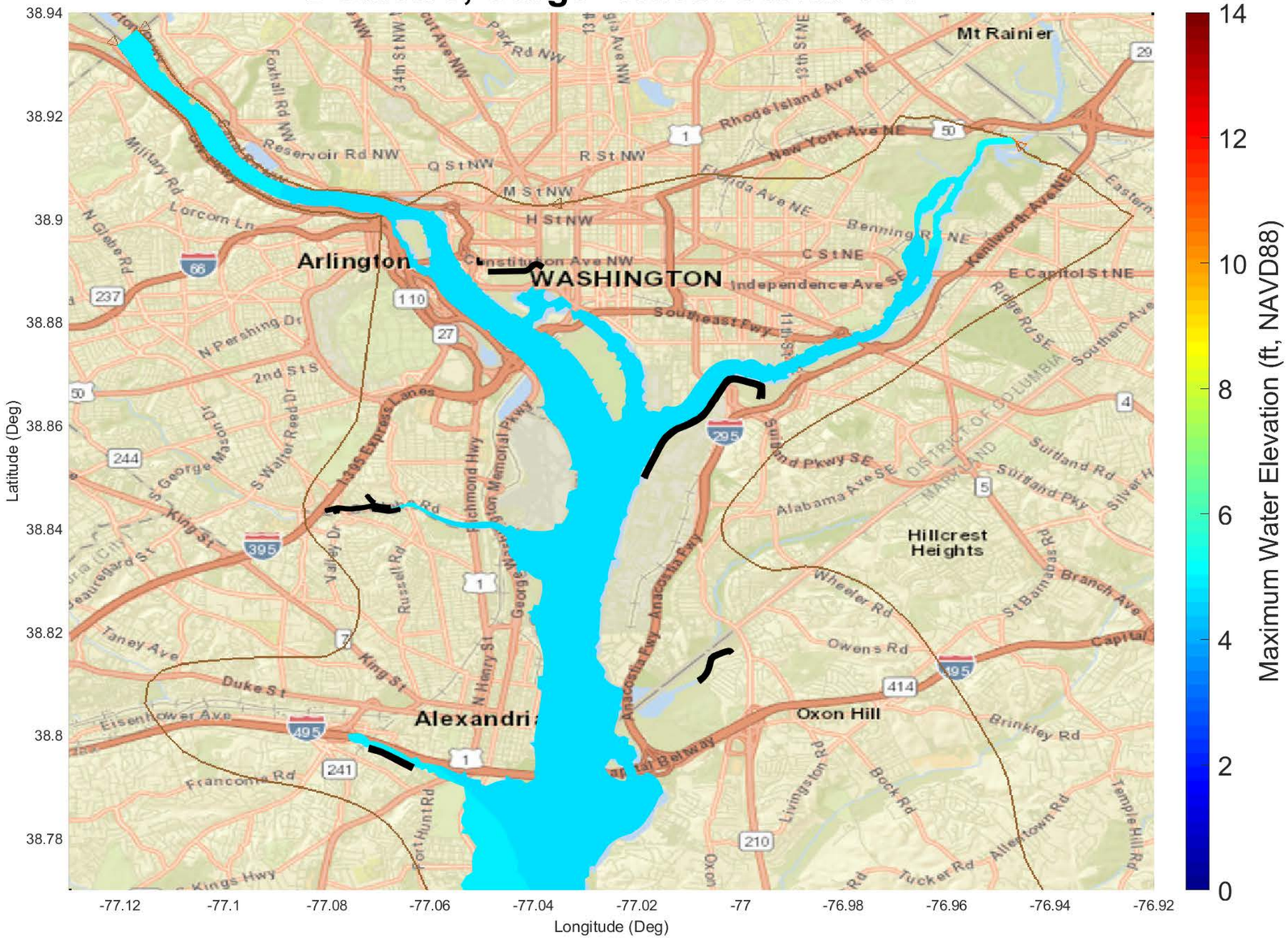

DCMetro, Surge+Tides: Storm 632

DCMetro, Surge+Tides: Storm 633

DCMetro, Surge+Tides: Storm 634

DCMetro, Surge+Tides: Storm 638

DCMetro, Surge+Tides: Storm 640

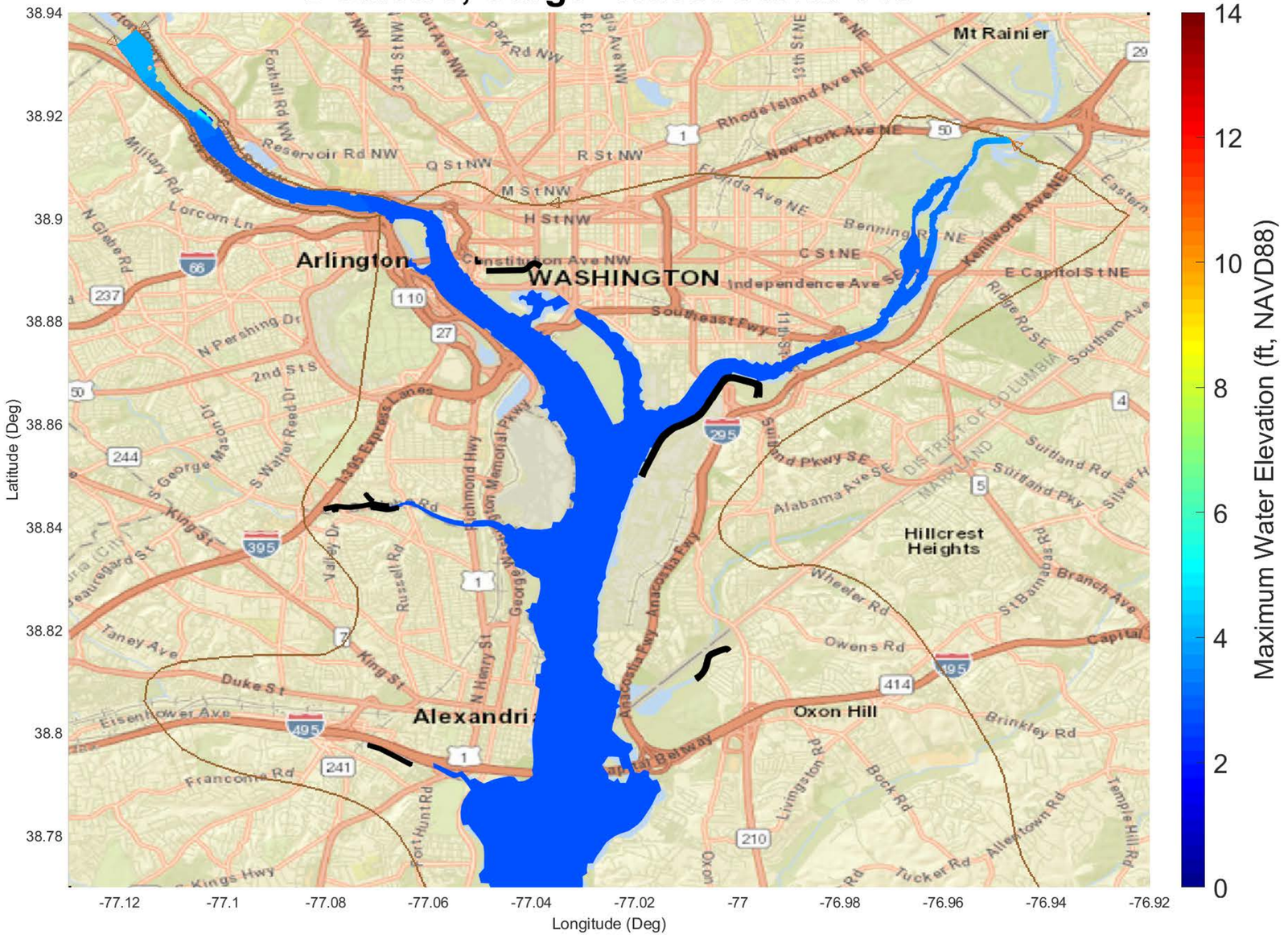

DCMetro, Surge+Tides: Storm 642

DCMetro, Surge+Tides: Storm 643

DCMetro, Surge+Tides: Storm 1003

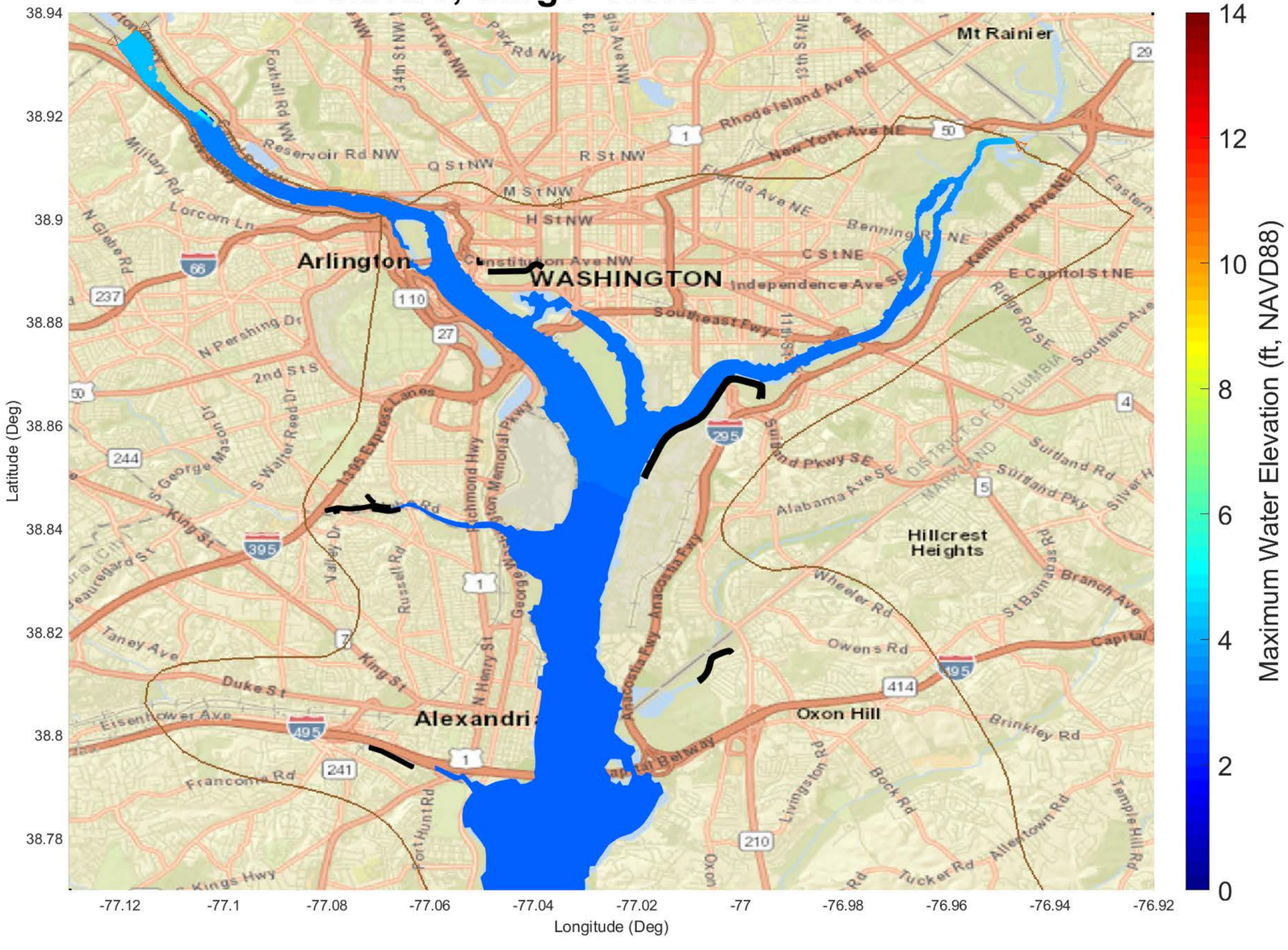

DCMetro, Surge+Tides: Storm 1005

Attachment # 2 Draft ERDC report entitled “Probabilistic Coastal Hazard Analysis: D.C. Metropolitan Coastal Study” dated January 2022

This page left intentionally blank.

ERDC/CHL TR-22-XX

2Coastal and Hydraulics Laboratory

US Army Corps of Engineers®
Engineer Research and Development Center

ERDC
INNOVATIVE SOLUTIONS for a safer, better world

Probabilistic Coastal Hazard Analysis: D.C. Metropolitan Coastal Study

Greg Slusarczyk, Madison C. Yawn, Norberto C. Nadal-Caraballo, Mary Cialone, Luke A. Aucoin, and Alexandros A. Taflanidis

January 2022

DRAFT

The U.S. Army Engineer Research and Development Center (ERDC) solves the nation's toughest engineering and environmental challenges. ERDC develops innovative solutions in civil and military engineering, geospatial sciences, water resources, and environmental sciences for the Army, the Department of Defense, civilian agencies, and our nation's public good. Find out more at www.erdc.usace.army.mil.

To search for other technical reports published by ERDC, visit the ERDC online library at http://acwc.sdp.sirsi.net/client/default.

ERDC/CHL TR-22-XX
January 2022

Probabilistic Coastal Hazard Analysis: D.C. Metropolitan Coastal Study

Greg Slusarczyk, Madison C. Yawn, Norberto C. Nadal-Caraballo, Mary Cialone, and Luke A. Aucoin

Coastal and Hydraulics Laboratory
U.S. Army Engineer Research and Development Center
3909 Halls Ferry Road
Vicksburg, MS 39180—6199

Alexandros A. Taflanidis

University of Notre Dame
Fitzpatrick Hall
Notre Dame, IN 46556

DRAFT

Prepared for

U.S. Army Corps of Engineers, Baltimore District

2 Hopkins Plaza

Baltimore, MD 21201

Abstract

This report summarizes the probabilistic analysis performed by the U.S. Army Engineer Research and Development Center (ERDC) Coastal and Hydraulics Laboratory (CHL) as part of the D.C. Metropolitan Coastal Study. The intent of this work, performed for the U.S. Army Corps of Engineers (USACE) Baltimore District (NAB) and Metropolitan Washington Council of Council of Governments (MWCOG), was to evaluate project alternatives to assess flooding risks induced by coastal storms for the metropolitan area surrounding Washington, D.C. This study applied the USACE's Probabilistic Coastal Hazard Analysis (PCHA) framework to quantify storm surge, leveraging existing synthetic tropical cyclones (TCs) from the North Atlantic Coast Comprehensive Study (NACCS). Using a reduced storm suite (RSS) of synthetic TCs and the historical extratropical cyclones (XCs) from NACCS, hydrodynamic model simulations were performed on an updated grid, including five proposed levee systems, to produce storm responses at 23 save point locations surrounding the D.C. Metropolitan area. Through application of the PCHA framework, the joint probability analysis of TC atmospheric-forcing parameters and their associate storm responses were assessed for the estimation of still water level (SWL) annual exceedance frequencies (AEFs) ranging from 10 to $1x10^{-4}$ yr^{-1}. The final AEFs were then compared to the NACCS SWL AEFs.

Contents

Figures and Tables

Figures

Tables

Preface

The study summarized in this report was conducted as a task within the Probabilistic Coastal Hazard Analysis: D.C. Metropolitan Coastal Study. The study was funded by the U.S. Army Corps of Engineers (USACE) Headquarters through the USACE Baltimore District (NAB) and conducted at the U.S. Army Engineer Research and Development Center (ERDC), Coastal and Hydraulics Laboratory (CHL), Vicksburg, MS, during the period of May 2020 – January 2022. Jacqueline Seiple (NAB) was the primary engineering point of contact.

This report was prepared by the Harbors, Entrances, and Structures (HES) Branch, the Coastal Processes (CP) Branch at CHL, and the University of Notre Dame.

At the time of publication of this report, Mr. Chad R. Bounds was Chief, Harbors Entrances Structures Branch; Ms. Lauren Dunkin, Acting Chief, Navigation Division. Dr. Ty V. Wamsley was Director, CHL, and Mr. Keith W. Flowers was Deputy Director, CHL.

The Commander of ERDC was COL Teresa A. Schlosser, and Dr. David W. Pittman was Director.

Unit Conversion Factors

Most measurements and calculations for this study were done in SI units. The following table can be used to convert SI units to English customary units.

Multiply	By	To Obtain
m	3.28084	ft
km	0.621371	mi
km	0.539957	nmi
km/h	0.621371	mph
km/h	0.539957	kn
hPa	1.0	mb

Notation

Δp	central pressure deficit of tropical cyclone, computed as the difference between a far-field atmospheric pressure of 1,013 hPa and central pressure (hPa)
θ	heading direction of tropical cyclone (deg)
ε	epsilon term
μ	mean
σ	standard deviation
λ	storm recurrence rate (storms/yr/km)
ρ	correlation coefficient
B	Holland B
C	copula
c_p	central pressure (hPa)
R_{max}	radius of maximum winds of tropical cyclone (km)
$tide_{sk}$	skew tide
V_t	translational speed of tropical cyclone (km/h)
x_0	tropical cyclone reference location
ADCIRC	ADvanced CIRCulation numerical model
AEF	annual exceedance frequency (yr^{-1})
ATCS	augmented tropical cyclone suite
BND	bivariate Gaussian (or Normal) probability distribution model

CCDF	complementary cumulative distribution function
CDF	cumulative distribution function
CHS	Coastal Hazards System
CHS-NA	Coastal Hazards System – North Atlantic study
CL	confidence limit
CRL	coastal reference location
CV	coefficient of variation
CSS	Composite Storm Set
DA	data assimilation process
DNC	dry-node correction
DSRR	directional storm recurrence rate
DTWD	doubly truncated Weibull distribution
EBTRK	extended best track database
EKF	Epanechnikov kernel function
EST	Empirical Simulation Technique
EVA	extreme value analysis
FIS	Flood Insurance Study
HI	High intensity
HURDAT	hurricane database
HWM	high water mark

IIF	intensity index function
IPET	Interagency Performance Evaluation Taskforce
GKF	Gaussian kernel function
GKS	Gaussian kernel surface
GPD	generalized Pareto distribution
GPM	Gaussian process metamodeling
GPR	Gaussian process regression
JPA	joint probability analysis
JPM	joint probability method
JPM-OS	joint probability method with optimal sampling
JPM-OS-RS	joint probability method with optimal sampling by response surface
JPM-OS-BQ	joint probability method with optimal sampling by Bayesian quadrature
LACPR	Louisiana Coastal Protection and Restoration
LI	Low intensity
MCAP	Mississippi Coastal Analysis Project
MGC	Meta-Gaussian copula
MI	Medium intensity
MLE	Maximum Likelihood Estimation
MRL	mean residual life

MSL	mean sea level
NACCS	North Atlantic Coast Comprehensive Study
NTR	non-tidal residual
PBL	planetary boundary layer numerical model
PCA	Principal Component Analysis
PCHA	Probabilistic Coastal Hazard Analysis
PDF	probability density function
PDS	partial duration series
RMSD	root-mean-square deviation
SLR	sea level rise (ft)
SRR	storm recurrence rate (storms/yr/km)
SRR_{200km}	recurrence rate associated with storms passing within 200 km of a given location (storms/yr)
SSHWS	Saffir-Simpson hurricane wind scale
STWAVE	STeady-state spectral WAVE numerical model
SWL	still water level
UKF	uniform kernel function
TC	tropical cyclone
XC	extratropical cyclone
Z	basic z-score

1 Introduction

In an effort to assess flood risk for the Washington, D.C. study area, the U.S. Army Corps of Engineers (USACE) Baltimore District (NAB) and the Metropolitan Washington Council of Council of Governments (MWCOG) sought assistance from the USACE Engineer Research and Development Center's (ERDC) Coastal and Hydraulics Laboratory (CHL) to evaluate project alternatives in the form of a levee system for flood risk reduction. Washington, D. C. is bordered by the Potomac and Anacostia Rivers which are tidally influenced by the Chesapeake Bay. Although the Chesapeake Bay offers some protection from wave hazards, this area is impacted by both tropical cyclones (TCs) and extratropical cyclones (XCs), making it vulnerable to the effects of storm-induced hazards like surge. In recent years, Washington, D.C. has seen the impacts of TCs, such as Hurricane Isabel, which produced an 8 ft storm surge (Beven and Cobb 2014).

Due to the governmental and cultural importance of Washington, D.C., the main goal of this study was to investigate the project alternatives and their impact on flood risk reduction for the study area. This work was completed by leveraging the existing North Atlantic Coast Comprehensive Study (NACCS) (Cialone et al. 2015; Nadal-Caraballo et al. 2015) storm suite to simulate a reduced storm suite (RSS) of synthetic TCs on an updated mesh that included the project alternatives. These alternatives were assessed by determining the magnitude of still water level (SWL) (surge + astronomical tide) annual exceedance frequencies (AEF) as compared to the SWL AEFs computed as part of the NACCS.

1.1 Background

Coastal flooding is primarily caused by rainfall, storm-induced water levels, and waves. For the northeastern U.S. Atlantic coastline, tides can have a significant influence on the degree of flooding given their large amplitudes. For the D.C. area, TCs and XCs have historically caused significant coastal flooding. The analysis conducted as part of this study for the quantification of coastal storm hazards focuses on the probabilistic characterization of storm forcing and responses for the study area. The primary goal of this study was the estimation of coastal storm hazard AEFs at 23 save point locations relative to the D.C. Metropolitan (D.C. Metro) study area. Estimating these AEFs required the development of a joint

probability model of TC atmospheric-forcing parameters and statistical analysis based on the StormSim-Stochastic Simulation Technique (StormSim-SST) for simulated responses of historical XCs.

The work described in this technical report follows the Coastal Hazards System's (CHS) (https://chs.erdc.dren.mil) Probabilistic Coastal Hazard Analysis (PCHA) framework developed by the USACE (Nadal-Caraballo et al. 2020) in collaboration with the University of Notre Dame. Since the D.C. Metro study area was included within the NACCS, this study leveraged the storm suite and hydrodynamic modeling grids from the 2015 regional study. As a result of the NACCS, a storm suite was developed to cover the probability and parameter spaces of TCs from Virginia to Maine, which resulted in a suite of 1050 synthetic TCs. Coastal hazards within this region are also influenced by XCs, therefore 100 historical XCs were included as part of the NACCS storm suite. The TCs and XCs from the NACCS were leveraged for this study in order to quantify coastal storm wave and water level extremal statistics for the D.C. Metro study area. Although the hydrodynamic modeling grids were also leveraged, they were significantly updated to include changes in bathymetry and mesh resolution as well as mesh alterations to include the project alternatives. For this study, the project alternatives considered were five proposed levee systems which are illustrated in Section 5.

1.2 Overview

The D.C. Metro study took advantage of the PCHA framework developed by ERDC-CHL as well as recent statistical and machine-learning improvements implemented other hurricane-exposed regions including the CHS' South Atlantic Study (SACS) (Nadal-Caraballo et al. 2022; Yawn et al. 2022a; Yawn et al. 2022b). The PCHA is a statistical and probabilistic framework that builds upon the methodology of the Joint Probability Method (JPM) for more robust and accurate quantification of coastal storm hazards and estimation of uncertainty. Generally, joint probabilistic analysis (JPA) of coastal storm hazards requires the evaluation of historical TC data, including the characterization of regional storm climatology and the development of a joint probability model of TC atmospheric-forcing parameters. Standard TC parameters used to describe hurricane and tropical storms are: track reference location, heading direction, central pressure deficit (intensity), radius of maximum winds (size), and translational speed. The magnitude and range of storm surge, for example, is primarily a function of storm intensity and size as well as

the along-shore location relative to the eye of the storm, as discussed in Toro et al. (2010).

Rather than relying on extrapolation beyond the historical record, the JPM applies marginal probability distributions and a joint probability model of TC forcing parameters; these distributions are subsequently discretized, resulting in multiple TC parameter combinations efficiently covering the parameter and probability spaces. Each of these combinations constitutes a synthetic TC. Weights, or probability masses, are computed for the resulting synthetic TC population, considering the relative likelihood of each synthetic TC event along with the magnitude of the storm response (e.g., storm surge, wave height) that it generates. The storm probability masses are integrated over the range of storm responses to compute the corresponding AEFs. The term *storm response* is used to describe a hydrodynamic reaction to storm forcing. *Storm forcing* refers to the characteristics of a storm, including atmospheric pressure and wind fields. Finally, results are conveyed through *hazard curves* which express the magnitude of a given coastal hazard as a function of AEFs.

1.3 Approach

Executing this study and conducting the PCHA required sampling sufficient number of synthetic TCs to efficiently blanket a wide range of hurricane atmospheric and hydrodynamic characteristics. Spanning the atmospheric-forcing parameter and probability spaces is necessary to accurately quantify coastal storm hazards such as storm surge and waves over the study area. For the NACCS, optimal sampling of the joint distribution of TC atmospheric parameters yielded 1050 unique TCs that encompassed the full range of the practical hazard, from frequent to very rare events (Nadal-Caraballo et al. 2015). As a means for capturing the climatology of the study region, this storm suite consists of landfalling, bypassing, and land-exiting synthetic TCs. An RSS of 60 storms was chosen from the NACCS synthetic TC suite for characterizing the SWL AEFs for the D.C. Metro study area.

As part of the CHS-North Atlantic (CHS-NA) study, a statistical update performed for the NACCS region, an augmented TC suite (ATCS) consisting of 1,098,720 storms was subsequently developed through hyper-discretization of the TC parameter space. The CHS-NA ATCS was leveraged for this study to perform a more robust probabilistic analysis of storm surge than was possible with the RSS alone. The hydrodynamic

responses of the ATCS were estimated through the application of Gaussian process metamodeling (GPM), a machine learning technique developed in collaboration with the University of Notre Dame.

An observation screening and sample-space optimization process (Nadal-Caraballo and Melby 2014; Nadal-Caraballo et al. 2012) was employed to select XCs for the NACCS storm suite. Storm surge and meteorological measurements corresponding to the 1938-2013 period were sampled to define significant extratropical events. The result was an efficient sample that yielded 100 historical XCs that were then modeled using high-fidelity climate and hydrodynamic numerical models. Due to instabilities in multiple simulations, the storm responses of 94 NACCS historical XCs were applied in the PCHA.

As a result of the analysis performed herein, the coastal storm induced hazards were quantified as AEFs ranging from 10 to $1x10^{-4}$ yr^{-1} for still water level (SWL) (surge + astronomical tide) at 23 save point locations surrounding Washington, D.C.

The following sections describe in detail the PCHA framework and its implementation within this study. Section 2 provides context to the probability analysis of TC responses using the JPM, and Section 2.4 describes advancements of the PCHA over the standard JPM approach. The storm climatology for the study area and storm recurrence analysis performed herein are discussed within Section 3. The joint probability analysis (JPA) of TC parameters through the development of marginal probability distributions and correlation coefficient matrices, as well as the characteristics of the storm suite applied in this study, are described in Section 4. In Section 5, the mesh modifications and the simulations are discussed. Section 6 provides details on the computation of hazards including the application of GPM techniques, the correction of bias and quantification of uncertainty, the correction applied to the ATCS responses, and the integration of TC responses. Section 6 also provides a comparison of the D.C. Metro P results with the NACCS results to illustrate the impacts of the mesh modifications. Section 7 provides the final conclusions and summary of the analysis conducted herein.

2 Probabilistic Coastal Hazard Analysis (PCHA)

The CHS (https://chs.erdc.dren.mil) is a national effort for quantification of coastal storm hazards along all United States coastlines. Coastal hazards from hurricanes and extreme extratropical storms can include storm surge, waves, wind, rainfall, compound coastal-inland flooding, seiche, and extreme tides, among others. Climate change and sea level rise (SLR), which are expected to significantly exacerbate coastal flooding in the upcoming decades, are also part of the CHS' scope. These coastal hazards can threaten the lives of millions of people living in coastal regions, and devastate coastal communities and infrastructure, resulting in profound adverse social, economic, and environmental impacts.

The foundation of the CHS is its PCHA framework. The PCHA is a comprehensive statistical and probabilistic framework for characterization of regional storm climatology, joint probability analysis of atmospheric forcing and storm responses, high-resolution numerical modeling, machine learning, and quantification of associated aleatory and epistemic uncertainties. In the CHS' PCHA framework, past tropical cyclones and hurricanes are parameterized according to their track path, heading direction, central pressure deficit, radius of maximum winds, and translational speed. These parameters and their dependencies are used to develop suites of synthetic TCs fully covering the range of storm parameter and probability spaces. The CHS also features a database hosting dozens of terabytes of coastal data, a web-tool for easy access to results, and a website with corresponding documentation and metadata.

The CHS database includes PCHA results currently encompassing more than 4,300 synthetic TCs, hundreds of XCs, and multiple future sea level conditions, totaling more than 15,000 unique high-resolution numerical hydrodynamic simulations resolving non-linear interactions between storm surge, wind waves, astronomical tide, and sea level rise. The CHS ensures accurate, robust, and consistent quantification of coastal hazards along most United States coastlines, thus facilitating the implementation of nation-wide coastal storm risk management and resilience strategies. CHS data also supports individual feasibility studies, economics analyses, evaluation of nature-based features, stochastic engineering design, and risk assessments.

A primary goal of the CHS-PCHA framework is addressing the limitations of the JPM and derived optimal sampling (OS) approaches which are discussed in the next sections.

2.1 Joint Probability Method (JPM)

The JPA of storm surge and waves from TCs, in most cases, suffers from a lack of historical observations resulting in small sample sizes. Moreover, some of the characteristics of the TCs that impact a particular area may make it necessary to consider them as belonging to different subpopulations, further reducing the already small sample sizes. Storm intensity has been identified as such a characteristic, since intense hurricanes tend to behave differently from weak TCs (Resio et al. 2007). The JPM addresses these limitations by focusing on characterizing storm forcing instead of their responses. In broad terms, TCs are defined by a number of forcing parameters and corresponding probability distribution functions (PDFs), which are discretized to generate the wind and pressure fields required for the simulation of storm surge and waves. TC forcing parameters include: track reference location (x_o), heading direction (θ), central pressure deficit (Δp), radius of maximum winds (R_{max}), and translational speed (V_t). The JPM has become the standard joint probabilistic model for estimating coastal storm hazards in hurricane-prone areas.

Gonzalez et al. (2019) summarized the development and evolution of the JPM. Early characterization and probabilistic analyses of individual hurricane parameters were performed by Myers (1954). The precursor of the JPM was pioneered in the late 1960s (Russell 1968a, 1968b) using a full Monte Carlo simulation to estimate probabilities of wind, storm surge, and wave loads on offshore structures. Beginning in the 1970s, NOAA further developed and adapted the JPM for hurricane climatology and probabilistic storm surge studies in the U.S. Atlantic and Gulf of Mexico coastal areas through several publications (e.g., Myers 1970, 1975; Ho 1974; Ho and Myers 1975). The total annual frequency of a given water level was determined by adding separately calculated frequencies from landfalling hurricanes, bypassing hurricanes, and XCs. By the late 1980s, FEMA had adopted the JPM (FEMA 1988) as presented in the National Weather Service report NWS-38 (Ho et al. 1987).

Although the JPM approach has been implemented since the 1970s, recent advancements in sampling techniques and the development of the JPM-

OS have made it possible to reduce the necessary number of synthetic storms, more efficiently characterizing the parameter and probability spaces. Different implementations of the JPM emerged as a result of several studies conducted following the devastation caused by Hurricane Katrina which occurred in 2005. These approaches, their advancements, and methods of implementation are discussed herein.

2.2 Joint Probability Method with Optimal Sampling (JPM-OS)

The destruction caused by Hurricane Katrina in 2005 led to the proliferation of storm surge hazard studies that brought further improvements to the JPM. Of particular importance was the work done by the IPET in which JPM with OS approaches were developed for the statistical analysis of extreme water levels to evaluate the performance of the Southeast Louisiana hurricane surge protection system. The IPET provided the basic framework for storm surge modeling approaches used in later works. This effort, led by a team of USACE, FEMA, NOAA, private sector, and academic researchers, was documented in the IPET (2009) report. The goal of these JPM-OS developments was the reduction in the number of storms required for populating the parameter space without sacrificing resolution and accuracy relative to the probability space.

JPM variants labeled as *OS* include the JPM by Bayesian Quadrature (JPM-OS-BQ), and the JPM with augmented sampling by means of Response Surface (JPM-OS-RS). In practice, the optimal sampling and thus the reduction in the number of storms is actually accomplished by either: 1) expert selection of TC parameter combinations (e.g., JPM-OS-RS); or 2) trial-and-error sampling of a storm subset that closely matches target hazard curves produced by a much larger storm set simulated using a low-fidelity hydrodynamic model or a high-fidelity model with a coarse grid (e.g., JPM-OS-BQ). The number of sampled storms generally decreased from potentially tens of thousands of storms (denoted as the reference set) to a few hundred.

The JPM-OS-RS approach (Resio et al. 2007), as described in Toro et al. (2010a), requires careful selection of TC parameter combinations based on expert judgment. This selection should yield a moderate number of synthetic TC simulations used to construct a response surface of storm surge elevation. The TC parameter space is filled in by interpolating intermediate surge values from the response surface using a finer discretization primarily considering the Δp-R_{max} bivariate space. In this

scheme the surge response is assumed to have small, linear variation along the θ-V_t space. Storm surge values interpolated from the response surface have been shown to introduce uncertainty with root-mean-square deviation (RMSD) on the order of 0.70 m (CPRA 2013). The JPM-OS-RS approach was applied to regional studies such as LACPR (USACE 2009) and the Flood Insurance Study (FIS) for Coastal Counties in Texas (USACE 2011).

As stated in Operating Guidance No. 8-12 document (FEMA 2012), FEMA's guidelines focused on JPM-OS-BQ (Toro 2008) approach "since it is more readily automated than the [JPM-OS-RS] which requires a greater degree of expert judgment in the selection of storms." This acknowledgement made JPM-OS-BQ the de facto JPM approach of FEMA's National Flood Insurance Program (NFIP) Risk MAP program. Beginning with the Mississippi Coastal Analysis Project (MCAP) (FEMA 2008), most FEMA studies to date have relied on this approach.

Reliance on choices made on the basis of judgment are not unique to the JPM-OS-RS. The JPM-OS-BQ approach requires the development and simulation of a JPM storm set consisting of thousands or tens of thousands of TCs to construct a reference set of storms and corresponding target hazard curves prior to conducting the storm sampling. The primary shortcoming of the JPM-OS-BQ approach is that, due to computational constraints, in practice it must rely on low-fidelity hydrodynamic models that do not incorporate all physical processes or models with coarse-resolution grids for efficient simulation of the storms that constitute the reference set.

Moreover, the JPM-OS-BQ employs a double-exponential covariance function (Toro et al. 2010a) as a pseudo dependence structure with correlation distances as inputs that dictate the discretization of TC marginal distributions. As discussed by Niedoroda et al. (2010) and Toro et al. (2010a, 2010b), the BQ correlation distances must be specified based on expert judgement. The JPM-OS-BQ sampling scheme consists of a trial-and-error process where various combinations of these correlation distances yield different storm sets, and the storm surge hazard curves from each set are compared to the target hazard curves from the reference set at select locations within the study area. The end goal is to select the storm set which storm surge hazard curves are closest to those of the reference set. However, the reliability of the target hazard curves is

unknown, particularly outside open water domains, and they potentially incorporate significant bias from the low-fidelity or coarse-grid simulations of the storm in the reference set. Another limitation of the so-called OS approaches is the lack of an actual joint probability model or consideration of joint probability distribution. In practice, TC parameters have been assumed to be independent, or pairs of TC parameters have been linked through simplified linear relationships.

In summary, the JPM-OS approaches initially adopted by federal agencies (e.g., BQ and RS) include some limitations that have not been adequately documented and corrected. This report discusses how the CHS-PCHA framework developed by USACE overcomes some of the previous JPM limitations related to the lack of a dependence structure correlating the TC atmospheric-forcing parameters, optimal sampling scheme, dry-node correction of hydrodynamic results, and quantification of spatially-varying bias correction and uncertainty.

2.3 The CHS' Probabilistic Coastal Hazard Analysis (PCHA)

As part of the CHS, the USACE initially developed a version of the JPM with a hybrid optimal sampling approach for the North Atlantic Coast Comprehensive Study (NACCS) (Cialone et al. 2015; Nadal-Caraballo et al. 2015) and the Coastal Texas Protection and Restoration Study (CTXS) (Nadal-Caraballo et al. 2018; Melby et al. 2021). This hybrid JPM-OS approach evolved into the PCHA framework through the incorporation of significant advancements further discussed in Section 2.5.

Although the details in the application of the JPM can vary significantly by study, the different approaches typically follow a common general methodology, depending on the dominant processes and respective solution strategies. The JPM methodology generally includes the following steps:

- characterization of historical storm climatology
- computation of historical storm recurrence rate (SRR)
- development of PDFs of historical TC parameters
- discretization of PDFs of TC parameters
- development of synthetic TC suite
- atmospheric and hydrodynamic modeling of synthetic TC suite
- quantification of uncertainties

- integration of joint probability of TC probability masses and responses, including error terms to compute AEF of coastal storm hazards

The AEF of coastal hazards such as storm surge or waves at any given site is a function of three main components: the SRR, the joint probability of characteristic TC parameters, and the storm responses. The AEF is computed from the JPM integral, which is presented in Nadal-Caraballo et al. (2019) with the form:

$$\lambda_{\tau(\hat{x})>\tau} = \lambda \int P[\tau(\hat{x}) > \tau|\hat{x}]\, f_{\hat{x}}(\hat{x}) d\hat{x} \quad (2\text{-}1a)$$

$$\approx \sum_i^n \hat{\lambda}_i\, P[\tau(\hat{x}_i) > \tau|\hat{x}_i] \quad (2\text{-}1b)$$

The JPM integral including uncertainty, which is presented in Nadal-Caraballo et al. (2019), takes the following form:

$$\lambda_{\tau(\hat{x})>\tau} = \lambda \int P[\tau(\hat{x}) + \varepsilon > \tau|\hat{x}, \varepsilon]\, f_{\hat{x}}(\hat{x}) f_{\varepsilon}(\varepsilon) d\hat{x} d\varepsilon \quad (2\text{-}2a)$$

$$\approx \sum_i^n \hat{\lambda}_i\, P[\tau(\hat{x}_i) + \varepsilon > \tau|\hat{x}_i, \varepsilon] \quad (2\text{-}2b)$$

where $\lambda_{\tau(\hat{x})>\tau}$ = AEF of TC response τ due to the atmospheric-forcing vector $\hat{x} = f(x_o, \theta, \Delta p, R_{max}, V_t)$; λ = SRR (storms/year/km); $P[\tau(\hat{x}) + \varepsilon > \tau|\hat{x}, \varepsilon]$ = conditional probability that the i-th TC with parameters $\hat{x}$ generates a response larger than τ; ε = unbiased error term or aleatory uncertainty of TC response; and n = number of TCs.

Recent CHS-PCHA studies, such as the SACS, employ the discrete form of the JPM integral without error term, ε, [Equation (2-1b)] as uncertainty is conveyed through confidence limits (CLs) as further discussed in Section 6.5.

In the discrete form of the JPM integral given in Equation (2-1b, 2-2b), $\hat{\lambda}_i$ is defined as the probability mass (storms/year) of i-th synthetic TC, where $\hat{\lambda}_i = \lambda p_i$, and p_i is the product of its discrete joint probability and the TC track spacing (in km) as defined in the JPM.

The TC atmospheric-forcing parameters commonly used in JPM for the characterization of TCs and included in the forcing vector $\hat{x}$ are

- track reference location (x_o)
- heading direction (θ)
- central pressure deficit (Δp)
- radius of maximum winds (R_{max})
- translational speed (V_t).

The parameter x_o is characterized through the computation of SRRs (Section 3.1.5). Subsequently, either a marginal or a conditional PDF is fitted to each of the remaining atmospheric-forcing parameter (i.e., θ, Δp, R_{max}, and V_t). This is done to properly capture the likelihood of occurrence of each of these parameters according to historical hurricane records. The PCHA implements a hybrid approach for discretizing these PDFs. To ensure optimal coverage of both probability and parameter spaces, as well as spatial coverage of the study region, a structured discretization approach is used for the θ and Δp distributions. Discretization of R_{max} and V_t is performed by BQ method. Synthetic TCs are thus developed as likely combinations of the atmospheric-forcing parameters, as sampled from their respective PDFs. The parameters of the synthetic TCs are used as inputs to the PBL model to estimate the time histories of the wind and pressure fields that drive high-fidelity storm surge and wave numerical hydrodynamic models.

Generally, two distinct types of uncertainty are recognized: aleatory and epistemic. *Aleatory* uncertainty acknowledges the presence of random variability in physical processes that cannot be exactly replicated. Estimates of such nondeterministic processes can be improved, yet they cannot be significantly reduced at present. *Epistemic* uncertainty refers to a lack of information or knowledge about the physical world. Epistemic uncertainty is reducible through selection and application of alternative data, models, and methods using approaches such as logic trees, which is outside the scope of this study. Sources of aleatory uncertainty often accounted for in JPM and PCHA studies generally include: (1) hydrodynamic modeling errors potentially arising from unresolved physical processes, inadequate resolution, and bathymetry inaccuracy; and (2) atmospheric modeling errors due to idealized wind and pressure fields and wind variations not captured by the PBL model.

2.4 Statistical Analysis of Extratropical Cyclones

Probabilistically assessing XC driven coastal storm hazards relies on the extreme value analysis (EVA) of historical storm responses. EVA is

performed on historical water level measurements available at gauges, since the JPM is not suitable for characterizing XC-driven coastal hazards. However, performing EVA when sufficient historical water level measurements are not available should rely on simulated storm responses developed by high-fidelity numerical models. When assessing XC responses using this methodology, time series data must first be collected by estimating the non-tidal residuals (NTRs). The way in which NTRs are estimated varies depending on the geographical region. In the North Atlantic and Pacific coasts, for example, the approach used to compute the NTR consists of subtracting a predicted astronomical tidal time series from a time series of verified water level measurements (Nadal-Caraballo and Melby 2014). For the selection of historical XCs, this approach to identify the NTRs was applied as part of the NACCS. The second step consists of identifying storm events within the period of the NTR time series. A method known as peaks-over-threshold (POT) is commonly used for censoring the time series. When performing POT, all NTRs above a certain threshold are identified and sampled from the historical record. An additional screening process of wind and pressure measurements is required to verify that sampled NTRs are actually wind-driven surges.

Nadal-Caraballo et al. (2012) developed the composite storm set (CSS) methodology in which the most significant XCs are sampled from water level stations throughout the study area using the POT method. If measurements are too sparse, then available hind-casts or metamodels can be used to generate additional data (Nadal-Caraballo et al. 2012). The CSS constitutes an optimized regional set of storms that is representative of the entire study area. Enough storms should be sampled for the water level distributions derived from the CSS to adequately match the distributions at the locations of the water level stations from which the CSS was sampled. Once sampled, the CSS storms are simulated using meteorological and hydrodynamic numerical models. Hind-cast wind and pressure fields are used to drive high fidelity storm surge and wave hydrodynamic models such as the ADCIRC (ADvanced CIRCulation) and STWAVE (STeady-state spectral WAVE) models.

For the analysis of XC-induced storm responses, a statistical approach known as the empirical simulation technique (EST) was developed by ERDC-CHL in the 1990s, which was adopted by the USACE and FEMA for their flood risk studies prior to implementation of the JPM. The EST encompasses limitations due to its application of nonparametric methods

(Borgman 2004) which results in the implementation of splines to complete low-frequency tails. However, the StormSim-SST developed by ERDC-CHL addresses the limitations of the univariate version of EST as StormSim-SST fits a generalized Pareto distribution (GPD)) (Coles 2001) to complete the low-frequency tail. Described as a bootstrap-based methodology, StormSim-SST utilizes observations or simulations from extreme events in the form of a partial duration series (PDS) to simulate multiple sequences of storm activity and associated responses. The GPD was selected for implementation in StormSim-SST based on extreme value theory for the analysis of PDS of extreme events (Coles 2001; Langousis et al. 2016). StormSim-SST also employs a mean residual life (MRL) automated threshold detection method (Langousis et al. 2016), for the objective selection of the GPD threshold parameter. The algorithm for the MRL method is as follows:

1. The PDS dataset, X, is sorted in ascending order and used as the initial set of values for the threshold θ.

2. For a given θ, a sample u is defined containing all values in X above the threshold ($X > \theta$). The arithmetic mean (ε) of these excesses is then computed for the sample:

$$\varepsilon = \frac{1}{n}\sum_{i=1}^{n}\left(u_i - \theta\right);\ i = 1, 2, \ldots, n \tag{2-3}$$

   where n is the sample size.

3. Assuming that the excesses are independent, a weight (ω) is also computed for the sample:

$$\omega = \frac{N - j}{Var\left(u - \theta\right)} \tag{2-4}$$

   in which N is the size of dataset X, and j is the rank of each value in the set of θ. Langousis et al. (2016) suggested repeating this step for up to $j = N - 10$ values of θ, to ensure a minimum sample size of $n = 10$ excesses for the computation of ε.

4. Afterwards, a linear regression model is fitted to a subsample of the set (θ, ε) using the weighted least squares method and the weighted mean square error (WMSE) computed from:

$$WMSE = \frac{1}{N_\theta}\sum_{i=1}^{N_\theta}\omega_i\left(\varepsilon_{p,i} - \varepsilon_i\right);\ i = 1, 2, \ldots, N_\theta \qquad (2\text{-}5)$$

   in which ε_p is the predicted excess, and N_θ is the subsample size. Langousis et al. (2016) suggested repeating this step for up to $j = N - 20$ subsamples of θ to ensure minimum sample size of $N_\theta = 10$ excesses for the linear fit.

5. The end result of this process is a third set of pairs (θ, *WMSE*) from which the threshold with minimum WMSE is selected as the parameter of the GPD.

In cases when multiple viable local WMSE minima are identified, the annual storm sample rate (or the average number of events sampled per year) is considered in the StormSim-SST metholodology as an additional criterion for threshold selection.

For this study, water levels were leveraged from the NACCS simulations completed using ADCIRC for 94 of the NACCS historical XCs. The simulation results for surge were applied as input to the StormSim-SST for the characterization of the SWL hazard produced by XCs within the study area. A more detailed description of the application of the StormSim-SST for this study is provided in Section 6.4.

2.5 Coastal Hazards System's PCHA Framework

In conjunction with the general JPM steps listed in Section 2.3, the following is a summary of the PCHA advancements over the standard JPM-OS approach included in this study:

- characterization of storm climate and TC hazards performed at over 1000 coastal reference locations (CRLs) along U.S. hurricane-exposed coastlines
- use of GPM, a machine learning method, to fill-in gaps in the HURDAT2 (HURricane DATa 2nd generation) database (Landsea and Franklin 2013) and incorporate long-term estimates of R_{max}

- use of GPM for development of ATCS to achieve hyper-resolution of the TC atmospheric-forcing parameter space
- computation of true joint probability model of TC forcing parameters through the use of meta-Gaussian copula (MGC) as dependence structure, explicitly accounting for the correlation between TC parameters
- performance of dry-node correction (DNC) to fill-in missing storm surge values
- spatially-varying bias correction and quantification of epistemic uncertainty

The main components of the PCHA framework and their interconnection are illustrated in Figure 2-1. The PCHA-related advancements are represented in the diagram below as red-colored boxes. In the diagram, processes related to TCs are shown by solid arrows whereas XC processes are illustrated by dashed arrows.

Gaussian process metamodeling (Jia et al. 2016; Zhang et al. 2018) is a machine learning method implemented in the PCHA framework for: i) performing data assimilation to fill-in gaps in the historical record and estimate missing TC parameters applied in the JPM; and ii) generating ATCSs of hundreds of thousands to millions of TCs that retain the high-fidelity nature of the initial TC suite (ITCS). The GPM component of the PCHA supersedes the OS-RS approach previously developed by USACE, as it has the capability of generating the storm surge response for augmented suites of thousands to millions of TCs. This finer discretization of the parameter space is coupled with the use of the MGC which simultaneously accounts for the correlation between relevant TC forcing parameters for a more truthful representation of the historical storm climatology.

Figure 2-1. Diagram of the main components of the PCHA framework (Nadal-Caraballo et al. 2020).

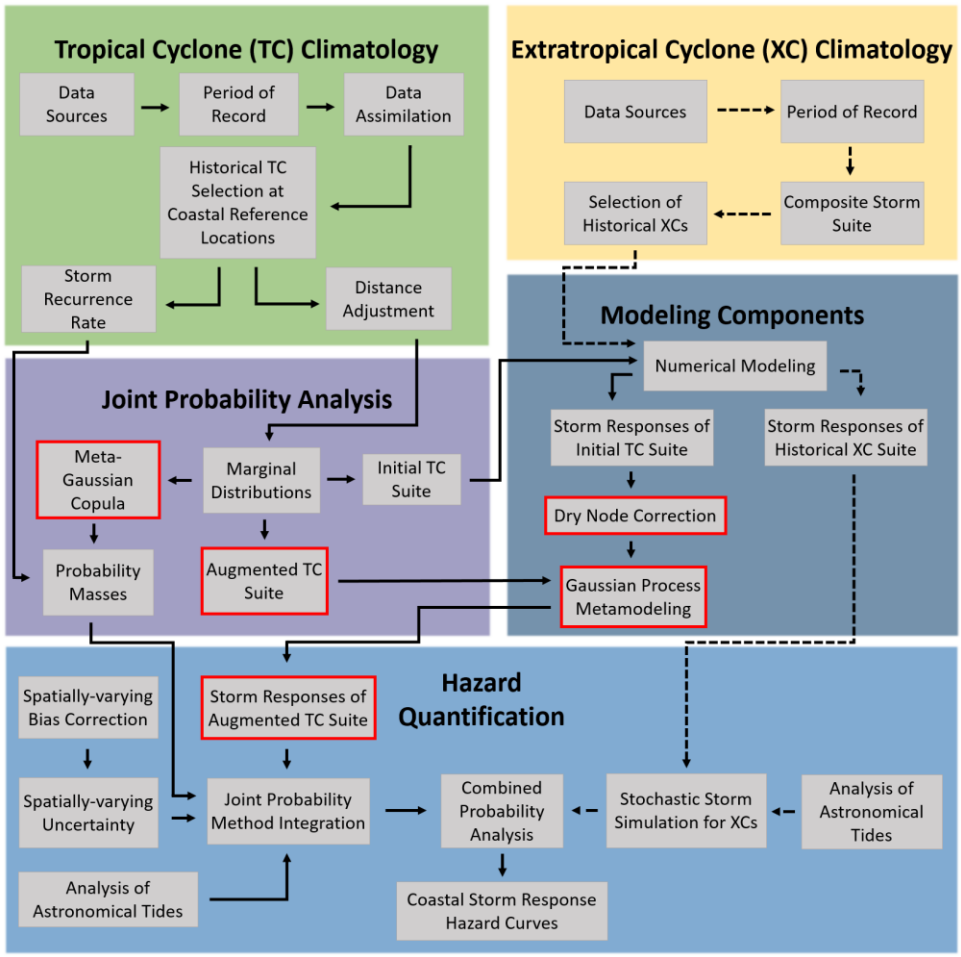

Following the interconnectivity of the components shown in Figure 2-1, the application of the PCHA to the D.C. Metro study area is detailed throughout Sections 3 through 6. The storm climatology analysis is documented in Section 3 which details the storm recurrence analysis and distance adjustment of TC parameters from historical storms. The joint probability analysis of the TC parameters including the application of the MGC and the development of the ATCS is discussed in Section 4. The mesh adjustments and simulation of the D.C. Metro RSS is documented in Section 5. Finally, Section 6 documents the post-processing of the hydrodynamic modeling results, the metamodel development, and application of the ATCS storm responses for developing hazard curves.

3 Characterization of Storm Climatology

The coastal storm hazards relative to the D.C. Metro study area are primarily dependent on large ocean-based storms consisting of TCs; however, XCs and transitional cyclones are also likely to affect this region. It is common to group the storms into statistical families of TCs and XCs with transitional cyclones that originated as tropical being categorized as tropical. A TC is a rotating, organized, warm-core system originating over tropical or subtropical waters and has a closed surface wind circulation about a well-defined center (e.g., tropical depression, tropical storm, or hurricane). An XC is a low-pressure system that primarily relies on baroclinic processes, getting its energy from the temperature contrast between warm and cold air masses in the atmosphere (e.g., Nor'easter). The climatology of both storm populations was assessed for the characterization of the SWL hazard in the study area.

3.1 Tropical Cyclones

As previously discussed, the characterization of historical TCs for purposes of the statistical analysis of coastal storm hazards is based on the primary TC parameters accounted for in the JPM: x_0, θ, Δp, R_{max}, and V_t. In this report, the definition of track and landfall conforms to that used within HURDAT2. The TC track is defined as the center of the eye which is computed as the location of minimum central pressure within HURDAT2. Landfall occurs when the track crosses the coastline where coastline is defined as the interface between mean-sea-level (MSL) and land. An idealized coastline was constructed from data obtained from NOAA's National Geophysical Data Center (NGDC).

Sections 3.1.1 through 3.1.6 describe the TC climatological data sources used in this study, period of record considered, selection of historical TCs, and the computation of spatially varying SRR for characterizing the climatology of TCs within the North Atlantic.

3.1.1 Data Sources

For TC screening, the main data source was HURDAT2. This database is a product of NOAA's National Hurricane Center (NHC) Re-Analysis Project and consists of the reanalysis of all historical TCs recorded in the North

Atlantic basin (i.e., North Atlantic Ocean, Gulf of Mexico, and the Caribbean Sea) beginning in 1851 (https://www.aoml.noaa.gov/hrd/hurdat/hurdat2.html).

A major limitation of HURDAT2 is the lack of R_{max} observations. The PCHA framework incorporates R_{max} from the extended best track (EBTRK) database (http://rammb.cira.colostate.edu) (Demuth et al. 2006). This database was created to supplement HURDAT2 best track data with storm structure information, including R_{max}. The EBTRK dataset applied in this study covers the 1988 to 2018 time period. Table 3-1 lists the sources used for the historical analysis of the primary TC parameters.

3.1.2 Period of Record for the PCHA

Prior to the selection of historical TCs, the specific period of record to be used for the JPA was assessed. The SRR and the marginal distributions of TC parameters are sensitive to the historical record length. The 1940s decade marked the dawn of modern aircraft reconnaissance missions to measure hurricane parameters, resulting in much more reliable estimates of both storm characteristics, including frequency and intensity.

Prior to 1944, the main data sources were land stations and ship reports (Jarvinen et al. 1984). During this period, it was typical for relatively weak storms to go undetected and for the intensity of strong storms to be underestimated. After 1944 and as a consequence of World War II, aerial reconnaissance led to increased data collection incidence and measurement accuracy, including storm position, track, wind speed, and pressure. The use of satellite imagery was introduced during the 1964 hurricane season (Neumann et al. 1985) and was considered one of the major advances in TC tracking (Jarvinen et al. 1984).

The high frequency of unsampled TCs prior to the 1940s has been well documented. Mann et al. (2007) estimated an undercount in the pre-aircraft reconnaissance era (1870–1943) ranging from 0.5 to 2.0 TC/yr, with a mean of 1.2 TC/yr. Landsea et al. (2010) discussed that the increase in reported TCs during the 1940s and until approximately 1960 had been interpreted as a result of climate change. This increase, however, is likely to be the consequence of improved observing and recording of short-lived TCs coinciding with the advent of aircraft reconnaissance and satellite imagery.

Worley et al. (2005) identified spikes in the number of unrecorded moderate to long-track TCs during the 1910s and 1940s as due to reduced ship observations during World War I and World War II, respectively. Vecchi and Knutson (2011), after adjusting HURDAT2 data for unrecorded TCs, concluded that the mid-twentieth century was a high-activity period that extended from the 1940s to the 1960s.

The review of technical literature indicates that although the 1940s decade saw improvements in the observation and recording of TCs, there was still a significant undercount during this period. In recent flood hazard studies where the JPM-OS methodology has been used, the period of record that was considered started in the early 1940s (FEMA 2008, 2012; Resio et al. 2007). The NACCS study performed by the USACE for the Virginia to Maine coastline used a period of record starting in 1938, corresponding to a few years before the dawn of Hurricane Hunter aircraft reconnaissance missions up to the present, to capture The Great New England Hurricane of 1938. Therefore, due to concerns of TC undercount prior to the 1940s and climatic non-stationarity, the PCHA framework uses the period of record from 1938 – 2019 for the computation of spatially-varying SRR and directional SRR (DSRR) (described in Section 3.1.5).

Due to issues with data collection, data gaps are present within the HURDAT2 database. To overcome this limitation of missing data values, GPM is also used in a data assimilation (DA) process to estimate missing values and fill in the database. The DA process within the PCHA framework is completed with two main goals: i) to fill-in central pressure gaps in the HURDAT2 database, and ii) to incorporate estimates of R_{max}. The GPM was used to conduct data assimilation (DA) to fill-in gaps in the HURDAT2 database, and to incorporate estimates of R_{max} obtained from EBTRK. The metamodel trained to predict Δp is trained on the following input vector: $\hat{x}_{\Delta p} = [lat, lon, W_{max}, V_t, \theta]$; where W_{max} = maximum sustained wind speed. Similarly, the metamodel trained to predict R_{max} considered the previous input vector, with the addition of Δp: $\hat{x} = [lat, lon, W_{max}, \Delta p, Vt, \theta]$. Examples of the reconstructed values for Δp and R_{max} are shown in Figures 3-1 through 3-4.

Figure 3-1. Reconstruction of Δ*p* for a 1938 historical TC using metamodeling techniques.

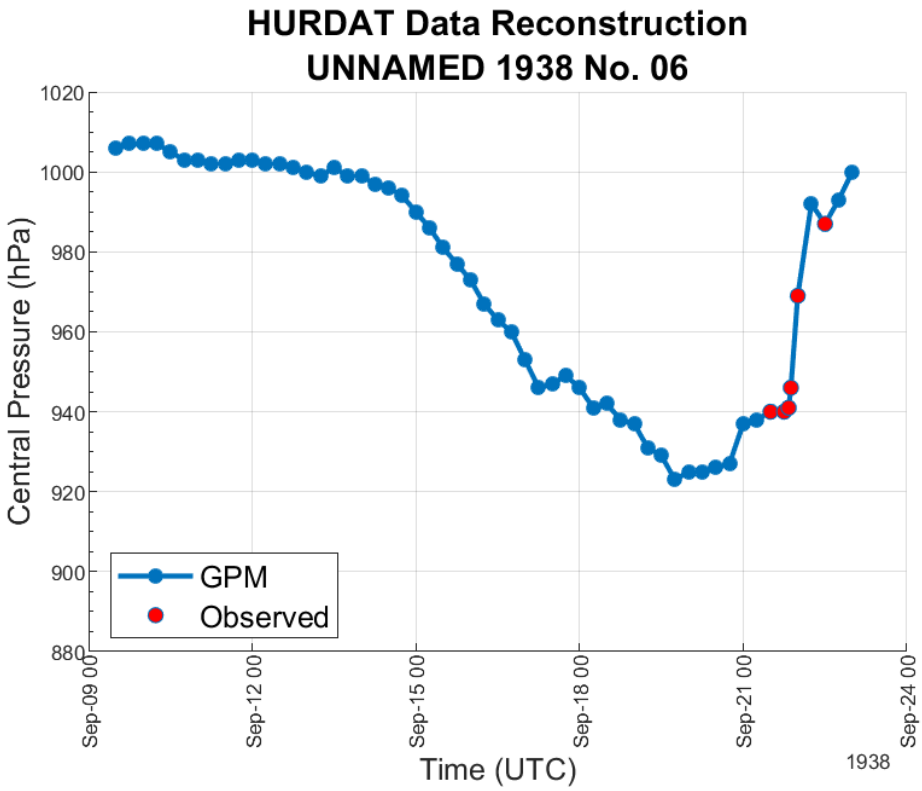

Figure 3-2. Reconstruction of Δ*p* for Hurricane Sandy using metamodeling techniques.

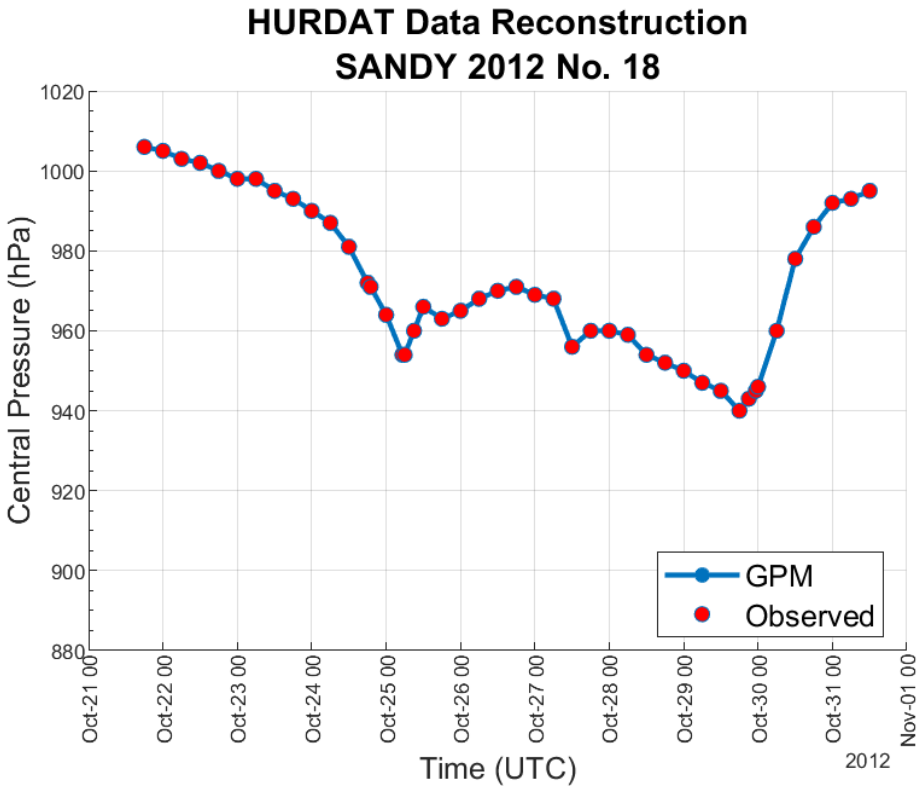

Figure 3-3. Reconstruction of R_{max} for a 1938 historical TC using metamodeling techniques.

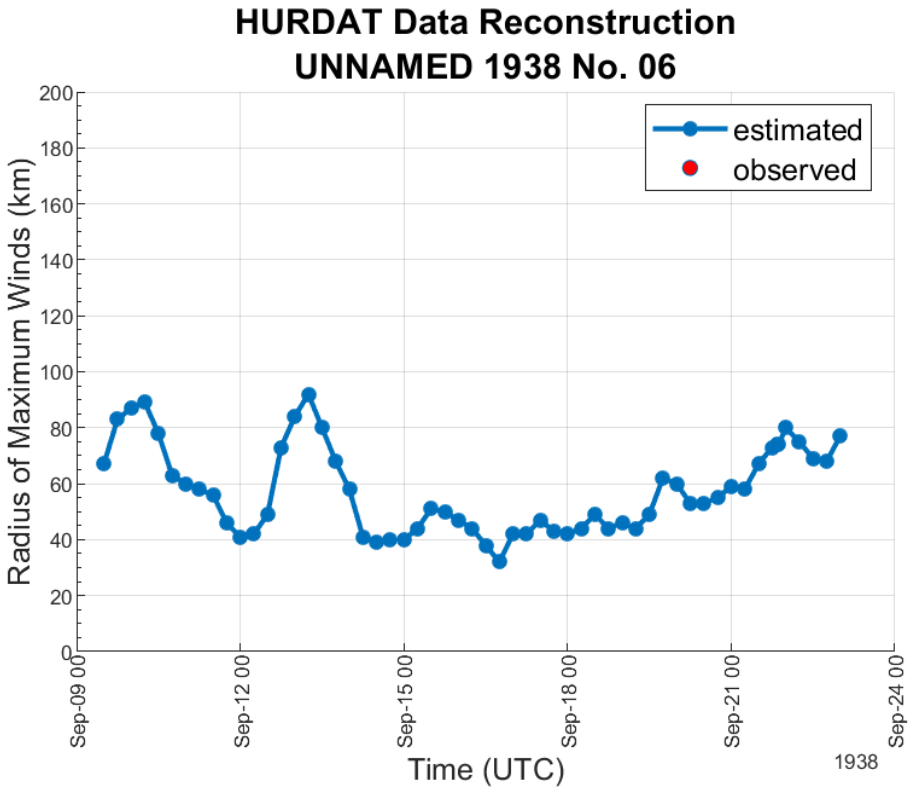

Figure 3-4. Reconstruction of R_{max} for Hurricane Sandy using metamodeling techniques.

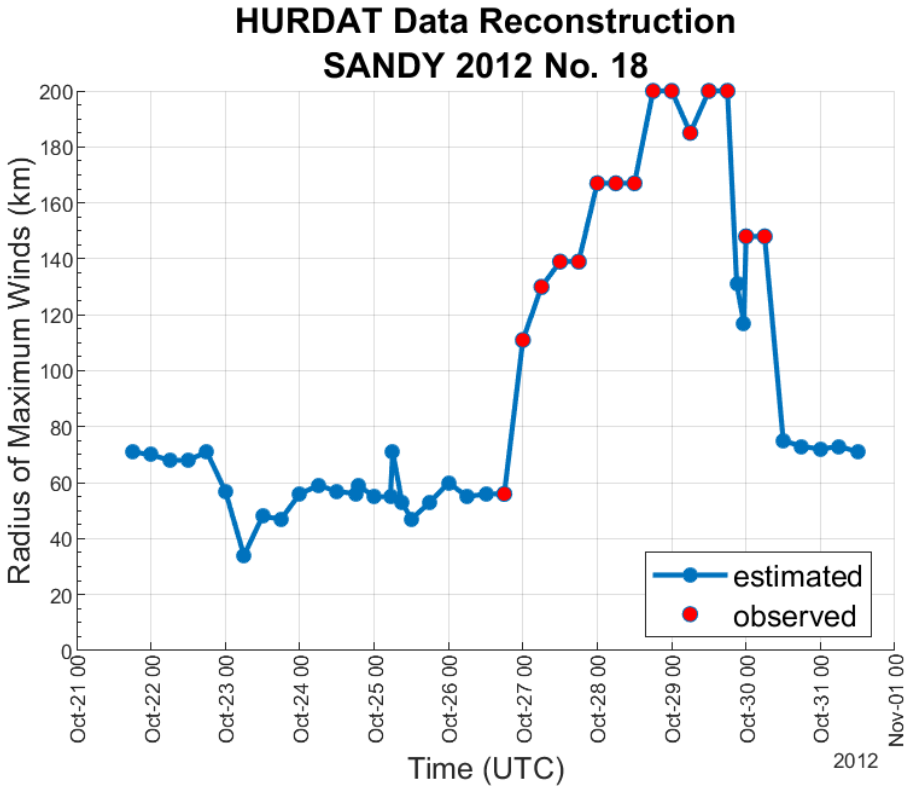

After performing the DA process using GPM, gaps in Δp were filled for the entire HURDAT2 period of record from 1851-2019. Likewise, for R_{max}, the DA process was used to fill in gaps in the EBTRK data record extending the record length to the 1851-2019 period. However, due to concerns of non-stationarity and undercounting of TC occurrences, only TC data from the 1938-2019 period was considered in the development of marginal distributions for the following TC parameters: Δp, V_t, θ, and R_{max}. Table 3-1 provides the period of record considered in the development of marginal distributions for each TC parameter.

Table 3-1. Source and period of record considered for each TC parameters.

Tropical Cyclone Parameter	Source and Availability	Period of Record
Track reference location	HURDAT2 (1851–2019)	1938–2019
Heading direction	Estimated from: HURDAT2 (1851–2019)	1938–2019
Central pressure deficit	HURDAT2 (1851–2019)	1938–2019
Translational speed	Estimated from: HURDAT2 (1851–2019)	1938–2019
Radius of maximum winds	EBTRK (1988 –2018)	1938–2019

3.1.3 Coastal Reference Locations (CRLs)

The quantification of coastal hazards performed for the CHS is completed on a national scale for the coverage of all hurricane-prone coastlines of the U.S. This requires the consistent characterization of storm climate to be conducted at a high spatial resolution.

The PCHA characterizes the storm climate at points along an idealized coastline referred to as CRLs. Additional CRLs are also positioned in offshore locations to characterize bypassing TCs in regions like the southern tip of Florida. These point locations mark where the 1) SRR, 2) each TC parameter PDF is fitted, and 3) computation of the joint probability through the MGC are defined to characterize the storm climate at that given location. The network of over 1000 CRLs allows for the computation of the TC probability masses at a high spatial resolution.

For the contiguous United States (CONUS), 663 CRLs (IDs 1 – 663) have been established along an idealized coastline starting south of the Mexico-Texas boundary (23.5°N) and ending in northern Nova Scotia (45.0°N).

The idealized coastline was constructed using data obtained from NOAA's National Centers for Environmental Information (NCEI) (https://www.ngdc.noaa.gov/mgg/shorelines), and can also be accessed directly through the "Global Self-consistent, Hierarchical, High-resolution Geography Database" (GSHHG) website (http://www.soest.hawaii.edu/pwessel/gshhg).

For offshore locations, 117 CRLs (IDs 664 – 780) were established around the North Atlantic Coast region from Virginia to Maine, and 65 CRLs were established off the southern tip of Florida (IDs 961-1025). For the Caribbean, 180 CRLs (IDs 781 – 960) were placed near Puerto Rico and the U.S. Virgin Islands, for a total of 1025 CRLs. Since this study leverages the work done as part of the CHS-NA study, all 368 CRLs within the North Atlantic (401-780) were used in the PCHA. However, CRLs 652 – 663 were excluded from application in the PCHA as they are north of Halifax, Nova Scotia, and are outside the area of interest for this study. Figure 3-5 illustrates the current network of 1025 CRLs (red circles), which has an average spacing of less than 10 km. Figure 3-6 shows a closer view of the CRLs relative to the North Atlantic basin. For this study, examples of the PCHA framework components are provided at CRL 458. Figure 3-7 illustrates the location of CRL 458.

Figure 3-5. Network of CRLs for the Coastal Hazards System.

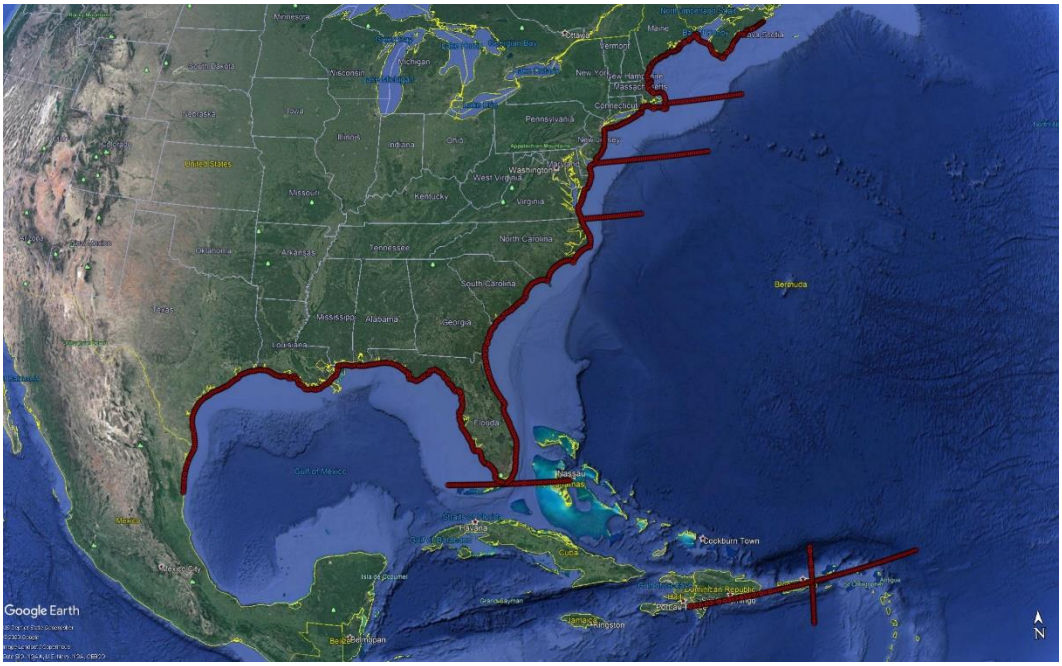

Figure 3-6. CRLs 401-780 (orange) relative to the NACCS study area.

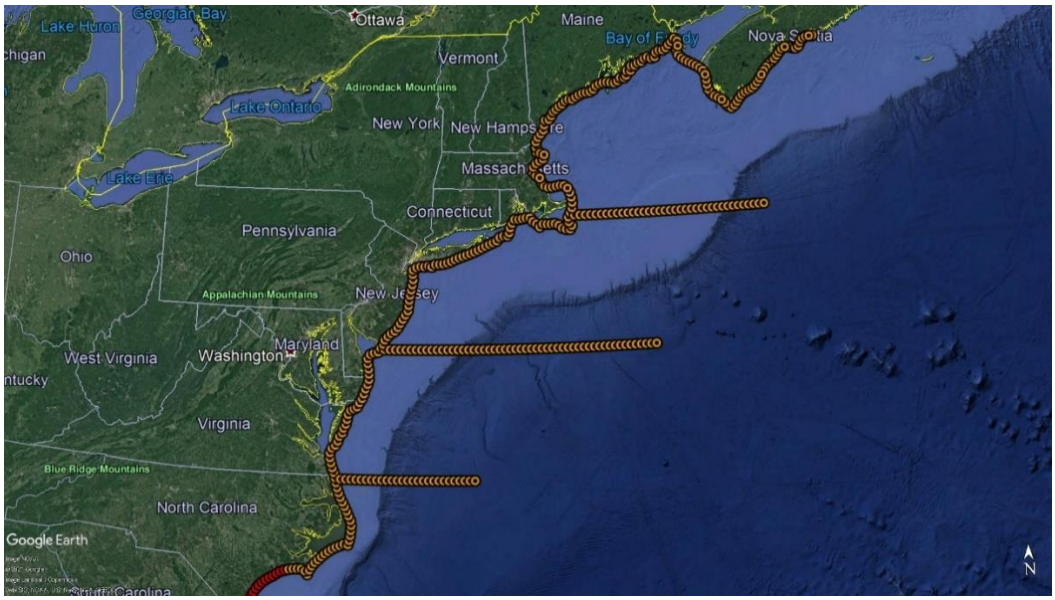

Figure 3-7. Example CRL 458 (yellow point) located near Washington, D.C.

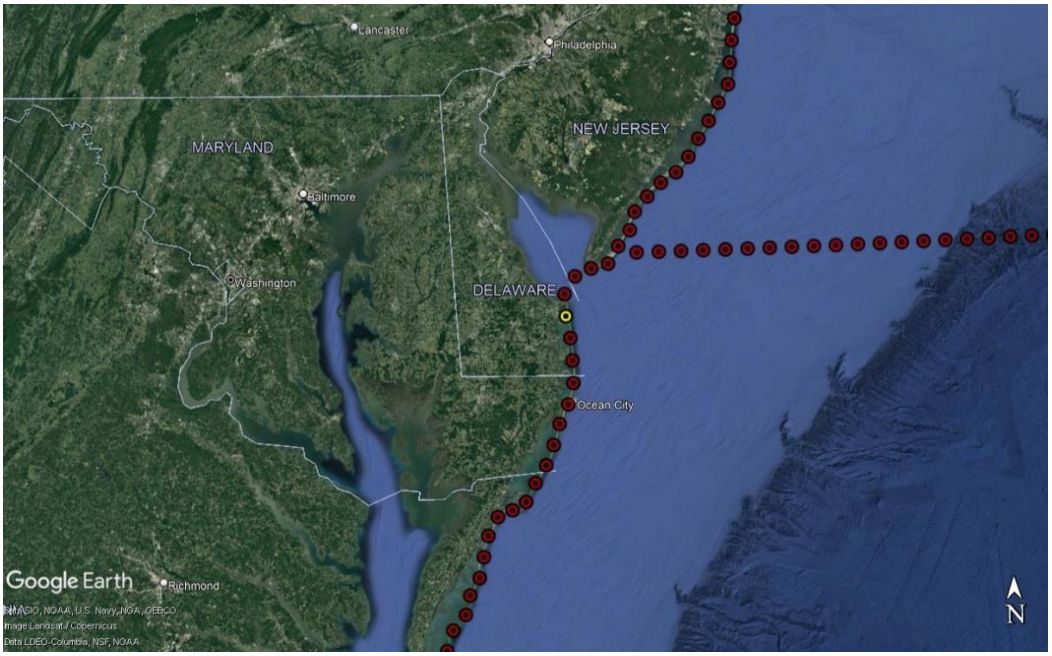

3.1.4 Selection of Historical TCs

Probabilistic characterization of storm climatology for the study area requires sampling a set of storms from the historical record (i.e., HURDAT2, EBTRK). The PCHA is then performed with this set of TCs as its basis, including the computation of SRR and development of marginal distributions of individual TC parameters. As previously discussed, for the SRR, the sampling of historical TCs was limited to the 1938–2019 period

for the fitting of marginal distributions. In the PCHA framework, TCs are sampled on a per CRL basis. TCs with $\Delta p \geq 8$ hPa that are within 600 km of a CRL are selected and assigned to that specific CRL. Note that Δp is computed as the difference between a far-field atmospheric pressure of 1,013 hPa and TC minimum central pressure (c_p) (FEMA 2008). The sampling process is repeated for each of the 1025 CRLs. For the NACCS storm suite, the 1050 synthetic TCs are encompassed by CRLs 401 through 780. Therefore, these 368 CRLs were chosen for the selection of historical TCs within the study area and characterization of the regional climatology.

For the selected TCs, an assessment of track points was performed to identify the closest high-intensity point to each CRL using Equation 3-1. For each TC, all track points within the 600 km radius are evaluated to ensure the selection of the most influential track location considering both TC intensity and distance from the CRL. The following intensity index function (IIF) (Nadal-Caraballo et al. 2015) is applied to determine the optimal sampling location along each track:

$$I_{\Delta p_i} = w(d_i)\Delta p_i \tag{3-1}$$

where: $I_{\Delta p_i}$ = TC intensity index for a given TC, computed at all track points within 600 km of a particular CRL; Δp_i = central pressure deficit at individual track points; $w(d_i)$ = distance-adjusted Gaussian weights from the Gaussian kernel function (GKF) method developed by Chouinard and Liu (1997); d_i = distance from the location of interest to a track point (km).

The distance-adjusted Gaussian weights were calculated considering the distance between TC track points and each CRL as follows:

$$w(d_i) = \frac{1}{\sqrt{2\pi}h_d} exp\left[-\frac{1}{2}\left(\frac{d_i}{h_d}\right)^2\right] \tag{3-2}$$

where h_d = optimal kernel size (km). The optimal kernel size was taken as 200 km, consistent with the value selected from numerical experiments described in Nadal-Caraballo et al. (2019). As part of the PCHA framework, each CRL within the boundaries of the study area will have its own set of sampled storms. For each CRL, the most influential track location in the probabilistic analysis is identified as the point along each TC track with the largest $I_{\Delta p_i}$. This results in a storm sampling approach that is consistent with the GKF method and balances the distance from TC

track to CRL with the TC intensity, thus avoiding bias that could be introduced if sampling was to be limited to the track point with the shortest distance to the CRL. Considering CRL and TC track pairs, the track point with the shortest distance to the CRL will generally be selected, unless one of the next closest track points (with similar distance) has significantly higher intensity, in which case the latter will be selected. The R_{max}, V_t, and θ were identified from this optimal sampling location for the marginal distribution development. Figure 3-8 shows the sampling location from TCs selected for CRL 458. The TCs and their associated parameters selected at this CRL are provided in Appendix A. Further discussion on using a kernel size of 200 km as well as sampling storms within 600 km of each CRL is provided in Section 3.1.5.

Figure 3-8. Selection of historical TCs within 600 km of CRL 458.

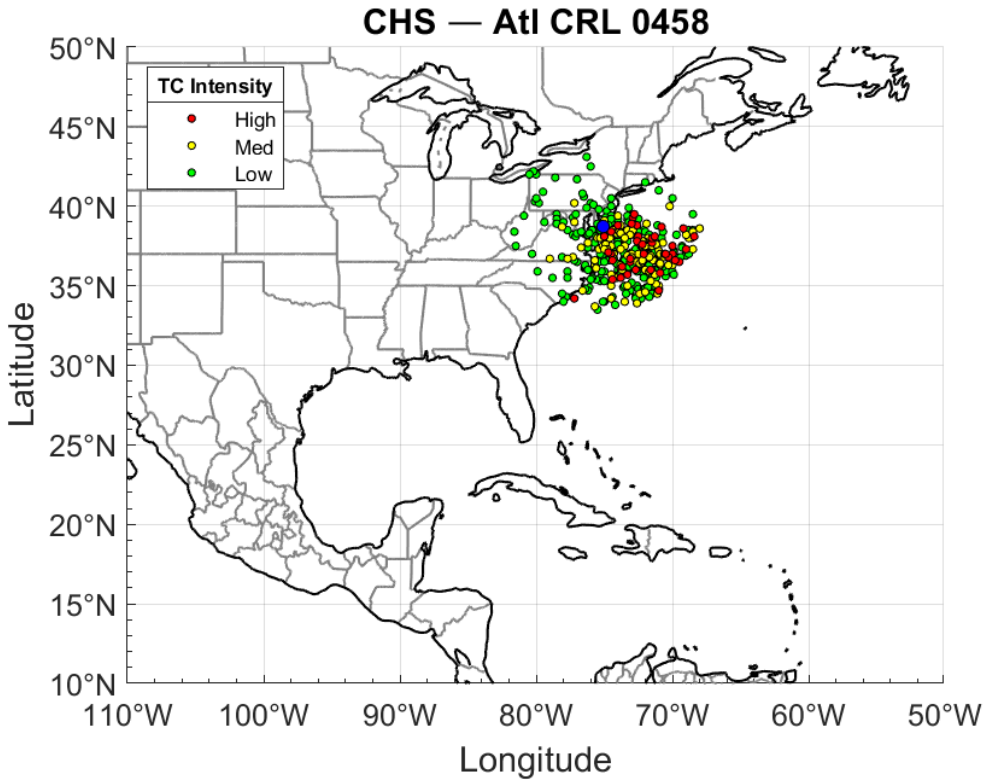

After the historical TCs are selected, they are partitioned into three bins, according to their intensity:

- Low intensity (LI); $8 \le \Delta p < 28$ hPa
- Medium intensity (MI); $28 \le \Delta p < 48$ hPa

- High intensity (HI); $\Delta p \geq 48$ hPa.

Partitioning TCs into low, medium, and high intensity bins is primarily done to account for potential differences in the correlation of pairs of atmospheric-forcing parameters between intense and weak cyclones. The PCHA seeks to represent the categories defined by the SSHWS using these three bins. In terms of the SSHWS, the LI bin captures TCs of tropical storm intensity whereas the MI bin contains Category 1 and 2 hurricanes. Category 3 through 5 hurricanes are captured by the HI bin. Note that historical TCs represent more variability in intensity than the defined bins.

3.1.5 Spatially-Varying Storm Recurrence Rate (SRR)

Efficient TC sampling from the historical record and statistical computation of SRR can be achieved using several different approaches. In recent studies, some of the approaches used to compute the spatial variation of SRR have included area-crossing, line-crossing, GKF, and other combined methods. Area-crossing and line-crossing are examples of capture zone methods. In the area-crossing approach, only storms passing through a particular area are counted in the computation of the SRR. The line-crossing approach usually consists of an idealized coastline or a reference line representing a segment of coastline. Only storms making landfall along the chosen segment of coastline are captured and counted towards the computation of the SRR. The SRR is the single most significant parameter in the JPM and PCHA framework as it describes the expected annual recurrence of storms at locations of interest, which are CRLs in this study.

Capture zones can also be defined in other ways, such as a rectangular or circular window, or any other finite spatial region. In past studies, the standard had been to apply any of the capture zone methods in order to count the storms and to assign uniform weights to all captured storms. The main limitation of the capture zone approach is that, while all storms within the chosen capture zone are given uniform weights, storms outside this zone are given a weight of zero. The conundrum lies in establishing a capture zone large enough to reduce the uncertainty associated with a sample size by capturing an adequate number of storms from which significant statistics can be derived but remains small enough to balance the uncertainty associated with spatial variability and population heterogeneity.

Nadal-Caraballo et al. (2019) conducted an extensive evaluation of different methods for the computation of SRR, including GKF, uniform kernel function (UKF), and the Epanechnikov kernel function (EKF). The curves of relative distance-adjusted weights for the UKF, GKF, and EKF with a kernel size of 200 km are shown in Figure 3-9. The curves are shown relative to the weight of a TC track point located at the CRL (distance = 0 km). All three kernel functions decrease with distance from the CRL, as expected. The weights of both UKF and EKF decrease to zero when the distance reaches the kernel size of 200 km. On the other hand, the GKF weight decreases following the well-known bell shape, decreasing almost to zero at a distance of 600 km and extending indefinitely afterwards.

Figure 3-9. UKF, GKF, and EKF weights as function of distance from CRL.

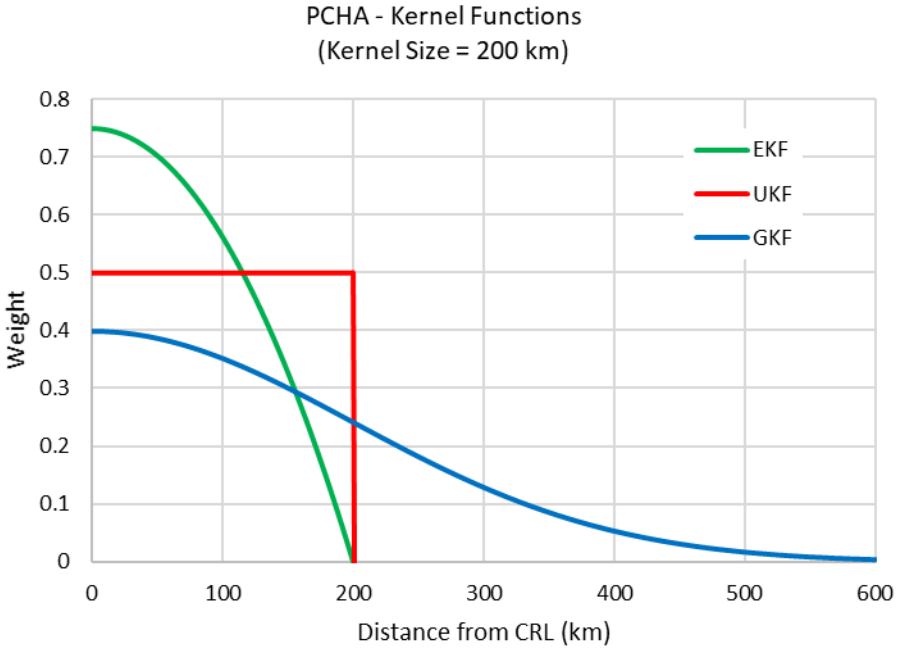

The study by Nadal-Caraballo et al. (2019) also found that the line-crossing approach can lead to underestimation of the hazard due to its exclusion of bypassing events. The area-crossing method was treated as a special case of the kernel approach through the application of the UKF. A significant advantage of the GKF is that it can consider a larger number of storms than the capture zone approach and the EKF. For the same ranges of optimal capture zone radii and Gaussian kernel sizes, the GKF SRR estimates exhibited a reduced coefficient of variation (CV) when compared

to UKF estimates. The GKF was deemed to be the best method to be used for conducting the SRR computational experiments.

As discussed above, the GKF method, developed by Chouinard and Liu (1997), can overcome the main limitations of capture zone approaches. The standard application of the GKF consists of establishing a grid of nodes where estimates of the SRR are sought. All storms within this gridded space can be counted at any given node, but the weight assigned to each storm decreases with increasing distance from storm to node. The distance-adjusted weights are computed using a Gaussian PDF with an optimal kernel size. The GKF equations are as follows:

$$\lambda = \frac{1}{T}\sum_i^n w(d_i) \tag{3-3}$$

where: λ = SRR in storms/yr/km; T = record length in (yr); $w(d_i)$ = distance weights from the GKF given by Equation (3-2); d_i = distance from location of interest to a track point (km); h_d = optimal kernel size (km). Use of the GKF weights minimizes sample size uncertainty by taking full advantage of all available storm data while significantly reducing the uncertainty associated with spatial variability and potentially heterogeneous populations.

The PCHA for this study adopted an optimal kernel size of 200 km. An optimal kernel size of 200 km was also chosen in the latest FEMA Region II study (FEMA 2014) and the NACCS (Nadal-Caraballo et al. 2015). Since the kernel size is representative of a standard deviation, TCs were sampled at a distance of 3 standard deviations, or $3*h_d$. In previous studies such as NACCS, a distance of 800 km chosen for sampling landfalling storms. However, further evaluations have shown that no measurable differences in SRR are observed between a sampling radius of 600 km and 800 km. This study subsequently used a sampling distance of 600 km for the calculation of SRR at each of the 368 selected CRLs. Table B-1 in Appendix B summarizes the SRR results for all CRLs considered for this study.

3.1.6 Distance Adjustment of Historical TCs

JPM-OS studies have often sampled TCs that are hundreds of kilometers away from a CRL simply because its track crossed an idealized coastline. The spatial and temporal occurrence of TCs is a natural stochastic process and, as an example, it is difficult to justify that a TC making landfall 500

km away from a CRL in Delaware is more relevant to the climatology of that area than a TC bypassing the CRL just 250 km away.

For this reason, the PCHA framework has adopted a normalization and distance-adjustment process for the sampled historical TCs. As discussed in Section 3.1.3, all TCs within 600 km from each CRL are sampled and assigned to that particular CRL. Continuing with the example above, and analogous to the computation of SRR, a bypassing TC just offshore of a CRL near Delaware should carry more weight relative to that CRL than a TC making landfall in Florida. Therefore, the concept of computing spatially-varying SRR through the application of the GKF and distance weights is extended to the selected TCs. The GKF is employed to generate distance weights required for the normalization of the TC parameters. The goal is to transform the TC parameters, so the sampled population reflects a distance-weighted mean and standard deviation.

Z-score normalization is a common technique used by machine learning practitioners to adjust population parameters even if the populations are not normally distributed. The first step in the normalization of TC parameter (x_i) is the computation of the mean (μ) and standard deviation (σ) of the sampled TCs:

$$\mu = \frac{\sum_{i=1}^{N} x_i}{N} \tag{3-4}$$

$$\sigma = \sqrt{\frac{\sum_{i=1}^{N} (x_i - \mu)^2}{N-1}} \tag{3-5}.$$

The normalized TC parameters (z_i) are determined through the basic z-score formula:

$$z_i = \frac{x_i - \mu}{\sigma} \tag{3-6}.$$

The next step is the computation of distance-weighted mean (μ_{DW}) and standard deviation (σ_{DW}) for each TC parameter:

$$\mu_{DW} = \frac{\sum_{i=1}^{N} w(d_i) x_i}{\sum_{i=1}^{N} w(d_i)} \tag{3-7}$$

$$\sigma_{DW} = \sqrt{\frac{\sum_{i=1}^{N} w(d_i)(x_i - \mu_{DW})^2}{\left(\frac{\acute{N}-1}{\acute{N}}\right)\sum_{i=1}^{N} w(d_i)}} \quad (3\text{-}8)$$

where $w(d_i)$ = distance weights computed using the GKF (Equation 3-2); x_i = individual parameter values of sampled TCs (e.g., one set of values per TC taken at the location of highest intensity relative to CRL); and N = number of sampled TCs, and $\acute{N}$= number of sampled TCs with non-zero weights. Finally, the adjusted TC parameters (x'_i) are obtained from the following equation:

$$x'_i = z_i \sigma_{DW} + \mu_{DW} \quad (3\text{-}9).$$

The historical TCs sampled from the HURDAT2 data set within 600 km from CRL 458 (1938–2019 period) and their distance-adjusted atmospheric parameters are listed in Appendix A.

3.2 Extratropical Cyclones

XCs differ from TCs in that their structure is rarely axially symmetric about a low pressure center meaning that XCs cannot be described by a set of parameters. XCs are formed as a result of differences in air masses meaning their energy relies on temperature differences. Greater differences in temperature between air masses results in greater instability and stronger XCs. Typically, this results in a more frequent occurrence of stronger XCs during the Northern Hemisphere winter.

In the U.S., one of the more recognized names for these storms is Nor'easters, which is derived from their common northeastward propagation along the East Coast of the U.S. Similarly to TCs, winds within an XC exhibit counterclockwise circulation about the low pressure center. However, they often produce smaller surge heights than TCs, since they typically exhibit lower intensity. However, TCs can convert to extratropical as they move from the tropics to the poles. When this occurs, it is referred to as an extratropical transition.

3.2.1 Data Sources and Period of Record

As discussed in Nadal-Caraballo et al. (2015), the selection of historical XCs for the storm suite was determined by examining water level measurements at NOAA gauges. Data at meteorological stations within the

NACCS study area was also applied in the selection process. Due to the non-stationarity concerns mentioned in Section 3.1.2, the selection of XCs for the NACCS storm suite was based on the 1938-2013 period of record which was maintained for this study. The application of the CSS methodology for the development of the historical XC storm suite is discussed in Nadal-Caraballo et al. (2015).

4 Joint Probability Analysis of Coastal Storm Hazards

As part of the NACCS, the development of synthetic TCs and respective storm parameters included TCs covering the entire coastal region from Virginia to Maine (Nadal-Caraballo et al. 2015). In the JPM, the primary parameters considered are:

- track reference location (x_o)
- heading direction (θ)
- central pressure deficit (Δp)
- radius of maximum winds (R_{max})
- translational speed (V_t).

These TC parameters are required as inputs to the PBL model used for the generation of wind and pressure fields. The work described in this section consists of the fitting of TC parameter probability distributions for the JPA relative to the D.C. Metro study area. The selection of a parametric or non-parametric probability distribution to characterize the likelihood of a given TC parameter is ultimately based on expert judgment. There is no single best solution. Past JPM studies have typically chosen either the Weibull or the Gumbel distribution to fit Δp with very similar storm surge hazard results (USACE 2009, 2011).

4.1 Marginal Distributions of TC Parameters

The characterization of storm climatology within the study area requires developing probability distributions of individual atmospheric-forcing parameters. These distributions were developed from the HURDAT2 1938–2019 data record and used to assess the historical maxima and variances of the TC parameters. This section discusses the PCHA steps to develop marginal distributions at the CRLs specific to the North Atlantic basin and provides examples plots and marginal distributions at CRL 458.

As discussed in Section 3.1.3, for each historical TC track, the forcing parameters were selected at an optimal location balancing intensity and distance from a given CRL through the use of the IIF (Equation (3-1)). The historical TCs sampled from the HURDAT2 data set within 600 km from CRL 458 (1938–2019 period) and their distance-adjusted atmospheric parameters are listed in Appendix A. Sections 4.1.1 through 4.1.4 discuss

the distribution fitted to each parameter. Note that the marginal distributions detailed here were explicitly used to assess the joint probability between TC parameters and were not discretized for the development of a synthetic storm suite.

4.1.1 Central Pressure Deficit (Δp)

The central pressure, c_p, is an inversely proportional measurement of TC intensity meaning that as TC intensity increases the value of c_p decreases. However, for convenience and to facilitate statistical analyses, hurricane intensity is usually expressed in terms of Δp. It is common practice to use these parameters interchangeably. In most JPM studies, the Δp has been computed from an assumed far-field atmospheric pressure of 1,013 hPa.

The probabilistic model of Δp is represented by the Weibull distribution:

$$F[\Delta p > x] = 1 - exp\left[-\left(\frac{x}{U}\right)^k\right] \quad (4\text{-}1)$$

where: U = scale parameter; and k = shape parameter. The Weibull best fit is shown in Figures 4-1 and 4-2. Since the PCHA employs three TC intensity bins (i.e. LI, MI, and HI), a doubly-truncated Weibull distribution (DTWD) is used to characterize the data from these bins. Figure 4-1 illustrates the Weibull best fit for Δp values ranging from $8 \leq x < 28$ hPa. In Figure 4-2, the Weibull is fit to central pressure deficit values truncated at 28 and 148 hPa.

Figure 4-1. DTWD for sampled Δp ranging from 8 to less than 28 hPa at CRL 458.

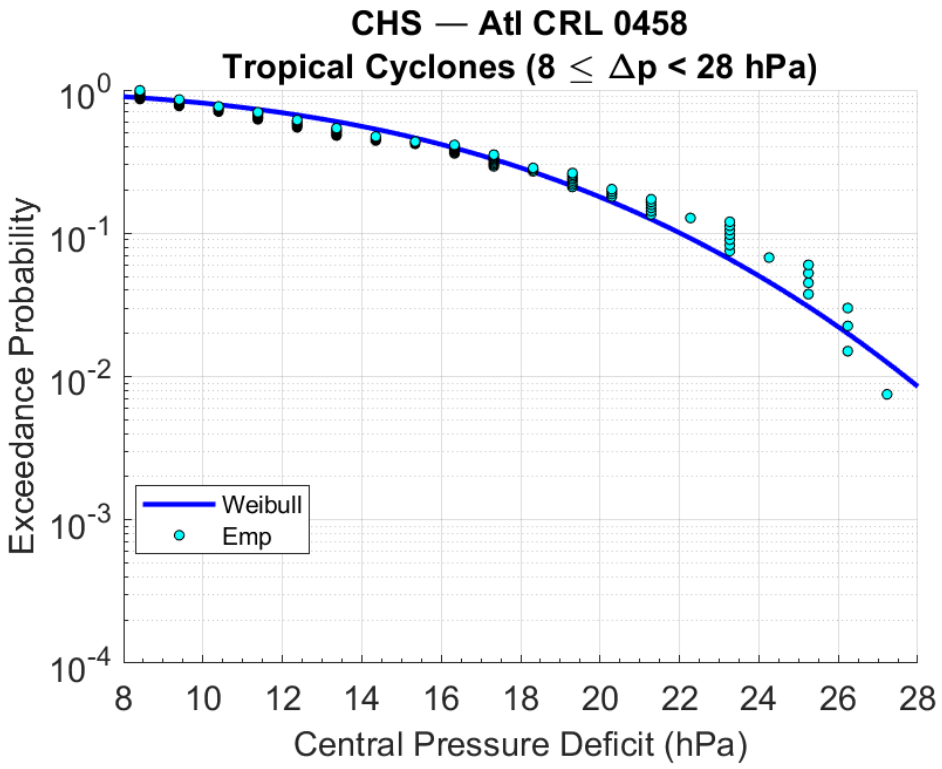

Figure 4-2. DTWD for sampled Δp of 28 to 148 hPa at CRL 458.

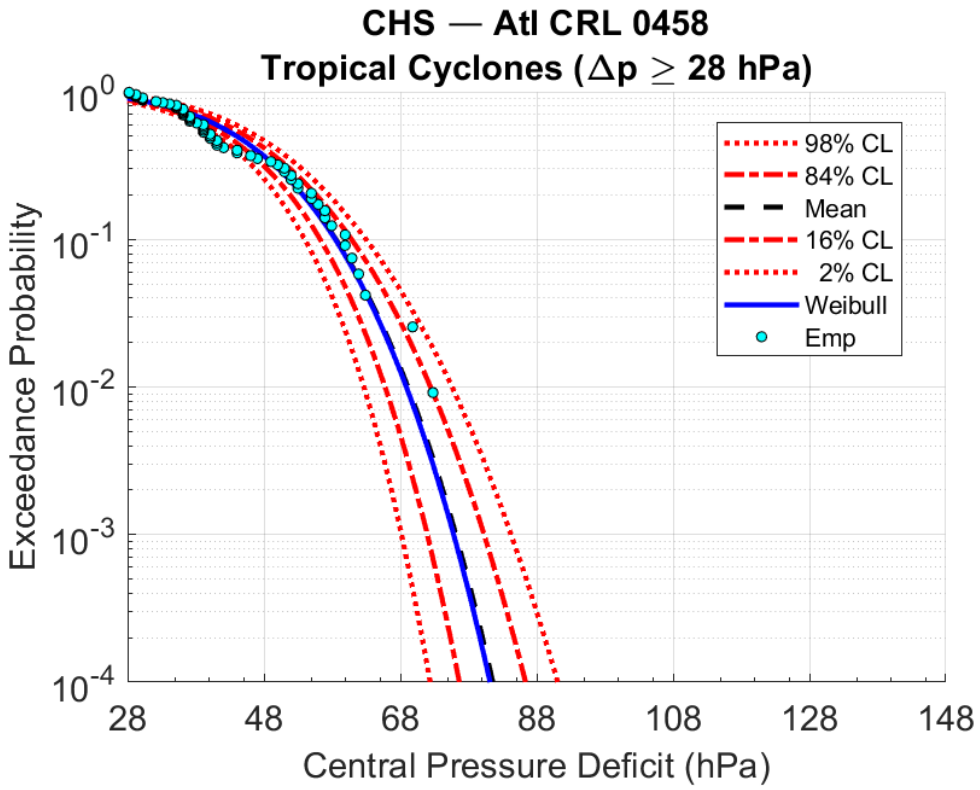

The scale parameter, shape parameter, and truncation limits of the Δp for CRL 458 are listed in Table 4-1. The Weibull distribution fits corresponding to each intensity group are shown in Figure 4-3, 4-4, and Figure 4-5.

Table 4-1. Marginal distribution parameters of Δp at CRL 458.

TC Intensity	U	k	Δp_1	Δp_2
High (DTWD)	48.0	4.23	48	148
Medium (DTWD)	48.0	4.23	28	48
Low (DTWD)	16.7	3.03	8	28

Figure 4-3. Marginal distribution (DTWD) of Δp for HI TCs at CRL 458.

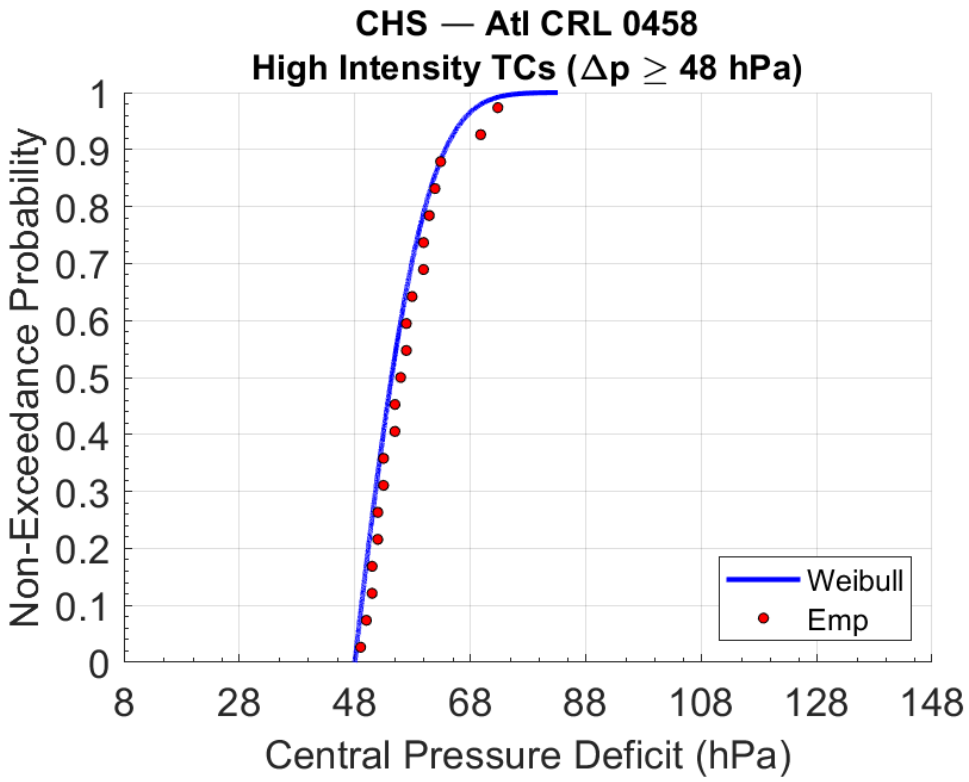

Figure 4-4. Marginal distribution (DTWD) of Δp for MI TCs at CRL 458.

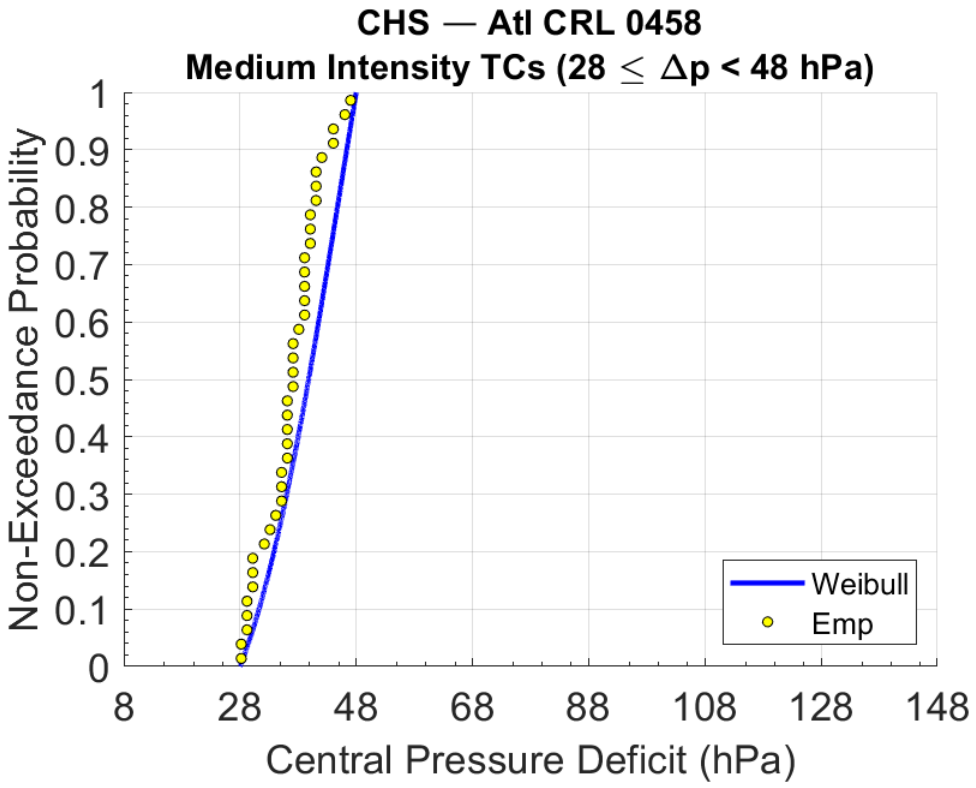

Figure 4-5. Marginal distribution (DTWD) of Δp for LI TCs at CRL 458.

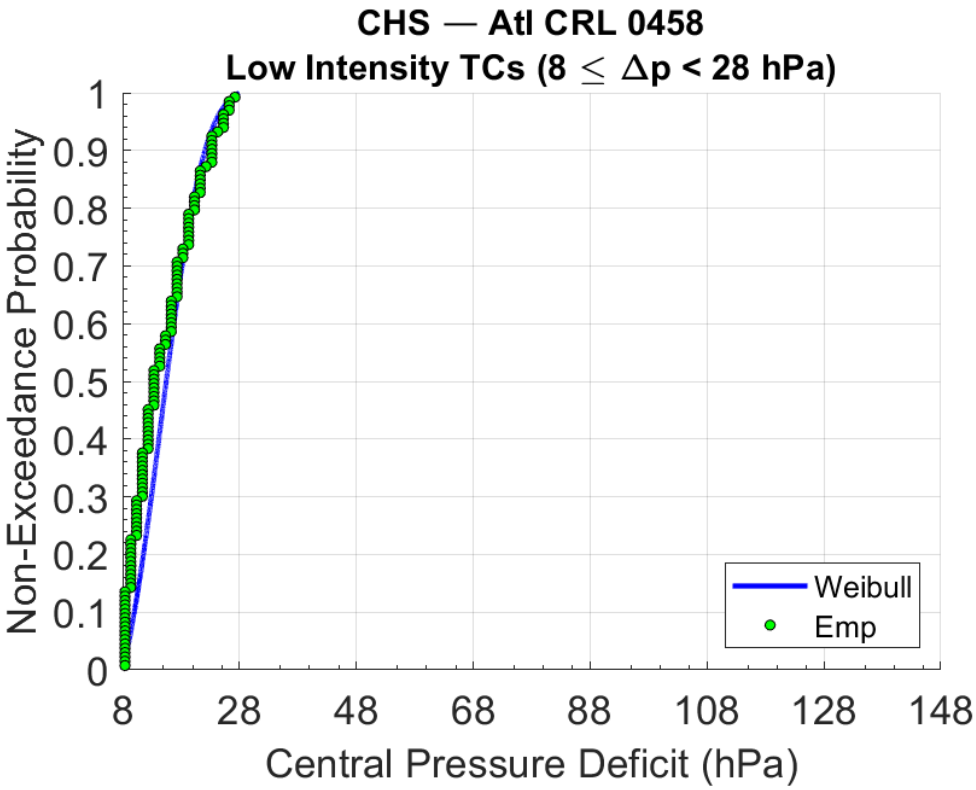

4.1.2 Radius of Maximum Winds (R_{max})

In this study, the parameter R_{max} is represented by the lognormal distribution which has the form:

$$f(x) = \frac{1}{x\sigma\sqrt{2\pi}} exp\left[-\frac{1}{2}\left(\frac{ln(x)-\mu}{\sigma}\right)^2\right] \quad (4\text{-}2)$$

where: μ = mean of $ln(x)$; σ= standard deviation of $ln(x)$. The main difference between the normal and lognormal distribution is that in the latter, $ln(x)$ is the normally distributed variable rather than x itself.

The R_{max} lognormal distribution parameters corresponding to CRL 458 are listed in Table 4-2. Figure 4-6, Figure 4-7, and Figure 4-8 show the marginal distribution fitted to R_{max} for each intensity bin.

Table 4-2. Marginal distribution parameters of R_{max} at CRL 458.

TC Intensity	$\mu_{ln(x)}$	$\sigma_{ln(x)}$
High	4.21	0.25
Medium	4.13	0.55
Low	4.14	0.49

Figure 4-6. Marginal distribution (lognormal) of R_{max} for HI TCs at CRL 458.

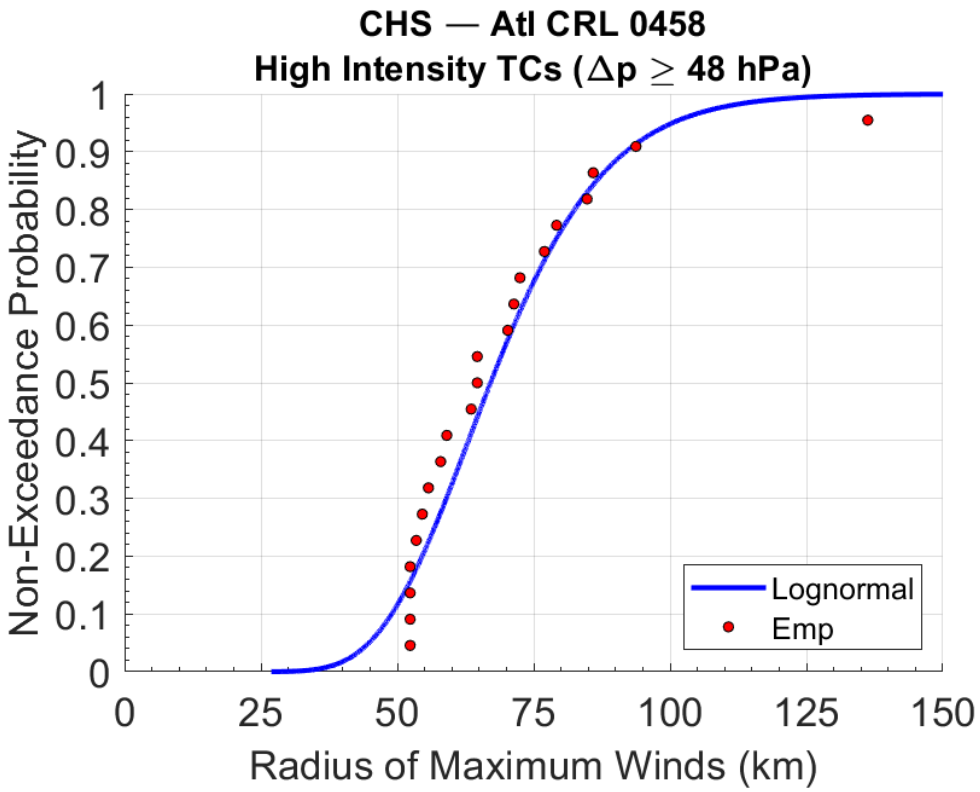

Figure 4-7. Marginal distribution (lognormal) of R_{max} for MI TCs at CRL 458.

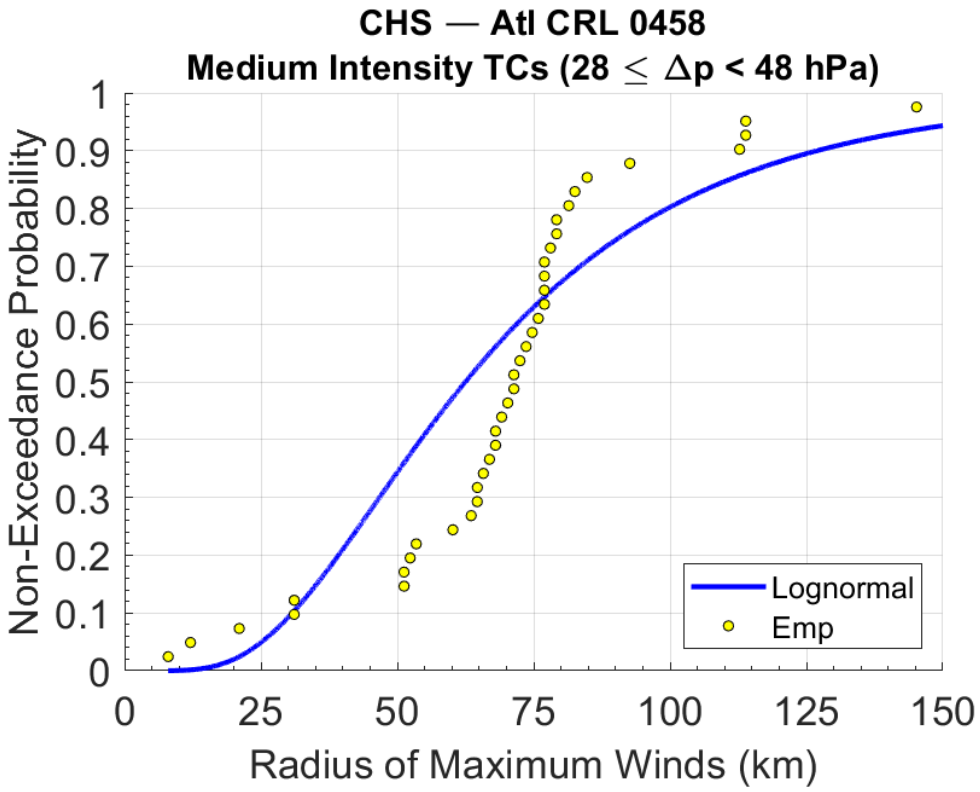

Figure 4-8. Marginal distribution (lognormal) of R_{max} for LI TCs at CRL 458.

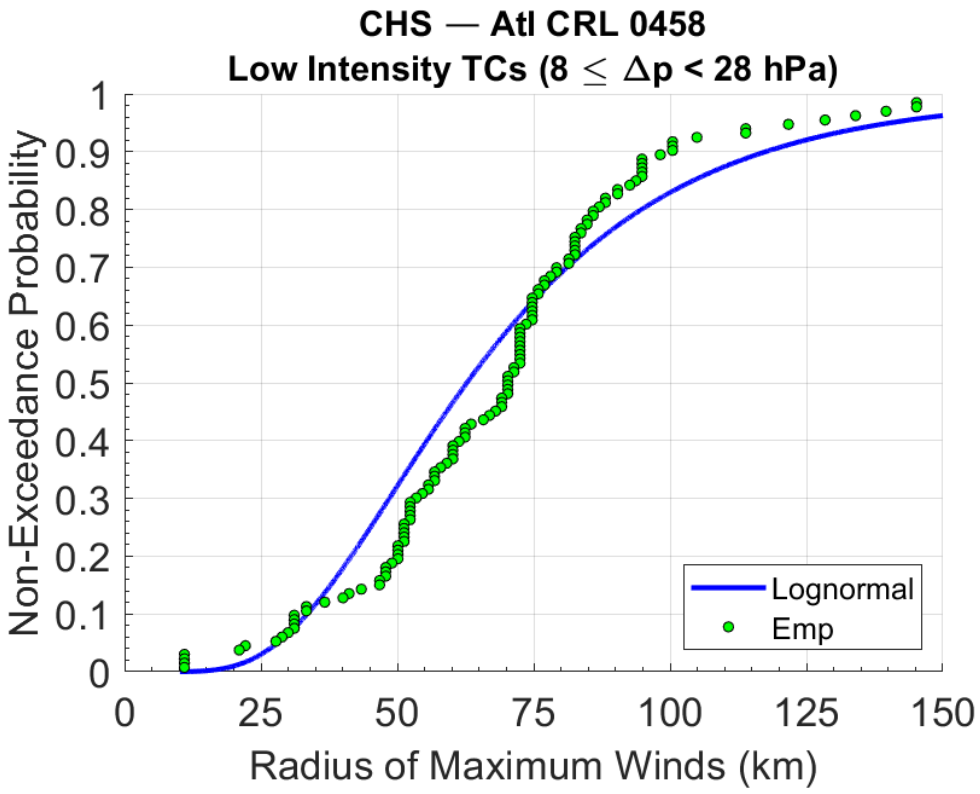

4.1.3 Translational Speed (V_t)

The V_t data requires two different parametric distributions. The lognormal distribution, discussed in the previous section (Equation 4-2), is used to fit LI TCs. The V_t of MI and HI TCs is represented by the normal distribution. A normal distribution has two parameters: mean (μ) and standard deviation (σ):

$$f(x) = \frac{1}{\sigma\sqrt{2\pi}} exp\left[-\frac{1}{2}\left(\frac{x-\mu}{\sigma}\right)^2\right] \quad (4\text{-}3)$$

where: μ = mean of random variable x; σ= standard deviation of x.

The marginal distribution of V_t for HI, MI, and LI TCs corresponding to CRL 458 are listed in Table 4-3. Figure 4-9, Figure 4-10, and Figure 4-11 show the marginal distribution fitted to V_t at CRL 458 or each intensity bin.

Table 4-3. Marginal distribution parameters of V_t at CRL 458.

TC Intensity (Normal)	μ	σ

High	41.1	14.9
Medium	34.2	15.0
TC Intensity (Lognormal)	$\mu_{ln(x)}$	$\sigma_{ln(x)}$
Low	3.44	0.51

Figure 4-9. Marginal distribution (normal) of V_t for HI TCs at CRL 458.

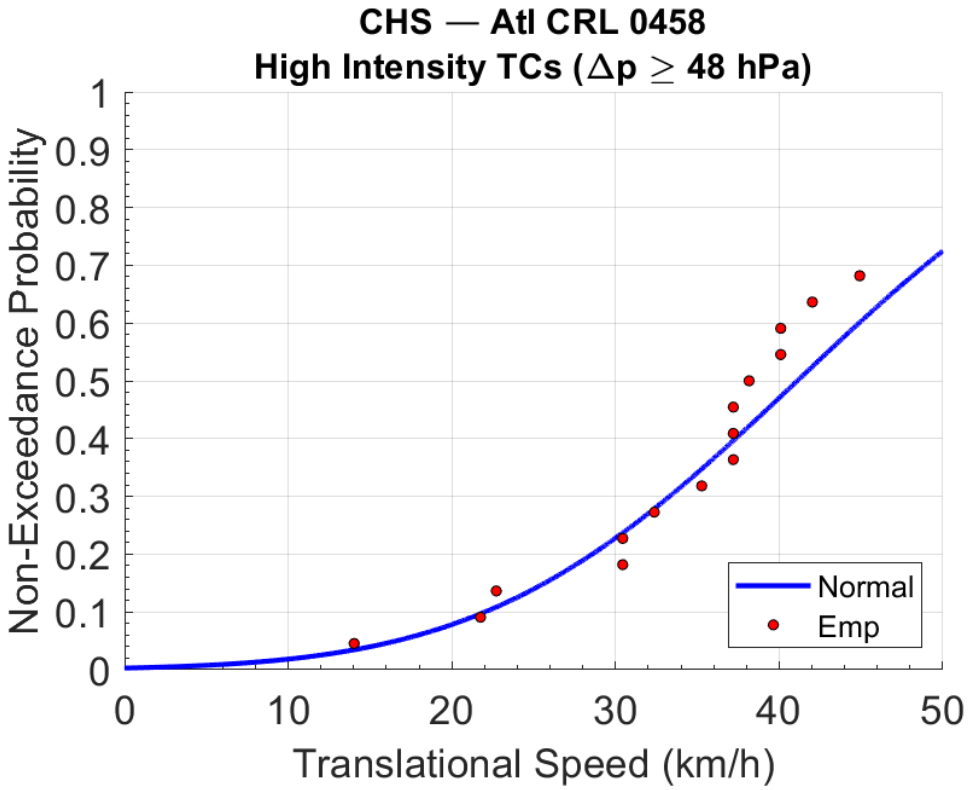

Figure 4-10. Marginal distribution (normal) of V_t for MI TCs at CRL 458.

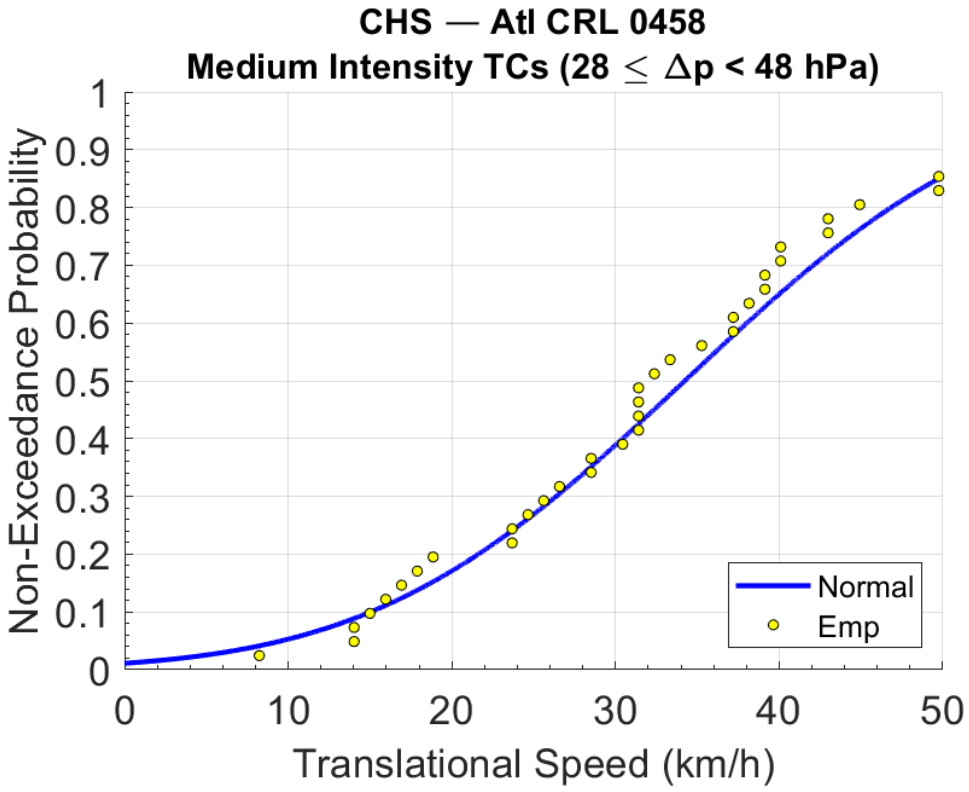

Figure 4-11. Marginal distribution (lognormal) of V_t for LI TCs at CRL 458.

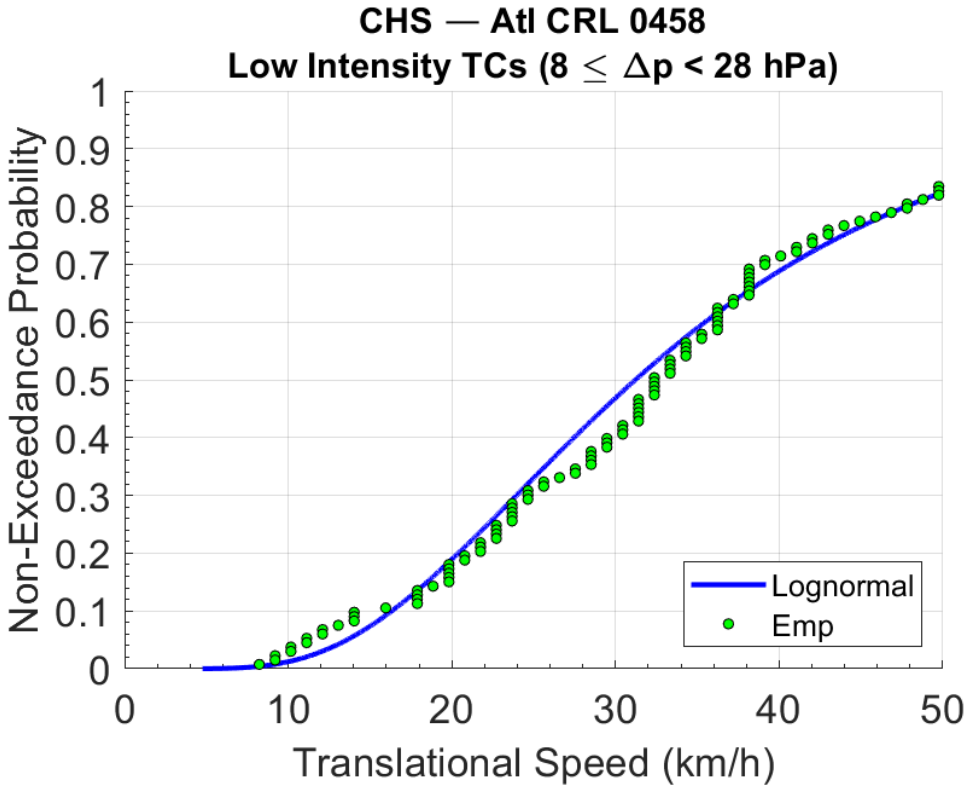

4.1.4 Heading Direction

In the PCHA, the θ marginal distribution is taken as the directional SRR (DSRR) that is computed from the GKF model (Chouinard and Liu 1997). The DSRR is given by

$$\lambda_\theta = \frac{1}{T}\sum_i^n w(d_i)\, w(\theta_i) \tag{4-4}$$

$$w(\theta_i) = \frac{1}{\sqrt{2\pi}h_\theta} exp\left[-\frac{1}{2}\left(\frac{\theta_i}{h_d}\right)^2\right] \tag{4-5}$$

where: λ_θ = the DSRR in storms/yr/km; T = record length in (yr); d_i = distance from location of interest to a track point (km); h_d = optimal kernel size (km); $w(\theta_i)$ = distance weights from the heading direction GKF (deg^{-1}); θ_i = heading direction (deg); h_θ = optimal directional kernel size (e.g., 30 deg); and $w(d_i)$ = distance weights computed using the GKF (Equation 3-2).

The θ normal distribution parameters corresponding to CRL 458 are listed in Table 4-4. Figure 4-12, Figure 4-13, and Figure 4-14 show the marginal distribution of θ derived from the DSSR for HI, MI, and LI TCs, respectively.

Table 4-4. Marginal distribution parameters of θ at CRL 458.

TC Intensity	μ	σ
High	13.9	40.0
Medium	32.8	36.2
Low	33.8	52.6

Figure 4-12. Marginal distribution (normal) of θ for HI TCs at CRL 458.

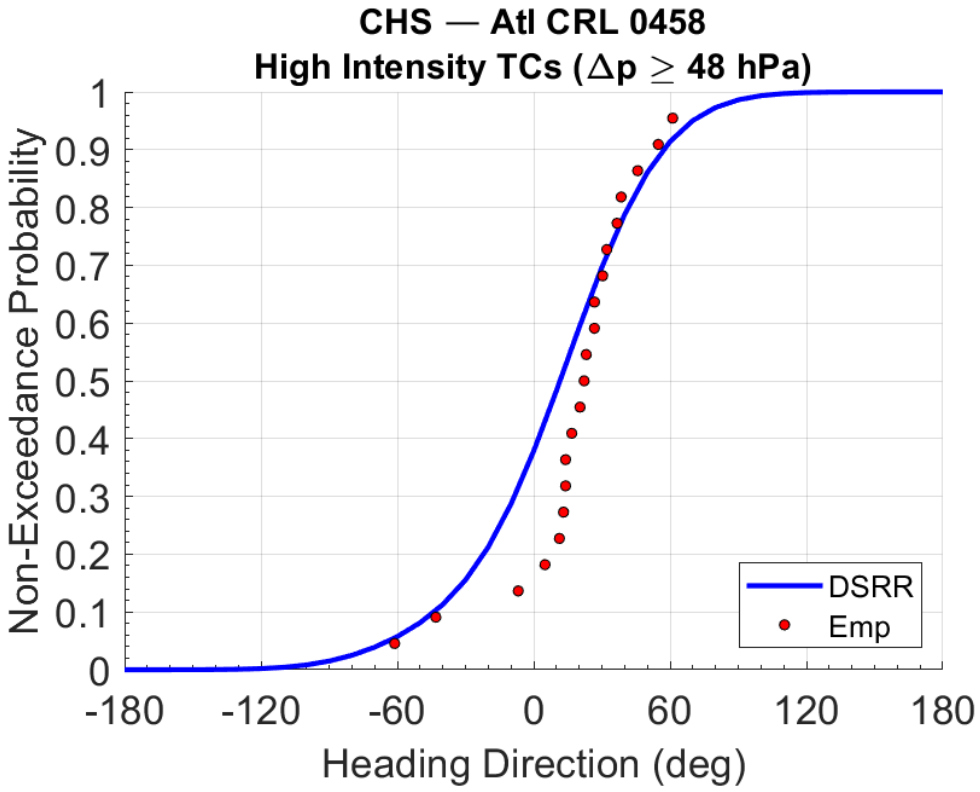

Figure 4-13. Marginal distribution (normal) of θ for MI TCs at CRL 458.

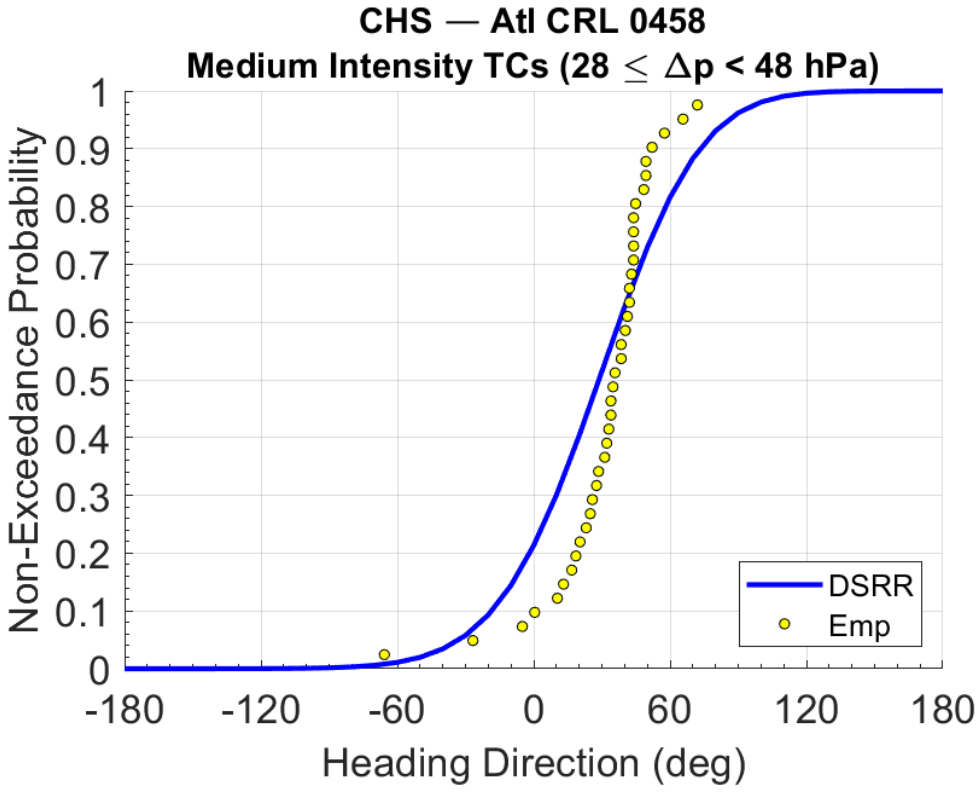

Figure 4-14. Marginal distribution (normal) of θ for LI TCs at CRL 458.

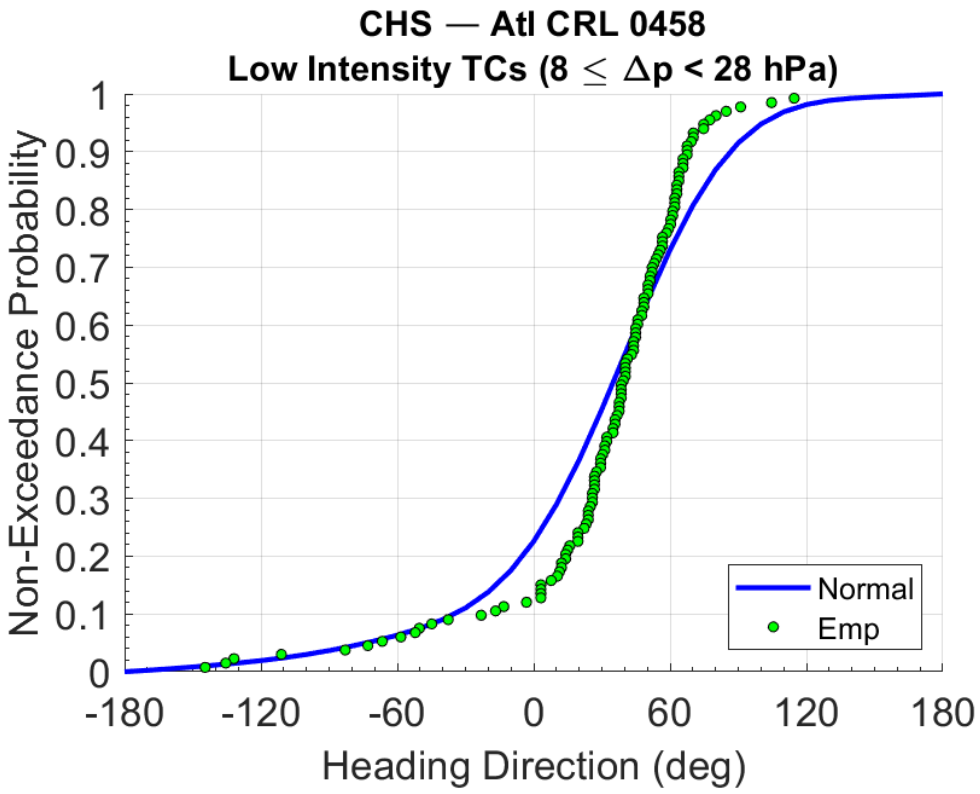

4.2 Joint Probability Analysis using the Meta-Gaussian Copula

The main deficiency in JPM studies to date is the lack of a true joint probability model. Typical joint probability approaches often involve unrealistic assumptions that either: 1) all random variables are independent, or 2) variables follow a joint normal distribution. TC parameters have some level of correlation between them (FEMA 2012). The correlation of TC parameters with location is implicitly considered, since the analysis is centered on a CRL; therefore, the SRR and the TC parameters used for fitting the probability distributions correspond to that location. The dependence between Δp and R_{max} is often considered in JPM studies, particularly if the latter is computed using a statistical model such as Vickery and Wadhera (2008) which explicitly uses Δp as input.

JPM-OS-BQ, for example, uses a double-exponential covariance function (Toro et al. 2010) as a pseudo dependence structure. Instead of computing the correlation between pairs of JPM atmospheric-forcing parameters, this approach relies on expert judgement to set correlation distances that dictate the discretization of marginal distributions of JPM parameters. Previous studies have either assumed independence between the

parameters (Equation 2-1) or used a correlation tree with 1:1 dependence as seen in the diagram in Figure 4-15. The latter approach was described by Resio et al. (2007):

$$P(x_0, \Delta p, R_{max}, V_f, \theta) = P(x_0) \cdot P(\Delta p) \cdot P(R_{max}) \cdot P(V_f) \cdot P(\theta) \quad (4\text{-}6).$$

Figure 4-15. TC parameter correlation tree with 1:1 dependence

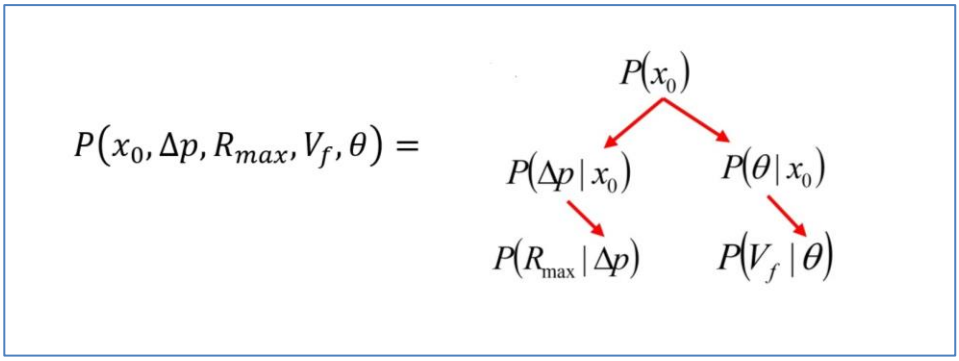

Other approaches have proposed the use of conditional distributions linking pairs of random variables, but in practice variables are often interconnected through simplified linear relationships.

The PCHA framework uses copula theory to overcome the aforementioned limitations. A copula is a dependence function that links a set of marginal distributions to form a unique joint probability distribution. According to the seminal Sklar's (1959) theorem, any joint (multivariate) distribution, H, can be deconstructed into marginal distributions, $F_{1,\ldots,n}$, and a copula, C, as follows:

$$H(x_1, \ldots, x_n) = C\left(F_1(x_1), \ldots, F_n(x_n)\right) \quad (4\text{-}7)$$

where n is the number of dimensions of the cumulative distribution function (CDF).

A copula must be expressed in terms of uniform marginal distributions (u_n) defined on the interval [0, 1]. The general formulation is:

$$C(u_1, \ldots, u_n) = H\left(F_1^{-1}(x_1), \ldots, F_n^{-1}(x_n)\right) \quad (4\text{-}8)$$

where $F^{-1}(\,)$ is the inverse of the marginal distribution.

Zhang and Singh (2019) recommend the use of meta-elliptical copulas, since this family frequently outperforms other multivariate copulas in capturing the full range of dependence, while also excelling due to simplicity of construction and ease of parameter estimation, particularly in the case of the MGC.

The MGC consists of a multivariate CDF constructed by linking a set of marginal probability distributions with a multivariate Gaussian copula as the dependence structure. The CDF of the Gaussian copula is expressed as:

$$C_R^{Gauss}(u) = \Phi_R\left(\Phi^{-1}(u_1), \ldots, \Phi^{-1}(u_n)\right) \tag{4-9}$$

where $\Phi^{-1}(\ )$ is the inverse of the standard Gaussian distribution; and Φ_R is the multivariate distribution of n Gaussian distributions with correlation matrix R, given by:

$$R = \begin{pmatrix} 1 & \rho_{1,2} & \cdots & \rho_{1,n} \\ \rho_{2,1} & 1 & \cdots & \rho_{2,n} \\ \vdots & \vdots & \ddots & \vdots \\ \rho_{n,1} & \rho_{n,2} & \cdots & 1 \end{pmatrix} \tag{4-10}.$$

The dependence between pairs of random variables is given by correlation coefficients (ρ). In the case of JPM, ρ must be computed for all pairs of TC forcing parameters. The correlation is accounted for by first computing the rank correlation between the TC atmospheric-forcing parameters using Kendall's Tau (Kendall 1970). By computing the rank correlation, the correlation between TC parameters is preserved following the non-linear transformations required for the MGC. The rank correlation is then transformed to Pearson's rho (Fang et al. 1990; 2002), a linear correlation, using the following form for application in the MGC approach:

$$\rho = \sin(\frac{\tau\pi}{2}) \tag{4-11}.$$

The dependence between pairs of random variables is given by correlation coefficients (ρ). For TCs, ρ is computed for all pairs of atmospheric-forcing parameters. Below are the correlation matrices (R) constructed for All, HI, MI, and LI TCs from Equation 4-10. For each of the intensity bins, Figures 4-16 through 4-19 illustrate the correlation between the JPM parameters computed as both the rank correlation and Pearson's correlation. In each

correlation matrix, the reported correlations correspond first to the rank correlation and secondly the Pearson's correlation shown in parentheses.

Figure 4-16. Correlation matrix for All TCs at CRL 458.

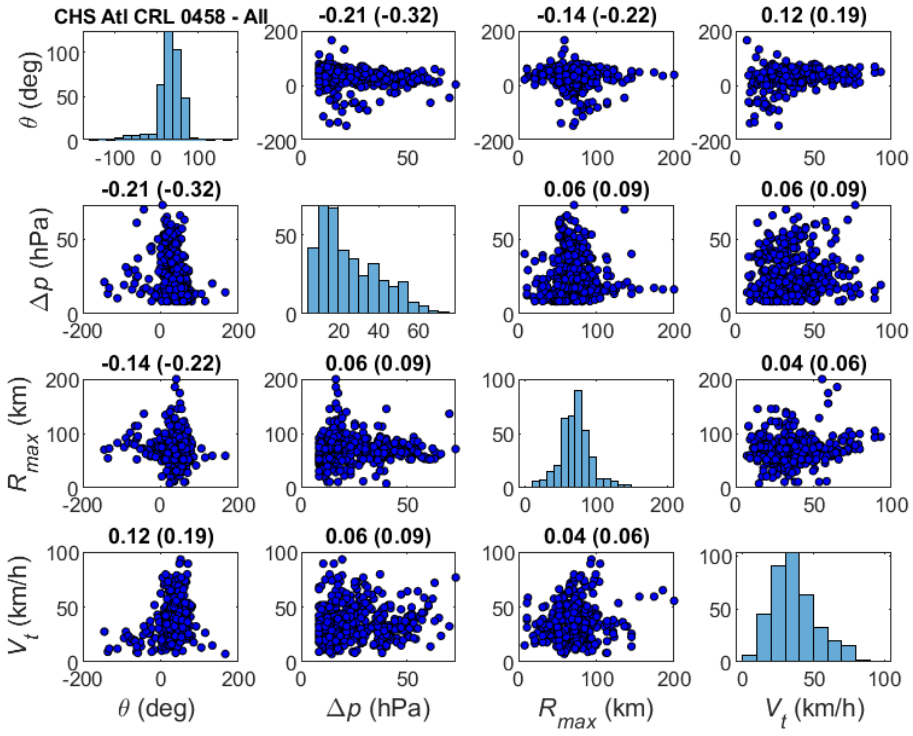

Figure 4-17. Correlation matrix for HI TCs at CRL 458.

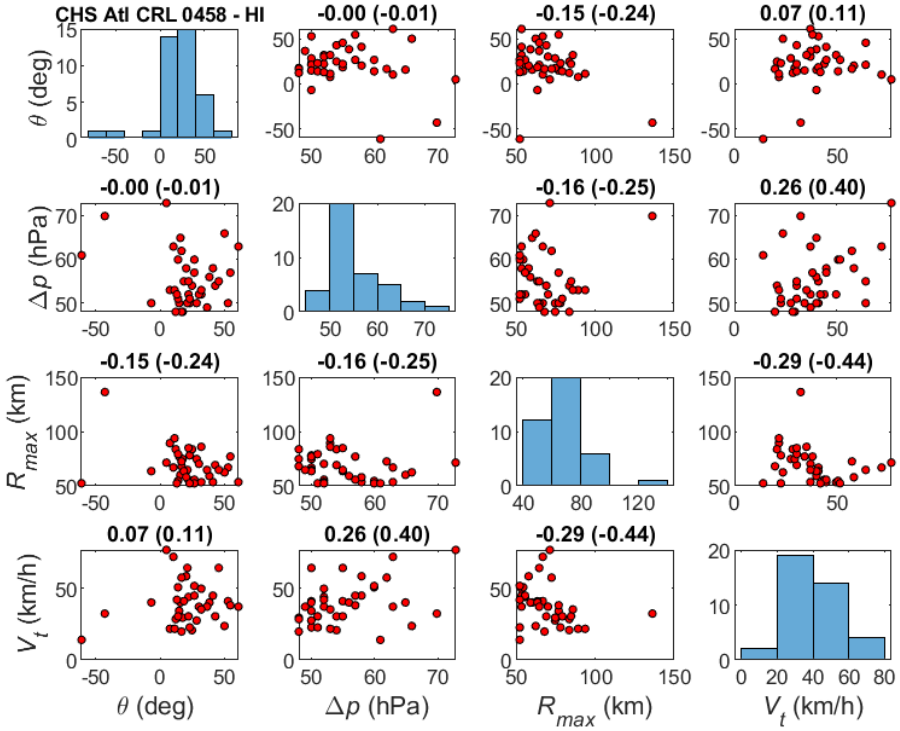

Figure 4-18. Correlation matrix for MI TCs at CRL 458.

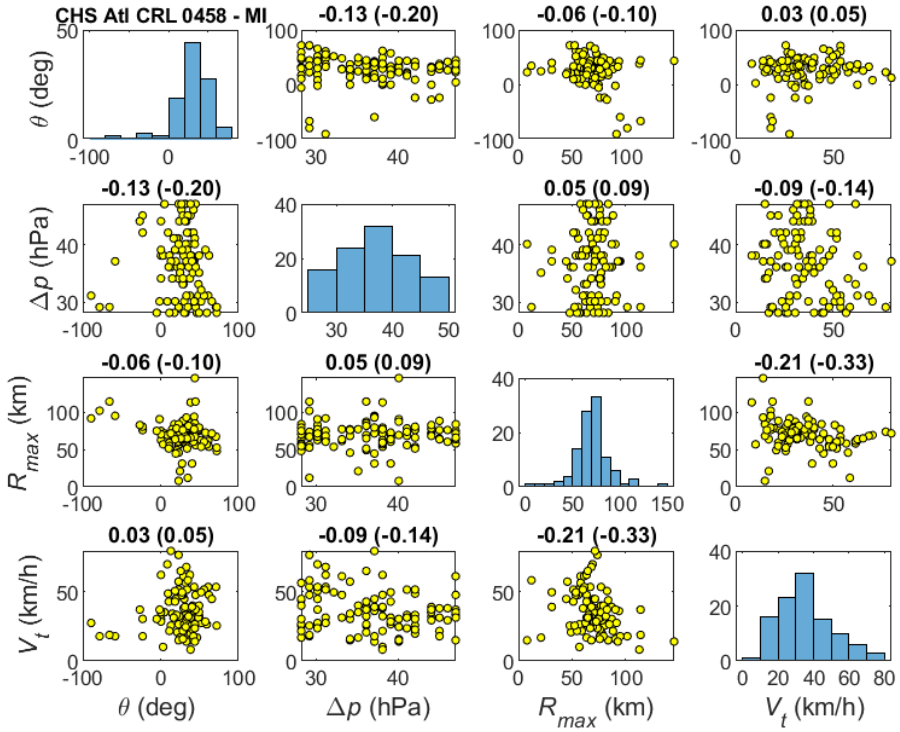

Figure 4-19. Correlation matrix for LI TCs at CRL 458.

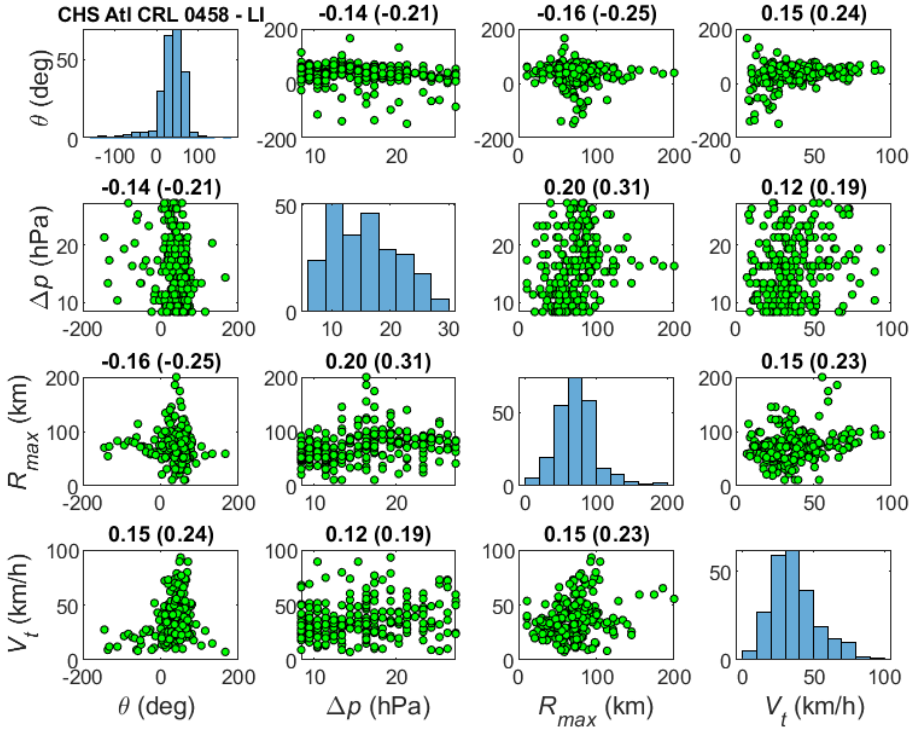

4.3 Selection of the Reduced Storm Suite (RSS)

The goal of the storm selection is to find the optimal combination of storms, given a predetermined number of events to be sampled out of the 1,050-storm ITCS, to obtain a reasonable estimation of the SWL hazard. The number of storms sampled for each RSS is limited by budget and/or schedule constraints and informed by previous studies where the Design of Experiments (DoE) has been applied (*e.g.*, Melby et al. 2020). The storm selection process is performed using the DoE approach documented in Taflanidis et al. (2017), and Zhang et al. (2018). The DoE compares the RSS SWL hazard curves to benchmark hazard curves corresponding to the ITCS at a given number of specific locations or save points. The difference between the RSS hazard curves and ITCS benchmark curves is minimized by initially sampling a small subset of TCs, and then iteratively adding additional TCs (*e.g.*, 5 by 5) until the difference between the two curves is significantly reduced or becomes negligible. The save points where the hazard curve optimization takes place correspond to critical locations within the study area.

The general steps in the DoE approach used for the selection of the TC RSS are as follows:

1. Identify a set of save points within the study area where the DoE optimization is to be performed.
2. Develop or use existing TC SWL hazard curves for the ITCS.
3. Determine the number of TCs to be sampled.
4. Develop new hazard curves for the ITCS.
5. Select the annual exceedance frequency (AEF) range at which the RSS and ITCS hazard curves will be compared. Differences can be computed along the entire hazard curve, segment of the hazard curve, or at specific AEFs (*e.g.*, 0.02 to 0.002 storms/year, equivalent to 50 to 500 years).
6. Calculate errors between the RSS and ITCS hazard curves at predetermined AEFs.
7. Conduct an iterative optimization analysis, described in Melby et al. (2020) to evaluate the benefit of increased RSS size; (*e.g.*, 5 by 5, from 10 to 25 TCs).
8. Once the sought number of storms is reached (*e.g.*, 25), in order to evaluate the overall RSS performance, the RSS selected through optimization indicated in Step 7 is compared to multiple RSS where TCs are sampled in a single batch.
9. Complete storm selection by choosing the optimal RSS from Step 8.
10. The selected storms are simulated in ADCIRC and the results used to reconstruct hazard curves.

For this study, an RSS of 60 TCs was selected for simulating in the hydrodynamic models. However, the probabilistic analysis applied surge responses from only 58 storms in the RSS, since two of the hydrodynamic simulations were unstable. The storm parameters of these 58 TCs are provided in Appendix C.

4.4 Augmented Synthetic TC Suite and Probability Masses

Generally, the PCHA workflow begins with the simulation of an ITCS of hundreds of storms (up to a few thousand in regional studies) to ensure high-resolution, high-fidelity results and introduces GPM to generate an ATCS of hundreds of thousands to millions of TCs that retain the high-fidelity nature of the initial suite (Jia et al. 2016; Zhang et al. 2018). The GPM establishes the relationship between the atmospheric-forcing vector

$\hat{x} = f(x_o, \theta, \Delta p, R_{max}, V_t)$ and the TC responses (e.g., storm surge, wave parameters).

The PCHA methodology includes the development of an ATCS to fully cover the parameter and probability spaces for the study area. The ATCS is developed by further discretizing the parameters of the ITCS, which is simulated in the hydrodynamic models, to create a higher density of synthetic TCs. However, to avoid an excessive computational cost, the number of augmented storms generated needs to be balanced with the number of point locations where the JPM integral is solved. The final result of developing and training the GPM is the development of a continuous surface of high-fidelity storm surge results produced for the construction of the final hazard curves. Using the high-fidelity hydrodynamic modeling results produced by simulating the ITCS, a GPM is then trained for predicting storm responses produced by the ATCS.

For this study, the GPM trained as part of the CHS-NA update was leveraged for the benefit of maintaining the high-fidelity nature of the regional hydrodynamic results. An ATCS containing 1,098,720 storms across 130 master tracks was developed from the NACCS ITCS. Table 4-5 outlines the discretization of the TC parameters for ATCS.

The ATCS was first defined by replicating a core set of 52,920 parameter combinations approximately 20.76 times to create an augmented suite of 1,098,720 storms. The parameters combined to develop this augmented suite were defined by further discretizing the parameters defined by the NACCS ITCS. The AEFs computed for this study are based on the GPM surge estimates forced by the ATCS as further discussed in Section 5.

Table 4-5 Atmospheric-forcing parameters from the ATCS.

TC Parameter	Range	Discretization	Number of Discrete Values
θ	-60°, -40°, -20°, 0°, +20°, +40° (clockwise from North)	20°	6
Δp	8 to 108 hPa	5 hPa	21
R_{max}	20 to 155 km	5 km	28
V_t	10 to 80 km/h	5 km/h	15
Master Tracks			130
Total number of TCs			1,098,720

4.4.1 Probability Masses for the ATCS

For each of the parameter combinations defined by the ATCS, a probability mass is computed as a function of SRR, TC weights, and track spacing. The SRR is of particular importance to the computation of AEFs, since it represents the number of storms a location is likely to experience in a year. Each TC in the synthetic suite constitutes a partition of the SRR. In other words, increasing the number of storms in the synthetic TC suite increases the resolution of both the probable and physical parameter spaces, while decreasing the weight of each individual storm. Following the development of the ATCS, the SRR, TC weights, and track spacing were then used to compute each storm's probability mass, as defined by $\hat{\lambda}_i$ in Equation 2-2, for each of the augmented storms.

5 Hydrodynamic Modeling

For this study, the simulations of the RSS were performed using ADCIRC to evaluate the effect of the updated mesh including the project alternatives on the storm responses. The project alternatives considered herein are proposed levees located within the D.C. Metro study area (Figure 5-3). The results of the ADCIRC simulations were output at a subset of save points selected from the NACCS which are listed in Table 5-1. The probabilistic analysis applied surge responses from 58 storms in the RSS due to the instabilities in two of the simulations.

The storm responses for the XCs were leveraged from the NACCS simulations as it was not feasible under this study to produce updated simulations of these storms. Due to instabilities in the NACCS simulations, the probabilistic analysis of XC-induced surge relied on 94 of the 100 storms in the XC suite. Although these simulations do not include the effects of the updated mesh, the influence of the XCs on the final SWL AEFs within the study area is small, and the differences in surge between the D.C. Metro and NACCS simulations are considered to be negligible.

The following section documents the changes made to the NACCS ADCIRC mesh for application in this study. Additionally, the conditions of the RSS simulations along with observed results are discussed here.

Table 5-1. Save points selected for D.C. Metro ADCIRC simulations.

Count	ADCIRC ID	Latitude	Longitude
1	14607	38.76	-77.03
2	5982	38.85	-77.03
3	5984	38.84	-77.03
4	5987	38.81	-77.03
5	5991	38.79	-77.03
6	7757	38.81	-77.04
7	14608	38.81	-77.03
8	14609	38.85	-77.02
9	14731	38.77	-77.04
10	14735	38.78	-77.04
11	5878	38.87	-77.02

12	5980	38.87	-77.01
13	6137	38.87	-77.02
14	7841	38.87	-77.02
15	14607	38.76	-77.03
16	14732	38.79	-77.02
17	5978	38.88	-77.05
18	5919	38.90	-77.08
19	14611	38.89	-77.05
20	14612	38.87	-77.00
21	14733	38.88	-76.97
22	5979	38.88	-77.02
23	14610	38.87	-77.02

5.1 ADCIRC Mesh Development

The ADCIRC mesh developed for the NACCS (Cialone et al. 2015) was modified to provide detailed representation of the D.C. Metro study area. There were two major changes implemented in the NACCS grid specific to this project, that is, refinement of the study area and de-refining of a remote area (Long Island, NY) while the original boundary of the domain (Figure 5-1) was not altered.

Figure 5-1. Outline plot showing the boundary of the ADCIRC computational domain.

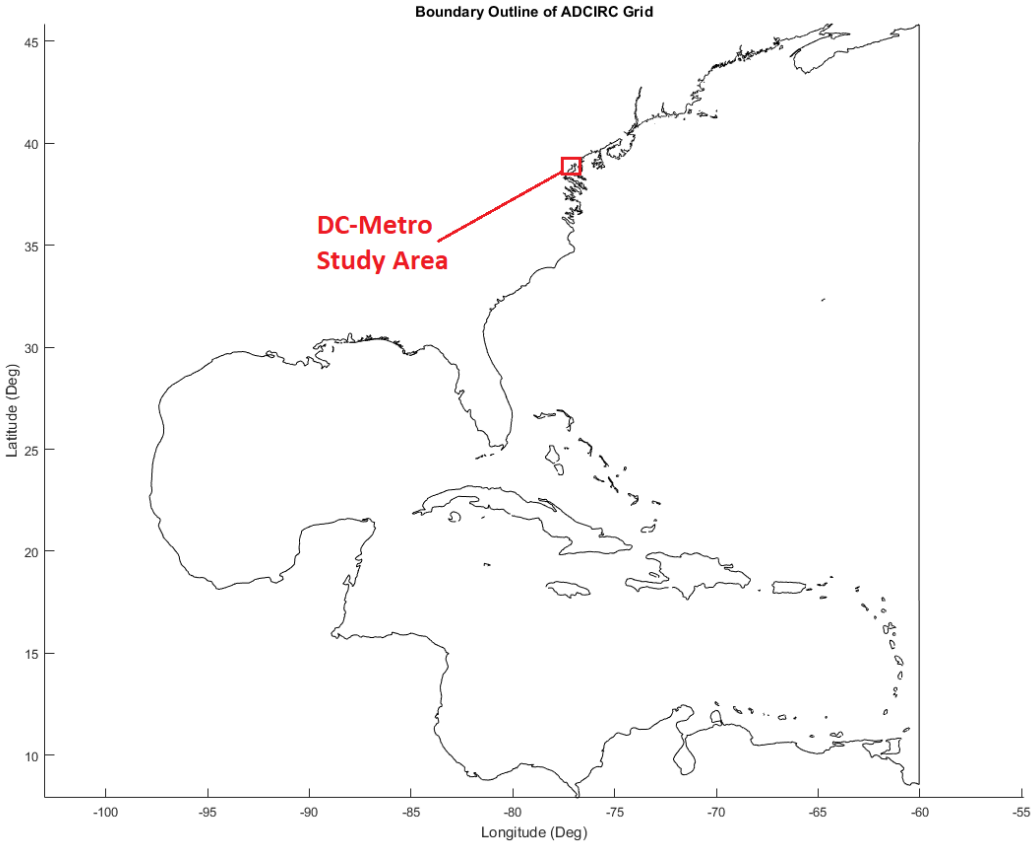

Refinement of the grid in the study area was necessary to fully capture and analyze the hydrodynamic processes in the area of interest. Moreover, this procedure facilitated the implementation of the complex levee system at the specific location required by the study sponsor (USACE NAB). The purpose of grid de-refining is to reduce the mesh resolution in areas remote from the area of interest in order to decrease model simulation times without significantly affecting the flow volume exchange between the de-resolved region and the study area. The total number of 3.12 million nodes in the NACCS grid was reduced to 2.95 million (approximately a 6% reduction) in the D.C. Metro grid due to the Long Island, NY region de-refining. Figure 5-2 shows the grid resolution before (a) and after (b) de-refining in the Long Island, NY area.

Figure 5-2. Long Island, NY area (a) before and (b) after de-refining.

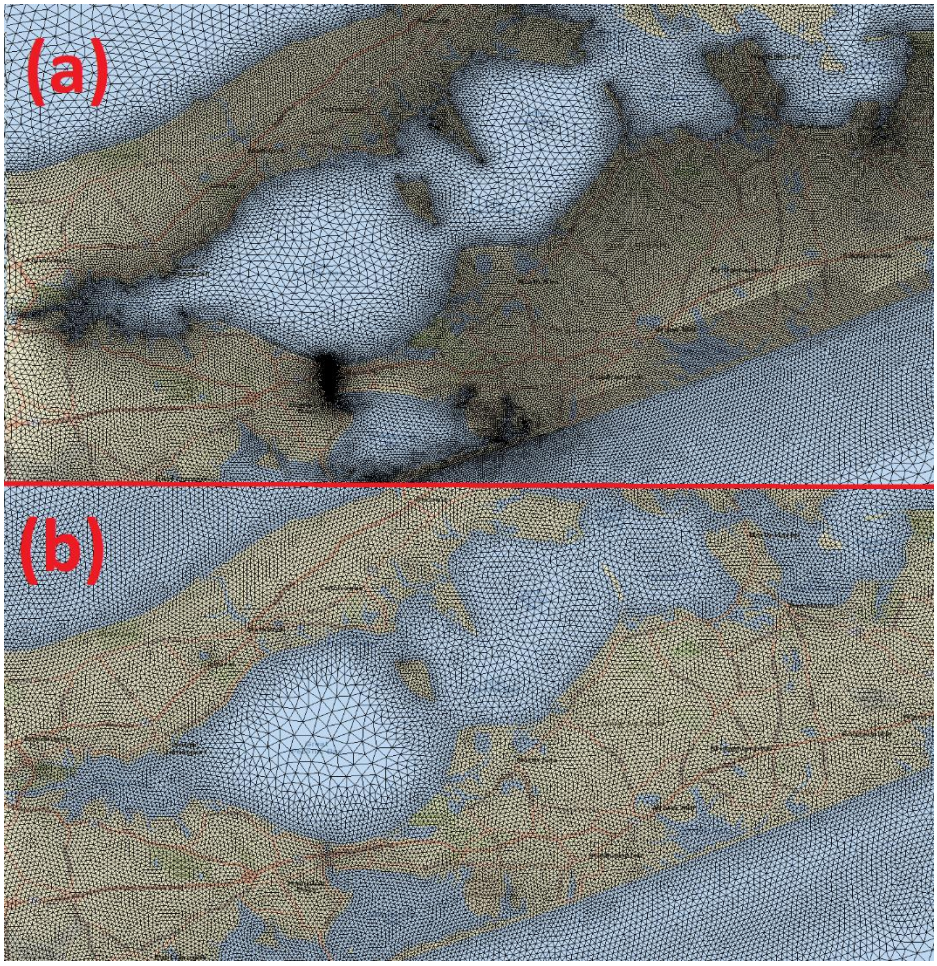

Figure 5-3(a) and Figure 5-3(b) show the ADCIRC mesh elements and boundary in the D.C. Metro study area for the NACCS mesh and D.C. Metro mesh, respectively. The resolution of the NACCS grid was locally increased in order to facilitate implementation of the levee structures (indicated as green lines in Figure 5-4) provided by the USACE NAB. Representing levees as ADCIRC weir-pair sub-grid features helps to maintain model stability. This is because the sub-grid scale formulation for weir-pairs prevents the model from transitioning from sub to supercritical flows during the course of the simulation in the event that the water elevation is high enough to overtop the structure. The D.C. Metro grid has a spatial resolution (element size) ranging from approximately 10 to 1000 m and MSL as the vertical datum.

Another noticeable difference between the NACCS grid and the D.C. Metro grid is the extent and boundary location in the Anacostia River. The NACCS grid was terminated southward from Route 50 in the D.C. Metro

grid (Figure 5-4 shows a detailed view of the grid termination) in order to properly accommodate the in-flow boundary condition for the Anacostia River.

Figure 5-3. (a) NACCS ADCIRC mesh in the D.C. Metro study area. (b) D.C. Metro ADCIRC mesh in the study area. Green lines indicate implemented levee structures.

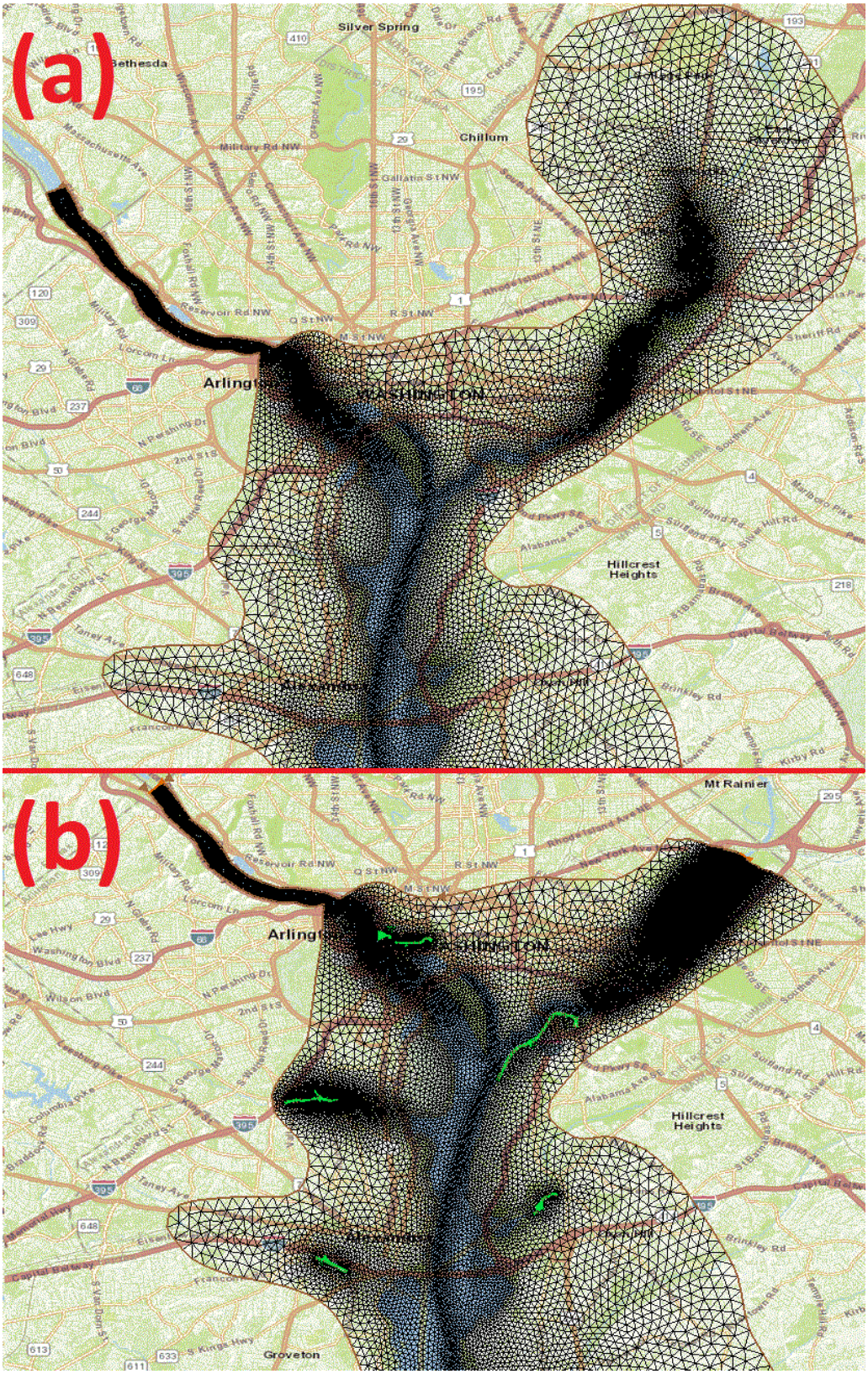

Figure 5-4. Zoom of ADCIRC grid at Anacostia River terminated boundary.

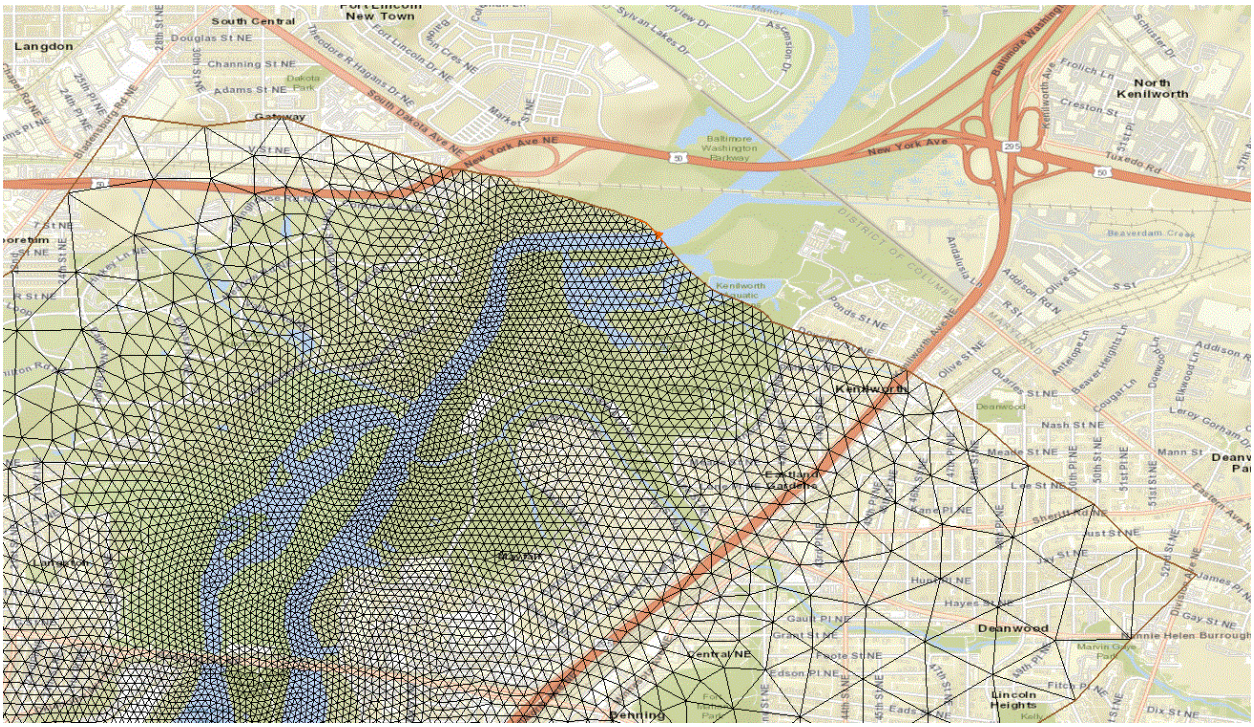

The final step in the grid modification was to update the bathymetry/topography in the study area with data from LIDAR surveys provided by the USACE NAB. Figure 5-5 shows a comparison of the bathymetry/topography relative to MSL before (a) and after (b) the update (the levee structures are indicated by black lines on Figure 5-5b).

Figure 5-5. Compression of the bathymetry/topography in the study area before (a) and after (b) update.

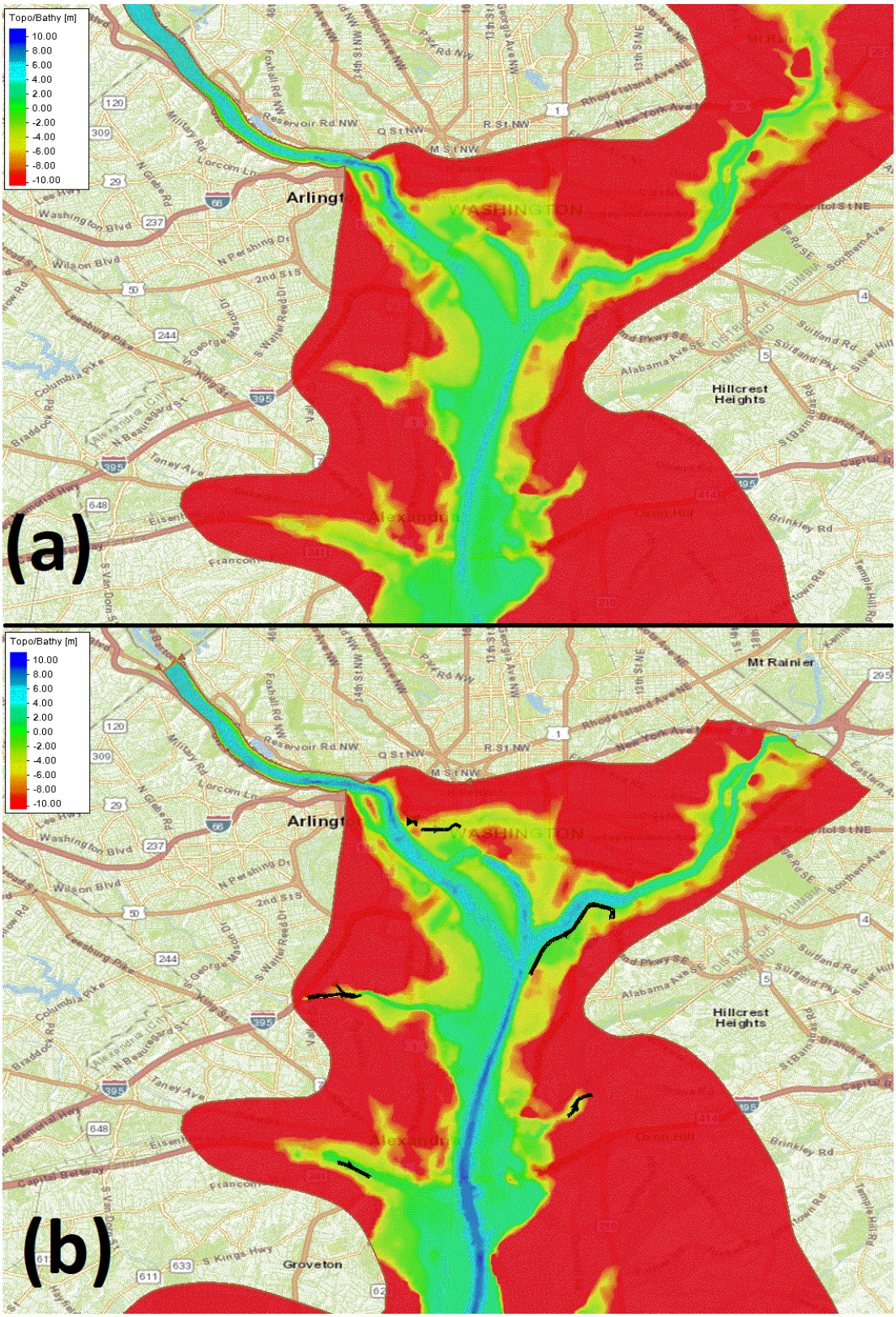

In order to show that the grid de-refining modification procedure did not significantly alter the model results in the region of interest and that the grid refining and updated bathymetry in the region of interest does improve model/data comparisons, an evaluation of the water surface elevation time-series from a simulation of Hurricane Irene was made at the Kiptopeke, Virginia gauge (NOAA Station 8632200) and the Washington, D.C. gauge (NOAA Station ID: 8594900); Figures 5-6 and 5-7, respectively. First, by comparing the NACCS water level time series with the D.C. Metro water level time-series, Figure 5-8 shows that the grid de-refining in the far-field did not alter the hydrograph at the entrance to Chesapeake Bay (Kiptopeke Station). Both the NACCS water level time series (red line) and the D.C. Metro water level time series (blue line) are nearly identical and compare well with the gauge data (green line)

Next, Figure 5-9 shows the water surface elevation time-series at the Washington, D.C. gauge, which is the region where the grid was refined and the bathymetry was updated with LIDAR data from the project sponsor. At this location, the Hurricane Irene D.C. Metro water level time series (blue line) shows great improvement over the time-series obtained from simulations with the NACCS mesh (red line) and the D.C. Metro water level time series compares well with the gauge data (green line). Figure 5-10 shows the water surface elevation time-series at the Washington, DC gauge, during Hurricane Isabel (2003). Once again, the Hurricane Isabel DCM water level time series (blue line) show very good agreement with DC gauge water level time series (green line). The gauge was nonoperational between 9/5/2003 and 9/11/2003 (“flat” green line between 125 and 275 hours).

In summary, de-refining the ADCIRC mesh has minimal impact on water levels in the region of interest and is simply a means to reduce model computation times. In contrast, improving the model bathymetry and grid resolution in the region of interest, greatly improves the model comparison/validation in the region of interest.

Figure 5-6. NOAA gauge: Kiptopeke, VA, ID 8632200.

Figure 5-7. NOAA gauge: Washington, DC, ID 8594900.

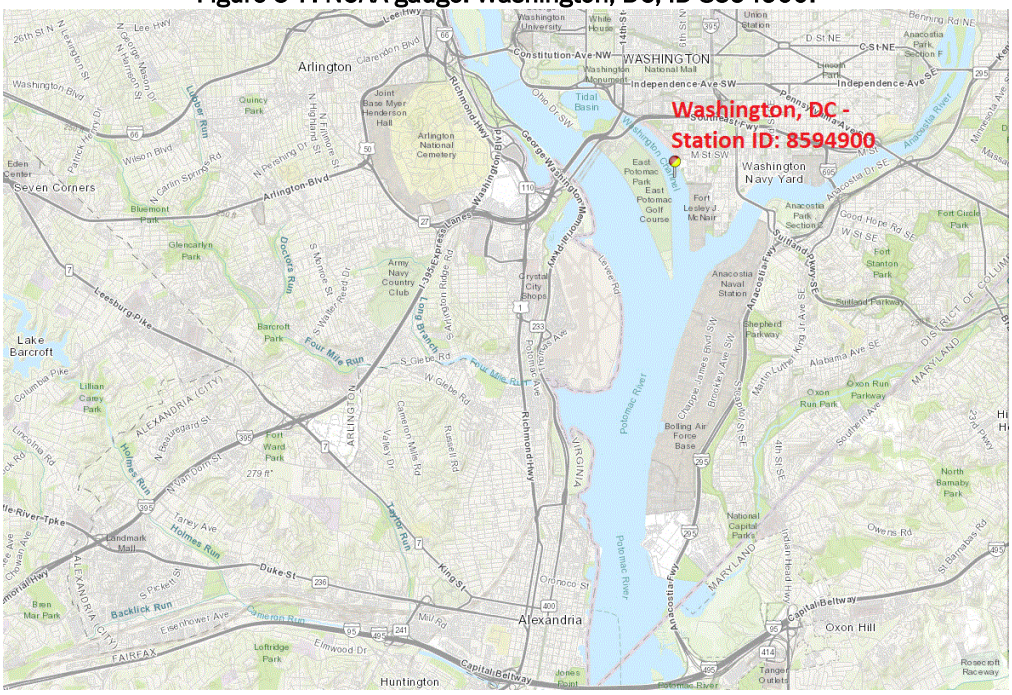

Figure 5-8. Water level time-series for simulated Hurricane Irene with D.C. Metro mesh (blue), NACCS mesh (red), and Kiptopeke, VA NOAA gauge (green).

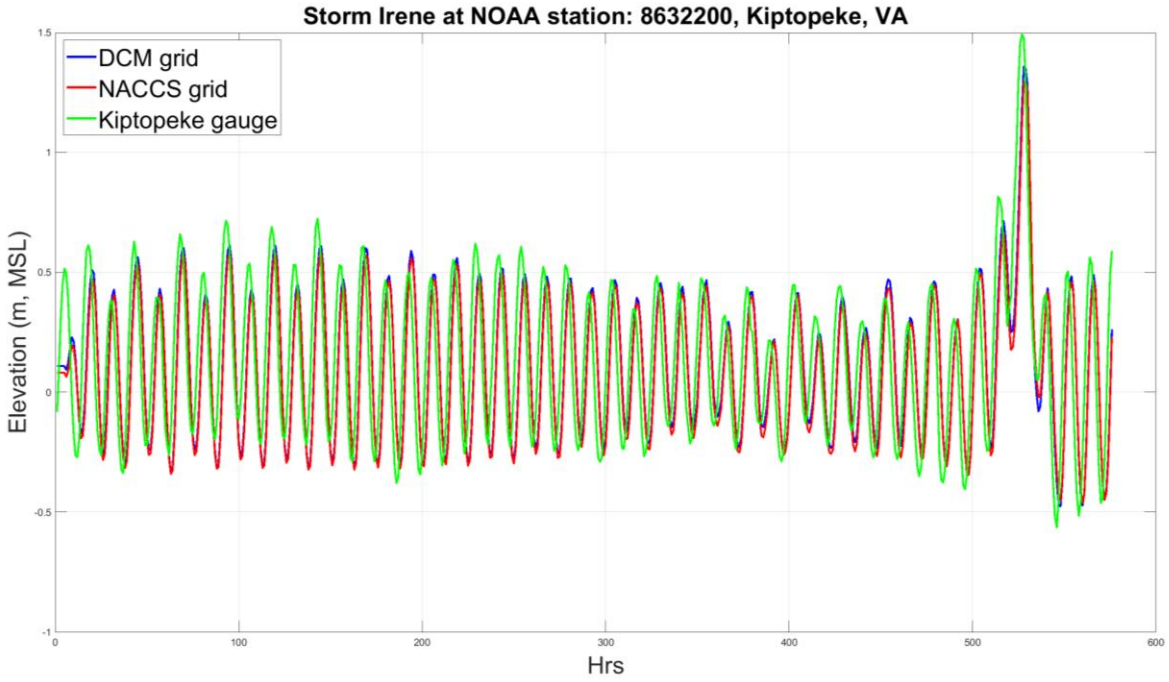

Figure 5-9. Water level time-series for simulated Hurricane Irene with D.C. Metro mesh (blue), NACCS mesh (red), and Washington, DC NOAA gauge (green).

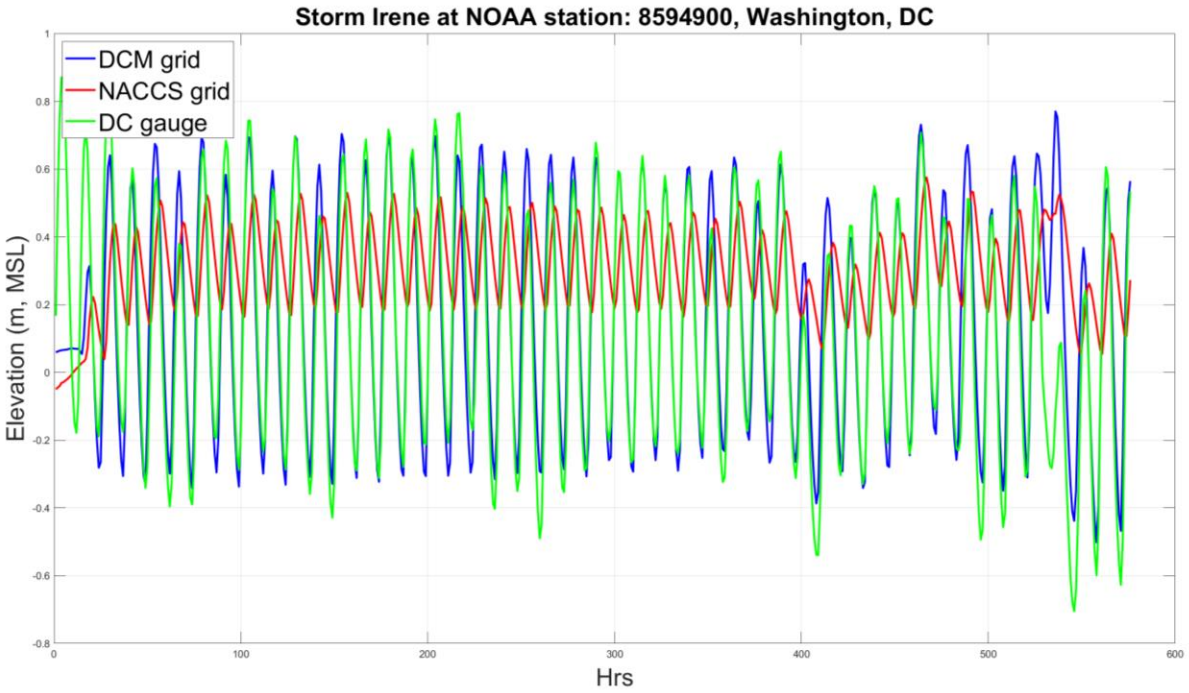

Figure 5-10. Water level time-series for simulated Hurricane Isabel with D.C. Metro mesh (blue), NACCS mesh (red), and Washington, DC NOAA gauge (green).

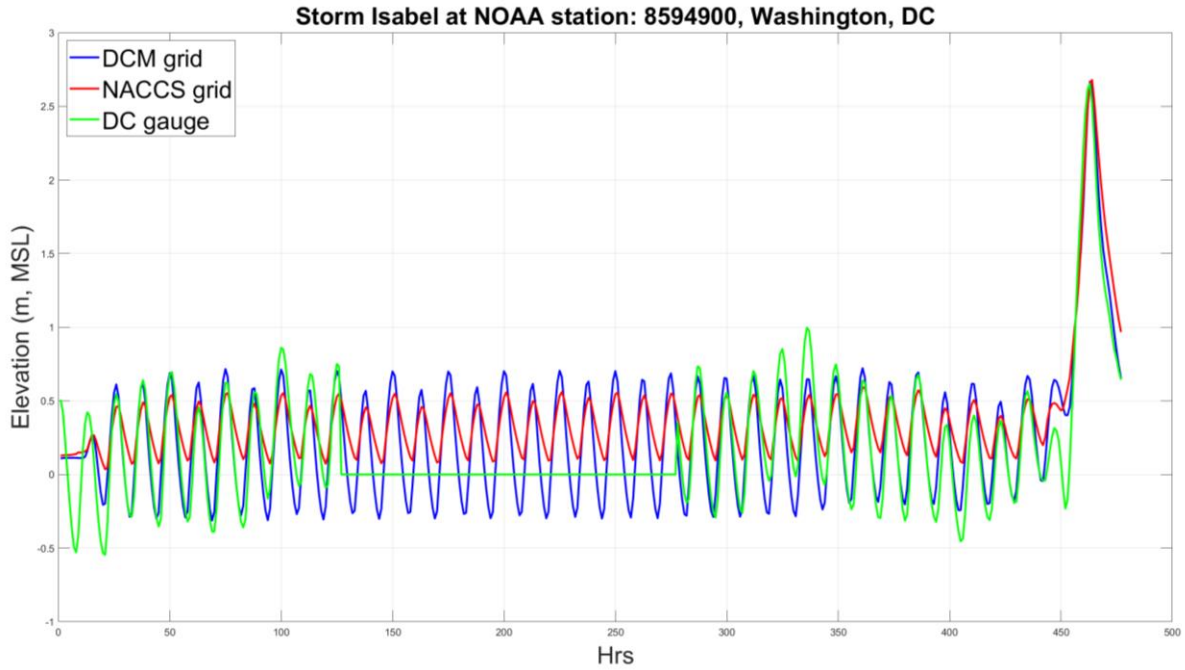

5.2 ADCIRC Simulation Results

The analysis of the maximum water level plots shows that surge generated by wind fields in 57% of the simulations is between 1 ft and 5 ft (Figure 5-11 shows Storm 640 that represents a typical response in this range), in 28% of the simulations the maximum water level is between 5 ft and 8 ft (Figure 5-12 shows Storm 17 that represents a typical response in this range), in 10% of the simulations the maximum water level is between 8 ft and 11 ft (Figure 5-13 shows Storm 110 that represents a typical response in this range), and in 5% of the simulations the maximum water level is between 11 ft and 14 ft (Figure 5-14 shows Storm 22 that represents typical response in this range). There is also one extreme case (Storm 72) where the maximum water elevation is between 14 ft and 15 ft (shown in Figure 5-15). As an example, the water level time-series plots for one of the save points provided by USACE NAB, point #5878 (shown in Figure 5-16), were generated for each of the above interval (Figures 5-17 through 5-21). The water level time-series show the evolution of water level at a predetermined location during a storm event. Storm 640 does not show a strong surge response in the hydrograph, but the remaining storms show a progressively stronger (higher) water level response in the water level time series.

Figure 5-11. Maximum water elevation: Storm 640, Surge only.

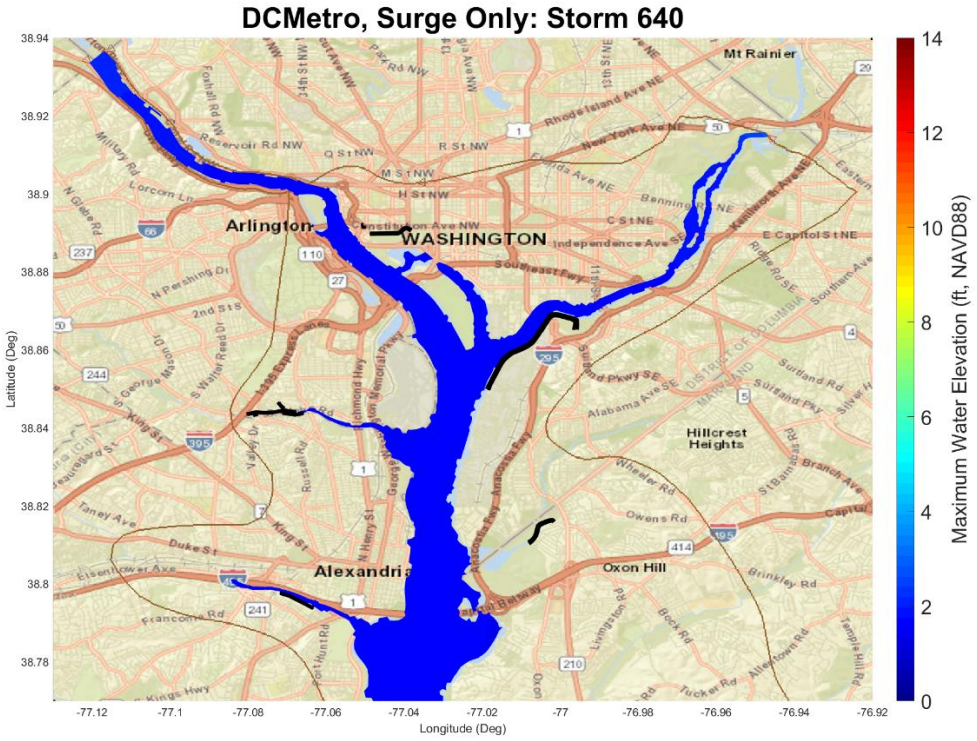

Figure 5-12. Maximum water elevation: Storm 17, Surge only.

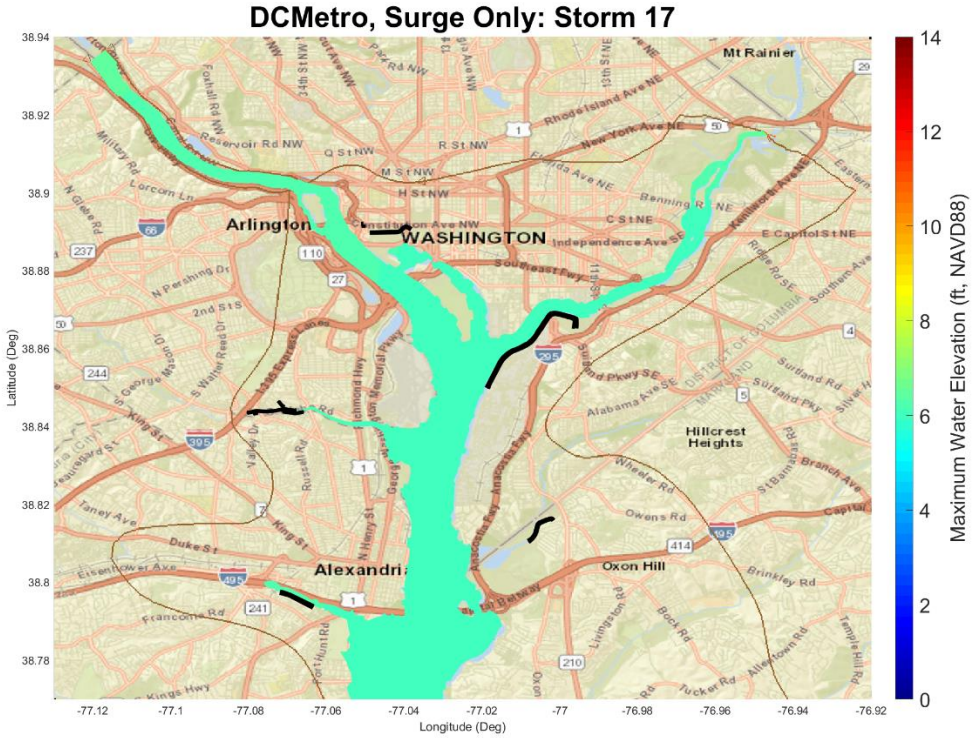

Figure 5-13. Maximum water elevation: Storm 110, Surge only.

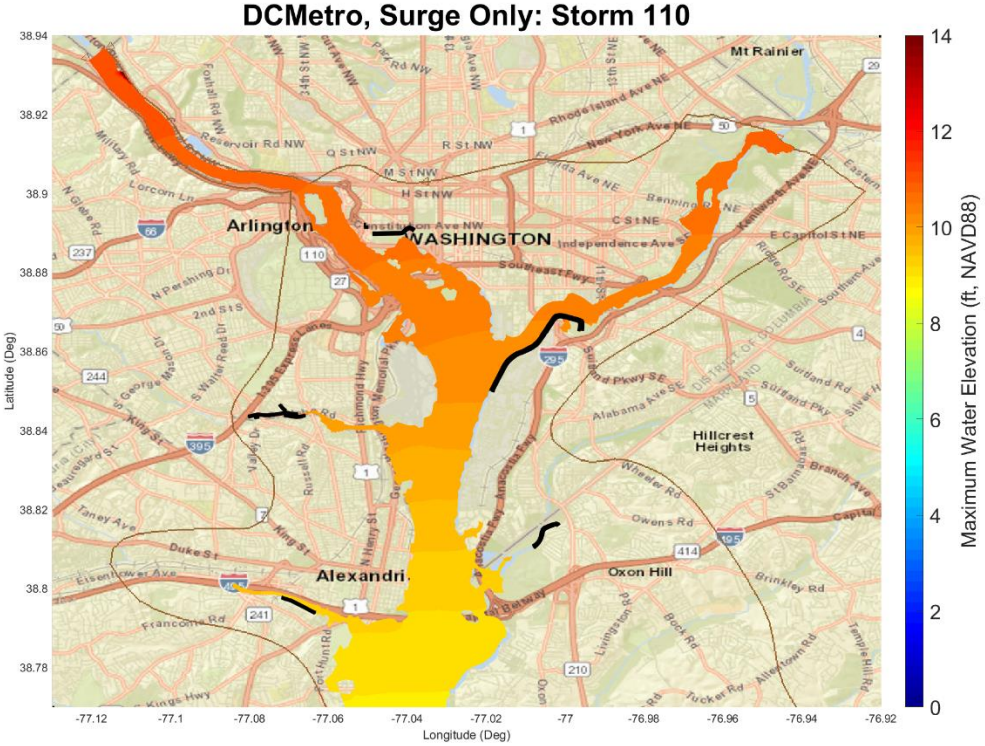

Figure 5-14. Maximum water elevation: Storm 22, Surge only.

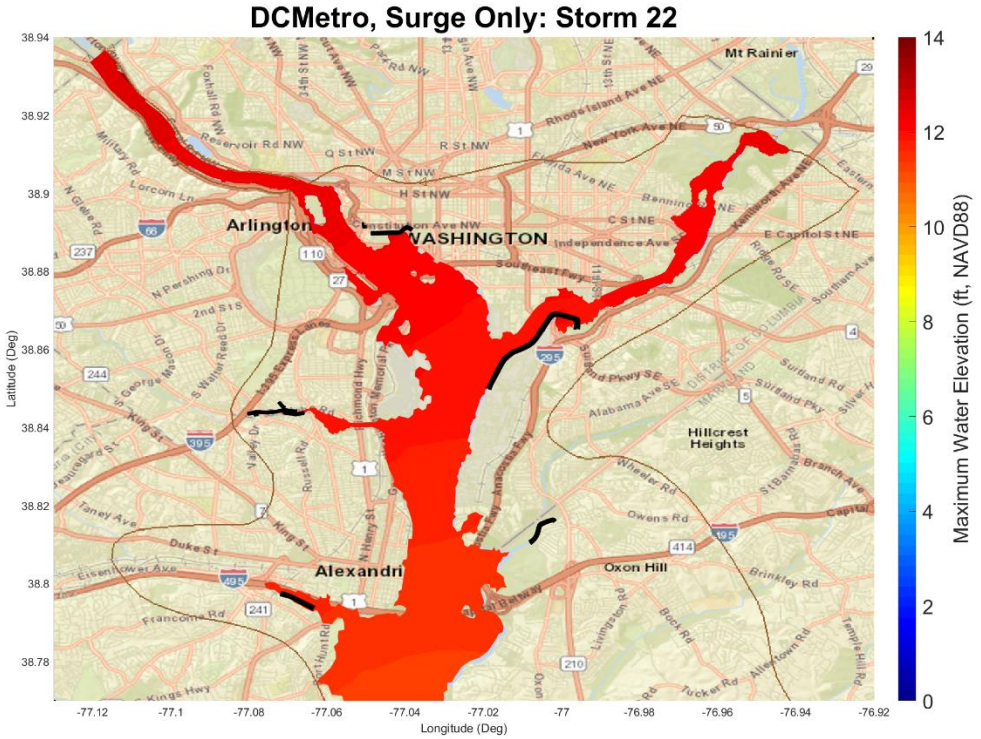

Figure 5-15. Maximum water elevation: Storm 72, Surge only.

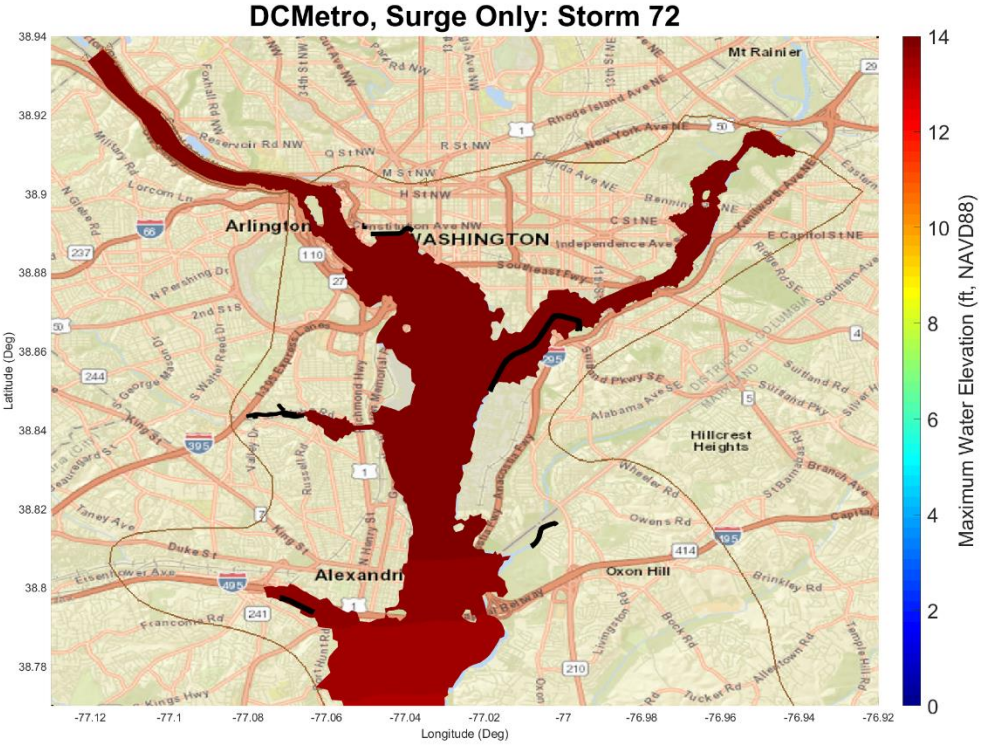

Figure 5-16. Save point #5878.

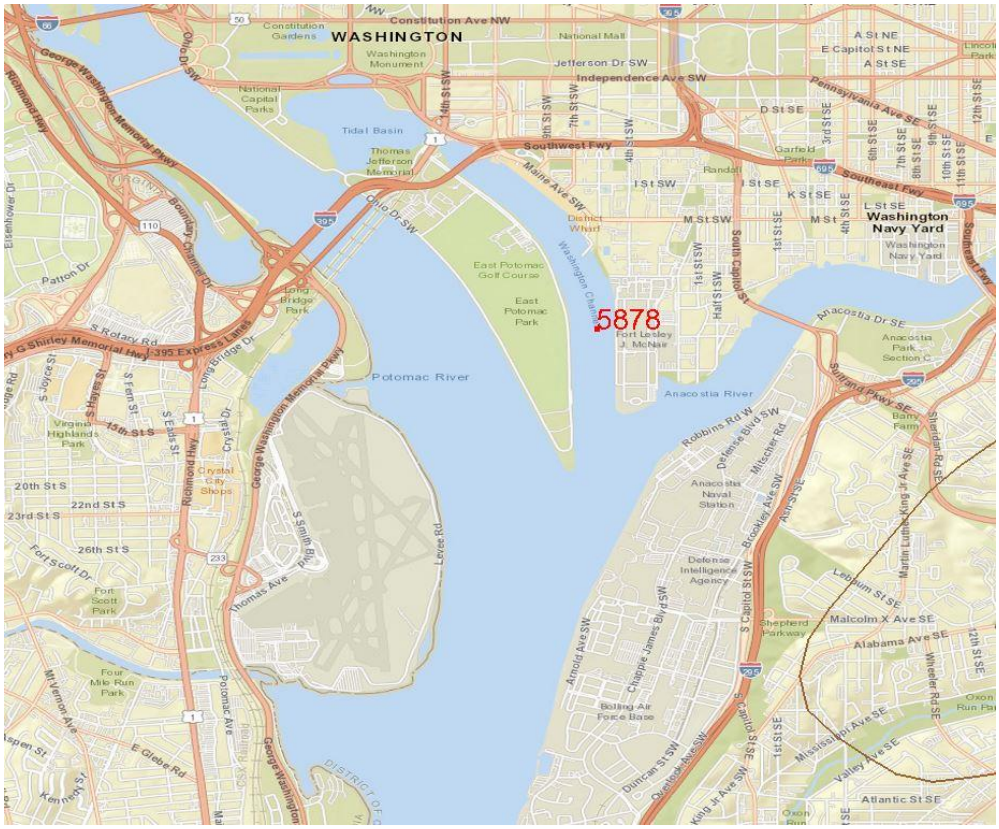

Figure 5-17. Water level time-series at save point #5878 (Storm 640, Surge only).

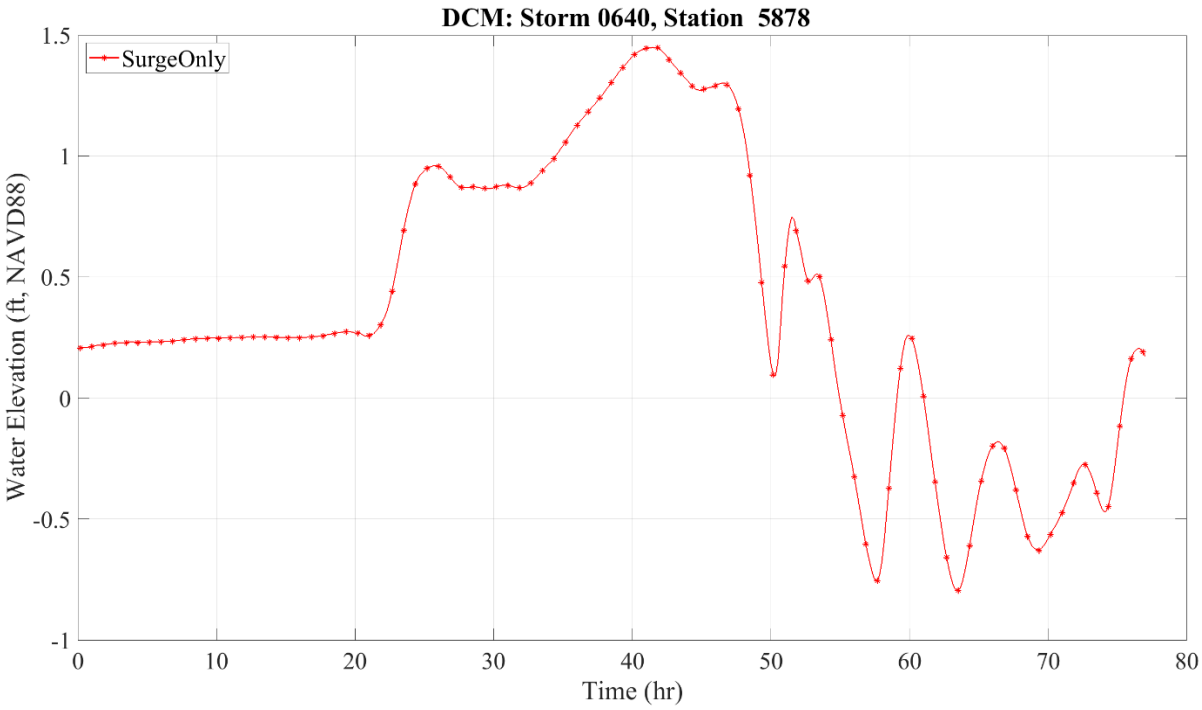

Figure 5-18. Water level time-series at save point #5878 (Storm 17, Surge only).

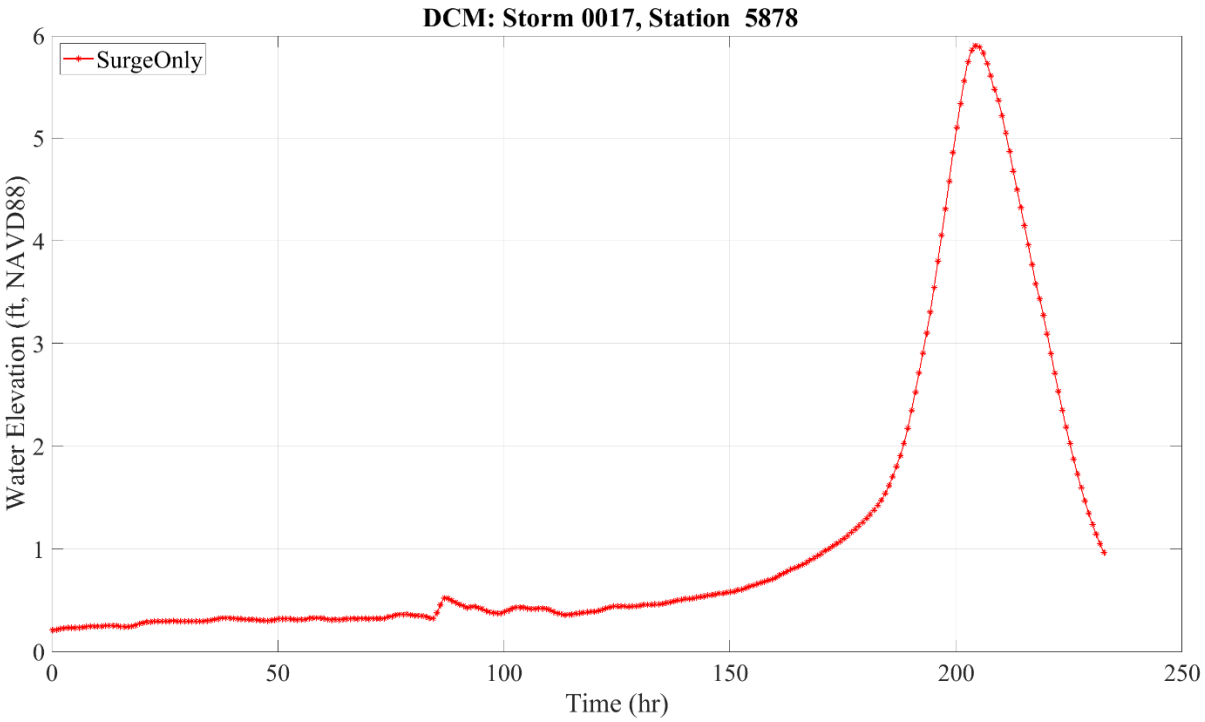

Figure 5-19. Water level time-series at save point #5878 (Storm 110, Surge only).

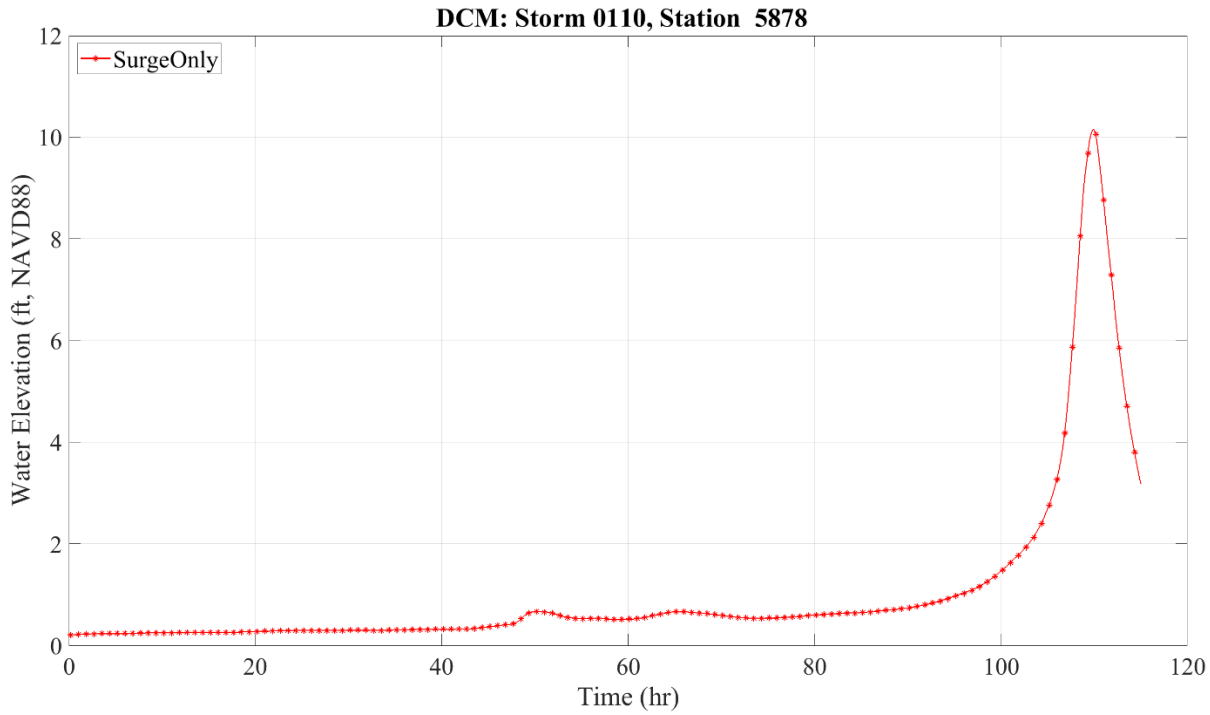

Figure 5-20. Water level time-series at save point #5878 (Storm 22, Surge only).

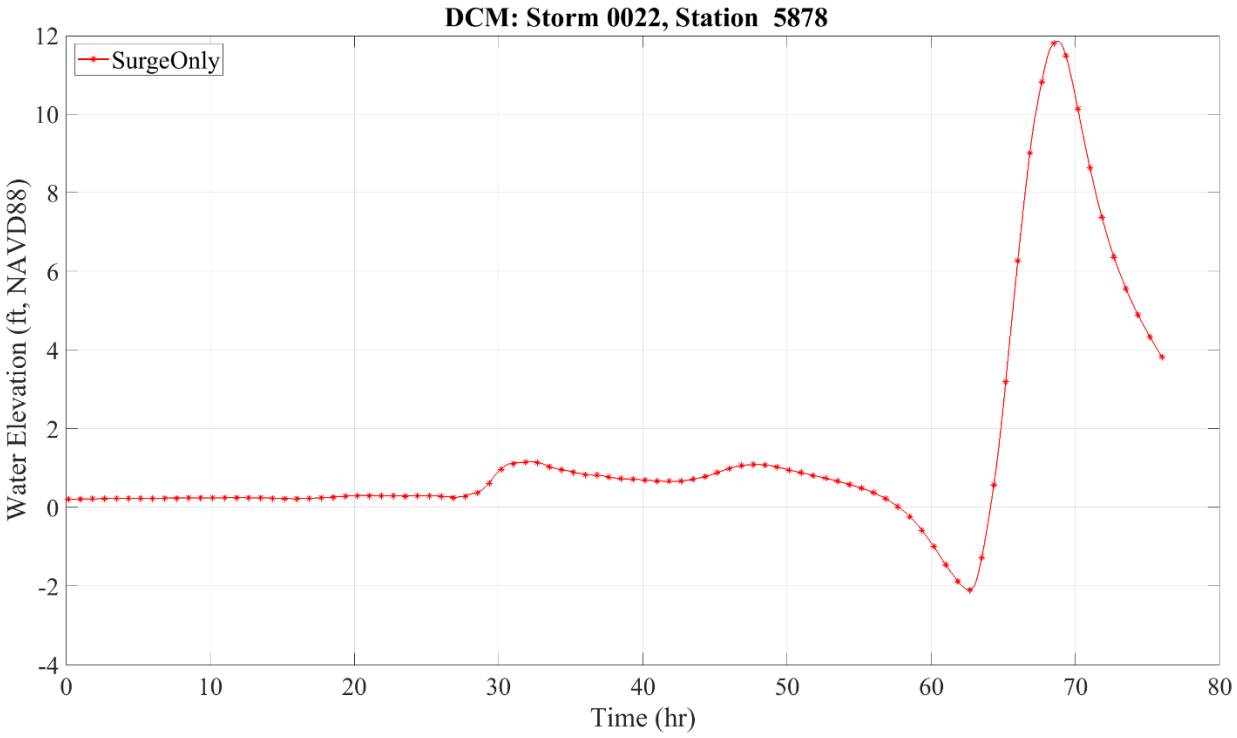

Figure 5-21. Water level time-series at save point #5878 (Storm 72).

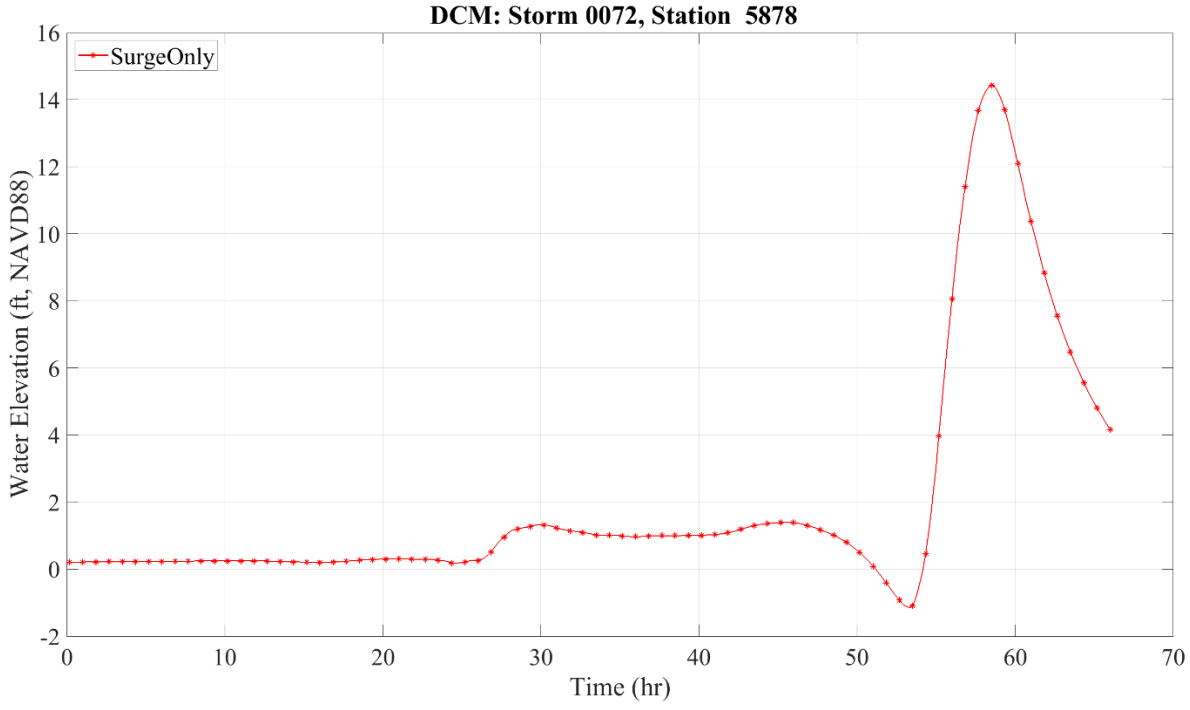

5.2.1 Synthetic Storm Simulations – Surge and Tide

The comparison of the maximum water level plots for Storm 640 with surge only (Figure 5-11) and with surge and tides (Figure 5-22) show a maximum water level increase of 1.16 ft (on average) due to tidal forcing. This observation was also confirmed by examining the water level time-series at save point #5878 where the peak surge for the Surge only (Figure 5-17) and Surge with Tides (Figure 5-27) cases are slightly below 1.5 ft and a little above 2.5 ft, respectively. For Storm 17, the average difference between the maximum water level for surge only (Figure 5-12) and with surge and tides (Figure 5-23) is approximately 0.65 ft; the maximum water level increase is attributed to the tides. Figure 5-18 and 5-28 provides additional proof for the above statement. The comparison of maximum water level plots for Storm 110 reveals a different behavior; the maximum water level of Surge only (Figure 5-13) is higher (by approximately 0.25 ft) than the maximum water level of Surge and Tides (Figure 5-24). The analysis of water level time-series shows consistency with the above statement (Figure 5-19 and Figure 5-29). This counterintuitive behavior is caused by the random nature of the tidal forcing and in this particular case, peak surge was more closely aligned with low tide. The comparison of Figure 5-14 and Figure 5-25 shows that Surge only maximum water level is lower on average by 0.3 ft than Surge and Tides maximum water level in the study area for Storm 22 (confirmed by peak water level shown in hydrographs of Figure 5-20 and 5-30). Behavior similar to Storm 110 takes place for Storm 72; the maximum water level for Surge only (Figure 5-15) is higher than the maximum water level for Surge with Tides (Figure 5-26) with a difference of 0.25-0.3 ft. The corresponding peak surge in Figure 5-21 (Surge only) is higher by 0.3 ft than peak surge observed in Figure 5-31 (Surge and Tides).

Figure 5-22. Maximum water elevation: Storm 640, Surge and Tides.

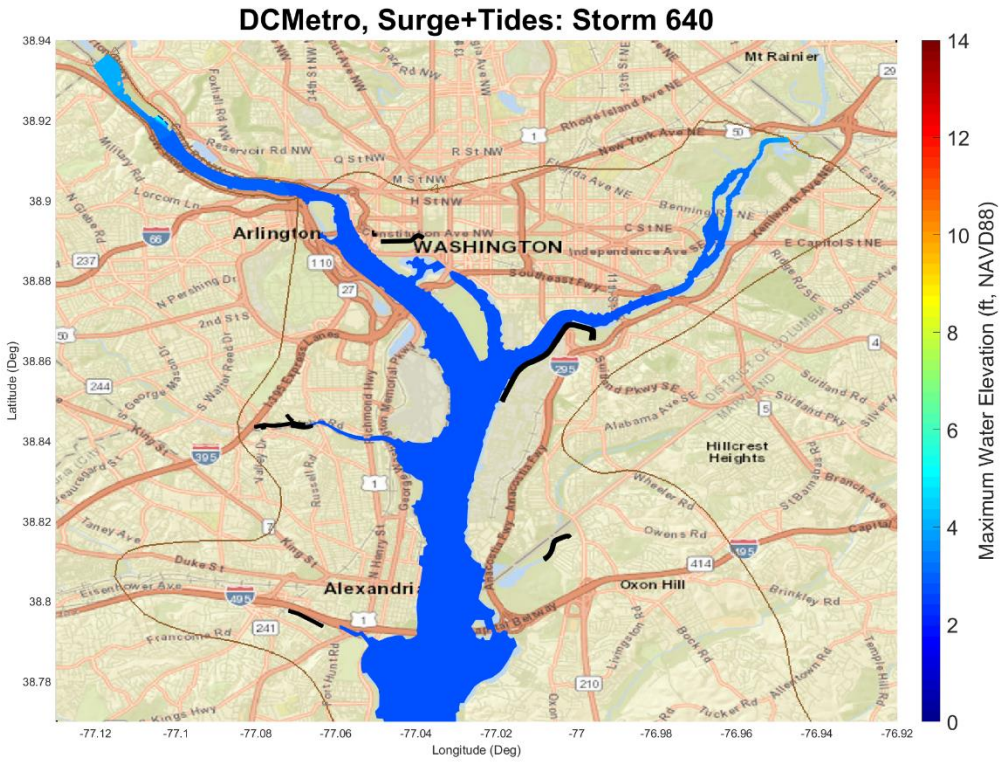

Figure 5-23. Maximum water elevation: Storm 17, Surge and Tides.

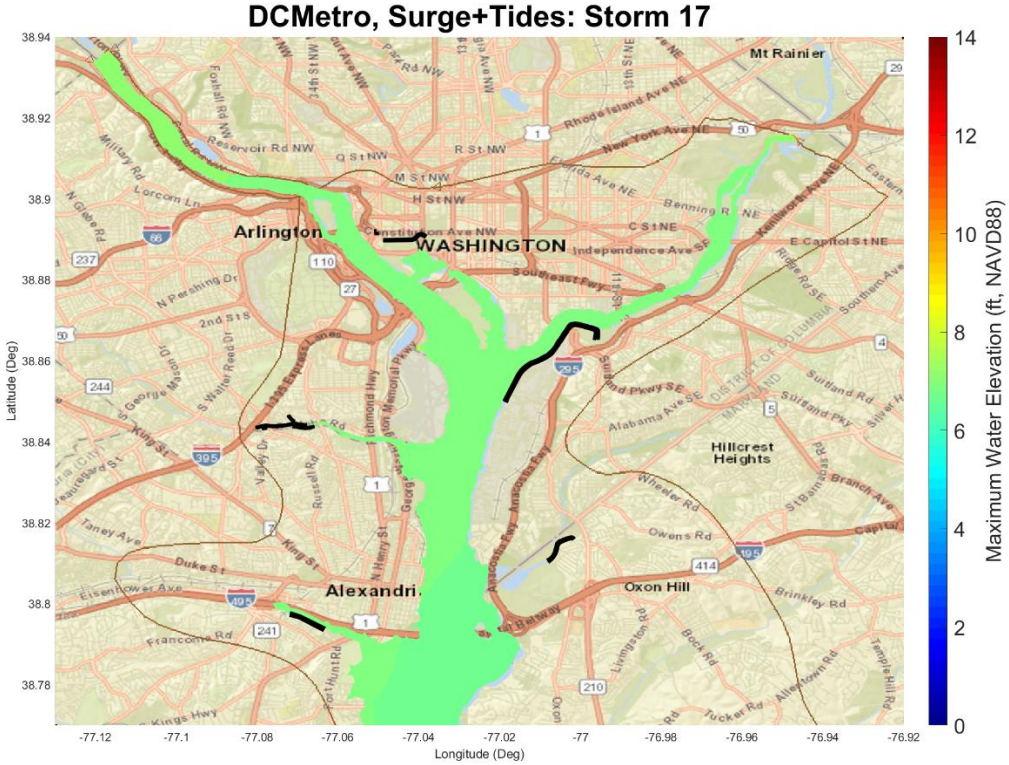

Figure 5-24. Maximum water elevation: Storm 110, Surge and Tides

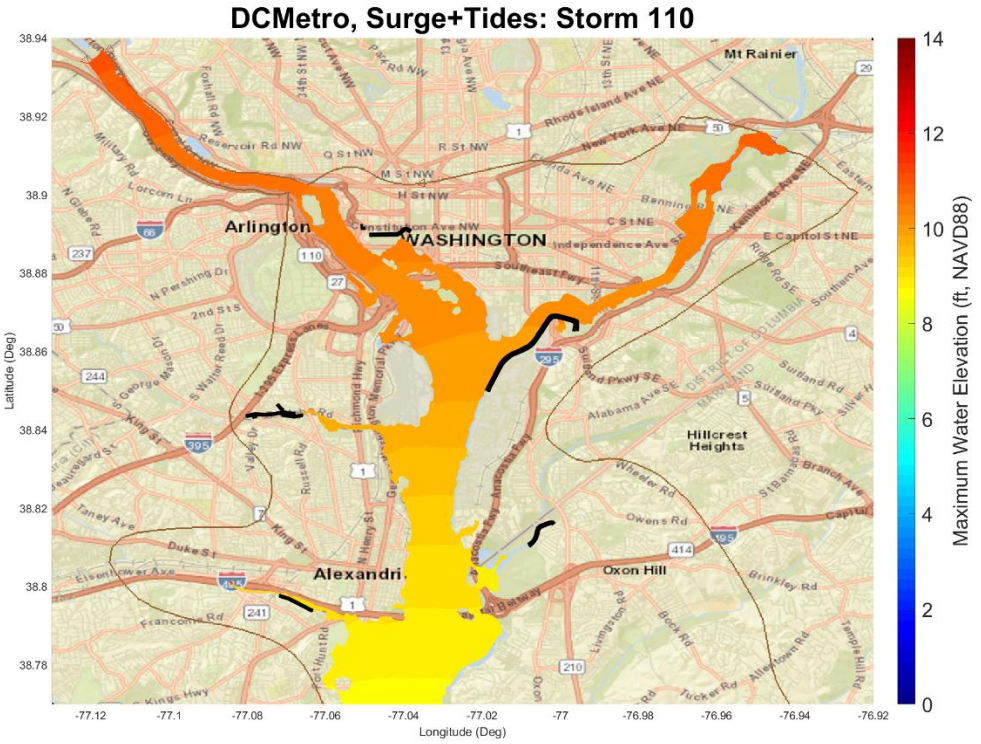

Figure 5-25. Maximum water elevation: Storm 22, Surge and Tides.

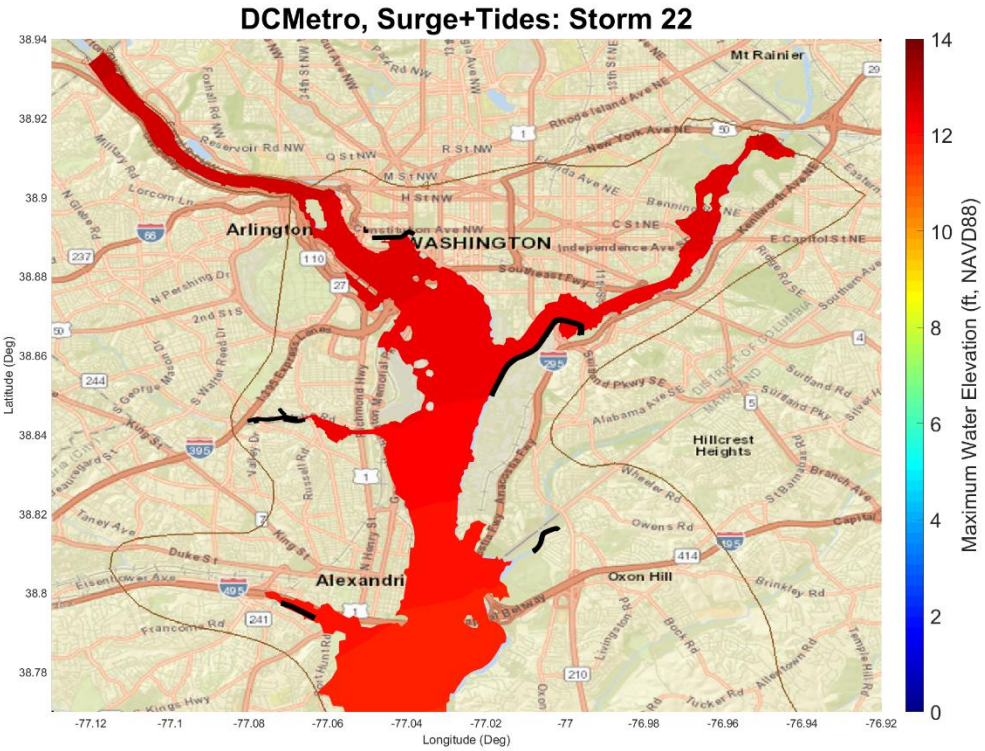

Figure 5-26. Maximum water elevation: Storm 72, Surge and Tides.

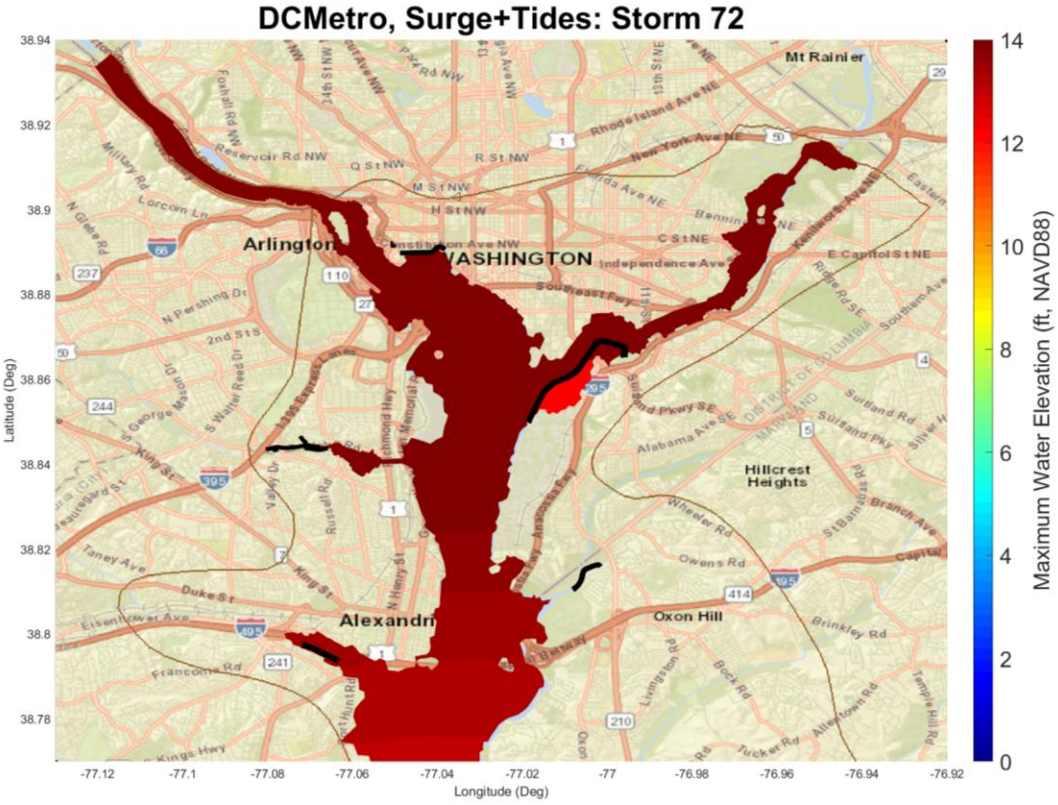

Figure 5-27. Water level time-series at save point #5878 (Storm 640, Surge and Tides).

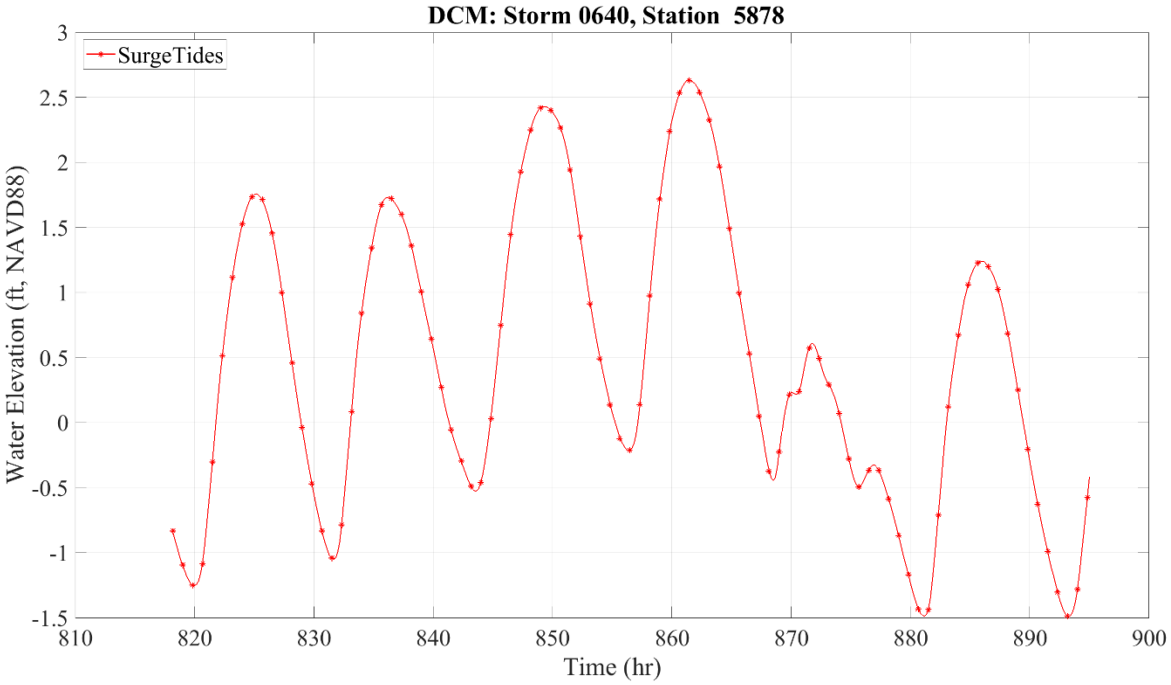

Figure 5-28. Water level time-series at save point #5878 (Storm 17, Surge and Tides).

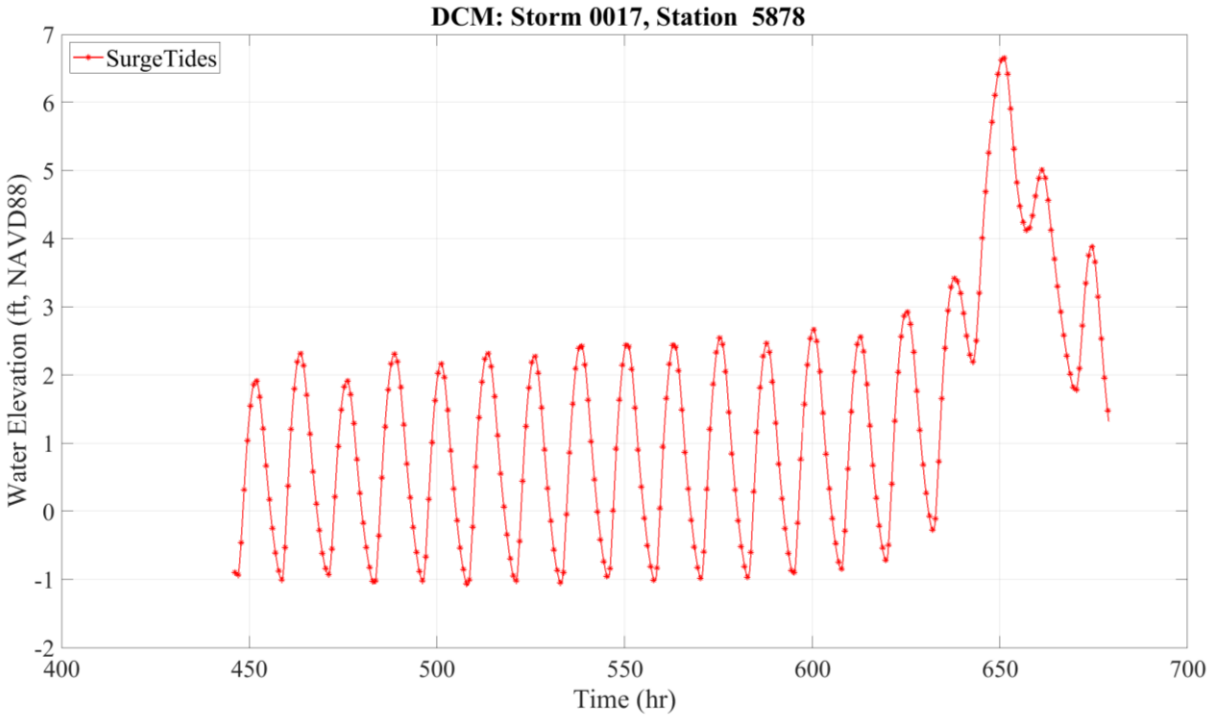

Figure 5-29. Water level time-series at save point #5878 (Storm 110, Surge and Tides).

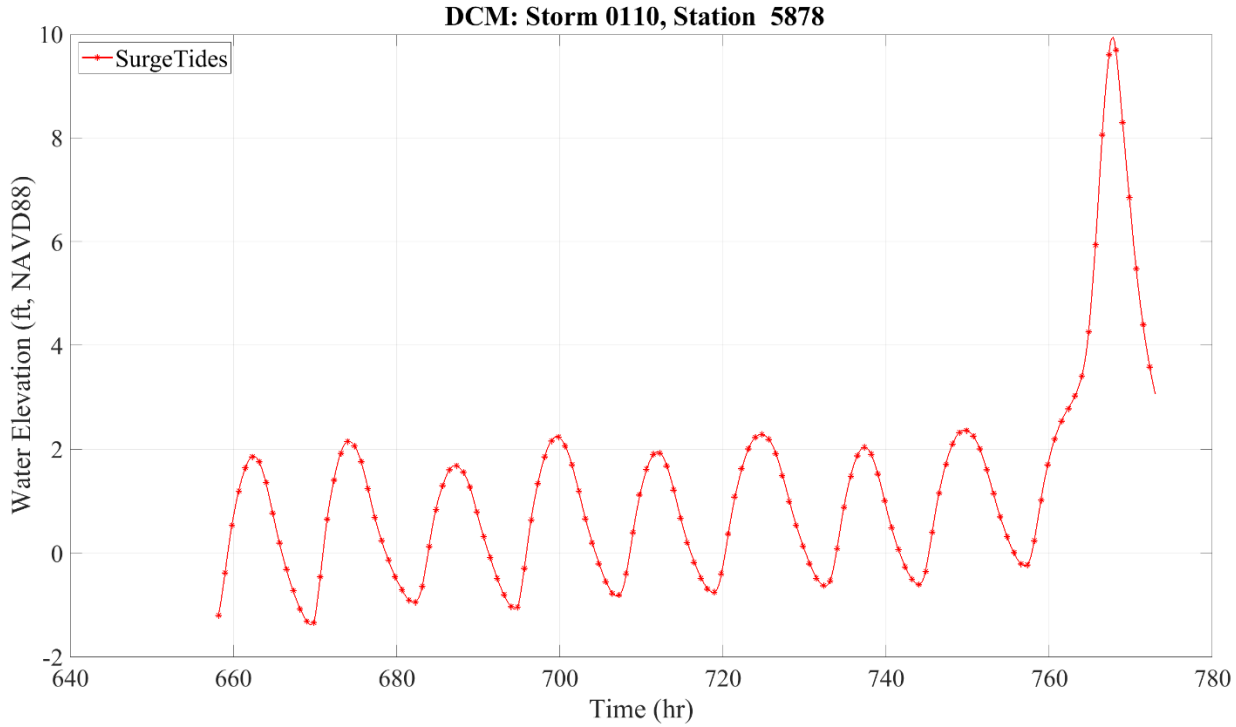

Figure 5-30. Water level time-series at save point #5878 (Storm 22, Surge and Tides).

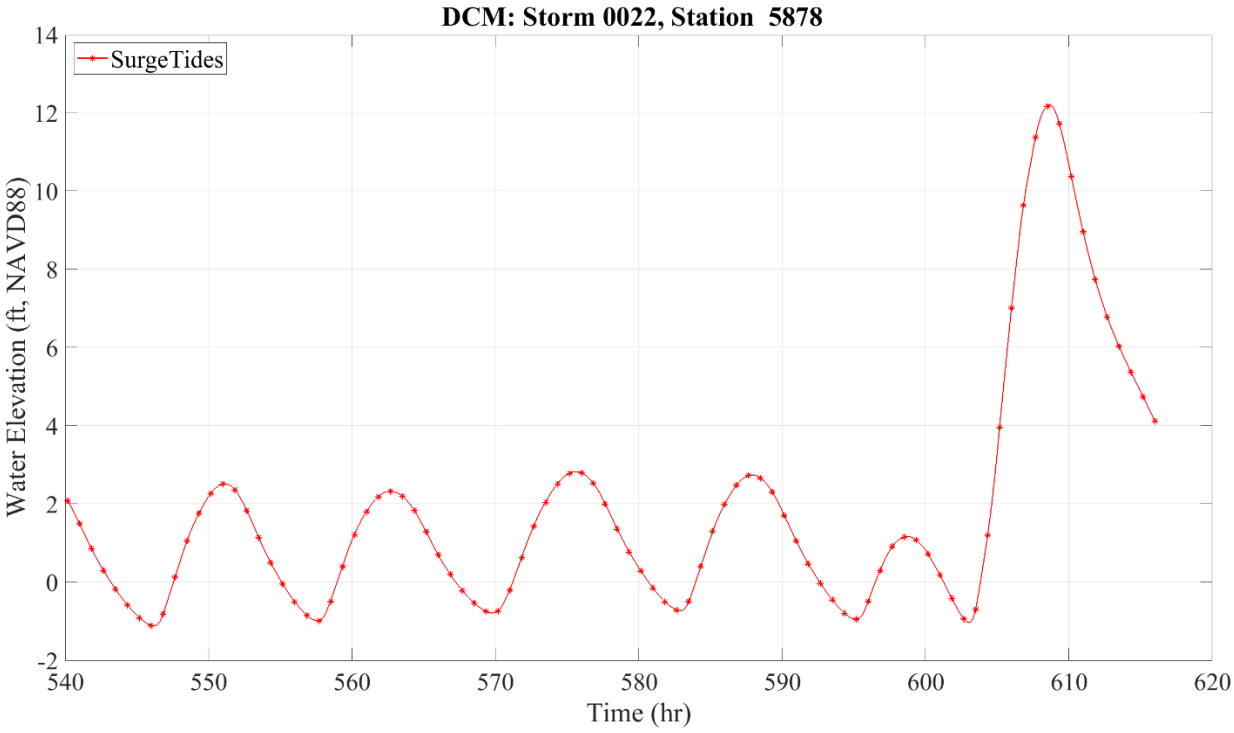

Figure 5-31. Water level time-series at save point #5878 (Storm 72, Surge and Tides).

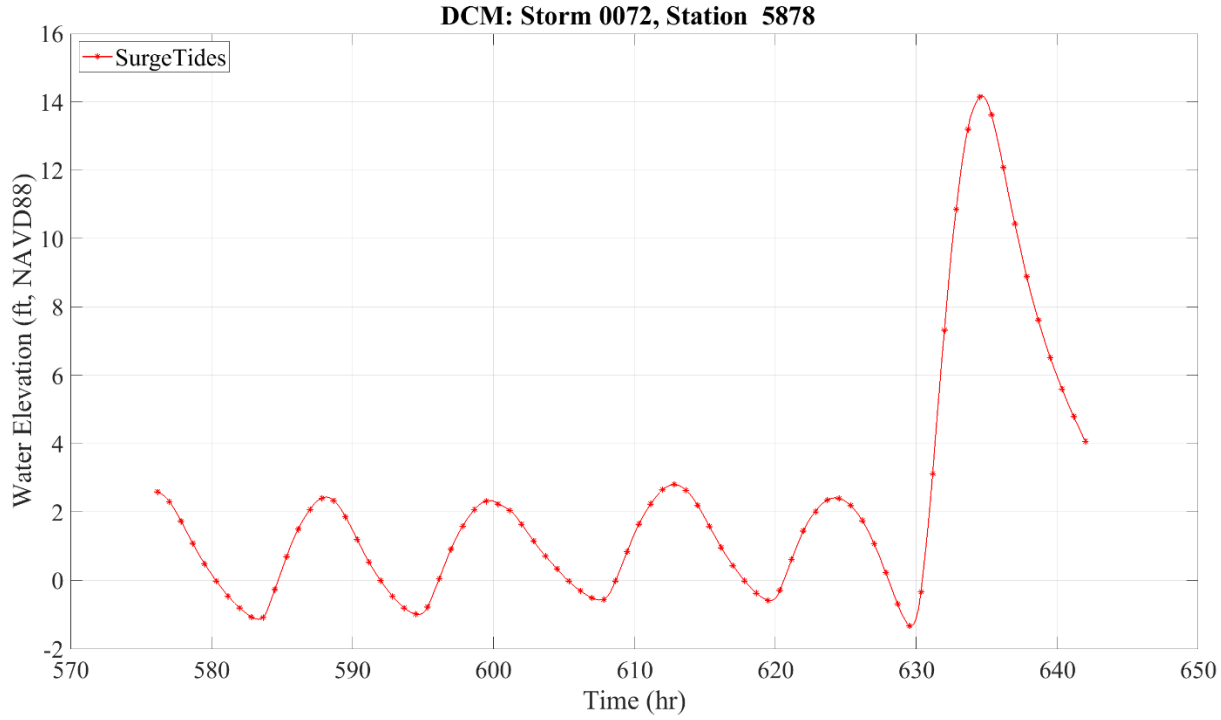

5.2.2 Synthetic Storm Simulations – Surge, Tide, and SLR

Simulations with a SLR of 1.62 ft, caused an increase in the maximum water surface elevations for each of the representative storms (640, 17, 110, 22, and 72). The average maximum water surface elevation for Surge+Tides+SLR for Storm 640 (Figure 5-32) is 4.2 ft (for Surge+Tides was approximately 2.75 – Figure 5-21). The Surge+Tides+SLR condition for Storm 17 (Figure 5-33) created an average maximum water level of 8.5 ft; for comparison, the Surge+Tides condition led to a maximum water level of 6.8 ft. Storm 110 with Surge+Tides+SLR (Figure 5-34) induced maximum water level between 10.5 ft and 11.5 ft (it was between 9 ft and 10 ft for Surge+Tides, Storm 110 – Figure 5-24). Figure 5-34 also shows flooded areas (encircled with blue color); in Anacostia Park and the southern part of Bolling Air Force Base. The flooding of these areas was also observed for Surge only (Figure 5-13) and Surge and Tides (Figure 5-24) conditions to a lesser extent. Figure 5-35 (maximum water level for Surge+Tides+SLR, Storm 22) shows two additional areas being flooded, that is, Ronald Reagan Airport and the northern part of Bolling Air Force Base (all flooded areas encircled with blue color). In this case, the maximum water elevation was between 13.5 ft and 14 ft (for Surge+Tides was between 11.8 ft and 12.5 ft). The maximum water elevation for Storm 72 (Surge+Tides+SLR; Figure 5-36) was between 15.4 ft and 16.4 ft where Surge+Tides condition for the same storm generated maximum water level between 13.3 ft and 14.7 ft. Due to this extreme water elevation, additional areas were flooded (the central part of Bolling Air Force Base, Navy Yard, and Constitution Ave between 17th and 14th St). The areas such as Ronald Reagan Airport, Anacostia Park and the southern and northern part of Bolling Air Force Base, that already were inundated during Surge only (Figure 5-15) and Surge+Tides (Figure 5-26) forcing conditions, experienced more extensive flooding due to the additional volume of water introduced by SLR.

Figures 5-37 through 5-41 confirm the above observation regarding maximum water, that is, the peak surges for save point #5878 are consistent with maximum water levels for each of the representative storms.

Figure 5-32. Maximum water elevation: Storm 640, Surge, Tides, and SLR.

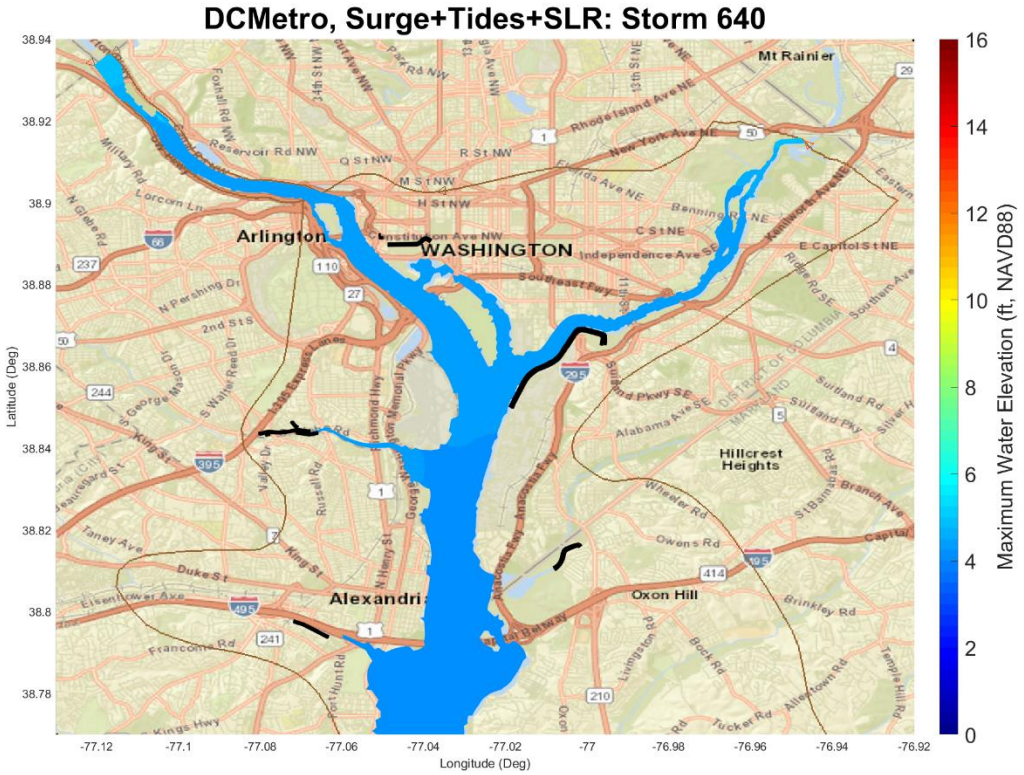

Figure 5-33. Maximum water elevation: Storm 151, Surge, Tides, and SLR.

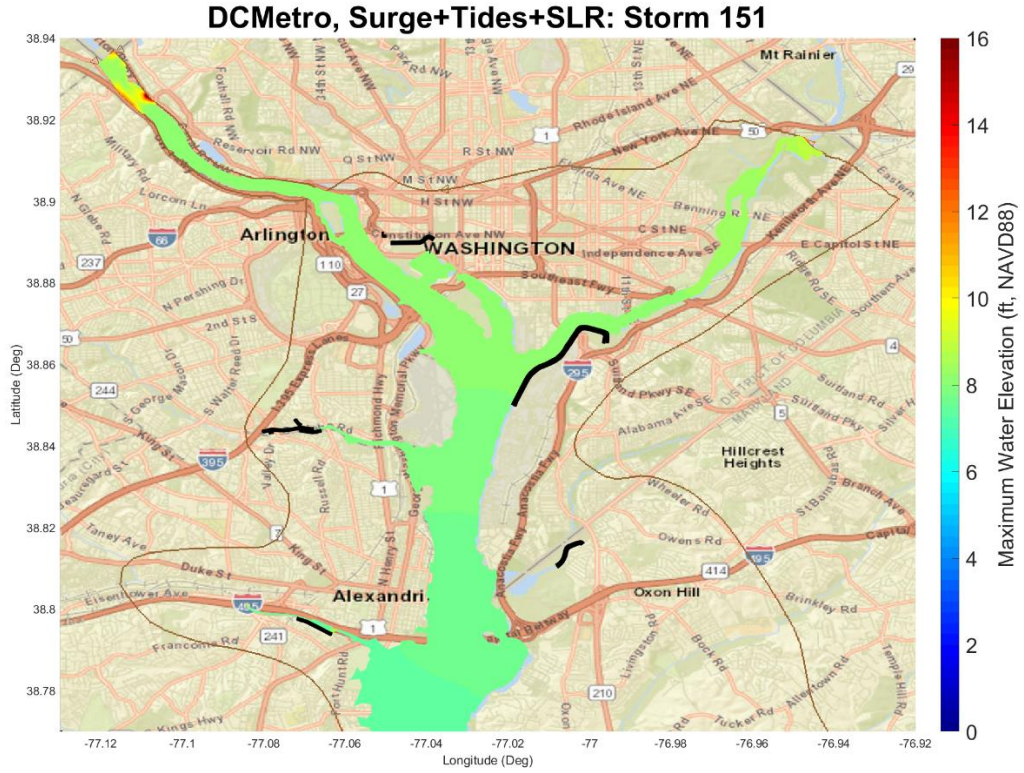

Figure 5-34. Maximum water elevation: Storm 110, Surge, Tides, and SLR.

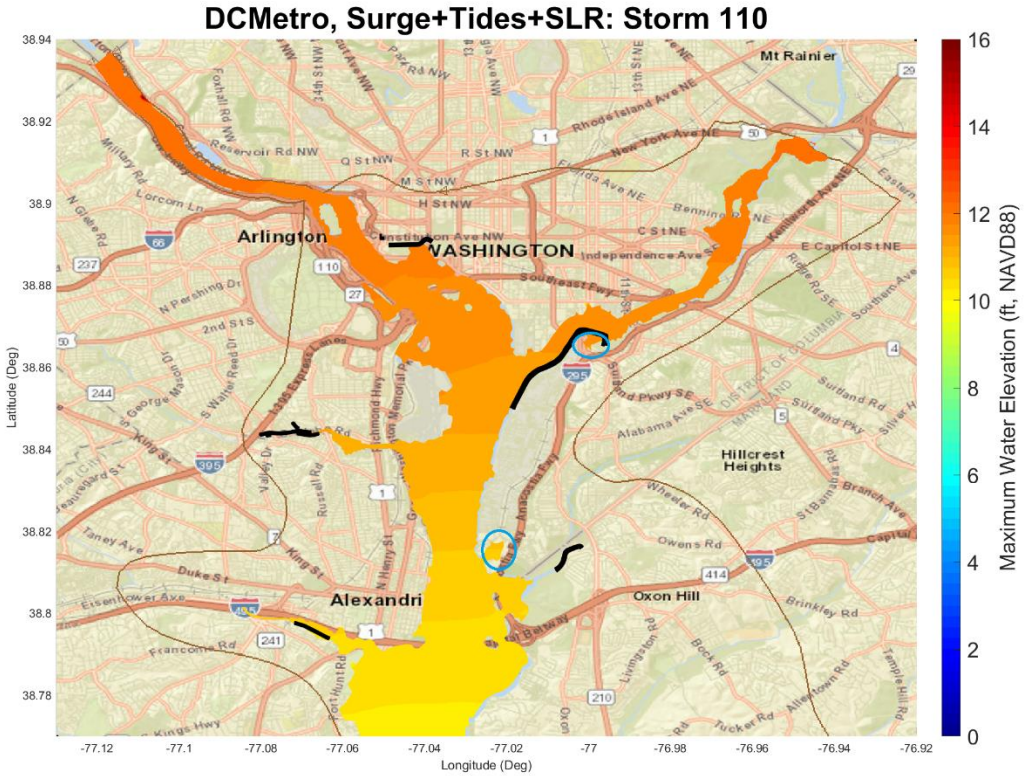

Figure 5-35. Maximum water elevation: Storm 22, Surge, Tides, and SLR.

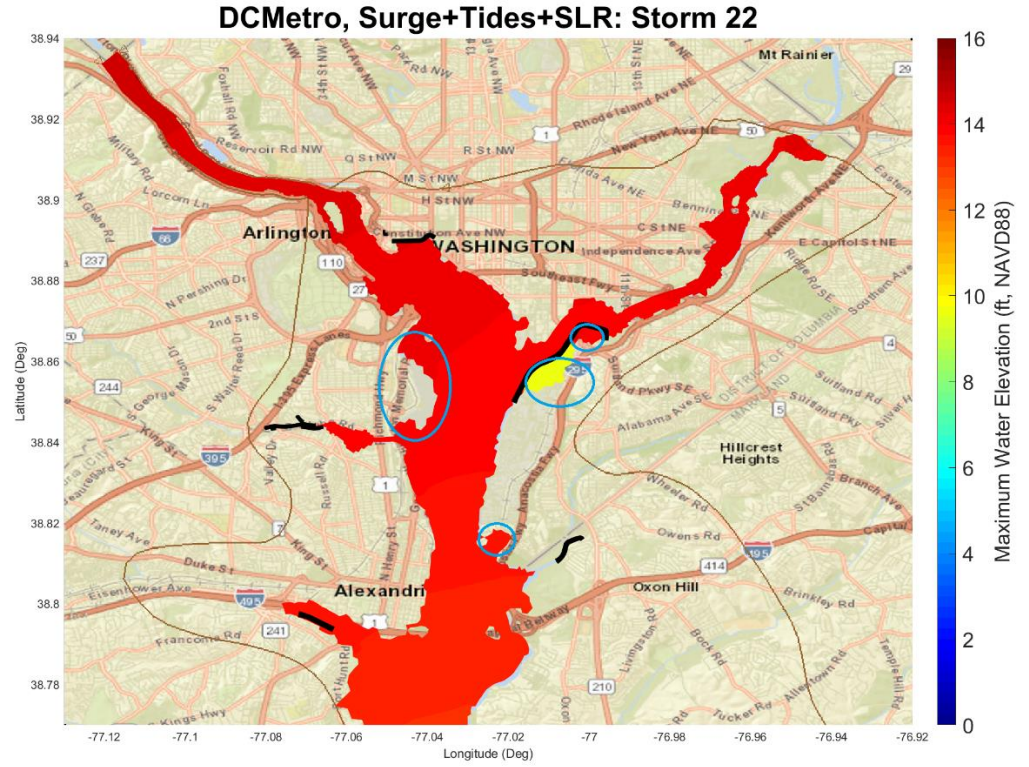

Figure 5-36. Maximum water elevation: Storm 72, Surge, Tides, and SLR.

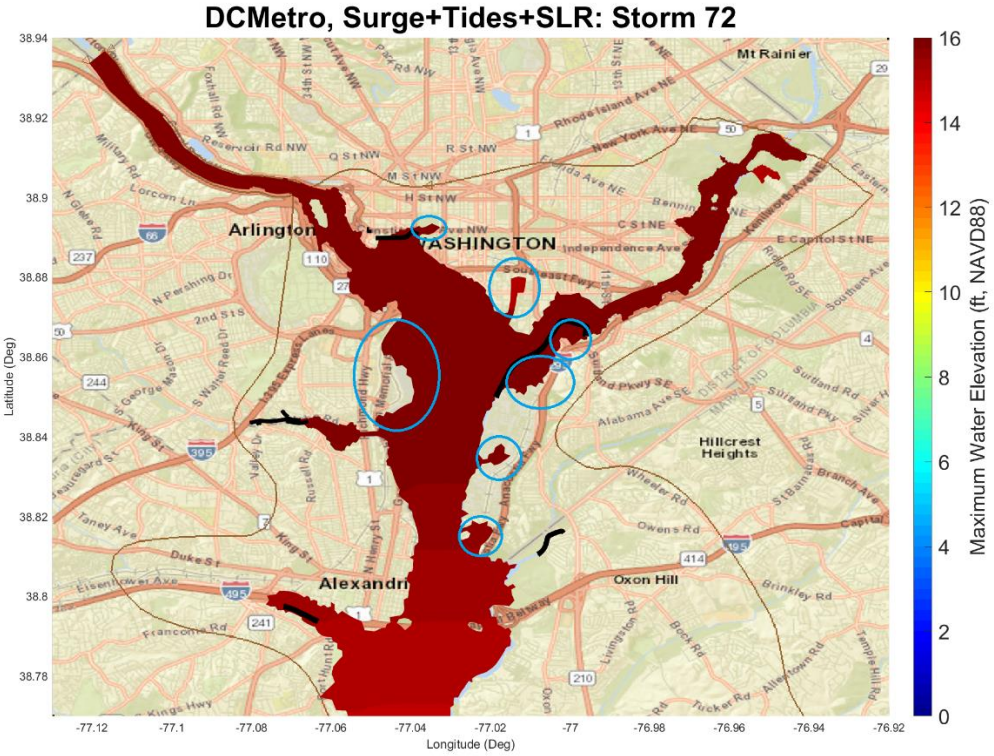

Figure 5-37. Water level time-series at save point #5878 (Storm 640, Surge, Tides, and SLR).

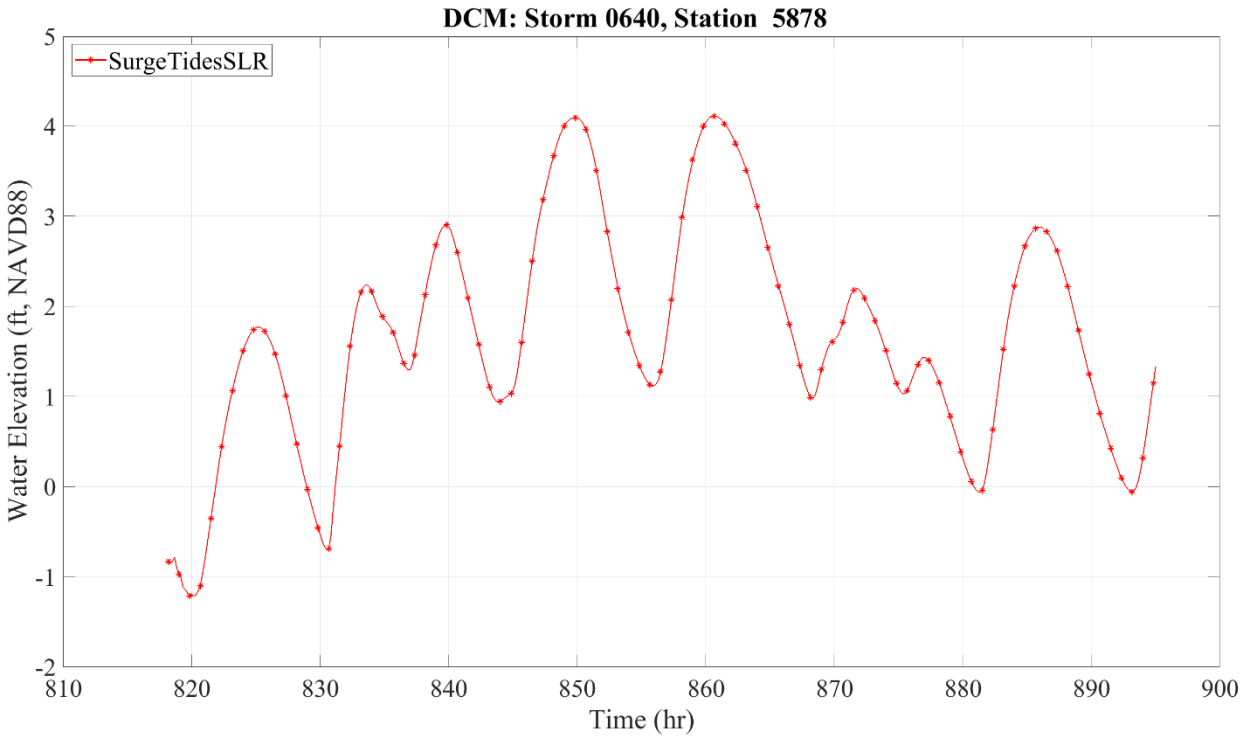

Figure 5-38. Water level time-series at save point #5878 (Storm 17, Surge, Tides, and SLR).

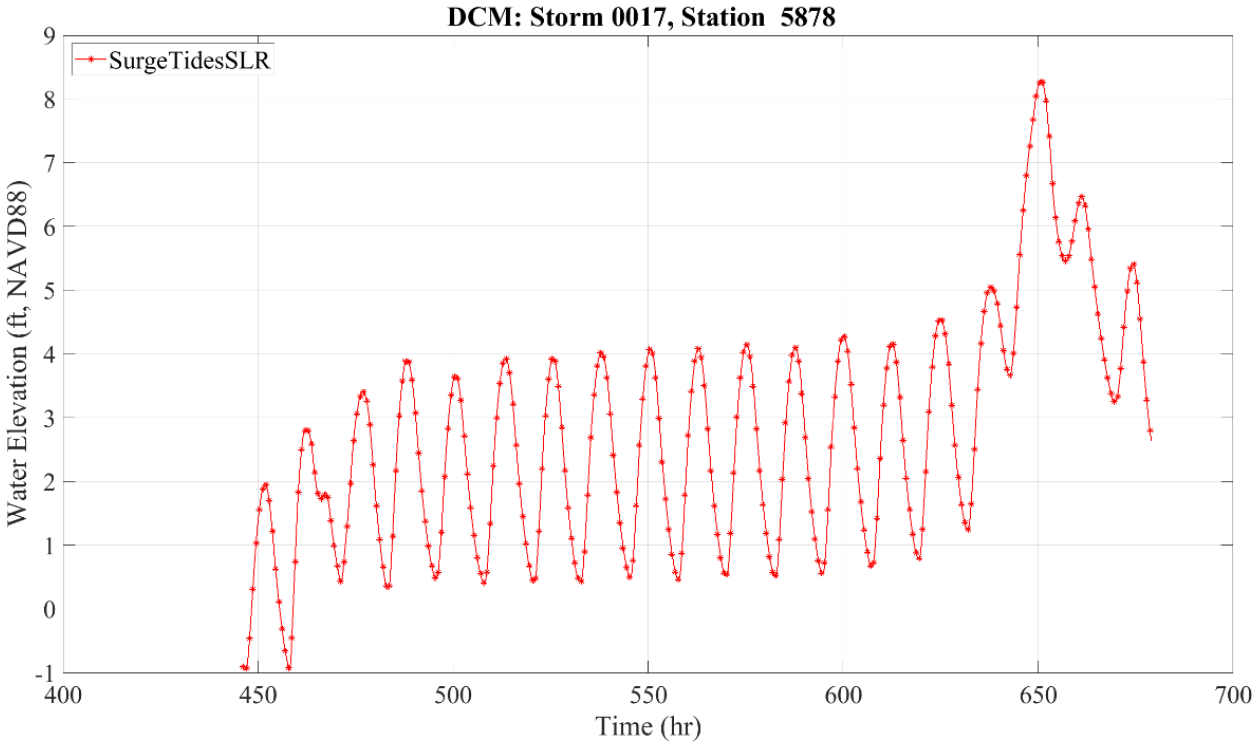

Figure 5-39. Water level time-series at save point #5878 (Storm 110, Surge, Tides, and SLR).

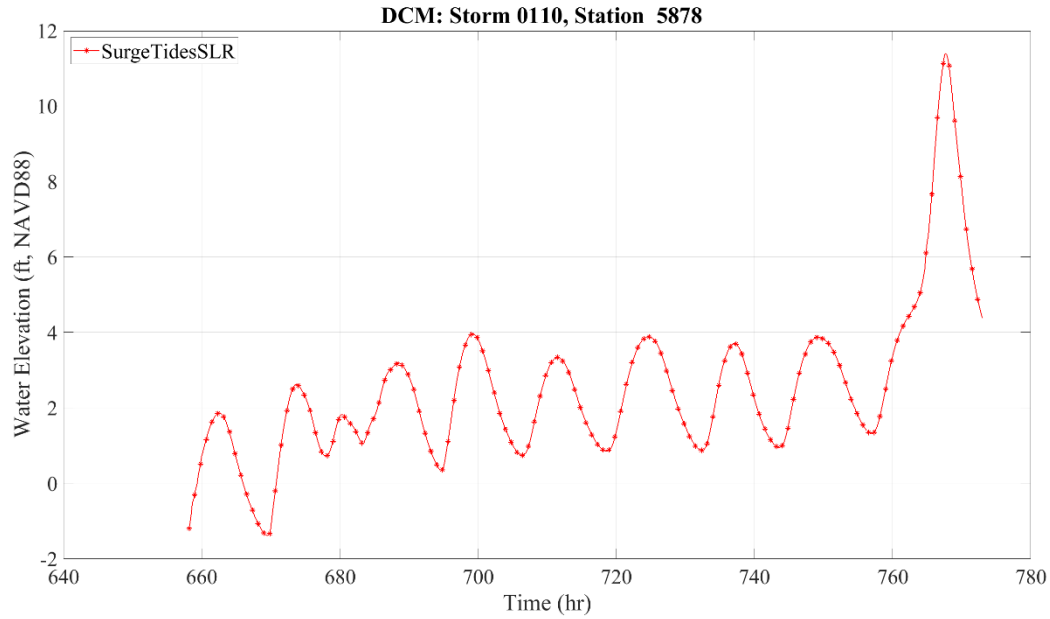

Figure 5-40. Water level time-series at save point #5878 (Storm 22, Surge, Tides, and SLR).

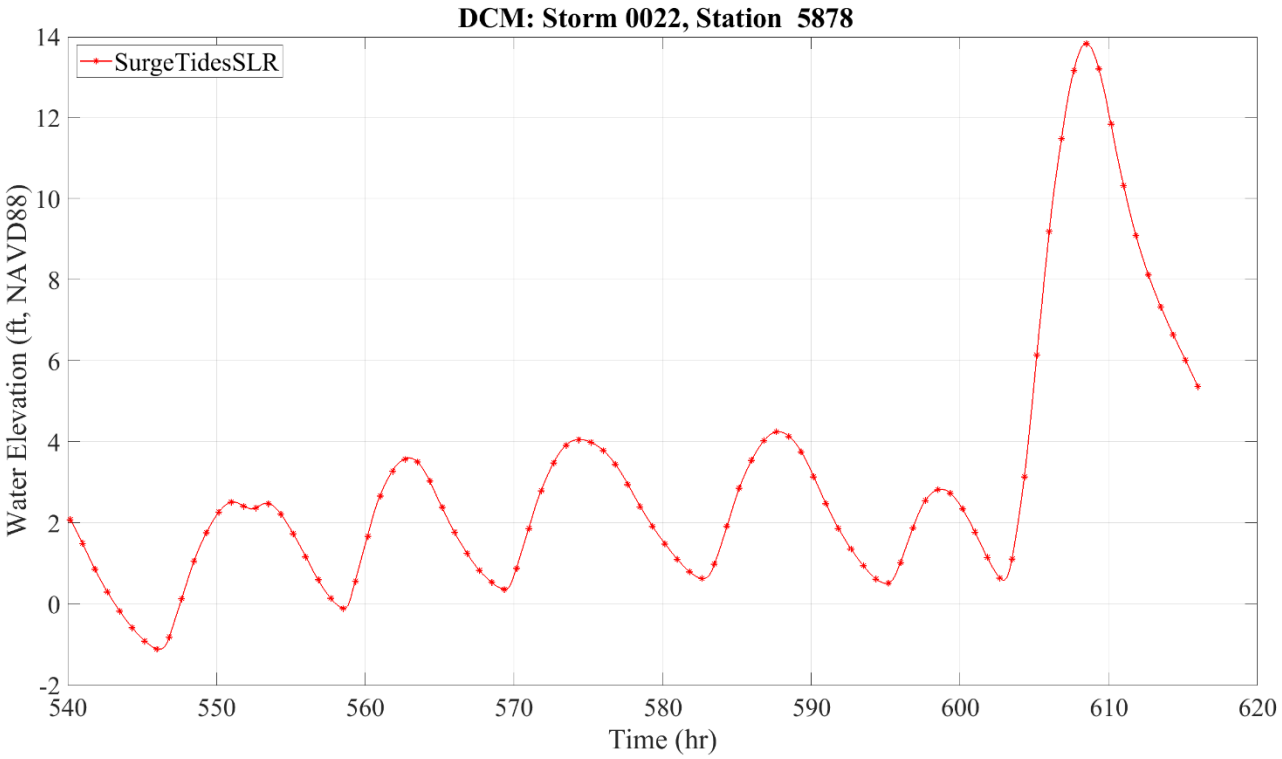

Figure 5-41. Water level time-series at save point #5878 (Storm 72, Surge, Tides, and SLR).

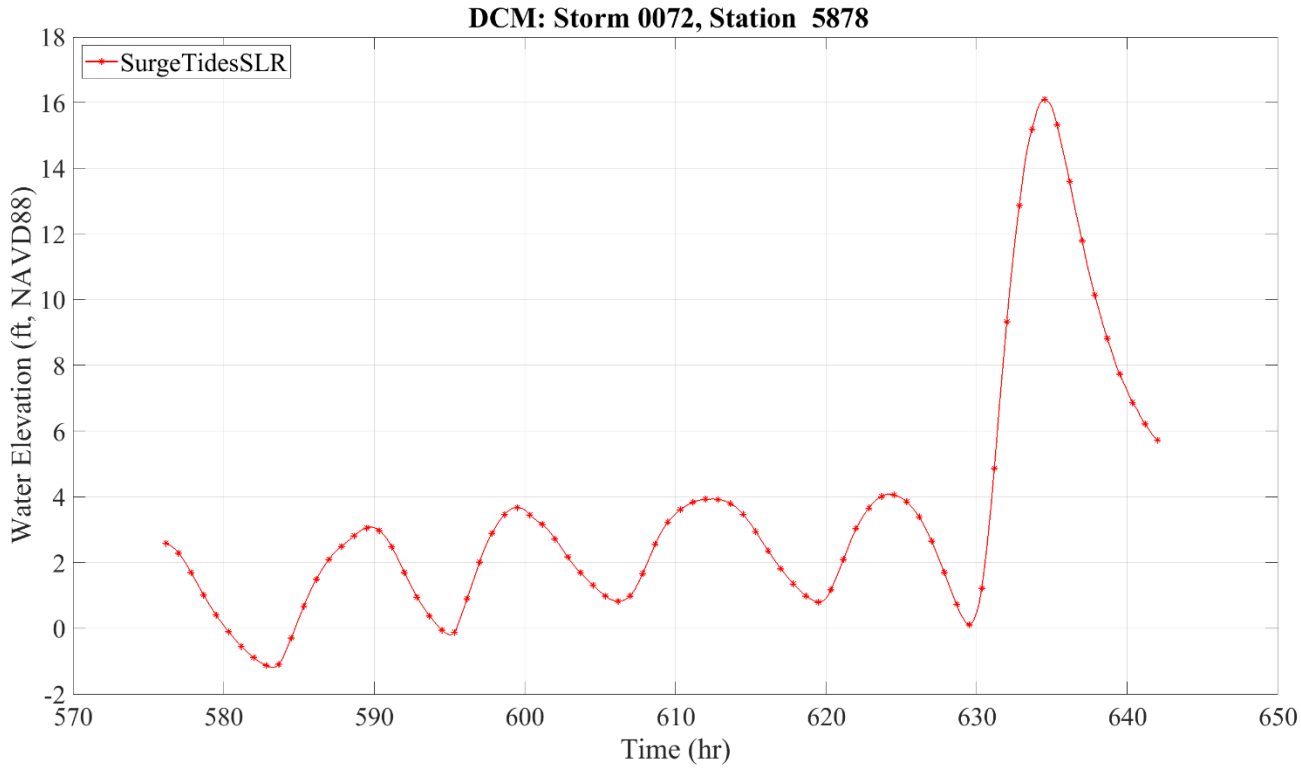

6 Estimation of Coastal Storm Hazards

For this study, the ATCS developed as part of the recently updated CHS-NA study was applied herein to leverage the metamodeling completed for the CHS-NA. The application of the ATCS allows for a more robust definition of the probability and parameter spaces of TCs relative to the D.C. Metro study area. As a result, the SWL AEFs are more accurately quantified than through application of the 60-storm RSS alone. However, to account for the impact of the ADCIRC mesh modifications (Section 5) on the final SWL AEFs, an adjustment of the ATCS storm responses was completed to correct the ATCS surge results based on the D.C. Metro simulationso. The process for developing the D.C. Metro SWL AEFs includes the following steps:

1. Using Equations 6-1 and 6-2, compute the absolute and relative differences of the surge at each save point using the D.C. Metro surge results (60-storm RSS) and the NACCS surge results (1050-storm ITCS):

$$\Delta_a = \tau_{DC\ Metro} - \tau_{NACCS} \tag{6-1}$$

$$\Delta_r = \frac{\Delta_a}{\tau_{NACCS}} \tag{6-2}$$

   where Δ_a = absolute difference in the surge, Δ_r = relative difference in surge, τ_{RSS} = surge response from the D.C. Metro RSS simulations, and τ_{NACCS} = surge response from the NACCS ITCS simulations.

2. Train individual GPMs to predict the absolute (Δ_a) and relative differences (Δ_r) of the ATCS surge results at each save point.

3. Apply the altitude equation (Equation 6-3) to estimate the total difference (h) in surge between the D.C. Metro study and the CHS-NA ATCS surge values:

$$h = \frac{\Delta_a}{\|\Delta_a\|} \frac{1}{\sqrt{\frac{1}{{\Delta_a}^2} + \frac{1}{{\Delta_r}^2}}} \tag{6-3}.$$

4. Compute spatially-varying bias and uncertainty.

5. Using the D.C. Metro study results, compute the skew-tide at each save point for quantifying the SWL AEFs.

6. Apply StormSim-SST for the quantification of XC-induced SWL AEFs using the NACCS XC surge responses.

7. Quantify the TC-induced SWL AEFs through JPM integration of the ATCS storm responses and associated probability masses.

8. Develop combined cyclone (CC) hazard curves by aggregating the TC and XC induced SWL AEFs.

The following sections describe the PCHA components applied for the development of SWL hazard curves for the study area. Section 6.1 documents the hydrodynamic modeling post-processing including the DNC and development of the CHS-NA surge metamodel. The results of the surge correction are provided in Section 6.1.3. Section 6.2 describes the correction of bias and computation of uncertainty for developing the SWL hazard curves. The methods applied to account for the effects of astronomical tides are detailed in Section 6.3. The application of the StormSim-SST for XC induced SWLs is documented in Section 6.4. The JPM integration of the storm responses from the ATCS is discussed in Section 6.5. Lastly, comparisons between the D.C. Metro and NACCS surge, skew tide, and SWL results are documented in Section 6.6.

6.1 Hydrodynamic Modeling Post-Processing

Upon completion of the hydrodynamic modeling, the PCHA includes two main post-processing components prior to the final probability analysis. These components include the DNC and training of the storm response metamodels. Only ADCIRC simulations were considered as part of the D.C. Metro, so only one metamodel was trained for predicting the surge responses from the CHS-NA ATCS. Additionally, the results from the D.C. Metro surge correction applied to the ATCS surge values are documented here.

6.1.1 Dry Node Correction (DNC)

When considering storm surge results from any given study, there are save points that remain dry (no surge information available) for some TCs within the hydrodynamic modeling. These save points, which are referred

to as dry nodes, can adversely affect the reliability of the hazard computation, if left uncorrected, due to the loss of probability mass associated with individual TCs that do not inundate the dry node. To address these problematic dry nodes, it is necessary to perform the DNC to avoid these potential inaccuracies in the hazard estimates. The DNC is also imperative for training a metamodel to predict accurate surge values from the augmented storm suite. The PCHA framework incorporates a DNC process that interpolates the missing storm surge at the dry nodes with a spatial GPM.

For the spatial GPM, the input data used in the optimization of the kriging parameters is the storm surge, which was recorded at the save points that were inundated during all the storm simulations ("always wet" save points). Maximum Likelihood Estimation (MLE) is then used to optimize the parameters in the kriging equation, which is evaluated at the dry nodes to fill in the missing data with pseudo-surges. The forcing vector for each of the always wet save points and the dry nodes was the latitude and longitude of each location. In order to fill-in the missing information at the dry nodes, the spatial GPM completes the SWL surface over the project domain, on a per-storm basis. Figure 6-1 shows an idealized cross-section to demonstrate the implementation of the DNC.

Figure 6-1. Idealized across-shore sketch illustrating the dry-node correction.

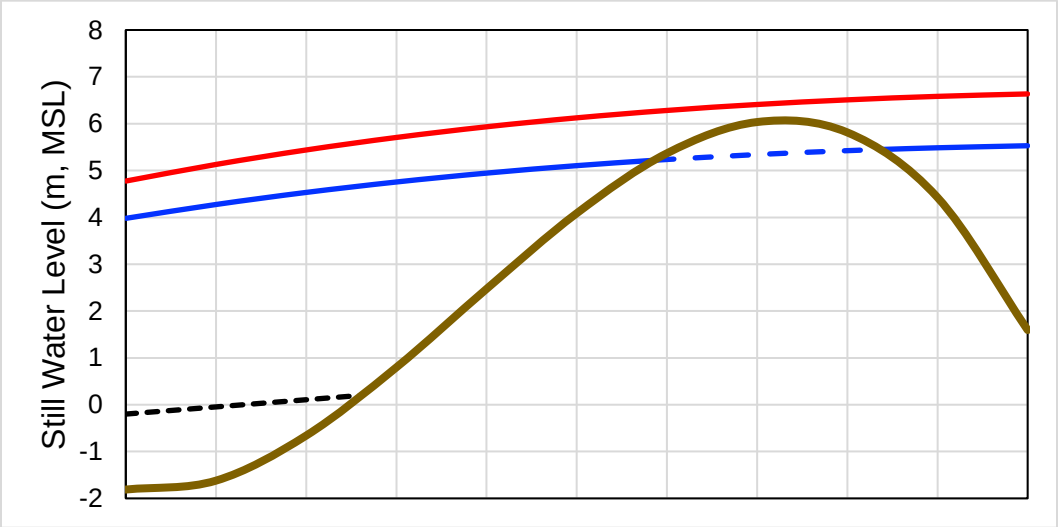

The dashed black curve and brown curve represent the initial water level and ground elevation, respectively. The SWL surface (solid blue curve) is interrupted by a section of high ground elevation (e.g., coastal bluff, dune, or barrier island). In typical JPM applications, nodes within this high

ground area are inundated by only the most extreme TCs leaving an incomplete representation of the SWL at this location, which can result in a significant underestimation of the storm surge hazard at these locations. For these uncorrected locations, the DNC completes the SWL surface over the entire domain, and across the high ground sections (dashed blue curve) to provide an accurate estimate along the entire blue line. Extending the SWL surface, even below ground, allows for proper integration of JPM uncertainty (per Equation 2-2). As a result, the SWL + uncertainty surface (red curve) may exceed the elevation of the high ground section. For the D.C. Metro, the DNC was completed prior to training a GPM for the prediction of the ATCS storm responses.

6.1.2 Surge Metamodel

For application of the ATCS in the probabilistic analysis, a metamodel must be trained to create a mathematical relationship between the input (storm parameters of the ITCS) and the output (storm responses of the ITCS). After training, predicted outputs can be obtained for future inputs, such as the ATCS, which maintain the high-fidelity simulations of the ITCS. Since this study leveraged the ATCS developed as part of the CHS-NA study, this section describes the kriging metamodel that was developed as part of that work.

The kriging procedure, the basis of the metamodel development, requires determining a correlation function for X, denoted $R = (x^l, x^m|s)$ and then following the subsequent steps in the kriging process outlined in Zhang et al. (2018). The essential part of the metamodel's kriging algorithm is the optimization of the parameter vector, s. In order to accomplish this optimization, the Leave One Out Cross Validation (LOOCV) error criterion were established.

The steric adjustment applied in the NACCS simulations was accounted for in the metamodeling procedure by correcting the input surge values by 0.1 meters (Cialone et al. 2015). Additionally, the input values were normalized with respect to Δp. The kriging equation used the adjusted inputs and the estimated correlation function to make raw predictions in a low-dimensional, latent space. To transform the latent predictions to the high-dimensional, original space, principle component analysis (PCA) was performed with enough components to account for 99% of the variation in the surge predictions.

After the metamodel was trained, it was validated against the NACCS ITCS simulations. The GPM was used to predict storm surge for the 1031 NACCS synthetic TCs with viable hydrodynamic simulations, and then the predictions were compared to the data from the ADCIRC simulations. The high accuracy of the GPM was confirmed as the model had average correlation coefficients greater than 98% and average square root of the squared errors less than 0.10 meters. Following the training of the GPM, it was applied to predict the surge induced by the ATCS. These surge values were then adjusted to account for the D.C. Metro mesh modifications as discussed in the following section.

6.1.3 D.C. Metro Surge Correction

As discussed at the beginning of Section 6, a correction was applied to the ATCS surge results to apply the effects of the ADCIRC mesh alterations and updates to the storm responses used in the development of the hazard curves. The method to compute the value of the correction included first determining the absolute (Δ_a) and relative (Δ_r) differences as shown in Equations 6-1 and 6-2 followed by computing a total difference through application of Equation 6-3. The correction was computed at each save point to avoid incurring bias in the final surge results applied in the JPM integration. The absolute and relative differences computed for the D.C. Metro save points are provided below in Table 6-1.

Table 6-1. Absolute and relative differences between the D.C. Metro and NACCS surge results.

Save Point	ADCIRC ID	Latitude	Longitude	Absolute Difference (Δ_a)	Relative Difference (Δ_r)
1	14607	38.76	-77.03	-0.01	-0.03
2	5982	38.85	-77.03	0.01	-0.01
3	5984	38.84	-77.03	0.01	-0.01
4	5987	38.81	-77.03	0.00	-0.02
5	5991	38.79	-77.03	-0.01	-0.02
6	7757	38.81	-77.04	0.02	0.00
7	14608	38.81	-77.03	0.02	-0.01
8	14609	38.85	-77.02	0.04	0.01
9	14731	38.77	-77.04	0.02	-0.01
10	14735	38.78	-77.04	0.04	0.00
11	5878	38.87	-77.02	0.06	0.02

12	5980	38.87	-77.01	0.05	0.02
13	6137	38.87	-77.02	0.07	0.02
14	7841	38.87	-77.02	0.39	0.31
15	14607	38.76	-77.03	0.36	0.28
16	14732	38.79	-77.02	0.37	0.30
17	5978	38.88	-77.05	0.39	0.31
18	5919	38.90	-77.08	0.41	0.32
19	14611	38.89	-77.05	0.38	0.29
20	14612	38.87	-77.00	0.07	0.03
21	14733	38.88	-76.97	0.10	0.05
22	5979	38.88	-77.02	0.01	-0.02
23	14610	38.87	-77.02	0.00	-0.02

6.2 Spatially-Varying Bias Correction and Uncertainty Quantification

A natural consequence of the inherent simplification associated with the modeling of complex natural systems is that model outputs will differ in some degree from the true or actual values of the evaluated phenomena. Quantification of the difference or error is necessary to calibrate model parameters, validate the results, and characterize model performance. Errors in hydrodynamic modeling, for example, may originate from the idealization of wind fields, shallow water approximations of the governing hydrodynamic equations, simplified wave model equations, and assumptions related to boundary conditions. The two main components of error are systematic error (bias) and spread (uncertainty), which respectively relate to model accuracy and precision. In the JPM methodology, it has been typically assumed that the error is unbiased, and the epistemic uncertainty has been addressed through the use of the epsilon term "ε" within the JPM. Bias correction is required prior to the JPM integration if found in the assessment of model error.

Generally, errors in SWL and wave height are evaluated by comparing the validation storm model results to measurements. For SWL, the comparison is primarily done with water level gage measurements and high-water marks (HWM). While the water level gage measurements are usually very accurate, HWMs can include wave effects that make them

inaccurate for comparing to SWL. As a result, HWM data is carefully culled to remove HWMs that contain significant wave effects.

In numerical storm surge modeling, there is bias if the computed water levels have a tendency to either over-predict or under-predict the measured water levels. Generally, the bias is computed as the mean of the differences between the modeled and measured water levels at a location of a water level measurement, which is termed the mean of the error. The bias has units of length, but a normalized bias can also be quantified. In cases where the bias is close to zero, the estimates are considered to be unbiased. The simplest bias correction is to apply a linear adjustment by subtracting the dimensional, or absolute, bias from the modeled. If the bias varies with SWL magnitude, the bias correction should be a multiplier applying normalized bias, or relative bias, rather than a uniform difference.

In the PCHA, both the spatially-varying absolute and relative forms of the bias are computed for the numerical models through application of a Gaussian kernel surface (GKS). This resulted in a two-dimensional (2D) surface of the relative and absolute forms of the bias for the study area. For the estimation of SWL AEFs, a total model bias is then computed by aggregating the relative biases (μ_{ε_r}) of both the ADCIRC and PBL models. Likewise, the absolute biases of these models are aggregated as the absolute total model bias (μ_{ε_a}). The total model bias for the relative and absolute forms is computed as the summation of individual biases:

$$\mu_{\varepsilon_a} = \mu_{\varepsilon_a 1} + \mu_{\varepsilon_a 2} + \ldots + \mu_{\varepsilon_a n} \quad \text{(6-4a)}$$

$$\mu_{\varepsilon_r} = \mu_{\varepsilon_r 1} + \mu_{\varepsilon_r 2} + \ldots + \mu_{\varepsilon_r n} \quad \text{(6-4b).}$$

The final step performed by the PCHA for the estimation of bias is computing a combined bias by synthesizing the relative total model and absolute total model biases. The combined bias applied in the PCHA bias correction uses Equation 6-7 as discussed below.

After quantifying any bias, the ATCS responses estimated using the GPM are corrected, and the unbiased uncertainty is then estimated. Three assumptions regarding uncertainties that are routinely applied are that the uncertainty terms are independent, their effects can be combined by addition, and the combined uncertainty can be represented as a Gaussian

distribution with mean zero. The uncertainty (σ_ε) can then be computed as:

$$\sigma_\varepsilon = \sqrt{\sigma_{\varepsilon 1}^2 + \sigma_{\varepsilon 2}^2 + \cdots + \sigma_{\varepsilon n}^2} \quad (6\text{-}5)$$

where the uncertainty is represented as the standard deviation of the error. If there is correlation between uncertainty terms, it must be accounted for in Equation 6-5.

The basic formulation of the JPM-OS incorporates uncertainty into the hazard curve in the integration process through the epsilon term. Therefore, the magnitude of this uncertainty will modify the mean hazard curve, which will affect its shape. The uncertainty can be characterized as an absolute quantity (e.g. +/- 0.60 m) or as a relative quantity (e.g. 20%). Exclusively accounting for absolute uncertainty is problematic when applied to small surges. A surge and uncertainty of the same magnitude could result in, for example, adding an uncertainty of 0.60 m to a 0.60 m surge. On the other hand, quantified relative uncertainty can be quite large if it is based on relatively small surge values. Thus, accounting for relative uncertainty alone could lead to the consideration of unrealistic uncertainty values for extreme surge elevations. The dynamics of applying either an absolute or relative uncertainty are illustrated in Figure 6-2. An example absolute uncertainty of 0.6 m is represented by the horizontal green line. The variation of uncertainty based on relative uncertainties of 20% and 40% are shown as the solid red and blue lines.

The PCHA framework overcomes these limitations through the combination of both the absolute and the relative forms of uncertainty following statistical DA methods. For the estimation of SWL AEFs, bias in the ADCIRC and PBL models is first corrected at all nodes within the study area. The spatially-varying absolute and relative forms of the uncertainty are then computed for the numerical models. Following a similar methodology as the bias, the relative total model uncertainty is computed by aggregating the relative uncertainties of both the ADCIRC and PBL models. Likewise, aggregating the absolute uncertainties for both models results in the absolute total model uncertainty. To synthesize the absolute and relative forms of the total model uncertainty, the equation corresponding to the scalar case of the DA error statistics described in Gao et al. (2021) is applied:

$$\frac{1}{{\sigma_{\varepsilon_c}}^2} = \frac{1}{{\sigma_{\varepsilon_a}}^2} + \frac{1}{(\sigma_{\varepsilon_r} \cdot \tau)^2} \tag{6-6a}$$

$$\sigma_{\varepsilon_c} = \frac{1}{\sqrt{\frac{1}{{\sigma_{\varepsilon_a}}^2} + \frac{1}{(\sigma_{\varepsilon_r} \cdot \tau)^2}}} \tag{6-6b}$$

where σ_{ε_c} = combined uncertainty (units of τ), σ_{ε_a} = absolute total model uncertainty (units of τ), and ($\sigma_{\varepsilon_r} \cdot \tau$) = relative total model uncertainty (units of τ). Using Equation 6-6, the relative total model uncertainty and absolute total model uncertainty are combined in a manner that prevents the over-estimation of uncertainty. This method accounts for both forms of uncertainty in a way that limits the over prediction of both low and high magnitude surge values. The effects of this application are shown in the example combined uncertainty curves shown in Figure 6-2. This example combined uncertainty curves apply an absolute uncertainty of 0.6 m to relative uncertainties of 20% and 40%. As seen in the red and blue dashed lines, the combined uncertainty increases as a function of the SWL, but the rate of increase follows an asymptotic behavior and diminishes upon approaching the absolute uncertainty.

For similar reasons, the PCHA also computes the combined bias as the summation of the aggregated relative and absolute total model biases as:

$$\mu_{\varepsilon_c} = \frac{\mu_{\varepsilon_a}}{\|\mu_{\varepsilon_a}\|} \frac{1}{\sqrt{\frac{1}{{\mu_{\varepsilon_a}}^2} + \frac{1}{{\mu_{\varepsilon_r}}^2}}} \tag{6-7}$$

where μ_{ε_c} = combined bias (units of τ), μ_{ε_a} = absolute total model bias (units of τ), ($\mu_{\varepsilon_r} \cdot \tau$) = relative total model bias (units of τ). Applying this form of the altitude equation for the estimation of bias retains the sign of the bias which is necessary for the correction done prior to uncertainty estimation.

Figure 6-2. Comparison of methods for characterizing uncertainty.

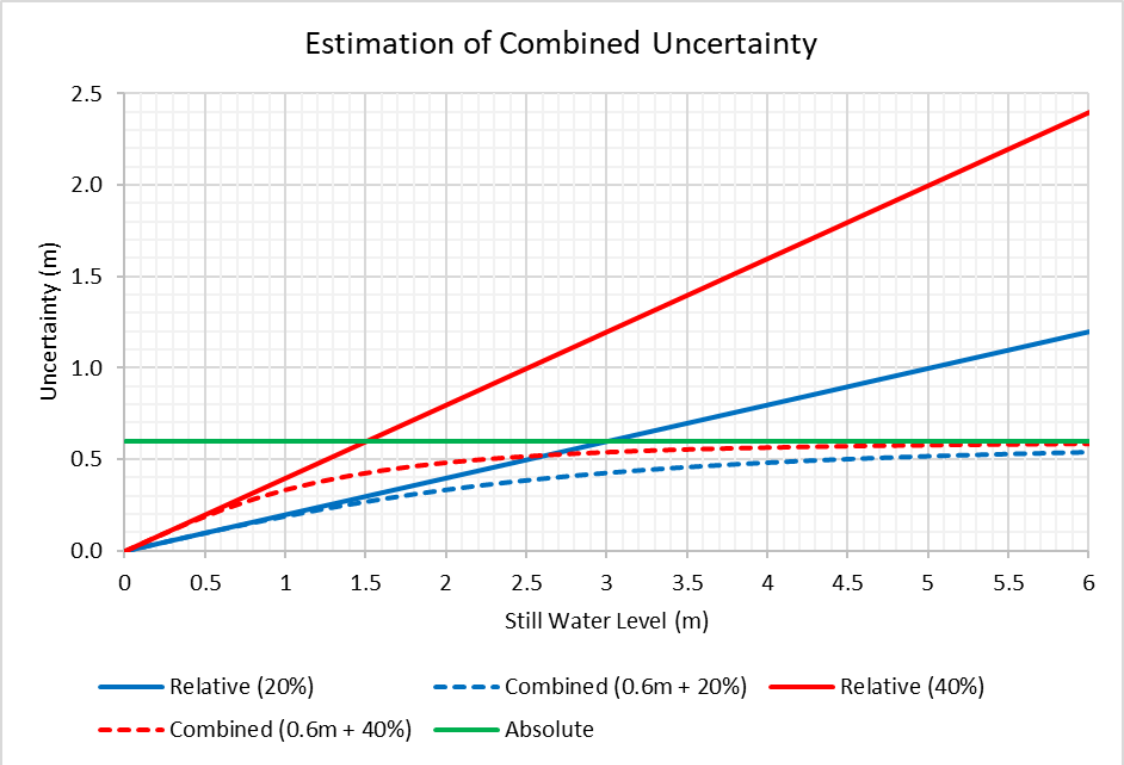

6.2.1 Spatially-Varying Bias

As part of the CHS-NA, the bias within the NACCS storm simulations was evaluated across all NACCS save point locations, including the subset of nodes within the D.C. Metro study area. The bias associated with the ADCIRC and PBL numerical model simulations was assessed by comparing historical measurement data with simulation results of the validation storms. The validation data considered for the NACCS were Hurricanes Sandy, Irene, Isabel, Josephine, and Gloria (Cialone et al. 2015).

The GKS approach was applied to create a 2D surface of the bias for the ADCIRC save points. From the perspective of each save point, weights are assigned to the validation data points based on their distance from the save points. These weights are calculated from Equation 3-2, with kernel size (h_d) estimated as the optimal value for estimating normal densities (Bowman and Azzalini 1997) as a function of the number of validation points and distance to save points. The average values for the relative and absolute forms of the bias as computed for the ADCIRC and PBL models are provided in Table 6-2. The bias correction was applied to the numerical modeling results prior to the computation of spatially-varying

uncertainty for ADCIRC and the PBL model. The uncertainty specific to each point location was estimated for these sources as discussed in the following section.

6.2.2 Spatially-Varying Uncertainty

The main sources of epistemic uncertainty are accounted for in the JPM through the uncertainty term defined as ε. The sources of errors, both bias and uncertainty, in this term include hydrodynamic modeling errors and meteorological modeling errors. The relative and absolute forms of uncertainty computed for each numerical model are described and presented below.

Estimating SWL AEFs required the estimation of combined uncertainty at each save point by applying the total model relative and absolute uncertainties in the altitude equation (Equation 6-5). The average values of the total model relative and absolute uncertainties computed as part of the CHS-NA, which accounts for the D.C. Metro save points, are provided in Table 6-3.

6.2.2.1 ADCIRC Modeling Error

The hydrodynamic modeling errors have been estimated as part of several recent FEMA studies. In the MCAP study (FEMA 2008), for example, the hydrodynamic modeling or calibration error was computed from the differences between simulated and measured storm surge elevations, or HWMs. The uncertainty associated with this error, however, was estimated based on the difference between the standard deviations of the calibration and measurement errors. The measurement error was estimated as a standard deviation representing the variability in HWMs from the actual maximum water level. The calibration and measurement uncertainties were estimated as 0.46 m and 0.40 m, respectively, resulting in a hydrodynamic modeling uncertainty of 0.23 m. The hydrodynamic modeling uncertainty calculated in the Coastal Texas FIS (USACE 2011) for the Gulf of Mexico region was estimated to be in the range of 0.53–0.76 m. However, for the NACCS, the hydrodynamic modeling uncertainty was computed based on the differences between ADCIRC results and high water marks and was estimated to be 0.48 m. For this study, ADCIRC modeling results were compared with HWM data for the validation storm simulations. As a result of this effort, relative and absolute forms of the

uncertainty were computed for all save points. Table 6-3 shows the average values of both forms for the hydrodynamic modeling.

6.2.2.2 Meteorological Modeling Error

The errors in meteorological modeling are estimated from the variability in water levels when comparing levels simulated using PBL winds to those simulated using handcrafted best-winds. The wind and pressure fields derived from best-winds employ techniques that combine inputs from a variety of meteorological sources. In previous studies such as the MCAP, the Coastal Texas FIS, and the NACCS (FEMA 2008; USACE 2011; and Nadal-Caraballo et al. 2015), a range of uncertainty of 0.30-0.75 m was determined from the validation efforts completed. In particular, the MCAP study, which was completed in parallel with LACPR, documented a standard deviation for the meteorological modeling of 0.36 m. Likewise, the NACCS reported a slight bias of -0.05 m as well an estimated uncertainty of 0.38 m for the meteorological modeling. The average values of the PBL absolute and relative uncertainty forms computed for this study are provided in Table 6-3.

6.2.3 Bias and Uncertainty Results

The following tables present the results obtained by applying the PCHA methodology for the estimation of bias and uncertainty. The total bias and uncertainty values reported in Tables 6-2 and 6-3 were computed as previously discussed.

Table 6-2. Absolute and relative components of bias.

Numerical Model	Average Bias	
	Absolute (m)	Relative
ADCIRC	-0.11	-0.09
PBL	-0.05	-0.21
Total (ADCIRC & PBL)	-0.18	-0.28

Table 6-3. Uncertainty for the hydrodynamic and meteorological modeling results computed for estimating AEFs.

Numerical Model	Average Uncertainty	
	Absolute (m)	Relative
ADCIRC	0.34	0.19

PBL	0.34	0.41
Total (ADCIRC & PBL)	0.46	0.39

6.3 Astronomical Tides

The GPM methodology is capable of accurately and efficiently predicting the storm surge and wave responses for tens or hundreds of thousands of TCs, beyond those simulated in ADCIRC. As previously mentioned, the GPM predictions are a function of the TC primary parameters (i.e., x_o, Δp, R_{max}, V_t, θ). The tides within the North Atlantic region are non-negligible and, therefore, were included in the D.C. Metro ADCIRC simulations. However, the astronomical tide is a stochastic process, which is uncorrelated to the TC parameters, and the current version of the GPM cannot replicate the behavior of the tides. As a result, tides must be added to the GPM predictions as a post-process by estimating the skew tide ($tide_{sk}$). The $tide_{sk}$ is computed as the difference between the with-tide and without-tide surge responses simulated by ADCIRC as shown in Figure 6-3.

Figure 6-3. Idealized example of water level components including the $tide_{sk}$.

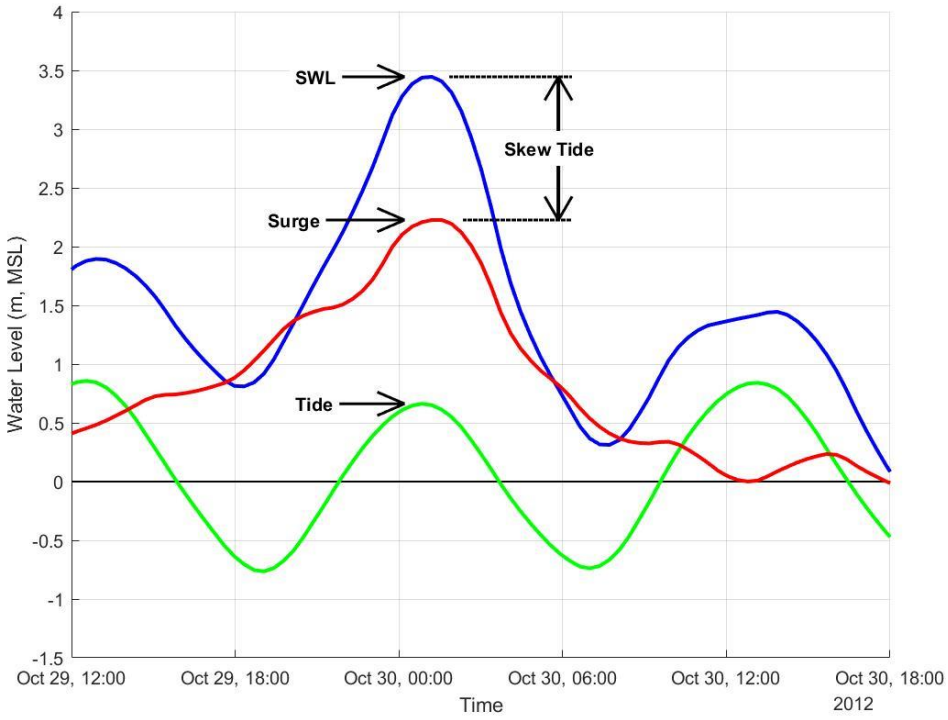

The following steps summarize the process of accounting for astronomical tides in the final SWL hazard curves through the $tide_{sk}$:

1. Use the GPM to simulate the surge-only responses for all storms in the ATCS. Note that the surge-only predictions include wave effects, such as wave setup, but exclude tides.

2. To account for the tides, compute the difference between the with-tide and without-tide scenarios simulated in ADCIRC. The remaining value is the $tide_{sk}$, which results from the random interaction between storm surge and astronomical tides and tends to be negatively correlated with the surge.

3. Fit a Gaussian process regression (GPR) model to the $tide_{sk}$ and storm surge pairs at each of the save points.

4. Predict a random $tide_{sk}$ for each storm in the ATCS using the GPR model.

5. Superimpose the $tide_{sk}$ and storm surge responses estimated for the ATCS prior to the development of the SWL hazard curves.

6.4 Application of StormSim-SST for XC Induced Responses

In order to assess the storm responses produced by the 94 NACCS XCs applied in this study, the StormSim-SST described in Section 2.3 was applied as part of the PCHA. The results of this analysis were SWL AEFs computed for the XCs. The storm response peaks (i.e., surge peaks) at the nodes were input into the StormSim-SST tool for the EVA and generation of the hazard curve. This tool was setup and applied for this study as follows:

1. Similarly to the methods applied in Section 6.3, a GPR model was fit with the $tide_{sk}$ computed as the difference between simulation results with-tides and without-tides. This approach enabled the tool to randomly include the effects of the $tide_{sk}$ by superimposing them in the POT dataset of XC responses without tides.

2. By incorporating the GPR model into the StormSim-SST tool, a second set of POT values was provided for the replacement of the empirical distribution of peaks without tides. This is usually done

for simulation responses not including SLR, where simulation output is available with- and without-tides. The replacement of peak values with those including the effects of tides in the simulation allows an apples-to-apples comparison of the peaks with the $tide_{sk}$.

3. The StormSim-SST processes the input using a bootstrap process of 1000 iterations, in which both the $tide_{sk}$ and the SLR offsets are also added to each random sample of data.

4. A GPD is fit to each random sample and the shape parameter values collected for assessment of the StormSim-SST performance. Outlier shape parameter values result from the bootstrapping process. Hence, the shape parameter values are truncated to the range of [-0.5, 0.3] to prevent unrealistic GPD fits.

5. The tool estimated the threshold parameter of the GPD through the MRL methodology described in Section 2.3. This objective selection process considered different possible threshold values based on the input POT dataset. The hazard was estimated after selecting the threshold value and comparing the values. The criteria considered were:

    a. Selection of a threshold that corresponds to the annual rate closest to 2 storms/yr, and

    b. Selection of the threshold parameter with the minimum weighted mean square error (WMSE; see Section 2.3).

For this study, StormSim-SST was executed with both threshold selection options, and the resulting hazard curves were compared across multiple nodes. The threshold with the minimum WMSE was selected for this study.

6.5 Integration of Joint Probability of Storm Responses

In the JPA of coastal storm hazards, the AEF of the TC responses, such as water levels, was computed by integrating the discrete form of the JPM integral (Equation 2-2). In PCHA applications, the discrete form of the JPM integral is employed without the epsilon term, since unbiased uncertainty is conveyed through CLs. When the epistemic uncertainty

associated with a given response is incorporated into the JPA, the JPM integral is modified as follows:

$$\lambda_{\tau(\hat{x})>\tau} \approx \sum_i^n \lambda_i P[\tau(\hat{x}) > \tau|\hat{x}] \quad (6\text{-}8).$$

For this study, four nonexceedance CLs are provided. The nomimal value of these CL applied in this study is 90%. It is standard practice to represent epistemic uncertainty as a Gaussian distribution process with mean zero (Resio et al. 2007; Toro 2008; FEMA 2012). Therefore, this requires the correction of any statistically significant bias. The CLs are then computed as follows:

$$CL = \mu_r + z\sigma_r \quad (6\text{-}9)$$

where: CL = confidence limit; μ_τ = mean value of a given TC response; z = Z-score or number of standard deviations the CL is above μ_τ; and σ_τ= standard deviation of the response.

The D.C. Metro-corrected peak responses produced by each storm in the ATCS at any given site are assigned the probability mass of the corresponding TC, computed as the product of (1) the SRR, (2) the joint probability from the discrete distributions, and (3) the track spacing. Computing the best-estimate (BE) water level AEF requires establishing a range of water elevation bins that encompass the entire range of water levels. The complementary cumulative distribution function (CCDF) of the response is developed by aggregating the probabilities of all water levels that exceed each of the established bins applying Equation 6-8.

The final flood hazard curves combine the probabilities and responses from both TCs and XCs. The probabilities of these two storm populations are combined, assuming independence, as follows:

$$P(CC) = P(TC) + P(XC) \quad (6\text{-}10)$$

where: $P(CC)$ = combined probability of a given response due to both TCs and XCs; $P(TC)$ = probability of a given response due to TCs; $P(XC)$ = probability of a given response due to XCs.

For this study, the SWL AEFs were computed at the 23 save point locations surrounding the D.C. Metro study area as shown in Figure 6-4.

The AEFs were computed ranging from 10 to $1x10^{-4}$ yr^{-1}, and the hazard curves show the BE curve and the 90% CL. Example hazard curves are provided at five example locations as illustrated in Figure 6-4. These example locations are also referenced in the hazard curves as "virtual gauges" (VGs). These example hazard curves (Figures 6-5 through 6-9) illustrate the effect of the ADCIRC mesh modifications on the SWLs (black curves) by comparing with the NACCS SWL results (red curves).

Figure 6-4. Distribution of D.C. Metro Study save point locations.

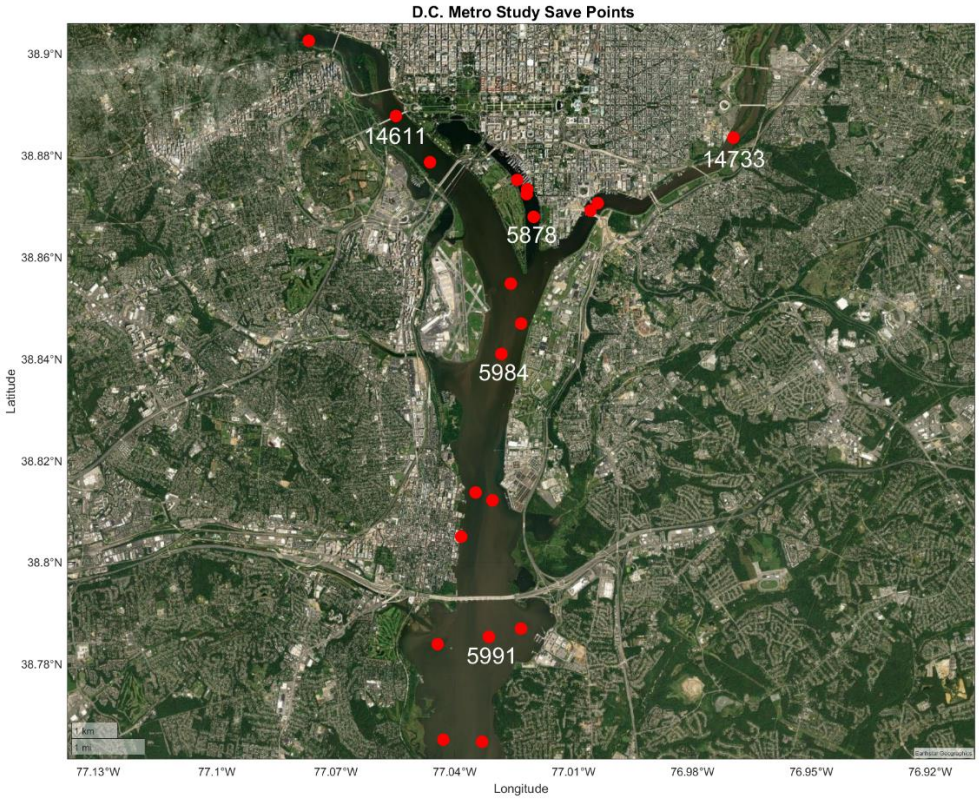

Figure 6-5. SWL hazard curve for Save Point 5878 (VG 11).

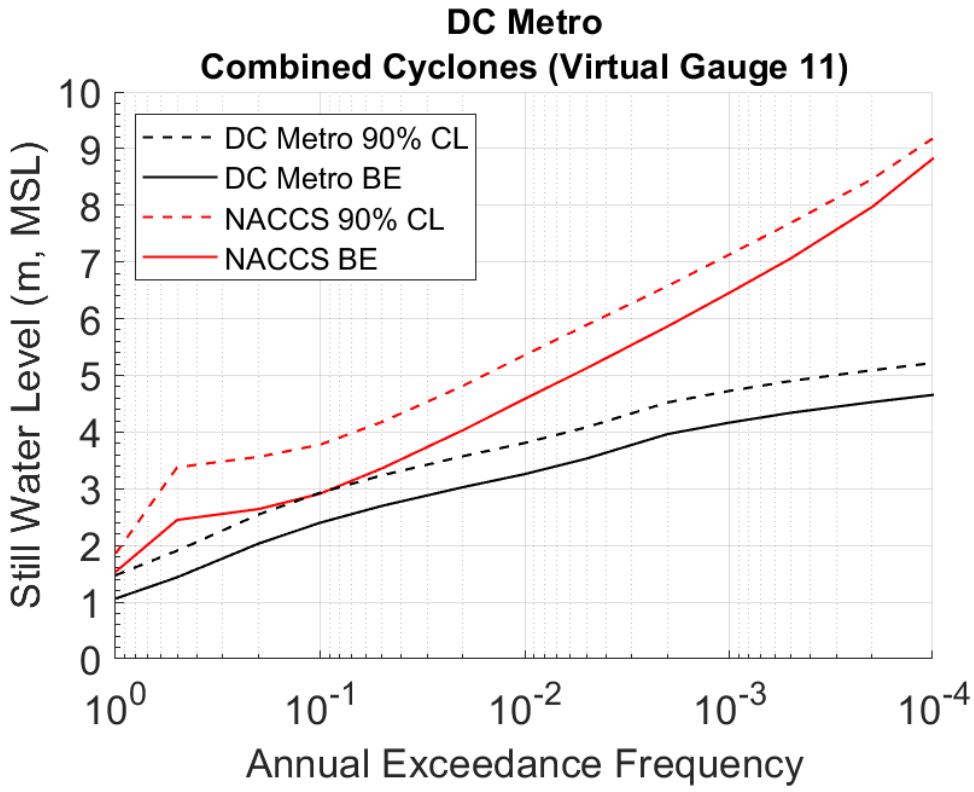

Figure 6-6. SWL hazard curve for Save Point 5984 (VG 3).

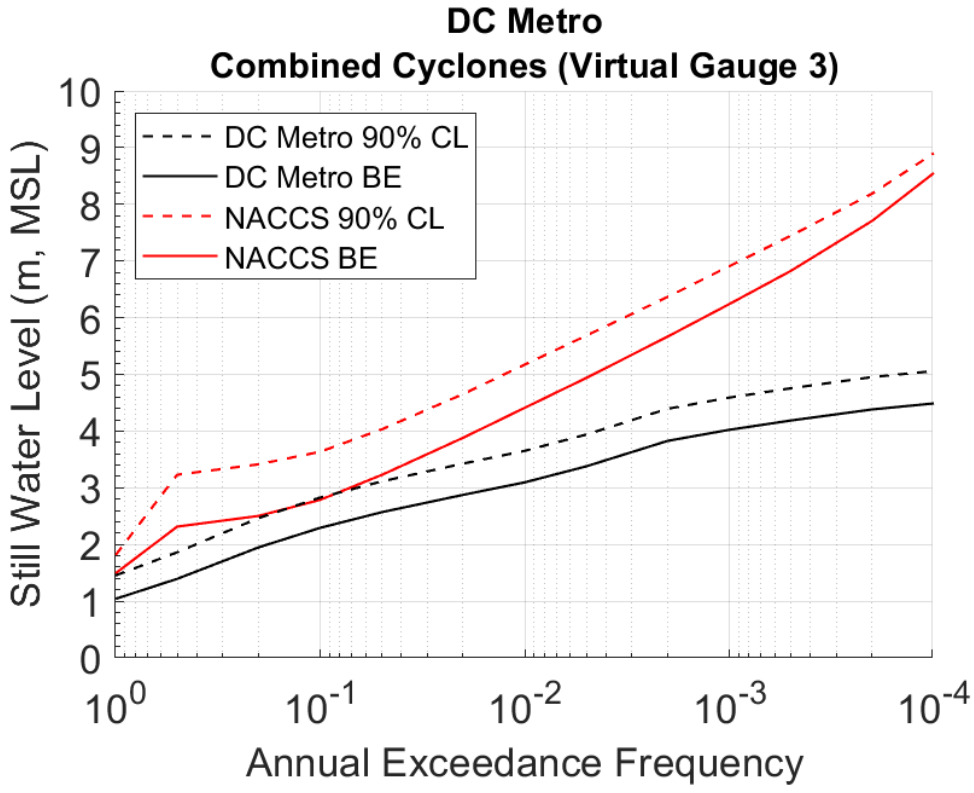

Figure 6-7. SWL hazard curve for Save Point 5991 (VG 5).

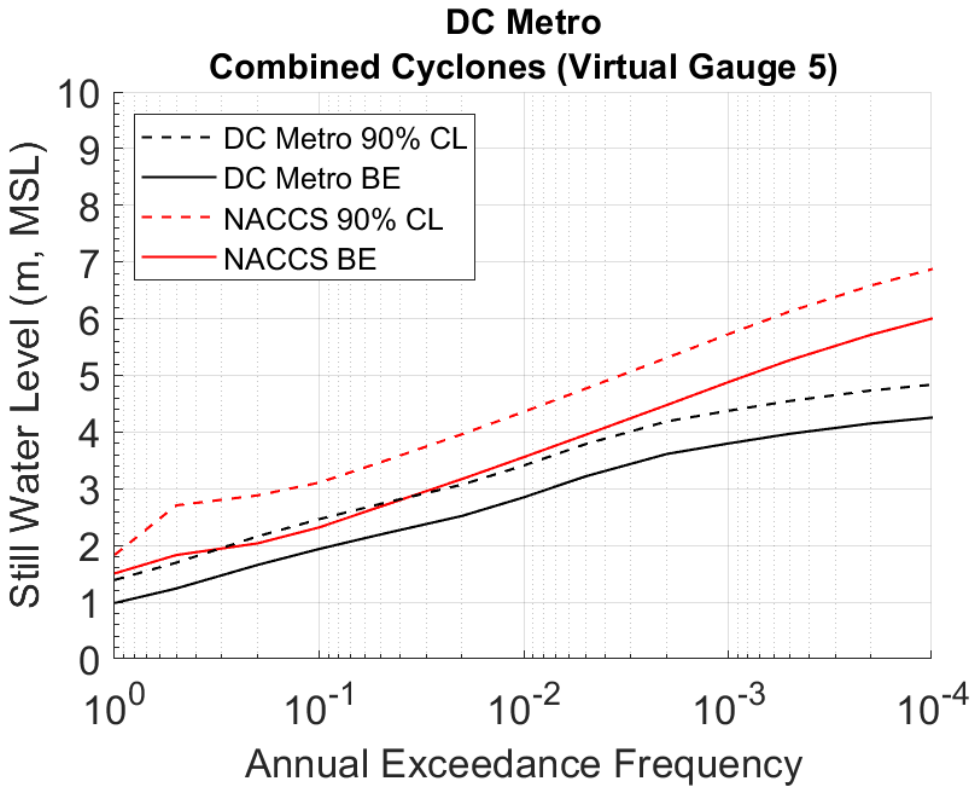

Figure 6-8. SWL hazard curve for Save Point 14611 (VG 19).

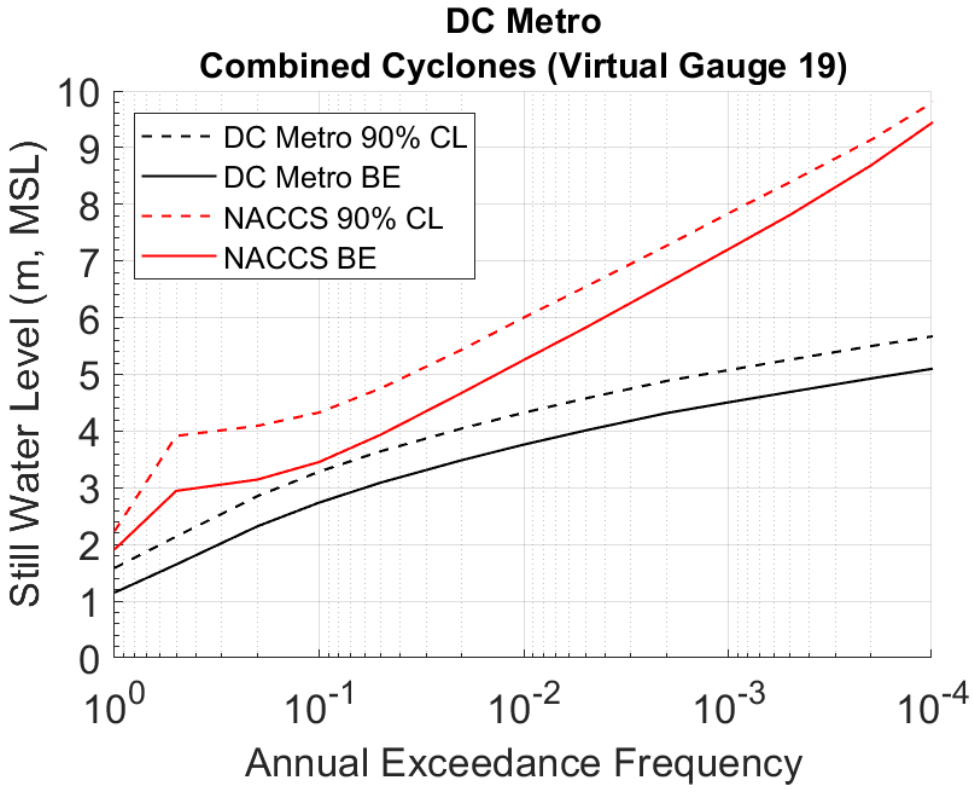

Figure 6-9. SWL hazard curve for Save Point 14733 (VG 21).

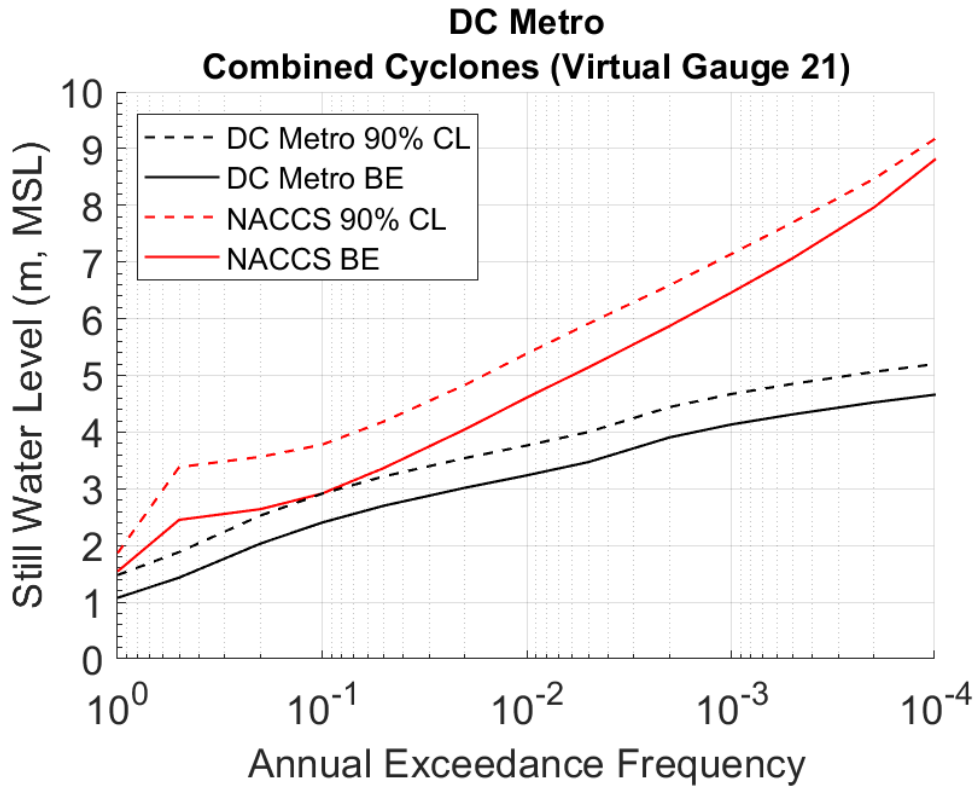

6.6 Analysis of D.C. Metro and NACCS Results

Additional comparisons were made between the D.C. Metro and NACCS results through application of a linear regression model. In Figures 6-10 through 6-12, a linear model is shown which illustrates the differences between surge, tides, and SWLs between the two studies. The trends shown in these images are reflected across each of the save points, or VGs, and can be attributed to the modifications made to the ADCIRC mesh. The updates to the mesh, which included increased resolution in the D.C. Metro area, updated bathymetry, and inclusion of the levee systems, resulted in a lowering of the tides and an increase in the storm surge. However, the overall effect of the D.C. Metro simulations contributed to lower SWL AEFs as compared to the NACCS results at each save point.

Figure 6-10. Results of storm surge level (SSL) linear regression at save point 5878 (VG 11).

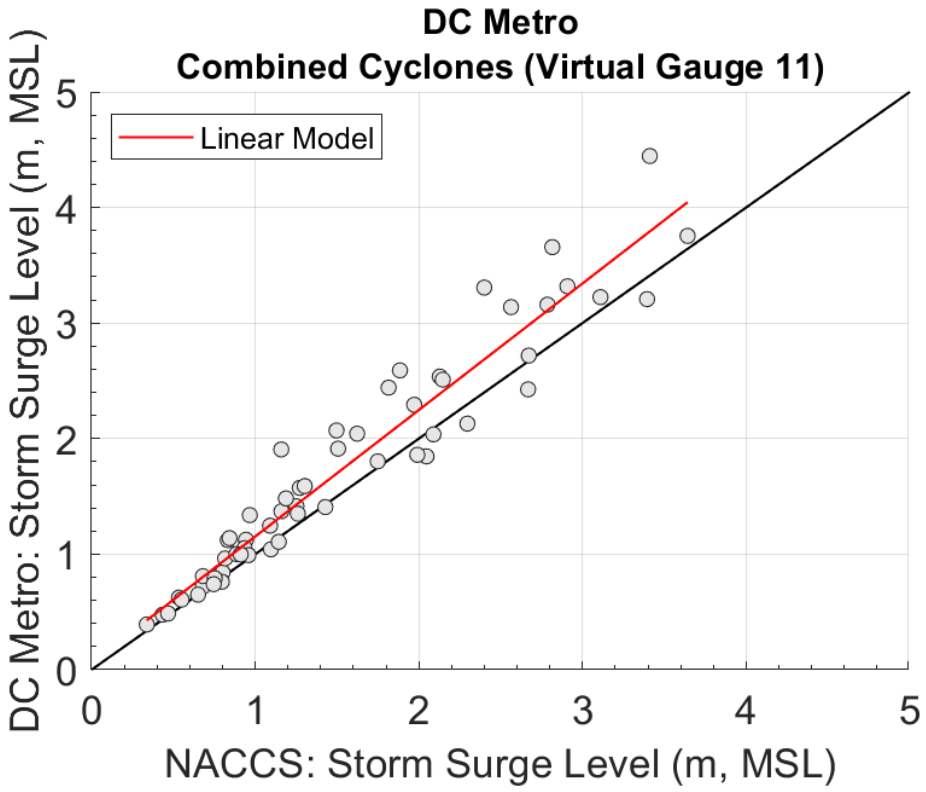

Figure 6-11. Results of skew tide linear regression at save point 5878 (VG 11).

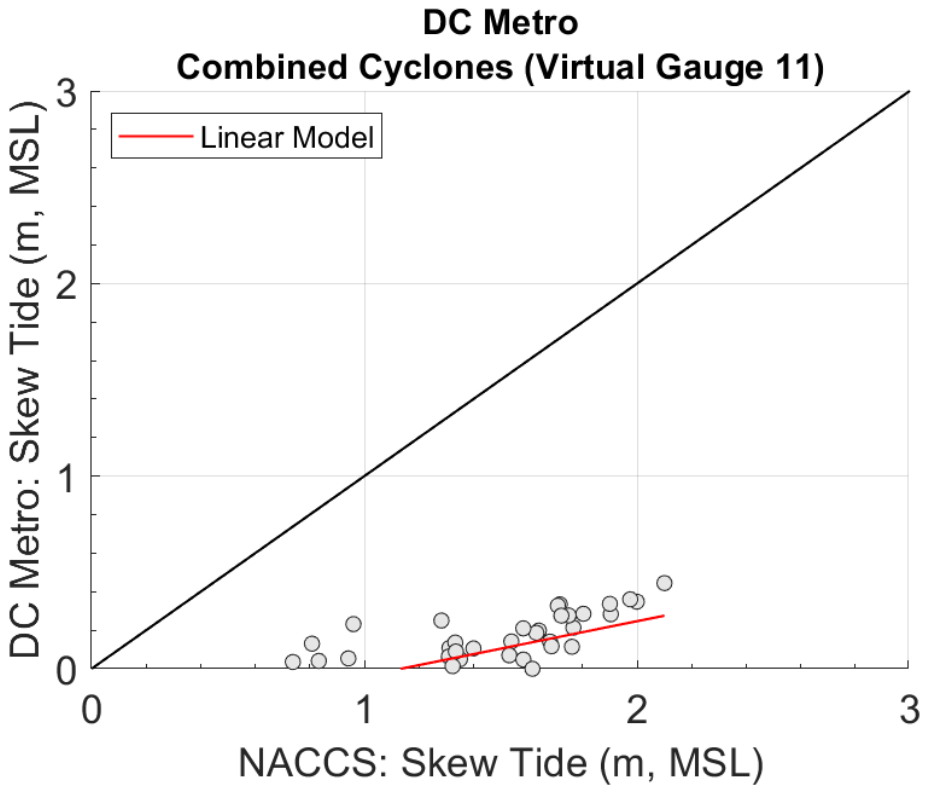

Figure 6-12. Results of SWL linear regression at save point 5878 (VG 11).

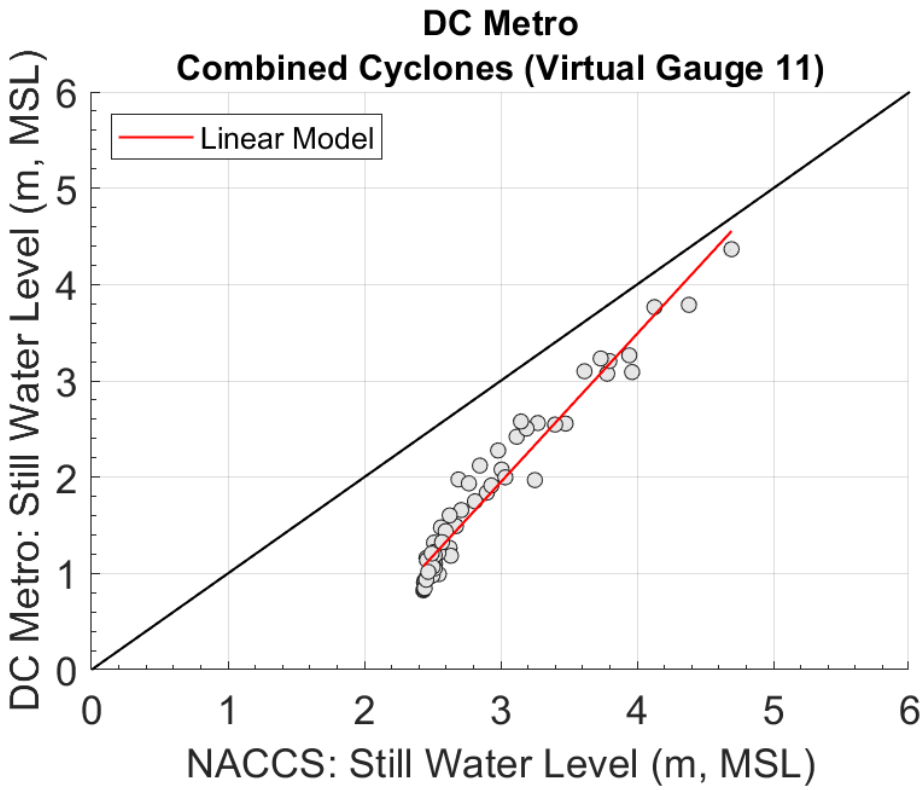

7 Conclusions

An evaluation of coastal storm hazards is summarized in this report for coastal locations surrounding the D.C. Metro study area. The intent of this study was to assess AEFs ranging from 10 to $1x10^{-4}$ yr^{-1} at 23 point locations for TC- and XC-induced SWLs. As a result, the statistics produced from this study will be used by USACE NAB and the MWCOG to assess the impact of the proposed levee systems on flood risk in the D.C. Metro study area.

Following the PCHA framework developed by ERDC-CHL, this study applied a variant of the JPM for the quantification of coastal storm hazards using advancements over standard JPM approaches such as GPM techniques, application of the MGC, and spatially-varying estimations of SRR, bias, and uncertainty. By leveraging the NACCS storm suite, a reduced suite of 58 synthetic TCs was simulated in ADCIRC using a modified mesh which included increased resolution, the proposed levee system, and updated bathymetry. However, to leverage the ATCS developed as part of the CHS-NA study, the D.C. Metro ADCIRC simulations were used to correct the ATCS surge responses. The ATCS accounted for a much denser coverage of the parameter and probability space of TCs, which benefited a more accurate quantification of the surge hazard than relying solely on the D.C. Metro RSS. Additionally, the XC-induced surge was leveraged from 94 historical XC simulations completed for NACCS.

After training a metamodel and producing storm surge estimates for the ATCS, an analysis was completed to estimate the absolute and relative differences of the D.C. Metro surge and the ATCS surge. These differences were applied to adjust the ATCS surge responses to account for the effects of the D.C. Metro simulations in the hazard curves. The storm responses induced by the XCs were then applied in StormSim-SST to quantify the surge hazard of this storm population. After performing the JPM integration with the ATCS-corrected surge, the final hazard curves were developed by combining the TC and XC SWL AEFs. By applying a linear regression to the D.C. Metro and NACCS SWL AEFs, the effects of the alterations to the D.C. Metro ADCIRC mesh were then illustrated as an overall lowering of the SWLs at all save points compared to the previous NACCS SWL results.

References

Beven, J., and H. Cobb. 2014. Tropical Cyclone Report: Hurricane Isabel 6-19 September 2003. Miami, FL: National Hurricane Center, National Weather Service.

Borgman, L. 2004. New Nonparametric Methods in Risk Analysis Based on Resampling Techniques and Empirical Simulation. ASCE 6th International Conference of Civil Engineering in the Oceans, October 20-22, 2004, Baltimore, MD.

Bowman, A. W., and A. Azzalini. 1997. Applied Smoothing Techniques for Data Analysis. New York: Oxford University Press Inc.

Chouinard, L. M., and C. Liu. 1997. Model for recurrence rate of hurricanes in Gulf of Mexico. Journal of Waterway, Port, Coastal and Ocean Engineering 123:113–119.

Cialone M. A., T. C. Massey, M. E. Anderson, A. S. Grzegorzewski, R. E. Jensen, A. Cialone, D. J. Mark, K. C. Peavey, B. L. Gunkel, T. O. McAlpin, N. C. Nadal-Caraballo, J. A. Melby, and J. J. Ratcliff. 2015. North Atlantic Coast Comprehensive Study (NACCS) coastal storm model simulations: Waves and water levels. ERDC/CHL TR-15-14. Vicksburg, MS: U.S. Army Engineer Research and Development Center.

Coastal Protection and Restoration Authority (CPRA). 2013. Greater New Orleans flood protection system notice of completion – Design assessment by non-federal sponsor. Bell City, LA: Lonnie G. Harper & Associates.

Coles, S. 2001. An Introduction to Statistical Modeling of Extreme Values. Lecture Notes in Control and Information Sciences. Springer.

Demuth, J., M. DeMaria, and J. A. Knaff. 2006. Improvement of advanced microwave sounder unit tropical cyclone intensity and size estimation algorithms. Journal of Applied Meteorology and Climatology 45:1573-1581.

Fang, K. T., S. Kotz, and K. W. Ng. 1990. Symmetric Multivariate and Related Distributions. Chapman and Hall.

Fang, H. B., K.-T. Fang, S. Kotz. 2002. The Meta-elliptical Distributions with Given Marginals. Journal of Multivariate Analysis 82:1-16.

Federal Emergency Management Agency (FEMA). 1988. Coastal flooding hurricane storm surge model. Volume 1 Methodology. Washington, DC: Office of Risk Management, Federal Insurance Administration, FEMA.

_____. 2008. Mississippi coastal analysis project. Final Report: HMTAP Task Order 18, prepared for the Federal Emergency Management Agency, Department of Homeland Security. Gaithersburg, MD: URS Group, Inc.

_____. 2012. Operating guidance No. 8-12 for use by FEMA staff and flood mapping partners: Joint probability – optimal sampling method for tropical storm surge. Washington, DC: Federal Emergency Management Agency, Department of Homeland Security.

_____. 2014. Redefinition of the coastal flood hazard zones in FEMA Region II: Analysis of the coastal storm surge flood frequencies. Final Report prepared for the Federal Emergency Management Agency, Department of Homeland Security. Fairfax, VA: Risk Assessment, Mapping, and Planning Partners.

Gao, F., X. Zhang, N. A. Jacobs, X.-Y. Huang, X. Zhang, and P. P. Childs. 1972. Estimation of TAMDAR Observational Error and Assimilation Experiments. Weather and Forecasting 27:856-877.

Gonzalez, V. M., N. C. Nadal-Caraballo, J. A. Melby, and M. A. Cialone. 2019. Quantification of Uncertainty in Probabilistic Storm Surge Models: Literature Review. ERDC/CHL SR-19-1. Vicksburg, MS: U.S. Army Engineer Research and Development Center.

Ho, F. P. 1974. Storm tide frequency analysis for the coast of Georgia. NOAA Technical Memorandum NWS HYDRO-19. Silver Spring, MD: U.S. Department of Commerce.

Ho, F. P., and V. A. Myers. 1975. Joint probability method of tide frequency analysis applied to Apalachicola Bay and St. George Sound, Florida. NOAA Technical Report NWS 18. Silver Spring, MD: National Weather Service, National Oceanic and Atmospheric Administration.

Ho, F. P., J. C. Su, K. L. Hanevich, R. J. Smith, and F. P. Richards. 1987. Hurricane climatology for the Atlantic and Gulf Coasts of the United States. NOAA Technical Report NWS 38. Silver Spring, MD: National Weather Service, National Oceanic and Atmospheric Administration.

Interagency Performance Evaluation Task Force (IPET). 2009. Performance evaluation of the New Orleans and Southeast Louisiana hurricane protection system. Final Report of the Interagency Performance Evaluation Task Force. Washington, DC: U.S. Army Corps of Engineers, Department of the Army.

Jarvinen, B. R., C. J. Neumann, and M. A. S. Davis. 1984. A tropical cyclone data tape for the North Atlantic basin, 1886–1983: Contents, limitations, and uses. NOAA Tech. Memo 22. Miami, FL: National Hurricane Center, National Weather Service.

Jia, G., Taflanidis, A.A., Nadal-Caraballo, N.C., Melby, J.A., Kennedy, A.B., and Smith, J.M. 2016. Surrogate modeling for peak or time-dependent storm surge prediction over an extended coastal region using an existing database of synthetic storms. Natural Hazards 81:909-938.

Kendall, M.G. 1970. Rank correlation methods. Griffin: Charles Griffin and Co. Ltd.

Landsea, C. W., G. A. Vecchi, L. Bengtsson, and T. R. Knutson. 2010. Impact of duration thresholds on Atlantic tropical cyclone counts. Journal of Climate 23:2508–19.

Landsea, C. W., and J. L. Franklin. 2013. Atlantic hurricane database uncertainty and presentation of a new database format. Monthly Weather Review 141:3576–3592.

Langousis, A., A. Mamalakis, M. Puliga, and R. Deidda. 2016. Threshold detection for the generalized Pareto distribution: Review of representative methods and application to the NOAA NCDC daily rainfall database. Water Resources Research 52:2659–2681.

Mann, M. E., T. A. Sabbatelli, and U. Neu. 2007. Evidence for a modest undercount bias in early historical Atlantic tropical cyclone counts. Geophysical Research Letters 34:L22707.

Melby, J. A., T. C. Massey, A. L. Stehno, N. C. Nadal-Caraballo, S. Misra, V. M. Gonzalez. 2020. Sabine Pass to Galveston Bay, TX Pre-Construction, Engineering and Design (PED) Hurricane Coastal Storm Surge and Wave Hazard Assessment Report 1- Background and Approach. ERDC/CHL Technical Report. Vicksburg, MS: U.S. Army Engineer Research and Development Center.

Melby, J. A., T. C. Massey, F. Diop, H. Das, N. C. Nadal-Caraballo, V. Gonzalez, M. Bryant, A. Tritinger, L. Provost. M. Owensby, and A. Stehno. 2021. Coastal Texas Protection and Restoration Feasibility Study – Coastal Texas Flood Risk Assessment: Hydrodynamic Response and Beach Morphology. ERDC/CHL TR-21-11. Vicksburg, MS: U.S. Army Engineer Research and Development Center.

Myers, V. A. 1954. Characteristics of United States hurricanes pertinent to levee design for Lake Okeechobee, Florida. Hydrometeorological Report No. 32. Washington, DC: Weather Bureau, U.S. Department of Commerce.

Myers, V. A. 1970. Joint probability method of tide frequency analysis applied to Atlantic City and Long Beach Island, NJ. ESSA Technical Memorandum WBTM HYDRO 11. Washington, DC: Weather Bureau, U.S. Department of Commerce.

Myers, V. A. 1975. Storm tide frequencies on the South Carolina Coast. NOAA Technical Report NWS-16. Washington, DC: National Weather Service, National Oceanic and Atmospheric Administration.

Nadal-Caraballo, N. C., J. A. Melby, and B. A. Ebersole. 2012. Statistical analysis and storm sampling approach for Lakes Michigan and St.

Clair. ERDC/CHL TR-12-19. Vicksburg, MS: U.S. Army Engineer Research and Development Center.

Nadal-Caraballo, N. C., and J. A. Melby. 2014. North Atlantic Coast Comprehensive Study – Phase I: Statistical analysis of historical extreme water levels with sea level change. ERDC/CHL TR-14-7. Vicksburg, MS: U.S. Army Engineer Research and Development Center.

Nadal-Caraballo, N. C., J. A. Melby, V. M. Gonzalez, and A. T. Cox. 2015. North Atlantic Coast Comprehensive Study – Coastal Storm Hazards from Virginia to Maine. ERDC/CHL TR-15-5. Vicksburg, MS: U.S. Army Engineer Research and Development Center.

Nadal-Caraballo, N.C., V. M. Gonzalez, T. C. Massey, and A. T. Cox. 2018. Coastal Texas Protection and Restoration Feasibility Study: Probabilistic Modeling of Coastal Storm Hazards. Draft Technical Report. Vicksburg, MS: U.S. Army Engineer Research and Development Center, in review.

Nadal-Caraballo, N. C., V. M. Gonzalez, and L. Chouinard. 2019. Storm Recurrence Rate Models for Tropical Cyclones – Report 1 of a series on the Quantification of Uncertainties in Probabilistic Storm Surge Models. ERDC/CHL TR-19-4. Vicksburg, MS: U.S. Army Engineer Research and Development Center.

Nadal-Caraballo, N. C., M. O. Campbell, V. Gonzalez, M. J. Torres, J. A. Melby, and A. A. Taflanidis. 2020. Coastal Hazards System: A Probabilistic Coastal Hazard Analysis Framework. Proceedings from the International Coastal Symposium (ICS) 2020. Journal of Coastal Research 95:1211-1216.

Nadal-Caraballo, N. C., M. C. Yawn, M. J. Torres, M. L. Carr, V. M. Gonzalez, E. Ramos-Santiago, T. C. Massey, A. A. Taflanidis, A. T. Cox. 2022. Coastal Hazards System: South Atlantic Coastal Study – Puerto Rico and the U.S. Virgin Islands. ERDC/CHL TR-22-XX. Vicksburg, MS: U.S. Army Engineer Research and Development Center, in review.

Neumann, C. J., G. W. Cry, E. L. Caso, and B. R. Jarvinen. 1985. Tropical cyclones of the North Atlantic Ocean, 1871-1980. Asheville, NC: National Climatic Center.

Niedoroda, A.W., D. T. Resio, G.R. Toro, D. Divoky, H. S. Has, and C. W. Reed. 2010. Analysis of the coastal Mississippi storm surge hazard. Ocean Engineering 37:82-90.

Resio, D. T., S. J. Boc, L. Borgman, V. Cardone, A. T. Cox, W. R. Dally, R. G. Dean, D. Divoky, E. Hirsh, J. L. Irish, D. Levinson, A. Niedoroda, M. D. Powell, J. J. Ratcliff, V. Stutts, J. Suhada, G. R. Toro, and P. J. Vickery. 2007. White Paper on estimating hurricane inundation probabilities. Consulting Report prepared by USACE for FEMA. Vicksburg, MS: U.S. Army Engineer Research and Development Center.

Russell, L. R. 1968a. Stochastic models for hurricane prediction for the Texas Gulf Coast. Master's thesis, Stanford University.

Russell, L. R. 1968b. Probability distributions for Texas Gulf Coast hurricane effects of engineering interest. PhD dissertation, Stanford University.

Taflanidis, A.A., J. Zhang, N. C. Nadal-Caraballo, and J. A. Melby. 2017. Advances in surrogate modeling for hurricane risk assessment: storm selection and climate change impact. In proceedings of 12th International Conference on Structural Safety & Reliability, August 6-10, Vienna, Austria.

Toro, G. R. 2008. Joint probability analysis of hurricane flood hazards for Mississippi – Final URS Group report in support of the FEMA-HMTAP flood study of the State of Mississippi. Boulder CO: Risk Engineering.

Toro, G. R., A.W. Niedoroda, C. W. Reed, and D. Divoky. 2010a. Quadrature-based approach for efficient evaluation of surge hazard. Ocean Engineering 37:114–124.

Toro, G. R., D. T. Resio, D. D., A.W. Niedoroda, and C. Reed. 2010b. Efficient joint probability methods for hurricane surge frequency analysis. Ocean Engineering 37:125–34.

U.S. Army Corps of Engineers (USACE). 2009. Louisiana Coastal Protection and Restoration (LACPR). Final Technical Report. New Orleans, LA: New Orleans District, Mississippi Valley Division, USACE.

_____. 2011. Flood insurance study: Coastal counties, Texas: Scoping and data review. Denton, TX: Federal Emergency Management Agency, Region 6.

Vecchi, G. A., and T. R. Knutson. 2011. Estimating annual numbers of Atlantic hurricanes missing from the HURDAT database (1878–1965) using ship track density. Journal of Climate 24:1736–1746.

Vickery, P. J., and B. O. Blanton. 2008. North Carolina coastal flood analysis system hurricane parameter development. Technical Report TR-08-06. Chapel Hill, NC: RENCI Renaissance Computing Institute.

Vickery, P. J., and D. Wadhera. 2008. Statistical models of Holland pressure profile parameter and radius to maximum winds of hurricanes from flight-level pressure and H*Wind data. Journal of Applied Meteorology and Climatology 47:2497–2517.

Worley, S. J., S. D. Woodruff, R. W. Reynolds, S. J. Lubker, and N. Lott. 2005. ICOADS release 2.1 data and products. Journal of Climatology 25:823–842.

Yawn, M.C., N. C. Nadal-Caraballo, M. L. Carr, E. Ramos-Santiago, V. M. Gonzalez, M. J. Torres, T. C. Massey, A. A. Taflanidis, and A. T. Cox. 2022. Coastal Hazards System: South Atlantic Coastal Study – North Carolina to South Florida. ERDC/CHL TR-22-XX. Vicksburg, MS: U.S. Army Engineer Research and Development Center, in review.

Yawn, M. C., N. C. Nadal-Caraballo, M. L. Carr, E. Ramos-Santiago, V. M. Gonzalez, M. J. Torres, T. C. Massey, A. A. Taflanidis, A. T. Cox.

2022. Coastal Hazards System: South Atlantic Coastal Study – South Florida to Mississippi. ERDC/CHL TR-22-XX. Vicksburg, MS: U.S. Army Engineer Research and Development Center, in review.

Zhang, J., Taflanidis, A.A., Nadal-Caraballo, N.C., Melby, J.A., and Diop, F. 2018. Advances in surrogate modeling for storm surge prediction: storm selection and addressing characteristics related to climate change. Natural Hazards 94:1225-1253.

Zhang, L., and Singh, V.P. 2019. Copulas and their Applications in Water Resources Engineering. Cambridge: Cambridge University Press.

Appendix A: Historical TC Selection

The TC parameters implemented for the development of marginal distributions (Section 4.1) at each CRL are reported here. The NHC ID indicates the chronological order the storm occurred in a given year. In Table A-1, the latitude, longitude, Δp and were selected based on the greatest intensity index computed for each storm (Section 3.1.4). The distance parameter reported indicates the distance from the CRL at which the intensity index was recorded. The adjusted Δp and z-score were computed as described in Section 3.1.6.

Table A-1. Historical TCs: coordinates, distance from CRL 458, and Δp.

Name	Year	NHC ID	Latitude	Longitude	Δp (hPa)	*z-score*	*Adj.* Δp (hPa)
UNNAMED	1938	6	39.3	-72.9	73	3.20	73
UNNAMED	1939	2	39.2	-74	8	-1.17	8
UNNAMED	1940	1	35.9	-72.3	18	-0.50	18
UNNAMED	1940	4	38.1	-71.3	52	1.79	52
UNNAMED	1940	5	37.3	-68.5	41	1.05	41
UNNAMED	1941	3	35.9	-71.7	36	0.71	36
UNNAMED	1942	9	35.5	-75.9	10	-1.04	10
UNNAMED	1943	2	34.8	-72.5	8	-1.17	8
UNNAMED	1943	5	36.8	-71.5	11	-0.97	11
UNNAMED	1943	7	37.7	-75.7	16	-0.63	16
UNNAMED	1944	3	39.2	-74.5	11	-0.97	11
UNNAMED	1944	7	37.1	-74.7	60	2.32	60
UNNAMED	1944	13	39.4	-73.3	20	-0.37	20
UNNAMED	1945	1	37.3	-73.8	35	0.64	35
UNNAMED	1945	9	38.3	-77	12	-0.90	12
UNNAMED	1946	2	37.8	-72.1	33	0.51	33
UNNAMED	1946	4	36.9	-69	23	-0.16	23
UNNAMED	1946	6	35.9	-75	10	-1.04	10
UNNAMED	1947	6	36.6	-74.8	11	-0.97	11
UNNAMED	1948	3	35.3	-71.6	35	0.64	35
UNNAMED	1948	10	35.7	-73.9	19	-0.43	19
UNNAMED	1949	1	35.7	-74.5	46	1.38	46

Name	Year	NHC ID	Latitude	Longitude	Δp (hPa)	*z-score*	*Adj.* Δp (hPa)
UNNAMED	1949	2	40.8	-76.6	15	-0.70	15
UNNAMED	1949	7	34.3	-77.8	13	-0.84	13
ABLE	1950	1	36	-72.7	56	2.06	56
DOG	1950	4	37.9	-71.4	41	1.05	41
ABLE	1951	2	36.1	-73.8	37	0.78	37
HOW	1951	9	36.9	-71.6	41	1.05	41
UNNAMED	1952	1	38.4	-72	26	0.04	26
ABLE	1952	2	39.5	-77.1	20	-0.37	20
UNNAMED	1953	2	38.2	-71.7	12	-0.90	12
BARBARA	1953	3	37.6	-74.9	40	0.98	40
CAROL	1953	4	37	-70.5	50	1.65	50
UNNAMED	1953	11	36.3	-72.5	17	-0.57	17
UNNAMED	1954	1	38.1	-71.3	14	-0.77	14
UNNAMED	1954	2	35.9	-72.6	16	-0.63	16
UNNAMED	1954	4	36.5	-72.1	9	-1.10	9
CAROL	1954	6	39.5	-72.8	58	2.19	58
EDNA	1954	8	38.1	-72.5	57	2.12	57
HAZEL	1954	14	40.2	-77.2	37	0.78	37
CONNIE	1955	2	37.7	-76.2	39	0.91	39
DIANE	1955	3	40.5	-74.5	12	-0.90	12
IONE	1955	8	36.6	-75.7	37	0.78	37
BETSY	1956	3	36.6	-69.8	49	1.58	49
FLOSSY	1956	7	38.5	-73	16	-0.63	16
UNNAMED	1956	9	34	-75.1	10	-1.04	10
UNNAMED	1956	11	37.5	-74.5	11	-0.97	11
AUDREY	1957	2	39.4	-80.9	19	-0.43	19
BECKY	1958	2	34.8	-72.1	11	-0.97	11
DAISY	1958	4	38	-72.6	44	1.25	44
HELENE	1958	8	35.5	-73.8	63	2.53	63
UNNAMED	1958	11	37	-70	17	-0.57	17
CINDY	1959	4	38	-74.6	14	-0.77	14
GRACIE	1959	8	41.7	-77	8	-1.17	8
UNNAMED	1959	12	35.2	-73	23	-0.16	23
UNNAMED	1959	14	39.5	-68.5	11	-0.97	11

Name	Year	NHC ID	Latitude	Longitude	Δp (hPa)	*z-score*	*Adj.* Δp (hPa)
BRENDA	1960	3	38.7	-75.3	21	-0.30	21
DONNA	1960	5	37.3	-74.8	42	1.11	42
ESTHER	1961	5	37.8	-72.6	51	1.72	51
UNNAMED	1961	6	38.3	-75.3	25	-0.03	25
GERDA	1961	8	37	-68.8	25	-0.03	25
ALMA	1962	1	36.9	-73.5	23	-0.16	23
UNNAMED	1962	6	35.4	-76	15	-0.70	15
UNNAMED	1962	7	36.4	-71	30	0.31	30
GINNY	1963	8	36.3	-70.3	47	1.45	47
UNNAMED	1963	10	38.2	-76.2	10	-1.04	10
CLEO	1964	5	36.3	-76.4	12	-0.90	12
DORA	1964	6	36.9	-73.3	28	0.17	28
GLADYS	1964	9	37.7	-70.7	39	0.91	39
ISBELL	1964	11	35.5	-77.7	17	-0.57	17
UNNAMED	1964	13	36.8	-72	9	-1.10	9
UNNAMED	1964	13	36.8	-72	9	-1.10	9
UNNAMED	1965	1	36	-76.2	16	-0.63	16
ALMA	1966	1	37.6	-73.5	11	-0.97	11
DORIA	1967	14	37.8	-73.3	27	0.11	27
CANDY	1968	3	42	-80	11	-0.97	11
DOLLY	1968	5	35	-71.3	19	-0.43	19
GLADYS	1968	14	37	-72	32	0.44	32
ANNA	1969	6	36.5	-72.5	16	-0.63	16
BLANCHE	1969	7	38.6	-68	36	0.71	36
CAMILLE	1969	9	37	-75.3	13	-0.84	13
GERDA	1969	16	37.8	-72.2	29	0.24	29
KARA	1969	25	34.9	-71.9	16	-0.63	16
ALMA	1970	1	36.5	-77	10	-1.04	10
UNNAMED	1970	8	37	-72.5	8	-1.17	8
ARLENE	1971	1	36.7	-72.9	12	-0.90	12
BETH	1971	6	37.2	-69.9	23	-0.16	23
DORIA	1971	9	38.5	-75.3	20	-0.37	20
GINGER	1971	14	36.8	-78.1	10	-1.04	10
HEIDI	1971	17	37.1	-69.9	19	-0.43	19

Name	Year	NHC ID	Latitude	Longitude	Δp (hPa)	*z-score*	*Adj.* Δp (hPa)
ALPHA	1972	1	34	-73.5	13	-0.84	13
AGNES	1972	2	38.2	-73.1	36	0.71	36
UNNAMED	1972	4	34	-78	9	-1.10	9
CARRIE	1972	11	38.8	-71.1	19	-0.43	19
DAWN	1972	13	36.6	-73.5	20	-0.37	20
ALFA	1973	6	36.3	-71.7	9	-1.10	9
UNNAMED	1974	2	33.5	-75.5	9	-1.10	9
DOLLY	1974	12	35.5	-72.1	8	-1.17	8
AMY	1975	2	35.9	-70.5	26	0.04	26
BLANCHE	1975	4	35.9	-70	26	0.04	26
ELOISE	1975	13	37.5	-81.5	9	-1.10	9
HALLIE	1975	19	35.7	-73.8	9	-1.10	9
UNNAMED	1976	1	34.8	-72	17	-0.57	17
UNNAMED	1976	2	36	-73.3	9	-1.10	9
BELLE	1976	7	38.8	-73.8	36	0.71	36
DAVID	1979	9	39.2	-78.5	24	-0.10	24
FREDERIC	1979	11	42.5	-76	15	-0.70	15
BRET	1981	6	36.6	-74.7	13	-0.84	13
DENNIS	1981	10	36.3	-73	18	-0.50	18
UNNAMED	1981	22	37.9	-71.4	35	0.64	35
UNNAMED	1982	2	37.1	-73	21	-0.30	21
DEAN	1983	6	34.8	-71	8	-1.17	8
DIANA	1984	10	37.2	-72.7	19	-0.43	19
ISIDORE	1984	15	34.3	-74.4	8	-1.17	8
JOSEPHINE	1984	16	36.8	-71.7	38	0.84	38
CLAUDETTE	1985	3	34.3	-72.7	9	-1.10	9
GLORIA	1985	9	38.4	-74.5	62	2.46	62
HENRI	1985	10	38.2	-74	8	-1.17	8
KATE	1985	13	34.7	-76.2	10	-1.04	10
ANDREW	1986	1	36.3	-72.7	11	-0.97	11
CHARLEY	1986	5	38.2	-74.1	21	-0.30	21
HUGO	1989	11	42.2	-80.2	25	-0.03	25
LILI	1990	14	36.6	-71.3	17	-0.57	17
ANA	1991	1	36.2	-70.7	10	-1.04	10

Name	Year	NHC ID	Latitude	Longitude	Δp (hPa)	*z-score*	*Adj.* Δp (hPa)
BOB	1991	3	38.9	-73	60	2.32	60
UNNAMED	1991	12	37.7	-71.5	21	-0.30	21
DANIELLE	1992	7	35.9	-75.2	12	-0.90	12
EMILY	1993	5	36.6	-74.4	51	1.72	51
GORDON	1994	12	33.7	-75.7	29	0.24	29
ALLISON	1995	1	37.1	-73.6	23	-0.16	23
FELIX	1995	7	36.5	-72.2	40	0.98	40
OPAL	1995	17	42	-80.5	22	-0.23	22
ARTHUR	1996	1	36.4	-74.1	8	-1.17	8
BERTHA	1996	2	38.3	-76.1	19	-0.43	19
EDOUARD	1996	5	37.5	-70	53	1.85	53
FRAN	1996	6	36.7	-79	28	0.17	28
JOSEPHINE	1996	10	38	-73.5	30	0.31	30
UNNAMED	1997	1	35.5	-74.1	9	-1.10	9
CLAUDETTE	1997	4	34.9	-71.8	8	-1.17	8
DANNY	1997	5	37.5	-73.5	17	-0.57	17
BONNIE	1998	2	36.7	-74.3	23	-0.16	23
EARL	1998	5	36.5	-75	13	-0.84	13
DENNIS	1999	5	35.5	-73.8	25	-0.03	25
FLOYD	1999	8	38	-75.3	39	0.91	39
IRENE	1999	13	35.4	-74.4	55	1.99	55
GORDON	2000	11	41.5	-72	8	-1.17	8
HELENE	2000	12	38	-72.5	12	-0.90	12
UNNAMED	2000	19	35.7	-69.9	21	-0.30	21
ALLISON	2001	1	38.6	-74.5	8	-1.17	8
ARTHUR	2002	1	36.1	-71	9	-1.10	9
GUSTAV	2002	8	36.8	-73	36	0.71	36
ISIDORE	2002	10	40.9	-79.5	14	-0.77	14
ISABEL	2003	13	36.7	-77.7	44	1.25	44
ALEX	2004	1	36	-73.7	39	0.91	39
CHARLEY	2004	3	34.5	-78.1	13	-0.84	13
FRANCES	2004	6	40.5	-80	12	-0.90	12
GASTON	2004	7	38.1	-74.8	12	-0.90	12
IVAN	2004	9	38.4	-76.7	13	-0.84	13

Name	Year	NHC ID	Latitude	Longitude	Δp (hPa)	*z-score*	*Adj.* Δp (hPa)
JEANNE	2004	11	38.8	-74.7	14	-0.77	14
OPHELIA	2005	16	37.3	-72.7	18	-0.50	18
TWENTY-TWO	2005	23	38.6	-73.8	8	-1.17	8
ALBERTO	2006	1	37	-73	14	-0.77	14
BERYL	2006	3	38.3	-73	11	-0.97	11
ERNESTO	2006	6	36.6	-77.2	16	-0.63	16
ANDREA	2007	1	34.3	-71.7	8	-1.17	8
BARRY	2007	2	39	-73.2	23	-0.16	23
GABRIELLE	2007	7	34.8	-76.4	8	-1.17	8
NOEL	2007	16	36.4	-70.9	39	0.91	39
CRISTOBAL	2008	3	36.2	-73.2	13	-0.84	13
HANNA	2008	8	40	-74.5	19	-0.43	19
KYLE	2008	11	37.4	-69.3	21	-0.30	21
BILL	2009	3	38.1	-68.4	52	1.79	52
EARL	2010	7	37.6	-72.2	53	1.85	53
IRENE	2011	9	38.1	-75	55	1.99	55
BERYL	2012	2	36.3	-72.9	17	-0.57	17
SANDY	2012	18	38.8	-74	70	3.00	70
ANDREA	2013	1	37.4	-76.2	16	-0.63	16
ARTHUR	2014	1	36.8	-74.4	37	0.78	37
BERTHA	2014	3	34.2	-72.7	8	-1.17	8
CLAUDETTE	2015	3	36.8	-69.4	8	-1.17	8
COLIN	2016	3	35.5	-74.4	17	-0.57	17
HERMINE	2016	9	39.2	-72.5	13	-0.84	13
MATTHEW	2016	14	35	-74.5	29	0.24	29
CINDY	2017	3	38.9	-78.5	10	-1.04	10
JOSE	2017	12	37.6	-71.2	40	0.98	40
MARIA	2017	15	36.6	-72.2	34	0.58	34
NATE	2017	16	43.1	-76.3	8	-1.17	8
FLORENCE	2018	6	34.2	-77.2	61	2.39	61
MICHAEL	2018	14	37.3	-75	30	0.31	30
DORIAN	2019	5	36.2	-73.7	57	2.12	57
ERIN	2019	6	36.9	-70.9	11	-0.97	11
MELISSA	2019	14	38.2	-69.7	17	-0.57	17

Name	Year	NHC ID	Latitude	Longitude	Δp (hPa)	*z-score*	*Adj.* Δp (hPa)
NESTOR	2019	16	37.5	-74.5	12	-0.90	12

Table A-2. Historical TCs with unadjusted atmospheric parameters for CRL 458.

Name	Year	NHC ID	Δp (hPa)	R_{max} (km)	V_f (km/h)	θ (deg)
UNNAMED	1938	6	73	73	76	2
UNNAMED	1939	2	8	83	49	85
UNNAMED	1940	1	18	94	7	39
UNNAMED	1940	4	52	72	35	30
UNNAMED	1940	5	41	79	31	19
UNNAMED	1941	3	36	85	24	45
UNNAMED	1942	9	10	65	8	-22
UNNAMED	1943	2	8	51	26	44
UNNAMED	1943	5	11	70	28	32
UNNAMED	1943	7	16	74	22	-53
UNNAMED	1944	3	11	48	28	62
UNNAMED	1944	7	60	58	49	12
UNNAMED	1944	13	20	29	32	50
UNNAMED	1945	1	35	78	38	42
UNNAMED	1945	9	12	60	35	38
UNNAMED	1946	2	33	78	29	50
UNNAMED	1946	4	23	90	43	25
UNNAMED	1946	6	10	72	29	67
UNNAMED	1947	6	11	36	36	59
UNNAMED	1948	3	35	78	33	51
UNNAMED	1948	10	19	85	42	23
UNNAMED	1949	1	46	63	36	43
UNNAMED	1949	2	15	90	47	29
UNNAMED	1949	7	13	74	11	-59
ABLE	1950	1	56	62	38	39
DOG	1950	4	41	70	29	15
ABLE	1951	2	37	92	11	33
HOW	1951	9	41	75	21	45
UNNAMED	1952	1	26	72	65	31
ABLE	1952	2	20	82	34	39
UNNAMED	1953	2	12	72	27	26
BARBARA	1953	3	40	71	22	32
CAROL	1953	4	50	66	38	-11

Name	Year	NHC ID	Δp (hPa)	R_{max} (km)	V_f (km/h)	θ (deg)
UNNAMED	1953	11	17	94	69	38
UNNAMED	1954	1	14	86	46	21
UNNAMED	1954	2	16	99	29	46
UNNAMED	1954	4	9	61	21	35
CAROL	1954	6	58	61	57	19
EDNA	1954	8	57	59	43	26
HAZEL	1954	14	37	73	79	11
CONNIE	1955	2	39	72	26	-3
DIANE	1955	3	12	63	18	71
IONE	1955	8	37	80	15	43
BETSY	1956	3	49	67	35	37
FLOSSY	1956	7	16	35	30	47
UNNAMED	1956	9	10	83	9	-126
UNNAMED	1956	11	11	37	29	45
AUDREY	1957	2	19	93	93	53
BECKY	1958	2	11	74	28	30
DAISY	1958	4	44	70	37	31
HELENE	1958	8	63	57	35	64
UNNAMED	1958	11	17	118	23	18
CINDY	1959	4	14	39	33	52
GRACIE	1959	8	8	66	36	54
UNNAMED	1959	12	23	54	26	69
UNNAMED	1959	14	11	51	30	46
BRENDA	1960	3	21	88	36	29
DONNA	1960	5	42	55	50	34
ESTHER	1961	5	51	80	28	12
UNNAMED	1961	6	25	88	49	25
GERDA	1961	8	25	68	68	18
ALMA	1962	1	23	63	41	40
UNNAMED	1962	6	15	75	8	12
UNNAMED	1962	7	30	69	21	45
GINNY	1963	8	47	68	29	39
UNNAMED	1963	10	10	76	34	-7
CLEO	1964	5	12	60	15	90

Name	Year	NHC ID	Δp (hPa)	R_{max} (km)	V_f (km/h)	θ (deg)
DORA	1964	6	28	80	38	51
GLADYS	1964	9	39	67	29	34
ISBELL	1964	11	17	65	25	-45
UNNAMED	1964	13	9	55	20	79
UNNAMED	1964	13	9	55	20	79
UNNAMED	1965	1	16	78	48	66
ALMA	1966	1	11	53	11	0
DORIA	1967	14	27	83	21	-95
CANDY	1968	3	11	76	50	82
DOLLY	1968	5	19	94	32	69
GLADYS	1968	14	32	57	48	54
ANNA	1969	6	16	80	52	26
BLANCHE	1969	7	36	67	64	25
CAMILLE	1969	9	13	46	30	97
GERDA	1969	16	29	20	57	35
KARA	1969	25	16	82	18	-84
ALMA	1970	1	10	42	29	59
UNNAMED	1970	8	8	52	48	67
ARLENE	1971	1	12	57	19	39
BETH	1971	6	23	78	31	32
DORIA	1971	9	20	99	41	25
GINGER	1971	14	10	77	11	8
HEIDI	1971	17	19	129	34	10
ALPHA	1972	1	13	74	10	112
AGNES	1972	2	36	82	30	36
UNNAMED	1972	4	9	97	13	13
CARRIE	1972	11	19	72	17	5
DAWN	1972	13	20	80	17	-77
ALFA	1973	6	9	84	27	26
UNNAMED	1974	2	9	86	68	46
DOLLY	1974	12	8	55	36	12
AMY	1975	2	26	94	7	39
BLANCHE	1975	4	26	69	22	42
ELOISE	1975	13	9	52	17	58

Name	Year	NHC ID	Δp (hPa)	R_{max} (km)	V_f (km/h)	θ (deg)
HALLIE	1975	19	9	55	34	49
UNNAMED	1976	1	17	94	34	64
UNNAMED	1976	2	9	62	40	45
BELLE	1976	7	36	55	41	8
DAVID	1979	9	24	87	33	26
FREDERIC	1979	11	15	92	89	50
BRET	1981	6	13	73	15	-61
DENNIS	1981	10	18	59	36	65
UNNAMED	1981	22	35	28	14	24
UNNAMED	1982	2	21	55	56	52
DEAN	1983	6	8	63	6	-29
DIANA	1984	10	19	54	31	53
ISIDORE	1984	15	8	74	31	64
JOSEPHINE	1984	16	38	110	5	39
CLAUDETTE	1985	3	9	54	21	74
GLORIA	1985	9	62	74	56	15
HENRI	1985	10	8	76	15	0
KATE	1985	13	10	65	50	67
ANDREW	1986	1	11	63	27	41
CHARLEY	1986	5	21	39	22	47
HUGO	1989	11	25	84	72	18
LILI	1990	14	17	139	23	27
ANA	1991	1	10	56	45	65
BOB	1991	3	60	56	50	26
UNNAMED	1991	12	21	72	25	-163
DANIELLE	1992	7	12	60	19	-18
EMILY	1993	5	51	56	20	22
GORDON	1994	12	29	111	16	-76
ALLISON	1995	1	23	71	44	50
FELIX	1995	7	40	139	11	45
OPAL	1995	17	22	76	37	41
ARTHUR	1996	1	8	74	26	49
BERTHA	1996	2	19	111	32	24
EDOUARD	1996	5	53	93	19	9

Name	Year	NHC ID	Δp (hPa)	R_{max} (km)	V_f (km/h)	θ (deg)
FRAN	1996	6	28	76	28	-9
JOSEPHINE	1996	10	30	78	52	44
UNNAMED	1997	1	9	71	46	23
CLAUDETTE	1997	4	8	56	21	36
DANNY	1997	5	17	19	52	66
BONNIE	1998	2	23	37	15	52
EARL	1998	5	13	52	35	71
DENNIS	1999	5	25	111	5	-68
FLOYD	1999	8	39	37	48	27
IRENE	1999	13	55	67	63	47
GORDON	2000	11	8	74	40	45
HELENE	2000	12	12	19	36	65
UNNAMED	2000	19	21	134	30	23
ALLISON	2001	1	8	64	20	41
ARTHUR	2002	1	9	83	36	71
GUSTAV	2002	8	36	111	35	46
ISIDORE	2002	10	14	83	59	54
ISABEL	2003	13	44	83	35	-33
ALEX	2004	1	39	74	26	60
CHARLEY	2004	3	13	74	48	35
FRANCES	2004	6	12	19	38	29
GASTON	2004	7	12	45	31	57
IVAN	2004	9	13	19	29	63
JEANNE	2004	11	14	56	26	69
OPHELIA	2005	16	18	37	21	38
TWENTY-TWO	2005	23	8	76	19	0
ALBERTO	2006	1	14	85	73	66
BERYL	2006	3	11	56	17	10
ERNESTO	2006	6	16	76	16	22
ANDREA	2007	1	8	59	24	123
BARRY	2007	2	23	77	39	31
GABRIELLE	2007	7	8	28	17	0
NOEL	2007	16	39	66	41	17
CRISTOBAL	2008	3	13	139	20	56

Name	Year	NHC ID	Δp (hPa)	R_{max} (km)	V_f (km/h)	θ (deg)
HANNA	2008	8	19	124	52	37
KYLE	2008	11	21	99	39	9
BILL	2009	3	52	56	40	11
EARL	2010	7	53	86	33	32
IRENE	2011	9	55	85	28	21
BERYL	2012	2	17	71	37	63
SANDY	2012	18	70	131	30	-51
ANDREA	2013	1	16	200	54	41
ARTHUR	2014	1	37	37	37	41
BERTHA	2014	3	8	37	32	14
CLAUDETTE	2015	3	8	54	29	59
COLIN	2016	3	17	79	76	55
HERMINE	2016	9	13	58	6	-153
MATTHEW	2016	14	29	56	23	76
CINDY	2017	3	10	103	89	74
JOSE	2017	12	40	9	12	22
MARIA	2017	15	34	77	13	28
NATE	2017	16	8	56	65	61
FLORENCE	2018	6	61	56	11	-71
MICHAEL	2018	14	30	73	43	69
DORIAN	2019	5	57	78	36	57
ERIN	2019	6	11	73	30	36
MELISSA	2019	14	17	74	9	-149
NESTOR	2019	16	12	34	34	73

Table A-3. Historical TCs with distance-adjusted atmospheric parameters for CRL 458.

Name	Year	NHC ID	Δp (hPa)	R_{max} (km)	V_f (km/h)	θ (deg)
UNNAMED	1938	6	73	71	77	5
UNNAMED	1939	2	8	83	51	80
UNNAMED	1940	1	18	95	10	38
UNNAMED	1940	4	52	70	37	30
UNNAMED	1940	5	41	78	33	20
UNNAMED	1941	3	36	85	27	44
UNNAMED	1942	9	10	62	11	-17
UNNAMED	1943	2	8	47	29	43
UNNAMED	1943	5	11	68	30	32
UNNAMED	1943	7	16	72	25	-45
UNNAMED	1944	3	11	43	30	59
UNNAMED	1944	7	60	55	51	14
UNNAMED	1944	13	20	22	34	48
UNNAMED	1945	1	35	77	40	41
UNNAMED	1945	9	12	57	37	38
UNNAMED	1946	2	33	77	31	48
UNNAMED	1946	4	23	90	45	26
UNNAMED	1946	6	10	70	31	64
UNNAMED	1947	6	11	30	38	57
UNNAMED	1948	3	35	77	35	49
UNNAMED	1948	10	19	85	44	24
UNNAMED	1949	1	46	60	38	42
UNNAMED	1949	2	15	90	49	29
UNNAMED	1949	7	13	72	14	-50
ABLE	1950	1	56	59	40	38
DOG	1950	4	41	68	31	17
ABLE	1951	2	37	93	14	33
HOW	1951	9	41	74	24	44
UNNAMED	1952	1	26	70	66	31
ABLE	1952	2	20	81	36	38
UNNAMED	1953	2	12	70	29	27
BARBARA	1953	3	40	69	25	32
CAROL	1953	4	50	64	40	-7

Name	Year	NHC ID	Δp (hPa)	R_{max} (km)	V_f (km/h)	θ (deg)
UNNAMED	1953	11	17	95	70	38
UNNAMED	1954	1	14	86	48	22
UNNAMED	1954	2	16	100	31	45
UNNAMED	1954	4	9	58	24	35
CAROL	1954	6	58	58	58	20
EDNA	1954	8	57	56	45	27
HAZEL	1954	14	37	71	80	13
CONNIE	1955	2	39	70	29	0
DIANE	1955	3	12	60	21	67
IONE	1955	8	37	79	18	42
BETSY	1956	3	49	65	37	37
FLOSSY	1956	7	16	29	32	46
UNNAMED	1956	9	10	83	12	-111
UNNAMED	1956	11	11	31	31	44
AUDREY	1957	2	19	94	93	51
BECKY	1958	2	11	72	30	30
DAISY	1958	4	44	68	39	31
HELENE	1958	8	63	53	37	61
UNNAMED	1958	11	17	122	26	19
CINDY	1959	4	14	33	35	50
GRACIE	1959	8	8	64	38	52
UNNAMED	1959	12	23	50	29	66
UNNAMED	1959	14	11	47	32	45
BRENDA	1960	3	21	88	38	29
DONNA	1960	5	42	51	52	34
ESTHER	1961	5	51	79	30	14
UNNAMED	1961	6	25	88	51	26
GERDA	1961	8	25	66	69	19
ALMA	1962	1	23	60	43	39
UNNAMED	1962	6	15	74	11	14
UNNAMED	1962	7	30	67	24	44
GINNY	1963	8	47	66	31	38
UNNAMED	1963	10	10	75	36	-3
CLEO	1964	5	12	57	18	85

Name	Year	NHC ID	Δp (hPa)	R_{max} (km)	V_f (km/h)	θ (deg)
DORA	1964	6	28	79	40	49
GLADYS	1964	9	39	65	31	34
ISBELL	1964	11	17	62	28	-38
UNNAMED	1964	13	9	51	23	75
UNNAMED	1964	13	9	51	23	75
UNNAMED	1965	1	16	77	50	63
ALMA	1966	1	11	49	14	3
DORIA	1967	14	27	83	24	-83
CANDY	1968	3	11	75	52	77
DOLLY	1968	5	19	95	34	66
GLADYS	1968	14	32	53	50	52
ANNA	1969	6	16	79	54	27
BLANCHE	1969	7	36	65	65	26
CAMILLE	1969	9	13	41	32	91
GERDA	1969	16	29	12	58	35
KARA	1969	25	16	81	21	-73
ALMA	1970	1	10	37	31	57
UNNAMED	1970	8	8	48	50	64
ARLENE	1971	1	12	53	22	38
BETH	1971	6	23	77	33	32
DORIA	1971	9	20	100	43	26
GINGER	1971	14	10	76	14	10
HEIDI	1971	17	19	134	36	12
ALPHA	1972	1	13	72	13	105
AGNES	1972	2	36	81	32	36
UNNAMED	1972	4	9	98	16	15
CARRIE	1972	11	19	70	20	8
DAWN	1972	13	20	79	20	-67
ALFA	1973	6	9	84	29	27
UNNAMED	1974	2	9	86	69	45
DOLLY	1974	12	8	51	38	14
AMY	1975	2	26	95	10	38
BLANCHE	1975	4	26	67	25	41
ELOISE	1975	13	9	48	20	56

Name	Year	NHC ID	Δp (hPa)	R_{max} (km)	V_f (km/h)	θ (deg)
HALLIE	1975	19	9	51	36	48
UNNAMED	1976	1	17	95	36	61
UNNAMED	1976	2	9	59	42	44
BELLE	1976	7	36	51	43	10
DAVID	1979	9	24	87	35	27
FREDERIC	1979	11	15	93	89	48
BRET	1981	6	13	71	18	-52
DENNIS	1981	10	18	56	38	62
UNNAMED	1981	22	35	21	17	25
UNNAMED	1982	2	21	51	57	50
DEAN	1983	6	8	60	9	-23
DIANA	1984	10	19	50	33	51
ISIDORE	1984	15	8	72	33	61
JOSEPHINE	1984	16	38	113	8	38
CLAUDETTE	1985	3	9	50	24	70
GLORIA	1985	9	62	72	57	17
HENRI	1985	10	8	75	18	3
KATE	1985	13	10	62	52	64
ANDREW	1986	1	11	60	29	40
CHARLEY	1986	5	21	33	25	46
HUGO	1989	11	25	84	73	19
LILI	1990	14	17	145	26	28
ANA	1991	1	10	52	47	62
BOB	1991	3	60	52	52	27
UNNAMED	1991	12	21	70	28	-145
DANIELLE	1992	7	12	57	22	-13
EMILY	1993	5	51	52	23	23
GORDON	1994	12	29	114	19	-66
ALLISON	1995	1	23	69	46	48
FELIX	1995	7	40	145	14	44
OPAL	1995	17	22	75	39	40
ARTHUR	1996	1	8	72	29	48
BERTHA	1996	2	19	114	34	25
EDOUARD	1996	5	53	94	22	11

Name	Year	NHC ID	Δp (hPa)	R_{max} (km)	V_f (km/h)	θ (deg)
FRAN	1996	6	28	75	30	-5
JOSEPHINE	1996	10	30	77	54	43
UNNAMED	1997	1	9	69	48	24
CLAUDETTE	1997	4	8	52	24	36
DANNY	1997	5	17	11	54	63
BONNIE	1998	2	23	31	18	50
EARL	1998	5	13	48	37	67
DENNIS	1999	5	25	114	8	-58
FLOYD	1999	8	39	31	50	28
IRENE	1999	13	55	65	64	46
GORDON	2000	11	8	72	42	44
HELENE	2000	12	12	11	38	62
UNNAMED	2000	19	21	140	32	24
ALLISON	2001	1	8	61	23	40
ARTHUR	2002	1	9	83	38	67
GUSTAV	2002	8	36	114	37	45
ISIDORE	2002	10	14	83	60	52
ISABEL	2003	13	44	83	37	-27
ALEX	2004	1	39	72	29	58
CHARLEY	2004	3	13	72	50	35
FRANCES	2004	6	12	11	40	29
GASTON	2004	7	12	40	33	55
IVAN	2004	9	13	11	31	60
JEANNE	2004	11	14	52	29	66
OPHELIA	2005	16	18	31	24	38
TWENTY-TWO	2005	23	8	75	22	3
ALBERTO	2006	1	14	85	74	63
BERYL	2006	3	11	52	20	12
ERNESTO	2006	6	16	75	19	23
ANDREA	2007	1	8	56	27	115
BARRY	2007	2	23	76	41	31
GABRIELLE	2007	7	8	21	20	3
NOEL	2007	16	39	64	43	19
CRISTOBAL	2008	3	13	145	23	54

Name	Year	NHC ID	Δp (hPa)	R_{max} (km)	V_f (km/h)	θ (deg)
HANNA	2008	8	19	128	54	37
KYLE	2008	11	21	100	41	11
BILL	2009	3	52	52	42	13
EARL	2010	7	53	86	35	32
IRENE	2011	9	55	85	30	22
BERYL	2012	2	17	69	39	60
SANDY	2012	18	70	136	32	-43
ANDREA	2013	1	16	200	56	40
ARTHUR	2014	1	37	31	39	40
BERTHA	2014	3	8	31	34	16
CLAUDETTE	2015	3	8	50	31	57
COLIN	2016	3	17	78	77	53
HERMINE	2016	9	13	55	9	-135
MATTHEW	2016	14	29	52	26	72
CINDY	2017	3	10	105	89	70
JOSE	2017	12	40	8	15	23
MARIA	2017	15	34	76	16	29
NATE	2017	16	8	52	66	58
FLORENCE	2018	6	61	52	14	-61
MICHAEL	2018	14	30	71	45	66
DORIAN	2019	5	57	77	38	55
ERIN	2019	6	11	71	32	36
MELISSA	2019	14	17	72	12	-132
NESTOR	2019	16	12	28	36	69

Appendix B: Storm Recurrence Rates

Table B-1. SRR results for all intensity bins and CRLs in the North Atlantic basin.

CRL	SRR (storms/yr/km)			
	LI	MI	HI	Total
401	1.52E-03	4.70E-04	6.06E-04	2.60E-03
402	1.52E-03	4.90E-04	6.13E-04	2.62E-03
403	1.53E-03	4.95E-04	6.21E-04	2.65E-03
404	1.54E-03	5.01E-04	6.29E-04	2.67E-03
405	1.56E-03	5.06E-04	6.39E-04	2.70E-03
406	1.57E-03	5.12E-04	6.45E-04	2.73E-03
407	1.56E-03	5.18E-04	6.47E-04	2.73E-03
408	1.56E-03	5.61E-04	6.04E-04	2.73E-03
409	1.56E-03	5.60E-04	6.06E-04	2.73E-03
410	1.57E-03	5.60E-04	6.09E-04	2.74E-03
411	1.58E-03	5.83E-04	5.87E-04	2.75E-03
412	1.59E-03	5.83E-04	5.88E-04	2.76E-03
413	1.60E-03	5.82E-04	5.90E-04	2.77E-03
414	1.61E-03	5.81E-04	5.91E-04	2.78E-03
415	1.61E-03	5.94E-04	5.92E-04	2.80E-03
416	1.61E-03	6.13E-04	5.93E-04	2.81E-03
417	1.63E-03	6.07E-04	5.93E-04	2.83E-03
418	1.64E-03	6.34E-04	5.73E-04	2.85E-03
419	1.66E-03	6.15E-04	5.67E-04	2.84E-03
420	1.66E-03	6.08E-04	5.60E-04	2.83E-03
421	1.65E-03	6.12E-04	5.42E-04	2.81E-03
422	1.65E-03	6.07E-04	5.33E-04	2.79E-03
423	1.66E-03	5.76E-04	5.26E-04	2.76E-03
424	1.65E-03	5.55E-04	5.19E-04	2.73E-03
425	1.64E-03	5.67E-04	4.88E-04	2.69E-03
426	1.63E-03	5.61E-04	4.62E-04	2.65E-03
427	1.63E-03	5.31E-04	4.54E-04	2.61E-03
428	1.59E-03	5.41E-04	4.46E-04	2.57E-03
429	1.57E-03	5.28E-04	4.38E-04	2.53E-03
430	1.54E-03	5.23E-04	4.22E-04	2.49E-03
431	1.53E-03	5.11E-04	3.99E-04	2.44E-03
432	1.51E-03	4.98E-04	3.91E-04	2.40E-03
433	1.51E-03	4.86E-04	3.63E-04	2.36E-03
434	1.48E-03	4.71E-04	3.55E-04	2.31E-03

CRL	SRR (storms/yr/km)			
	LI	MI	HI	Total
435	1.45E-03	4.60E-04	3.43E-04	2.26E-03
436	1.42E-03	4.70E-04	3.10E-04	2.20E-03
437	1.42E-03	4.75E-04	2.67E-04	2.16E-03
438	1.38E-03	4.87E-04	2.65E-04	2.13E-03
439	1.37E-03	4.88E-04	2.68E-04	2.13E-03
440	1.37E-03	4.71E-04	2.66E-04	2.11E-03
441	1.35E-03	4.61E-04	2.63E-04	2.07E-03
442	1.35E-03	4.45E-04	2.65E-04	2.06E-03
443	1.33E-03	4.37E-04	2.62E-04	2.03E-03
444	1.31E-03	4.57E-04	2.55E-04	2.02E-03
445	1.29E-03	4.59E-04	2.31E-04	1.98E-03
446	1.27E-03	4.58E-04	2.28E-04	1.95E-03
447	1.25E-03	4.53E-04	2.28E-04	1.93E-03
448	1.26E-03	4.58E-04	2.31E-04	1.95E-03
449	1.28E-03	4.44E-04	2.35E-04	1.96E-03
450	1.25E-03	4.54E-04	2.34E-04	1.94E-03
451	1.24E-03	4.41E-04	2.33E-04	1.92E-03
452	1.22E-03	4.33E-04	2.32E-04	1.89E-03
453	1.22E-03	4.20E-04	2.16E-04	1.85E-03
454	1.20E-03	4.13E-04	2.16E-04	1.83E-03
455	1.18E-03	3.96E-04	2.16E-04	1.79E-03
456	1.14E-03	3.77E-04	2.16E-04	1.74E-03
457	1.11E-03	3.63E-04	2.11E-04	1.68E-03
458	1.08E-03	3.48E-04	2.05E-04	1.63E-03
459	1.05E-03	3.18E-04	2.17E-04	1.58E-03
460	1.03E-03	3.13E-04	2.19E-04	1.56E-03
461	1.03E-03	3.16E-04	2.24E-04	1.57E-03
462	1.04E-03	3.20E-04	2.31E-04	1.59E-03
463	1.02E-03	3.18E-04	2.32E-04	1.57E-03
464	1.01E-03	3.15E-04	2.35E-04	1.56E-03
465	9.88E-04	3.22E-04	2.22E-04	1.53E-03
466	9.79E-04	3.19E-04	2.24E-04	1.52E-03
467	9.71E-04	3.19E-04	2.27E-04	1.52E-03
468	9.68E-04	3.20E-04	2.32E-04	1.52E-03
469	9.59E-04	3.19E-04	2.34E-04	1.51E-03
470	9.44E-04	3.15E-04	2.34E-04	1.49E-03
471	9.32E-04	3.12E-04	2.34E-04	1.48E-03

CRL	SRR (storms/yr/km)			
	LI	MI	HI	Total
472	9.20E-04	3.07E-04	2.34E-04	1.46E-03
473	8.88E-04	3.22E-04	2.34E-04	1.44E-03
474	8.66E-04	3.12E-04	2.31E-04	1.41E-03
475	8.43E-04	3.03E-04	2.27E-04	1.37E-03
476	8.20E-04	2.94E-04	2.24E-04	1.34E-03
477	7.89E-04	2.97E-04	2.22E-04	1.31E-03
478	7.72E-04	2.86E-04	2.19E-04	1.28E-03
479	7.50E-04	2.79E-04	2.15E-04	1.24E-03
480	7.27E-04	2.69E-04	2.09E-04	1.21E-03
481	7.08E-04	2.61E-04	2.06E-04	1.17E-03
482	7.06E-04	2.64E-04	2.08E-04	1.18E-03
483	7.10E-04	2.69E-04	2.11E-04	1.19E-03
484	7.19E-04	2.77E-04	2.16E-04	1.21E-03
485	7.24E-04	2.83E-04	2.19E-04	1.23E-03
486	7.28E-04	3.05E-04	2.16E-04	1.25E-03
487	7.25E-04	3.08E-04	2.18E-04	1.25E-03
488	7.32E-04	3.20E-04	2.17E-04	1.27E-03
489	7.38E-04	3.27E-04	2.20E-04	1.28E-03
490	7.40E-04	3.32E-04	2.22E-04	1.29E-03
491	7.41E-04	3.43E-04	2.18E-04	1.30E-03
492	7.40E-04	3.47E-04	2.20E-04	1.31E-03
493	7.42E-04	3.52E-04	2.22E-04	1.32E-03
494	7.45E-04	3.57E-04	2.23E-04	1.33E-03
495	7.50E-04	3.63E-04	2.25E-04	1.34E-03
496	7.47E-04	3.76E-04	2.25E-04	1.35E-03
497	7.53E-04	3.82E-04	2.26E-04	1.36E-03
498	7.57E-04	3.86E-04	2.27E-04	1.37E-03
499	7.62E-04	3.89E-04	2.27E-04	1.38E-03
500	7.69E-04	3.90E-04	2.27E-04	1.39E-03
501	7.75E-04	3.94E-04	2.27E-04	1.40E-03
502	7.81E-04	4.00E-04	2.25E-04	1.41E-03
503	7.86E-04	4.04E-04	2.25E-04	1.41E-03
504	7.84E-04	4.02E-04	2.25E-04	1.41E-03
505	7.90E-04	4.06E-04	2.26E-04	1.42E-03
506	8.01E-04	4.15E-04	2.27E-04	1.44E-03
507	7.95E-04	4.26E-04	2.11E-04	1.43E-03
508	7.80E-04	4.16E-04	2.09E-04	1.40E-03

CRL	SRR (storms/yr/km)			
	LI	MI	HI	Total
509	7.60E-04	4.17E-04	2.09E-04	1.39E-03
510	7.52E-04	4.13E-04	2.07E-04	1.37E-03
511	7.61E-04	4.17E-04	2.12E-04	1.39E-03
512	7.67E-04	4.22E-04	2.12E-04	1.40E-03
513	7.73E-04	4.28E-04	2.12E-04	1.41E-03
514	7.74E-04	4.43E-04	2.13E-04	1.43E-03
515	8.00E-04	4.51E-04	2.15E-04	1.47E-03
516	8.08E-04	4.74E-04	2.17E-04	1.50E-03
517	8.24E-04	4.89E-04	2.19E-04	1.53E-03
518	8.23E-04	4.88E-04	2.18E-04	1.53E-03
519	8.33E-04	4.97E-04	2.19E-04	1.55E-03
520	8.41E-04	5.04E-04	2.19E-04	1.56E-03
521	8.41E-04	5.20E-04	2.20E-04	1.58E-03
522	8.55E-04	5.33E-04	2.21E-04	1.61E-03
523	8.71E-04	5.49E-04	2.23E-04	1.64E-03
524	8.84E-04	5.61E-04	2.24E-04	1.67E-03
525	8.91E-04	5.70E-04	2.25E-04	1.69E-03
526	8.82E-04	5.63E-04	2.25E-04	1.67E-03
527	8.64E-04	5.45E-04	2.23E-04	1.63E-03
528	8.48E-04	5.28E-04	2.21E-04	1.60E-03
529	8.36E-04	5.37E-04	2.03E-04	1.58E-03
530	8.21E-04	5.29E-04	2.01E-04	1.55E-03
531	8.15E-04	4.99E-04	2.01E-04	1.52E-03
532	7.95E-04	4.84E-04	1.97E-04	1.48E-03
533	7.80E-04	4.85E-04	1.71E-04	1.44E-03
534	7.61E-04	4.70E-04	1.67E-04	1.40E-03
535	7.48E-04	4.56E-04	1.64E-04	1.37E-03
536	7.41E-04	4.46E-04	1.62E-04	1.35E-03
537	7.39E-04	4.16E-04	1.85E-04	1.34E-03
538	7.33E-04	4.14E-04	1.84E-04	1.33E-03
539	7.29E-04	4.07E-04	1.83E-04	1.32E-03
540	7.28E-04	3.86E-04	1.80E-04	1.29E-03
541	7.10E-04	3.70E-04	1.77E-04	1.26E-03
542	6.96E-04	3.59E-04	1.67E-04	1.22E-03
543	6.82E-04	3.47E-04	1.64E-04	1.19E-03
544	6.67E-04	3.33E-04	1.61E-04	1.16E-03
545	6.52E-04	3.45E-04	1.34E-04	1.13E-03

CRL	SRR (storms/yr/km)			
	LI	MI	HI	Total
546	6.46E-04	3.44E-04	1.33E-04	1.12E-03
547	6.42E-04	3.67E-04	1.09E-04	1.12E-03
548	6.39E-04	3.69E-04	1.09E-04	1.12E-03
549	6.27E-04	3.63E-04	1.07E-04	1.10E-03
550	6.18E-04	3.54E-04	1.05E-04	1.08E-03
551	6.10E-04	3.45E-04	1.03E-04	1.06E-03
552	5.93E-04	3.34E-04	1.01E-04	1.03E-03
553	5.78E-04	3.27E-04	9.81E-05	1.00E-03
554	5.87E-04	3.06E-04	9.68E-05	9.90E-04
555	5.81E-04	3.06E-04	9.61E-05	9.83E-04
556	5.75E-04	3.41E-04	5.97E-05	9.76E-04
557	5.65E-04	3.36E-04	5.71E-05	9.58E-04
558	5.56E-04	3.30E-04	5.51E-05	9.41E-04
559	5.60E-04	3.36E-04	5.67E-05	9.52E-04
560	5.59E-04	3.30E-04	5.70E-05	9.46E-04
561	5.54E-04	3.33E-04	5.07E-05	9.38E-04
562	5.53E-04	3.28E-04	5.86E-05	9.40E-04
563	5.53E-04	3.29E-04	6.00E-05	9.42E-04
564	5.55E-04	3.31E-04	6.21E-05	9.48E-04
565	5.70E-04	3.30E-04	4.92E-05	9.49E-04
566	5.98E-04	3.09E-04	5.11E-05	9.59E-04
567	6.06E-04	3.16E-04	5.38E-05	9.75E-04
568	6.12E-04	3.28E-04	4.15E-05	9.81E-04
569	6.15E-04	3.30E-04	4.42E-05	9.89E-04
570	6.18E-04	3.34E-04	4.61E-05	9.97E-04
571	6.22E-04	3.40E-04	4.85E-05	1.01E-03
572	6.26E-04	3.41E-04	5.51E-05	1.02E-03
573	6.35E-04	3.36E-04	5.68E-05	1.03E-03
574	6.34E-04	3.36E-04	5.78E-05	1.03E-03
575	6.37E-04	3.39E-04	6.02E-05	1.04E-03
576	6.42E-04	3.44E-04	6.31E-05	1.05E-03
577	6.49E-04	3.49E-04	6.65E-05	1.06E-03
578	6.61E-04	3.53E-04	7.04E-05	1.08E-03
579	6.69E-04	3.61E-04	7.43E-05	1.10E-03
580	6.73E-04	3.62E-04	7.67E-05	1.11E-03
581	6.74E-04	3.61E-04	7.81E-05	1.11E-03
582	6.82E-04	3.67E-04	8.25E-05	1.13E-03

CRL	SRR (storms/yr/km)			
	LI	MI	HI	Total
583	6.82E-04	3.66E-04	8.36E-05	1.13E-03
584	6.75E-04	3.58E-04	8.17E-05	1.11E-03
585	6.82E-04	3.63E-04	8.58E-05	1.13E-03
586	6.74E-04	3.57E-04	8.37E-05	1.11E-03
587	6.80E-04	3.61E-04	8.76E-05	1.13E-03
588	6.80E-04	3.61E-04	8.93E-05	1.13E-03
589	6.84E-04	3.65E-04	9.23E-05	1.14E-03
590	6.82E-04	3.64E-04	9.33E-05	1.14E-03
591	7.07E-04	3.43E-04	9.59E-05	1.15E-03
592	7.15E-04	3.51E-04	1.01E-04	1.17E-03
593	7.18E-04	3.54E-04	1.04E-04	1.18E-03
594	7.08E-04	3.49E-04	1.01E-04	1.16E-03
595	7.07E-04	3.50E-04	1.03E-04	1.16E-03
596	7.19E-04	3.47E-04	1.07E-04	1.17E-03
597	7.17E-04	3.49E-04	1.09E-04	1.17E-03
598	7.32E-04	3.34E-04	1.02E-04	1.17E-03
599	7.28E-04	3.33E-04	1.02E-04	1.16E-03
600	7.29E-04	3.27E-04	1.02E-04	1.16E-03
601	7.39E-04	3.36E-04	1.07E-04	1.18E-03
602	7.47E-04	3.50E-04	1.12E-04	1.21E-03
603	7.57E-04	3.56E-04	1.15E-04	1.23E-03
604	7.52E-04	3.76E-04	1.29E-04	1.26E-03
605	7.65E-04	3.85E-04	1.35E-04	1.29E-03
606	7.75E-04	3.93E-04	1.41E-04	1.31E-03
607	7.84E-04	4.01E-04	1.47E-04	1.33E-03
608	7.93E-04	4.08E-04	1.52E-04	1.35E-03
609	8.03E-04	4.16E-04	1.58E-04	1.38E-03
610	8.13E-04	4.23E-04	1.64E-04	1.40E-03
611	8.25E-04	4.32E-04	1.71E-04	1.43E-03
612	8.16E-04	4.65E-04	1.77E-04	1.46E-03
613	8.31E-04	4.75E-04	1.83E-04	1.49E-03
614	8.45E-04	4.85E-04	1.90E-04	1.52E-03
615	8.52E-04	4.78E-04	2.20E-04	1.55E-03
616	8.68E-04	4.87E-04	2.27E-04	1.58E-03
617	8.81E-04	4.95E-04	2.33E-04	1.61E-03
618	8.85E-04	5.08E-04	2.38E-04	1.63E-03
619	8.96E-04	5.15E-04	2.44E-04	1.65E-03

CRL	SRR (storms/yr/km)			
	LI	MI	HI	Total
620	9.10E-04	5.24E-04	2.49E-04	1.68E-03
621	9.25E-04	5.32E-04	2.55E-04	1.71E-03
622	9.34E-04	5.38E-04	2.59E-04	1.73E-03
623	9.31E-04	5.37E-04	2.59E-04	1.73E-03
624	9.25E-04	5.34E-04	2.58E-04	1.72E-03
625	9.19E-04	5.30E-04	2.55E-04	1.70E-03
626	9.13E-04	5.28E-04	2.55E-04	1.70E-03
627	9.28E-04	5.11E-04	2.55E-04	1.69E-03
628	9.27E-04	5.13E-04	2.56E-04	1.70E-03
629	9.47E-04	4.95E-04	2.56E-04	1.70E-03
630	9.44E-04	5.38E-04	2.13E-04	1.69E-03
631	9.69E-04	5.06E-04	2.10E-04	1.68E-03
632	9.60E-04	5.02E-04	2.07E-04	1.67E-03
633	9.69E-04	4.78E-04	2.04E-04	1.65E-03
634	9.58E-04	4.91E-04	1.85E-04	1.63E-03
635	9.51E-04	4.90E-04	1.83E-04	1.62E-03
636	9.46E-04	4.90E-04	1.81E-04	1.62E-03
637	9.47E-04	4.86E-04	1.80E-04	1.61E-03
638	9.68E-04	4.62E-04	1.79E-04	1.61E-03
639	9.62E-04	4.87E-04	1.53E-04	1.60E-03
640	9.56E-04	4.87E-04	1.52E-04	1.60E-03
641	9.51E-04	4.90E-04	1.51E-04	1.59E-03
642	9.69E-04	4.75E-04	1.50E-04	1.59E-03
643	9.75E-04	4.81E-04	1.51E-04	1.61E-03
644	9.82E-04	4.88E-04	1.53E-04	1.62E-03
645	9.89E-04	4.95E-04	1.54E-04	1.64E-03
646	9.79E-04	5.07E-04	1.53E-04	1.64E-03
647	9.57E-04	5.24E-04	1.44E-04	1.63E-03
648	9.70E-04	5.05E-04	1.44E-04	1.62E-03
649	9.69E-04	5.08E-04	1.43E-04	1.62E-03
650	9.71E-04	5.13E-04	1.44E-04	1.63E-03
651	9.75E-04	5.19E-04	1.45E-04	1.64E-03
664	8.52E-04	5.53E-04	2.06E-04	1.61E-03
665	8.61E-04	5.65E-04	2.07E-04	1.63E-03
666	8.69E-04	5.78E-04	2.09E-04	1.66E-03
667	8.76E-04	5.86E-04	2.16E-04	1.68E-03
668	8.83E-04	5.99E-04	2.18E-04	1.70E-03

CRL	SRR (storms/yr/km)			
	LI	MI	HI	Total
669	8.99E-04	6.21E-04	2.02E-04	1.72E-03
670	9.06E-04	6.35E-04	2.05E-04	1.75E-03
671	9.17E-04	6.45E-04	2.08E-04	1.77E-03
672	9.29E-04	6.55E-04	2.11E-04	1.80E-03
673	9.41E-04	6.67E-04	2.14E-04	1.82E-03
674	9.53E-04	6.78E-04	2.18E-04	1.85E-03
675	9.66E-04	6.89E-04	2.22E-04	1.88E-03
676	9.81E-04	6.97E-04	2.25E-04	1.90E-03
677	9.95E-04	7.06E-04	2.29E-04	1.93E-03
678	1.02E-03	7.07E-04	2.33E-04	1.96E-03
679	1.03E-03	7.14E-04	2.36E-04	1.98E-03
680	1.04E-03	7.20E-04	2.40E-04	2.00E-03
681	1.06E-03	7.25E-04	2.44E-04	2.02E-03
682	1.07E-03	7.19E-04	2.58E-04	2.04E-03
683	1.08E-03	7.47E-04	2.36E-04	2.06E-03
684	1.09E-03	7.50E-04	2.39E-04	2.08E-03
685	1.10E-03	7.56E-04	2.43E-04	2.10E-03
686	1.11E-03	7.66E-04	2.41E-04	2.11E-03
687	1.12E-03	7.69E-04	2.46E-04	2.13E-03
688	1.13E-03	7.76E-04	2.47E-04	2.15E-03
689	1.14E-03	7.79E-04	2.52E-04	2.17E-03
690	1.17E-03	7.63E-04	2.57E-04	2.19E-03
691	1.18E-03	7.66E-04	2.62E-04	2.20E-03
692	1.21E-03	7.25E-04	2.87E-04	2.22E-03
693	1.22E-03	7.27E-04	2.90E-04	2.23E-03
694	1.22E-03	7.34E-04	2.87E-04	2.25E-03
695	1.24E-03	7.07E-04	3.09E-04	2.26E-03
696	1.24E-03	7.15E-04	3.11E-04	2.26E-03
697	1.24E-03	7.04E-04	3.25E-04	2.27E-03
698	1.27E-03	6.84E-04	3.26E-04	2.28E-03
699	1.26E-03	6.99E-04	3.27E-04	2.29E-03
700	1.26E-03	7.10E-04	3.24E-04	2.30E-03
701	1.04E-03	3.26E-04	2.43E-04	1.61E-03
702	1.06E-03	3.40E-04	2.48E-04	1.64E-03
703	1.07E-03	3.50E-04	2.57E-04	1.68E-03
704	1.08E-03	3.61E-04	2.65E-04	1.71E-03
705	1.10E-03	3.72E-04	2.73E-04	1.74E-03

CRL	SRR (storms/yr/km)			
	LI	MI	HI	Total
706	1.11E-03	3.80E-04	2.81E-04	1.77E-03
707	1.13E-03	4.10E-04	2.70E-04	1.81E-03
708	1.14E-03	4.18E-04	2.79E-04	1.84E-03
709	1.16E-03	4.34E-04	2.85E-04	1.87E-03
710	1.17E-03	4.45E-04	2.91E-04	1.91E-03
711	1.18E-03	4.56E-04	2.96E-04	1.94E-03
712	1.18E-03	4.88E-04	3.01E-04	1.97E-03
713	1.20E-03	5.00E-04	3.06E-04	2.00E-03
714	1.21E-03	5.11E-04	3.10E-04	2.04E-03
715	1.23E-03	5.23E-04	3.14E-04	2.06E-03
716	1.22E-03	5.52E-04	3.18E-04	2.09E-03
717	1.22E-03	5.72E-04	3.20E-04	2.11E-03
718	1.24E-03	5.73E-04	3.22E-04	2.14E-03
719	1.25E-03	5.81E-04	3.24E-04	2.16E-03
720	1.24E-03	6.11E-04	3.27E-04	2.18E-03
721	1.26E-03	6.36E-04	3.11E-04	2.20E-03
722	1.26E-03	6.53E-04	3.13E-04	2.22E-03
723	1.27E-03	6.59E-04	3.14E-04	2.24E-03
724	1.27E-03	6.72E-04	3.14E-04	2.26E-03
725	1.28E-03	6.78E-04	3.15E-04	2.28E-03
726	1.29E-03	6.93E-04	3.06E-04	2.29E-03
727	1.30E-03	7.08E-04	3.05E-04	2.31E-03
728	1.30E-03	7.16E-04	3.03E-04	2.32E-03
729	1.31E-03	7.24E-04	3.02E-04	2.34E-03
730	1.32E-03	7.33E-04	3.02E-04	2.36E-03
731	1.33E-03	7.41E-04	3.02E-04	2.37E-03
732	1.35E-03	7.35E-04	3.03E-04	2.39E-03
733	1.36E-03	7.45E-04	3.04E-04	2.41E-03
734	1.37E-03	7.53E-04	3.05E-04	2.43E-03
735	1.35E-03	7.93E-04	3.01E-04	2.45E-03
736	1.36E-03	8.14E-04	2.91E-04	2.47E-03
737	1.37E-03	8.19E-04	2.96E-04	2.48E-03
738	1.38E-03	8.49E-04	2.76E-04	2.50E-03
739	1.36E-03	8.79E-04	2.78E-04	2.52E-03
740	1.37E-03	8.87E-04	2.80E-04	2.54E-03
741	1.38E-03	8.94E-04	2.82E-04	2.55E-03
742	1.38E-03	9.00E-04	2.85E-04	2.57E-03

CRL	SRR (storms/yr/km)			
	LI	MI	HI	Total
743	1.39E-03	9.15E-04	2.83E-04	2.58E-03
744	1.39E-03	9.22E-04	2.85E-04	2.60E-03
745	1.40E-03	9.28E-04	2.88E-04	2.61E-03
746	1.39E-03	9.43E-04	2.89E-04	2.63E-03
747	1.40E-03	9.36E-04	3.05E-04	2.64E-03
748	1.40E-03	9.50E-04	3.07E-04	2.65E-03
749	1.40E-03	9.49E-04	3.16E-04	2.66E-03
750	1.40E-03	9.53E-04	3.19E-04	2.67E-03
751	1.40E-03	9.58E-04	3.22E-04	2.68E-03
752	1.40E-03	9.62E-04	3.25E-04	2.69E-03
753	1.38E-03	9.84E-04	3.27E-04	2.69E-03
754	1.53E-03	5.10E-04	4.03E-04	2.45E-03
755	1.56E-03	5.31E-04	3.92E-04	2.48E-03
756	1.59E-03	5.42E-04	3.88E-04	2.52E-03
757	1.60E-03	5.53E-04	3.97E-04	2.55E-03
758	1.61E-03	5.63E-04	4.05E-04	2.58E-03
759	1.61E-03	5.96E-04	4.13E-04	2.62E-03
760	1.64E-03	5.88E-04	4.21E-04	2.65E-03
761	1.65E-03	5.94E-04	4.32E-04	2.67E-03
762	1.66E-03	6.03E-04	4.38E-04	2.70E-03
763	1.65E-03	6.40E-04	4.38E-04	2.73E-03
764	1.67E-03	6.51E-04	4.43E-04	2.76E-03
765	1.71E-03	6.40E-04	4.47E-04	2.79E-03
766	1.71E-03	6.76E-04	4.40E-04	2.82E-03
767	1.73E-03	7.08E-04	4.20E-04	2.85E-03
768	1.74E-03	7.17E-04	4.23E-04	2.88E-03
769	1.74E-03	7.49E-04	4.26E-04	2.91E-03
770	1.75E-03	7.56E-04	4.28E-04	2.94E-03
771	1.74E-03	7.86E-04	4.29E-04	2.96E-03
772	1.79E-03	7.51E-04	4.30E-04	2.98E-03
773	1.79E-03	7.97E-04	4.08E-04	2.99E-03
774	1.80E-03	8.03E-04	4.08E-04	3.01E-03
775	1.81E-03	8.09E-04	4.08E-04	3.02E-03
776	1.80E-03	8.25E-04	4.09E-04	3.04E-03
777	1.81E-03	8.28E-04	4.10E-04	3.05E-03
778	1.81E-03	8.30E-04	4.12E-04	3.06E-03
779	1.84E-03	8.09E-04	4.14E-04	3.06E-03

CRL	SRR (storms/yr/km)			
	LI	MI	HI	Total
780	1.84E-03	8.10E-04	4.15E-04	3.06E-03

Appendix C: Atmospheric-Forcing Parameters for D.C. Metro Study RSS

Table C-1. Atmospheric-forcing parameters of the subset of 58 NACCS TCs.

TC Count	NACCS Storm ID	NACCS Region	Master Track ID	θ (deg)	Δp (hPa)	R_{max} (km)	V_t (km/h)
1	31	3	5	-60	68	62	12
2	33	3	5	-60	48	49	25
3	57	3	25	-40	88	53	20
4	69	3	26	-40	38	63	48
5	72	3	27	-40	78	66	45
6	75	3	27	-40	48	26	20
7	76	3	27	-40	38	39	42
8	77	3	27	-40	28	74	23
9	83	3	28	-40	38	62	38
10	109	3	50	-20	68	113	32
11	110	3	50	-20	58	25	23
12	115	3	51	-20	78	68	43
13	117	3	51	-20	58	72	12
14	119	3	51	-20	38	31	12
15	122	3	52	-20	78	115	27
16	123	3	52	-20	68	70	39
17	136	3	54	-20	78	87	44
18	142	3	72	0	83	53	12
19	143	3	72	0	78	77	35
20	146	3	72	0	63	26	13
21	147	3	72	0	58	29	38
22	148	3	72	0	53	55	21
23	149	3	72	0	48	51	48
24	151	3	72	0	38	59	39
25	155	3	73	0	83	39	12
26	165	3	73	0	33	50	12
27	174	3	74	0	53	114	25
28	204	3	107	20	33	41	22
29	205	3	107	20	28	59	35
30	206	3	108	20	88	59	33
31	210	3	108	20	68	31	29
32	275	3	125	40	78	139	30
33	282	3	125	40	43	79	21

TC Count	NACCS Storm ID	NACCS Region	Master Track ID	θ (deg)	Δp (hPa)	R_{max} (km)	V_t (km/h)
34	283	3	125	40	38	47	27
35	289	3	126	40	73	61	30
36	296	3	126	40	38	63	47
37	391	2	32	-40	78	47	57
38	524	2	98	20	78	74	38
39	530	2	98	20	48	59	22
40	532	2	98	20	38	92	51
41	534	2	98	20	28	45	35
42	629	2	119	40	58	98	29
43	630	2	119	40	53	29	50
44	631	2	119	40	48	46	14
45	632	2	119	40	43	66	53
46	633	2	119	40	38	52	34
47	634	2	120	40	88	69	39
48	638	2	120	40	68	60	45
49	640	2	120	40	58	34	56
50	642	2	120	40	48	54	41
51	643	2	120	40	43	73	17
52	1003	1	113	40	48	58	52
53	1005	1	113	40	38	69	45
54	31	3	5	-60	68	62	12
55	33	3	5	-60	48	49	25
56	57	3	25	-40	88	53	20
57	69	3	26	-40	38	63	48
58	72	3	27	-40	78	66	45

Attachment # 3, ERDC Final Report entitled” Northern Virginia Infrastructure System Vulnerability Assessment”, dated May 19, 2022

This page left intentionally blank.

Metropolitan Washington District of Columbia (MWDC) Coastal Storm Risk Management (CSRM) Feasibility Study

Northern Virginia Infrastructure System Vulnerability Assessment

Martin T. Schultz, Scott G. Bourne, Christina L. Saltus, and Laars C. Helenius[1]

Environmental Laboratory
Engineer Research and Development Center
US Army Corps of Engineers
Vicksburg, MS 39180

Final Report

May 19, 2022

[1] Deceased

Table of Contents

1.0 Introduction

The tidal zone of the Potomac River extends to the fall line, just upstream of Chain Bridge in Washington DC. Below the fall line, areas adjacent to the Potomac River are vulnerable to flooding caused by coastal storms. Sea level rise will increase the probability and extent of flooding. This report seeks to identify infrastructure that is vulnerable to flooding, and understand what impacts of sea level rise might have on the vulnerability. This study was undertaken as part of the US Army Corps of Engineers (USACE) Baltimore District (NAB) Metropolitan Washington, District of Columbia (MWDC) Coastal Storm Risk Management (CSRM) Feasibility Study. The purpose of the feasibility study is to evaluate and screen out alternatives for flood risk reduction in the Potomac River. Despite the title of this feasibility study, its focus is on the west bank of the Potomac River in Northern Virginia. An outline of the study area and its planning units is illustrated in (Figure 1.1).

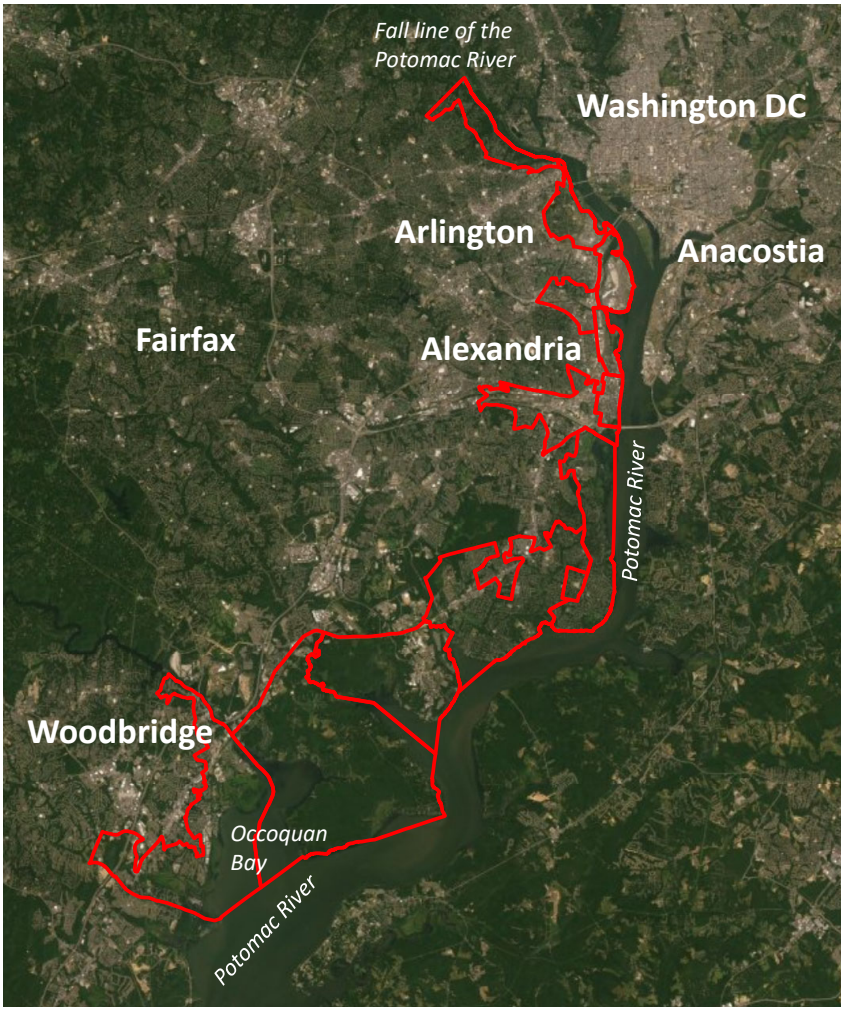

Figure 1.1: Study Area and its Planning Units on the West Bank of the Potomac River in Northern Virginia.

NAB compiled a geographic information system (GIS) database containing information about utility and transportation infrastructure in the northern Virginia study area. The Engineer Research and Development Center (ERDC) Coastal and Hydraulics Laboratory modeled the water levels generated by coastal storms for selected return periods ranging from 1 to 1000 years. Sea-level rise will increase the extent and depth of flooding caused by storms of a given return period. Using sea-level in 2020 as a baseline, sea-level change was projected for low, medium, and high rates of change and evaluated in years 2030, 2080, and 2130. ERDC CHL simulated water surface elevations and the extent of flooding for each year and rate of change in sea level. NAB used these results to estimate inundation depths by comparing water surface elevations to digital elevation models to calculate water depths at regular grid points in the study area.

This vulnerability assessment focuses on seven sea level change scenarios, outlined in Table 1.1. Scenarios are numbered 1 through 7. Each scenario corresponds to a change in sea level as shown in column two, and a year and rate of change in sea level as shown in columns three and four. The rationale for down selecting to seven sea level change scenarios is that seven of the ten original scenarios exhibited less than two feet of sea level rise. In terms of the absolute difference in sea level from baseline, three of the original scenarios were within 0.2 feet of each other. Only one of each pair of these scenarios was analyzed because each pair would have produced almost identical impacts to infrastructure systems.

For each sea level rise scenario, the impacts to infrastructure systems are assessed for coastal storms with a 100-year return period and a 1000-year return period. These two levels of storm severity were selected to represent the weakest storm that might have any significant impact on infrastructure, and the most severe storm that might reasonably be expected to occur, respectively. This effectively bounds the range of potential impacts to infrastructure given the change in sea level.

Scenario	**Change in Sea Level** (feet)	**Corresponding MWDC CSRM Sea Level Rise Scenario**	
		Year	**Rate of Sea Level Change**
1	0	2020	Intermediate
2	0.67	2030	Intermediate
3	1.08	2030	High
4	1.75	2080	Intermediate
5	3.27	2130	Intermediate
6	3.93	2080	High
7	8.64	2130	High

Table 1.1: Mapping of Sea Level Rise Scenarios to MWDC CSRM Sea Level Rise Scenarios.

Most infrastructure is in a continuous stage of development and today, nobody can predict how the infrastructure systems in the study area will look a century from now when the sea level forecasts might be realized. Therefore, it is reasonable to ask why one should be concerned about the potential effect of a sea level that is forecast for many years in the future on the present day infrastructure system. It is possible that sea levels could rise faster than expected. However, by neglecting time and asking how static changes in sea level would affect the system as it exists today, it is possible to identify where and what kind of improvements in existing

infrastructure would be needed first. Many of the vulnerabilities identified in this report can be addressed gradually over time as the opportunities for infrastructure replacement present themselves in the normal course of business operations. In that sense, this vulnerability assessment should be a guide for planners who are concerned with how to evolve the infrastructure system over the long term.

Coastal storm impacts to infrastructure systems were assessed for selected transportation and utility systems. Impacts were assessed for the following transportation systems: Ronald Reagan Washington National Airport (DCA), Washington Metro (Metro), CSX freight and Virginia Rail Express (VRE) commuter rail systems, and road transportation. Impacts were assessed for the following utility systems: drinking water treatment, wastewater treatment and natural gas. This study found no impacts of coastal storms or sea level rise on drinking water treatment and supply systems and the local electric utility, Dominion Energy, declined to provide information that would support this study.

This report consists of six sections that describe potential flood impacts to each of the transportation and utility systems potentially affected by coastal storms and sea level rise. The components and structures associated with each of the systems that are potentially damaged under at least one of the coastal storm and sea level rise scenarios are identified and the depth of inundation at that component or structure is estimated. In most cases, there is very little other information upon which to infer the consequences of that inundation. The strategy here is to present the information and enable readers with more complete information about the vulnerability and design of specific components and structures assess those consequences.

Assessment endpoints for each of the infrastructure systems considered in this study are as follows. For DCA, the focus is on disruption of air transportation caused by inundation of electrical components, aids to navigation, or flooding of the runways. For Metro, the focus is on disruption of commuter rail service caused by inundation of WMATA infrastructure. For CSX Freight and VRE Express, which run on the same rail line, the focus is on disruption of freight and commuter rail service caused by inundation of CSX tracks and VRE rail stations. For road transportation, a network analysis is performed to estimate the percent reduction in average daily traffic capacity of the road network caused by flooding of road segments. The analysis of wastewater systems identifies the water treatment plants and wastewater pump stations within the planning area that are vulnerable to flooding. The components and structures associated with each wastewater treatment plant are identified and the inundation depths at those components and structures are estimated for each coastal storm and sea level rise scenario. For the natural gas system, the percent of service population that would be affected by disruption of natural gas service in the low pressure distribution system in Old Town Alexandria is estimated. No other impacts to the natural gas distribution system were identified.

2.0 Ronald Reagan Washington National Airport

Ronald Reagan Washington National Airport (DCA) is located in Virginia on the western bank of the Potomac River. The airport was constructed on a landfill that extends into the tidally-affected portion of the river, making it vulnerable to flooding from storms and sea level rise. The purpose of this study is to assess the extent to which sea level rise would contribute to flooding at the airport and the impacts that flooding would have on air transportation. Flooding could disrupt air transportation in several ways. Floods could damage electrical components that support runway lights or aids to navigation (NAVAIDs). Damage to NAVAIDs could also limit air travel to certain types of aircraft or aircraft with certain types of navigational equipment. Each of the three runways are also vulnerable to flooding and flooding on any portion of a runway would prevent the use of that runway.

The Metropolitan Washington Airports Authority (MWAA) provided a geographic information system (GIS) database containing information about the location of electrical infrastructure components and NAVAIDs. The locations of those components considered in this study are shown in Figure 2.1. This study focuses on those components located between the river and the runways because these are potentially flooded before the runways. There are critical infrastructure components located west of the runways as well, but these are generally higher in elevation and would not be flooded before the runways. The components are described in Table 2.1. The numbers in that table refer to the labels in Figure 2.1. Emphasis is placed on electrical components and control structures that support NAVAIDs. In many cases NAVAIDS include systems of lights that are adjacent to runways and sensors that are distributed throughout the airfield. This study did not consider the distributed sub-components of those systems because there was little information to identify and characterize those sub-components in the database.

Inundation water depths were calculated at each of these infrastructure components given each of the coastal storm and seven sea level rise scenarios (Tables 2.2 and 2.3). For the runways, maximum inundation water depth and the percent of runway covered in water (Table 2.4) were calculated. Inundation depths in Tables 2.2 and 2.3 reflect the difference between water and ground surface elevations. Information on existing flood proofing of electrical components and NAVAIDs was not available for this study and was not taken into account. Several electrical components and NAVAIDs are vulnerable to flooding from a 100-year storm under existing sea levels (Table 2.2). These include the TV-900 electric station, portions of the fuel depot, the crew lot electric substation, the maintenance shops, and the High Intensity Approach Lighting System (HIALS) control building. For a 100-year storm, it appears that flood impacts would remain limited to this small number of electrical components and NAVAIDs.

The 1000-year flood is an example of low probability event that, for the purpose of this study, represents a worst case scenario. Under existing sea-level conditions, the 1000-year storm floods substantial portions of each runway (Table 2.3) and this would disrupt air transportation prior to flooding of most electrical components and NAVAIDs. A 1000-year storm would also produce up to two feet of flooding at several electrical components (e.g., TV-150, TV-100, TV-600, and Visual Approach Slope Indicator Substation) and NAVAIDs (e.g., Very High Frequency (VHF) Omnidirectional Range (VOR) System, Precision Approach Path Indicators (PAPI) Control Station, and Airport Surface Detection System). However, Flood damage to electrical components and NAVAIDs, or their distributed components, might require extensive repair, extending the period of air travel disruption following a coastal storm.

Sea level rise will increase the probability of realizing coastal storm impacts to infrastructure. This is illustrated in Tables 2.2 and 2.3, which show an increasing number of electrical components and NAVAIDs affected by coastal storms given higher sea levels. For example, in Table 2.2, the extent of flooding given 3.27 feet of sea level rise approaches nearly the same extent of flooding that would be produced by a 1000-year coastal storm under current sea level (Table 2.3). Interpreted, this suggests that something between 1.75 and 3.27 feet of sea level rise could increase the probability that air travel would be disrupted by almost an order of magnitude, from one in a thousand to one in a hundred (*e.g.*, $p = 0.001$ to $p = 0.01$).

Runways are essential components of the infrastructure system at any airport. Staff at DCA indicated that, if any portion of a runway were inundated, regulations would prohibit the use of that runway. At DCA, runways are among the first infrastructure components to be flooded. Table 2.3 lists the maximum depth of flooding and the percent of runway area flooded for each coastal storm and sea level rise scenario. For example, a 100-year flood under existing sea level would inundate about 4.0% of runway 04-22 to a depth of as much as 2.2 feet. All runways exhibit some amount of flooding given 1.75 feet of sea level rise. The extent of inundation under the various coastal storm and sea level rise alternatives is illustrated in Figures 2.2 and 2.3. For example, Figure 2.2 shows that, given a 100-year coastal storm under existing sea level, the flooded portion of Runway 4-22 is located at the southern end of the runway. In Figures 2.2, it appears that the eastern tip of Runway 15-33 would also be flooded given a 100-year coastal storm under existing sea level. This is not correct. The digital elevation model underlying the imagery pre-dates improvements to this runway that would prevent flooding by a 100-year coastal storm given existing sea level. However, some portion of all runways would be inundated by a 100-year coastal storm given 1.75 feet of sea level rise. Figure 2.3 shows the extent of inundation for a 1000-year coastal storm.

The flood protection originally proposed for the Reagan Airport (Alternative 4a) involved increasing the height of the levee road around the perimeter of the airport. This alternative was made more expensive because of the need for deployable floodwall at the end of each runway. As a result, this alternative did not satisfy the benefit cost criteria for implementation. However, had this alternative been adopted, it would have protected the assets at the airport from a 100-year storm up to at least 3.93 feet of sea level rise and from a 1000-year storm up to 1.75 feet of sea level rise. Both storms overtop the proposed protection given a change in sea level somewhere between these changes in sea level and the next highest change in sea-level, respectively (*i.e.*, 8.64 feet for a 100-year storm and 3.27 feet for a 1000-year storm).

This study has considered changes in sea level up to 8.64 feet. This corresponds to sea level rise in 2130 under the high sea level rise scenario used in the MWDC CSRM feasibility study. Nobody can say how long it will be before an 8.64 foot change in sea level is realized. However, it is likely that air travel and infrastructure systems at DCA will change substantially between now and then. In the meantime, the information provided here can be used to identify the most vulnerable infrastructure components and suggest improvements that reduce risk. Efforts to build resilience to coastal storms should address potential flooding of the electrical components and fuel farm in the southern part of the airport and perhaps raising the runways to reduce their vulnerability to flooding.

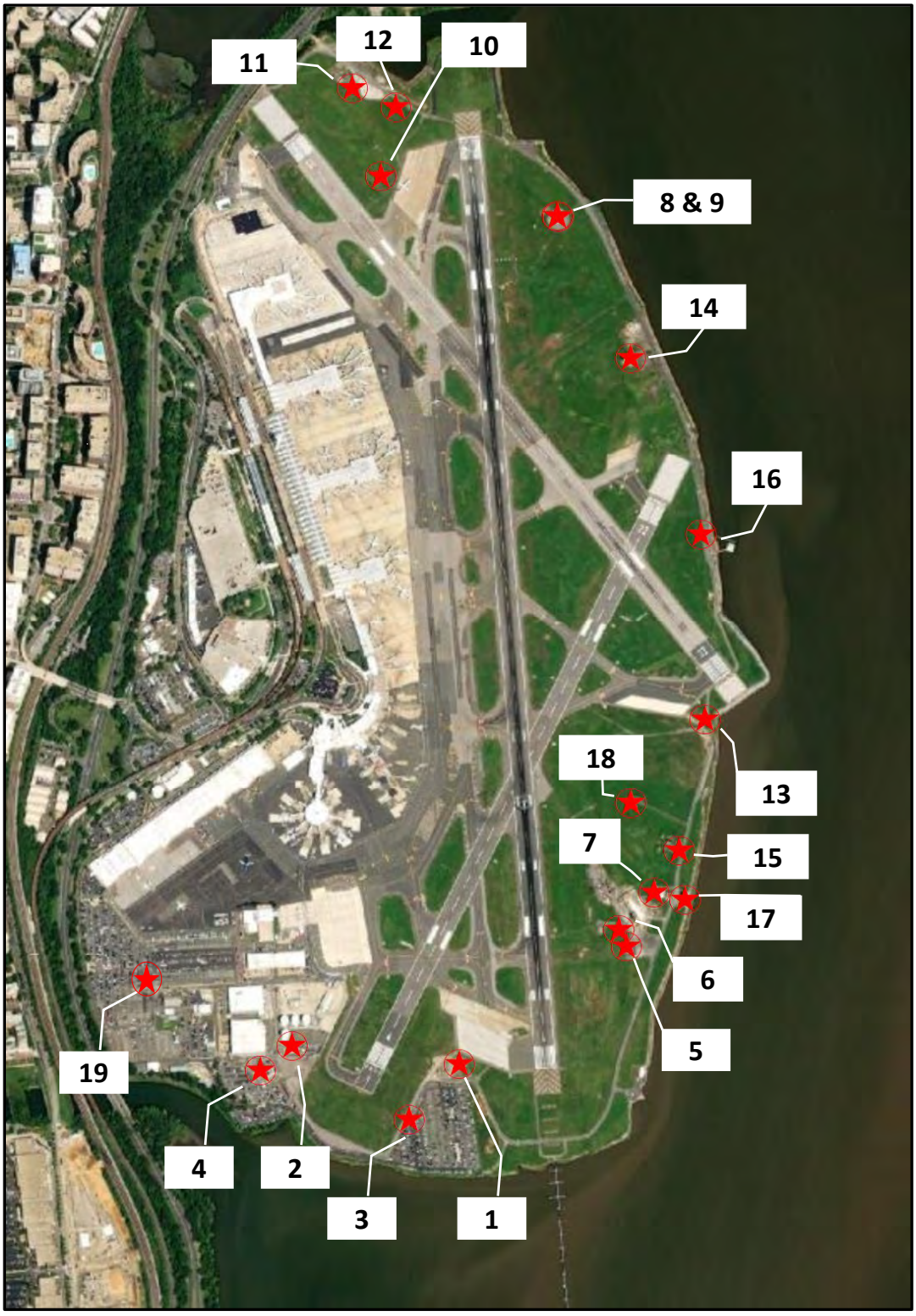

Figure 2.1: Critical Infrastructure Components and Runways

Label	Electrical Component or NAVAID	Description
1	TV-900 Electric Station	Supplies power to lighting on Runways 01-19 and 04-22.
2	Fuel Depot	Store and supply fuel to aircraft. Fuel is stored in above ground tanks and distributed via a pipeline aircraft at the gates.
3	Crew Lot Electric Sub-Station	-
4	Maintenance Shops	-
5	High Intensity Approach Lighting System (HIALS) Building (ALSF-2-XFMR)	This building houses controls for the HIALS system, which is a system of lights designed to assist the pilots transition from instrument flight to visual flight for landing.
6	Control Room @ Transformers 45 and 46.	-
7	Workshop	-
8	Visual Approach Slope Indicator (VASI) Substation	Supplies power to the VASI, a system of lights located on the side of the runway. These lights provide visual descent guidance pilots who are landing.
9	Very High-Frequency (VHF) Omnidirectional Range (VOR) System	Short range radio navigation system that transmits navigational information to aircraft with receiving equipment to assist them in maintaining course. These systems are becoming obsolete and being replaced by satellite navigation systems such as global positioning system (GPS).
10	Precision Approach Path Indicators (PAPI) Control Station	Controls for the PAPI, a system of lights located on the side of the runway that provide visual descent guidance to pilots who are landing. Similar to VASI, but more modern and efficient.
11	TV-150 Electric Station	-
12	TV-100 Electric Station	-
13	TV-600 Electric Station	-
14	Airport Surface Detection Equipment (ASDE) Transformer	ASDE is a system of sensors that collects information on the identity and location of aircraft and vehicles on the ground and transmits that information to air traffic controllers who track their surface movements.
15	Apparent Aid to Navigation	-
16	TV-800 Electric Station	-
17	Radar Facility	-
18	Apparent Aid to Navigation or Lighting Control	-
19	South Distribution Station	Supplies power to TV-900, FAA Facilities, TV-800, Aircraft Rescue and Firefighting (ARFF-301), and the Fuel Farm.

Table 2.1: Descriptions of Structures, Electrical Components and NAVAIDs.

Label	Electrical Component or NAVAID	Sea Level Rise (feet)						
		0.0	**0.67**	**1.08**	**1.75**	**3.27**	**3.93**	**8.64**
1	TV-900 Electric Station	3.0	3.1	3.5	4.1	5.4	6.0	10.3
2	Fuel Depot	1.4	1.5	1.9	2.5	3.8	4.4	8.7
3	Crew Lot Electric Sub-Station	1.2	1.3	1.7	2.3	3.6	4.2	8.5
4	Maintenance Shops	1.1	1.2	1.6	2.2	3.5	4.1	8.4
5	High Intensity Approach Lighting System (HIALS) Building (ALSF-2-XFMR)	0.8	0.9	1.3	1.9	3.2	3.8	8.1
6	Control Room @ Transformers 45 and 46.	0.5	0.6	1.0	1.6	2.9	3.5	7.8
7	Workshop	-	-	-	0.2	1.5	2.1	6.4
8	Visual Approach Slope Indicator (VASI) Substation	-	-	-	-	1.4	2.0	6.3
9	Very High-Frequency (VHF) Omnidirectional Range (VOR) System	-	-	-	-	1.2	1.8	6.1
10	Precision Approach Path Indicators (PAPI) Control Station	-	-	-	-	1.0	1.6	5.9
11	TV-150 Electric Station	-	-	-	-	0.9	1.5	5.8
12	TV-100 Electric Station	-	-	-	-	0.6	1.2	5.5
13	TV-600 Electric Station	-	-	-	-	0.6	1.2	5.5
14	Airport Surface Detection Equipment (ASDE)	-	-	-	-	-	0.4	4.7
15	Apparent Aid to Navigation	-	-	-	-	-	-	3.7
16	TV-800 Electric Station	-	-	-	-	-	-	3.5
17	Radar Facility	-	-	-	-	-	-	3.4
18	Apparent Aid to Navigation or Lighting Control	-	-	-	-	-	-	3.1
19	South Distribution Station (Electric Station)	-	-	-	-	-	-	3.1

Table 2.2: Inundation Depths at Critical Infrastructure Components for a 100-year Storm.

Label	Electrical Component or NAVAID	Sea Level Rise (feet)						
		0.0	**0.67**	**1.08**	**1.75**	**3.27**	**3.93**	**8.64**
1	TV-900 Electric Station	6.0	6.1	6.5	7.1	8.5	9.1	13.3
2	Fuel Depot	4.4	4.5	4.9	5.5	6.9	7.5	11.7
3	Crew Lot Electric Sub-Station	4.2	4.3	4.7	5.3	6.7	7.3	11.5
4	Maintenance Shops	4.1	4.2	4.6	5.2	6.6	7.2	11.4
5	High Intensity Approach Lighting System (HIALS) Building (ALSF-2-XFMR)	3.8	3.9	4.3	4.9	6.3	6.9	11.1
6	Control Room @ Transformers 45 and 46.	3.5	3.6	4.0	4.6	6.0	6.6	10.8
7	Workshop	2.1	2.2	2.6	3.2	4.6	5.2	9.4
8	Visual Approach Slope Indicator (VASI) Substation	2.0	2.1	2.5	3.1	4.5	5.1	9.3
9	Very High-Frequency (VHF) Omnidirectional Range (VOR) System	1.8	1.9	2.3	2.9	4.3	4.9	9.1
10	Precision Approach Path Indicators (PAPI) Control Station	1.6	1.7	2.1	2.7	4.1	4.7	8.9
11	TV-150 Electric Station	1.5	1.6	2.0	2.6	4.0	4.6	8.8
12	TV-100 Electric Station	1.2	1.3	1.7	2.3	3.7	4.3	8.5
13	TV-600 Electric Station	1.2	1.3	1.7	2.3	3.7	4.3	8.5
14	Airport Surface Detection Equipment (ASDE)	0.4	0.5	0.9	1.5	2.9	3.5	7.7
15	Apparent Aid to Navigation	-	-	-	0.5	1.9	2.5	6.7
16	TV-800 Electric Station	-	-	-	0.3	1.7	2.3	6.5
17	Radar Facility	-	-	-	0.2	1.6	2.2	6.4
18	Apparent Aid to Navigation or Lighting Control	-	-	-	-	1.3	1.9	6.1
19	South Distribution Station	-	-	-	-	1.3	1.9	6.1

Table 2.3. Inundation Depths at Critical Infrastructure Components for a 1000-year Storm.

Runway	Sea Level Rise (feet)	100-year Storm		1000-year Storm	
		Maximum Water Depth (ft)	Percent Coverage	Maximum Water Depth (feet)	Percent Coverage
15-33	0	0.0	0.0%	2.9	91.4%
	0.67	0.0	0.0%	3.0	94.3%
	1.08	0.4	8.9%	3.4	98.1%
	1.75	1.0	18.5%	4.0	99.8%
	3.27	2.3	54.6%	5.4	100.0%
	3.93	2.9	91.4%	6.0	100.0%
	8.64	7.2	100.0%	10.2	100.0%
1-19	0	0.0	0.0%	2.3	64.3%
	0.67	0.0	0.0%	2.4	67.8%
	1.08	0.0	0.0%	2.8	80.2%
	1.75	0.4	0.4%	3.4	95.5%
	3.27	1.7	35.3%	4.8	96.2%
	3.93	2.3	64.3%	5.4	96.2%
	8.64	6.6	96.2%	9.6	96.2%
4-22	0	2.2	3.9%	5.2	76.1%
	0.67	2.3	4.0%	5.3	80.7%
	1.08	2.7	4.3%	5.7	89.6%
	1.75	3.3	11.7%	6.3	90.4%
	3.27	4.6	41.0%	7.7	90.4%
	3.93	5.2	76.1%	8.3	90.4%
	8.64	9.5	90.4%	12.5	90.4%

Table 2.3: Maximum Inundation Depths and Percent Coverage on Runways.

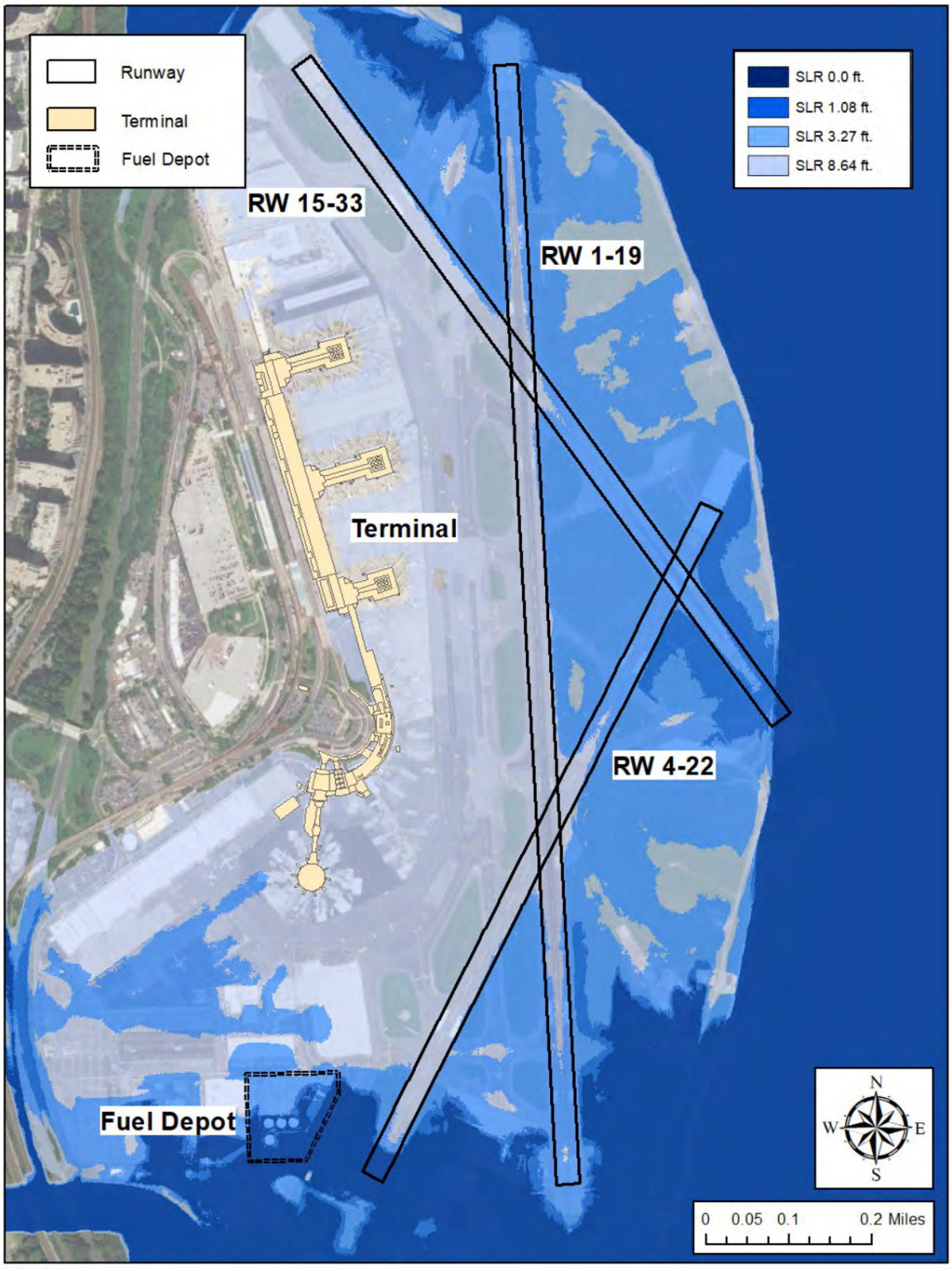

Figure 2.2: DCA Runways, 100 year. Inundation of DCA runways given a 100-year coastal storm for four sea level rise scenarios. Areas of dark blue represent the flood extent given a 100-year coastal storm under existing sea level and successively lighter shades represent 1.08 feet, 3.27 feet and 8.64 feet, respectively.

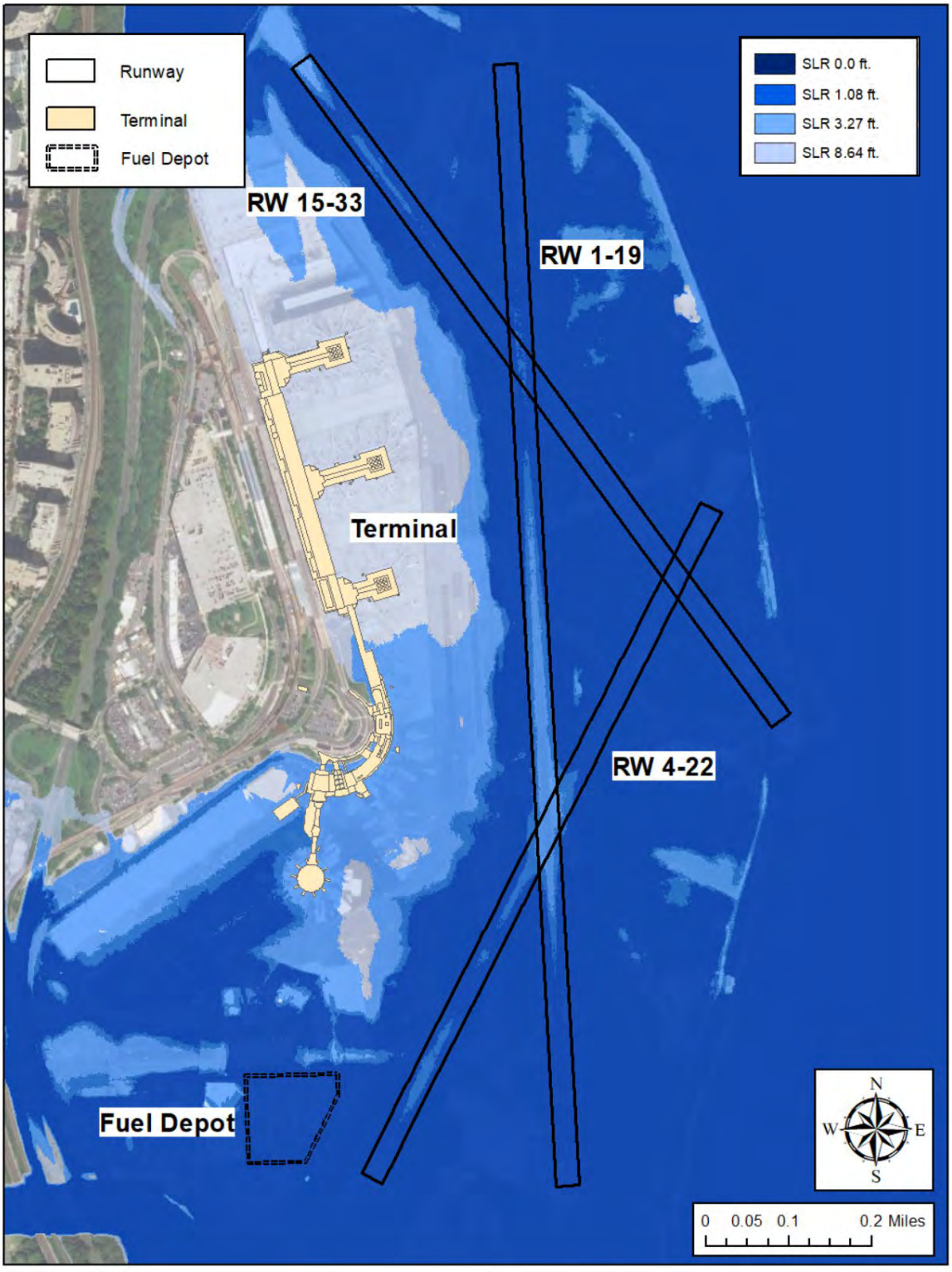

Figure 2.3: DCA Runways, 1000 year. Inundation of DCA runways given a 1000-year coastal storm for four sea level rise scenarios. Areas of dark blue represent the flood extent given a 1000-year coastal storm under existing sea level and successively lighter shades represent 1.08 feet, 3.27 feet and 8.64 feet, respectively.

3.0 Washington Metro

The Washington Metropolitan Area Transit Authority (WMATA or Metro) provides bus and light rail service to commuters throughout Metropolitan Washington DC (MWDC). Prior to the COVID-19 pandemic, total daily entries into the light rail system ranged from 606,000 – 737,000. Riders west of the Potomac River are served by four rail lines, including the Orange, Blue, Silver, and Yellow Lines (Figure 3.1). The potential impacts of floods on light rail systems include inundation of tracks, traction power substations (TPSS), tie breaker stations (TBS), and ventilation shafts. Surface tracks can be inundated by flood waters and tracks in underground tunnels may be flooded either by flood waters entering through rail tunnel entrances, ventilation shafts, or leakage caused by an increase in hydrostatic pressure on the tunnel walls. Impacts on the western side of the Potomac River (Table 3.1) were primarily limited to coastal storms with a 1000-year return period and 8.64 feet of sea level rise.

Figure 3.1: Washington Metrorail System.

Flood impacts to the Orange Line and Silver Line were found to be minimal under all coastal storm and sea level rise scenarios. These two lines run from western Fairfax County to downtown Washington DC. Together with the Blue Line, these lines run through a tunnel underneath the Potomac River between the Rosslyn Station in Arlington, VA and the Foggy Bottom Station in Washington DC. Coastal storm and sea level rise will increase water surface elevations in the Potomac by as much as 10.3 feet (1000-year storm with 8.64 feet of sea level rise). Excess hydrostatic pressure caused by increases in water surface elevations in the Potomac River could cause leakage in the tunnel, but this seems unlikely because the tunnel has been designed for permanent service under the Potomac River. There was no evidence that entrances to the tunnel underneath the Potomac River might be inundated by the most severe storm and sea level rise scenarios (1000-year coastal storm and 8.64 feet of sea level rise). However, the tunnel is potentially flooded through a ventilation shaft on the east bank of the Potomac River, at 2902 Virginia Avenue NW. This ventilation shaft appears to be elevated, but its elevation is not known.

The Blue Line runs from Rosslyn Station in Arlington Virginia to Franconia-Springfield and serves Arlington Cemetery, the Pentagon, DCA, and Old Town Alexandria. Flood impacts to the Blue Line are summarized in Table 3.1 and in Figures 3.2 and 3.3, which show the location of selected Blue Line features and flood polygons given selected coastal storm and sea level rise scenarios. Blue line surface tracks that are subject to flooding include the stretch between the southern entrance to the Rosslyn Station tunnel entrance and the north entrance to the Pentagon Station tunnel, including Arlington Cemetery Station (1000-year storm with 8.64 feet of sea level rise, Table 3.1). There is also a small section of surface track between DCA and Braddock Road Station, just north of the Four Mile Run Bridge, which may be flooded given a 100-year storm with 8.64 feet of sea level rise or a 1000-year storm with at least 3.23 feet of sea level rise (Table 3.1). The Pentagon Tunnel is potentially flooded at both its entrance (1000-year storm with 8.64 feet of sea level rise) and through a ventilation shaft located at 220F Boundary Channel Drive. Impacts were also observed at King Street Station under the most extreme sea level rise scenarios (100-year storm with 8.64 feet of sea level rise and 1000-year storm with at least 3.93 feet of sea level rise). While the station at King Street Station is elevated, access to the station would be impeded by flooding of the parking area and station entrances (100-year storm with 8.64 feet of sea level rise and 1000-year storm with 3.93 feet of sea level rise).

The Yellow Line transports commuters between Washington DC and Virginia across the Potomac River via the Fenwick Bridge, which is one of five bridges forming the 14th Street Bridge Complex. The Pentagon Station tunnel entrance is located approximately 0.2 miles from the bridge. The tunnel entrance is potentially flooded by a 1000-year coastal storm with between 3.93 and 8.64 feet of sea level rise. Water could also enter the tunnel via the ventilation shaft at 225 Boundary Channel Drive, which is also flooded. The Yellow Line merges with the Blue Line at Pentagon Station and continues south to King Street Station. It diverges from the Blue Line south of King Street and continues on to Eisenhower Station. There may be some indication of surface track flooding between the tunnel north of Eisenhower Station and Eisenhower Station itself. Although Eisenhower Station is elevated, access to Eisenhower Station and parking areas could be impeded by flood waters surrounding the station. Additional impacts to the Yellow Line include potential flooding of the TPSS at 2502 Huntington Avenue in Alexandria (100-year and 1000-year storms with 8.64 feet of sea level rise).

Component	Description	Line	100-year Storm Severity							1000-year Storm Severity						
			Sea Level Rise (feet)							Sea Level Rise (feet)						
			0.00	0.67	1.08	1.75	3.23	3.93	8.64	0.00	0.67	1.08	1.75	3.23	3.93	8.64
Stations	Arlington Cemetery	Blue	-	-	-	-	-	-	-	-	-	-	-	-	-	1.53
Station Entrances & Parking	Eisenhower Avenue	Yellow	-	-	-	-	-	-	-	-	-	-	-	-	-	0.61
	King Street	Blue	-	-	-	-	-	-	2.93	-	-	-	-	1.13	1.73	5.93
Ventilation Shafts	225 Boundary Channel Drive	Yellow	-	-	-	-	-	-	-	-	-	-	-	-	-	1.56
	220F Boundary Channel Drive	Blue	-	-	-	-	-	-	0.90	-	-	-	-	-	-	3.90
Tie Breaker Stations (TBS)	C14 (Eisenhower Station)	Yellow	-	-	-	-	-	-	0.37	-	-	-	-	-	-	3.66
	C06 (Arlington Cemetery)	Blue	-	-	-	-	-	-	-	-	-	-	-	-	-	9.07
Traction Power Substations (TPSS)	Jefferson Davis (Subsurface, East of Pentagon Station)	Yellow	-	-	-	-	-	-	-	-	-	-	-	-	-	0.28
	Huntington Avenue TPSS (Surface, North of Eisenhower Station)	Yellow	-	-	-	-	-	-	-	-	-	-	-	-	-	2.81
Tunnel Entrances	Pentagon Tunnel Entrances	Yellow	-	-	-	-	-	-	-	-	-	-	-	-	-	12.03
		Blue	-	-	-	-	-	-	-	-	-	-	-	-	-	14.85
Surface Tracks	Arlington Cemetery - Rosslyn	Blue	-	-	-	-	-	-	-	-	-	-	-	-	-	1.9
	Pentagon – Arlington Cemetery	Blue	- -	-	-	-	-	-	-	-	-	-	-	-	-	15.7
	Braddock Rd. - DCA	Blue/Yellow	-	-	-	-	-	-	2.5	-	-	-	-	0.7	1.3	5.5
	Huntington – Eisenhower Ave.	Yellow	-	-	-	-	-	-	-	-	-	-	-	-	-	6.0
	Pentagon – L'Enfant Plaza	Yellow	-	-	-	-	-	-	-	-	-	-	-	-	-	9.0

Table 3.1: Summary of Storm and Sea Level Rise Impacts to WMATA Metrorail Infrastructure Components. Inundation depths shown in feet for given levels of coastal storm severity and sea level change (feet).

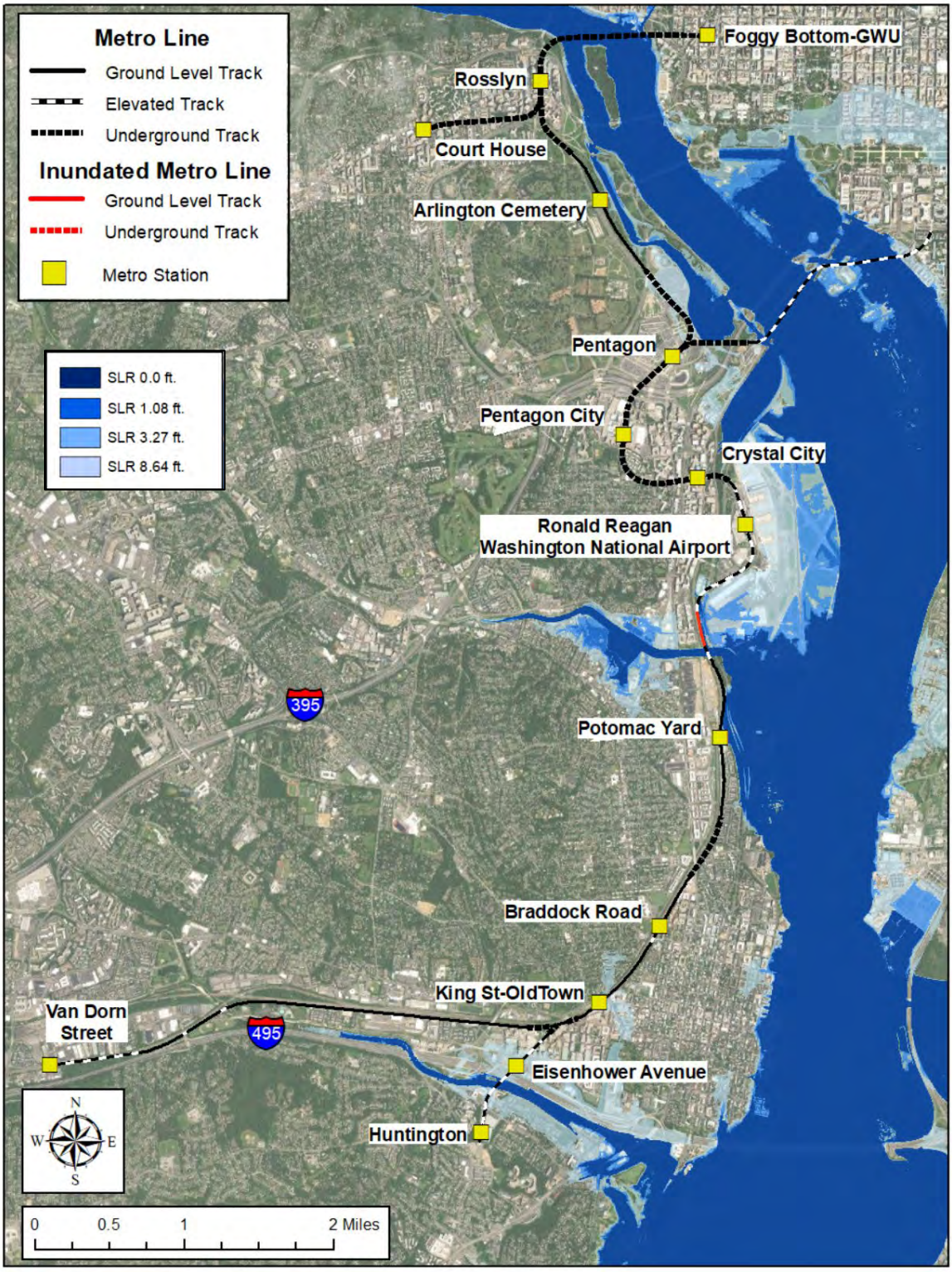

Figure 3.2: Washington Metro Blue and Yellow Lines, 100 year. Metro railroad track inundation caused by a 100-year coastal storm under four sea level rise scenarios. Shades of blue indicate the extent of inundation given different changes in sea level.

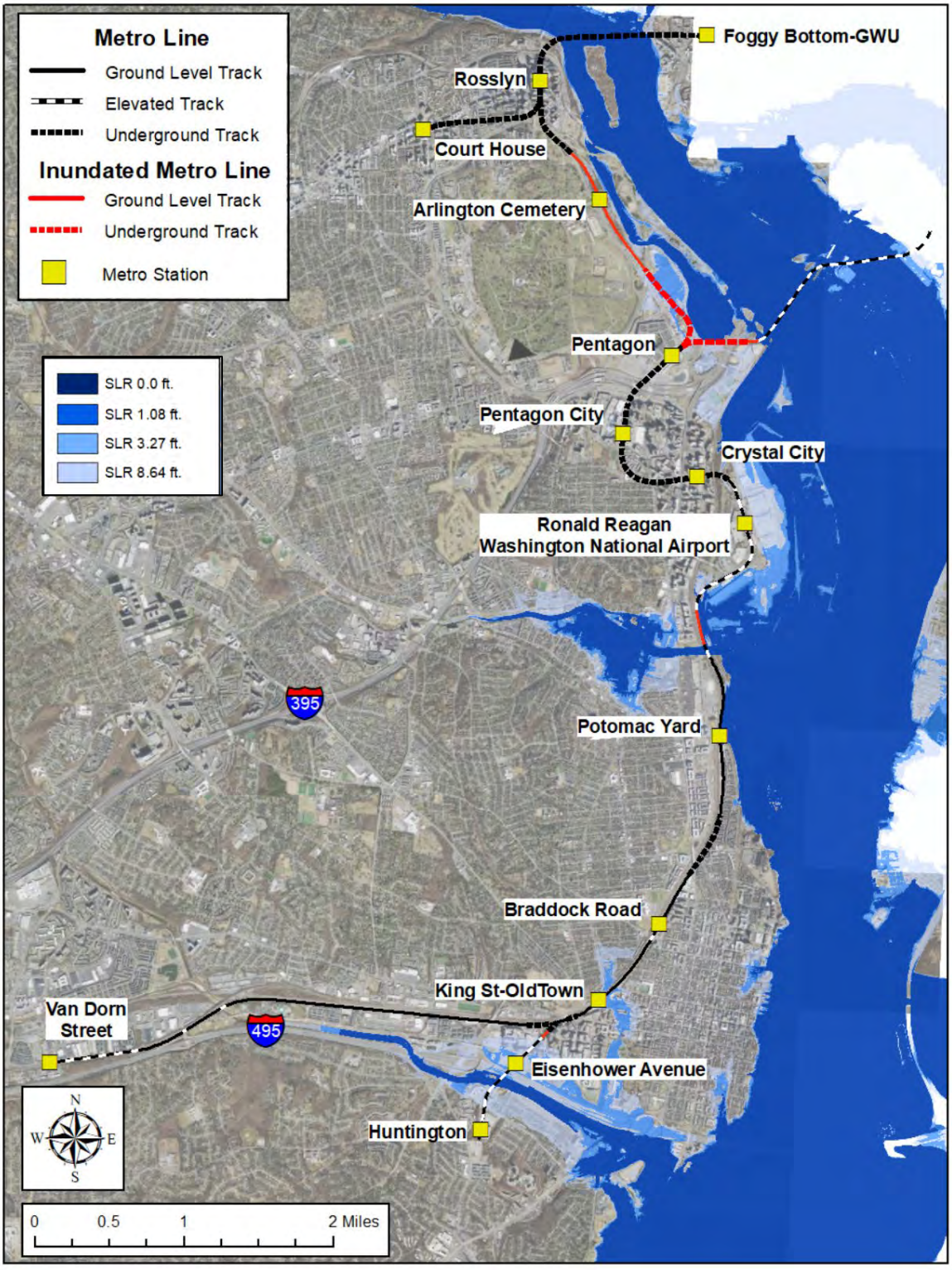

Figure 3.3: Washington Metro, Blue and Yellow Lines, 1000 year. Metro railroad track inundation caused by a 1000-year coastal storm under four sea level rise scenarios. Shades of blue indicate the extent of inundation given different changes in sea level.

4.0 CSX Freight and Virginia Rail Express (VRE)

Commercial railways in the study area are operated by CSX Transportation and Virginia Railway Express (VRE). CSX Transportation is a Class 1 freight railroad that operates east of the Mississippi River. VRE is a publicly owned corporation that operates commuter rail service in Virginia on tracks owned by CSX Transportation and Norfolk Southern Railroad. In 2019, VRE estimated that its average daily ridership was 17,000 people per day. Within the planning area, the railroad infrastructure that is potentially affected by floods includes segments of railroad track between Long Bridge, a railroad bridge that crosses the Potomac River into the District of Columbia, and Quantico Station, which is located outside the planning area just south of Occoquan Bay.

There are two rail segments that are potentially inundated during coastal storm events (Table 4.1). The locations of these rail segments are shown in Figure 4.1 for a 100-year coastal storm and in Figure 4.2 for a 1000-year coastal storm. The first is a roughly one-half mile segment of rail between Long Bridge Park and Roaches Run, just north of Crystal City. This segment is potentially flooded given a 1000-year storm and 8.64 feet of sea level rise (Table 4.1). This would disrupt rail service between Alexandria Station in Virginia and L'Enfant Station in the District of Columbia. The second is a three mile segment of track just north of Rippon Station and adjacent to Occoquan Bay. This section of track is susceptible to flooding under a 100-year storm with 8.64 feet of sea level rise, and 1000-year storm with 3.23 feet of sea level rise. Flooding of this segment would disrupt rail service between Woodbridge Station and Rippon Station. There is also a short spur line just north of Old Town Alexandria that previously served the now defunct Potomac River Power Generating Plant that appears to be susceptible to flooding. However, this segment has been excluded from the table because it no longer appears to be in use.

Rail Segment	Southern Station	Northern Station	100-year Storm Severity							1000-year Storm Severity						
			Sea-Level Rise (feet)							Sea-Level Rise (feet)						
			0.00	0.67	1.08	1.75	3.23	3.93	8.64	0.00	0.67	1.08	1.75	3.23	3.93	8.64
1	Quantico	Rippon	0	0	0	0	0	0	0	0	0	0	0	0	0	0
2	Rippon	Woodbridge	0	0	0	0	0	0	1.6	0	0	0	0	0.4	1.1	5.2
3	Woodbridge	Lorton	0	0	0	0	0	0	0	0	0	0	0	0	0	0
4	Lorton	Franconia-Springfield	0	0	0	0	0	0	0	0	0	0	0	0	0	0
5	Franconia-Springfield	Alexandria	0	0	0	0	0	0	0	0	0	0	0	0	0	0
6	Alexandria	Crystal City	0	0	0	0	0	0	0	0	0	0	0	0	0	0
7	Crystal City	L'Enfant Station	0	0	0	0	0	0	1.4	0	0	0	0	0	0	4.4

Table 4.1: Flood impacts to CSX Freight and Virginia Rail Express (VRE).

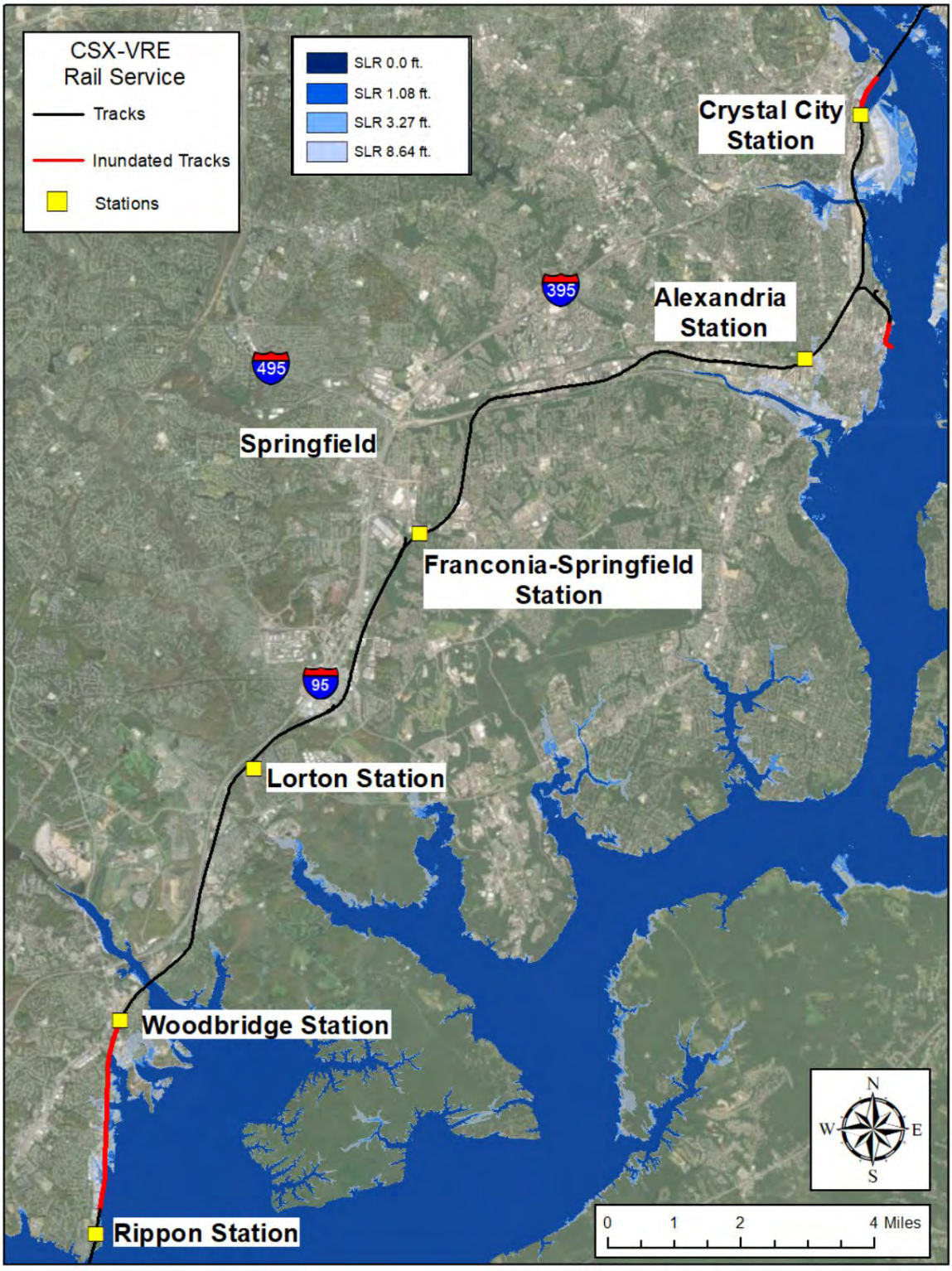

Figure 4.1: CSX Freight and Virginia Rail Express (VRE), 100-year. Potentially inundated segments of CSX rail lines are shown in red. The extent of inundation is shown for a 100-year coastal storm given existing sea levels and three sea level rise scenarios (1.08 ft, 3.23 ft., and 8.64 ft.).

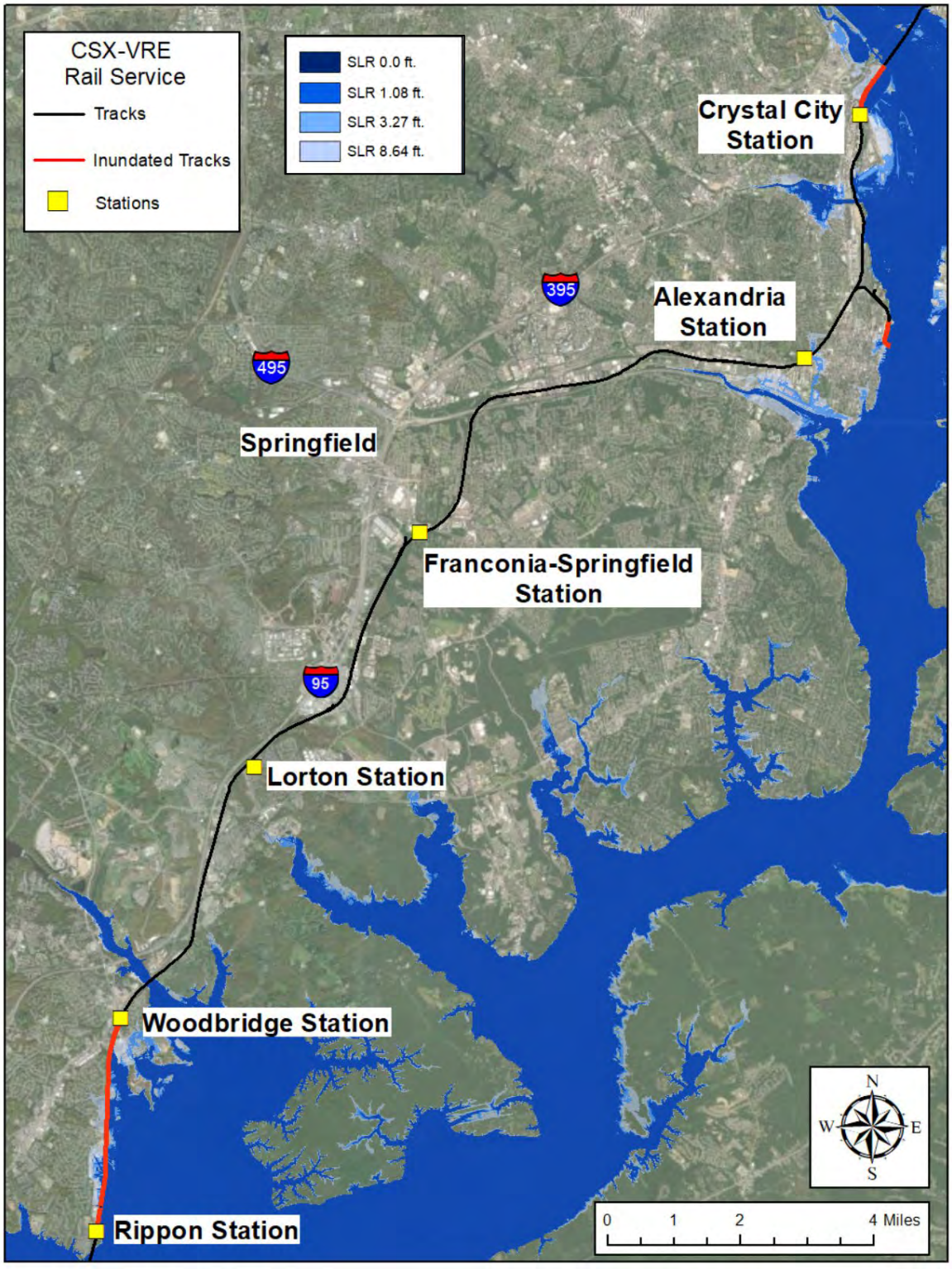

Figure 4.2: CSX Freight and Virginia Rail Express (VRE), 1000-year. Potentially inundated segments of CSX rail lines are shown in red. The extent of inundation is shown for a 100-year coastal storm given existing sea levels and three sea level rise scenarios (1.08 ft., 3.23 ft., and 8.64 ft.).

5.0 Road Transportation Network

Coastal storms can interfere with road transportation by inundating road segments and forcing drivers to find alternate routes. These impacts on road transportation are assessed through a network analysis that estimates the percent reduction in traffic capacity caused by coastal storms and sea level rise. The analysis accounts for differences in the location and connectivity of road segments within the network and differences in average daily traffic (ADT) among road segments. A database representing the statewide road network was obtained from the State of Virginia Department of Transportation. The road network was trimmed to include only those road segments within the twelve contiguous planning unit boundaries. The trimmed network consisted of 16,145 road segments (Figure 5.1). Each segment was defined by a road or route name, the latitude and longitude of each terminus, whether the road segment was one way or two way, and ADT. There were 12,237 two-way road segments and 3,908 one-way road segments. ADT was missing for 8,472 road segments. These were assigned the minimum value of ADT in the database (10).

The road network was represented as a directed graph with nodes representing road segments and edges (arcs) between nodes representing the traffic flow in each direction between two road segments. One node is distinguished as a source, another as a sink, and all other nodes as intermediate nodes. Traffic in the road network is modeled as flow through the digraph from the source to the sink such that the flow along any edge never exceeds its capacity and the flow out of and into the network are equal. Maximal flow through a digraph with a defined source and a defined sink is found using the Ford Fulkerson algorithm.[2] The effect of flooding is modeled by removing inundated road segments from the digraph and recalculating maximum flow. The percent change in maximal flow is equated with percent decrease in traffic capacity.

In the aforementioned digraph, one node is defined arbitrarily as a source and another as a sink. In fact, traffic is entering and exiting the road network through many road segments. This is called a circulation problem. Tardos' method can be used to solve the circulation problem using the Ford Fulkerson maximal flow algorithm.[3] Tardos' method modifies the digraph by designating nodes with net positive flows into the network as semi-sources and net negative flows out of the network as semi-sinks. Edges are introduced between semi-sources and the source node and between semi-sinks and the sink node. Each edge has a capacity equal to net flow. This method enables the circulation problem to be solved using the maximal flow algorithm.

For the MWDC CSRM road network, the modified digraph has 1,014 semi-sources and 1,021 semi-sinks. The Ford-Fulkerson algorithm is applied to the modified digraph to determine the maximum flow. Then for each coastal storm and sea level rise scenario, the nodes for inundated road segments are removed. The Ford Fulkerson algorithm is used to recalculate maximum flow. The difference in maximal flow through the full network and the network with the nodes for inundated road segments removed is the reduction in traffic flow.

---

[2] Ford, L.R., and D.R. Fulkerson. 1956. "Maximal flow through a network." *Canadian Journal Of Mathematics* 8: 399-404. doi:10.4153/CJM-1956-045-5.

[3] Tardos, Eva. 1985. "A strongly polynomial minimum cost circulation algorithm." *Combinatorica* 5: 247–255. doi:10.1007/BF02579369.

Figure 5.1: Road Network in the MWDC CSRM Planning Area.

Reduction in Traffic Capacity – No Action Alternative

Given the No Action alternative at existing sea levels, the inundation caused by a 100-year storm would reduce traffic capacity within the planning area by 4.2% and the inundation caused by a 1000-year storm would reduce traffic capacity by 6.0%. Sea level rise will increase the extent of inundation caused by storms of a given intensity and the number of inundated road segments, further reducing traffic capacity. Results of the traffic analysis show that, as sea level

rises, the number of inundated road segments and the reduction in traffic capacity increase (Table 5.1). The change in traffic capacity is plotted on changes in sea level in Figure 5.2. In terms of its effect on traffic capacity, these results suggest that a four foot increase in sea level has the same effect on traffic capacity as increasing storm severity from a 100-year to a 1000-year storm at baseline sea level.

SLR Scenario	**Sea Level Change** (ft)	**Inundated Road Segments** (Number)		**Change in Traffic Capacity** (Percent)	
		100 Year	**1000 Year**	**100 Year**	**1000 Year**
1	0	401	652	-4.2%	-6.0%
2	0.67	415	660	-4.2%	-6.2%
3	1.08	455	691	-4.6%	-6.3%
4	1.75	495	725	-5.1%	-6.4%
5	3.27	594	969	-5.8%	-11.7%
6	3.93	652	1,043	-6.0%	-12.5%
7	8.64	1,246	1,651	-14.5%	-17.3%

Table 5.1: Number of Inundated Road Segments and Reduction in Traffic Capacity, No Action Alternative.

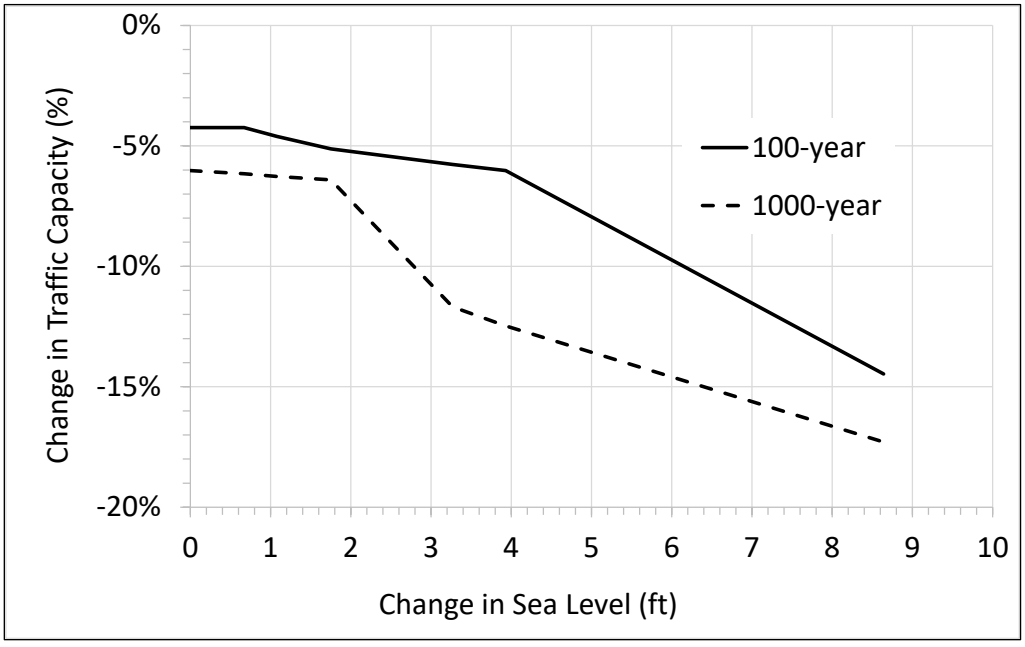

Figure 5.2: Effect of Sea Level Change on the Change in Traffic Capacity within the Planning Area under the No Action Alternative.

Contribution of Roads or Routes to the Reduction in Traffic Capacity

A road segment can be thought of as a length of road between two intersections. Each road or route in the study area is composed of many road segments. An inundated road or route contains at least one inundated road segment. When a road segment is inundated, traffic is forced to navigate around the inundated road segment. When inundated, road segments with higher ADTs have the potential to make a larger contribution toward a reduction in traffic capacity than road segments with lower ADT, depending upon the capacity of alternate routes. This section of the traffic analysis explores how much each road or route contributes to the reduction in traffic flow. Those roads or routes that make the greatest contribution to the reduction in traffic capacity at lower levels of storm severity and sea level rise should receive priority for flood mitigation. Flood mitigation can be accomplished either by reducing flood risk or increasing the capacity of alternate routes. Those impacts that are forecast at higher sea levels may still be decades away and can be addressed through a regular transportation planning process.

This study identified 58 distinct roads or routes that were inundated under at least one of the various coastal storm and sea level rise scenarios considered in this study. The contribution of each inundated road or route to the overall reduction in traffic flow was estimated by restoring all inundated road segments along a given road or route and then recalculating the reduction in traffic flow. The contribution to reduction in traffic flow is then calculated:

$$c_{ij} = \frac{r_{ij} - r'_{ij}}{r_{ij}}$$

Where r_{ij} is the reduction in traffic flow for coastal storm *i* and sea level rise scenario *j* and r'_{ij} is the reduction in traffic flow for coastal storm *i* and sea level rise scenario *j* with all inundated road segments associated with the given road or route restored to service. c_{ij} is the proportional contribution of the road or route to the reduction in traffic capacity. For example, suppose a 100-year coastal storm would reduce traffic flow in the planning area by 4.2%. The potential benefit of protecting the George Washington Parkway (VA-90005) would be estimated by restoring all of the flooded road segments associated with that route to the road network and recalculating the traffic capacity. In this example, restoration of VA-90005 reduces the reduction in traffic capacity to 2.25%. Therefore, the approximate contribution of VA-2005 to the overall reduction in traffic capacity is: $\frac{0.042-0.0215}{0.042} = 0.487\%$, or 48.7% (Table 5.2). The estimate is approximate because some road segments may be shared by multiple routes, but each route has been restored individually in this assessment.

A small number of the largest roads and routes account for the largest fraction of reduction in traffic capacity. The top sixteen roads and routes are listed in Table 2 in rank order of their contribution to the reduction in traffic capacity given a 100-year storm event over all potential sea levels. Route VA-90005 (George Washington Parkway (GWP)) contributes the most to the reduction in traffic capacity, accounting for 48.7% of the 4.2% reduction. This is equivalent to a 2.04% reduction in overall traffic capacity (e.g., $0.487 \times 0.042 = 0.0204$). Inundated segments of VA-90005 (GWP) extend from the Belle Haven neighborhood to north of Key Bridge. Key sites were traffic capacity is interrupted include access to I-66 ramps, I-395 ramps, and Ronald Reagan Washington National Airport (DCA).

Route US-1 (Richmond Highway) accounts for the second largest contribution to the reduction in traffic capacity given a 100-year coastal storm and baseline sea level. The reduction in traffic capacity (13.6%) appears to be primarily attributed to inundation of segments of US-1 (Richmond Highway) between Cameron Run and Huntington Avenue. Route SC-1510 accounts for 8% of the reduction in traffic capacity. The flooded portions of SC-1510 are located in the Belle Haven neighborhood between VA-90005 (GWP) and Fort Hunt Drive. This segment has an average daily traffic capacity (ADT) of 8,000 vehicles per day. Flood risks to this route would potentially be reduced by the flood wall proposed in the Belle Haven neighborhood. CR-6915 accounts for 4.9% of the reduction in traffic flow given a 100-year storm under baseline sea levels. This route carries traffic away from the arrivals and departure area of DCA and merges with the northbound lanes of VA-90005 (GWP) just south of Roaches Run. It should be noted that the digital road network used in this assessment differs from available maps and imagery and may not accurately reflect recent improvements at the southern entrance to DCA.

The number of inundated road segments will increase as the extent of area inundated during coastal storms increases with sea level rise. Overall, for a 100-year coastal storm, the reduction in traffic capacity increases from 4.2% to 6.0% given an increase in sea level of 3.93 feet and to 14.5% given an increase in sea level of 8.64 feet (Table 5.1). As sea level rises, the relative contribution of the various routes to the overall reduction in traffic capacity remains consistent for a 100-year storm up to 3.93 feet of increase in sea level (Tables 5.2) and for a 1000-year storm up to 1.75 feet of sea level (Table 5.3). Greater changes in sea level result in the inundation of several new routes, including I-95/I-495, VA-241, and VA-110. This drastically alters the relative contribution of the various routes to the overall reduction in traffic capacity. Segments of I-95/I-495 (Capital Beltway) along Cameron Run become inundated, accounting for 20.5% of the reduction in traffic capacity for a 100-year storm (Table 5.2) and 24.6% of the reduction in traffic capacity for a 1000-year storm (Table 5.3). Similarly, VA-110 and VA-241 become significant contributors to the reduction in traffic capacity. Segments of VA-110 become inundated east of the Pentagon and segments of VA-241 (Telegraph Road) become inundated beneath I-95/I-495.

Increases in the extent of inundation can be caused either by increases in storm severity or by increases in sea level. At least with respect to percent reductions in traffic capacity, the increase in coastal storm severity from a 100-year to a 1000-year return period is equivalent to approximately four feet of sea level rise. In other words, a 6% reduction in traffic capacity could be caused either by a 1000-year coastal storm given the current sea level or a 100-year coastal storm given four feet of sea level rise (Table 5.1).

The extent of road segments inundated by each of the various coastal storm and sea level rise scenarios is illustrated at four locations that account for some of the large reductions in traffic capacity. These include: 1) VA-90005 (GWP) north of DCA (Figures 5.2 & 5.3); 2) I-95/I-495 along Cameron Run (Figures 5.4 & 5.5); 3) Belle Haven (Figures 5.6 & 5.7); and 4) Old Town Alexandria (Figures 5.8 & 5.9). Figures 5.2 and 5.3 illustrate inundated road segments along VA-90005 (GWP) north of DCA. Each road segment is one of four colors to indicate which of the four selected sea level rise scenarios would cause inundation of that road segment given the coastal storm. The four sea level rise scenarios considered here are 0.0 feet, 1.08 ft., 3.27 ft., and 8.64 ft. The other sea level change scenarios have not been shown here because those differences would be difficult to visualize and interpret at this scale. Flood polygons representing the extent of flooding given these four changes in sea level are also shown, with lighter shades of blue representing greater changes in sea level.

100 yr Road or Route	Sea Level Change (ft)						
	0.00	**0.67**	**1.08**	**1.75**	**3.27**	**3.93**	**8.64**
VA-90005 (GWP)	48.7%	48.7%	52.8%	47.5%	48.5%	46.4%	19.3%
US-1	13.6%	13.6%	12.5%	14.6%	12.0%	13.0%	12.7%
SC-1510	8.0%	8.0%	7.3%	6.6%	6.7%	6.4%	3.0%
CR-6915	4.9%	4.9%	4.5%	4.1%	3.6%	3.5%	1.4%
I-395 (Ramps 9 & 10)	4.8%	4.8%	4.4%	3.9%	3.5%	3.4%	1.2%
SC-629	3.2%	3.2%	3.0%	5.1%	4.8%	4.6%	1.9%
SC-99016 (Ramp)	4.2%	4.2%	3.9%	4.1%	3.7%	3.5%	1.6%
SC-628	3.9%	3.9%	3.6%	4.3%	3.8%	3.6%	1.5%
I-95 / I-495	-	-	-	-	-	-	20.5%
SC-632	3.0%	3.0%	2.8%	2.5%	2.2%	2.1%	1.2%
VA-120				2.7%	2.4%	2.0%	1.8%
I-66 (Ramp 75A)	1.5%	1.5%	1.4%	1.3%	1.1%	1.1%	0.5%
VA-241	-	-	-	-	-	-	7.9%
VA-110	-	-	-	-	-	-	5.4%
SC-636	0.0%	0.0%	0.0%	0.0%	1.0%	2.0%	1.1%
SC-1208	0.5%	0.5%	0.4%	0.4%	0.3%	0.3%	0.2%
SC-2100	0.4%	0.4%	0.3%	0.3%	0.3%	0.5%	0.2%
Total	**96.7%**	**96.7%**	**96.9%**	**97.4%**	**93.9%**	**92.4%**	**81.4%**

Table 5.2: Percent Contribution of Roads and Routes to Reduction in Traffic Capacity under Different Sea Level Change Scenarios, 100-year Storm.

1000-yr Road or Route	Sea Level Change (ft)						
	0.00	**0.67**	**1.08**	**1.75**	**3.27**	**3.93**	**8.64**
VA-90005 (GWP)	46.4%	45.3%	44.5%	43.5%	23.9%	22.4%	16.2%
US-1	13.0%	15.0%	14.7%	14.4%	12.5%	13.4%	14.9%
I-95 / I-495	-	-	-	-	24.6%	23.0%	17.5%
SC-1510	6.4%	6.3%	6.9%	6.8%	3.7%	3.5%	2.5%
SC-629	4.6%	4.5%	4.4%	4.3%	2.4%	2.2%	1.6%
VA-120	2.0%	4.2%	4.1%	3.0%	2.2%	2.1%	2.0%
SC-628	3.6%	3.6%	3.5%	3.4%	1.9%	1.8%	1.3%
SC-99016 Ramp	3.5%	3.4%	3.4%	3.3%	1.8%	1.7%	1.3%
CR-6915	3.5%	3.4%	3.3%	3.3%	1.8%	1.7%	1.2%
I-395 (Ramps 9 & 10)	3.4%	3.3%	3.2%	3.2%	1.3%	1.3%	1.0%
VA-110	-	-	-	-	3.6%	6.3%	4.6%
SC-632	2.1%	2.1%	2.0%	2.0%	1.4%	1.4%	1.0%
SC-636	2.0%	1.9%	1.9%	1.9%	1.0%	1.0%	1.3%
VA-241	-	-	-	-	-	-	9.3%
SC-622	0.7%	0.7%	1.3%	1.3%	1.1%	1.0%	0.7%
I-66 (Ramp 75A)	1.1%	1.1%	1.0%	1.0%	0.6%	0.5%	0.4%
VA-236	-	-	-	-	2.1%	2.0%	1.4%
Total	**92.3%**	**94.8%**	**94.2%**	**91.4%**	**85.9%**	**85.3%**	**78.2%**

Table 5.3: Percent Contribution of Roads and Routes to Reduction in Traffic Capacity under Different Sea Level Change Scenarios, 1000-year Storm.

Significant reductions in traffic capacity are attributed to the inundation of road segments along route VA-90005 (GWP). Inundated segments of route VA-90005 (GWP) north of DCA are shown in Figures 5.2 and 5.3 for each of the coastal storm and sea level rise scenarios. VA-90005 (GWP) is high traffic corridor with an estimated average daily traffic (ADT) of 62,000 vehicles per day. Given a 100-year coastal storm, segments of VA-90005 (GWP) along Roaches Run and underneath I-395 are inundated, as are the access ramps that provide access to and from I-395 (Exit 10). The Richmond Highway follows US-1 to I-395 and continues north of I-395 along Route VA-110, on the east side of the Pentagon. Sections of VA-110 would be inundated during a 100-year coastal storm given more than 3.93 feet of sea level rise (Figure 5.2). Impacts of a 1000-year storm are illustrated in Figure 5.3.

Potential flooding of road segments in the vicinity of Four Mile Run and Arlandria is illustrated in Figures 5.4 and 5.5. While this is not a particularly high traffic area it is shown here because it is prone to flooding and has been considered for a flood risk reduction project.

Given larger increases sea level, low lying segments of the I-95/I-495 (the Capital Beltway) corridor along Cameron Run south of Old Town Alexandria are vulnerable to flooding. This route has ADT of 154,000 vehicles per day and, if inundated, these road segments would account for a large fraction of reductions in traffic capacity. Figures 5.6 and 5.7 show inundated road segments between the VA-241 and I-95/I-495 interchange and the Potomac River. Low lying segments of the Capital Beltway would become inundated given a 100-year coastal storm and 8.64 feet of sea level rise (Figure 5.6) or a 1000-year storm with at least 3.93 feet of sea level rise. Also of interest is the extensive flooding of US-1 east of Huntington. This problem is more immediate, with inundation potentially occurring given a 100-year coastal storm and existing sea levels. For comparison, Route US-1 has an ADT of 48,000 vehicles per day.

Two additional areas are of note. These include Old Town Alexandria and Belle Haven. Although they would not contribute significantly to reductions in traffic capacity, both of these areas have been considered for flood risk reduction projects. Inundation of road segments in Old Town Alexandria is shown for the various coastal storm and sea-level rise scenarios in Figures 5.8 and 5.9. Inundation of road segments in Belle Haven is shown for the various coastal storm and sea-level rise scenarios in Figures 10 and 11. Routes of note in the Belle Haven neighborhood are SC-1510 (Belle Haven Boulevard), which has an ADT of 8100 vehicles per day, and SC-632 (Belle Haven Road), which has an ADT of 7100 vehicles per day. Both of these routes feed VA-90005 (GWP) and are listed in Tables 5.2 and 5.3 as significant contributors to reductions in traffic capacity under all coastal storm and sea level rise scenarios.

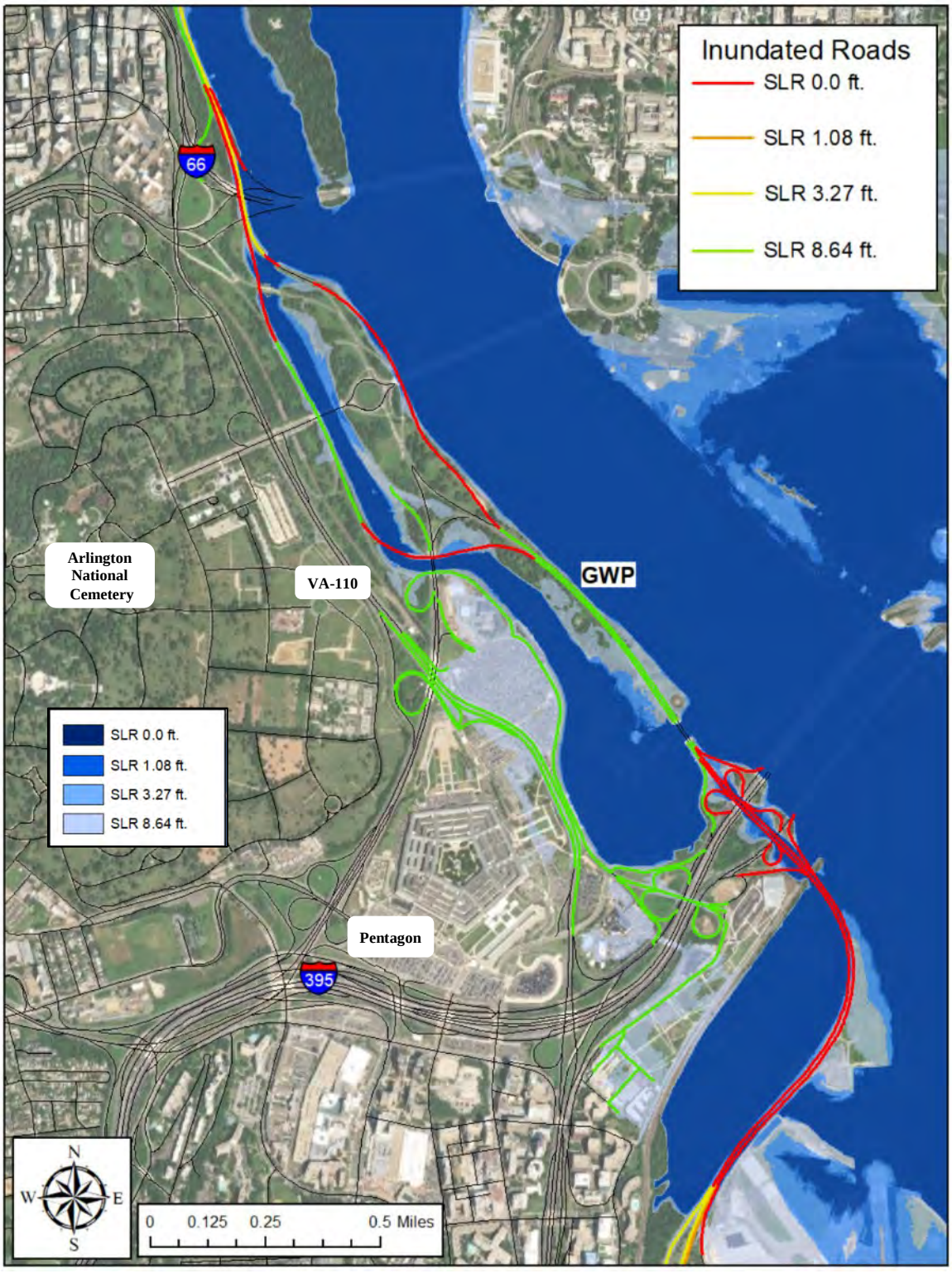

Figure 5.2: VA-90005 (GWP) between Ronald Reagan National Airport and Key Bridge, 100-year. Road inundation caused by a 100-year coastal storm under four sea level rise scenarios. The State of Virginia road network used in this assessment terminated at the Potomac River. None of the bridges crossing the Potomac River are inundated.

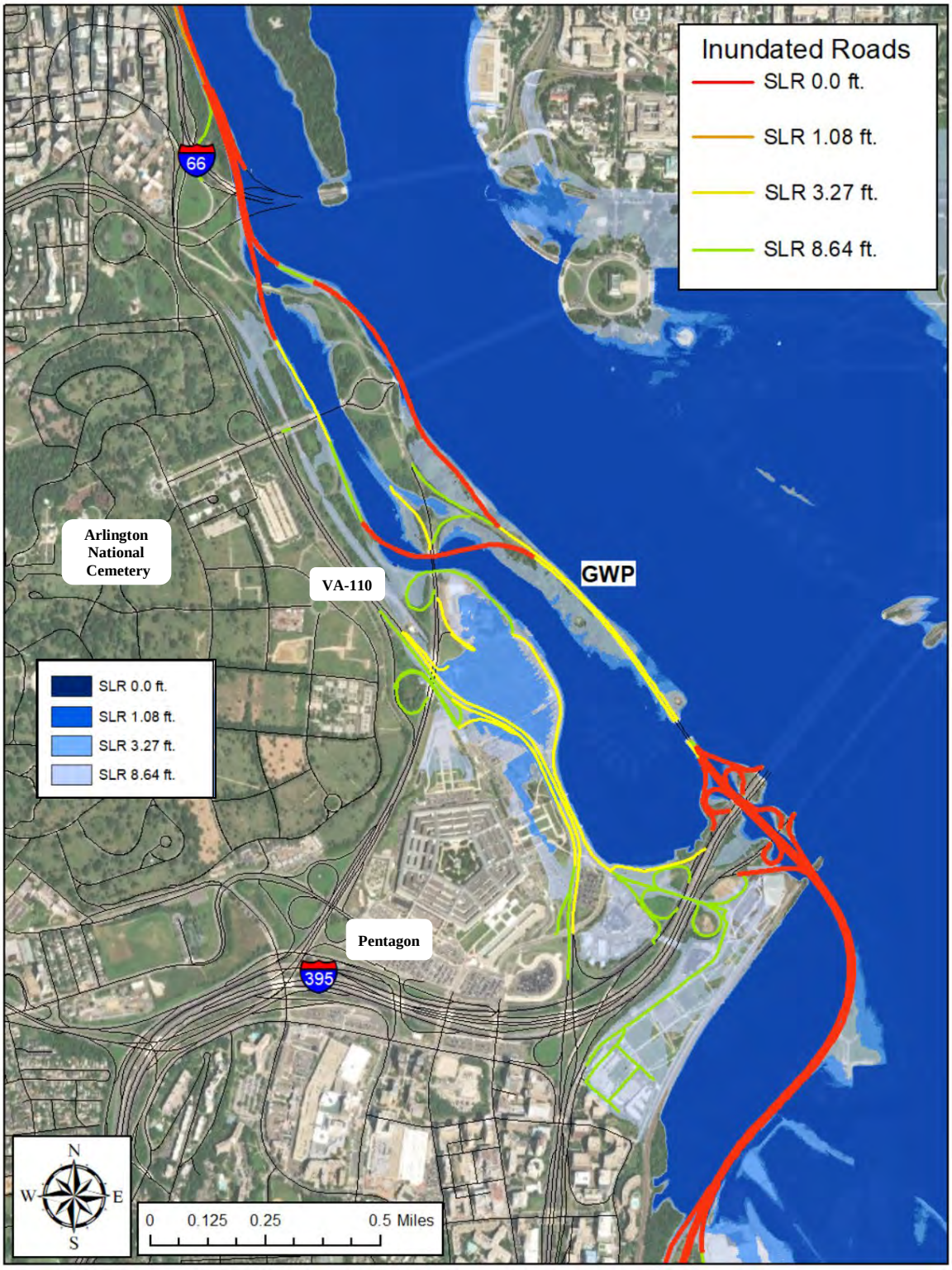

Figure 5.3: VA-90005 (GWP) between Ronald Reagan National Airport and Key Bridge, 1000-year. Road inundation caused by a 1000-year coastal storm under four sea level rise scenarios. The State of Virginia road network used in this assessment terminated at the Potomac River. None of the bridges crossing the Potomac River are inundated.

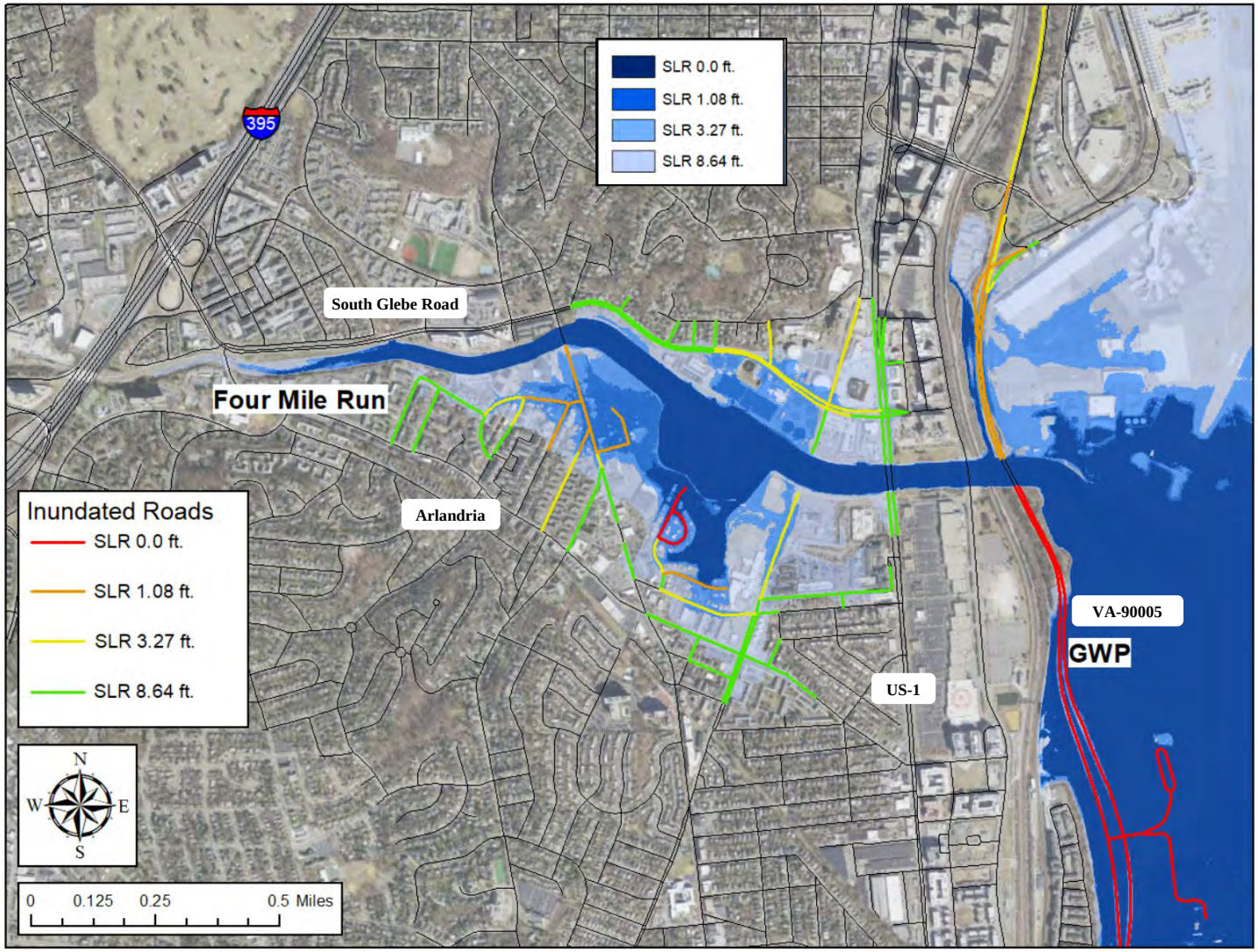

Figure 5.4: Four Mile Run and Arlandria, 100 year. Road inundation caused by a 100-year coastal storm under four sea level rise scenarios.

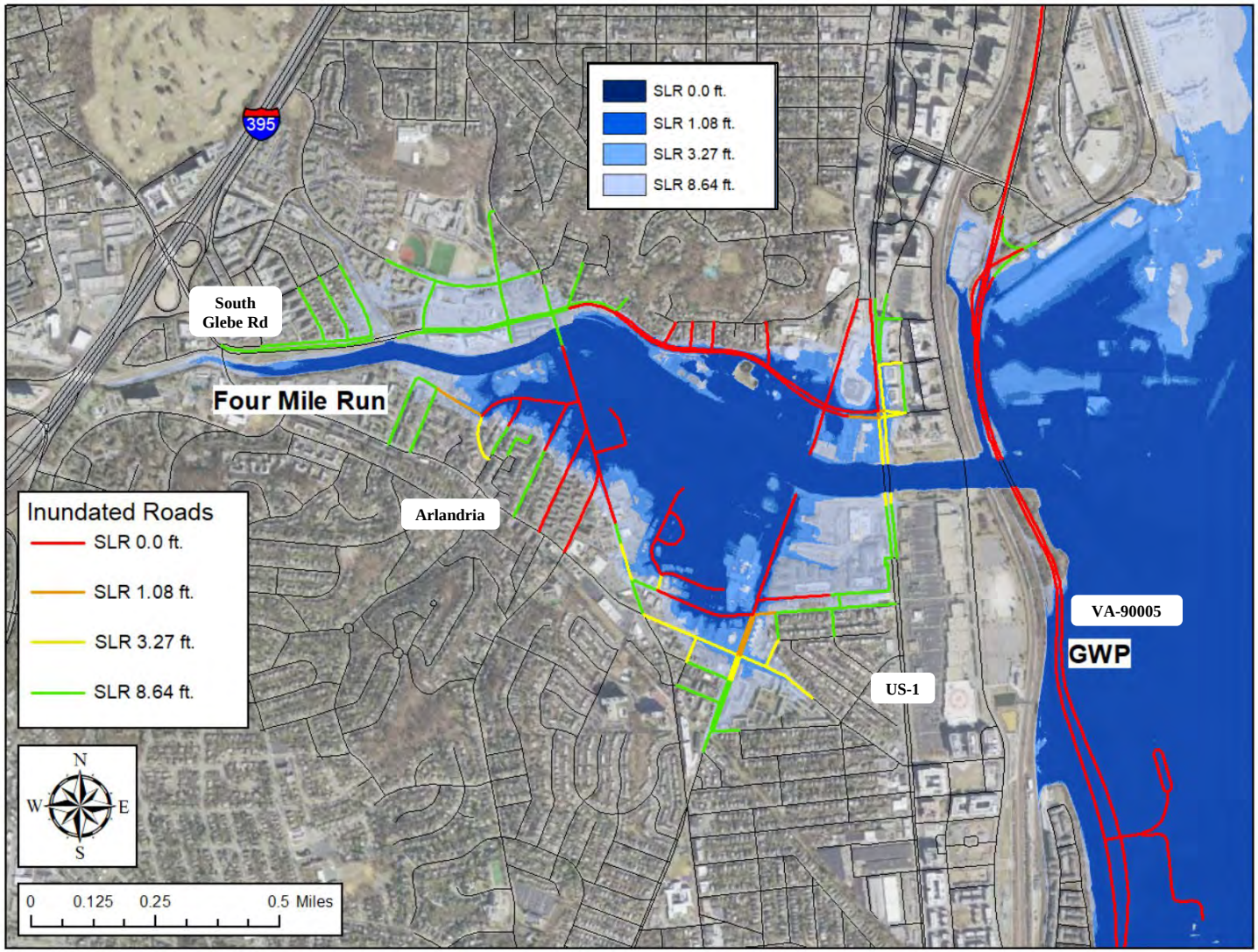

Figure 5.5: Four Mile Run and Arlandria, 1000 year. Road inundation caused by a 1000-year coastal storm under four sea level rise scenarios.

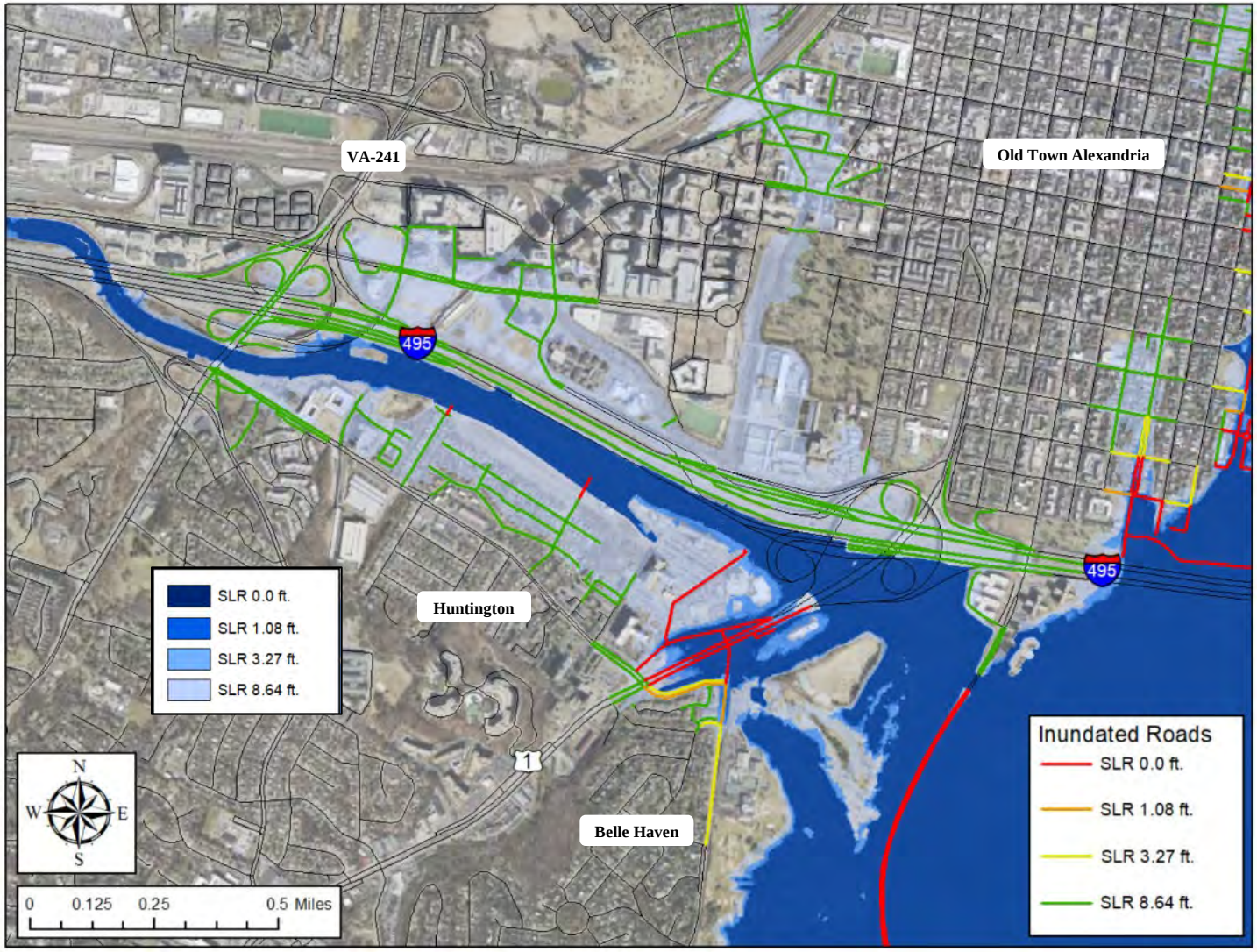

Figure 5.6: I-95/I-495 Corridor between Telegraph Road (VA-241) and the Potomac River, 100 year. Road inundation caused by a 100-year coastal storm under four sea level rise scenarios.

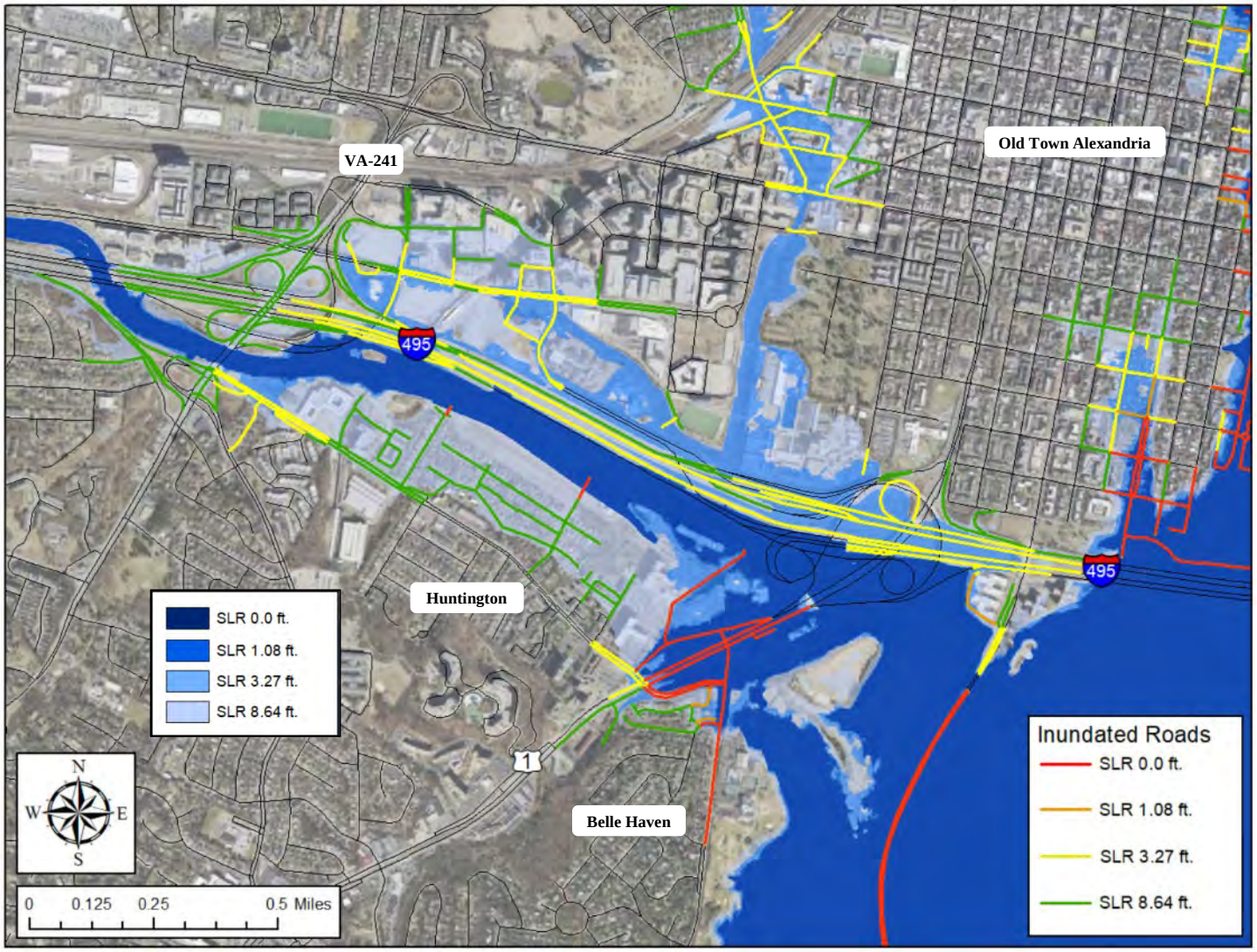

Figure 5.7: I-95/I-495 Corridor between Telegraph Road (VA-241) and the Potomac River, 1000 year. Road inundation caused by a 1000-year coastal storm under four sea level rise scenarios.

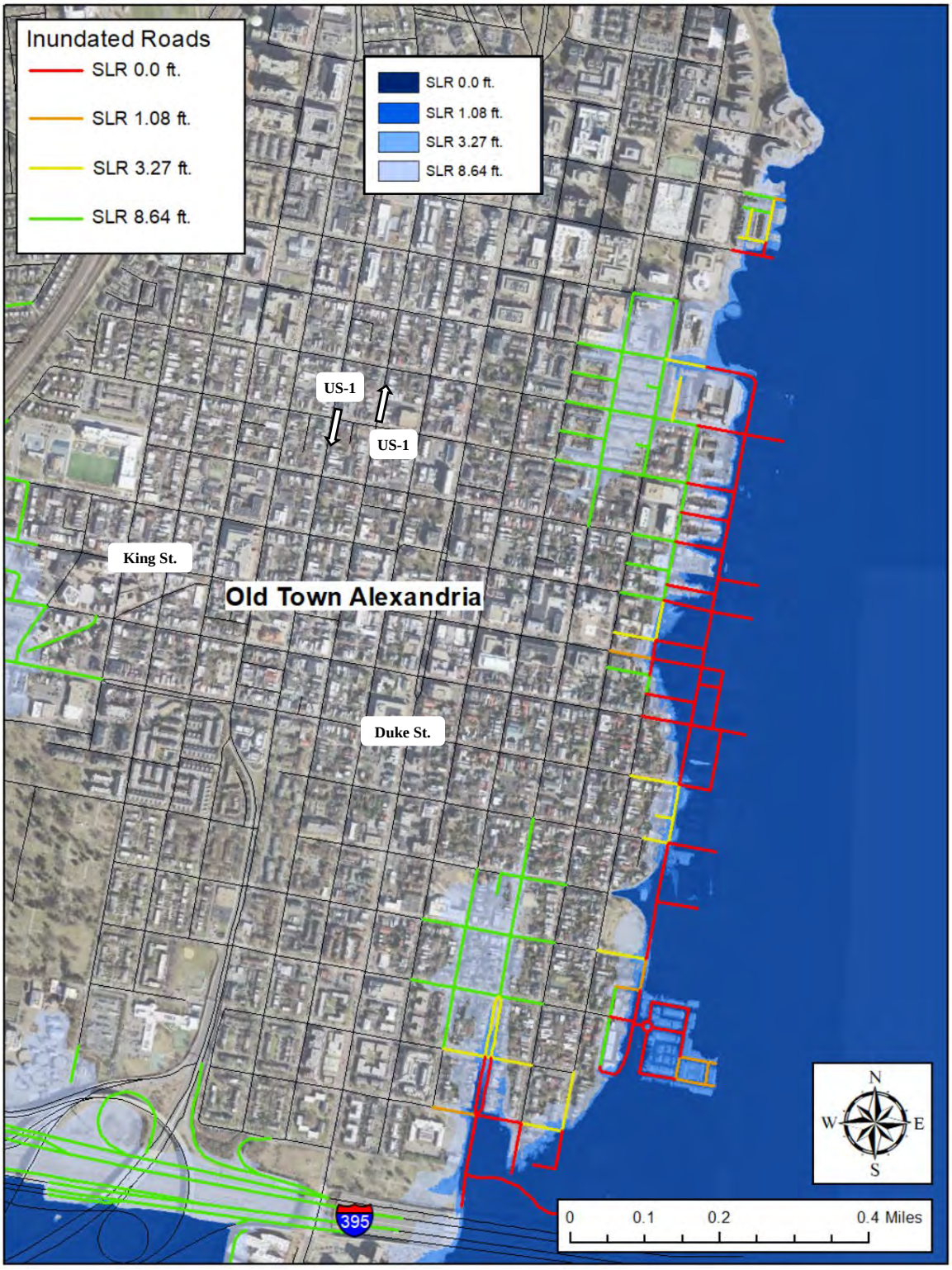

Figure 5.8: Old Town Alexandria, 100 year. Road inundation caused by a 100-year coastal storm under four sea level rise scenarios.

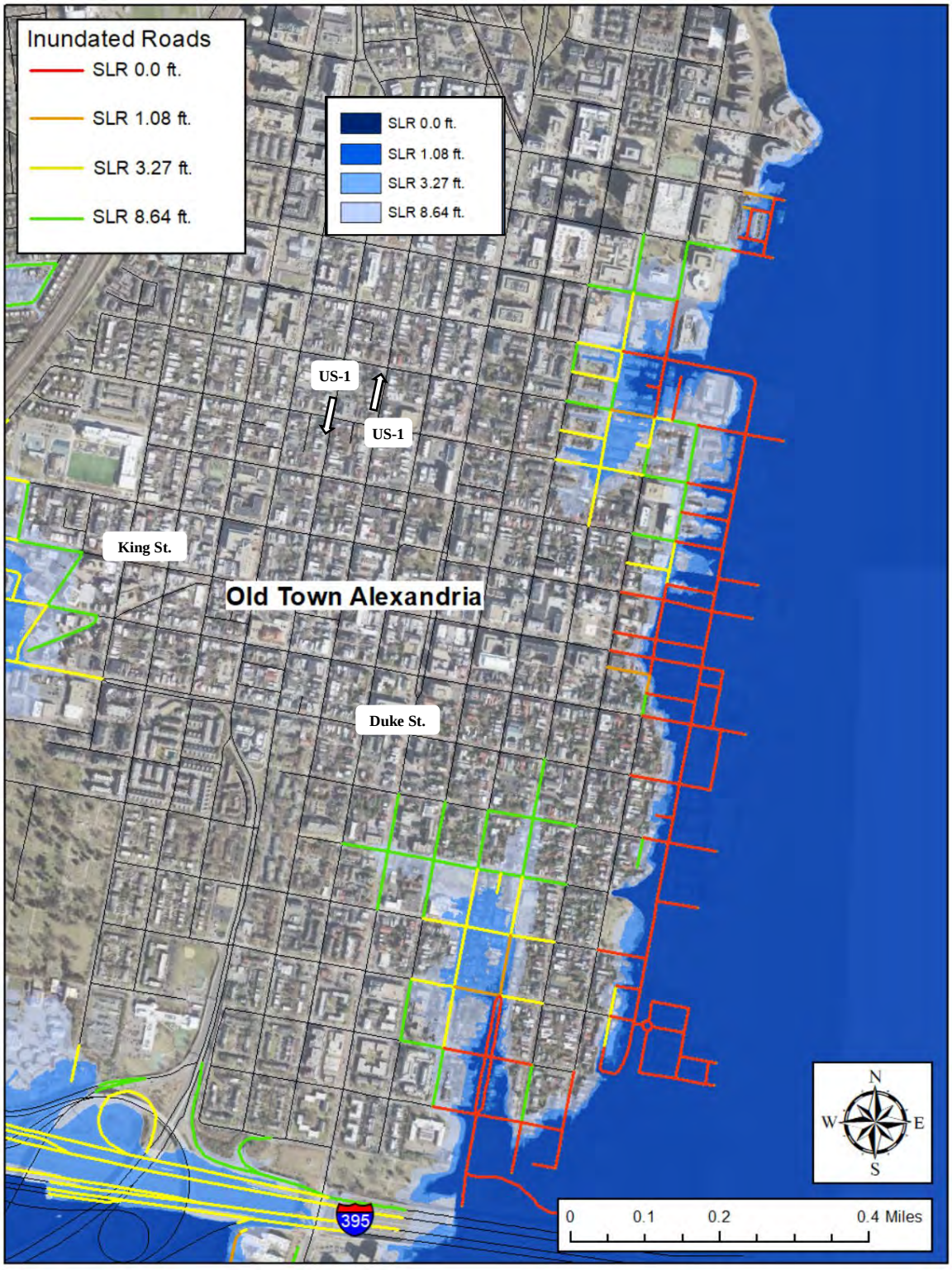

Figure 5.9: Old Town Alexandria, 1000 year. Road inundation caused by a 1000-year coastal storm under four sea level rise scenarios.

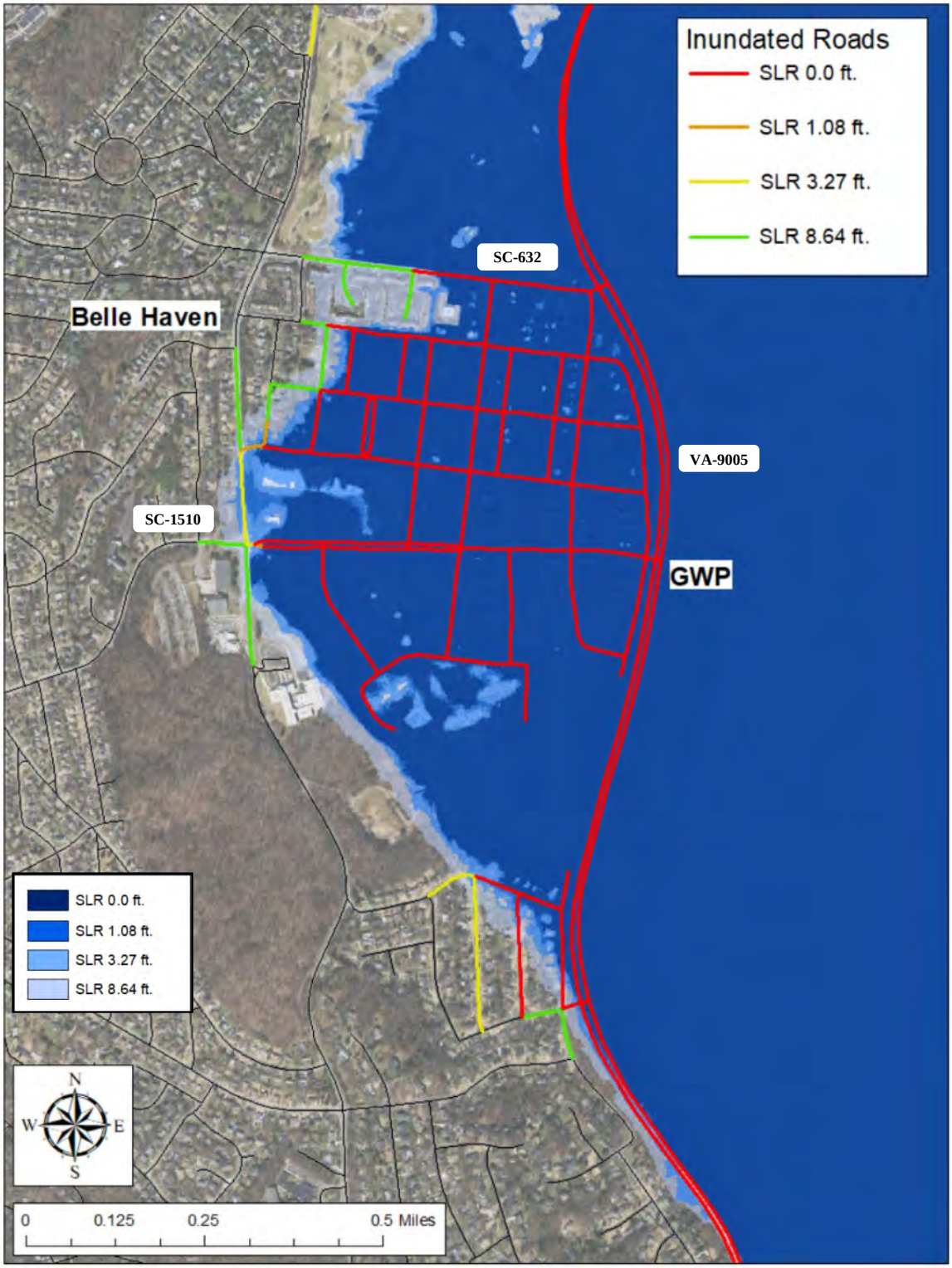

Figure 5.10: Belle Haven, 100 year. Road inundation caused by a 100-year coastal storm under four sea level rise scenarios.

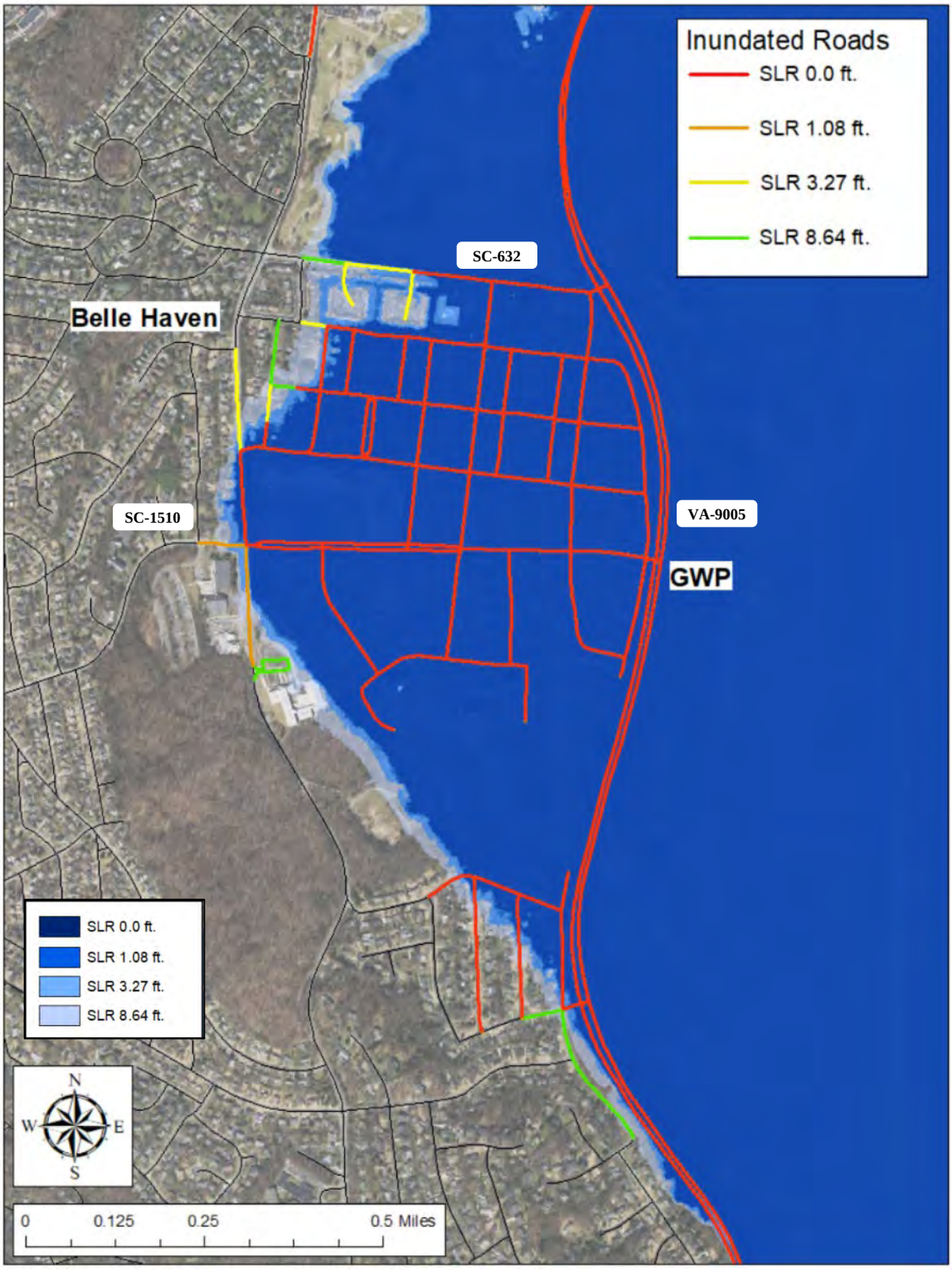

Figure 5.11: Belle Haven, 1000 year. Road inundation caused by a 1000-year coastal storm under four sea level rise scenarios.

Benefits of MWDC CSRM Alternatives

The MWDC CSRM Feasibility Study alternatives considered an array of alternatives that were designed to protect specific areas from coastal flooding. These areas included Ronald Reagan Washington National Airport, the Arlington Water Pollution Control Plant (AWPCP), Arlandria, Old Town Alexandria, and Belle Haven. Over the course of the planning study, three of these alternatives were eliminated. The tentatively selected plan (TSP) includes the AWPCP and Belle Haven alternatives. The potential for each of these alternatives to mitigate reductions in traffic capacity is considered here. However, it should be noted that these alternatives were not designed to achieve reductions in traffic capacity and their benefits are relatively minor.

Benefits of the AWPCP and Belle Haven alternatives are summarized in Table 5.4, which reports the change in percent reduction in traffic capacity realized under each alternative and each sea level rise and coastal storm scenario. Given a 100-year coastal storm, AWPCP would have no effect on traffic capacity without more than a 1.08 foot increase in sea level. Given increases in sea level between 1.08 and 3.93 feet, AWPCP would reduce the percent change in traffic capacity by as much as 0.288%. That is equivalent to a 4.8% reduction in the percent reduction in traffic capacity. These benefits diminish as sea level increases from 3.93 feet to 8.64 feet. Given an 8.64 foot increase in sea level, the AWPCP alternative would provide no benefits in terms of reducing flood impacts on traffic capacity. In terms of mitigating impacts of a 100-year coastal storm on traffic capacity, the Belle Haven alternative offers more than twice the benefits of AWPCP over the first few feet of sea level rise, but these benefits diminish given higher levels of sea level rise and higher coastal storm severities.

SLR Scenario	**Sea Level Change** (ft)	**Arlington Water Pollution Control Plant (AWPCP)**		**Belle Haven**	
		100 Year	**1000 Year**	**100 Year**	**1000 Year**
1	0.00	-	-	-	-
2	0.67	-	-0.425 (6.9%)	-0.332 (7.8%)	-0.503 (8.2%)
3	1.08	-	-0.425 (6.8%)	-0.332 (7.2%)	-
4	1.75	-0.136 (2.7%)	-0.425 (6.6%)	-0.454 (8.9%)	-
5	3.27	-0.193 (3.3%)	-	-0.503 (8.7%)	-
6	3.93	-0.288 (4.8%)	-	-0.503 (8.3%)	-
7	8.64	-	-	-	-

Table 5.4: Benefit of AWPCP and Belle Haven alternatives in terms of reducing impacts on traffic capacity. The absolute change in percent reduction in traffic capacity is shown for each alternative and each sea level rise and coastal storm scenario. The change is shown as a percentage of percent reduction in traffic capacity under the No Action alternative.

Appendix: Traffic Capacity Network Analysis: Mathematical Summary

A directed graph (digraph) $D(V, E)$ consists of a set of nodes V with one node distinguished as a *source node* and another as a *sink node* while all other nodes are said to be *intermediate nodes*, a set of arcs $E \subseteq V \times V$, and a function $c: E \to \mathbb{N}$ called a *capacity function*. Given two nodes $u, v \in V$ the arcs (u, v) and (v, u) are distinct as the former is the arc from u to v and the latter is the arc from v to u. For each arc $e = (u, v) \in V \times V = E$, $c(e)$ is the capacity of arc e or $c(u, v)$ is the capacity of the arc (u, v). For any $v \in V$ the *out-neighborhood* $N^+(v) = \{u \in V | (v, u) \in E\}$ and the *in-neighborhood* $N^-(v) = \{u \in V | (u, v) \in E\}$. A flow network can be intuitively thought of as a model for how traffic flows along the digraph from the source to the sink such that the flow along any arc never exceeds the capacity of that arc and that the flow of traffic into and out of any intermediate node are exactly the same. Technically, a network flow is a function $f: E \to \mathbb{N}$ such that for each $(u, v) \in E$ we have $0 \leq f(u, v) \leq c(u, v)$ and $f^+(v) = f^-(v)$ for all intermediate nodes v where:

$$f^+(v) = \sum_{u \in N^+(v)} f(v, u)$$
$$f^-(v) = \sum_{u \in N^-(v)} f(u, v).$$

Consider the example illustrated in Figure 5.A1. This network has source u and sink v and each arc is labeled with a pair of numbers, the capacity of the arc and the flow along that arc. Observe that the flow never exceeds the capacity and that for each intermediate node, the flow into a node is equal to the flow out of the node and that the net flow out of the source is the same as the net flow into the sink, 3. So we say the flow for this network is 3.

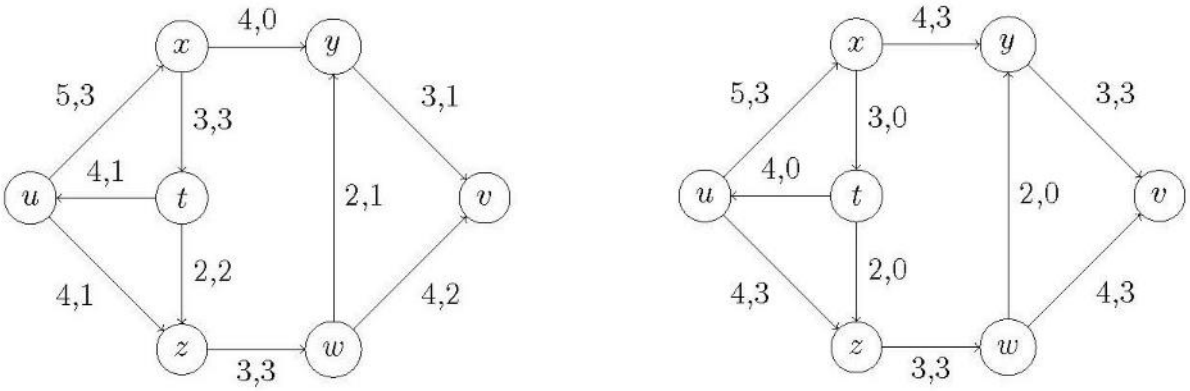

Figure 5.A1: Illustration of Network Flow (a) A flow from u to v. (b) A maximum flow from u to v.

A natural question arises: what is the maximum amount of flow from the source to the sink for this network? It turns out that the maximal flow for our network in Figure 5.A1 is 6 and a flow that achieves this maximum is illustrated in Figure 5.A2. The question of finding maximal flows was answered in general by developing the Ford-Fulkerson algorithm. The algorithm will always find the maximal flow for a given network from a defined source to a defined sink.

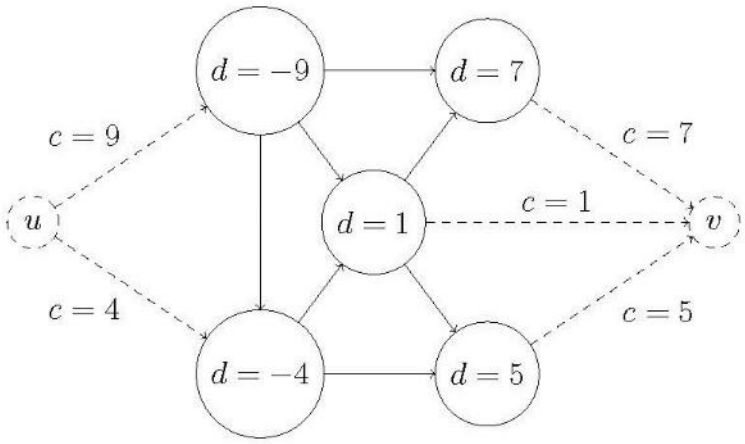

Figure 5.A2: Transformation of a circulation problem into a maximum flow problem.

We want to understand how traffic flow is interrupted by flooding, so using the GIS data along with the inundation lists, we derive a flow network for the road system spanning the 12 planning areas and calculate the maximum flow. Then using the inundation data, we remove flooded road segments from our digraph and recompute the maximal flow for the altered network. Then we assume that the percentage change in maximal flow represents the percentage change in traffic capacity.

We begin with the GIS data described above to construct a digraph $D(V, E)$ that models the road network spanning the 12 planning areas under consideration. Each node $v \in V$ of our digraph is either an intersection of two or more roads or a terminal point for a road. Each arc $(u, v) \in E$ represents a road segment and indicates the traffic flow from u to v. If a road segment was labeled as two-way between nodes u and v, we added an arcs (u, v) and (v, u) to our digraph. If a road segment was labeled as one-way between nodes u and v we added either (u, v) or (v, u) depending upon the direction of travel for the road. Thus we ended up with a digraph $D(V, E)$ with $|V| = 13{,}916$ and $|E| = 16{,}145$. We only wanted to analyze the largest contiguous piece of this network, so we eliminated any components that were not connected to the largest network. See Figure 1 (above) for a visual representation.

In order to complete the flow network, we need to determine the arc capacities and define a source and sink. For each arc we set the capacity equal to the ADT, but we do not have a natural way of defining a source or sink for our traffic model. When we want to consider flow in a network without special nodes, this is known as a *circulation problem*. We solve the circulation problem by adding a source node and a sink node to the digraph and connect them to the digraph with fixed capacities creating an augmented flow network that can be analyzed with the Ford-

Fulkerson algorithm. So for each $v \in V$ we compute the *demand* of vertex v, $d(v)$, as $d(v) = c^{-}(v) - c^{+}(v)$.

Now for any node that has $d(v) < 0$, the node has more outgoing capacity than incoming capacity and we call these nodes *semi-sources*. Similarly when $d(v) > 0$, the node has more incoming capacity than outgoing capacity and we call these nodes *semi-sinks*. Then the source node is connected to each semi-source by an arc with capacity equal to the negative of the demand at the semi-source. All semi-sinks are connected by an arc to the sink with capacity equal to the demand at the semi-sink. Figure 4 illustrates this process. Solid nodes and solid arcs are part of the original digraph and the dashed nodes and arcs are added components. We identified 1,014 semi-sources and 1,021 semi-sinks in our digraph and we connected the semi-sources to a single source node and all the semi-sinks to a single sink node. All the other vertices were left unaltered.

With these changes, our circulation problem has been transformed into a maximum flow problem across our network from the source to the sink. Then we apply the Ford-Fulkerson algorithm to the altered network to determine the maximum flow of our traffic network. Then for each flood scenario, we remove the flooded road segments and repeat the analysis to determine the maximum flow for each flooding scenario.

6.0 Wastewater Systems

The planning area contains four wastewater treatment plants that serve populations both within the planning area and other areas within the MWDC region. The Arlington Water Pollution Control Plant (AWPCP) serves the City of Arlington. The AlexRenew wastewater treatment plant (WWTP) serves the City of Alexandria. The Noman M. Cole Wastewater Treatment Plant serves Fairfax County, and the H.L. Mooney Advanced Water Reclamation Facility serves Prince William County. Only AWPCP and AlexRenew are within one or more of the flood footprints for the coastal storm and sea level rise scenarios considered. This study also identified 29 wastewater pumps that are vulnerable to flooding. These are distributed throughout the four counties that border the Potomac River.

The location of various water treatment structures and buildings within AWPCP and the AlexRenew WWTP were obtained from publicly available GIS layers. Many of these structures may be surrounded by barriers or have raised first floor elevations that reduce their vulnerability to flooding. This information is not reflected in those GIS layers. An assessment of those impacts will require accurate information about what inundation depths might jeopardize the ability of these water treatment system components to function as intended. This information was not available for this study and any assessment of the impacts of inundation on the ability to treat wastewater is left to readers who have that information.

In this section of the report, several tables report inundation depths at WWTP components and structures. These depths are taken one meter away from the perimeter of the polygon representing that component or structure. The mean and maximum inundation depths within the perimeter area are reported as is the fraction of perimeter area that is inundated. Estimates of maximum and minimum flood depth should be interpreted carefully. For example, a maximum water depth may appear to be high, but if only a small fraction of perimeter area is inundated, the impacts may be limited. Thus, the estimate of mean water depth and percent of perimeter area inundated should both be considered. Within a given perimeter area, both the maximum water depth and fraction of perimeter area will increase monotonically with increases in coastal storm severity and sea level rise. However, mean water depths will not increase monotonically because the average depth of inundation was calculated only over the inundated portions of the perimeter. Therefore, as a larger area becomes inundated, the mean may decrease if the inundation depths over the newly inundated portions of the perimeter are shallower. Therefore, in the tables that follow, one will occasionally observe that higher sea levels cause decreases in mean inundation depths. This simply reflects the change in land surface elevation over the inundated perimeter area.

The digital elevation model used to estimate flood inundation depths sometimes reports inaccurate information about the elevation of WWTP components and structures. This is particularly true where tanks were built into the ground and may have been empty at the time that LIDAR elevation data were collected. This resulted in estimates of excessive inundation depths at some components and structures. In an effort to prevent this issue from distorting the severity of flood impacts, inundation depths were estimated at the perimeter of each component or structure. While this strategy was successful at some components or structures, it was not successful at all components or structures. The decision was made to fully report inundation depths as estimated and flag the maximum and mean inundation depths that appeared to be unreasonable. Those results that are believed to be inaccurate have been flagged using red font and their identification numbers are flagged with an asterisk.

Arlington Water Pollution Control Plant (AWPCP)

As with many wastewater treatment plants, AWPCP is located in low lying area and, as a result of its proximity to the tidal region of the Potomac River, it is susceptible to flooding caused by coastal storms and sea level rise. The AWPCP is located on South Glebe Road adjacent to Four Mile Run approximately 0.75 miles upstream of its confluence with the Potomac River. The components of the AWPCP are listed in Table 6.1. A description of the component or structure and an estimate of its value have also been provided where that information was available in the GIS data file. The year of these estimates is not known.

Inundation water depths were estimated at the perimeter of 63 distinct components or structures. Maximum and mean water depths are summarized for 100-year coastal storms in Table 6.2 and for 1000-year coastal storms in Table 6.3. There are ten estimates of inundation water depth that appear questionable. These are highlighted in red and the identification numbers in the first column of the table are marked with an asterisk. While it is likely that these components and structures would still be flooded under these coastal storm and sea-level rise scenarios, the inundation depths may be greatly overstated because LIDAR measurements captured the bottom of the structures rather than the ground elevation at the perimeter of the structure. Figures 6.1 and 6.2 show the extent of the AWPCP inundated under each of the coastal storm and sea level rise scenarios.

The extent of wastewater service disruption in the service area will depend upon the combination of components and structures that are inundated and the depth of inundation. Many of the components and structures at AWPCP are elevated in a way that might protect them from flood damage or from flood service disruption. For example, operational controls may be housed in buildings with elevated first floors or aeration tanks may be surrounded by rims that protect them from up to several feet of flooding. Critical inundation depths for individual components and structures were not available for this study. An assessment of what impacts floods would have in terms of disruption of service should be made in consultation with those who have knowledge of this particular treatment plant.

ID #	Facility Name	Facility Value	Facility Type
1	Dissolved Air Floatation Thickener (DAFT)		Wastewater Treatment
2	Preliminary Treatment Building		Wastewater Treatment
3	New Maintenance Building (NMB)		Operations Building
4	Wet Weather Filtration Facility Building (WWFF)	$ 16,192,436	Wastewater Treatment - High Water Facility
5	Unidentified Facility		-
6	ASE1 Meter Vault		Electrical/Controls
7	East Secondary Services Pump Station (SPSB)		Pump Station
8	ASE 1 Pump Station Electrical Building (DC3)		Electrical/Controls - High Water Facility
9	Secondary Aeration Tanks (SAT) 4, 3, 2, & 1	$ 41,800,000	Wastewater Treatment
10	Secondary Blower Building (SBB)		Wastewater Treatment
11	Flow Equalization Tanks (FEQ1)		Wastewater Treatment
12	Operations and Control Building (OCB)		Operations Building
13	Activated Sludge Effluent Pumping Station 1 (ASE1)	$ 54,276,200	Pump Station
14	West Secondary Services Pump Station (WSPSB) & ASE2		Pump Station/Electrical/Controls
15	Post Aeration Facility (PAF)		Wastewater Treatment
16	Chlorine Contact Tanks (CCT)		Wastewater Treatment
17	Filtration and Disinfection Facility (FADF)	$ 49,676,600	Wastewater Treatment
18	Methanol Feed Facility (MFF)	$ 53,086,500	Wastewater Treatment
19	Standby Generator Facility (SGF)	$ 5,350,781	Back-up Electric Generation
20	Primary Gravity Thickener Building		Wastewater Treatment
21	Sludge Storage Tanks 06-2		Wastewater Treatment
22	Sludge Storage Tanks 06-1		Wastewater Treatment
23	Unidentified Facility		-
24	Flow Equalization Pump Station		Pump Station
25	Primary Effluent Pump Station (PEPS)		Pump Station
26	Four Mile Run Lift Station		Lift Station
27	Flow Equalization Tanks (FEQ3)		Wastewater Treatment
28	Flow Equalization Tanks (FEQ2)		Wastewater Treatment
29	North Ferric/Odor Control Facility	$ 6,793,800	Wastewater Treatment
30	Secondary Aeration Tanks (SAT) 6 & 5	$ 20,900,000	Wastewater Treatment
31	Unidentified Facility		-
32	Distribution Center Building		Back-up Electric Generation
33	Unidentified Facility		-
34	Surface Waste Pump Station (SWPS)		Pump Station
35	Foam Collection Pump Station (FCPS)	$ 7,052,100	Pump Station
36	Chemical Storage?		Chemical Storage
40	Electrical Distribution Center Building 5 (DCB5)	$ 824,230	Electrical/Controls
41	South Ferric Facility (SFF)		Wastewater Treatment
42	Advanced Backwash Building (ABWB)		Wastewater Treatment
43	Distribution Center Building		Back-up Electric Generation
44	Four Mile Run Intercept		Wastewater Treatment
45	Secondary Clarifier 9 (SCL9)		Wastewater Treatment
46	Secondary Clarifier 8 (SCL8)		Wastewater Treatment
47	Secondary Clarifier 7 (SCL7)		Wastewater Treatment
48	Secondary Clarifier 6 (SCL6)		Wastewater Treatment
49	Secondary Clarifier 5 (SCL5)		Wastewater Treatment
50	Secondary Clarifier 2 (SCL2)		Wastewater Treatment
51	Secondary Clarifier 4 (SCL4)		Wastewater Treatment
52	Secondary Clarifier 1 (SCL1)		Wastewater Treatment
53	Secondary Clarifier 3 (SCL3)		Wastewater Treatment
54	Plant Effluent Water Facility (PEWF)		Wastewater Treatment
56	Primary Clarifiers 1-10 (PCL)	$ 12,712,000	Wastewater Treatment
57	PTB Backup Flow Distribution Structure		Wastewater Treatment
58	Potomac Interceptor Backup Structure (PTB)		Wastewater Treatment
60	Potomac Yard Pump Station		Pump Station
61	East Mixed Liquor Flow	$ 5,250,000	Wastewater Treatment
62	West Mixed Liquor Flow	$ 5,250,000	Wastewater Treatment
63	Primary Effluent Flume	$ 56,600,000	Wastewater Treatment

Table 6.1: Components and Structures of AWPCP.

ID#	Facility Description	S1 (0.0 ft.)			S2 (0.67 ft.)			S3 (1.08 ft.)			S4 (1.75 ft.)			S5 (3.23 ft.)			S6 (3.93 ft.)			S7 (8.64 ft.)		
		Max. (ft.)	Avg. (ft.)	Area (%)	Max. (ft.)	Avg. (ft.)	Area (%)	Max. (ft.)	Avg. (ft.)	Area (%)	Max. (ft.)	Avg. (ft.)	Area (%)	Max. (ft.)	Avg. (ft.)	Area (%)	Max. (ft.)	Avg. (ft.)	Area (%)	Max. (ft.)	Avg. (ft.)	Area (%)
6	ASE1 Meter Vault	0.1	0.1	11.3	0.2	0.1	19.8	0.6	0.4	33.9	1.2	0.8	45.2	2.5	1.4	99.0	3.1	2.0	99.0	7.4	6.3	99.0
35	Foam Collection PS (FCPS)	0.0	0.0	0.0	0.1	0.1	1.6	0.8	0.3	47.6	1.4	0.6	88.9	2.7	1.9	98.5	3.3	2.5	98.5	7.6	6.8	98.5
31	Unidentified Facility	0.0	0.0	0.0	0.0	0.0	0.0	6.8	3.4	90.8	7.4	3.7	97.3	8.7	4.8	100.0	9.3	5.4	103.8	13.6	9.7	100.0
30*	Secondary Aeration Tank 5-6	0.0	0.0	0.0	0.0	0.0	0.0	17.4	7.8	67.4	18.0	7.9	71.7	19.3	7.3	93.2	19.9	7.4	99.1	24.2	11.7	99.1
53	Secondary Clarifier 3 (SCL3)	0.0	0.0	0.0	0.0	0.0	0.0	1.2	0.4	56.7	1.8	0.7	98.4	3.1	2.0	100.0	3.7	2.6	100.0	8.0	6.9	100.0
52	Secondary Clarifier 1 (SCL1)	0.0	0.0	0.0	0.0	0.0	0.0	1.2	0.5	40.1	1.8	0.7	84.1	3.1	1.9	97.4	3.7	2.5	97.4	8.0	6.8	97.4
9*	Secondary Aeration Tank 1-4	0.0	0.0	0.0	0.0	0.0	0.0	23.3	7.1	39.8	23.9	7.1	43.4	25.2	4.0	98.3	25.8	4.5	100.0	30.1	8.8	100.0
62*	West Mixed Liquor Flow	0.0	0.0	0.0	0.0	0.0	0.0	23.3	12.4	36.0	23.9	9.7	48.5	25.2	6.4	89.2	25.8	6.5	95.5	30.1	10.8	95.5
61	East Mixed Liquor Flow	0.0	0.0	0.0	0.0	0.0	0.0	2.2	1.4	13.8	2.8	0.7	55.1	4.1	1.6	98.1	4.7	2.2	98.1	9.0	6.5	98.1
14	West Secondary Serv. PS, ASE2	0.0	0.0	0.0	0.0	0.0	0.0	0.0	0.0	0.0	0.5	0.3	2.3	6.7	1.5	68.0	7.3	1.8	80.9	11.6	5.7	99.6
48	Secondary Clarifier 6 (SCL6)	0.0	0.0	0.0	0.0	0.0	0.0	0.0	0.0	0.0	2.1	0.7	88.3	3.4	1.9	100.0	4.0	2.5	100.0	8.3	6.8	100.0
50	Secondary Clarifier 2 (SCL2)	0.0	0.0	0.0	0.0	0.0	0.0	0.0	0.0	0.0	1.9	0.7	82.0	3.2	1.8	104.1	3.8	2.4	100.0	8.1	6.7	100.0
51	Secondary Clarifier 4 (SCL4)	0.0	0.0	0.0	0.0	0.0	0.0	0.0	0.0	0.0	3.4	0.7	81.9	4.7	1.9	92.2	5.3	2.5	92.9	9.6	6.8	92.9
34	Surface Waste PS (SWPS)	0.0	0.0	0.0	0.0	0.0	0.0	0.0	0.0	0.0	1.5	0.4	78.6	2.8	1.6	100.0	3.4	2.2	100.0	7.7	6.5	100.0
49	Secondary Clarifier 5 (SCL5)	0.0	0.0	0.0	0.0	0.0	0.0	0.0	0.0	0.0	2.1	0.8	78.0	3.4	1.8	99.2	4.0	2.4	100.0	8.3	6.7	100.0
41	South Ferric Facility (SFF)	0.0	0.0	0.0	0.0	0.0	0.0	0.0	0.0	0.0	0.8	0.4	65.7	2.1	1.6	84.0	2.7	2.2	84.0	7.0	6.5	84.0
28	Flow Equalization Tanks (FEQ2)	0.0	0.0	0.0	0.0	0.0	0.0	0.0	0.0	0.0	4.8	1.7	49.2	6.1	2.2	78.6	6.7	2.6	87.5	11.0	6.5	99.2
7	East Secondary Serv. PS (SPSB)	0.0	0.0	0.0	0.0	0.0	0.0	0.0	0.0	0.0	0.9	0.4	25.7	2.2	1.0	86.9	2.8	1.5	97.9	7.1	5.7	100.0
12	Operation & Control Bldg (OCB)	0.0	0.0	0.0	0.0	0.0	0.0	0.0	0.0	0.0	0.7	0.3	22.6	2.0	1.1	70.5	2.6	1.7	72.6	6.9	5.5	89.0
19	Standby Generator Fac. (SGF)	0.0	0.0	0.0	0.0	0.0	0.0	0.0	0.0	0.0	0.7	0.4	16.9	2.0	0.9	78.2	2.6	1.4	86.7	6.9	5.5	98.3
43	Distribution Center Building	0.0	0.0	0.0	0.0	0.0	0.0	0.0	0.0	0.0	0.1	0.1	13.9	1.4	0.8	63.9	2.0	1.4	69.5	6.3	5.4	86.2
27	Flow Equalization Tanks (FEQ3)	0.0	0.0	0.0	0.0	0.0	0.0	0.0	0.0	0.0	0.2	0.1	2.1	1.5	0.8	40.6	2.1	0.9	71.6	6.4	4.8	96.4
47*	Secondary Clarifier 7 (SCL7)	0.0	0.0	0.0	0.0	0.0	0.0	0.0	0.0	0.0	0.0	0.0	0.0	20.3	8.0	86.9	20.9	7.7	97.8	25.2	11.8	100.0
46*	Secondary Clarifier 8 (SCL8)	0.0	0.0	0.0	0.0	0.0	0.0	0.0	0.0	0.0	0.0	0.0	0.0	17.1	4.4	85.5	17.7	4.7	91.6	22.0	8.8	95.7
13	Activ. Sludge Eff. PS 1 (ASE1)	0.0	0.0	0.0	0.0	0.0	0.0	0.0	0.0	0.0	0.0	0.0	0.0	0.7	0.4	79.2	1.3	0.9	94.8	5.6	5.2	96.1
32	Distribution Center Building	0.0	0.0	0.0	0.0	0.0	0.0	0.0	0.0	0.0	0.0	0.0	0.0	0.8	0.5	53.4	1.4	0.7	84.3	5.7	4.9	95.6
8	ASE 1 PS Electrical Bldg (DC3)	0.0	0.0	0.0	0.0	0.0	0.0	0.0	0.0	0.0	0.0	0.0	0.0	1.0	0.6	51.3	1.6	0.9	72.6	5.9	4.7	97.4
10	Secondary Blower Bldg (SBB)	0.0	0.0	0.0	0.0	0.0	0.0	0.0	0.0	0.0	0.0	0.0	0.0	1.4	0.7	40.1	2.0	1.0	61.7	6.3	4.5	98.2
36	Chemical Storage (?)	0.0	0.0	0.0	0.0	0.0	0.0	0.0	0.0	0.0	0.0	0.0	0.0	0.9	0.4	35.1	1.5	0.7	79.0	5.8	5.0	79.0
42*	Adv. Backwash Bldg (ABWB)	0.0	0.0	0.0	0.0	0.0	0.0	0.0	0.0	0.0	0.0	0.0	0.0	10.3	6.7	25.1	10.9	7.0	26.1	15.2	4.6	97.1
5	Unidentified Facility	0.0	0.0	0.0	0.0	0.0	0.0	0.0	0.0	0.0	0.0	0.0	0.0	0.8	0.3	21.2	1.4	0.6	48.3	5.7	4.0	100.0
45	Secondary Clarifier 9 (SCL9)	0.0	0.0	0.0	0.0	0.0	0.0	0.0	0.0	0.0	0.0	0.0	0.0	1.2	0.7	21.1	1.8	1.0	32.6	6.1	4.7	42.1
29	N. Ferric/Odor Control Facility	0.0	0.0	0.0	0.0	0.0	0.0	0.0	0.0	0.0	0.0	0.0	0.0	0.2	0.1	15.2	0.9	0.4	94.6	5.2	4.7	94.6
33	Unidentified Facility	0.0	0.0	0.0	0.0	0.0	0.0	0.0	0.0	0.0	0.0	0.0	0.0	0.1	0.0	12.4	0.7	0.4	43.4	5.0	4.0	93.1
4*	Wet Weather Filtr. Fac. (WWFF)	0.0	0.0	0.0	0.0	0.0	0.0	0.0	0.0	0.0	0.0	0.0	0.0	9.2	6.3	3.6	9.8	3.5	43.5	14.1	4.4	100.0
17*	Filt. & Disinfection Fac. (FADF)	0.0	0.0	0.0	0.0	0.0	0.0	0.0	0.0	0.0	0.0	0.0	0.0	0.0	0.0	0.0	10.5	4.1	31.7	14.8	4.6	94.4
63	Primary Effluent Flume	0.0	0.0	0.0	0.0	0.0	0.0	0.0	0.0	0.0	0.0	0.0	0.0	0.0	0.0	0.0	0.6	0.2	25.2	4.9	4.2	100.0
40	Elect. Dist. Ctr. Bldg. 5 (DCB5)	0.0	0.0	0.0	0.0	0.0	0.0	0.0	0.0	0.0	0.0	0.0	0.0	0.0	0.0	0.0	5.3	2.2	13.6	9.6	3.5	81.8
18	Methanol Feed Facility (MFF)	0.0	0.0	0.0	0.0	0.0	0.0	0.0	0.0	0.0	0.0	0.0	0.0	0.0	0.0	0.0	0.0	0.0	0.0	4.2	2.3	94.3
15	Post Aeration Facility (PAF)	0.0	0.0	0.0	0.0	0.0	0.0	0.0	0.0	0.0	0.0	0.0	0.0	0.0	0.0	0.0	0.0	0.0	0.0	4.1	2.3	97.7
57*	PTB Backup Flow Dist. Struct.	0.0	0.0	0.0	0.0	0.0	0.0	0.0	0.0	0.0	0.0	0.0	0.0	0.0	0.0	0.0	0.0	0.0	0.0	13.9	10.4	100.0
23	Unidentified Facility	0.0	0.0	0.0	0.0	0.0	0.0	0.0	0.0	0.0	0.0	0.0	0.0	0.0	0.0	0.0	0.0	0.0	0.0	2.2	1.3	51.9
16	Chlorine Contact Tanks (CCT)	0.0	0.0	0.0	0.0	0.0	0.0	0.0	0.0	0.0	0.0	0.0	0.0	0.0	0.0	0.0	0.0	0.0	0.0	4.3	2.8	99.8
2	Preliminary Treatment Building	0.0	0.0	0.0	0.0	0.0	0.0	0.0	0.0	0.0	0.0	0.0	0.0	0.0	0.0	0.0	0.0	0.0	0.0	1.7	1.1	23.1
25	Primary Effluent PS (PEPS)	0.0	0.0	0.0	0.0	0.0	0.0	0.0	0.0	0.0	0.0	0.0	0.0	0.0	0.0	0.0	0.0	0.0	0.0	4.0	2.8	97.6
24	Flow Equalization Pump Station	0.0	0.0	0.0	0.0	0.0	0.0	0.0	0.0	0.0	0.0	0.0	0.0	0.0	0.0	0.0	0.0	0.0	0.0	3.3	3.0	96.2
56	Primary Clarifiers 1-10 (PCL)	0.0	0.0	0.0	0.0	0.0	0.0	0.0	0.0	0.0	0.0	0.0	0.0	0.0	0.0	0.0	0.0	0.0	0.0	9.8	3.2	81.9
54	Plant Eff. Water Fac. (PEWF)	0.0	0.0	0.0	0.0	0.0	0.0	0.0	0.0	0.0	0.0	0.0	0.0	0.0	0.0	0.0	0.0	0.0	0.0	3.5	2.5	88.9
11	Flow Equalization Tanks (FEQ1)	0.0	0.0	0.0	0.0	0.0	0.0	0.0	0.0	0.0	0.0	0.0	0.0	0.0	0.0	0.0	0.0	0.0	0.0	2.8	1.5	50.8
58*	PTB Structure (PTB)	0.0	0.0	0.0	0.0	0.0	0.0	0.0	0.0	0.0	0.0	0.0	0.0	0.0	0.0	0.0	0.0	0.0	0.0	11.8	5.5	40.9
1	Diss. Air Float. Thick. (DAFT)	0.0	0.0	0.0	0.0	0.0	0.0	0.0	0.0	0.0	0.0	0.0	0.0	0.0	0.0	0.0	0.0	0.0	0.0	0.0	0.0	0.0
20	Prim. Gravity Thickener Bldg.	0.0	0.0	0.0	0.0	0.0	0.0	0.0	0.0	0.0	0.0	0.0	0.0	0.0	0.0	0.0	0.0	0.0	0.0	0.0	0.0	0.0
21	Sludge Storage Tanks 06-2	0.0	0.0	0.0	0.0	0.0	0.0	0.0	0.0	0.0	0.0	0.0	0.0	0.0	0.0	0.0	0.0	0.0	0.0	0.0	0.0	0.0
3	New Maint. Building (NMB)	0.0	0.0	0.0	0.0	0.0	0.0	0.0	0.0	0.0	0.0	0.0	0.0	0.0	0.0	0.0	0.0	0.0	0.0	0.0	0.0	0.0
22	Sludge Storage Tanks 06-1	0.0	0.0	0.0	0.0	0.0	0.0	0.0	0.0	0.0	0.0	0.0	0.0	0.0	0.0	0.0	0.0	0.0	0.0	0.0	0.0	0.0
26	Four Mile Run Lift Station	0.0	0.0	0.0	0.0	0.0	0.0	0.0	0.0	0.0	0.0	0.0	0.0	0.0	0.0	0.0	0.0	0.0	0.0	0.0	0.0	0.0
44	Four Mile Run Intercept	0.0	0.0	0.0	0.0	0.0	0.0	0.0	0.0	0.0	0.0	0.0	0.0	0.0	0.0	0.0	0.0	0.0	0.0	0.0	0.0	0.0
60	Potomac Yard PS	0.0	0.0	0.0	0.0	0.0	0.0	0.0	0.0	0.0	0.0	0.0	0.0	0.0	0.0	0.0	0.0	0.0	0.0	0.0	0.0	0.0

Table 6.2: Inundation by a 100-year Coastal Storm under Seven Sea-Level Rise Scenarios.

ID#	Facility Description	S1 (0.0 ft.)			S2 (0.67 ft.)			S3 (1.08 ft.)			S4 (1.75 ft.)			S5 (3.23 ft.)			S6 (3.93 ft.)			S7 (8.64 ft.)		
		Max. (ft.)	Avg. (ft.)	Area (%)	Max. (ft.)	Avg. (ft.)	Area (%)	Max. (ft.)	Avg. (ft.)	Area (%)	Max. (ft.)	Avg. (ft.)	Area (%)	Max. (ft.)	Avg. (ft.)	Area (%)	Max. (ft.)	Avg. (ft.)	Area (%)	Max. (ft.)	Avg. (ft.)	Area (%)
6	ASE1 Meter Vault	3.1	2.0	99.0	3.2	2.1	99.0	3.6	2.5	99.0	4.2	3.1	99.0	5.6	4.5	35.0	6.2	5.1	99.0	10.4	9.3	99.0
35	Foam Collection PS (FCPS)	3.3	2.5	98.5	3.4	2.6	98.5	3.8	3.0	98.5	4.4	3.6	98.5	5.8	5.0	62.0	6.4	5.6	98.5	10.6	9.8	98.5
31	Unidentified Facility	9.3	5.4	100.0	9.4	5.5	100.0	9.8	5.9	100.0	10.4	6.5	100.0	11.8	7.9	32.0	12.4	8.5	100.0	16.6	12.7	100.0
30*	Secondary Aeration Tank 5-6	19.9	7.4	99.1	20.0	7.5	99.1	20.4	7.9	99.1	21.0	8.5	99.1	22.4	9.9	253.0	23.0	10.5	99.1	27.2	14.7	99.1
53	Secondary Clarifier 3 (SCL3)	3.7	2.6	100.0	3.8	2.7	100.0	4.2	3.1	100.0	4.8	3.7	100.0	6.2	5.1	129.0	6.8	5.7	100.0	11.0	9.9	100.0
52	Secondary Clarifier 1 (SCL1)	3.7	2.5	97.4	3.8	2.6	97.4	4.2	3.0	97.4	4.8	3.6	97.4	6.2	5.0	124.0	6.8	5.6	97.4	11.0	9.8	97.4
9*	Secondary Aeration Tank 1-4	25.8	4.5	100.0	25.9	4.6	100.0	26.3	5.0	100.0	26.9	5.6	100.0	28.3	7.0	444.0	28.9	7.6	100.0	33.1	11.8	100.0
62*	West Mixed Liquor Flow	25.8	6.5	95.5	25.9	6.6	95.5	26.3	7.0	95.5	26.9	7.6	95.5	28.3	9.0	61.0	28.9	9.6	95.5	33.1	13.8	95.5
61	East Mixed Liquor Flow	4.7	2.2	98.1	4.8	2.3	98.1	5.2	2.7	98.1	5.8	3.3	98.1	7.2	4.7	57.0	7.8	5.3	98.1	12.0	9.5	98.1
14	West Secondary Serv. PS, ASE2	7.3	1.8	80.9	7.4	1.9	83.2	7.8	2.0	96.1	8.4	2.5	99.6	9.8	3.9	85.0	10.4	4.5	99.6	14.6	8.7	99.6
48	Secondary Clarifier 6 (SCL6)	4.0	2.5	100.0	4.1	2.6	100.0	4.5	3.0	100.0	5.1	3.6	100.0	6.5	5.0	128.0	7.1	5.6	100.0	11.3	9.8	100.0
50	Secondary Clarifier 2 (SCL2)	3.8	2.4	100.0	3.9	2.5	100.0	4.3	2.9	100.0	4.9	3.5	100.0	6.3	4.9	132.0	6.9	5.5	100.0	11.1	9.7	100.0
51	Secondary Clarifier 4 (SCL4)	5.3	2.5	92.9	5.4	2.6	92.9	5.8	3.0	92.9	6.4	3.6	92.9	7.8	5.0	118.0	8.4	5.6	92.9	12.6	9.8	92.9
34	Surface Waste PS (SWPS)	3.4	2.2	100.0	3.5	2.3	100.0	3.9	2.7	100.0	4.5	3.3	100.0	5.9	4.7	48.0	6.5	5.3	100.0	10.7	9.5	100.0
49	Secondary Clarifier 5 (SCL5)	4.0	2.4	100.0	4.1	2.5	100.0	4.5	2.9	100.0	5.1	3.5	100.0	6.5	4.9	127.0	7.1	5.5	100.0	11.3	9.7	100.0
41	South Ferric Facility (SFF)	2.7	2.2	84.0	2.8	2.3	84.0	3.2	2.7	84.0	3.8	3.3	84.0	5.2	4.7	46.0	5.8	5.3	84.0	10.0	9.5	84.0
28	Flow Equalization Tanks (FEQ2)	6.7	2.6	87.5	6.8	2.6	88.2	7.2	2.9	92.3	7.8	3.3	99.2	9.2	4.7	145.0	9.8	5.3	99.2	14.0	9.5	99.2
7	East Secondary Serv. PS (SPSB)	2.8	1.5	97.9	2.9	1.5	99.2	3.3	1.9	99.2	3.9	2.5	100.0	5.3	3.9	82.0	5.9	4.5	100.0	10.1	8.7	100.0
12	Operation & Control Bldg (OCB)	2.6	1.7	72.6	2.7	1.8	72.6	3.1	2.1	75.3	3.7	2.6	79.0	5.1	3.7	168.0	5.7	4.3	89.0	9.9	8.4	90.0
19	Standby Generator Fac. (SGF)	2.6	1.4	86.7	2.7	1.4	91.9	3.1	1.7	98.3	3.7	2.3	98.3	5.1	3.7	93.0	5.7	4.3	98.3	9.9	8.5	98.3
43	Distribution Center Building	2.0	1.4	69.5	2.1	1.2	86.2	2.5	1.6	86.2	3.1	2.2	86.2	4.5	3.6	31.0	5.1	4.2	86.2	9.3	8.4	86.2
27	Flow Equalization Tanks (FEQ3)	2.1	0.9	71.6	2.2	1.0	72.1	2.6	1.3	82.2	3.2	1.6	96.4	4.6	3.0	183.0	5.2	3.6	96.4	9.4	7.8	96.4
47*	Secondary Clarifier 7 (SCL7)	20.9	7.7	97.8	21.0	7.8	98.5	21.4	8.1	99.8	22.0	8.6	100.0	23.4	10.0	148.0	24.0	10.6	100.0	28.2	14.8	100.0
46*	Secondary Clarifier 8 (SCL8)	17.7	4.7	91.6	17.8	4.8	92.3	18.2	5.1	95.0	18.8	5.6	95.7	20.2	7.0	141.0	20.8	7.6	95.7	25.0	11.8	95.7
13	Activ. Sludge Eff. PS 1 (ASE1)	1.3	0.9	94.8	1.4	1.0	94.8	1.8	1.4	96.1	2.4	2.0	96.1	3.8	3.4	74.0	4.4	4.0	96.1	8.6	8.2	96.1
32	Distribution Center Building	1.4	0.7	84.3	1.5	0.7	92.8	1.9	1.1	95.6	2.5	1.7	95.6	3.9	3.1	34.0	4.5	3.7	95.6	8.7	7.9	95.6
8	ASE 1 PS Electrical Bldg (DC3)	1.6	0.9	72.6	1.7	1.0	74.4	2.1	1.4	76.1	2.7	1.9	77.9	4.1	2.9	55.0	4.7	3.5	97.4	8.9	7.7	97.4
10	Secondary Blower Bldg (SBB)	2.0	1.0	61.7	2.1	1.0	64.1	2.5	1.3	70.7	3.1	1.6	85.6	4.5	2.9	157.0	5.1	3.4	95.8	9.3	7.5	98.2
36	Chemical Storage (?)	1.5	0.7	79.0	1.6	0.8	79.0	2.0	1.2	79.0	2.6	1.8	79.0	4.0	3.2	27.0	4.6	3.8	79.0	8.8	8.0	79.0
42*	Adv. Backwash Bldg (ABWB)	10.9	7.0	26.1	11.0	7.1	26.1	11.4	7.5	26.1	12.0	7.8	27.1	13.4	3.2	84.0	14.0	3.5	95.0	18.2	7.6	97.1
5	Unidentified Facility	1.4	0.6	48.3	1.5	0.6	51.8	1.9	0.9	57.7	2.5	1.3	73.0	3.9	2.2	86.0	4.5	2.8	100.0	8.7	7.0	100.0
45	Secondary Clarifier 9 (SCL9)	1.8	1.0	32.6	1.9	1.0	34.0	2.3	1.4	36.0	2.9	1.9	38.0	4.3	3.2	57.0	4.9	3.8	38.7	9.1	6.4	53.0
29	N. Ferric/Odor Control Facility	0.9	0.4	94.6	1.0	0.5	94.6	1.4	0.9	94.6	2.0	1.5	94.6	3.4	2.9	87.0	4.0	3.5	94.6	8.2	7.7	94.6
33	Unidentified Facility	0.7	0.4	43.4	0.8	0.4	51.7	1.2	0.8	57.9	1.8	1.1	72.4	3.2	2.2	45.0	3.8	2.8	93.1	8.0	7.0	93.1
4*	Wet Weather Filtr. Fac. (WWFF)	9.8	3.5	43.5	9.9	3.5	44.0	10.3	3.9	44.0	10.9	4.5	44.0	12.3	3.8	159.0	12.9	3.5	92.1	17.1	7.4	100.0
17*	Filt. & Disinfection Fac. (FADF)	10.5	4.1	31.7	10.6	4.2	32.0	11.0	4.6	32.0	11.6	3.7	45.1	13.0	3.2	248.0	13.6	3.6	90.6	17.8	7.6	94.4
63	Primary Effluent Flume	0.6	0.2	25.2	0.7	0.2	50.5	1.1	0.4	100.0	1.7	1.0	100.0	3.1	2.4	17.0	3.7	3.0	100.0	7.9	7.2	100.0
40	Elect. Dist. Ctr. Bldg 5 (DCB5)	5.3	2.2	13.6	5.4	2.3	13.6	5.8	2.0	19.1	6.4	1.9	27.3	7.8	1.7	30.0	8.4	2.3	81.8	12.6	6.5	81.8
18	Methanol Feed Facility (MFF)	0.0	0.0	0.0	0.0	0.0	1.7	0.4	0.2	6.7	1.0	0.4	26.9	2.4	1.1	32.0	3.0	1.1	94.3	7.2	5.3	94.3
15	Post Aeration Facility (PAF)	0.0	0.0	0.0	0.0	0.0	0.0	0.0	0.0	0.0	0.0	0.0	0.0	2.3	0.9	80.0	2.9	1.2	95.2	7.1	5.1	100.0
57*	PTB Backup Flow Dist. Struct.	0.0	0.0	0.0	0.0	0.0	0.0	0.0	0.0	0.0	0.0	0.0	0.0	12.1	8.6	67.0	12.7	9.2	100.0	16.9	13.4	100.0
23	Unidentified Facility	0.0	0.0	0.0	0.0	0.0	0.0	0.0	0.0	0.0	0.0	0.0	0.0	0.4	0.2	4.0	1.0	0.5	34.0	5.2	3.2	99.9
16	Chlorine Contact Tanks (CCT)	0.0	0.0	0.0	0.0	0.0	0.0	0.0	0.0	0.0	0.0	0.0	0.0	2.5	1.0	141.0	3.1	1.6	99.8	7.3	5.8	99.8
2	Preliminary Treatment Building	0.0	0.0	0.0	0.0	0.0	0.0	0.0	0.0	0.0	0.0	0.0	0.0	0.0	0.0	0.0	0.5	0.4	12.0	4.7	1.9	98.9
25	Primary Effluent PS (PEPS)	0.0	0.0	0.0	0.0	0.0	0.0	0.0	0.0	0.0	0.8	0.4	14.6	2.2	1.0	40.0	2.8	1.6	97.6	7.0	5.8	97.6
24	Flow Equalization Pump Station	0.0	0.0	0.0	0.0	0.0	0.0	0.0	0.0	0.0	0.1	0.1	10.4	1.5	1.2	37.0	2.1	1.8	96.2	6.3	6.0	96.2
56	Primary Clarifiers 1-10 (PCL)	0.0	0.0	0.0	0.0	0.0	0.0	0.0	0.0	0.0	5.8	1.6	30.9	8.0	2.0	193.0	8.6	2.3	72.4	12.8	5.6	95.4
54	Plant Eff. Water Fac. (PEWF)	0.0	0.0	0.0	0.0	0.0	0.0	0.0	0.0	0.0	0.0	0.0	0.0	1.7	0.9	40.0	2.3	1.3	88.9	6.5	5.5	88.9
11	Flow Equalization Tanks (FEQ1)	0.0	0.0	0.0	0.0	0.0	0.0	0.0	0.0	0.0	0.0	0.0	0.0	1.0	0.5	35.0	1.6	0.8	33.0	5.8	3.3	86.3
58*	PTB Structure (PTB)	0.0	0.0	0.0	0.0	0.0	0.0	0.0	0.0	0.0	0.0	0.0	0.0	10.0	4.9	20.0	10.6	5.5	32.7	14.8	5.2	73.6
1	Diss. Air Float. Thick. (DAFT)	0.0	0.0	0.0	0.0	0.0	0.0	0.0	0.0	0.0	0.0	0.0	0.0	0.0	0.0	0.0	0.0	0.0	0.0	0.3	0.2	6.2
20	Prim. Gravity Thickener Bldg.	0.0	0.0	0.0	0.0	0.0	0.0	0.0	0.0	0.0	0.0	0.0	0.0	0.0	0.0	0.0	0.0	0.0	0.0	0.1	0.1	2.1
21	Sludge Storage Tanks 06-2	0.0	0.0	0.0	0.0	0.0	0.0	0.0	0.0	0.0	0.0	0.0	0.0	0.0	0.0	0.0	0.0	0.0	0.0	0.1	0.1	1.7
3	New Maint. Building (NMB)	0.0	0.0	0.0	0.0	0.0	0.0	0.0	0.0	0.0	0.0	0.0	0.0	0.0	0.0	0.0	0.0	0.0	0.0	0.0	0.0	0.0
22	Sludge Storage Tanks 06-1	0.0	0.0	0.0	0.0	0.0	0.0	0.0	0.0	0.0	0.0	0.0	0.0	0.0	0.0	0.0	0.0	0.0	0.0	0.0	0.0	0.0
26	Four Mile Run Lift Station	0.0	0.0	0.0	0.0	0.0	0.0	0.0	0.0	0.0	0.0	0.0	0.0	0.0	0.0	0.0	0.0	0.0	0.0	0.0	0.0	0.0
44	Four Mile Run Intercept	0.0	0.0	0.0	0.0	0.0	0.0	0.0	0.0	0.0	0.0	0.0	0.0	0.0	0.0	0.0	0.0	0.0	0.0	0.0	0.0	0.0
60	Potomac Yard PS	0.0	0.0	0.0	0.0	0.0	0.0	0.0	0.0	0.0	0.0	0.0	0.0	0.0	0.0	0.0	0.0	0.0	0.0	0.0	0.0	0.0

Table 6.3: Inundation by a 1000-year Coastal Storm under Seven Sea-Level Rise Scenarios.

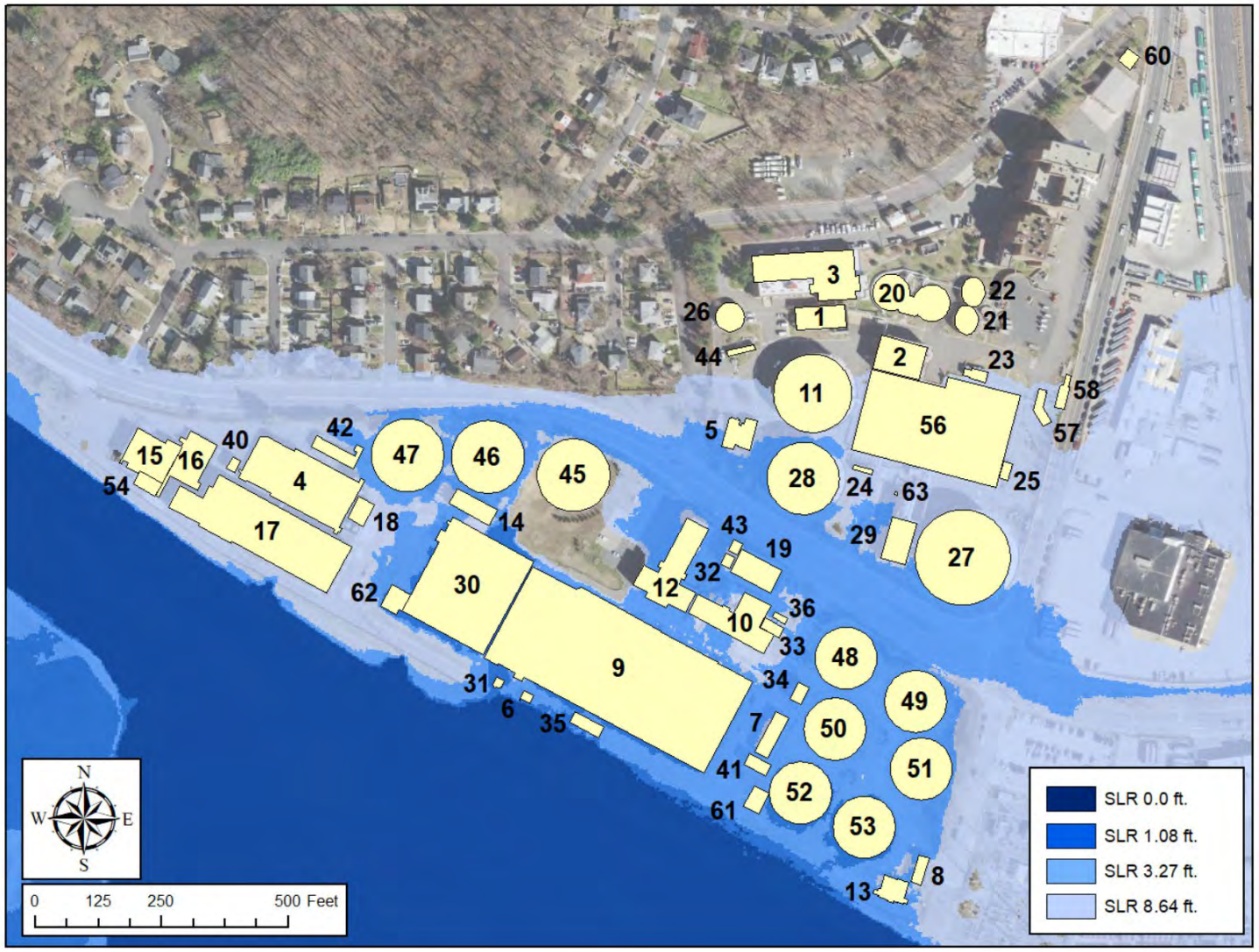

Figure 6.1: Arlington Water Pollution Control Plant (AWPCP), 100-year coastal storm. Inundation of AWPCP components and structures by a 100-year coastal storm given existing sea level and three sea level rise scenarios (1.08 ft., 3.27 ft., 8.64 ft.).

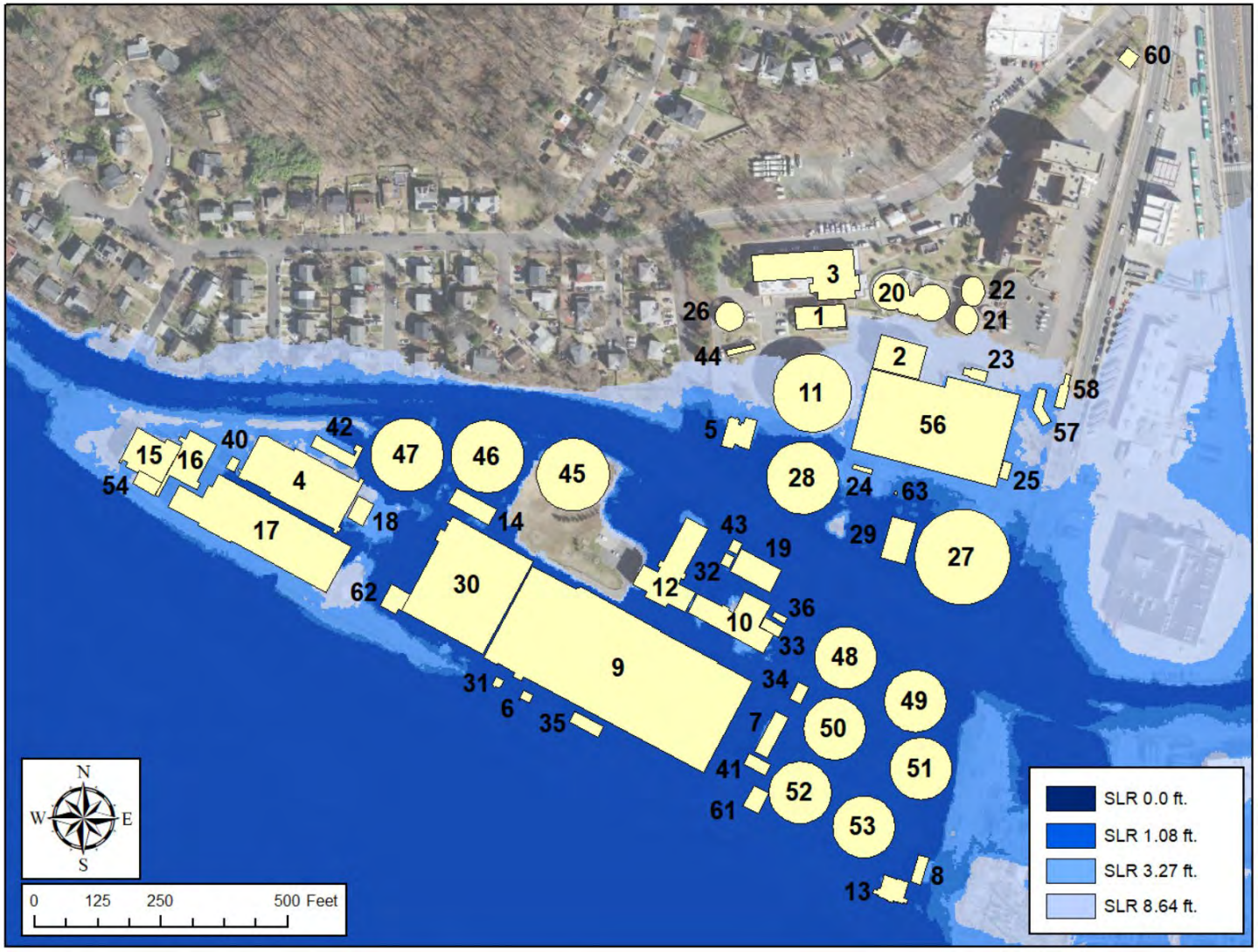

Figure 6.2: Arlington Water Pollution Control Plant (AWPCP), 1000-year coastal storm. Inundation of AWPCP components and structures by a 1000-year coastal storm given existing sea level and three sea level rise scenarios (1.08 ft., 3.27 ft., 8.64 ft.).

AlexRenew Wastewater Treatment Plant (AlexRenew)

AlexRenew serves the City of Alexandria, Virginia. As with many wastewater treatment plants, AlexRenew is located in low lying area and, as a result of its proximity to the tidal region of the Potomac River, it is susceptible to flooding caused by coastal storms and sea level rise. The AlexRenew WWTP is located north of I-95/I-495 (Capitol Beltway) and north of Cameron Run approximately 0.65 miles upstream of its confluence with the Potomac River. The facility is potentially impacted by bank overflow from Cameron Run at higher levels of coastal storm severity and sea level rise. The components of the AlexRenew are listed in Table 6.4. Each is assigned a unique sequential identification number (ID#) and, where it was available in the GIS data file, a unique identifier and description.

Inundation water depths were estimated at the perimeter of 63 distinct components or structures. Maximum and mean water depths are summarized for 100-year coastal storms in Table 6.5 and for 1000-year coastal storms in Table 6.6. There are six estimates of inundation water depth that appear questionable. These are highlighted in red and the identification numbers in the first column of the table are marked with an asterisk. While it is likely that these components and structures would still be flooded under these coastal storm and sea-level rise scenarios, the inundation depths may be greatly overstated. For example, this might occur if LIDAR measurements captured the bottom of the structures rather than the ground elevation at the perimeter of the structure. Figures 6.3 and 6.4 show the extent of the AWPCP inundated under each of the coastal storm and sea level rise scenarios.

The extent of wastewater service disruption in the service area will depend upon the combination of components and structures that are inundated and the depth of inundation. Many of the components and structures at AlexRenew may be elevated in a way that might protect them from flood damage or from flood service disruption. Critical inundation depths for individual components and structures was not available for this study. An assessment of what impacts floods would have in terms of disruption of service should be made in consultation with those who have knowledge of this particular treatment plant.

Identification Number	Structure Identifier	Description
1	002018BLDS	Unidentified
2	002020BLDS	Unidentified
3	002022BLDS	Unidentified
4	002023BLDS	Unidentified
5	002024BLDS	Unidentified
6	003136BLDS	Biological Reactor Basins (BRB)
7	007074BLDS	Solids Processing Building L (SPBL)
8	007102BLDS	Sludge Thickening Building (STB)
9	007103BLDS	Unidentified
10	007104BLDS	Preliminary Treatment Building K (PTBK)
11	009254BLDS	Twenty (20) Digester Complex (TDC)
12	009255BLDS	Main Building (MAIN)
13	007795BLDS	Unidentified
14	008748BLDS	Process Air Compressor Building (PACB)
15	011784BLDS	Unidentified
16	020555BLDS	Unidentified
17	020556BLDS	Advance Treatment Facility (ATF)
18	020561BLDS	Unidentified
19	039232BLDS	Unidentified
20	040176BLDS	Unidentified
21	040775BLDS	Unidentified
22	040777BLDS	Unidentified
23	040780BLDS	Unidentified
24		20/3 Digester No. 4
26		20/2 Digester No. 2
27		20/1 Digester No. 1
28		20/3 Digester No. 3
29		Unidentified
30		Unidentified
31		Secondary Settling Tanks 1 (SST1)
32		Secondary Settling Tanks 2 (SST2)
33		Secondary Settling Tanks 3 (SST3)
34		Primary Settling Tanks (PST)
35		Secondary Settling Tanks 4 (SST4)
36		Secondary Settling Tanks 5 (SST5)
37		Secondary Settling Tanks 6 (SST6)
38		Post Aeration Basins 45 (PAB45)
39	020556BLDS	Admin/Lab Building J (ALBJ)
40	008748BLDS	UV Disinfection Building N (UVDB-N)
41	007102BLDS	Pre-Pasteurization Building (PPB)

Table 6.4: AlexRenew WWTP Components and Structures.

ID #	Facility Description	S1 (0.0 ft.)			S2 (0.67 ft.)			S3 (1.08 ft.)			S4 (1.75 ft.)			S5 (3.23 ft.)			S6 (3.93 ft.)			S7 (8.64 ft.)		
		Max. (ft.)	Avg. (ft.)	Area (%)	Max. (ft.)	Avg. (ft.)	Area (%)	Max. (ft.)	Avg. (ft.)	Area (%)	Max. (ft.)	Avg. (ft.)	Area (%)	Max. (ft.)	Avg. (ft.)	Area (%)	Max. (ft.)	Avg. (ft.)	Area (%)	Max. (ft.)	Avg. (ft.)	Area (%)
37*	Sec. Set. Tanks (SST6)	0.0	0.0	0.0	0.0	0.0	0.0	0.0	0.0	0.0	0.0	0.0	0.0	0.0	0.0	0.0	0.0	0.0	0.0	14.4	10.0	97.9
13*	Unidentified	0.0	0.0	0.0	0.0	0.0	0.0	0.0	0.0	0.0	0.0	0.0	0.0	0.0	0.0	0.0	0.0	0.0	0.0	14.4	11.1	95.0
19*	Unidentified	0.0	0.0	0.0	0.0	0.0	0.0	0.0	0.0	0.0	0.0	0.0	0.0	0.0	0.0	0.0	0.0	0.0	0.0	14.4	5.5	100.0
36*	Sec. Set. Tanks (SST5)	0.0	0.0	0.0	0.0	0.0	0.0	0.0	0.0	0.0	0.0	0.0	0.0	0.0	0.0	0.0	0.0	0.0	0.0	14.3	8.6	98.4
35*	Sec. Set. Tanks (SST4)	0.0	0.0	0.0	0.0	0.0	0.0	0.0	0.0	0.0	0.0	0.0	0.0	0.0	0.0	0.0	0.0	0.0	0.0	14.3	7.0	96.6
2*	Unidentified	0.0	0.0	0.0	0.0	0.0	0.0	0.0	0.0	0.0	0.0	0.0	0.0	0.0	0.0	0.0	0.0	0.0	0.0	9.8	4.2	72.0
6	Biol. Reactor Basins (BRB)	0.0	0.0	0.0	0.0	0.0	0.0	0.0	0.0	0.0	0.0	0.0	0.0	0.0	0.0	0.0	0.0	0.0	0.0	6.1	2.9	99.2
11	20 Digester Comp. (TDC)	0.0	0.0	0.0	0.0	0.0	0.0	0.0	0.0	0.0	0.0	0.0	0.0	0.0	0.0	0.0	0.0	0.0	0.0	5.2	1.8	95.4
28	20/3 Digester No. 3	0.0	0.0	0.0	0.0	0.0	0.0	0.0	0.0	0.0	0.0	0.0	0.0	0.0	0.0	0.0	0.0	0.0	0.0	5.1	2.2	98.4
40	UV Dis. Bldg. N (UVDB-N)	0.0	0.0	0.0	0.0	0.0	0.0	0.0	0.0	0.0	0.0	0.0	0.0	0.0	0.0	0.0	0.0	0.0	0.0	4.6	2.6	99.9
38	Post Aeration B 45 (PAB45)	0.0	0.0	0.0	0.0	0.0	0.0	0.0	0.0	0.0	0.0	0.0	0.0	0.0	0.0	0.0	0.0	0.0	0.0	4.5	2.8	100.0
24	20/3 Digester No. 4	0.0	0.0	0.0	0.0	0.0	0.0	0.0	0.0	0.0	0.0	0.0	0.0	0.0	0.0	0.0	0.0	0.0	0.0	4.3	2.0	99.3
17	Adv. Treat. Fac. (ATF)	0.0	0.0	0.0	0.0	0.0	0.0	0.0	0.0	0.0	0.0	0.0	0.0	0.0	0.0	0.0	0.0	0.0	0.0	4.2	1.8	89.9
21	Unidentified	0.0	0.0	0.0	0.0	0.0	0.0	0.0	0.0	0.0	0.0	0.0	0.0	0.0	0.0	0.0	0.0	0.0	0.0	3.2	2.1	100.0
14	Process Air Comp. (PACB)	0.0	0.0	0.0	0.0	0.0	0.0	0.0	0.0	0.0	0.0	0.0	0.0	0.0	0.0	0.0	0.0	0.0	0.0	3.1	2.0	99.9
33	Sec. Set. Tanks (SST3)	0.0	0.0	0.0	0.0	0.0	0.0	0.0	0.0	0.0	0.0	0.0	0.0	0.0	0.0	0.0	0.0	0.0	0.0	3.0	0.9	32.6
18	Unidentified	0.0	0.0	0.0	0.0	0.0	0.0	0.0	0.0	0.0	0.0	0.0	0.0	0.0	0.0	0.0	0.0	0.0	0.0	2.9	2.0	78.2
30	Unidentified	0.0	0.0	0.0	0.0	0.0	0.0	0.0	0.0	0.0	0.0	0.0	0.0	0.0	0.0	0.0	0.0	0.0	0.0	2.9	2.1	97.2
31	Sec. Set. Tanks (SST1)	0.0	0.0	0.0	0.0	0.0	0.0	0.0	0.0	0.0	0.0	0.0	0.0	0.0	0.0	0.0	0.0	0.0	0.0	2.9	1.7	92.5
8	Sludge Thick. Bldg. (STB)	0.0	0.0	0.0	0.0	0.0	0.0	0.0	0.0	0.0	0.0	0.0	0.0	0.0	0.0	0.0	0.0	0.0	0.0	2.9	1.7	63.2
32	Sec. Set. Tanks (SST2)	0.0	0.0	0.0	0.0	0.0	0.0	0.0	0.0	0.0	0.0	0.0	0.0	0.0	0.0	0.0	0.0	0.0	0.0	2.8	1.2	94.3
23	Unidentified	0.0	0.0	0.0	0.0	0.0	0.0	0.0	0.0	0.0	0.0	0.0	0.0	0.0	0.0	0.0	0.0	0.0	0.0	2.6	1.9	100.0
16	Unidentified	0.0	0.0	0.0	0.0	0.0	0.0	0.0	0.0	0.0	0.0	0.0	0.0	0.0	0.0	0.0	0.0	0.0	0.0	2.5	1.0	54.6
15	Unidentified	0.0	0.0	0.0	0.0	0.0	0.0	0.0	0.0	0.0	0.0	0.0	0.0	0.0	0.0	0.0	0.0	0.0	0.0	2.4	0.8	0.0
29	Unidentified	0.0	0.0	0.0	0.0	0.0	0.0	0.0	0.0	0.0	0.0	0.0	0.0	0.0	0.0	0.0	0.0	0.0	0.0	2.3	1.0	75.8
22	Unidentified	0.0	0.0	0.0	0.0	0.0	0.0	0.0	0.0	0.0	0.0	0.0	0.0	0.0	0.0	0.0	0.0	0.0	0.0	2.1	1.4	99.7
41	Pre-Pasteurization Bldg.	0.0	0.0	0.0	0.0	0.0	0.0	0.0	0.0	0.0	0.0	0.0	0.0	0.0	0.0	0.0	0.0	0.0	0.0	1.9	1.4	99.7
39	Admin/Lab Bldg. J (ALBJ)	0.0	0.0	0.0	0.0	0.0	0.0	0.0	0.0	0.0	0.0	0.0	0.0	0.0	0.0	0.0	0.0	0.0	0.0	1.9	1.1	100.0
20	Unidentified	0.0	0.0	0.0	0.0	0.0	0.0	0.0	0.0	0.0	0.0	0.0	0.0	0.0	0.0	0.0	0.0	0.0	0.0	1.9	1.4	100.0
12	Main Building (MAIN)	0.0	0.0	0.0	0.0	0.0	0.0	0.0	0.0	0.0	0.0	0.0	0.0	0.0	0.0	0.0	0.0	0.0	0.0	1.8	0.8	100.0
26	20/2 Digester No. 2	0.0	0.0	0.0	0.0	0.0	0.0	0.0	0.0	0.0	0.0	0.0	0.0	0.0	0.0	0.0	0.0	0.0	0.0	1.6	0.9	99.2
27	20/1 Digester No. 1	0.0	0.0	0.0	0.0	0.0	0.0	0.0	0.0	0.0	0.0	0.0	0.0	0.0	0.0	0.0	0.0	0.0	0.0	1.4	0.7	12.7
5	Unidentified	0.0	0.0	0.0	0.0	0.0	0.0	0.0	0.0	0.0	0.0	0.0	0.0	0.0	0.0	0.0	0.0	0.0	0.0	1.1	0.6	0.0
4	Unidentified	0.0	0.0	0.0	0.0	0.0	0.0	0.0	0.0	0.0	0.0	0.0	0.0	0.0	0.0	0.0	0.0	0.0	0.0	0.0	0.0	0.0
34	Prim. Settling Tanks (PST)	0.0	0.0	0.0	0.0	0.0	0.0	0.0	0.0	0.0	0.0	0.0	0.0	0.0	0.0	0.0	0.0	0.0	0.0	0.0	0.0	0.0
7	Solid. Proc. Bldg. L (SPBL).	0.0	0.0	0.0	0.0	0.0	0.0	0.0	0.0	0.0	0.0	0.0	0.0	0.0	0.0	0.0	0.0	0.0	0.0	0.0	0.0	0.0
10	Prelim. Tr. Bldg. K (PTBK)	0.0	0.0	0.0	0.0	0.0	0.0	0.0	0.0	0.0	0.0	0.0	0.0	0.0	0.0	0.0	0.0	0.0	0.0	0.0	0.0	0.0
9	Unidentified	0.0	0.0	0.0	0.0	0.0	0.0	0.0	0.0	0.0	0.0	0.0	0.0	0.0	0.0	0.0	0.0	0.0	0.0	0.0	0.0	0.0
1	Unidentified	0.0	0.0	0.0	0.0	0.0	0.0	0.0	0.0	0.0	0.0	0.0	0.0	0.0	0.0	0.0	0.0	0.0	0.0	0.0	0.0	0.0
3	Unidentified	0.0	0.0	0.0	0.0	0.0	0.0	0.0	0.0	0.0	0.0	0.0	0.0	0.0	0.0	0.0	0.0	0.0	0.0	0.0	0.0	0.0

Table 6.5: AlexRenew WWTP, 100-year coastal storm. Inundation of AlexRenew WWTP components and structures by a 100-year coastal storm under seven sea-level rise scenarios.

ID #	Facility Description	S1 (0.0 ft.)			S2 (0.67 ft.)			S3 (1.08 ft.)			S4 (1.75 ft.)			S5 (3.23 ft.)			S6 (3.93 ft.)			S7 (8.64 ft.)		
		Max. (ft.)	Avg. (ft.)	Area (%)	Max. (ft.)	Avg. (ft.)	Area (%)	Max. (ft.)	Avg. (ft.)	Area (%)	Max. (ft.)	Avg. (ft.)	Area (%)	Max. (ft.)	Avg. (ft.)	Area (%)	Max. (ft.)	Avg. (ft.)	Area (%)	Max. (ft.)	Avg. (ft.)	Area (%)
6	Biol. Reactor Basins (BRB)	0.0	0.0	0.0	0.0	0.0	0.0	0.0	0.0	0.0	0.0	0.0	0.0	4.3	2.0	61.2	4.9	2.4	68.6	9.1	5.6	99.3
11	20 Digester Complex (TDC)	0.0	0.0	0.0	0.0	0.0	0.0	0.0	0.0	0.0	0.0	0.0	0.0	3.4	2.3	28.5	4.0	2.8	30.2	8.2	4.6	97.0
28	20/3 Digester No. 3	0.0	0.0	0.0	0.0	0.0	0.0	0.0	0.0	0.0	0.0	0.0	0.0	3.3	1.8	47.4	3.9	2.2	54.0	8.1	5.2	95.7
40	UV Dis. Bldg N (UVDB-N)	0.0	0.0	0.0	0.0	0.0	0.0	0.0	0.0	0.0	0.0	0.0	0.0	2.8	1.3	67.5	3.4	1.7	80.7	7.6	5.6	94.6
38	Post Aeration B 45 (PAB45)	0.0	0.0	0.0	0.0	0.0	0.0	0.0	0.0	0.0	0.0	0.0	0.0	2.7	1.0	98.1	3.3	1.6	98.1	7.5	5.8	98.1
24	20/3 Digester No. 4	0.0	0.0	0.0	0.0	0.0	0.0	0.0	0.0	0.0	0.0	0.0	0.0	2.5	1.7	37.0	3.1	1.9	44.5	7.3	5.0	94.8
17	Adv. Treat. Fac. (ATF)	0.0	0.0	0.0	0.0	0.0	0.0	0.0	0.0	0.0	0.0	0.0	0.0	2.4	0.6	44.7	3.0	0.9	70.1	7.2	4.6	100.0
21	Unidentified	0.0	0.0	0.0	0.0	0.0	0.0	0.0	0.0	0.0	0.0	0.0	0.0	1.4	0.6	68.2	2.0	1.0	96.3	6.2	5.1	99.0
14	Process Air Comp (PACB)	0.0	0.0	0.0	0.0	0.0	0.0	0.0	0.0	0.0	0.0	0.0	0.0	1.3	0.8	43.1	1.9	0.8	95.3	6.1	5.0	98.0
18	Unidentified	0.0	0.0	0.0	0.0	0.0	0.0	0.0	0.0	0.0	0.0	0.0	0.0	1.1	0.6	54.2	1.7	1.1	67.0	5.9	4.5	100.0
30	Unidentified	0.0	0.0	0.0	0.0	0.0	0.0	0.0	0.0	0.0	0.0	0.0	0.0	1.1	0.5	65.4	1.7	1.0	87.5	5.9	5.0	97.0
31	Sec. Set. Tanks 1 (SST1)	0.0	0.0	0.0	0.0	0.0	0.0	0.0	0.0	0.0	0.0	0.0	0.0	1.1	0.6	32.6	1.7	0.8	59.0	5.9	4.5	87.6
8	Sludge Thick Bldg. (STB)	0.0	0.0	0.0	0.0	0.0	0.0	0.0	0.0	0.0	0.0	0.0	0.0	1.1	0.4	32.9	1.7	0.8	47.0	5.9	3.8	99.2
32	Sec. Set. Tanks 2 (SST2)	0.0	0.0	0.0	0.0	0.0	0.0	0.0	0.0	0.0	0.0	0.0	0.0	1.0	0.5	23.1	1.6	0.9	34.3	5.8	4.0	87.3
23	Unidentified	0.0	0.0	0.0	0.0	0.0	0.0	0.0	0.0	0.0	0.0	0.0	0.0	0.8	0.4	57.2	1.4	0.7	91.2	5.6	4.9	96.3
16	Unidentified	0.0	0.0	0.0	0.0	0.0	0.0	0.0	0.0	0.0	0.0	0.0	0.0	0.7	0.3	9.8	1.3	0.6	19.4	5.5	3.6	78.8
29	Unidentified	0.0	0.0	0.0	0.0	0.0	0.0	0.0	0.0	0.0	0.0	0.0	0.0	0.5	0.2	8.0	1.1	0.4	28.8	5.3	3.6	92.0
33	Sec. Set. Tanks 3 (SST3)	0.0	0.0	0.0	0.0	0.0	0.0	0.0	0.0	0.0	0.0	0.0	0.0	0.4	0.3	2.7	1.0	0.6	6.7	6.0	3.2	87.0
41	Pre-Pasteuriz. Bldg. (PPB)	0.0	0.0	0.0	0.0	0.0	0.0	0.0	0.0	0.0	0.0	0.0	0.0	0.1	0.1	8.6	0.7	0.3	77.5	4.9	4.4	95.5
39	Admin/Lab Bldg. J (ALBJ)	0.0	0.0	0.0	0.0	0.0	0.0	0.0	0.0	0.0	0.0	0.0	0.0	0.0	0.0	0.6	0.7	0.3	33.3	4.9	4.1	97.5
37*	Sec. Set. Tanks 6 (SST6)	0.0	0.0	0.0	0.0	0.0	0.0	0.0	0.0	0.0	0.0	0.0	0.0	0.0	0.0	0.0	13.2	10.5	51.4	17.4	11.1	74.5
13*	Unidentified	0.0	0.0	0.0	0.0	0.0	0.0	0.0	0.0	0.0	0.0	0.0	0.0	0.0	0.0	0.0	13.2	11.5	77.9	17.4	13.3	96.0
19*	Unidentified	0.0	0.0	0.0	0.0	0.0	0.0	0.0	0.0	0.0	0.0	0.0	0.0	0.0	0.0	0.0	13.2	5.4	80.2	17.4	8.5	98.1
36*	Sec. Set. Tanks 5 (SST5)	0.0	0.0	0.0	0.0	0.0	0.0	0.0	0.0	0.0	0.0	0.0	0.0	0.0	0.0	0.0	13.1	9.5	70.1	17.3	11.0	93.8
35*	Sec. Set. Tanks 4 (SST4)	0.0	0.0	0.0	0.0	0.0	0.0	0.0	0.0	0.0	0.0	0.0	0.0	0.0	0.0	0.0	13.1	9.8	45.1	17.3	7.9	98.7
2*	Unidentified	0.0	0.0	0.0	0.0	0.0	0.0	0.0	0.0	0.0	0.0	0.0	0.0	0.0	0.0	0.0	8.6	5.9	45.3	12.8	6.1	100.0
4	Unidentified	0.0	0.0	0.0	0.0	0.0	0.0	0.0	0.0	0.0	0.0	0.0	0.0	0.0	0.0	0.0	0.0	0.0	0.0	10.2	2.4	81.9
34	Prim. Settling Tanks (PST)	0.0	0.0	0.0	0.0	0.0	0.0	0.0	0.0	0.0	0.0	0.0	0.0	0.0	0.0	0.0	0.0	0.0	0.0	8.9	2.8	40.2
15	Unidentified	0.0	0.0	0.0	0.0	0.0	0.0	0.0	0.0	0.0	0.0	0.0	0.0	0.0	0.0	0.0	0.0	0.0	0.0	5.4	2.4	83.4
22	Unidentified	0.0	0.0	0.0	0.0	0.0	0.0	0.0	0.0	0.0	0.0	0.0	0.0	0.0	0.0	0.0	0.0	0.0	0.0	5.1	4.4	98.2
20	Unidentified	0.0	0.0	0.0	0.0	0.0	0.0	0.0	0.0	0.0	0.0	0.0	0.0	0.0	0.0	0.0	0.0	0.0	0.0	4.9	4.4	100.0
12	Main Building (MAIN)	0.0	0.0	0.0	0.0	0.0	0.0	0.0	0.0	0.0	0.0	0.0	0.0	0.0	0.0	0.0	0.0	0.0	0.0	4.8	3.8	100.0
26	20/2 Digester No. 2	0.0	0.0	0.0	0.0	0.0	0.0	0.0	0.0	0.0	0.0	0.0	0.0	0.0	0.0	0.0	0.0	0.0	0.0	4.6	3.9	89.1
27	20/1 Digester No. 1	0.0	0.0	0.0	0.0	0.0	0.0	0.0	0.0	0.0	0.0	0.0	0.0	0.0	0.0	0.0	0.0	0.0	0.0	4.4	2.8	93.8
5	Unidentified	0.0	0.0	0.0	0.0	0.0	0.0	0.0	0.0	0.0	0.0	0.0	0.0	0.0	0.0	0.0	0.0	0.0	0.0	4.1	2.1	88.1
7	Solids Proc. Bldg. L (SPBL)	0.0	0.0	0.0	0.0	0.0	0.0	0.0	0.0	0.0	0.0	0.0	0.0	0.0	0.0	0.0	0.0	0.0	0.0	2.4	1.4	100.0
10	Prelim. Tr. Bldg. K (PTBK)	0.0	0.0	0.0	0.0	0.0	0.0	0.0	0.0	0.0	0.0	0.0	0.0	0.0	0.0	0.0	0.0	0.0	0.0	2.4	1.5	45.8
9	Unidentified	0.0	0.0	0.0	0.0	0.0	0.0	0.0	0.0	0.0	0.0	0.0	0.0	0.0	0.0	0.0	0.0	0.0	0.0	1.7	0.9	8.0
1	Unidentified	0.0	0.0	0.0	0.0	0.0	0.0	0.0	0.0	0.0	0.0	0.0	0.0	0.0	0.0	0.0	0.0	0.0	0.0	1.6	1.1	98.3
3	Unidentified	0.0	0.0	0.0	0.0	0.0	0.0	0.0	0.0	0.0	0.0	0.0	0.0	0.0	0.0	0.0	0.0	0.0	0.0	0.4	0.2	6.9

Table 6.6: AlexRenew WWTP, 1000-year coastal storm. Inundation of AlexRenew WWTP components and structures by a 1000-year coastal storm under seven sea-level rise scenarios.

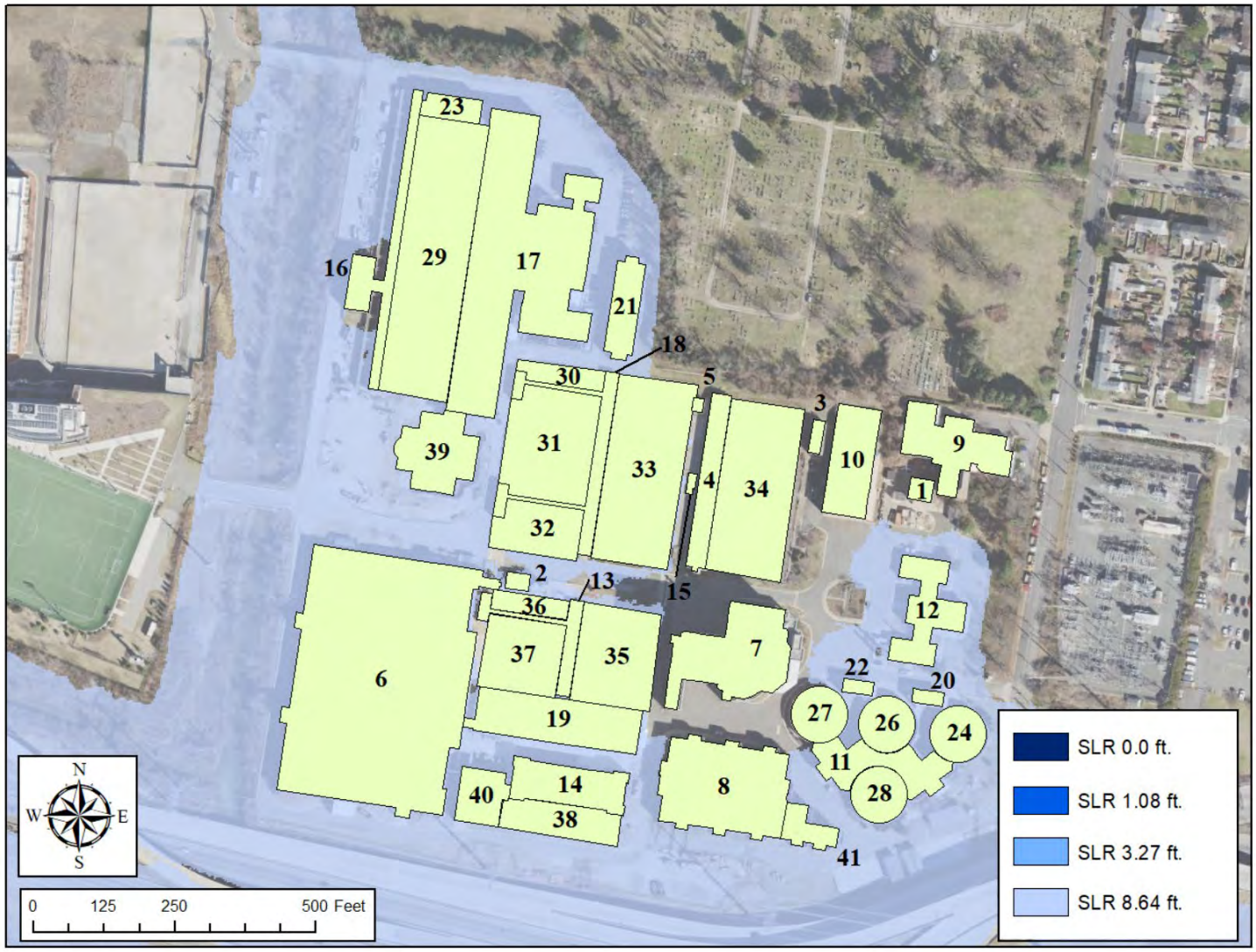

Figure 6.3: AlexRenew WWTP, 100-year coastal storm. Inundation of AlexRenew WWTP components and structures given existing sea level and three sea level scenarios (1.08 ft., 3.27 ft., and 8.64 ft.).

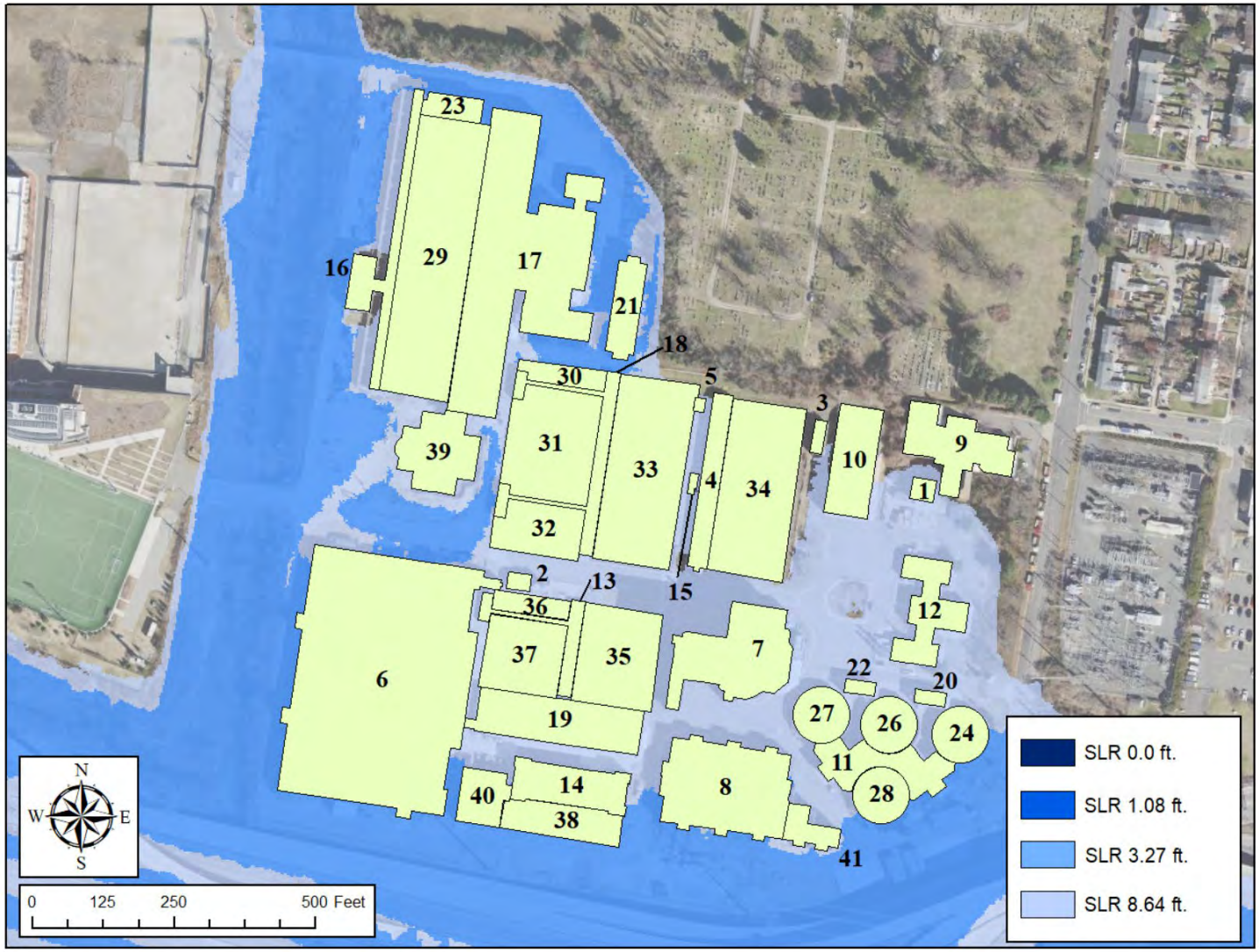

Figure 6.4: AlexRenew WWTP, 1000-year coastal storm. Inundation of AlexRenew WWTP components and structures given existing sea level and three sea level scenarios (1.08 ft., 3.27 ft., and 8.64 ft.).

Wastewater Pump Stations

The role of wastewater pump stations is to force sewage from lower to higher elevations in sanitary sewer mains. These components of the wastewater system tend to be vulnerable to flooding because they are located in low-lying areas. There are 89 wastewater pump stations located within the planning area. Traditionally, wastewater pump stations have been built with separate dry and wet wells. The dry well contains the mechanical and electrical equipment and the wet well holds the sewage that must be pumped to a higher elevation. Recently, submersible pumps have become increasingly more common. Pump stations that are equipped with submersible pumps may remain in service during flood events. None of the information provided by the various jurisdictions indicated whether or not any of the pump stations were of the submersible variety.

There are 29 pump stations within the planning area that are vulnerable to flooding caused by coastal storms and sea level rise. These pump stations are listed by county in Table 6.7. The identification numbers and structure identifiers in Table WWPS1 are those that were provided in the GIS data files by the various jurisdictions. Alexandria did not provide information on the location of its wastewater pump stations. There are four pump stations located in Alexandria, including Four Mile Run Pump Station (3650 Commonwealth Avenue), Potomac Run Pump Station (1901 Potomac Boulevard), Slater's Lane Pump Station, and Mark Center Pump Station. Of these four pump stations, only the Four Mile Run Pump Station is vulnerable to flooding from the coastal storm and sea level rise scenarios considered in this study. The locations of these pump stations are shown in Figure 6.5. Pump stations in the figure are labelled using the unique structure identifiers that were provided by each jurisdiction.

Inundation of pump stations would disrupt wastewater service for customers located upstream. When determining whether service would be disrupted at a particular pump station, inundation depths should be considered in relation to critical flood depths, which is the flood depth at a pump station that would cause the dry well to flood. Some pump stations, particularly those located in low lying areas, may have been designed to withstand some amount of inundation before the dry well becomes flooded. Information on critical flood depths at wastewater pump stations in the planning area was not available for this study. Similarly, information on the areas served by each wastewater pump station was not available for this study. Thus, it was not possible to determine what number of customers would be affected. However, most pump stations appear to serve populations that are nearest the river. Thus, it seems that a relatively small fraction of customers would be affected.

County	ID#	Structure ID	100-year Storm and Sea Level Rise (ft)							1000-year Storm and Sea Level Rise (t)						
			0.00 ft.	0.67 ft.	1.08 ft.	1.75 ft.	3.23 ft.	3.93 ft.	8.64 ft.	0.00 ft.	0.67 ft.	1.08 ft.	1.75 ft.	3.23 ft.	3.93 ft.	8.64 ft.
Arlington	8949	LFST007	1.6	1.7	2.1	2.7	4.0	4.6	8.9	4.6	4.7	5.1	5.7	7.1	7.7	11.9
	14102	LFST012	0.0	0.0	0.0	0.0	0.0	0.0	2.7	0.0	0.0	0.0	0.0	0.9	1.5	5.7
	10375	LFST011	0.0	0.0	0.0	0.0	0.0	0.0	2.3	0.0	0.0	0.0	0.0	0.0	0.0	5.3
	14042	LFST013	0.0	0.0	0.0	0.0	0.0	0.0	0.0	0.0	0.0	0.0	0.0	0.0	0.0	1.7
Alexandria	1	Four Mile Run	0.0	0.0	0.0	0.0	0.2	0.8	5.1	0.8	0.8	1.3	1.9	3.3	3.9	8.1
Fairfax	28	112-2-004	6.0	6.1	6.5	7.1	8.4	9.0	13.3	9.0	9.1	9.5	10.1	11.5	12.1	16.3
	32	117-2-021	4.7	4.8	5.2	5.8	7.1	7.7	12.0	7.7	7.8	8.2	8.8	10.2	10.8	15.0
	30	110-3-122	3.7	3.8	4.2	4.8	6.1	6.7	11.0	6.7	6.8	7.2	7.8	9.2	9.8	14.0
	27	112-2-001	3.5	3.6	4.0	4.6	5.9	6.5	10.8	6.5	6.6	7.0	7.6	9.0	9.6	13.8
	1	102-2-286	3.3	3.4	3.8	4.4	5.7	6.3	10.6	6.3	6.4	6.8	7.4	8.8	9.4	13.6
	24	083-4-153	2.1	2.2	2.6	3.2	4.5	5.1	9.4	5.1	5.2	5.6	6.2	7.6	8.2	12.4
	11	093-2-155	1.1	1.2	1.6	2.2	3.5	4.1	8.4	4.1	4.2	4.6	5.2	6.6	7.2	11.4
	19	110-3-209	0.8	0.9	1.3	1.9	3.2	3.8	8.1	3.8	3.9	4.3	4.9	6.3	6.9	11.1
	10	102-2-349	0.0	0.0	0.0	0.0	0.6	1.2	5.5	1.2	1.3	1.7	2.3	3.7	4.3	8.5
	25	093-2-156	0.0	0.0	0.0	0.0	0.2	0.8	5.1	0.8	0.9	1.3	1.9	3.3	3.9	8.1
	33	109-2-098	0.0	0.0	0.0	0.0	0.0	0.0	3.5	0.0	0.0	0.0	0.3	1.7	2.3	6.5
	4	102-3-454	0.0	0.0	0.0	0.0	0.0	0.0	3.5	0.0	0.0	0.0	0.3	1.7	2.3	6.5
	17	109-3-020	0.0	0.0	0.0	0.0	0.0	0.0	2.6	0.0	0.0	0.0	0.0	0.8	1.4	5.6
	9	102-4-311	0.0	0.0	0.0	0.0	0.0	0.0	2.5	0.0	0.0	0.0	0.0	0.7	1.3	5.5
	20	083-1-230	0.0	0.0	0.0	0.0	0.0	0.0	0.7	0.0	0.0	0.0	0.0	0.0	0.0	3.7
Prince William County	8	292-SLS-00001	2.8	2.9	3.3	3.9	5.2	5.8	10.1	5.8	5.9	6.3	6.9	8.3	8.9	13.1
	29	358-SLS-00001	0.0	0.0	0.0	0.0	5.0	5.6	9.9	5.6	5.7	6.1	6.7	8.1	8.7	12.9
	16	315-SLS-00002	0.6	0.7	1.1	1.7	3.0	3.6	7.9	3.6	3.7	4.1	4.7	6.1	6.7	10.9
	2	378-SLS-00001	0.0	0.0	0.0	0.0	0.0	0.4	4.7	0.4	0.5	0.9	1.5	2.9	3.5	7.7
	25	314-SLS-00001	0.0	0.0	0.0	0.0	0.0	0.0	4.1	0.0	0.0	0.3	0.9	2.3	2.9	7.1
	34	336-SLS-00001	0.0	0.0	0.0	0.0	0.0	0.0	5.1	0.0	0.0	0.0	0.0	0.0	3.9	8.1
	17	269-SLS-00003	0.0	0.0	0.0	0.0	0.0	0.0	3.1	0.0	0.0	0.0	0.0	1.3	1.9	6.1
	18	269-SLS-00001	0.0	0.0	0.0	0.0	0.0	0.0	2.8	0.0	0.0	0.0	0.0	1.0	1.6	5.8
	15	379-SLS-00002	0.0	0.0	0.0	0.0	0.0	0.0	2.4	0.0	0.0	0.0	0.0	0.6	1.2	5.4

Table 6.7. Inundation depths at wastewater sewer pumps for each coastal storm and sea level rise scenario.

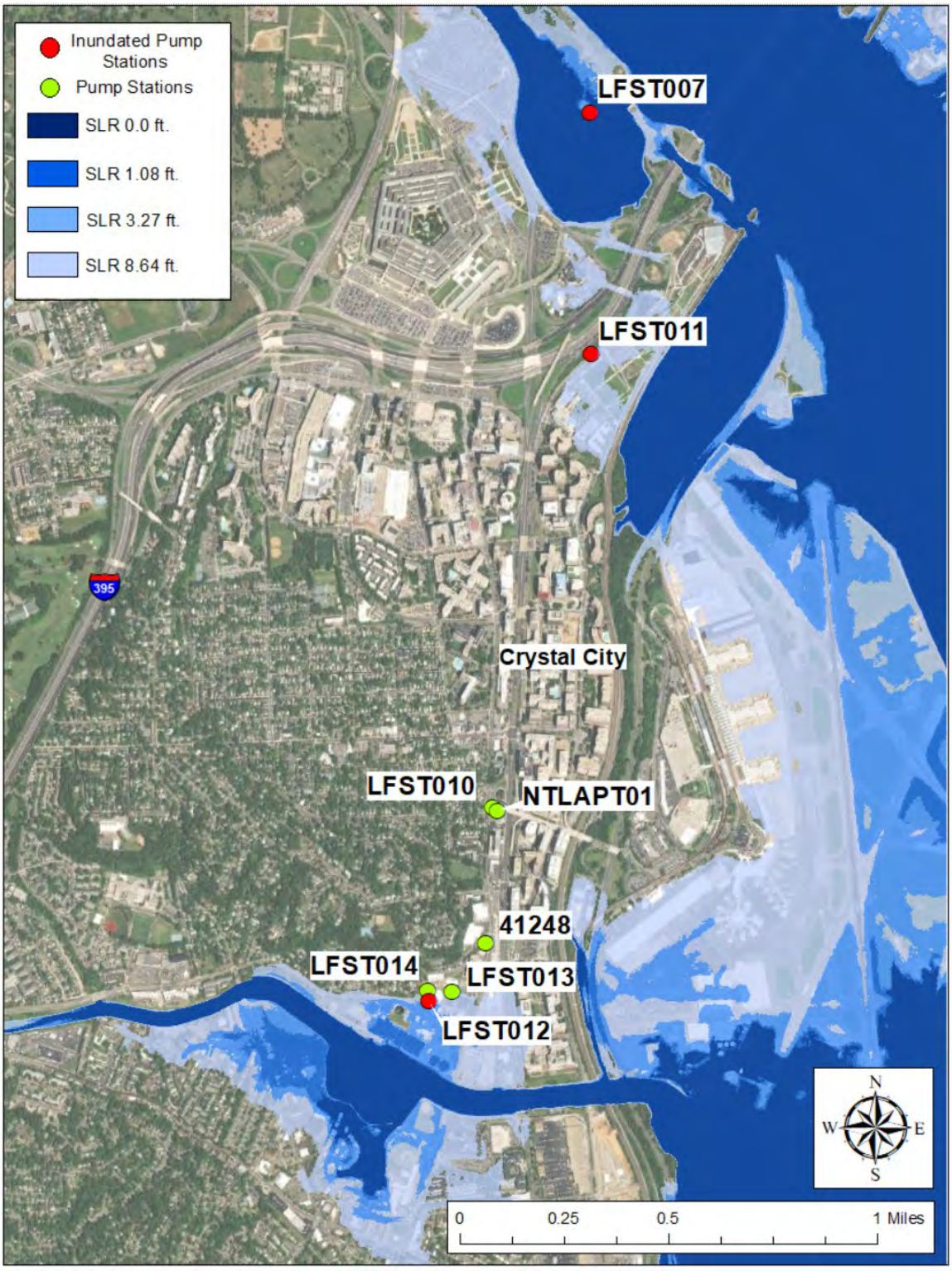

Figure 6.5: Arlington Wastewater Pump Stations, 100 year.

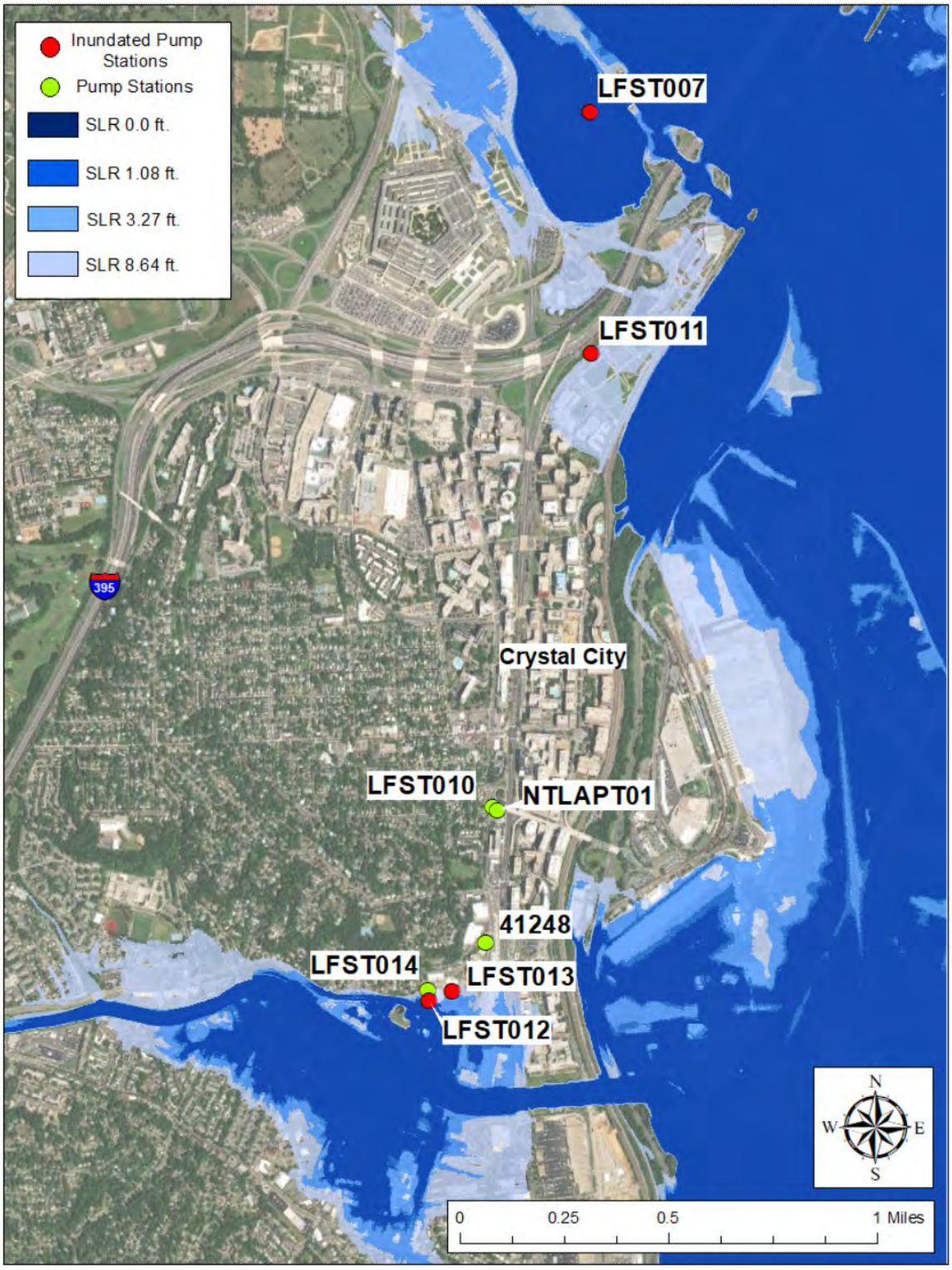

Figure 6.6: Arlington Wastewater Pump Stations, 1000-year.

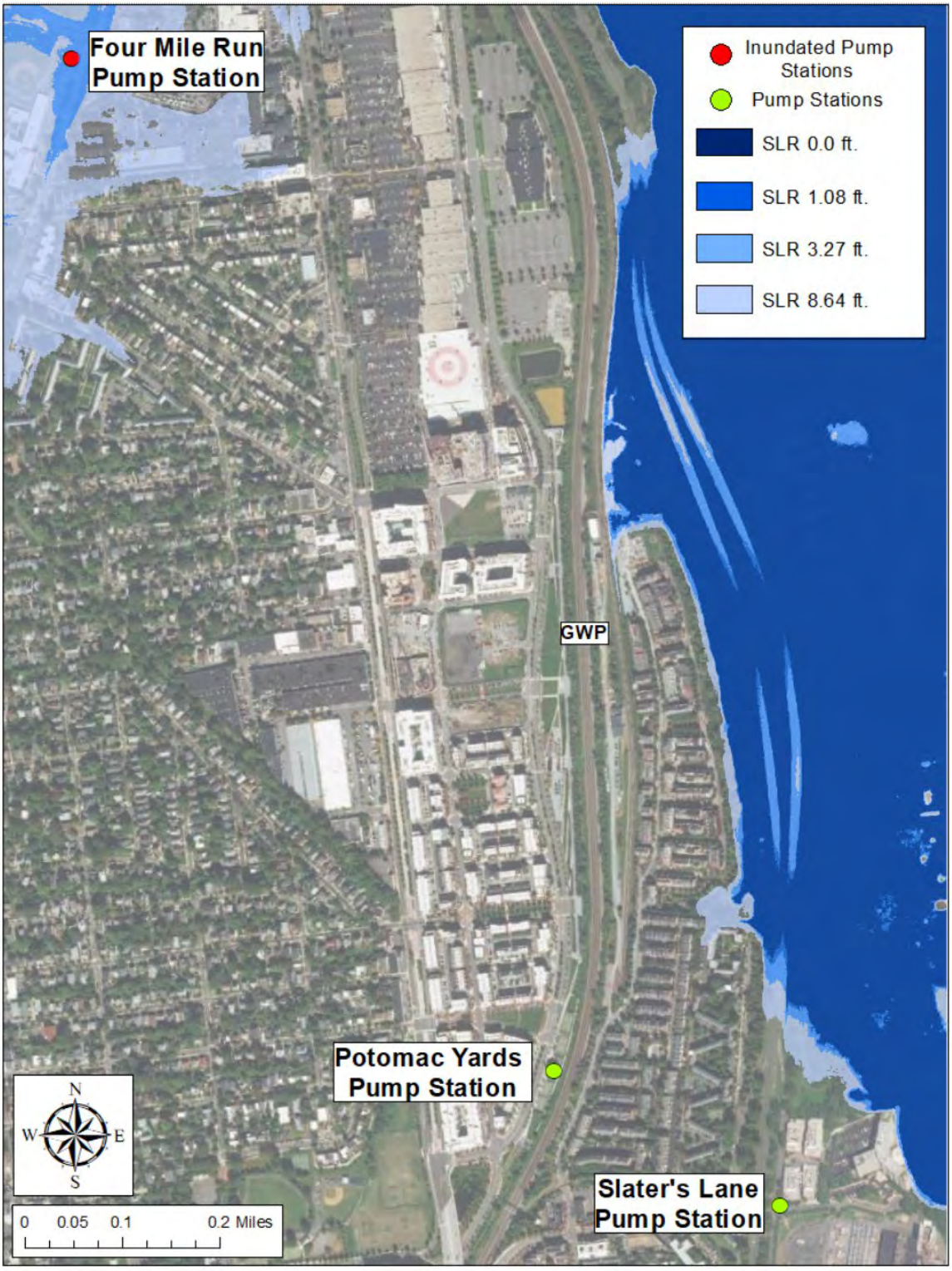

Figure 6.7: Alexandria Wastewater Pump Stations, 100-year.

Figure 6.8: Alexandria Wastewater Pump Stations, 1000 year.

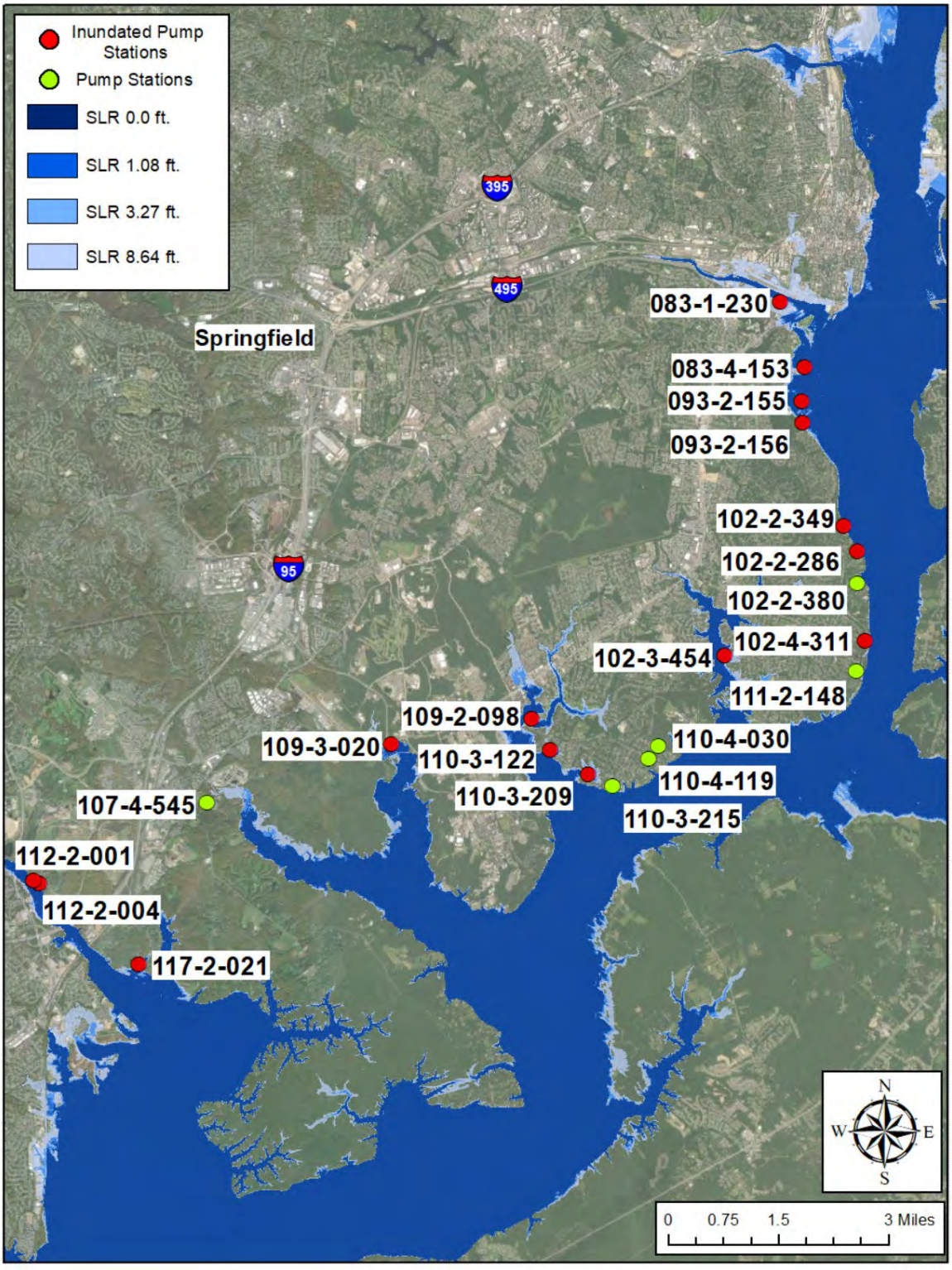

Figure 6.9: Fairfax Wastewater Pump Stations, 100 year.

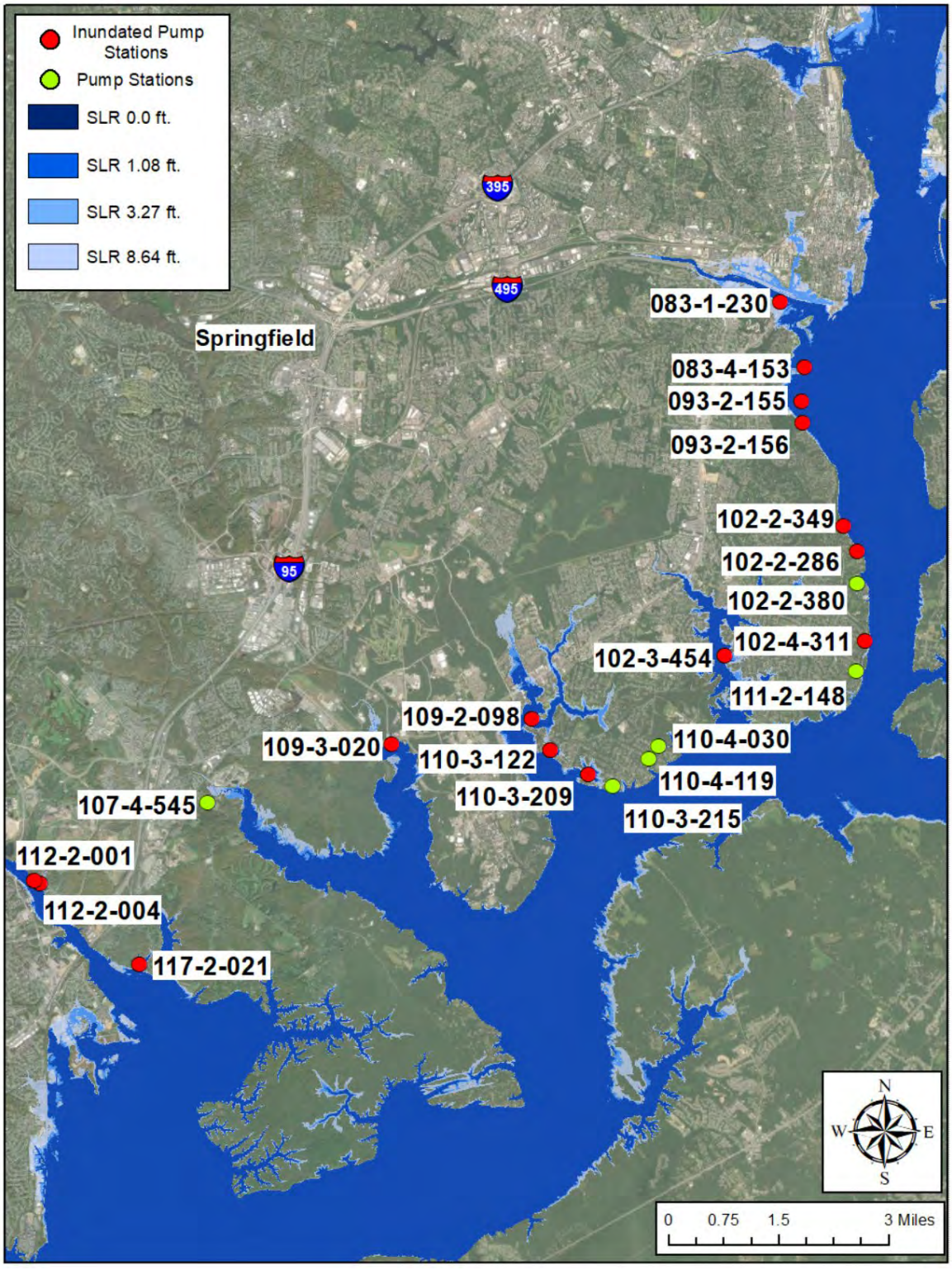

Figure 6.10: Fairfax Wastewater Pump Stations, 1000 year.

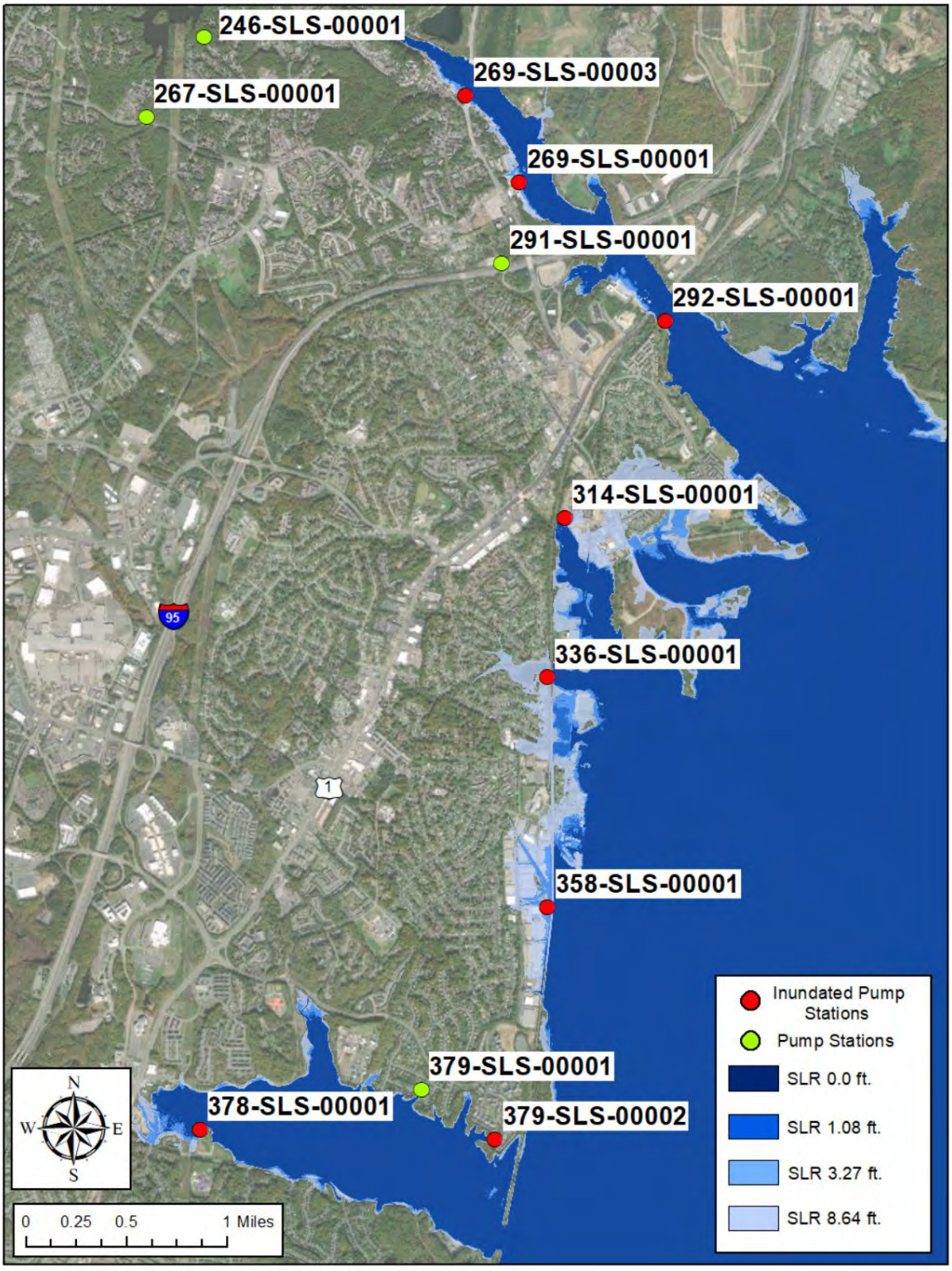

Figure 6.11: Prince William County Wastewater Pump Stations, 100 year.

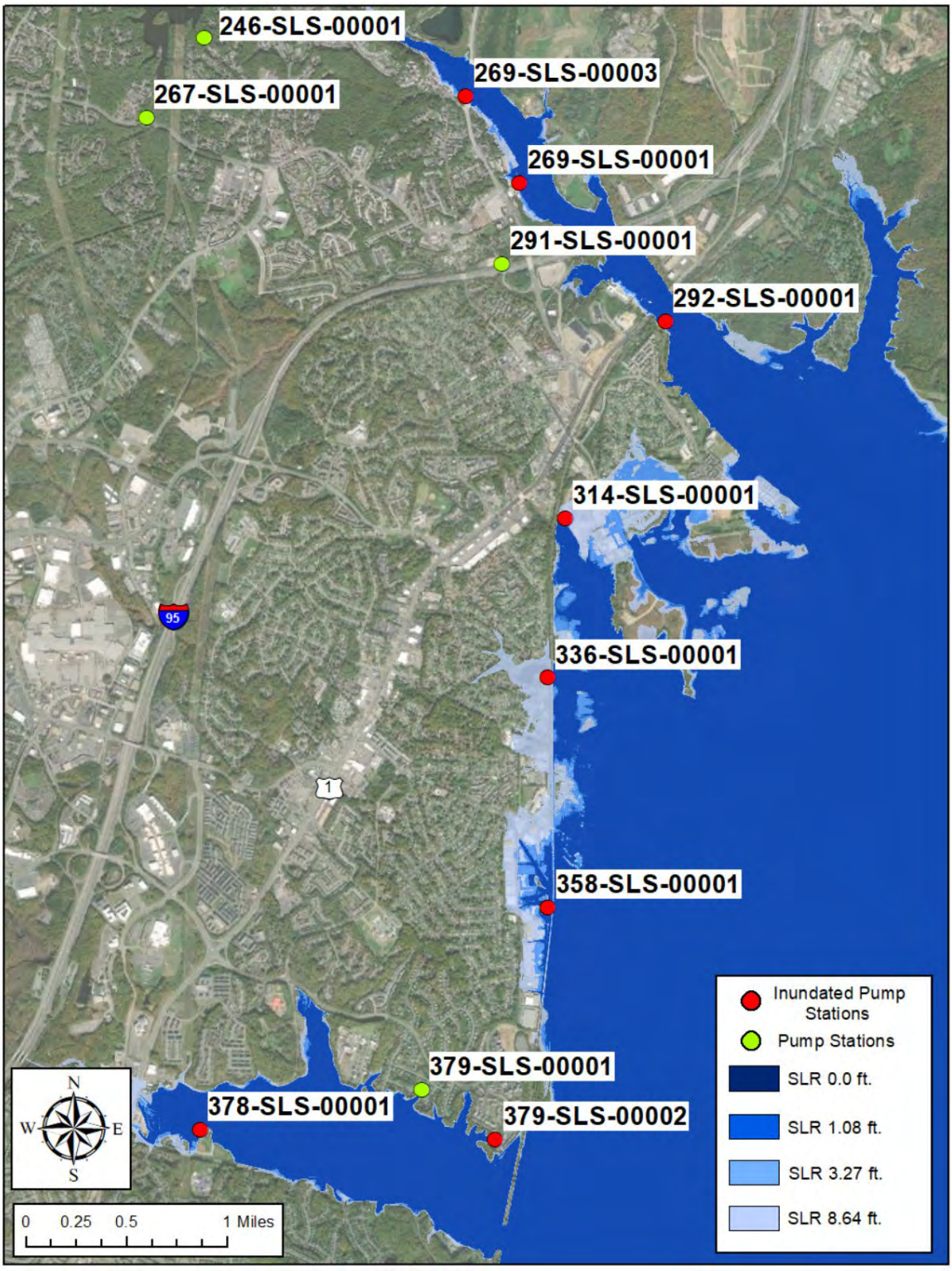

Figure 6.12: Prince William County Wastewater Pump Stations, 1000 year.

6.0 Natural Gas

Washington Gas, a wholly-owned subsidiary of AltaGas Ltd., supplies natural gas to more than one million customers in the vicinity of greater Metropolitan Washington DC, which includes the MWDC CSRM planning area. Within the MWDC CSRM planning area, there are 30,340 residential gas meters and 1,434 commercial gas meters. Washington Gas declined to provide information on its distribution system for security reasons. However, representatives of Washington Gas collaborated with the study to identify vulnerabilities and assess their potential impacts on customers within the planning area. The major threat to natural gas systems from floods is water intrusion into the natural gas distribution system. Water could enter the system through natural gas regulators, which are distributed throughout the system to maintain a stable level of pressure within the system, and through intrusion of low pressure gas distribution pipelines.

One natural gas regulator was identified as potentially being flooded under the range of coastal storm and sea level rise scenarios considered in this study. This regulator serves approximately 180 meters. Given forewarning of a flood event, Washington Gas could prevent flood water from entering the system at this location by installing risers. Beyond that, additional measures would be needed to protect the system. Water inundation depths at the location of the natural gas regulator exceed the critical depth given a 100-year coastal storm with between 3.93 and 8.64 feet of sea level rise and given a 1000-year coastal storm with at least 3.93 feet of sea level rise.

Most of the gas distribution lines in the planning area are high pressure lines and therefore not vulnerable to water intrusion. There is one low pressure gas distribution system in Old Town Alexandria that serves approximately 3000 meters. That distribution system could be vulnerable to water intrusion given as little as one foot of flood inundation. Based on information provided by Washington Gas, it was estimated that up to 4.2 % of customers served by the low pressure distribution system could be affected by a 100-year coastal storm with 8.64 feet of sea level rise. Given a 1000-year coastal storm, approximately 1% of customers could be affected with 1.75 feet of sea level rise, 2.2% of customers could be affected with 3.27 feet of sea level rise, 2.6% of customers would be affected with 3.93 feet of sea level rise, and 8.3% of customers could be affected with 8.64 feet of sea level rise. However, there is also a reasonable chance this system could continue to operate normally if sufficient backfeeds are available.